

When Cubic Cobalt Sulfide Meets Layered Molybdenum Disulfide: A Core–Shell System Toward Synergetic Electrocatalytic Water Splitting

Han Zhu, Junfeng Zhang, Ruoping Yanzhang, Mingliang Du,* Qingfa Wang,*
Guohua Gao,* Jiandong Wu, Guangming Wu, Ming Zhang, Bo Liu,
Juming Yao, and Xiangwen Zhang

Electrocatalysts have grown to play prominent roles in the design of alternative energy devices due to the need of clean and sustainable energy.^[1,2] The future energy supply strongly relies on innovative breakthroughs regarding the design of sustainable, low cost, and efficient systems for the conversion and storage of renewable energy sources. Electrocatalytic water splitting to hydrogen and oxygen is a promising and appealing solution that has attracted significant attention.^[3,4] Noble metals and their alloys, such as Pt and IrO₂, have been demonstrated as state-of-the-art catalysts for hydrogen evolution reaction (HER) and oxygen evolution reaction (OER).^[5,6] Nevertheless, the scarcity and high cost of noble metals impede their large-scale practical application and necessitate the development of alternative earth-abundant materials with high electrocatalytic performance and wide availability.^[7]

Transition metals,^[8,9] transition metal oxides,^[10] carbon materials,^[11,12] and non-metallic element doped carbon^[13–16] catalysts have attracted considerable attentions. However, most studies focus on how to improve the electrocatalytic activity for HER or OER and ignore how to develop a bifunctional electrocatalyst that promotes both high HER and OER activity. The controllable integration of HER and OER catalysts into a single nanostructure with the expected synergetic electrocatalytic for both HER and OER has recently become one of the hottest research topics in the field.^[5–7,9] Recently, we developed molybdenum

disulfide (MoS₂) with different trigonal prismatic (2H) and octahedral (1T) structures as HER catalysts under acidic conditions.^[17,18] Besides the molybdenum disulfide, molybdenum phosphide also have been regarded as the promising high active HER catalysts.^[19–21] In addition, cobalt chalcogenides, including Co₃S₄, CoS₂, Co_{1–x}S, etc., are widely used in dye-sensitized solar cells,^[22] supercapacitors,^[23] and Li ions batteries,^[24] and to date, cobalt sulfide and phosphide are regarded as the most active HER and OER catalysts.^[25–30] To our best knowledge, there are no reports on the synergetic effects of an MoS₂–Co₉S₈ system for electrocatalytic water splitting.

The first combination of Co and MoS₂ was used as a hydridesulfurization (HDS) catalyst, and researchers confirmed that the addition of Co, called the promoted phase, indeed improved the HDS activity of the Co–Mo–S catalyst.^[31–33] Recently, Ramos *et al.*^[31] offered a model based on a density functional theory (DFT) analysis to determine a reasonable description of the surface contact region between the individual MoS₂ and Co₉S₈ phases and predicted that the synergetic effect between the interface region of the two phases would lead to remarkably improved activity for HDS. Afterward, the researchers devoted to finding an effective approach to engineer the nanostructure of MoS₂ and Co₉S₈, with the aim to create a surface contact region to employ the synergetic effects. However, to date, few approaches can be found for the nanostructuring of a Co–Mo–S catalyst with a high surface contact region. Multicomponent nanomaterials with core–shell structures display tunable and unique properties, providing superior electrochemical performance compared to alloying and doping modifications due to the interaction and electronic transfer among the materials used in the structure.^[10,34,35]

Here, we provide a new strategy for the first design and synthesis of a cubic cobalt sulfide–layered molybdenum disulfide core–shell/carbon nanofibers (Co₉S₈@MoS₂/CNFs) hybrid system obtained through a simple S vapor assisted graphitization of polyacrylonitrile (PAN) nanofibers containing cobalt nitrate (Co(NO₃)₂) and ammonium tetrathiomolybdate ((NH₄)₂MoS₄). The Co₉S₈@MoS₂ core–shell nanostructure consists of a core of Co₉S₈ nanoparticle surrounded by a shell of fullerene-like MoS₂ layers. The CNFs not only serve as a substrate for the anchor of Co₉S₈@MoS₂ but are also used as hosts and reactors for the inoculation of Co₉S₈@MoS₂. The unique Co₉S₈@MoS₂/CNFs cocatalysts system not only serves as a bifunctional catalyst for OER and HER by combining the intrinsic properties of individual MoS₂ and Co₉S₈, but also

Dr. H. Zhu, Prof. M.-L. Du, Dr. M. Zhang, Prof. J.-M. Yao
College of Materials and Textiles
Key Laboratory of Advanced Textile Materials and
Manufacturing Technology of the Ministry of Education
Zhejiang Sci-Tech University
Hangzhou 310018, P. R. China
E-mail: du@zstu.edu.cn



Dr. J.-F. Zhang, R.-P. Yangzhang, Dr. Q.-F. Wang, Prof. X.-W. Zhang
Key Laboratory for Green Chemical Technology
of the Ministry of Education
School of Chemical Engineering and Technology
Tianjin University
92 Weijin Road, Tianjin 300072, P. R. China
E-mail: qfwang@tju.edu.cn

Dr. G.-H. Gao, J.-D. Wu, Prof. G.-M. Wu, Dr. B. Liu
Shanghai Key Laboratory of Special Artificial
Microstructure Materials and Technology
Tongji University
Shanghai 200092, P. R. China
E-mail: gao@tongji.edu.cn

DOI: 10.1002/adma.201501969

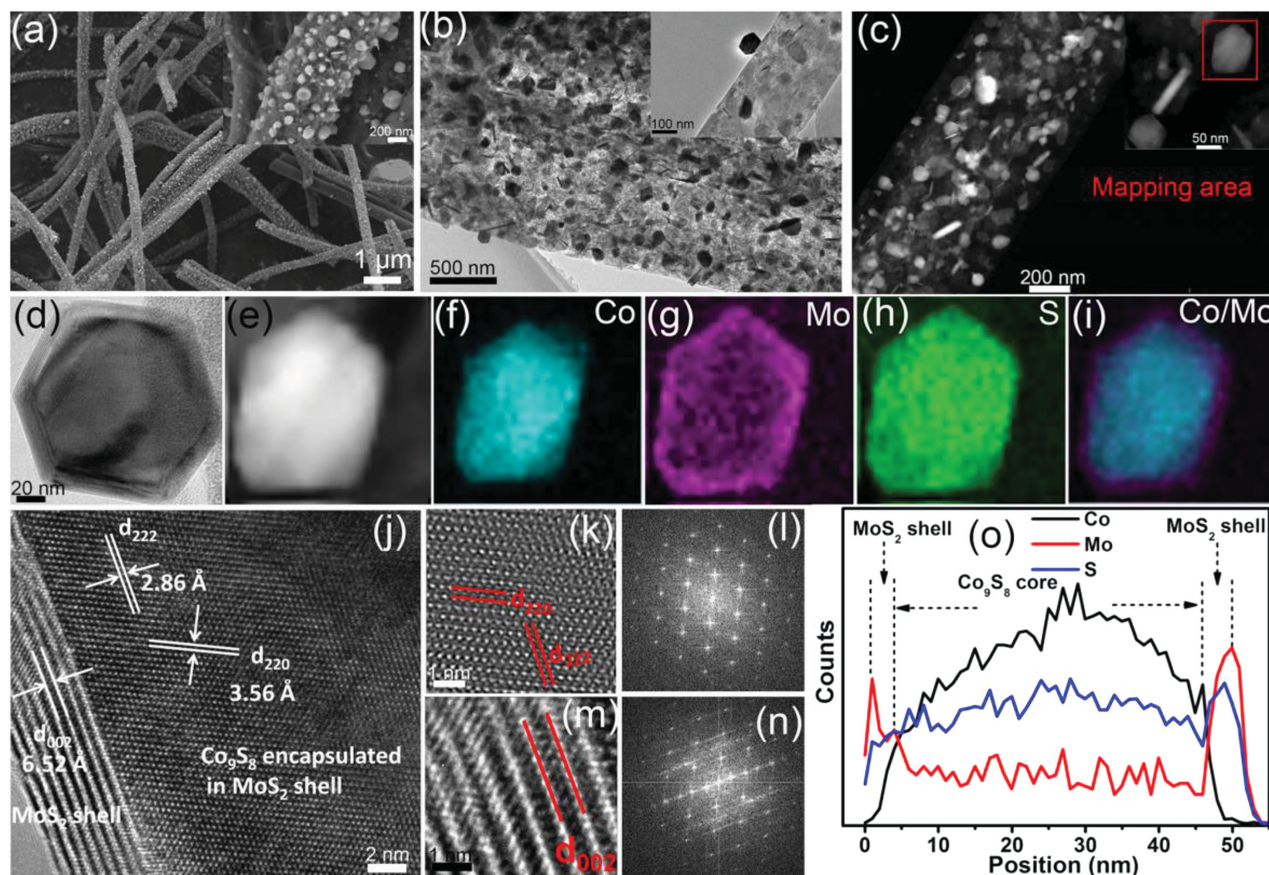


Figure 1. a) FE-SEM, b) TEM, and c) STEM images of the $\text{Co}_9\text{S}_8@\text{MoS}_2/\text{CNFs}$ hybrid nanostructures. Insets in (a)–(c) are the corresponding high-magnification images. d) TEM, e) STEM, and f–i) STEM-EDS element mapping images of the $\text{Co}_9\text{S}_8@\text{MoS}_2$ nanocrystal; HRTEM images of the j) $\text{Co}_9\text{S}_8@\text{MoS}_2$, k) Co_9S_8 core, m) MoS_2 shell and the corresponding FFT images of the l) Co_9S_8 core and the n) MoS_2 shell; line-scan EDX spectra of the $\text{Co}_9\text{S}_8@\text{MoS}_2$ nanocrystal. The mass ratio of the Co to Mo precursor is 1:1.

exhibits impressive improved HER and OER activities compared to pure MoS_2/CNFs and $\text{Co}_9\text{S}_8/\text{CNFs}$ nanostructures. The $\text{Co}_9\text{S}_8@\text{MoS}_2/\text{CNFs}$ hybrid can be directly used as an electrode for HER and OER and displays excellent stability. The enhanced electrocatalytic activities are attributed to the synergistic effects between Co and Mo at the proposed localized interface region between the MoS_2 and Co_9S_8 phases. Density functional theory calculations to model the nanointerfaces revealed that the improved catalytic activities stem from a large reduction of the kinetic energy barrier of H_2 molecule desorption on the nanointerfaces in the core-shell structure.

Figure 1a,b shows the field-emission scanning electron microscopy (FE-SEM) and transmission electron microscopy (TEM) images of the $\text{Co}_9\text{S}_8@\text{MoS}_2$ core-shell CNFs hybrid. Compared to the Co–Mo–PAN precursor nanofibers (Figure S1, Supporting Information), after the S vapor assisted graphitization, large amounts of nanocrystals sprang up and uniformly anchored on the CNFs. The CNFs as the substrate are important hosts and reactors for the formation of unique $\text{Co}_9\text{S}_8@\text{MoS}_2$. The sizes of the $\text{Co}_9\text{S}_8@\text{MoS}_2$ nanocrystals range from 30 to 120 nm, and most possess octahedral shapes, which also can be verified via the high-angle annular dark field scanning TEM (HAADF-STEM) images (Figure 1c). Figure 1d displays

a typical octahedral morphology of a $\text{Co}_9\text{S}_8@\text{MoS}_2$ core-shell nanocrystal grown on the CNFs. From Figure 1d–i, uniform distributions of Co, Mo, and S form a hexagonal morphology, which are in accordance with the mapping area of $\text{Co}_9\text{S}_8@\text{MoS}_2$. The Co is mainly located in the center of the hexagon, whereas the Mo is located in the entire area of the hexagon with strong signals at the edges. When the signal areas of Co and Mo are mixed, the Co is completely encapsulated by the Mo (Figure 1i). In addition, the S signal area is the same as that of Mo and exhibits uniform signals, revealing a core-shell structure with Mo and S in the shell and Co and S in the core (Figure 1e–i).

The high-resolution TEM (HRTEM) image (Figure 1j) clearly exhibits two distinguished phases side-by-side: cubic Co_9S_8 and layered MoS_2 . The sizes of the Co_9S_8 cores range from 20 to 100 nm, whereas the thicknesses of the MoS_2 shells range from 4 to 8 nm, consisting of 5–12 layers. The HRTEM images and the associated fast Fourier transform (FFT) of the Co_9S_8 and MoS_2 nanocrystals are shown in Figure 1k–n. The interfringe distances of 3.56 and 2.86 Å correspond to the (220) and (222) planes of the cubic Co_9S_8 phase.^[22] The layer-to-layer spacing between the stripes of the MoS_2 shell is 6.52 Å, which is slightly larger than the spacing of bulk MoS_2 (6.1 Å).^[17,36] The line-scan

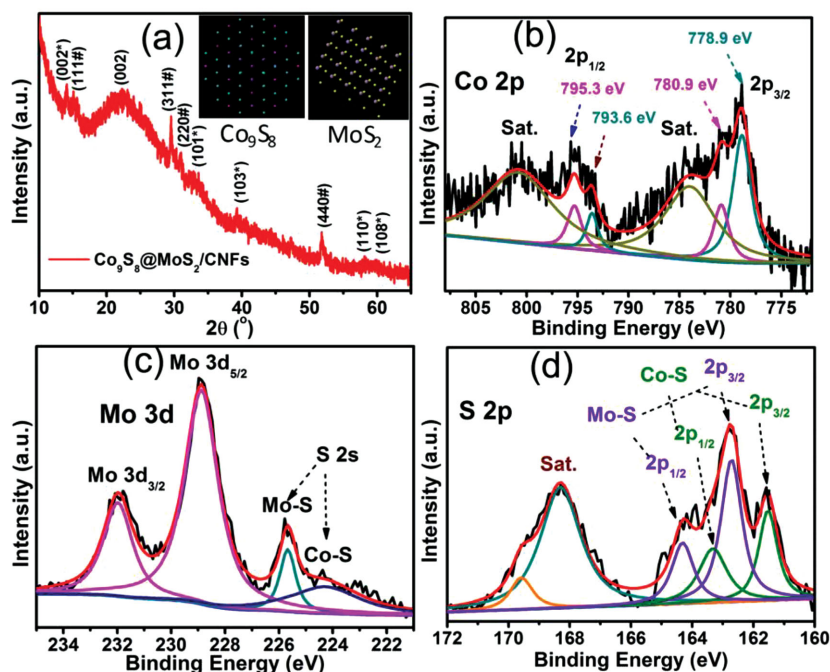


Figure 2. a) XRD patterns of the $\text{Co}_9\text{S}_8@\text{MoS}_2/\text{CNFs}$ membrane. Insets are the unit cells of Co_9S_8 and MoS_2 nanocrystals. The peaks of Co_9S_8 are marked by #, and the peaks of MoS_2 are marked by *. b) Co 2p, c) Mo 3d, and d) S 2p XPS spectra for the $\text{Co}_9\text{S}_8@\text{MoS}_2/\text{CNFs}$ membrane.

energy-dispersive X-ray spectroscopy (EDX) spectra of the $\text{Co}_9\text{S}_8@\text{MoS}_2$ nanocrystal also strongly demonstrates the core-shell structures with a 1:1.95:4.01 Mo:Co:S molar ratio, and the mass fraction of the $\text{Co}_9\text{S}_8@\text{MoS}_2$ nanocrystals is $\approx 10\%$ (Figure S2, Supporting Information). As shown in Figure 1o, the Co only exists in the area ranging from 5 to 45 nm, whereas the Mo and S both exist in the entire area. In particular, the Mo and S possess strong signals in the MoS_2 shell region, and the thickness of the MoS_2 shell is ≈ 5 nm. The fullerene-like MoS_2 shells were directly grown around the Co_9S_8 cores and, therefore, more direct contact surface area between the two sulfide phases was generated.

The physical and chemical structures and surface chemical states of the $\text{Co}_9\text{S}_8@\text{MoS}_2/\text{CNFs}$ were further investigated via the X-ray diffraction (XRD) and X-ray photoelectron (XPS). As a control, the XRD patterns of the CNFs and the Co-Mo-PAN precursor nanofibers are shown in Figure S3 (Supporting Information). The $\text{Co}_9\text{S}_8@\text{MoS}_2/\text{CNFs}$ hybrid (Figure 2a) displays several peaks at 14.1° , 33.1° , 39.3° , 58.2° , and 59.9° corresponding to the (002^*) , (101^*) , (103^*) , (110^*) , and (008^*) planes, respectively, which are consistent with hexagonally structured MoS_2 (2H- MoS_2 , JCPDS 37-1492) (inset in Figure 2a). The peaks of the $(111^\#)$, $(311^\#)$, $(222^\#)$, and $(440^\#)$ planes located at 15.2° , 29.6° , 31.4° , and 52.0° , respectively, are indexed perfectly with the Co_9S_8 fcc phase (JCPDS No. 86-2273) with the cell parameter $a = 9.92 \text{ \AA}$ (inset in Figure 2a).^[22] The broadband at $\approx 24^\circ$ corresponds to the (002) plane of the CNFs indicative of the crystalline graphitic carbon.

The C 1s and N 1s XPS spectra are shown in Figure S4 and S5 (Supporting Information), respectively. The core level of the

Co 2p spectrum was deconvoluted into two spin-orbit doublets and two shakeup satellites (identified as "Sat.") (Figure 2b). The first doublet at 778.9 and 793.6 eV and the second at 780.9 and 795.3 eV are attributed to $\text{Co } 2p_{3/2}$ and $\text{Co } 2p_{1/2}$, respectively.^[22] The doublets were assigned to Co^{3+} and Co^{2+} , which agrees with previous reports and manifests the formation of Co_9S_8 nanocrystals. Compared to the XPS spectra of pure Co_9S_8 nanocrystals^[22] (778.5 and 793.9 eV), the binding energies of Co 2p shifted to 778.9 and 793.6 eV, suggesting a strong interaction between the Co_9S_8 and the surrounding MoS_2 shell.

For the Mo 3d, two significant peaks located at 228.9 and 232.0 eV are ascribed to the $\text{Mo } 3d_{5/2}$ and $\text{Mo } 3d_{3/2}$, indicative of a +4 oxidation state (Figure 2c). The Mo 3d peaks also exhibit shifts compared to the pure MoS_2 nanoplates,^[17,18] providing further evidence of the strong interaction between the Co_9S_8 and MoS_2 . The nearby S 2s peaks were deconvoluted into two peaks at 225.7 and 224.2 eV, corresponding to the two chemical states of S species bonding with Mo and Co ions. In the S 2p spectra (Figure 2d), the binding energy centered at 168.3 eV can be fitted by one main peak and one shakeup

satellite peak. The S 2p peaks at 164.3 and 162.7 eV are attributed to the $\text{S } 2p_{1/2}$ and $\text{S } 2p_{3/2}$ orbitals of divalent sulfide ions (S_2^{2-}), in accordance with the formation of MoS_2 . The other two S 2p peaks at 161.5 and 163.3 eV are assigned to $\text{S } 2p_{3/2}$ and $\text{S } 2p_{1/2}$ of Co-S bondings, respectively, which is in good agreement with a previous report on Co_9S_8 crystals.^[22] Therefore, the XPS spectra further manifest the successful synthesis of $\text{Co}_9\text{S}_8@\text{MoS}_2$ core-shell nanostructures and suggest a strong interaction between the two phases.

Morphology and structure evolutions generated when the cubic cobalt sulfide meets layered molybdenum disulfide. When the cubic cobalt sulfide meets layered molybdenum sulfide, the unique $\text{Co}_9\text{S}_8@\text{MoS}_2$ core-shell nanostructures are formed. To investigate the differences and relationships between the structure and electrocatalytic activity of the MoS_2 and Co_9S_8 phases, we further synthesized individual Co_9S_8 and MoS_2 nanocrystals grown on CNFs using the same S vapor assisted graphitization. The FE-SEM images of the three nanostructures are shown in Figure S6 (Supporting Information). The individual MoS_2 phase on the CNFs indicates a 2D plate morphology, and most of the nanoplates are perpendicular to the nanofiber axis (Figure 3a). The exposed edges of the MoS_2 nanoplates consist of 4–10 layers (Figure S7, Supporting Information).

The STEM-EDS mapping images (Figure 3d) clearly show the presence of Mo and S elements. The edges of the nanoplates and a perfect match between the Mo and S elements are easily visible. As shown in Figure 3b, the Co_9S_8 nanocrystals with facet shapes are densely grown on the CNFs. The particle sizes of the Co_9S_8 range from 20 to 100 nm. The chemical

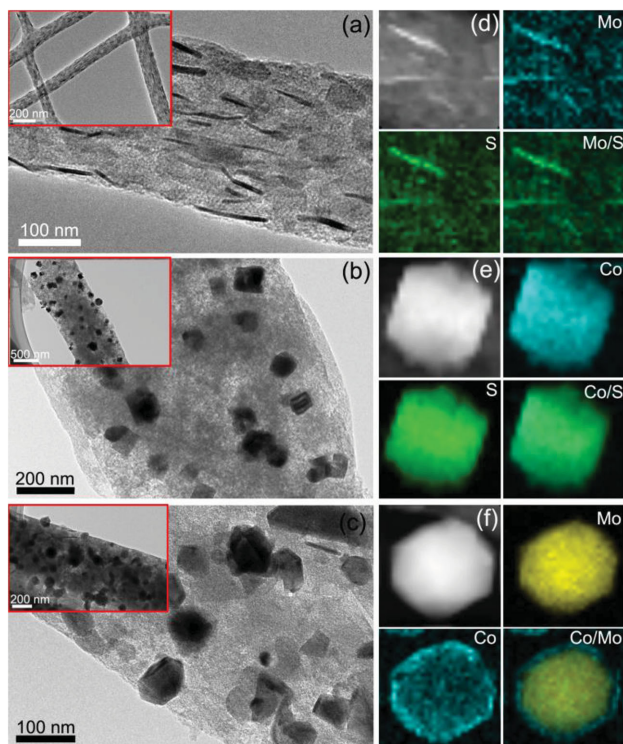


Figure 3. TEM and STEM-EDS mapping images of the a,d) MoS_2/CNFs , b,e) $\text{Co}_9\text{S}_8/\text{CNFs}$, and c,f) $\text{Co}_9\text{S}_8@/\text{MoS}_2/\text{CNFs}$ hybrid. Insets are the corresponding low-magnification TEM images.

composition of the Co_9S_8 nanocrystals is verified in Figure 3e. The Co and S element both exhibit hexagonal shapes, and the mapping area of the Co and S match well, demonstrating the formation of Co_9S_8 nanocrystals. When the Co and Mo precursors were mixed into PAN nanofibers and after S-assisted graphitization, the MoS_2 and Co_9S_8 nanocrystals grew individually, forming the unique core-shell structures (Figure 3c). Similarly, the Co signal area is encapsulated in the Mo area, presenting the core-shell structure. The XRD patterns and the Raman spectra of the three different nanostructures are discussed in Figure S8 and S9 (Supporting Information). These results illustrate the changes in physical properties caused by the morphology and structure evolutions and suggest the existence of the interactions between the Co_9S_8 and MoS_2 phases due to the direct contact of the two phases caused by the unique core-shell structures.

HER and OER make up the two half reactions of electrocatalytic water splitting, which are the key electrocatalytic reactions to obtain clean and sustainable energy.^[1,8,9,37,38] For MoS_2 -based HER catalysts, the structure of earth-abundant MoS_2 with high crystallinity is hexagonal 2H- MoS_2 , which is a semiconductor whose poor bulk conduction and anisotropic electrical transport limit its overall catalytic efficiency.^[39] Finding an effective approach to improve the electrocatalytic activity of the stable and earth-abundant 2H- MoS_2 has drawn attention for use in wide applications. In our work, by combining two components, the unique $\text{Co}_9\text{S}_8@/\text{MoS}_2$ core-shell nanostructures are expected to provide promising enhanced 2H- MoS_2 HER activity.

The electrocatalytic performances of CNFs, MoS_2/CNFs , $\text{Co}_9\text{S}_8/\text{CNFs}$, and $\text{Co}_9\text{S}_8@/\text{MoS}_2/\text{CNFs}$ for HER in Ar-saturated 0.5 M H_2SO_4 and for OER in Ar-saturated 1 M KOH are shown in Figure 4. All the results shown by solid lines were corrected for iR losses. The cyclic voltammetry (CV) of these nanostructures obtained in 0.5 M H_2SO_4 and 1 M KOH are shown in Figure S10 (Supporting Information). As shown in Figure 4A, the CNFs guarantee a negligible background activity for H_2 evolution. The cathodic current increases as the potential become more negative, corresponding to catalytic H_2 evolution. The $\text{Co}_9\text{S}_8@/\text{MoS}_2/\text{CNFs}$ exhibit a very small onset potential of 64 mV and an overpotential (η_{10}) of 190 mV for significant H_2 evolution ($J = 10 \text{ mA cm}^{-2}$). In contrast, the individual MoS_2 nanoplates and Co_9S_8 nanocrystals grown on the CNFs both exhibit inferior HER activity with larger onset potentials of 224 and 282 mV, respectively, and lower catalytic currents. At high current densities, the $\text{Co}_9\text{S}_8@/\text{MoS}_2/\text{CNFs}$ hybrid ($J = 10 \text{ mA cm}^{-2}$, 190 mV) also exhibits more efficient activity than MoS_2/CNFs ($J = 10 \text{ mA cm}^{-2}$, 342 mV), whereas the $\text{Co}_9\text{S}_8/\text{CNFs}$ cannot reach this value at -0.4 V versus RHE (Table 1). The HER kinetics of the above catalysts were identified using the corresponding Tafel plots (Figure 4C). The Tafel slope for the $\text{Co}_9\text{S}_8@/\text{MoS}_2/\text{CNFs}$ obtained at $J = 10 \text{ mA cm}^{-2}$ was 110 mV dec^{-1} , whereas the MoS_2/CNFs and $\text{Co}_9\text{S}_8/\text{CNFs}$ corresponded to 110 and 203 mV dec^{-1} , respectively. Benefiting from the unique core-shell structures, the $\text{Co}_9\text{S}_8@/\text{MoS}_2/\text{CNFs}$ catalyst exhibits significant improved HER activity compared to the MoS_2/CNFs and $\text{Co}_9\text{S}_8/\text{CNFs}$.

As one of the important electrocatalytic reactions, OER is much harsher than HER because, at the anode, it suffers a complex four-electron oxidation process with slow kinetics, which imposes considerable electrochemical overpotential requirements that lead to significant losses in the overall efficiency of water splitting.^[1] However, in this work, the unique $\text{Co}_9\text{S}_8@/\text{MoS}_2/\text{CNFs}$ also exhibit exceptional OER activity, except for HER. The OER performances were investigated and are shown in Figure 4B,D.

In Figure 4B, the polarization curve of $\text{Co}_9\text{S}_8@/\text{MoS}_2/\text{CNFs}$ exhibits a much earlier OER onset potential ($\approx 1.580 \text{ V}$ vs RHE) and a greater catalytic current compared to individual $\text{Co}_9\text{S}_8/\text{CNFs}$ ($\approx 1.624 \text{ V}$) and MoS_2/CNFs ($\approx 1.662 \text{ V}$). In addition, no obvious voltammetric responses were observed for the CNFs. It is very important to compare the overpotential requirements for achieving a current density of 10 mA cm^{-2} , which is a metric relevant to solar fuel synthesis. Remarkably, the $\text{Co}_9\text{S}_8@/\text{MoS}_2/\text{CNFs}$ could induce such a current density at an η as small as $\approx 0.430 \text{ V}$, which is much smaller than those of $\text{Co}_9\text{S}_8/\text{CNFs}$ ($\approx 0.512 \text{ V}$) (Table 1). Meanwhile, the MoS_2/CNFs cannot reach a current density of 10 mA cm^{-2} , suggesting its poor OER activity. For HER, the $\text{Co}_9\text{S}_8@/\text{MoS}_2/\text{CNFs}$ hybrid exhibits remarkable activity at an onset potential at 64 mV and an η_{10} at 190 mV, which represents almost the best semiconductor MoS_2 -based (2H- MoS_2) electrocatalyst^[40–45] and are very close to the recently reported metallic MoS_2 (1T- MoS_2),^[44,46,47] molybdenum phosphide,^[19–21] and cobalt chalcogenides.^[25–29,48] In addition, the OER activity at an onset potential of 1.580 V versus RHE, the η at 350 mV and the η_{10} at 430 mV also exhibit higher activities than those reported for Co-based electrocatalysts, including $\text{Co}_3\text{O}_4/\text{SWCNTs}$ (1.76 V),^[49] $\text{Mn}_3\text{O}_4/\text{CoSe}_2$

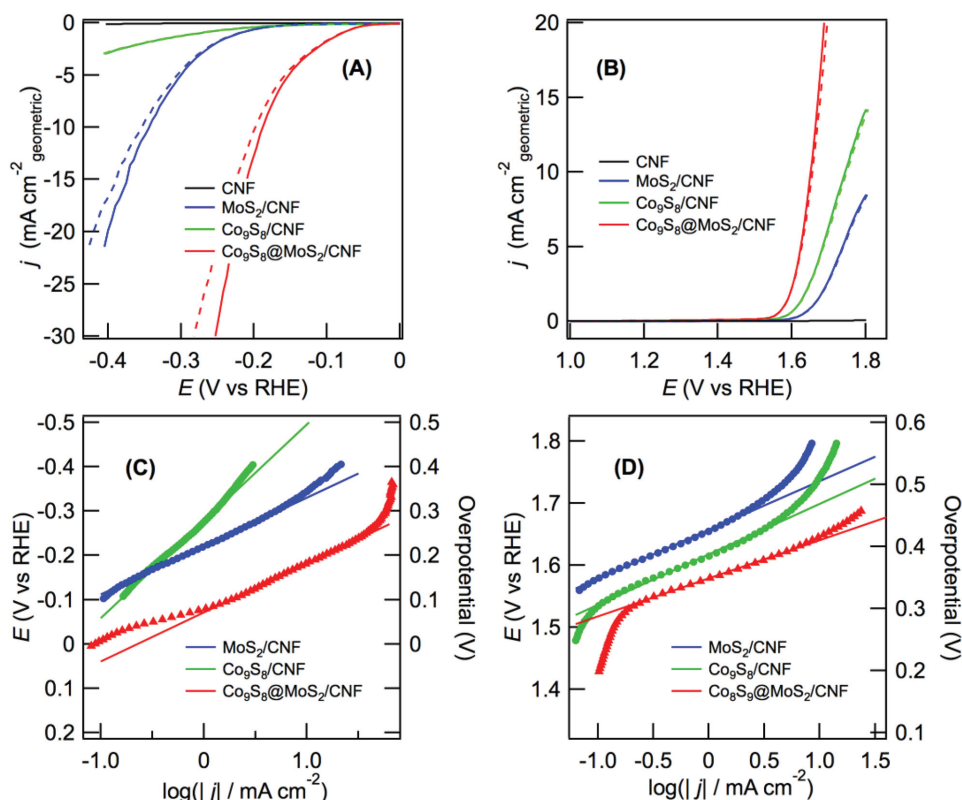


Figure 4. Polarization curves of $\text{Co}_9\text{S}_8@\text{MoS}_2/\text{CNFs}$, MoS_2/CNFs , $\text{Co}_9\text{S}_8/\text{CNFs}$, and CNFs at 2 mV s^{-1} in A) $0.5 \text{ M H}_2\text{SO}_4$ and B) 1 M KOH . All the results shown by solid lines were corrected for iR losses. The dashed lines exhibit the original results. The corresponding Tafel plots of (A) and (B) after iR corrected are shown in (C) and (D), respectively. The catalyst loading is $\approx 212 \mu\text{g cm}^{-2}$, and all of the data reflect the catalytic activity after potential sweeps for 1000 cycles between 0 and 1.2 V versus SCE.

(1.68 V),^[50] and $\text{NiCo}_2\text{S}_4/\text{graphene}$ (1.70 V).^[51] Tafel analysis yielded Tafel plots of 61, 80, and 78 mV dec^{-1} for $\text{Co}_9\text{S}_8@\text{MoS}_2/\text{CNFs}$, MoS_2/CNFs , and $\text{Co}_9\text{S}_8/\text{CNFs}$, respectively, further indicating the outstanding intrinsic OER kinetics of the $\text{Co}_9\text{S}_8@\text{MoS}_2/\text{CNFs}$. The Nyquist plots (Figure S11, Supporting Information) of $\text{Co}_9\text{S}_8@\text{MoS}_2/\text{CNFs}$, MoS_2/CNFs , and $\text{Co}_9\text{S}_8/\text{CNFs}$ obtained in $0.5 \text{ M H}_2\text{SO}_4$ and 1 M KOH electrolyte both reveal dramatically decreased charge transfer resistance (R_{CT}) for the $\text{Co}_9\text{S}_8@\text{MoS}_2/\text{CNFs}$, exhibiting more facile electrode kinetics for enhancing the catalytic activity.

Stability is another important criterion for catalysts regarding their wide practical applications. The CVs of

the $\text{Co}_9\text{S}_8@\text{MoS}_2/\text{CNFs}$ in $0.5 \text{ M H}_2\text{SO}_4$ and 1 M KOH , the MoS_2/CNFs in $0.5 \text{ M H}_2\text{SO}_4$ and the $\text{Co}_9\text{S}_8/\text{CNFs}$ in 1 M KOH were obtained from 1 to 1000 cycles (Figure S12, Supporting Information). The $\text{Co}_9\text{S}_8@\text{MoS}_2/\text{CNFs}$ demonstrate small changes in current density under acidic and alkaline conditions, suggesting superior durability. In addition, the morphology of the $\text{Co}_9\text{S}_8@\text{MoS}_2/\text{CNFs}$ over 1000 cycles did not reveal obvious changes (Figure S13, Supporting Information).

For practical applications in electrocatalytic water splitting, we fabricated the $\text{Co}_9\text{S}_8@\text{MoS}_2/\text{CNFs}$ membrane for direct use as the working electrode. The electrolysis process was

Table 1. Comparison of HER and OER activity data among various catalysts.

Catalyst	Reaction	E versus RHE [V]		η [V]		Tafel slope [mV dec^{-1}]
		Onset	10 mA cm^{-2}	Onset	10 mA cm^{-2}	
$\text{Co}_9\text{S}_8@\text{MoS}_2/\text{CNFs}$	HER	−0.064	−0.190	0.064	0.190	110
	OER	1.580	1.66	0.350	0.430	61
MoS_2/CNFs	HER	−0.224	−0.342	0.224	0.342	110
	OER	1.662	—	0.432	—	80
$\text{Co}_9\text{S}_8/\text{CNFs}$	HER	−0.282	—	0.282	—	203
	OER	1.624	1.742	0.394	0.512	78

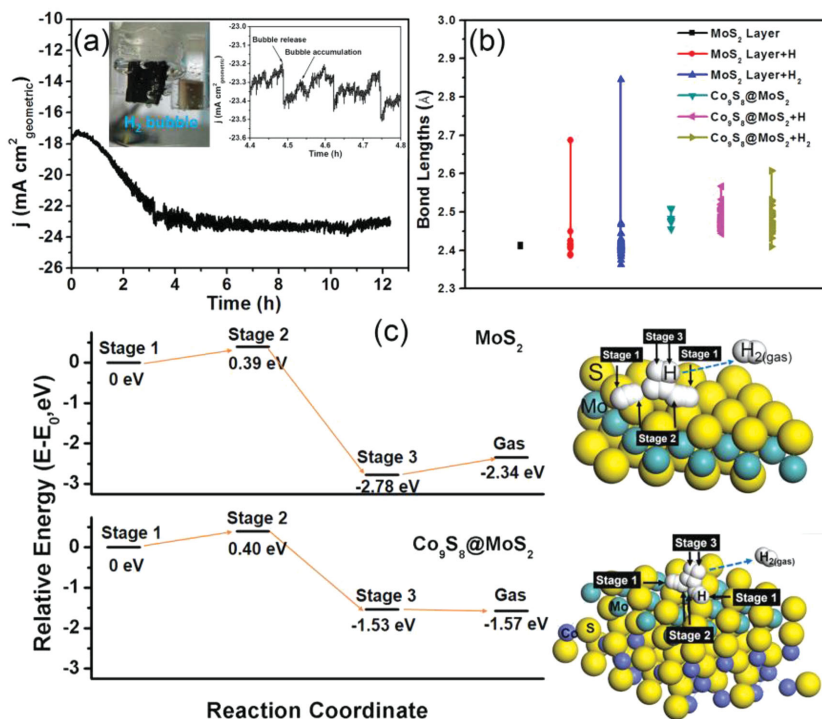


Figure 5. a) Chronoamperometric responses (j - t) recorded on the Co_9S_8 @ MoS_2 /CNF membrane electrode at a constant applied potential of -0.190 V versus RHE. Inset of photograph shows the generation of H_2 bubbles on the Co_9S_8 @ MoS_2 /CNF membrane electrode. Another inset is the enlargement of the stability test. All the measurements were performed in an Ar-saturated 0.5 M H_2SO_4 electrolyte. b) The Mo-S bond lengths in MoS_2 and Co_9S_8 @ MoS_2 during H (0, 1, 2) adsorption. c) The kinetic energy barrier profiles of HER on the MoS_2 (top) and Co_9S_8 @ MoS_2 (down) catalysts. The right side shows the diffusion paths of H_2 on the MoS_2 and Co_9S_8 @ MoS_2 surfaces.

performed at a constant potential of -0.190 V (as significant H_2 evolution ($J = 10$ mA cm^{-2})) versus RHE in 0.5 M H_2SO_4 for 12 h. As shown in **Figure 5a**, at the initiation of the process, the current density of the Co_9S_8 @ MoS_2 /CNFs electrode increased gradually, and reached the maximum current density of 24 mA cm^{-2} after 3 h operation. Then the Co_9S_8 @ MoS_2 /CNFs exhibit well stability under continuous operation for the following 9 h (**Figure 5a**). The insets in **Figure 5a** clearly indicate the alternate processes of bubble accumulation and the bubble release. The enhanced HER activity is due to the nanointerfaces between the MoS_2 and Co_9S_8 . With increased electrolysis time, more electrolyte can access the Co_9S_8 - MoS_2 nanointerfaces, yielding the increased HER activity. The electrolysis process for O_2 evolution was also performed at a constant potential of -1.600 V versus RHE in 1 M KOH. For the continuous operation for 10 h, the current density exhibits small degradation (**Figure S14**, Supporting Information). It is noted that the individual Co_9S_8 nanocrystal may dissolve in the acid condition. In the present work, the Co_9S_8 were encapsulated and protected by layered MoS_2 shells, which can improve the stability of Co_9S_8 in acid condition. In addition, the CNFs substrate not only assures charge transfer between the electrode and the Co_9S_8 @ MoS_2 but also serves as a host for protection against electrolyte erosion. Recently

published results demonstrate that the Co_9S_8 encapsulated inside the carbon shells exhibit a remarkable chemical stability.^[52] The continuous operations for hydrogen in acid and oxygen in alkaline demonstrate the good stability of the membrane electrode.

It is known that small differences in structures lead to significant changes in the physical and chemical properties.^[40,41] MoS_2 and Co_9S_8 are effective HER and OER catalysts, respectively. When Co_9S_8 meets MoS_2 , the unique core-shell structure not only combines the functions of MoS_2 and Co_9S_8 , serving as an electrocatalyst for both OER and HER, but the new structure also exhibits synergistic effects, leading to substantially improved HER and OER activities. Due to the contact regions between the Co_9S_8 and the MoS_2 shell, we propose that Co_9S_8 - MoS_2 nanointerfaces may provide the synergistically active sites for HER and OER catalysis. The nanointerfaces lead to the creation of open latent vacancy sites on Mo atoms interacting with Co and the formation of direct Co-Mo bonds.^[31,32] These advantages can generate strong electron transfer between Co and Mo through the intermediate sulfur atoms bonded to both metals. These changes in coordination and electronic properties are expected to favor a synergetic effect between Co and Mo at the proposed localized interface region between the MoS_2 and Co_9S_8 phases, leading to the promising promoted electrocatalytic activity.

To understand the synergistic effects originating from the nanointerfaces on the catalytic activity of Co_9S_8 @ MoS_2 , we investigated the hydrogen evolution pathway on MoS_2 and Co_9S_8 @ MoS_2 surfaces by first-principles calculations. The hydrogen evolution in acidic solutions can be divided into hydrogen atom adsorbed on the catalyst surface, hydrogen molecule formation, and hydrogen molecule desorption on the catalyst surface. In the first step, we studied hydrogen adsorption on the MoS_2 and Co_9S_8 @ MoS_2 surfaces. The optimized structures of the MoS_2 , Co_9S_8 @ MoS_2 , H- MoS_2 , and H- Co_9S_8 @ MoS_2 are shown in **Figure S13** (Supporting Information). The obtained lattice parameters of the MoS_2 , Co_9S_8 , and Co_9S_8 @ MoS_2 were compared with previous experimental data, as shown in **Table S1** (Supporting Information). For bulk MoS_2 and Co_9S_8 , the lattice parameters agree well with experimental data. Interestingly, for Co_9S_8 @ MoS_2 , the MoS_2 exhibits good matching on the Co_9S_8 surfaces. As shown in **Figure S15f** (Supporting Information), the interface between the MoS_2 and the Co_9S_8 is connected by the S atoms in the MoS_2 layer. Doping of MoS_2 on Co_9S_8 enlarge the Mo-S bond length from 2.412 Å in the MoS_2 layer to 2.454 – 2.507 Å in Co_9S_8 @ MoS_2 , which also agrees with the experimental data. The adsorption energy of H and H_2 on the surface of MoS_2 and Co_9S_8 @ MoS_2 surfaces were derived as:

$$\Delta E_{H_2} = \frac{1}{n} (E(\text{surf} + nH_2) - E(\text{surf}) - nE(H_2)) \quad (1)$$

$$\Delta E_H = \frac{1}{n} (E(\text{surf} + nH) - E(\text{surf}) - nE(H)) \quad (2)$$

where n is the number of adsorbed hydrogen atoms, $E(\text{surf})$ is the total energy of the surface without H adsorption, and $E(\text{surf} + nH)$ is the total energy of the surface with n adsorbed atoms or molecules. The results are shown in Table S2 (Supporting Information).

For the adsorption of one H atom, the H—S bond is located parallel to the MoS₂ surface and perpendicular to the Co₉S₈@MoS₂ surfaces (Figure S16g,h, Supporting Information). For the adsorption of two H atoms, there are eight isomers for 2H-MoS₂, as shown in Figure S16c–i (Supporting Information). Additionally, the structures with perpendicular H—S bonds exhibit better stability. Moreover, Co₉S₈@MoS₂ with two perpendicular H—S bonds exhibits a higher hydrogen atom adsorption energy than the MoS₂ surface, which indicates easier H atom absorption on the Co₉S₈@MoS₂ surface. There are two stable chemical absorptions of hydrogen molecules on the MoS₂ surface (Figure S16a,b, Supporting Information). However, there is no chemical absorption but only one physical absorption of hydrogen molecules on the Co₉S₈@MoS₂ surface (Figure S17a, Supporting Information). Thus, the Co₉S₈@MoS₂ surfaces exhibited a much smaller hydrogen molecule adsorption energy (E_{H_2}) than the MoS₂ surface, demonstrating the highly active nature of the Co₉S₈@MoS₂ catalysts in stabilizing the HER intermediate and releasing H₂ gas. Moreover, the Mo—S bond length changes induced by hydrogen adsorption are shown in Figure 5b. Based on the Co doping, the changes in the Mo—S bond are largely reduced, which is favorable for recycle stability.

Next, we investigated the kinetic energy barrier profiles of HER on the MoS₂ and Co₉S₈@MoS₂ surfaces using the climbing-image nudged elastic band (CI-NEB) method implemented in Vienna Ab Initio Simulation Package (VASP), as shown in Figure 5c. The right side of Figure 5c shows the reaction path of hydrogen atom adsorption and hydrogen molecule desorption. Both MoS₂ and Co₉S₈@MoS₂ exhibit similar maximum energy barriers (0.4 eV) of hydrogen atom adsorption ($H_{\text{ads}} + H_{\text{ads}}$) during stage 2. However, the high chemical binding of hydrogen molecules forms another barrier of 0.4 eV for H₂ desorption from the MoS₂ surface. Without chemical hydrogen absorption, H₂ desorption from Co₉S₈@MoS₂ is much easier. Overall, compared to MoS₂, the Co₉S₈@MoS₂ catalysts exhibit almost the same H atom adsorption energy, a lower H₂ molecule desorption energy, and a similar kinetic energy barrier for promoting H—H bond formation of two adjacently adsorbed H atoms.

These Co₉S₈@MoS₂/CNFs cocatalysts systems have three main advantages: i) The core-shell structures create the high contact area of interfaces between MoS₂ and Co₉S₈ nanocrystals, and therefore, electron transfer occurs through intermediate sulfur atoms bonded to both metals at the interfaces; ii) fullerene-like MoS₂ shells around the Co₉S₈ cores favor an increase in the contact surface area between the two phases and could present stacking faults and possibly bending effects,

which are important factors for electrocatalytic activity;^[24,25] and iii) the CNFs substrate not only serves as a host for the formation of Co₉S₈@MoS₂ and for protection against electrolyte erosion, but also assures charge transfer between the electrode and the Co₉S₈@MoS₂. This synergistic strategy can be applied to other transition metal sulfide systems, such as WS₂, FeS₂, and NiS₂, and these novel hybrid nanomaterials could also be applied to dye-sensitized solar cells, supercapacitors, and Li ion batteries.

In summary, we describe a new class of Co₉S₈@MoS₂ core-shell structures formed on CNFs with cubic Co₉S₈ as the core and layered MoS₂ as the shell. The investigations of HER and OER electrocatalytic performances suggest that the unique Co₉S₈@MoS₂/CNFs hybrid demonstrates significant enhancement in both HER and OER performance and superior durability and thus can serve as cocatalyst for HER and OER in electrocatalytic water splitting. The high hydrogen and oxygen evolution activities of the Co₉S₈@MoS₂ are due to the electrocatalytic synergetic effects of the nanointerfaces generated by the directly contacting regions between the Co₉S₈ core and the MoS₂ shell. These advantages generate strong electron transfer between Co and Mo through the intermediate sulfur atoms bonded to both metals, leading to promising promoted electrocatalytic activity.

Supporting Information

Supporting Information is available from the Wiley Online Library or from the author.

Acknowledgements

H.Z. and J.Z. contributed equally to this work. The authors gratefully acknowledge the financial support from the National Natural Science Foundation of China (51373154, 21203137, and 51472182), the Shanghai Committee of Science and Technology (11nm0501300 and 13JC1408700), the Program for Innovative Research Team of Zhejiang Sci-Tech University, and the 521 Talent Project of Zhejiang Sci-Tech University.

Received: April 24, 2015

Revised: June 5, 2015

Published online: July 14, 2015

- [1] S. Cobo, J. Heidkamp, P. Jacques, J. Fize, V. Fourmond, L. Guetaz, B. Jousselme, V. Ivanova, H. Dau, S. Palacin, M. Fontecave, V. Artero, *Nat. Mater.* **2012**, *11*, 802.
- [2] M. Ledendecker, G. Clavel, M. Antonietti, M. Shalom, *Adv. Funct. Mater.* **2015**, *25*, 393.
- [3] A. Yamaguchi, R. Inuzuka, T. Takashima, T. Hayashi, K. Hashimoto, R. Nakamura, *Nat. Commun.* **2014**, *5*, 4256.
- [4] S. Chen, S. Z. Qiao, *ACS Nano* **2013**, *7*, 10190.
- [5] B. T. Sneed, A. P. Young, D. Jalalpoor, M. C. Golden, S. Mao, Y. Jiang, Y. Wang, C. K. Tsung, *ACS Nano* **2014**, *8*, 7239.
- [6] S. Zhang, Y. Z. Hao, D. Su, V. V. T. Doan-Nguyen, Y. T. Wu, J. Li, S. Sun, C. B. Murray, *J. Am. Chem. Soc.* **2014**, *136*, 15921.
- [7] M. S. Faber, S. Jin, *Energy Environ. Sci.* **2014**, *7*, 3519.

- [8] R. Subbaraman, D. Tripkovic, K. C. Chang, D. Strmcnik, A. P. Paulikas, P. Hirunsit, M. Chan, J. Greeley, V. Stamenkovic, N. M. Markovic, *Nat. Mater.* **2012**, *11*, 550.
- [9] M. Gong, W. Zhou, M. C. Tsai, J. G. Zhou, M. Y. Guan, M. C. Lin, B. Zhang, Y. F. Hu, D. Y. Wang, J. Yang, S. J. Pennycook, B. J. Hwang, H. J. Dai, *Nat. Commun.* **2014**, *5*, 4695.
- [10] Z. Chen, D. Cummins, B. N. Reinecke, E. Clark, M. K. Sunkara, T. F. Jaramillo, *Nano Lett.* **2011**, *11*, 4168.
- [11] M. Shalom, S. Gimenez, F. Schipper, I. Herraiz-Cardona, J. Bisquert, M. Antonietti, *Angew. Chem. Int. Ed.* **2014**, *53*, 3654.
- [12] H. T. Chung, J. H. Won, P. Zelenay, *Nat. Commun.* **2013**, *4*, 1922.
- [13] M. Zhou, C. Z. Yang, K. Y. Chan, *Adv. Energy Mater.* **2014**, *4*, 1400840.
- [14] J. Liang, R. F. Zhou, X. M. Chen, Y. H. Tang, S. Z. Qiao, *Adv. Mater.* **2014**, *26*, 6074.
- [15] H. Zhu, M. L. Du, M. Zhang, M. L. Zou, T. T. Yang, S. L. Wang, J. M. Yao, B. C. Guo, *Chem. Commun.* **2014**, *50*, 15435.
- [16] M. Seredych, E. Rodriguez-Castellon, T. J. Bandoz, *J. Mater. Chem. A* **2014**, *2*, 20164.
- [17] H. Zhu, F. L. Lyu, M. L. Du, M. Zhang, Q. F. Wang, J. M. Yao, B. C. Guo, *ACS Appl. Mater. Interfaces* **2014**, *6*, 22126.
- [18] H. Zhu, M. L. Du, M. Zhang, M. L. Zou, T. T. Yang, Y. Q. Fu, J. M. Yao, *J. Mater. Chem. A* **2014**, *2*, 7680.
- [19] J. M. McEnaney, J. C. Crompton, J. F. Callejas, E. J. Popczun, A. J. Biacchi, N. S. Lewis, R. E. Schaak, *Chem. Mater.* **2014**, *26*, 4826.
- [20] Z. Xing, Q. Liu, A. M. Asiri, X. Sun, *Adv. Mater.* **2014**, *26*, 5702.
- [21] P. Xiao, M. A. Sk, L. Thia, X. Ge, R. J. Lim, J. Y. Wang, K. H. Lim, X. Wang, *Energy Environ. Sci.* **2014**, *7*, 2624.
- [22] S. H. Chang, M. D. Lu, Y. L. Tung, H. Y. Tuan, *ACS Nano* **2013**, *7*, 9443.
- [23] Z. N. Yu, L. Tetard, L. Zhai, J. Thomas, *Energy Environ. Sci.* **2015**, *8*, 702.
- [24] W. H. Shi, J. X. Zhu, X. H. Rui, X. H. Cao, C. Chen, H. Zhang, H. H. Hng, Q. Y. Yan, *ACS Appl. Mater. Interfaces* **2012**, *4*, 2999.
- [25] Y. Sun, C. Liu, D. C. Grauer, J. Yano, J. R. Long, P. Yang, C. J. Chang, *J. Am. Chem. Soc.* **2013**, *135*, 17699.
- [26] E. J. Popczun, C. G. Read, C. W. Roske, N. S. Lewis, R. E. Schaak, *Angew. Chem. Int. Ed.* **2014**, *53*, 5427.
- [27] Q. Liu, J. Tian, W. Cui, P. Jiang, N. Cheng, A. M. Asiri, X. Sun, *Angew. Chem. Int. Ed.* **2014**, *53*, 6710.
- [28] J. Tian, Q. Liu, A. M. Asiri, X. Sun, *J. Am. Chem. Soc.* **2014**, *136*, 7587.
- [29] M. S. Faber, R. Dziedzic, M. A. Lukowski, N. S. Kaiser, Q. Ding, S. Jin, *J. Am. Chem. Soc.* **2014**, *136*, 10053.
- [30] H. L. Wang, Y. Y. Liang, Y. G. Li, H. J. Dai, *Angew. Chem. Int. Ed.* **2011**, *50*, 10969.
- [31] M. Ramos, G. Berhault, D. A. Ferrer, B. Torres, R. R. Chianelli, *Catal. Sci. Technol.* **2012**, *2*, 164.
- [32] G. Hagenbach, P. H. Courty, B. Delmon, *J. Catal.* **1973**, *31*, 264.
- [33] Y. Y. Zhu, Q. M. Ramasse, M. Brorson, P. G. Moses, L. P. Hansen, C. F. Kisielowski, S. Helveg, *Angew. Chem. Int. Ed.* **2014**, *53*, 10723.
- [34] D. L. Wang, H. L. Xin, R. Hovden, H. Wang, Y. C. Yu, D. A. Muller, F. J. DiSalvo, H. D. Abruna, *Nat. Mater.* **2013**, *12*, 81.
- [35] G. Y. Chen, H. Ågren, T. Y. Ohulchanskyy, P. N. Prasad, *Chem. Soc. Rev.* **2015**, *44*, 1680.
- [36] F. Hoshyargar, A. Yella, M. Panthofer, W. Tremel, *Chem. Mater.* **2011**, *3*, 4716.
- [37] L. L. Feng, G. D. Li, Y. P. Liu, Y. Y. Wu, H. Chen, Y. Wang, Y. C. Zou, D. J. Wang, X. X. Zou, *ACS Appl. Mater. Interfaces* **2015**, *7*, 980.
- [38] M. Jahan, Z. L. Liu, K. P. Loh, *Adv. Funct. Mater.* **2013**, *23*, 5363.
- [39] J. D. Benck, T. R. Hellstern, J. Kibsgaard, P. Chakthranont, T. F. Jaramillo, *ACS Catal.* **2014**, *4*, 3957.
- [40] A. Kumar, F. Ciucci, A. N. Morozovska, S. V. Kalinin, S. Jesse, *Nat. Chem.* **2011**, *3*, 707.
- [41] T. M. Gür, S. F. Bent, F. B. Prinz, *J. Phys. Chem. C* **2014**, *118*, 21301.
- [42] J. Kibsgaard, Z. Chen, B. N. Reinecke, T. F. Jaramillo, *Nat. Mater.* **2012**, *11*, 963.
- [43] H. Wang, Z. Lu, D. Kong, J. Sun, T. M. Hymel, Y. Cui, *ACS Nano* **2014**, *8*, 4940.
- [44] M. A. Lukowski, A. S. Daniel, F. Meng, A. Forticaux, L. Li, S. Jin, *J. Am. Chem. Soc.* **2013**, *135*, 10274.
- [45] J. Xie, J. Zhang, S. Li, F. Grote, X. Zhang, H. Zhang, R. Wang, Y. Lei, B. Pan, Y. Xie, *J. Am. Chem. Soc.* **2013**, *135*, 17881.
- [46] D. Voiry, M. Salehi, R. Silva, T. Fujita, M. Chen, T. Asefa, V. B. Shenoy, G. Eda, M. Chhowalla, *Nano Lett.* **2013**, *13*, 6222.
- [47] Y. Yang, H. Fei, G. Ruan, C. Xiang, J. M. Tour, *Adv. Mater.* **2014**, *26*, 8163.
- [48] E. J. Popczun, J. R. McKone, C. G. Read, A. J. Biacchi, A. M. Wiltrout, N. S. Lewis, R. E. Schaak, *J. Am. Chem. Soc.* **2013**, *135*, 9267.
- [49] J. Wu, Y. Xue, X. Yan, W. S. Yan, Q. M. Cheng, Y. Xie, *Nano Res.* **2012**, *5*, 521.
- [50] M. R. Gao, Y. F. Xu, J. Jiang, Y. R. Zheng, S. H. Yu, *J. Am. Chem. Soc.* **2012**, *134*, 2930.
- [51] Q. Liu, J. T. Jin, J. Y. Zhang, *ACS Appl. Mater. Interfaces* **2013**, *5*, 5002.
- [52] L. L. Feng, G. D. Li, Y. Liu, Y. Wu, H. Chen, Y. Wang, Y. C. Zou, D. Wang, X. Zou, *ACS Appl. Mater. Interfaces* **2015**, *7*, 980.

Probing the unexpected behavior of AuNPs migrating through nanofibers: a new strategy for the fabrication of carbon nanofiber–noble metal nanocrystal hybrid nanostructures†

Cite this: *J. Mater. Chem. A*, 2014, 2, 11728

Han Zhu,^a MingLiang Du,^{*ab} Ming Zhang,^{ab} MeiLing Zou,^a TingTing Yang,^a LiNa Wang,^b JuMing Yao^{ab} and BaoChun Guo^c

The intimate relationship of electrochemical sensors with high sensitivity and reliability has stimulated intensive research on developing versatile materials with excellent electrocatalytic activity. Here, we reported a novel strategy for the design of novel nanostructure-based electrochemical biosensors originating from an unexpected behavior of Au nanoparticles (AuNPs) embedded in the interior of polyacrylonitrile nanofibers (Au–PANFs), which can migrate to the external surfaces of the carbon nanofibers (Au–CNFs) during the graphitization process. Small and uniform AuNPs embedded in PANFs were synthesized *via* a combination of electrospinning and *in situ* reduction. With the conversion from the amorphous structures of PANFs to graphene layered structures of CNFs, the AuNPs can migrate from the interior of PANFs to the external surfaces of CNFs. The migration of AuNPs through the nanofiber matrix is strongly dependent on the graphitization temperature and heating rates. Three different heating rates of 2, 5, and 10 °C min^{−1} and graphitization temperatures of 600, 800, and 1000 °C were employed to investigate the migration and the exposed density of AuNPs on the CNFs. These novel nanomaterials were constructed as a nonenzymatic H₂O₂ electrochemical sensor and the sensors based on Au–CNFs with increased density of exposed AuNPs exhibit significantly promoted electrochemical activity. The Au–CNFs (1000 °C, 2 °C min^{−1}) with high exposed density and small sizes of AuNPs possess higher specific surface area and active sites, leading to higher electrocatalytic activity. The present investigations provide a general route for the fabrication of nanostructures for novel electrochemical sensors, energy storage devices and so on.

Received 3rd April 2014

Accepted 9th May 2014

DOI: 10.1039/c4ta01624f

www.rsc.org/MaterialsA

Introduction

Over the last two decades, the development of new electronic devices for wide applications in the sensitive detection of clinical, environmental, and food safety is currently an area of intensive research.^{1,2} In this context, materials with dimensions at the nanoscale appear highly promising due to their exciting physical and chemical properties for the selective detection with low limits. Nanomaterial-based sensors exhibit extremely high surface area to volume ratio, which can increase the number of binding sites available for biological recognition element

immobilization.^{3–6} In addition, the utilization of nanomaterials usually leads to faster mass transfer rates, resulting in lower limits of detection and faster analyte detection rates than those seen in conventional sensors.^{5,7,8}

Large amounts of nanomaterials, such as noble metal NPs, carbon nanotubes (CNTs) and graphene, are employed to construct the electrochemical biosensors.^{9–14} Electrochemical detection of biomolecules using nanomaterials can often achieve high sensitivity because nanomaterials are extremely sensitive to electronic perturbations in the surrounding environment. Considerable efforts were devoted to novel nanomaterials to coordinate mass- and charge-transport and electron-transfer kinetics for realizing simultaneous minimization of primary resistances in biosensing: electrochemical reaction occurring at electrolyte/electrode interface, mass transport of analyte in electrolyte and electrode, and the electron conduction in electrode and current collector.^{1,12–14}

Carbonaceous materials, such as CNTs and graphene, are of enormous interest, mainly due to their superior electrocatalytic activity for various chemical and biological systems.^{15–17} The

^aDepartment of Materials Engineering, College of Materials and Textile, Zhejiang Sci-Tech University, Hangzhou 310018, P. R. China. E-mail: du@zstu.edu.cn; Tel: +86-571-86843255

^bKey Laboratory of Advanced Textile Materials and Manufacturing Technology, Zhejiang Sci-Tech University, Ministry of Education, Hangzhou 310018, P. R. China

^cDepartment of Polymer Materials and Engineering, South China University of Technology, Guangzhou 510640, P. R. China

† Electronic supplementary information (ESI) available. See DOI: 10.1039/c4ta01624f

control of heterogeneous electron-transfer kinetics through judicious design and structural manipulation of advanced carbon materials is of importance in the fabrication of many electrochemical devices such as biosensors.^{8,15} Several groups have demonstrated the successful fabrication of sensitive biosensors using CNTs and graphene.^{16–19} These sensors utilize the fast mass transfer and large surface areas provided by the carbonaceous nanomaterials. Myung *et al.* have reported the construction of a graphene-encapsulated nanoparticle-based biosensor for the selective detection of cancer biomarkers.⁹ Chen *et al.* have fabricated the CNT-based electrochemical devices for the electronic sensing of proteins.¹⁰

Up to date, one-dimensional electrospun carbon nanofibers (CNFs) have been widely used as ideal electron pathways because of their intriguing chemical and physical properties such as good conductivity ($\rho = (3\text{--}7) \times 10^{-3} \text{ } \Omega \text{ cm}$).^{17,20–23} Electrospinning is a highly versatile method to produce nanofibers of various polymers with diameters ranging from a few tens of nanometers to a few micrometers in different forms such as nonwoven mats, yarns, *etc.*^{21–23} It is a relatively simple and low-cost strategy to produce continuous nanofibers from polymer solutions or melts. CNFs synthesized *via* electrospinning and subsequent graphitization had attracted attention mainly because their structures and properties can be easily adjusted by changing the processing conditions. Similar to other carbonaceous materials, electrospun CNFs are mostly used in the electrochemical applications related to the energy storage devices including lithium-ion batteries, supercapacitors, and fuel cells.^{24–27} Only a few studies focus on the electrochemical sensor applications of the electrospun CNFs. In addition, the electrocatalytic activities of CNFs are often adjusted through the utilization of additional active components, such as loading or deposition of metal NPs onto the nanofibers.

Combining different materials with precise control of their interface at the nanoscale would lead to significantly enhanced properties. Noble metal nanostructures, especially Au nanostructures, have proven to be the most intriguing platforms suitable for a broad spectrum of bioapplications due to their bioinertness and biocompatibility, relatively simple and facile synthetic control and bioconjugation.^{1,8,15} Recent years have witnessed tremendous efforts devoted to the design and synthesis of Au nanostructures in the application of electrochemical biosensors.^{1,16} Au nanostructure-based electrochemical biosensors are extremely sensitive to the sizes, shapes and dispersion of Au nanostructures.^{15,18,28,29} Recently, our group has reported the designs of noble metal nanostructure decorated one-dimensional organic nanofibers, employing as the electrochemical biosensors for the detection of H_2O_2 , glucose and glutathione.^{30–33} Small sizes of Au nanocrystals usually can dramatically influence their physical and chemical properties arising from their large surface-area-to-volume ratio and the spatial confinement of electrons, phonons, and electric fields in and around these particles.^{30,31} These novel nanocrystal–nanofiber hybrid architectures exhibit high surface area and strong electrochemical activities, leading to advanced materials for electrochemical sensors, nanoelectronics, energy storage devices and catalysts.

Unlike organic nanofibers, CNFs lack functional groups and are consequently relatively chemically inert. Common strategies to decorate the CNFs with nanocrystals include surface treatments by ultrasonication and acid-assisted oxidation, vapor deposition and solution growth.^{34–36} Hermans *et al.* have reported that CNTs and CNFs functionalized with HNO_3 can produce surface carboxyl groups, serving as anchoring points for the grafting of PdNPs.³⁷ Liang *et al.* have synthesized PdNP functionalized CNF composites through a two-step chemical vapor deposition of Pd(allyl)(Cp) .³⁸ However, because of the complex interfacial reactions involved and more demanding process conditions imposed, the size and distribution control of nanocrystals on CNFs become considerable problems. How to synthesize excellent electrochemical sensors based on CNFs incorporated with small and uniform nanocrystals still remains a huge challenge.

Recently, Yang *et al.* have reported an approach to prepare CNFs decorated with SnO_2 nanocrystals by combining the PANFs and stannous chloride salt solution.³⁹ After the carbonization in an $\text{Ar}/\text{H}_2\text{O}$ atmosphere, the SnO_2 -NPs were formed on the surfaces of the CNFs. Similarly, Hou *et al.* prepared the PANFs mixed with $\text{Fe(acetylacetonate)}_3$ to synthesize CNF/Fe nanocomposites and the FeNPs immobilized on the CNFs can serve as the catalysts for the growth of CNTs.⁴⁰

Unlike the above common strategies and newly raised thermal decomposition approaches, we proposed a new strategy and synthesized a new system, CNF–Au nanostructures. In the procedure, accompanied with the conversion from PANFs to CNFs, the nanostructure of CNF–Au and can be assembled and tailored by the migration of AuNPs in PANFs to the outside of CNFs during the graphitization process. Our previous work has reported a green and facile approach for the synthesis of small and uniform AuNPs embedded in the interior of the PANFs *via* a combination of electrospinning and *in situ* reduction.^{41,42} Note that intriguing phenomena can be observed during the graphitization process. With the conversion from the amorphous structures of PANFs to graphene layered structures of CNFs, the initial AuNPs migrate from the interior of PANFs to the exterior of CNFs. The migration of AuNPs through the nanofiber matrix is strongly dependent on the graphitization temperature and heating rates. We employed three different heating rates of 2, 5, and $10 \text{ } ^\circ\text{C min}^{-1}$ and graphitization temperatures of 600, 800, and $1000 \text{ } ^\circ\text{C}$, respectively, to investigate the migration and the exposed density of AuNPs on the CNFs. The conversion from embedded AuNPs to exposed AuNPs attached to the external surfaces of CNFs is explained by an atom diffusion mechanism. In addition, we also investigate the conversion in the chemical structures from the $\text{--C}\equiv\text{N}$ structure to the $\text{--C}=\text{C--C}=\text{N}$ structure during the graphitization process. Similar phenomena can be obtained by Pt–CNF hybrid nanostructures, indicating that this new strategy will provide a general approach for the fabrication of CNF–noble metal nanostructures. These novel nanomaterials were constructed as a nonenzymatic H_2O_2 electrochemical sensor. The electrochemical sensors based on Au–CNFs with increased density of exposed AuNPs exhibit significantly promoted electrochemical activity with increased density of exposed AuNPs. The Au–CNFs with high density of

exposed AuNPs possess higher specific surface area and active sites. It means that more AuNPs will take part in the reactions, leading to higher electrocatalytic activity. The sensors show a lower detection limit and wider responding range, indicating that the fabricated sensor could be potentially used for monitoring the concentration of H_2O_2 without any enzyme.

Experiment section

Materials and methods

Materials. Chloroauric acid ($\text{HAuCl}_4 \cdot 4\text{H}_2\text{O}$, 99.9%), hydrogen per-oxide (30%), hydroquinone (HQ), phosphate buffered saline (PBS) and dimethyl formamide (DMF, 99.5%) were commercially available from Shanghai Civi Chemical Technology Co., Ltd. Polyacrylonitrile (PAN, $M_w \approx 1.4 \times 10^5$, copolymerized with 10 wt% methyl acrylate) was manufactured by Sinopec Shanghai Petrochemical Co., Ltd. Epigallocatechingallate (EGCG, 98%) were purchased from Xuan-ChengBaiCao Plant Industry and Trade Co., Ltd. All of the chemicals were used without further purification. Deionized water (DIW, 18.2 M Ω) was used for all solution preparations.

Synthesis of Au-PANF precursor solution. The first step involved the synthesis of AuNPs in PAN/DMF solution *via* an *in situ* reduction method.⁴¹ Briefly, 6 g PAN powder was dissolved in 44 mL DMF under magnetic stirring at 65 °C to get a homogenous solution. Then, 0.30 mmol $\text{HAuCl}_4 \cdot 4\text{H}_2\text{O}$ was added to the PAN/DMF solution and the mixture were stirred at 65 °C for 1 h. Finally, 0.025 g EGCG was immediately added to the above mixture and the mixture was stirred using a magnetic agitator for 3 h. Therefore, the mass fraction of PAN in the DMF solution was 12 wt% and the mass ratio of $\text{HAuCl}_4 \cdot 4\text{H}_2\text{O}$ and the PAN powder was 1.0 wt%.

Fabrication of PANF and Au-PANF nanofibrous mats. The PAN/DMF (12%) and Au-PANF precursor solution with the mass ratio of 1.0 wt% ($\text{HAuCl}_4 \cdot 4\text{H}_2\text{O}$ to PAN) was used to prepare nonwoven mats *via* an electrospinning technique. The precursor solution was transferred into a syringe with a stainless copper needle at the tip. The needle was connected to a high voltage power supply. The applied voltage was 12 kV, the needle to collector distance was 12 cm and the flow rate of the solution was 0.6 mL h⁻¹. All experiments were performed at room temperature. The electrospun PANF and Au-PANF nanofibrous mats were collected onto a piece of aluminum foil.

Fabrication of CNF and Au-CNF nanofibrous mats. The as-collected electrospun PANF and Au-PANF nanofibrous mats were peeled off from the aluminum foil and placed into a home-built CVD tube furnace for heat treatment. The nanofibrous mats were heated to 280 °C in air at a rate of 5 °C min⁻¹ and maintained for 6 h for stabilization, then the samples were heated up to 800 °C at a rate of 5 °C min⁻¹ under Ar gas flow (50 Sccm) for the graphitization. The desired graphitization temperature was held constant for 8 h and then the products were cooled to room temperature under an Ar atmosphere.

Fabrication of Au-CNF nanofiber biosensors for H_2O_2 detection. For the fabricating procedure of the Au-CNF/GCE biosensor, the glassy carbon electrode (GCE) with a diameter of 3 mm was polished carefully using alumina slurry as a polisher

to get a mirror-like surface, followed by rinsing with DIW and ethanol and then drying with nitrogen. The Au-CNF fibrous mat was glued by Nafion aqueous solution (1 wt%) on the pretreated GCE and left to dry by N_2 at room temperature. The modified electrode was washed gently with DIW and then soaked in PB at 4 °C. This modified electrode is denoted as Au-CNF/GCE. The control sample, CNFs, was fabricated using similar procedures for the preparation of CNF/GCE biosensors. All the modified electrodes were stored at 4 °C in a refrigerator before further characterizations.

Electrocatalytic measurement. Amperometric experiments were conducted with a CHI660H workstation (Shanghai Chenhua, Shanghai). All experiments were carried out using a conventional three-electrode system in 0.1 M PBS, where CNF/GCE and Au-CNF/GCE were used as the working electrode, a platinum foil as the auxiliary electrode and a saturated Ag/AgCl electrode as the reference electrode. The buffer was purged with high-purity nitrogen for at least 30 min prior to each amperometric experiment, and the nitrogen environment was then maintained over the solution to protect the solution from oxygen. Electrochemical performances of the fabricated electrodes were tested using a three-electrode system by cyclic voltammetry (CV).

Instrumentation. The morphology evolution of the PANFs, CNFs, Au-PANFs, Au-CNFs, Pt-PANFs and Pt-CNFs were characterized by JSM-2100 transmission electron microscopy (JEOL, Japan) at an acceleration voltage of 200 kV and JSM-6700F FE-SEM (JEOL, Japan) at an acceleration voltage of 3 kV. X-ray photoelectron spectra of the products were recorded using an X-ray photoelectron spectrometer (Kratos Axis Ultra DLD) with an aluminum (mono) K_α source (1486.6 eV). The aluminum K_α source was operated at 15 kV and 10 mA. Fourier transform infrared (FTIR) spectra were recorded on a Nicolet 5700 FTIR spectrometer in transmittance mode at a resolution of 4 cm⁻¹ and 32 scans in the range from 4000 nm to 400 nm. XRD patterns of the nanofibrous mats were characterized with a SIEMENS Diffraktometer D5000 X-ray diffractometer using a Cu K_α radiation source at 35 kV, with a scan rate of 0.02° 2 θ s⁻¹ in the 2 θ range of 10–80°. Raman spectra of all the samples were recorded using a RenishawinVia Raman microscope using a 532 nm laser excitation source. The excitation light intensity in front of the objective was 10 mW with a spectral collection time of 1 s. The integration time for our measurements was set to 10 s. The high-angle annular dark field scanning TEM (HAADF-STEM) image, STEM mapping and line-scan energy dispersive X-ray spectroscopy (EDX) images were recorded using a STEM (Technai G2 F30 S-Twin, Philips-FEI) at an acceleration voltage of 300 kV.

Results and discussion

The morphologies of the electrospun polyacrylonitrile nanofibers with embedded AuNPs (Au-PANFs) and carbon nanofibers with immobilized AuNPs on surfaces (Au-CNFs) were determined by using the FE-SEM and TEM characterizations. As shown in Fig. 1a, the distinct and continuous Au-PANFs are straight and have smooth surfaces with an average diameter of

about 512 ± 54 nm. The hybrid nanofibers are up to hundreds of micrometers in length, leading to high surface-to-volume ratios. In addition, no AuNPs can be seen on the surfaces of the Au-PANFs. However, from the TEM image of Au-PANFs shown in Fig. 1b, small AuNPs with an average diameter of 2.3 ± 0.5 nm are evenly dispersed in the whole PANFs, indicating that the AuNPs are mainly embedded in the interior of PANFs. In addition, the inset in Fig. 1b exhibits a HRTEM image of AuNPs, showing lattice fringes of the Au (111) plane with an interplanar distance of 0.23 nm.

Compared with the smooth surfaces of Au-PANFs, as shown in Fig. 1d, large amounts of AuNPs were immobilized on the surfaces of CNFs. It means that after the graphitization process, the initial AuNPs embedded in the interior of PANFs broke through the nanofiber and formed on the external surfaces of CNFs. The average diameter of the Au-CNFs decreases to 200 ± 44 nm after graphitization, indicating the significant shrinkage of the nanofibers. The TEM image of Au-CNFs exhibits small and uniform AuNPs distributed on CNFs and the lattice fringes shown in the inset in Fig. 1e are visible with a spacing of about 0.23 nm, which corresponds to the lattice spacing of the (111) planes of Au.⁴¹ Meanwhile, after the graphitization treatment at 800 °C, the diameter of AuNPs formed on the surfaces of CNFs increased to 5.6 ± 0.7 nm and no aggregated NPs are observed.

The interfacial structures of Au-CNFs can be resolved in greater detail by HAADF-STEM imaging (Fig. 1c). The HAADF-

STEM image of the Au-CNFs can also indicate that the AuNPs are evenly immobilized on the surfaces of CNFs. As shown in Fig. 1c and f, it is apparent that the brighter spots are the AuNPs, and the STEM-EDS mapping (Fig. 1g) demonstrates that the quasi-spherical shapes of the AuNPs are immobilized on the external surfaces. Compared with Fig. 1f, the positions of AuNPs in the mapping image (Fig. 1g) are nearly consistent with the AuNPs anchored on CNFs.

XRD patterns can provide much information about the crystal structures of Au-PANFs and Au-CNFs. As shown in Fig. 1h, the Au-PANF nanofibrous mats exhibit a sharp peak and a broad band, locating at 16.9° and 27.7° , which are ascribed to the PAN crystalline phase of the (110) plane and the amorphous phase.^{43,44} However, no diffraction peaks of Au crystals emerged on the XRD pattern. Meanwhile, the representative diffraction peak (002) of the stacked graphite layers (JCPDS 75-1621) in the Au-CNFs is detected at $2\theta = 24.7^\circ$, demonstrating the crystalline structures of graphitic carbon in the nanofibers.^{45,46} Interplanar *d*-spacing of the graphite layers were calculated using Bragg's Law.^{45,46} By using $\lambda = 0.154$ nm (Cu K_α), the calculated value of d_{002} of Au-CNFs is 3.60 Å. Compared with Au-PANFs, four new strong peaks appeared at 38.3° , 44.4° , 64.8° , and 77.8° , which are consistent with the (111), (200), (220) and (311) planes of Au crystals, respectively (JCPDS 04-0784).^{47,48} The strong differences in the diffraction peaks of the Au crystals between the Au-PANFs and Au-CNFs

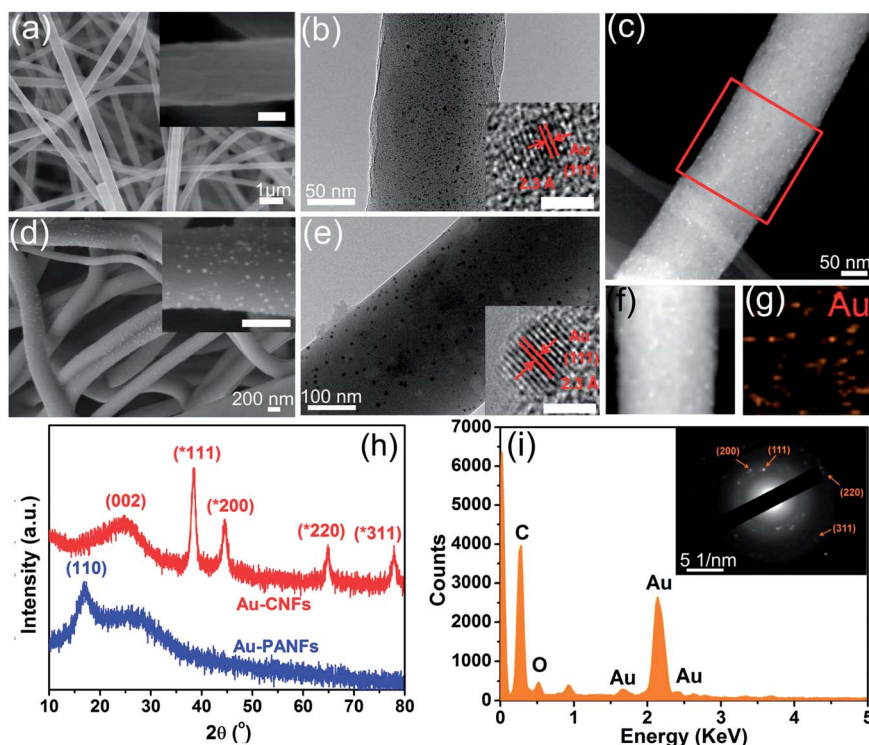


Fig. 1 FE-SEM and TEM images of the (a and b) Au-PANFs and (d and e) Au-CNFs graphitized at 800 °C. Insets in (a and d) are the high-magnification FE-SEM images of the Au-PANFs and Au-CNFs (scale bar 200 nm). Insets in (b and e) are the HRTEM images of the AuNPs embedded in PANFs and on the surfaces of CNFs, respectively (scale bar 2 nm). (c and f) HAADF-STEM images of the Au-CNFs and the (g) STEM-EDS mapping image of the selective area of Au-CNFs. (h) XRD patterns of the Au-PANF and Au-CNF nanofibrous mats. (i) EDX spectrum of the Au-CNFs. Inset in (i) is the SAED pattern of the Au-CNFs.

demonstrate that the Au–CNFs have much exposed AuNPs on the surfaces, which are consistent with the FE-SEM and STEM results. We have further performed the EDX spectroscopy of Au–CNFs, and Fig. 1i shows the Au, C and O elements, confirming the presence of AuNPs. The SAED pattern (inset in Fig. 1i) recorded on the mapping region of Au–CNFs as indicated by the red square in Fig. 1c further verifies that the AuNPs are polycrystalline in nature and consist of face-centered cubic-phase nanocrystallites. The concentric diffraction rings from inside to outside are indexed to the (111), (200), (220), and (311) planes of Au crystals.^{18,48}

XPS was used to investigate the chemical states of the surfaces of Au–PANFs and Au–CNFs. As shown in Fig. 2a, the Au 4f XPS spectra of Au–PANFs can be deconvoluted to two peaks at 88.0 and 84.3 eV, which are associated with the binding energies (BEs) of Au 4f_{7/2} and Au 4f_{5/2}, respectively. Compared with the BEs of Au⁰ (87.7 eV and 84.0 eV), the higher BEs of Au 4f indicate that the AuNPs embedded in PANFs are surrounded by the PAN molecules, leading to a substantial electron donation from AuNPs to the stabilizer molecules.^{41,49,50} Tanaka and Negishi *et al.* have reported that the relatively high binding energy of Au

4f was due to the binding of surface Au atoms in AuNPs with the stabilizer or passive molecules surrounding the nanoparticles, which led to a substantial electron donation from AuNPs to the stabilizer molecules.^{49,50} These indicate that the AuNPs were embedded in the interior of PANFs and surrounded by large amounts of PAN molecules.

Focusing on the XPS spectrum of Au–CNFs, two sharp and distinct peaks can be observed at 84.2 and 87.8 eV. Compared with that of the Au–PANFs, the BEs of Au 4f of Au–CNFs are close to the BEs of Au⁰, indicating that the AuNPs on the surfaces of CNFs are surrounded by few molecules. A few molecules around the exposed AuNPs on CNFs lead to weaker substantial electron donation, and the small changes in the BEs of Au 4f. The intensity of the Au 4f peaks of Au–CNFs is much higher than that of Au–PANFs, demonstrating that the Au–CNFs have more exposed AuNPs on the surfaces of the nanofibers. The XPS results are consistent with the FE-SEM, STEM and XRD results and more discussion can be found in the following studies.

To investigate the evolution of the AuNPs transferred from the interior to the external surfaces, we performed a control experiment to study the graphitization of the PANFs. The morphologies, microstructures and crystal structures were examined by TEM, FESEM, STEM, XRD and Raman characterizations. Fig. 3a shows the amorphous structure of PANFs and as shown in Fig. 3b, the carbonaceous matrix of CNFs was constructed by graphitic carbon layers. The insets in Fig. 3b show the lattice spacing of 0.36 nm corresponding to the (002) lattice plane of graphite and the typical diffraction pattern of the CNFs, reflecting randomly oriented polycrystallites.^{45,46} Therefore, along with the carbonization from PANFs to CNFs, the amorphous structures of PANFs converted to the graphitic carbon layered structures.

The HAADF-STEM and STEM-EDS mapping images of CNFs clearly show three different elements, which are ascribed to carbon, oxygen and nitrogen. We have further performed line-scanned EDX spectroscopy on individual CNF. Fig. 3l shows the line-scanned EDX spectra of CNFs along the red-line (Fig. 3f) across the nanofiber, which clearly shows the existences of carbon, oxygen and nitrogen.

Comparing the FE-SEM images of PANFs with CNFs, the average diameters of nanofibers decreased from 560 nm to 200 nm, indicating the significant shrinkage of the PANFs. Based on the above results, we suppose that the AuNPs transferred from the interior of PANFs to the exterior of CNFs was caused by the carbonization process, and more experiments and discussion will be performed in the following studies. XRD patterns also indicate the structure conversion from PANFs to CNFs. As shown in Fig. 3j, the PANF mats exhibit two peaks, locating at 17.1° and 26.7°, which are ascribed to the PAN crystalline phase and the amorphous phase, respectively. The broader diffraction peaks of CNFs centered at 24.1° and 44.1° are attributed to carbon (002) and (100) planes. The *d*₀₀₂ calculated value of pure CNFs is 3.69 Å. Compared with the *d*₀₀₂ value of graphite (0.335 nm), the expanded *d*₀₀₂ value of CNFs (0.369 nm) and Au–CNFs (0.360 nm) implies that the graphene layers are displaced due to many layer-sequential

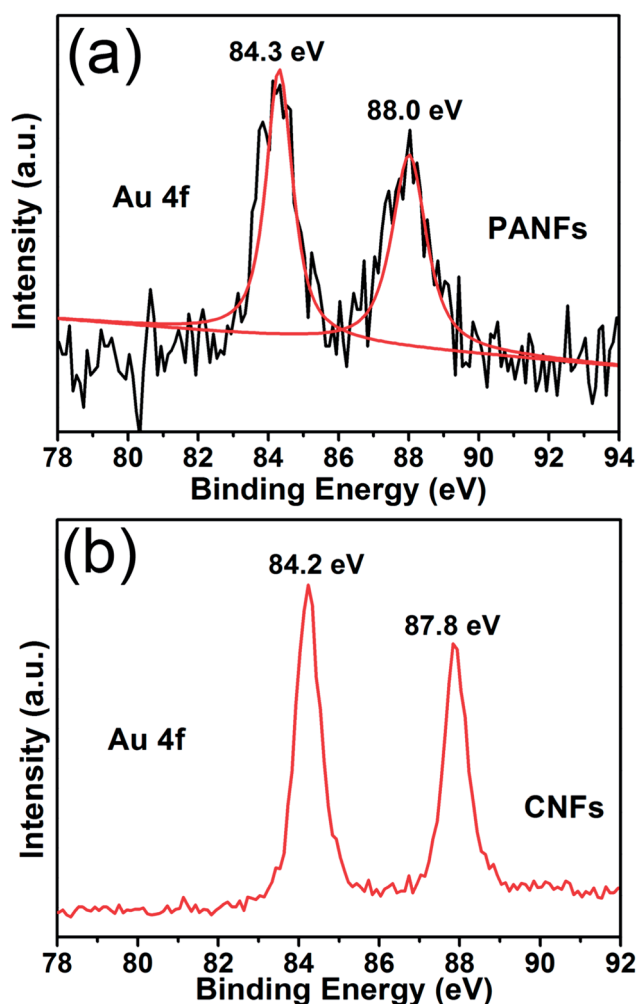


Fig. 2 XPS spectra of the Au 4f of (a) Au–PANFs and (b) Au–CNFs graphitized at 800 °C.

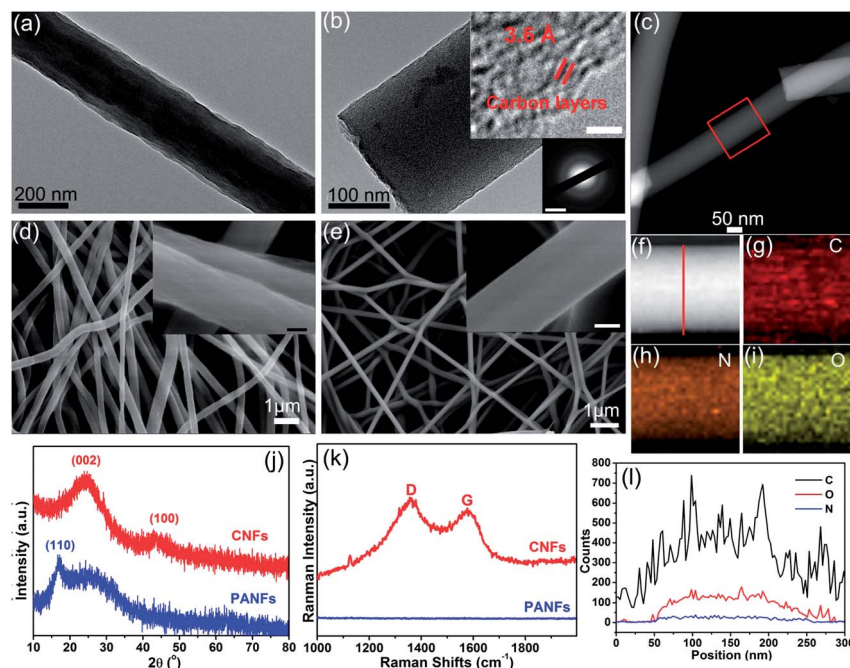


Fig. 3 TEM and FE-SEM images of the (a and d) PANFs and (b and e) CNFs graphitized at 1000 °C. (c and f) HAADF-STEM images of the Au-CNFs and the (g–i) STEM-EDS mapping images of the selective area of CNFs. (j) XRD patterns and (k) Raman spectra of the PANF and CNF nanofibrous mats. (l) Line-scan EDX spectra of the CNF. Insets in (b) are the HRTEM image and SAED pattern of the CNFs (scale bars, 2 nm and 5 nm⁻¹). Insets in (d and e) are the high-magnification FE-SEM images of CNFs (scale bars, 200 nm and 100 nm).

mismatches occurring in the CNFs and that there is much space for energy storage.^{24,45,46}

The Raman spectrum of the PANFs does not show any peaks in the range from 1000 to 2000 cm⁻¹, while the CNFs exhibit two fundamental vibrations, which are observed at 1357 and 1577 cm⁻¹. The primary peak (D band) corresponds to the breaking symmetry caused by defects or structural disorders, while the later peak (G band) is related to in-plane tangential stretch vibration mode of the graphitic layer.^{48,51} The intensity ratio of D and G bands (I_D/I_G) was calculated to be 1.09, showing that the CNFs indeed composed of graphitic rolls mixed with a small amount of amorphous carbon and a number of pores.

FTIR and XPS were used to study the evolution in chemical structures, surface compositions and chemical states of the PANFs and CNFs during the graphitization process. As shown in Fig. 4a, the FTIR spectra of PANFs, pre-oxidation PANFs at 280 °C (PANOF) and CNFs graphitized at 1000 °C were performed to investigate the evolution in chemical structures during the graphitization process.

The PANFs displays a broad band centered at 3472 cm⁻¹ ascribed to the stretching vibration of O–H groups. The other three characteristic peaks at 1670, 2242 and 2931 cm⁻¹ correspond to the C=O stretching in carboxylate groups, C≡N stretching in nitrile groups and C–H stretching in C–H and CH₂ groups, which are consistent with the previous literature.^{41,43,52} After the pre-oxidation at 280 °C, the FTIR spectrum of PANOFs exhibits weaker intensity of C≡N peaks (2242 cm⁻¹). In addition, the two strong peaks located at 1590 and 1372 cm⁻¹ are ascribed to the C=N and C=C stretching vibration and the C–H in-plane bending vibration, indicating the conversion

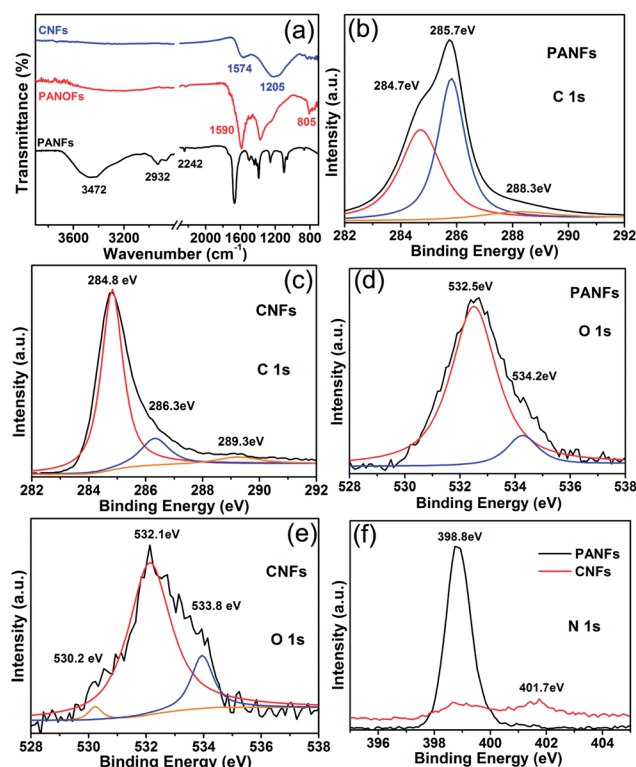


Fig. 4 (a) FTIR spectra of the PANFs, pre-oxidation PANFs at 280 °C and CNFs carbonized at 1000 °C. XPS spectra of C 1s of (b) PANFs and (c) CNFs. XPS spectra of O 1s of (d) PANFs and (e) CNFs. (f) XPS spectra of N 1s of PANFs and CNFs.

from the $\text{C}\equiv\text{N}$ structure to the $\text{C}=\text{C}-\text{C}=\text{N}$ structure during the pre-oxidation process.^{52,53} What is more, a strong peak ascribed to the $\text{C}=\text{C}-\text{H}$ bending vibration can be observed at 805 cm^{-1} . The above FTIR results demonstrate that the $\text{C}\equiv\text{N}$ structures were converted to the $\text{C}=\text{C}-\text{C}=\text{N}$ structure, forming the aromatic structures. After the carbonization at $800\text{ }^{\circ}\text{C}$, the characteristic peaks for $\text{O}-\text{H}$, $\text{C}\equiv\text{N}$ are vanished, the peaks located at 1574 and 1205 cm^{-1} are attributed to the $\text{C}=\text{C}$ or $\text{C}=\text{N}$ stretching vibration and $\text{C}-\text{N}$ bending vibration. Such chemical changes can clearly demonstrate the chemical structure conversion during the graphitization process.

The XPS spectra of PANF and CNF nanofibrous mats are shown in Fig. 4b–f. As shown in the $\text{C } 1\text{s}$ spectra of PANFs in Fig. 4b, three different types of carbon with different chemical states are observed at 284.7 , 285.7 and 288.3 eV , respectively. These peaks are ascribed to the carbon atoms in different functional groups: the $\text{C}-\text{C}$, the C in $\text{C}\equiv\text{N}$ bonds and the C in $\text{C}=\text{O}$ bonds, respectively.^{53,54} Meanwhile, the CNFs show a distinct peak located at 284.8 eV corresponding to the graphitized carbon. The other two weaker peaks located at 286.3 and 289.3 eV are ascribed to the $\text{C}-\text{O}$ or $\text{C}-\text{N}$ bonds and $\text{C}=\text{O}$ bonds. The $\text{C}=\text{O}$ groups of PANFs are due to the two different chemical environments of oxygen in methyl acrylate (PAN contains 10 wt% of methyl acrylate), while the $\text{C}=\text{O}$ groups of CNFs are due to the oxygen-containing groups on the surface of the nanofibers, which are similar to those of our previous studies.⁴¹ The $\text{O } 1\text{s}$ XPS spectra of PANFs exhibit two peaks at 532.5 eV and 534.2 eV associated with the chemical environments of oxygen in carbonyl groups of methyl acrylate. Focusing on the CNFs, the $\text{O } 1\text{s}$ spectra show two peaks located at 530.2 and 532.1 eV may be due to adsorbed oxygen, and carbonyl groups.

The higher binding energy peak at 533.8 eV possibly originates from absorbed H_2O , which is similar to the previous reports.^{53–55} The $\text{N } 1\text{s}$ spectra of the PANFs exhibit a significant peak at 398.8 eV and it can be assigned to the nitrogen atoms that bond with carbon atoms in the form of $\text{C}\equiv\text{N}$ bonds.⁵¹ Meanwhile, after the graphitization process, the CNFs show two very weak bands centered at 399.0 eV and 401.7 eV , which are attributed to the $\text{C}\equiv\text{N}$ species and pyridinic nitrogen, demonstrating the formation of the $\text{C}=\text{C}-\text{C}=\text{N}$ structure. The above results confirm the conversion in the chemical structures from $\text{C}\equiv\text{N}$ to $\text{C}=\text{C}-\text{C}=\text{N}$ structure during the graphitization process. Based on the FTIR and XPS results, the conversion in chemical structures from PANFs to CNFs is illustrated in Fig. S1.† The graphitization processes for the conversion from PANFs to CNFs are divided into three steps: oxidative stabilization, high-temperature carbonization, and graphitization.⁵⁶ The stabilization of PANFs treated at $280\text{ }^{\circ}\text{C}$ can ensure both the molecules and the molecular orientation. At this stage, the adjacent cyano groups reacted with each other and thus, the macromolecules cross-link together through the chemical bonds. Through the carbonization and graphitization process, the chemical structures convert from $\text{C}\equiv\text{N}$ to $\text{C}=\text{C}-\text{C}=\text{N}$ structure, forming the aromatic structure and then graphene layered structures.

Based on the above results, the graphitization process would lead to the significant shrinkages of the nanofibers and the structure conversions from amorphous to graphene layered

structures. The high graphitization temperature and fast heating rate could lead to the dramatic shrinkage of the nanofibers, which are the key for the migration of AuNPs from the interior to the exterior of the nanofibers.

In the follow study, we performed the control experiments for the conversion from Au-PANFs to Au-CNf with different graphitization temperatures and heating rates. As shown in Fig. 5a and e, the Au-PANFs with higher mass ratio of $\text{HAuCl}_4\cdot 4\text{H}_2\text{O}$ (2.5 wt %) were synthesized to explore the migration and evolution of the AuNPs. As shown in Fig. 5a, large amounts of spherical AuNPs with an average diameter of about $2.5 \pm 0.6\text{ nm}$ are evenly embedded in the interior of PANFs. From the edges of the PANFs (inset in Fig. 5a) and the FE-SEM image of the Au-PANFs, nearly no AuNPs can be observed at the surfaces of PANFs. After the graphitization at $600\text{ }^{\circ}\text{C}$, the average diameter of spherical AuNPs increases to $4.1 \pm 1.1\text{ nm}$ and the AuNPs trend to migrate to the edges of the CNFs, which can be observed in Fig. 5b and f. From Fig. 5f, the FE-SEM image of Au-CNf ($600\text{ }^{\circ}\text{C}$, $2\text{ }^{\circ}\text{C min}^{-1}$) exhibits that a lot of AuNPs break through the CNFs and immobilize on the surfaces of CNFs. In addition, there is still space among the AuNPs and non-aggregated AuNPs.

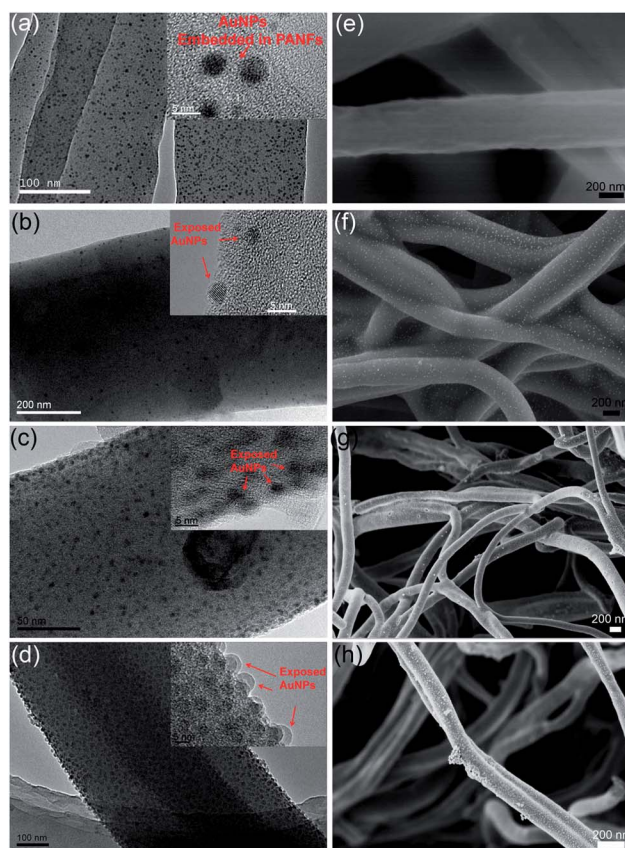


Fig. 5 (a) TEM and (e) FE-SEM images of the Au-PANFs with the mass ratio of 2.5 wt% (PAN and HAuCl_4). TEM and FE-TEM images of Au-CNf with various graphitization temperatures at (b and f) $600\text{ }^{\circ}\text{C}$, (c and g) $800\text{ }^{\circ}\text{C}$ and (a and h) $1000\text{ }^{\circ}\text{C}$, respectively. Insets are the corresponding HRTEM images of the Au-PANFs and Au-CNf. The heating rate of the graphitization process is $2\text{ }^{\circ}\text{C min}^{-1}$.

Meanwhile, the diameter of Au-PANFs is about 530 ± 52 nm while that of the Au-CNFs is about 320 ± 64 nm, indicating the significant shrinkage of the nanofibers. With an increased graphitization temperature of 800°C , as shown in Fig. 5c and g, more and more spherical AuNPs can be found on the surfaces of CNFs and the distance among each AuNP becomes less. In addition, it can be seen from the HRTEM image (inset in Fig. 5c) of the edges of Au-CNFs that the AuNPs are emigrating from the interior of CNFs. The average diameter of the AuNPs increases to 4.9 ± 1.2 nm and the diameter of the Au-CNFs decreases to 260 ± 43 nm, indicating the continuous migration of AuNPs and shrinkage of the nanofibers. When the temperature increased to 1000°C , most of the spherical AuNPs are exposed on the surfaces of the CNFs and the AuNPs are right next to each other (Fig. 5d). The average diameter of the AuNPs increased to 6.9 ± 1.4 nm and the diameter of the Au-CNFs decreased to 210 ± 45 nm. However, although large amounts of AuNPs formed, there were still no aggregated NPs, demonstrating that at the low heating rate, the Au-CNFs with a higher density of exposed AuNPs with small and uniform sizes can be obtained.

Table 1 summarizes the XPS atomic concentrations, mass concentrations and Au 4f BES of the Au-PANFs and CNFs graphitized at 600 , 800 , and 1000°C min^{-1} at a heating rate of 2°C min^{-1} . In our present investigations, we used the same Au-PANF samples to prepare Au-CNF nanofibrous mats and it means that the mass concentration of Au in PANFs before graphitization is constant. The Au-PANFs exhibit the lowest atomic and mass concentrations of Au, which are 0.06 and 0.96% , suggesting the lowest density of exposed AuNPs on the surfaces. Through graphitization at 600 , 800 , and 1000°C , the atomic and mass concentrations increase to 0.21% and 3.12% , 0.38% and 4.92% , and 0.95% and 8.04% , demonstrating the increased densities of exposed AuNPs on the surfaces of CNFs. Compared with the BES of Au 4f of Au-PANFs (84.3 and 88.0 eV), the Au-CNFs graphitized at 600 , 800 , and 1000°C exhibit lower BES. With increased graphitization temperatures, the BES of Au 4f get closer to the BES of Au^0 (87.7 eV and 84.0 eV), suggesting the migration of AuNPs through the matrix of nanofibers. The changes in the mass concentration and atomic concentration of Au-PANFs and Au-CNFs- 600 , Au-CNFs- 800 and Au-CNFs- 1000 can strongly indicate the migration of AuNPs from the interior to the exterior of CNFs.

Fig. 6 shows the TEM and FE-TEM images of Au-CNFs with various graphitization temperatures at 600 , 800 and 1000°C , respectively. The heating rate of the graphitization process is

5°C min^{-1} . As shown in Fig. 6a to c, a series of evolution can be clearly observed. With increased graphitization temperatures from 600 to 1000°C , compared with the AuNPs embedded in PANFs (3.4 ± 0.6 nm), the average diameters of the AuNPs increased to 5.8 ± 1.1 , 8.3 ± 2.3 and 10.2 ± 2.7 nm, respectively, which are similar to those shown in Fig. 6. In addition, compared with those of Au-PANFs (530 ± 52 nm), the diameters of Au-CNFs decrease to 306 ± 67 , 234 ± 52 , and 195 ± 48 nm, respectively, indicating the enormous shrinkage of nanofibers. The evolution of the migration of AuNPs can be clearly observed in the HRTEM images in Fig. 6a–c. At 600°C , a little area of AuNPs is exposed and coated by three graphene layers, indicating the migration of AuNPs. Both the fringe of the AuNPs and graphitic carbon shells can be simultaneously observed in the insets of Fig. 6a. The lattice spacings of 0.23 nm and 0.36 nm are ascribed to the (111) plane of Au crystals and the (002) lattice plane of graphite, respectively.

Typically, upon increasing the temperature to 800°C , more area of AuNPs are exposed from the interior of the nanofibers and coated by two graphene layers. With continuous increase to 1000°C , the AuNPs are almost broken through the nanofibers and immobilized on the surfaces (Fig. 6c). The exposed AuNPs are also coated by two graphene layers. The complete migration process of AuNPs from the interior of PANFs to the exterior of CNFs can be clearly observed. The exposed AuNPs are surrounded by several graphene layers while the AuNPs embedded in PANFs are surrounded by large amounts of PAN macromolecules, which are consistent with the XPS results (Fig. 2). Note that as shown in Fig. 6c and f, more and more adjacent AuNPs formed, indicating the aggregation of AuNPs.

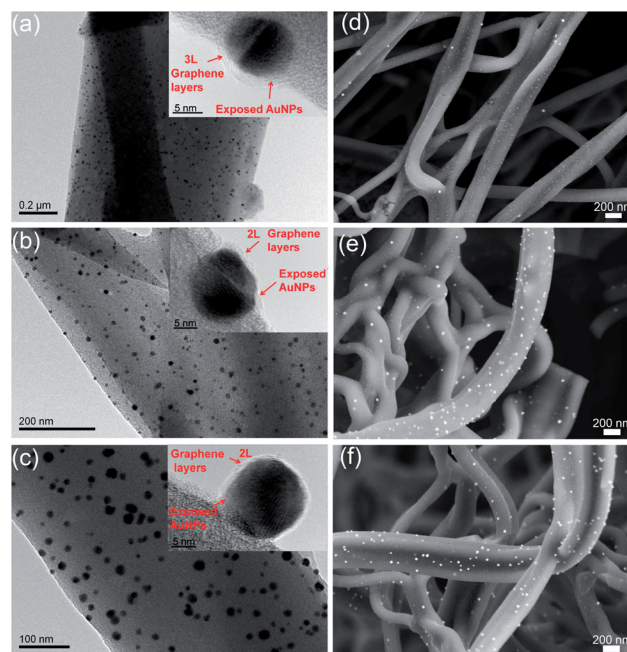


Fig. 6 TEM and FE-TEM images of Au-CNFs with various graphitization temperatures at (a and d) 600°C , (b and e) 800°C and (c and f) 1000°C , respectively. Insets are the corresponding HRTEM images of the AuNPs. The heating rate of the graphitization process is 5°C min^{-1} .

Table 1 XPS atomic concentrations, mass concentrations and Au 4f BES of the Au-PANFs and CNFs graphitized at 600 , 800 , and 1000°C min^{-1} at a heating rate of 2°C min^{-1}

Samples	Au 4f binding energy (eV)	Atomic concentrations (%)	Mass concentrations (%)
Au-PANFs	84.3, 88.0	0.06	0.92
Au-CNFs-600	84.2, 87.9	0.21	3.12
Au-CNFs-800	84.2, 87.8	0.38	4.92
Au-CNFs-1000	84.1, 87.8	0.95	8.04

When the heating rate increased to $10\text{ }^{\circ}\text{C min}^{-1}$, as shown in Fig. 7a and d, the Au–CNFs ($600\text{ }^{\circ}\text{C}$) exhibit high density of exposed AuNPs on the surfaces of CNFs. Compared with Au–PANFs, the average diameter of the AuNPs increases to $10.7 \pm 2.8\text{ nm}$ and at this temperature and heating rate, the AuNPs still remain spherical. With the temperature increased to $800\text{ }^{\circ}\text{C}$, the exposed AuNPs tend to collide with adjacent NPs and grow up to larger sized AuNPs with irregular shape (Fig. 7b and e). Fig. 7c and f show the Au–CNFs carbonized at $1000\text{ }^{\circ}\text{C}$, and the spherical AuNPs embedded in PANFs grew up to larger sized AuNPs with irregular shapes immobilized on the CNFs, indicating the migration and ripening phenomena of AuNPs. The average diameter of the AuNPs with irregular shapes graphitized at 800 and $1000\text{ }^{\circ}\text{C}$ are 18.2 ± 3.7 and $25.5 \pm 5.1\text{ nm}$. Compared with Au–PANFs, the diameter of Au–CNFs decreased to $260\text{ nm} \pm 42$, 205 ± 38 and $180 \pm 36\text{ nm}$, demonstrating the remarkable shrinkage of the nanofibers.

The heating temperature ranging from 300 to $500\text{ }^{\circ}\text{C}$ belongs to the carbonization process. At a low heating rate ($2\text{ }^{\circ}\text{C min}^{-1}$) and heating temperature ($600\text{ }^{\circ}\text{C}$), the AuNPs with low exposed area have already emerged from the nanofibers (Fig. 6b). However, the AuNPs did not completely come out from the interior of nanofibers until the temperature increased to $1000\text{ }^{\circ}\text{C}$ (Fig. 6d). However, at $1000\text{ }^{\circ}\text{C}$, the exposed AuNPs still remain small ($6.9 \pm 1.4\text{ nm}$) and are uniformly spherical in shape without any aggregated NPs. Upon increasing the heating rate to $5\text{ }^{\circ}\text{C min}^{-1}$, the migration of AuNPs became faster in comparison with those shown in Fig. 7. The diameters of the AuNPs of Au–CNFs increase from 5.8 ± 1.1 to $10.2 \pm 2.7\text{ nm}$

along with the increased heating temperatures from 600 to $800\text{ }^{\circ}\text{C}$, indicating that the faster heating rate results in the greater shrinkage and collisions of AuNPs to form larger sized AuNPs. Based on the above results, with the heating rate at $5\text{ }^{\circ}\text{C min}^{-1}$ and graphitization temperature at $1000\text{ }^{\circ}\text{C}$, the AuNPs can completely expose on the surfaces of CNFs. Table 2 summarizes the statistics of the diameter of AuNPs embedded in PANFs and AuNPs immobilized on CNFs at different graphitization temperatures of 600 , 800 and $1000\text{ }^{\circ}\text{C}$ and heating rates of 2 , 5 , and $10\text{ }^{\circ}\text{C min}^{-1}$.

It can be concluded that the higher graphitization temperature and faster heating rate can strongly influence the shrinkage of the nanofibers and the sizes of AuNPs. In addition, the higher graphitization temperature and fast heating rate could result in the aggregation of AuNPs into larger ones that are inclined to be exposed on the surface of the CNFs. Therefore, these results can strongly support the assumption, that is, during the graphitization, with the conversion from amorphous structures to graphene layered structures, the pre-formed AuNPs embedded in PANFs can move around the randomly oriented graphene layers. Meanwhile, along with the shrinkage of nanofibers, the AuNPs can migrate to the surfaces of the CNFs.

To further investigate the migration of the AuNPs on the external surfaces of AuNPs, we performed a control experiment to count the number of AuNPs on CNFs. Fig. 8 shows the TEM and HAADF-STEM images of the Au–CNFs with low mass ratio of HAuCl_4 ($0.5\text{ wt}\%$) treated at $1000\text{ }^{\circ}\text{C}$ ($5\text{ }^{\circ}\text{C min}^{-1}$). As shown in Fig. 8a, the AuNPs are evenly dispersed in the CNFs and however, it cannot be determined whether the AuNPs are embedded in the interior of CNFs or immobilized on the exterior of the CNFs. Focusing on the HAADF-STEM images of the Au–CNFs, it can be clearly observed that the AuNPs (bright spots) are indeed immobilized on the surfaces of the CNFs. The exposed density of the AuNPs in Fig. 8b is almost consistent with the AuNPs dispersed in CNFs in Fig. 8a. The STEM-EDS mapping images of the Au–CNFs taken randomly were to further investigate the locations of the AuNPs.

Fig. 8c shows the mapping area of the Au–CNFs and Fig. 8d exhibits the STEM-EDS mapping image of CNF constructed by

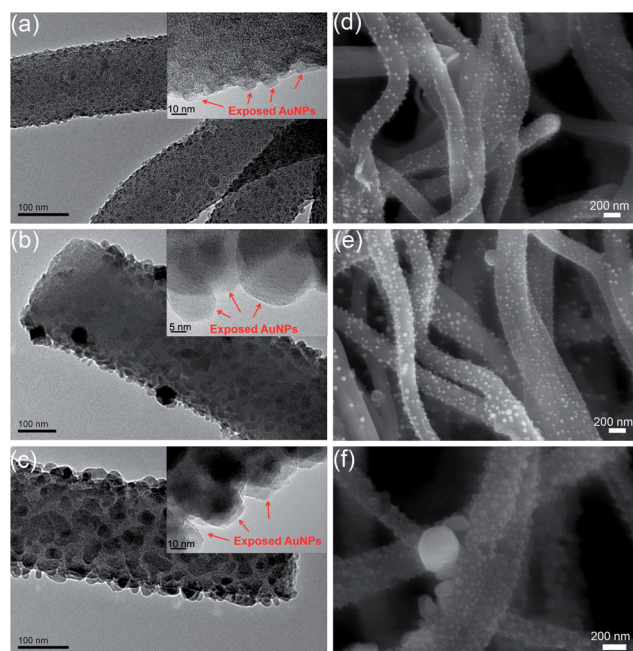


Fig. 7 TEM and FE-TEM images of Au–CNFs with various graphitization temperatures at (a and d) $600\text{ }^{\circ}\text{C}$, (b and e) $800\text{ }^{\circ}\text{C}$ and (c and f) $1000\text{ }^{\circ}\text{C}$, respectively. Insets are the corresponding HRTEM images of the AuNPs. The heating rate of the graphitization process is $10\text{ }^{\circ}\text{C min}^{-1}$.

Table 2 The statistics of the AuNPs embedded in PANFs and AuNPs immobilized on CNFs at different graphitization temperatures and heating rates

Samples	Average diameters of AuNPs (nm)	Average diameters of nanofibers (nm)	Heating rates ($^{\circ}\text{C min}^{-1}$)
Au–PANFs	2.5 ± 0.6	530 ± 52	
Au–CNFs-600	4.1 ± 1.1	320 ± 64	2
Au–CNFs-800	4.9 ± 1.2	260 ± 43	2
Au–CNFs-1000	6.9 ± 1.4	210 ± 45	2
Au–CNFs-600	5.8 ± 1.1	306 ± 67	5
Au–CNFs-800	8.3 ± 2.3	234 ± 52	5
Au–CNFs-1000	10.2 ± 2.7	195 ± 48	5
Au–CNFs-600	10.7 ± 2.8	260 ± 42	10
Au–CNFs-800	18.2 ± 3.7	205 ± 38	10
Au–CNFs-1000	23.5 ± 5.1	180 ± 36	10

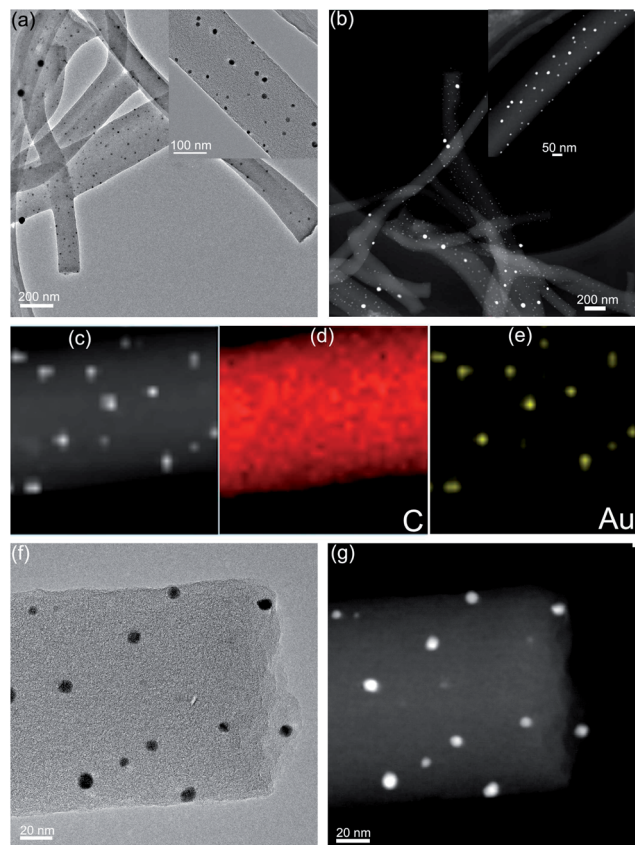


Fig. 8 (a) TEM and (b) HAADF-STEM images of the Au-CNFs graphitized at 1000 °C (5 °C min⁻¹) with low mass ratio of HAuCl₄ (0.5 wt%). Insets are the corresponding high-resolution TEM and HAADF-STEM images of single Au-CNFs. (c) HAADF-STEM and (d and e) STEM-EDS mapping images of the randomly selective area of the Au-CNFs. (f) TEM and (g) HAADF-STEM images of the Au-CNFs taken at the same areas.

carbon elements. Compared with the mapping area of CNFs in Fig. 8c, the yellow bright spots in Fig. 8e are constructed by Au elements and the shapes, locations and sizes are exactly the same. Twelve yellow spots (AuNPs) can be clearly observed, which are consistent with the number of the AuNPs in Fig. 8c, confirming the exposed AuNPs on the surfaces of CNFs. As shown in Fig. 8f, there are eleven AuNPs dispersed on CNFs. Compared with Fig. 8f, the HAADF-STEM image of the same area also exhibits eleven AuNPs with the same locations, shapes and sizes, locating on the surface of the CNF. Therefore, at a heating rate of 5 °C min⁻¹ and graphitization temperature of 1000 °C, the initial AuNPs embedded in PANFs were migrated to the surfaces of CNFs.

On the basis of the above investigations, a schematic is displayed in Fig. 9 to summarize the behaviours of AuNPs migrated from the interior of PANFs to the external surfaces of CNFs during the graphitization process. According to our previous study, the small and well-dispersed AuNPs embedded in PANFs were synthesized by an *in situ* reduction approach.^{41,42} The PAN macromolecule with abundant cyano groups (C≡N) can effectively anchor the AuNPs because of the strong chelating effect.^{41,42} In addition, the PAN macromolecules both

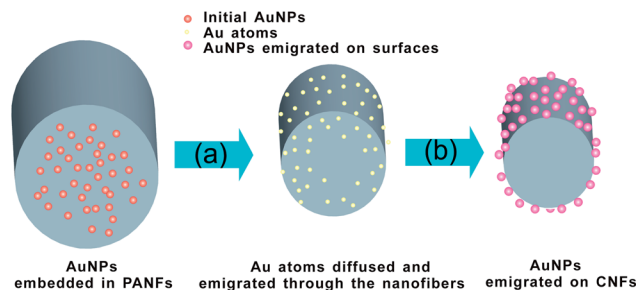


Fig. 9 Schematics of the behaviours of AuNPs migrated through the nanofibers during the graphitization process: (a) the melting of initial AuNPs embedded in PANFs and the diffusion and migration of Au atoms through the matrix of nanofibers. (b) The Au atoms diffused and migrated to the surfaces of the CNFs and grew up to AuNPs.

acted as chelating agents and stabilizers to protect the AuNPs from aggregations, leading to uniform and well-dispersed AuNPs. During the carbonization process, the C≡N structure started to get converted to the C=C-C≡N structure, forming the aromatic structures and the graphene layer structures. Without the stabilization of the C≡N groups, the pre-formed AuNPs embedded in PANFs can migrate around the randomly oriented graphene layers.

It is reported that the metal NPs exhibit size-dependent meltings.⁵⁷ For particles of spherical geometry with diameter D :

$$T_m/T_b = 1 - C/D,$$

where T_m is the melting temperature of the NPs with diameter D , T_b is the melting temperature of bulk solids (Au: $T_b = 1338$ K), and C is the material constant (Au: $C = 1.1281$ nm). As discussed above, the average diameter of the initial AuNPs embedded in PANFs is 2.5 ± 0.6 nm and according to the equation, the melting temperature of the AuNPs is 734 K (461 °C), which is below the graphitization temperatures at 600 °C. Therefore, when AuNPs were treated at elevated temperatures, the initial AuNPs melted into an atom scale. The size of Au atoms is smaller than the spaces of graphene layers of the CNFs (0.37 nm) and therefore, the Au atoms can migrate and diffuse through the graphene layers. In our case, the randomly oriented graphene layers provide many potential paths (nanochannels) connecting the inner nanofibers and the external environment. However, these paths are not straight, but tortuous, thus, the distance for atoms to pass the nanofibers to the surfaces is largely exceeding the nanofiber thickness.

Under the same conditions, the Au atoms closer to the surfaces of nanofibers had smaller migratory distances and preferentially migrated to the surfaces. More and more preferentially migratory Au atoms were nucleated at the surfaces and grew up to NPs. The migration rates and diffusion of Au atoms were strongly dependent on the graphitization temperatures and heating rates. Higher graphitization temperatures and heating rates lead to faster molecular movement, indicating the faster migration and diffusion of Au atoms. Therefore, Au atoms with faster migration and diffusion rates get easily exposed on the surfaces of nanofibers, while the slower ones still remain in

the matrix of nanofibers. Along with the shrinkages of nanofibers, more and more Au atoms diffused and migrated to the surfaces of the CNFs and grew up to AuNPs. The larger size of AuNPs immobilized on CNFs was caused by the aggregation of the small AuNPs because of the faster diffusion of Au atoms during the carbonization process. Because of the high treatment temperature and the migration of the AuNPs, the neighboring AuNPs may collide with each other and then age to larger AuNPs.

To confirm this new strategy is a general approach for the fabrication of CNF-noble metal nanostructures, Pt-CNF hybrid nanostructures were also prepared by the method. As shown in Fig. 10a and c, the PtNPs with an average diameter of 4.4 ± 0.9 nm were evenly dispersed in the interior of PANFs. After graphitization at 1000°C with the heating rate of 5°C min^{-1} , most of the PtNPs were exposed on the surfaces of CNFs and the diameter of PtNPs increases to 10.7 ± 2.5 nm. The observed phenomena are similar to the Au-CNF systems, indicating that the new strategy is not only applicable to the Au system but also employed for the fabrication of other noble metal-CNF nanostructures.

Compared with the bulk metal electrode, such small, uniform and well-dispersed AuNPs immobilized on the surfaces of CNFs possess high ratio of surface atoms with free valences to the cluster of total atoms and can provide electrochemical reversibility for the redox reactions.^{6,7} Fig. 11 shows the cyclic voltammograms (CVs) of CNFs and Au-CNF functionalized GCE with H_2O_2 in the presence of hydroquinone (HQ). According to the reported literature,^{22,51} high graphitization temperatures would lead to the higher conductivity because of their increasing degree of graphitization of CNFs. Therefore, we investigated the electrochemical properties of CNFs and Au-CNFs with different graphitization temperatures and heating rates to study their morphology-dependent electrochemical activities. As shown in Fig. 11A, curve a is ascribed to the CVs of CNFs (graphitized at 1000°C) with H_2O_2 in 5 mM HQ and much weak redox peaks can be observed. The curves b, c and d are ascribed to the CVs of Au-CNFs graphitized at 600, 800, and 1000°C with a heating rate of 2°C min^{-1} . Compared to the CVs

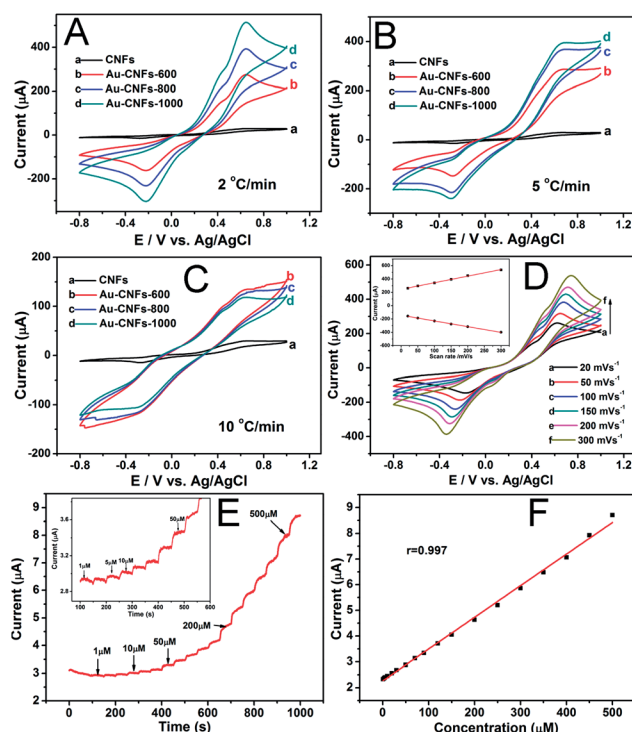


Fig. 11 (A–C) The electrochemical properties of CNFs and Au-CNFs with different graphitization temperatures and heating rates. CVs of (a) CNF/GCE, (b) Au-CNFs-600/GCE, (c) Au-CNFs-800/GCE and Au-CNFs-1000/GCE biosensor with 5.0 mM HQ in 0.1 M PBS in the presence of 5.0 mM H_2O_2 (scan rate, 50 mV s^{-1}). (D) CVs of Au-CNFs-1000/GCE (2°C min^{-1}) in 1.0 mM H_2O_2 with different scan rates and the inset shows the relationship between the redox peak currents and scan rates; (E) amperometric response of the fabricated Au-CNFs-1000/GCE (2°C min^{-1}) sensor to successive addition of different concentrations of H_2O_2 to 1.0 M PBS and the inset shows the response of the sensor from $1\text{ }\mu\text{M}$ to $50\text{ }\mu\text{M}$ H_2O_2 ; and (F) relationship of the calibration curve and the linear fitting curve between the currents and the H_2O_2 concentration.

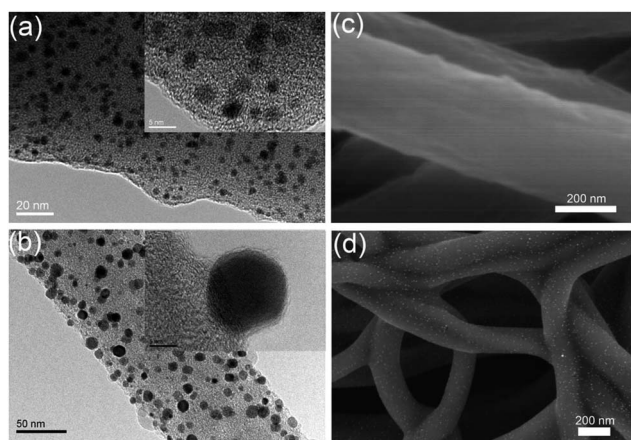


Fig. 10 TEM and FE-SEM images of the (a and c) Pt-PANFs and (b and d) Pt-CNFs (1000°C , 5°C min^{-1}) hybrid nanostructures. Insets are the corresponding HRTEM images.

of CNFs (curve a) with Au-CNFs in HQ with H_2O_2 (curve b to d), significant redox peaks of Au-CNFs are obtained, indicating the electroactive property of Au-CNFs. It can be clearly observed that even the sizes of the AuNPs on CNFs increased from 4.1 to 6.9 nm, the intensity of the redox peaks significantly increased with the increased density of exposed AuNPs (Fig. 11A, curve b to d). The Au-CNFs-1000 with high density of exposed AuNPs possesses higher specific surface area and active sites. It means that more AuNPs will take part in the reactions, leading to the higher electrocatalytic activity. The redox peak currents of HQ (curve d) are about 298.4 and $511.6\text{ }\mu\text{A}$, with potentials at -0.22 and 0.65 V , respectively. When the Au-CNFs were treated by a relatively high heating rate (5°C min^{-1}), the sizes of the AuNPs on CNFs increased from 5.8 to 10.2 nm and the redox peaks of HQ still exhibit a similar trend (Fig. 11B). However, when the heating rate increased to $10^\circ\text{C min}^{-1}$, Fig. 11C indicates an inverse phenomenon that the intensities of the redox peaks of HQ decreased with the graphitization temperature. The sizes of the AuNPs on CNFs increased from 10.7 to 23.5 nm and more serious aggregated AuNPs can be found, resulting in the weak

Table 3 Summary of the response time, detection range, and detection time of as-prepared H₂O₂ electrochemical sensors in comparison with other reported sensors

Electrochemical sensor	Response time (s)	Detection range (μM)	Detection limit (μM)	Ref.
Au-CNFs	1	1–500	0.42	This work
HRP-AuNP-PVA	1	1–500	0.5	58
HRP-AgNP-PVA/PEI	2	5–550	2.5	30
HRP-Ag-PVA	2	10–560	5.6	31
HRP-AuNP cellulose NFs	1	1–500	1	59
HRP-Fe ₃ O ₄ -silica	No data	2–24	0.43	60
HRP-sonogel-carbon	No data	4–100	1.6	61

electrochemical activity of AuNPs. The increased density of the AuNPs on CNFs cannot offset the decrease in the activities of AuNPs caused by the larger size and aggregation.

Therefore, slower heating rates ($2\text{--}5\text{ }^{\circ}\text{C min}^{-1}$) would lead to a small increase in the sizes of AuNPs (below 10 nm) and the higher graphitization temperatures would bring about the higher exposed density of AuNPs on the surfaces of CNFs (600–1000 $^{\circ}\text{C}$). The synergistic effects between the smaller size and higher exposed density of AuNPs lead to the increased electrochemical activity. Because of the highest electrochemical activity, we use the Au-CNFs-1000/GCE ($2\text{ }^{\circ}\text{C min}^{-1}$) to evaluate the detection limits of the constructed biosensors. Fig. 11D exhibits CV curves of Au-CNFs-1000 ($2\text{ }^{\circ}\text{C min}^{-1}$) at different scan rates ranging from 20 to 300 mV s^{-1} . It is obvious that the shape of the CVs almost does not change in the range varied from 20 to 300 mV s^{-1} and the total peak current density increases with increasing potential scan rates, which demonstrates a good rate property and excellent electrochemical behavior for the Au-CNFs-1000 ($2\text{ }^{\circ}\text{C min}^{-1}$) functionalized electrode. Meanwhile, the inset in Fig. 11B shows that there is a linear relationship between the redox peak current density and the scan rate for the electrode materials, indicating that the electrode process is a surface-controlled process.

For the amperometric sensing application, the Au-CNFs-1000 ($2\text{ }^{\circ}\text{C min}^{-1}$) functionalized GCE electrodes are generally evaluated by measuring the current response at a working potential of 0.0 V for the detection of H₂O₂. Fig. 11E displays the amperometric response at the CNFs and the Au-CNFs-1000 ($2\text{ }^{\circ}\text{C min}^{-1}$) modified GCE towards the successive addition of H₂O₂. As shown in Fig. S2,† the CNF/GCE exhibits a weaker response to the addition of H₂O₂, while the Au-CNF/GCE shows a larger catalytic current to the changes of the H₂O₂ concentration (Fig. 11E). The rapid electrode response to the change of the H₂O₂ concentration could be attributed largely to the well-dispersed AuNPs immobilized on the Au-CNFs, which could effectively promote the electron transfer rate between the H₂O₂ and the electrode. With the continued addition of H₂O₂, the sensor responded rapidly to the substrates and could achieve 90% of the steady-state current within 3 s, indicating the fast amperometric response to the reduction of H₂O₂. Fig. 11F shows a linear relationship of the concentration of H₂O₂ with the correlation coefficient of 0.997. The detection limit of 0.42 μM was estimated at a signal-to-noise ratio of 3.

Most of the biosensors for the detection of H₂O₂ should be assisted by immobilizing the horseradish peroxidase (HRP). In

our present investigations, the constructed nonenzymatic sensors show lower detection limit and wider responding range for H₂O₂ without any enzyme. Table 3 summaries the response time, detection range, and detection time of as-prepared H₂O₂ electrochemical sensors in comparison with other reported sensors. It can be clearly observed that our sensors without any enzyme exhibit lower detection limits and faster response than those systems with HRP as reported in the literature.

In addition, the Au-CNF electrochemical sensors exhibit good reproducibility in the detection of H₂O₂ with a relative standard deviation (RSD) of about 3.3% in the presence of 5.0 mM of H₂O₂ obtained by recycling for more than 10 measurements. The fabricated Au-CNF electrodes used 10 times were compared by the CV curves (Fig. S3†) and the redox peaks are almost the same, indicating the excellent stability and reusability of electrochemical sensors. The sensors show lower detection limit and wider responding range, indicating that the fabricated sensor could be potentially used for monitoring the concentration of H₂O₂ without any enzyme.

Conclusions

A novel strategy for the design of novel nanostructures to show an unexpected behavior of AuNPs embedded in the interior of PANFs, which can migrate to the external surfaces of the CNFs during the graphitization process have been demonstrated. With the conversion from the amorphous structures of PANFs to graphene layered structures of CNFs, the initial AuNPs embedded in the interior of the PANFs migrate to the external surfaces of CNFs. The migration of AuNPs through the nanofiber matrix are strongly dependent on the graphitization temperature and heating rates. Three different heating rates at 2, 5, and 10 $^{\circ}\text{C min}^{-1}$ and graphitization temperatures at 600, 800, and 1000 $^{\circ}\text{C}$, respectively, were performed to investigate the migration and the exposed density of AuNPs on the CNFs. In addition, the conversion in the chemical structures from the $\text{C}\equiv\text{N}$ structure to the $\text{C}=\text{C}-\text{C}=\text{N}$ structure during the graphitization process was investigated. The migration phenomena of AuNPs are explained by an atom diffusion mechanism. These novel nanomaterials were constructed as a nonenzymatic H₂O₂ electrochemical sensor. The electrochemical sensors based on AuNPs with different densities of exposed AuNPs exhibit significant promoted electrochemical activity with increased density of exposed AuNPs. The Au-CNFs with high density of exposed AuNPs possess higher specific surface area and active

sites. It means that more AuNPs will take part in the reactions, leading to higher electrocatalytic activity. The sensor showed lower detection limit and wider responding range, indicating that the fabricated sensor could be potentially used for monitoring the concentration of H_2O_2 without any enzyme. The present investigations provide a general route for the fabrication of nanostructures for novel electrochemical sensors, energy storage devices and so on.

Acknowledgements

This work was supported by the National Natural Science Foundation of China (NSFC) (51373154), the 521 Talent Project of Zhejiang Sci-Tech University and the Key Discipline Open Fund of the Zhejiang Province (2014KF01).

Notes and references

- 1 X. Y. Lang, H. Y. Fu, C. Hou, G. F. Han, P. Yang, Y. B. Liu and Q. Jiang, *Nat. Commun.*, 2013, **4**, 2169.
- 2 P. Lin and F. Yan, *Adv. Mater.*, 2012, **24**, 34–51.
- 3 C. Marichy, M. Bechelany and N. Pinna, *Adv. Mater.*, 2012, **24**, 1017–1032.
- 4 L. Matlock-Colangelo and A. J. Baeumner, *Lab Chip*, 2012, **12**, 2612–2620.
- 5 Y. Q. Wang, B. Yan and L. X. Chen, *Chem. Rev.*, 2013, **113**, 1391–1428.
- 6 L. N. Cella, W. Chen, N. V. Myung and A. Mulchandani, *J. Am. Chem. Soc.*, 2010, **132**, 5024–5026.
- 7 X. M. Feng, R. M. Li, Y. W. Ma, R. F. Chen, N. E. Shi, Q. L. Fan and W. Huang, *Adv. Funct. Mater.*, 2011, **21**, 2989–2996.
- 8 Y. D. Jin, *Adv. Mater.*, 2012, **24**, 5153–5165.
- 9 S. Myung, A. Solanki, C. Kim, J. Park, K. S. Kim and K. B. Lee, *Adv. Mater.*, 2011, **23**, 2221–2225.
- 10 R. J. Chen, H. C. Choi, S. Bangsaruntip, E. Yenilmez, X. W. Tang, Q. Wang, Y. L. Chang and H. J. Dai, *J. Am. Chem. Soc.*, 2004, **126**, 1563–1568.
- 11 H. Im, X. J. Huang, B. Gu and Y. K. Choi, *Nat. Nanotechnol.*, 2007, **2**, 430–434.
- 12 Y. Xiang and Y. Lu, *Nat. Chem.*, 2011, **3**, 697–703.
- 13 N. J. Ronkainen, H. B. Halsall and W. R. Heineman, *Chem. Soc. Rev.*, 2010, **39**, 1747–1763.
- 14 J. Wang, *Chem. Rev.*, 2008, **108**, 814–825.
- 15 S. Mao, G. H. Lu, K. H. Yu, Z. Bo and J. H. Chen, *Adv. Mater.*, 2010, **22**, 3521–3526.
- 16 J. Lu, I. Do, L. T. Drzal, R. M. Worden and I. Lee, *ACS Nano*, 2008, **2**, 1825–1832.
- 17 A. L. Torre, M. D. C. Gimenez-Lopez, M. W. Fay, G. A. Rance, W. A. Solomonsz, T. W. Chamberlain, P. D. Brown and A. N. Khlobystov, *ACS Nano*, 2012, **6**, 2000–2007.
- 18 K. Besteman, J. O. Lee, F. G. M. Wiertz, H. A. Heering and C. Dekker, *Nano Lett.*, 2003, **3**, 727–730.
- 19 J. Wang, M. Musameh and Y. H. Lin, *J. Am. Chem. Soc.*, 2003, **125**, 2048–2049.
- 20 J. B. Mu, C. L. Shao, Z. C. Guo, Z. Y. Zhang, M. Y. Zhang, P. Zhang, B. Chen and Y. C. Liu, *ACS Appl. Mater. Interfaces*, 2011, **3**, 590–596.
- 21 A. Stein, Z. Y. Wang and M. A. Fierke, *Adv. Mater.*, 2009, **21**, 265–293.
- 22 X. W. Mao, F. Simeon, G. C. Rutledge and T. A. Hatton, *Adv. Mater.*, 2013, **25**, 1309–1314.
- 23 A. Greiner and J. H. Wendorff, *Angew. Chem., Int. Ed.*, 2007, **46**, 5670–5703.
- 24 L. W. Ji, O. Toprakci, M. Alcoutlabi, Y. F. Yao, Y. Li, S. Zhang, B. K. Guo, Z. Lin and X. W. Zhang, *ACS Appl. Mater. Interfaces*, 2012, **4**, 2672–2679.
- 25 X. F. Lu, X. J. Bian, G. D. Nie, C. C. Zhang, C. Wang and Y. Wei, *J. Mater. Chem.*, 2012, **22**, 12723–12730.
- 26 P. Q. Wang, D. Zhang, F. Y. Ma, Y. Ou, Q. N. Chen, S. H. Xie and J. Y. Li, *Nanoscale*, 2012, **4**, 7199–7204.
- 27 J. S. Bonso, G. D. Kalaw and J. P. Ferraris, *J. Mater. Chem. A*, 2014, **2**, 418–424.
- 28 M. R. Langille, M. L. Personick and C. A. Mirkin, *Angew. Chem., Int. Ed.*, 2013, **52**, 13910–13940.
- 29 A. S. Urban, X. S. Shen, Y. M. Wang, N. Large, H. Wang, M. W. Knight, P. Nordlander, H. Y. Chen and N. J. Halas, *Nano Lett.*, 2013, **13**, 4399–4403.
- 30 H. Zhu, M. L. Du, M. Zhang, P. Wang, S. Y. Bao, L. N. Wang, Y. Q. Fu and J. M. Yao, *Biosens. Bioelectron.*, 2013, **49**, 210–215.
- 31 H. Zhu, M. L. Du, M. Zhang, P. Wang, S. Y. Bao, Y. Q. Fu and J. M. Yao, *Sens. Actuators, B*, 2013, **185**, 608–619.
- 32 H. Zhu, M. Zhang, S. Y. Cai, Y. T. Cai, P. Wang, S. Y. Bao, M. L. Zou and M. L. Du, *RSC Adv.*, 2014, **4**, 794–804.
- 33 H. Zhu, M. L. Du, M. Zhang, P. Wang, S. Y. Bao, M. L. Zou, Y. Q. Fu and J. M. Yao, *Biosens. Bioelectron.*, 2014, **54**, 91–101.
- 34 J. Li, S. B. Tang, L. Lu and H. C. Zeng, *J. Am. Chem. Soc.*, 2007, **129**, 9401–9409.
- 35 I. Kvande, J. Zhu, T. J. Zhao, N. Hammer, M. Ronning, S. Raaen, J. C. Walmsley and D. Chen, *J. Phys. Chem. C*, 2010, **114**, 1752–1762.
- 36 D. Y. Shin, B. Jeong, B. S. Mun, H. Jeon, H. J. Shin, J. Baik and J. Lee, *J. Phys. Chem. C*, 2013, **117**, 11619–11624.
- 37 S. Hermans, V. Bruyr and M. A. Devillers, *J. Mater. Chem.*, 2012, **22**, 14479–14486.
- 38 C. H. Liang, W. Xia, M. V. D. Berg, Y. M. Wang, H. Soltani-Ahmadi, O. Schluter, R. A. Fischer and M. Muhler, *Chem. Mater.*, 2009, **21**, 2360–2366.
- 39 Z. X. Yang, G. D. Du, Z. P. Guo, X. B. Yu, S. Li, Z. X. Chen, P. Zhang and H. K. Liu, *Nanoscale*, 2010, **2**, 1011–1017.
- 40 H. Q. Hou and D. H. Reneker, *Adv. Mater.*, 2004, **16**, 69–73.
- 41 H. Zhu, M. L. Du, M. L. Zou, C. S. Xu, N. Li and Y. Q. Fu, *J. Mater. Chem.*, 2012, **22**, 9301–9307.
- 42 M. L. Zou, M. L. Du, H. Zhu, C. S. Xu, N. Li and Y. Q. Fu, *Polym. Eng. Sci.*, 2013, **53**, 1099–1108.
- 43 L. J. Wang, J. H. Hu, H. Y. Zhang and T. Zhang, *Chem. Commun.*, 2011, **47**, 6837–6839.
- 44 C. Y. Su, Y. F. Tong, M. Y. Zhang, Y. Zhang and C. L. Shao, *RSC Adv.*, 2013, **3**, 7503–7512.
- 45 Y. Aykut, *ACS Appl. Mater. Interfaces*, 2012, **4**, 3405–3415.
- 46 B. S. Lee, S. B. Son, K. M. Park, G. S. Lee, K. H. Oh, S. H. Lee and W. R. Yu, *ACS Appl. Mater. Interfaces*, 2012, **4**, 6702–6710.
- 47 Z. C. Xu, Y. L. Hou and S. H. Sun, *J. Am. Chem. Soc.*, 2007, **129**, 8698–8699.

- 48 H. Zhu, M. L. Du, D. L. Yu, Y. Wang, L. N. Wang, M. L. Zou, M. Zhang and Y. Q. Fu, *J. Mater. Chem. A*, 2013, **1**, 919–929.
- 49 Y. Negishi, K. Nobusada and T. Tsukuda, *J. Am. Chem. Soc.*, 2005, **127**, 5261–5270.
- 50 A. Tanaka, Y. Takeda, M. Imamura and S. Sato, *Phys. Rev. B: Condens. Matter Mater. Phys.*, 2003, **68**, 195415.
- 51 W. Li, L. S. Zhang, Q. Wang, Y. Yu, Z. Chen, C. Y. Cao and W. G. Song, *J. Mater. Chem.*, 2012, **22**, 15342–15347.
- 52 J. Q. Wang, K. Pan, E. P. Giannelis and B. Cao, *RSC Adv.*, 2013, **3**, 8978–8987.
- 53 A. G. El-Deen, N. A. M. Barakat, K. A. Khalil and H. Y. Kim, *J. Mater. Chem. A*, 2013, **1**, 11001–11010.
- 54 M. Zhang, E. Uchaker, S. Hu, Q. F. Zhang, T. H. Wang, G. Z. Cao and J. Y. Li, *Nanoscale*, 2013, **5**, 12342–12349.
- 55 J. N. Wang, W. Qin, X. Q. Liu and H. Q. Liu, *RSC Adv.*, 2013, **3**, 11132–11139.
- 56 W. B. Li, Z. H. Yang, G. L. Zhang and Q. Meng, *Ind. Eng. Chem. Res.*, 2013, **52**, 6492–6501.
- 57 K. K. Nanda, S. N. Sahu and S. N. Behera, *Phys. Rev. A: At., Mol., Opt. Phys.*, 2002, **66**, 013208.
- 58 J. Wang, H. B. Yao, D. He, C. L. Zhang and S. H. Yu, *ACS Appl. Mater. Interfaces*, 2012, **4**, 1963–1971.
- 59 T. Zhang, W. Wang, D. Zhang, X. Zhang, Y. Ma, Y. Zhou and L. Qi, *Adv. Funct. Mater.*, 2010, **20**, 1152–1160.
- 60 Y. H. Won, D. Aboagye, H. S. Jang, A. Jitianu and L. A. Stanciu, *J. Mater. Chem.*, 2010, **20**, 5030–5034.
- 61 J. L. H. H. de Cisneros, M. Elkaoutit, I. Naranjo-Rodriguez, M. Dominguez, M. P. Hernandez-Artiga and D. Bellida-Milla, *Electrochim. Acta*, 2008, **53**, 7131–7137.

The design and construction of 3D rose-petal-shaped MoS₂ hierarchical nanostructures with structure-sensitive properties†

Cite this: *J. Mater. Chem. A*, 2014, 2, 7680

Received 27th February 2014
Accepted 28th March 2014

Han Zhu,^a MingLiang Du,^{*ab} Ming Zhang,^{ab} MeiLing Zou,^a TingTing Yang,^a YaQin Fu^{ab} and JuMing Yao^{ab}

DOI: 10.1039/c4ta01004c

www.rsc.org/MaterialsA

Rose-petal-shaped MoS₂ hierarchical nanostructures were designed and constructed using carbonized electrospun nanofibers as a template, which exhibit highly structure-sensitive properties for the hydrogen evolution reaction (HER). We first synthesized carbon nanofiber (CNF) mats by combining the electrospinning and carbonization processes, and then the CNF mats were used as a substrate for the direct growth of MoS₂ nanocrystals via the CVD method. By controlling the MoS₂ morphology at the nanoscale, we constructed evolutions in the structures and preferentially exposed more catalytically active edge sites, enabling improved performance for electrochemical catalytic activity. Because of their highly exposed edges and excellent chemical and electrical coupling to the underlying CNFs, MoS₂-CNF fiber mats exhibited excellent HER activity with a small overpotential of ~0.12 V and a small Tafel slope of 45 mV per decade. Our findings provide a feasible way to design and engineer advanced nanostructures for catalysis, electronic devices, and other potential applications.

Introduction

The rational design and construction of materials with structure-sensitive properties at the nanoscale is paramount in developing advanced nanomaterials. Novel properties may arise when the size of a material is decreased to the nanoscale and the dimensionality is lowered, due to quantum confinement effects and edge effects.¹⁻³ As a new member of the 2D material family, molybdenum disulfide (MoS₂) has recently been discovered to have a unique combination of optical, mechanical, electronic and chemical properties and is fundamentally and technologically intriguing.^{1,2,4-6} Although traditionally used as an industrial hydrosulfurization catalyst, MoS₂ is an

exciting hydrogen evolution reaction (HER) catalyst that exhibits promising HER activity in crystalline or amorphous materials and molecular mimics.⁵ However, its HER electrocatalytic activity is currently limited by the density and reactivity of active sites, poor electrical transport, and inefficient electrical contact with the catalyst.⁷

Previous studies have reported that the HER activity stemmed from the sulfur edges of the MoS₂ plates, while the basal planes were catalytically inert.^{5,8} As a result, tremendous efforts have been made to design and engineer the structures of MoS₂ catalysts with exposed active sites.^{1,9} In addition, MoS₂ is a semiconductor whose poor bulk conduction and anisotropic electrical transport can limit overall catalytic efficiency. Previous studies reported MoS₂ catalysts supported on Au,⁵ graphene,⁸ graphite⁷ and carbon paper,¹⁰ which were prepared by physical vapor deposition or annealing of molybdate in H₂ or H₂S. In addition, various overpotentials (from 0.1 to 0.4 V) and Tafel slopes (from 41 to 120 mV per decade) have been reported.^{5,7-10} Moreover, the morphology and distribution of the catalytically important edge sites of MoS₂ are found to be sensitive to preparation conditions, edge-attached promoter atoms, and interactions with support media.

Carbon nanotubes (CNTs) are widely used as substrates for the support of catalysts, and they have attracted a lot of attention in recent years as a result of their unique structure and wide potential application in electrochemical devices and energy conversion and storage devices.¹¹⁻¹⁴ Similar to CNTs, electrospun carbon nanofibers (CNFs), with wide application in electrochemical devices, are now at the cutting edge of materials science.¹⁴⁻¹⁶ CNFs are composed of graphene layers that form stacked cones, while CNTs are composed of concentric hollow graphene cylinders.^{15,16} Compared with CNTs, CNFs have several advantages, including qualitatively reproducible synthesis, controlled morphology, and larger functionalized surface area for the immobilization of molecules. Electrospinning is currently the only technique that allows the fabrication of continuous fibers with diameters down to a few nanometers.¹⁶⁻¹⁸ In the present investigations, we have

^aDepartment of Materials Engineering, College of Materials and Textile, Zhejiang Sci-Tech University, Hangzhou 310018, P. R. China

^bKey Laboratory of Advanced Textile Materials and Manufacturing Technology, Zhejiang Sci-Tech University, Ministry of Education, Hangzhou 310018, P. R. China. E-mail: du@zstu.edu.cn; Tel: +86-571-86843255

† Electronic supplementary information (ESI) available. See DOI: 10.1039/c4ta01004c

developed a simple electrospun polyacrylonitrile nanofiber (PANF) based graphitization method to fabricate 1D CNFs that are composed of graphitic nanorolls and possess good conductivity and numerous active sites, which can serve as nuclear sites for the growth of MoS₂ nanocrystals.

Solution-phase production of MoS₂ by exfoliation or hydrothermal synthesis holds promise for large-scale production, and Zafropoulou *et al.* have reported the deposition of MoS₂ material on CNTs and CNFs by *in situ* thermal decomposition of (NH₄)₂MoS₄ in oleylamine.¹⁹ However, the structure, morphology, size and thickness are not controllable, and the design and engineering of structures of MoS₂ with exposed edge sites still remains a huge challenge.^{6,20–22} Very recently, chemical vapor deposition (CVD) has been successful in growing high-quality graphene, and several groups have used it to synthesize MoS₂ thin films on 2D insulating substrates such as SiO₂ and sapphire.^{3,23,24} Here, we report the first synthesis of MoS₂ nanosheets on 1D conductive CNFs by the CVD method, demonstrating the rational design and engineering of MoS₂ layered structures, and realizing the construction of structure-sensitive properties for HER with low overpotential and small Tafel slope. Moreover, by incorporating MoS₂ into a large nanostructured conductive substrate and a membrane electrode, we have successfully minimized the charge and mass transport limitations, lowering the resistivity of the MoS₂ crystal.

We first synthesized the CNF mats by combining the electrospinning and carbonization processes, and then the CNF mats were used as the substrate for the direct growth of MoS₂ nanocrystals *via* the CVD method. The synthesis strategy for hierarchical MoS₂–CNF nanomaterials is schematically illustrated in Fig. 1. In brief, MoO₃ powder was first thermally evaporated and reduced by sulfur vapor in the gas phase at 700–900 °C, and then the resulting MoO₂ was nucleated on the surfaces of the CNFs and grown into tubular shells along the entire CNF in a CVD furnace (see details in ESI†). The MoO₂ tubular shells were then annealed in sulfur vapor carried by Ar at 900 °C for 6 h. Because of the high-temperature annealing, the surface of the MoO₂ shells was sulfurized to MoS₂, with varying numbers of layers depending on the annealing duration. A series of morphological evolutions of MoS₂–CNF nanomaterials can be obtained, namely (i) bicontinuous MoS₂ scrolls with controlled layers grown around the CNFs, (ii) small 2D

MoS₂ nanosheets grown on the MoS₂ scrolls along the CNFs, and (iii) 3D rose-petal-shaped MoS₂ nanosheet–CNFs hierarchical nanomaterials with controlled layers and a high density of exposed edges.

Results and discussion

Distinct and continuous PAN nanofibers with random orientation were obtained through the electrospinning process (Fig. S1a†). The PANFs, with smooth surfaces and uniform diameter of 525 ± 52 nm (Fig. S2a†), are up to hundreds of micrometers in length, leading to high surface-to-volume ratios. After carbonization treatment at 1000 °C, the diameter of the CNFs significantly reduces to 215 ± 48 nm (Fig. S2b†) and the continuous nanofibers can still be up to several tens of micrometers in length (Fig. S1b†). As shown by field emission scanning electron microscopy (FE-SEM) and transmission electron microscopy (TEM) in Fig. 2a and b, large-scale MoS₂ ultra nanosheets are grown along the CNFs to form continuous 3D rose-petal-shaped nanostructures. Fig. 2a and low-magnification FE-SEM images (Fig. S3†) clearly show that uniform and continuous 3D rose-petal-shaped MoS₂ nanosheets were grown along the whole CNF substrate and on nanofibers up to several hundred micrometers in length.

Fig. 2b also illustrates that the CNFs are completely covered by the MoS₂ nanosheets; the size of the nanosheets is several

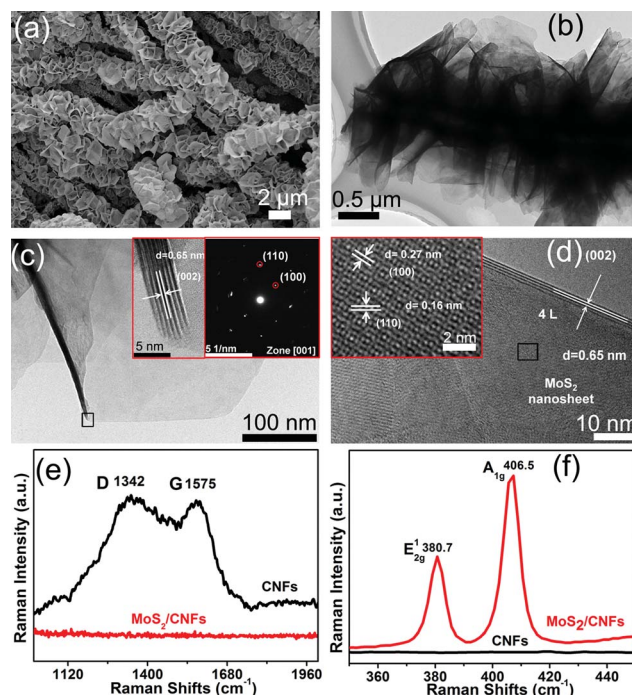


Fig. 2 (a) FE-SEM and (b) TEM image of MoS₂–CNF hierarchical nanomaterials. (c) and (d) TEM images of the rose-petal-shaped MoS₂ nanosheets. Inset in (c): SAED pattern of the MoS₂ nanosheet shown in (c) and HRTEM image of the MoS₂ wrinkle taken on the area marked in the rectangle in (c). Inset in (d): HRTEM image of the MoS₂ nanosheet taken on the area marked in the rectangle in (d). (e) and (f) Raman spectra of the CNF and hierarchical MoS₂–CNF nanomaterials.

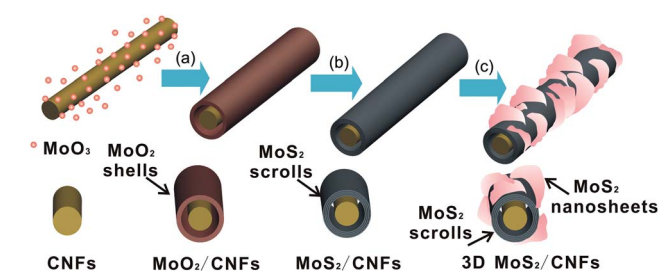


Fig. 1 Synthesis procedure for hierarchical MoS₂–CNF nanomaterials. (a) The nucleation of MoO₂ along the CNFs and the formation of MoO₂ shells; (b) the formation of MoS₂ scrolls after surface sulfurization by S vapor; (c) the growth of 2D MoS₂ nanosheets around the whole MoS₂ scroll–CNFs to form 3D architectures.

micrometers (Fig. 2c). To verify the number of layers of MoS₂ nanosheets, we imaged the folded edges randomly taken on the nanosheets and observed four parallel dark lines with a spacing of 0.65 nm (Fig. 2d). In addition, we also imaged the wrinkled part of the MoS₂ nanosheets and eight parallel dark lines were observed (inset in Fig. 2c). These images confirm the layers of the rose-petal-shaped MoS₂ nanosheets. The inset in Fig. 2c displays the selected area electron diffraction (SAED) pattern taken on a single MoS₂ nanosheet, indicating the highly crystalline structure. The high-resolution TEM image of the MoS₂ nanosheet shows a honeycomb arrangement of the atoms with lattice spacing of 0.16 and 0.27 nm, corresponding to the (110) and (100) planes. Meanwhile, some disordered graphene-like hexagonal lattices emerged because of the mis-orientated stacking of Mo and S pairs in multilayer structures. Raman spectroscopy was further used to confirm the complete sulfuration of the MoS₂ from MoO₃. Fig. 2e shows the Raman spectra of pure CNF and MoS₂-CNF hierarchical nanomaterials. Two Raman peaks in the range of 1000–2000 cm⁻¹ under 514 nm excitation were assigned to the D and G bands of carbon (1342 and 1575 cm⁻¹). After vapor growth and surface sulfuration, as shown in Fig. 2f the as-prepared MoS₂-CNF hierarchical nanomaterials have two distinct Raman peaks located at 380.7 (E_{2g}) and 406.5 (A_{1g}) cm⁻¹, respectively. The Raman spectrum of the MoS₂-CNFs in the range of 1000–2000 cm⁻¹ did not show any peaks of carbon, indicating that MoS₂ nanosheets completely covered the CNFs. In order to verify the reproducibility of the synthesized MoS₂-CNF mats, we measured ten samples of Raman spectra of the MoS₂-CNF mats, and the results exhibit similar Raman peaks of MoS₂ (Fig. S4†).

X-ray photoelectron spectroscopy (XPS) was employed to investigate graphitization of the CNFs from PANFs and the chemical states of Mo and S in the MoS₂-CNF nanomaterials. Fig. 3a and b show the XPS spectra of C 1s and N 1s of the PANFs and the CNFs after graphitization at 1000 °C under an Ar

protecting environment. The C 1s spectrum of the PANFs displays two peaks with binding energies at 284.7 and 285.8 eV, which accord with the carbon atoms in C–C bonds and C≡N bonds, respectively. After thermal annealing at 1000 °C, the CNFs only exhibit one sharp peak located at 284.7 eV (C–C bonds), indicating the formation of graphitic CNFs. For the PANFs, the N 1s spectrum depicts a strong peak located at 398.8 eV, and it can be assigned to the nitrogen atoms that bond with carbon atoms in the form of C≡N (Fig. 3b).¹⁵ On the sample CNFs, two weaker N 1s peaks emerged at 398.8 eV and 401.2 eV. The former is ascribed to the C≡N species as mentioned above, while the latter is attributed to pyridine type nitrogen. In addition, the weak intensity of the N 1s peaks demonstrates that most of the nitrogen vanishes after the carbonization process. Fig. 3c and d show the XPS spectra of Mo 3d and S 2p of the 3D rose-petal-shaped MoS₂ ultra nanosheets grown on the continuous scrolled MoS₂-CNFs. The Mo 3d orbit of the MoS₂-CNFs exhibits two peaks located at 229.1 and 232.2 eV, which are ascribed to the doublet of Mo 3d_{5/2} and Mo 3d_{3/2}, respectively (Fig. 3a).^{23–25} The binding energies for S 2p_{3/2} and 2p_{1/2} were 162.5 and 163.2 eV, respectively (Fig. 3d). These measured binding energies of Mo and S accord with the MoS₂ crystals. X-ray diffraction (XRD) patterns of the CNF and MoS₂-CNF hybrid fibrous mats were obtained to investigate the crystalline phase compositions. As shown in Fig. S5,† the CNFs display the representative diffraction peak (002) of the stacked graphite layers at 25.2° and the *d*-spacing of CNFs is *d*(002) = 3.52 Å, indicating the crystalline structure of graphitic carbon in the nanofibers.^{26,27} Besides the (002) peaks of the CNFs, the MoS₂-CNF nanomaterials exhibit four new peaks at 14.9°, 34.3°, 40.4° and 60.3°, and they are ascribed to the (002), (100), (103) and (100) crystal planes, respectively, indicating MoS₂ crystal domains with hexagonal structure [(PDF) no. 771716].^{24,25} The strong intensity of (002) planes of MoS₂ displays the high density of exposed edge sites.

By changing the amounts of MoO₃, a series of morphological evolutions can be obtained. At low amounts of MoO₃, as shown in Fig. 4a and d, the rough CNFs are completely covered by layers of MoS₂ nanosheets, and several small isolated 2D MoS₂ nanosheets grow on the layered nanosheets along with the CNFs. With increasing amounts of MoO₃, small 2D MoS₂ nanosheets appear and the density of nanosheets increases throughout the CNF (Fig. 4b and e). At the highest amounts, 2D MoS₂ nanosheets grow throughout the MoS₂-coated CNFs to produce 3D continuous MoS₂-CNF hierarchical nanomaterials (Fig. 4c and f). The 2D rose-petal-shaped MoS₂ nanosheets grow densely and uniformly along with the CNFs. Based on the above results, different morphologies of the MoS₂-CNFs can be easily obtained by adjustment of the amount of MoO₃. The carbonaceous matrix of CNFs consisted of small and random graphene layers (Fig. S6†). As shown in the TEM images, at 0.020 g of MoO₃ it is clearly observed from the edge of the MoS₂-CNFs that a MoS₂ scroll with about 20 layers is assembled around the whole CNF. The well-defined layered structure of the MoS₂ scroll has an interlayer distance of 0.65 nm for (002) planes (inset in Fig. 4d). In addition, the phenomenon of wrinkled MoS₂ nanosheets on the surface of the CNF indicates that the CNF substrates were encapsulated in the MoS₂ scrolls.

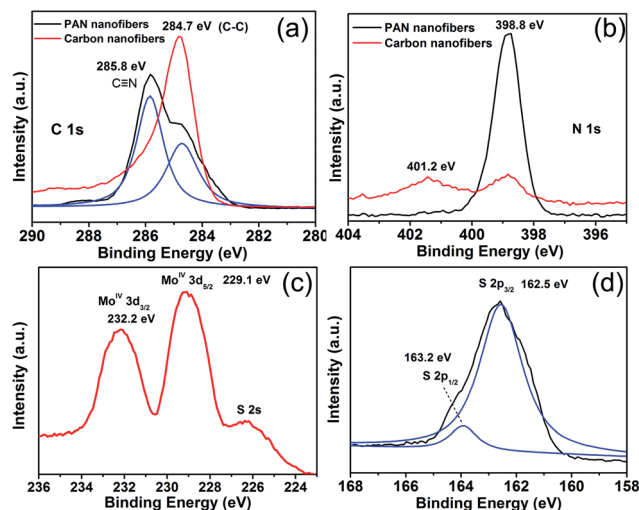


Fig. 3 XPS spectra of C 1s (a) and N 1s (b) of the PAN and carbon nanofibers. XPS spectra of Mo 3d (c) and S 2p (d) of the MoS₂-CNF hierarchical nanostructure.

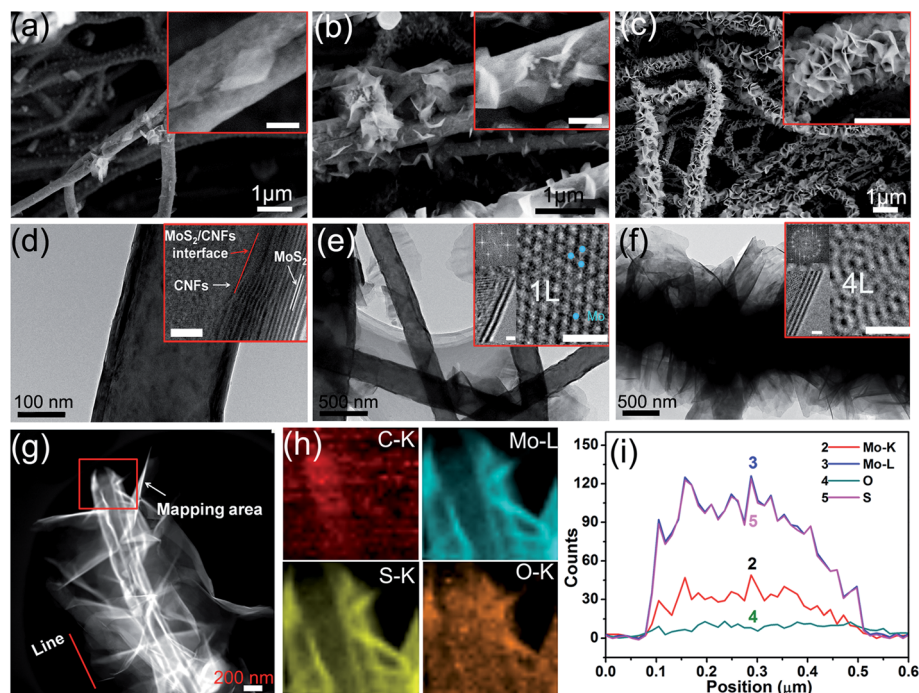


Fig. 4 (a) FE-SEM and TEM images of the morphological evolutions of MoS₂-CNFs with different amounts of MoO₃: (a and d) 0.020 g, (b and e) 0.035 g and (c and f) 0.05 g. Insets in (a–c) are high-magnification FE-SEM images of MoS₂-CNFs (scale bar, 100 nm). The inset in (d) is a HRTEM image of the edges of the scrolled MoS₂-CNFs (scale bar, 5 nm). Insets in (e–f) are HRTEM images of the MoS₂ nanosheets, the folded MoS₂ edges, and the corresponding FFT patterns (scale bar, 1 nm). HAADF-STEM images (g) and STEM-EDX element mappings (h) taken on the scrolled MoS₂-CNFs. (i) Line-scan EDX spectra taken on the MoS₂ nanosheets grown on the MoS₂ scroll-CNFs.

As amounts were continuously increased to 0.020 g, small 2D MoS₂ nanosheets began to grow on the surfaces of the MoS₂ scrolls (Fig. 4e). The HRTEM image shown in Fig. 3e exhibits the honeycomb arrangements of the Mo and S atoms, and the folded edges of the MoS₂ nanosheet presents one dark fringe with a space of ~ 0.65 nm, confirming the bilayer nanostructure of MoS₂. The light spots are ascribed to Mo atoms (blue). The fast Fourier transform (FFT) also shows the hexagonal symmetry of the MoS₂ structure. When the amount was increased to 0.05 g, large 2D MoS₂ nanosheets grew densely and uniformly on the scroll MoS₂-CNF substrates (Fig. 4f). As shown in the insets of Fig. 4f, the HRTEM image of the rose-petal-shaped MoS₂ nanosheets displays a disordered hexagonal structure and the folded edges of the MoS₂ nanosheets present four dark fringes, confirming the multilayer nanostructure of MoS₂. Shi *et al.*²¹ have reported that the arrangement of the atoms can reflect the layer structures. If the MoS₂ domains have a layer number ≥ 2 , both AB stacking and mis-orientated stacking would emerge.

The AB stacking bilayer region in Fig. 4e shows uniform intensity for the hexagonal lattice due to the overlapping of the Mo and S pairs in the top and bottom layers. With increasing number of layers, for example 4 layers, the orientation of the atoms becomes disordered and the FFT patterns also confirm the mis-orientated stacking (insets in Fig. 4f). Therefore, along with the growth of 2D MoS₂ nanosheets from small to larger size, the number of layers also increased from 1 layer to 4 layers.

Fig. 4g shows a high-angle annular dark field scanning TEM (HAADF-STEM) image of the 3D MoS₂-CNF nanomaterials. The

MoS₂ scrolls can be clearly observed and the STEM-EDX mapping of Mo and S elements indicates the semi-hollow structure of the MoS₂ scrolls. The STEM-EDX mapping displays four different elements and the red, blue, yellow and orange regions in the images correspond to the elements C, Mo, S and O. In the mapping of C (Fig. 4h), the dense signal area belongs to the CNFs and the other C signals are ascribed to the carbon-coated Cu grid. The line-scan EDX spectrum of the 2D MoS₂ nanosheet demonstrates the strong Mo and S signals and the very much weaker O signal, indicating complete sulfurization from MoO₂ to MoS₂. The Raman spectra of the three samples also provide evidence for the morphological evolutions (Fig. S7†). The scrolled MoS₂-CNF (sample a) exhibits four distinct Raman peaks, which are ascribed to E_{2g} and A_{1g} of MoS₂ and the D and G bands of carbon. With the morphological evolution of the MoS₂-CNF architecture, the intensities of the peaks of MoS₂ increase and the D and G bands of carbon decrease. The Raman spectra of the 3D MoS₂-CNF nanomaterials did not display the D and G bands of carbon, demonstrating that the CNFs are densely covered by the MoS₂ nanosheets.

The morphological evolution of 3D hierarchical MoS₂-CNF nanomaterials brings us a promising way to design and engineer surface structures at the nanoscale, which is paramount in developing effective catalysts. In order to show the structure-sensitive properties of the MoS₂-CNF hierarchical nanomaterials, we evaluated the electrochemical activity of the scrolled MoS₂-CNFs (sample a), the small 2D MoS₂ nanosheets grown on the scrolled MoS₂-CNFs (sample b), and the 3D MoS₂-CNF

nanomaterials (sample c) for the HER. An excellent catalyst for the HER should reduce the overpotential and consequently increase the efficiency of this important electrochemical process, depending on the highly catalytic edge sites of the MoS₂ nanosheets.^{7,8,25} In our systems, the constructed 3D rose-petal-shaped MoS₂ nanosheets grown on the scrolled MoS₂-CNFs can offer densely exposed active edge sites for HER. The direct growth of MoS₂ nanosheets on conducting CNF substrates enabled a convenient evaluation of their catalytic activity by attachment of the MoS₂-CNF mats to electrode holders in 0.5 M H₂SO₄ solution using a typical three-electrode setup (see ESI† for details). As shown in Fig. 5A, the polarization curves (*i*-*V* plot) recorded with our three samples showed overpotentials of ~0.2 V (sample d), 0.15 V (sample e), and 0.12 V (sample f), respectively. In addition, the linear portions of the Tafel plots (Fig. 5B) were fit to the Tafel equation ($\eta = b \log j + a$, where *j* is the current density and *b* is the Tafel slope).^{7,8} The Tafel slopes of the three samples are ~160, ~97, and ~45 mV per decade, respectively. As a control experiment, the HER activity of pure CNFs (sample a), MoS₂ powder (sample b) and a mixture of MoS₂ powder and CNFs (sample c) were also examined. As shown in Fig. 5, the samples show much lower activity and current density than the MoS₂-CNF hierarchical nanostructures. In addition, sample f, in comparison with the other samples, exhibits the lowest overpotential and Tafel slope because of the large numbers of exposed edge sites, demonstrating excellent HER activity. Note that a trend can be clearly observed, with the morphological evolutions along with increased amounts of exposed edge sites leading to smaller Tafel slopes.

The high electrocatalytic activity of the hierarchical MoS₂-CNF hybrid catalysts in the HER is attributed to the strong chemical and electronic coupling between the conducting CNFs and the MoS₂ nanosheets with various structures. Unlike the deposition of catalysts on conducting substrates, such as Ni foams and graphene, the CNFs serve as the nucleation sites and templates for growth of MoS₂ scrolls and rose-petal-shaped 3D MoS₂ nanosheets. Chemical coupling helps the direct growth of highly uniform MoS₂ around the CNFs to form scrolls and rose-petal-shaped nanosheets. Electrical coupling to the underlying CNFs in an interconnected conducting network affords rapid electron transport from the less-conducting MoS₂ nanosheets to the electrodes. To measure this effect and verify the strong

chemical and electrical coupling, an electrochemical impedance measurement at an overpotential of $\eta = 0.12$ V was performed (Fig. S8†). In a control experiment, the pure CNFs, bulk MoS₂ powder and mixture of MoS₂ powder and CNFs show charge-transfer resistance (*R*_{CT}) of ~3.5 kΩ (sample a), 10 kΩ (sample b), and 8 kΩ (sample c), respectively. However, the MoS₂-CNF nanomaterials (from sample d to f) exhibit much lower *R*_{CT} of ~300, ~150 and ~45 Ω, supporting the strong chemical and electrical coupling effects. The remarkable decrease of *Z*_f offers markedly faster HER kinetics with the MoS₂-CNF hybrid catalysts.

Besides HER activity, high durability is another important criterion for a good catalyst. To evaluate the stability in an acidic environment, we cycled the hierarchical MoS₂-CNF mats (sample c) continuously for 1000 cycles. After the continuous operation, the MoS₂-CNFs showed a 5% decay in the electrocatalytic current density (Fig. S9†), suggesting the high stability of the electrocatalyst based on MoS₂-CNF mats during long-term cycling. Compared with Pt-based electrocatalysts, the activity of the present MoS₂-CNF nanomaterials must still be further improved. However, due to the high costs of Pt, the results of the present investigation provide a promising alternative for the production of hydrogen energy.

Conclusions

In summary, we have synthesized large-scale continuous hierarchical MoS₂-CNF nanomaterials with highly exposed edge site architecture of MoS₂, with tunable structures from 1D scrolls to 2D nanosheets that exhibit structure-sensitive properties for the HER. By controlling the MoS₂ morphology at the nanoscale, we have produced evolutions in the structure and preferentially exposed more catalytically active edge sites, enabling improved performance for electrochemical catalytic activity. Because of the highly exposed edges and excellent chemical and electrical coupling to the underlying CNFs, the MoS₂-CNFs nanofiber mats exhibited excellent HER activity with a small overpotential of ~0.12 V and small Tafel slope of 45 mV per decade. The construction of structure-sensitive nanomaterials with enhanced HER activity provide a feasible way to design and engineer advanced nanostructures for catalysis, electronic devices and other potential applications.

Acknowledgements

This work was supported by the National Natural Science Foundation of China (NSFC) (51373154) and the 521 Talent Project of Zhejiang Sci-Tech University.

Notes and references

- 1 J. Kibsgaard, Z. B. Chen, B. N. Reinecke and T. F. Jaramillo, *Nat. Mater.*, 2012, **11**, 963–969.
- 2 Z. Y. Wang, H. Li, Z. Liu, Z. J. Shi, J. Lu, K. Suenaga, S. K. Joung, T. Okazaki, Z. N. Gu, J. Zhou, Z. X. Gao, G. P. Li, S. Sanvito, E. G. Wang and S. Iijima, *J. Am. Chem. Soc.*, 2010, **132**, 13840–13847.

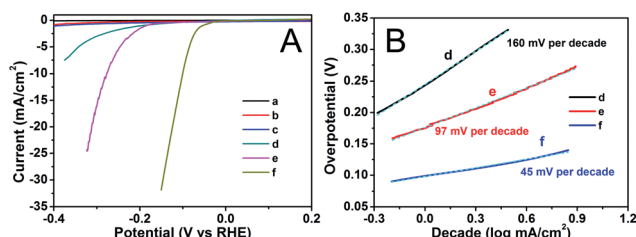


Fig. 5 Electrocatalytic activities of hierarchical MoS₂-CNF nanomaterials for the hydrogen evolution reaction. (A) Polarisation curves obtained with different morphologies of MoS₂-CNF nanomaterials: (a) CNFs, (b) MoS₂ powder, (c) mixture MoS₂ powder and CNFs, (d) scrolled MoS₂-CNFs, (e) small 2D MoS₂ nanosheets grown on the scrolled MoS₂-CNFs and (f) 3D MoS₂-CNF nanostructures. (B) The corresponding Tafel plots of the three samples (d–f).

- 3 K. Yan, L. Fu, H. L. Peng and Z. F. Liu, *Acc. Chem. Res.*, 2013, **46**, 2263–2274.
- 4 M. S. Choi, G. H. Lee, Y. J. Yu, D. Y. Lee, S. H. Lee, P. Kim, J. Hone and W. J. Yoo, *Nat. Commun.*, 2013, **4**, 1624–1630.
- 5 T. F. Jaramillo, K. P. Jorgensen, J. Bonde, J. H. Nielsen, S. Horch and I. Chorkendorff, *Science*, 2007, **317**, 100–102.
- 6 J. N. Coleman, M. Lotya, A. O'Neill, S. D. Bergin, P. J. King, U. Khan, K. Young, A. Gaucher, S. De, R. J. Smith, *et al.*, *Science*, 2011, **331**, 568–571.
- 7 M. A. Lukowski, A. S. Daniel, F. Meng, A. Forticaux, L. S. Li and S. Jin, *J. Am. Chem. Soc.*, 2013, **135**, 10274–10277.
- 8 Y. G. Li, H. L. Wang, L. M. Xie, Y. Y. Liang, G. S. Hong and H. J. Dai, *J. Am. Chem. Soc.*, 2011, **133**, 7296–7299.
- 9 J. F. Xie, J. J. Zhang, S. Li, F. Grote, X. D. Zhang, H. Zhang, R. X. Wang, Y. Lei, B. C. Pan and Y. Xie, *J. Am. Chem. Soc.*, 2013, **135**, 17881–17888.
- 10 T. F. Jaramillo, J. Bonde, J. D. Zhang, B. L. Ooi, K. Andersson, J. Ulstrup and I. Chorkendorff, *J. Phys. Chem. C*, 2008, **112**, 17492–17498.
- 11 Y. B. Chen, Z. Y. Shen, Z. W. Xu, Y. Hu, H. T. Xu, S. Wang, X. L. Guo, Y. F. Zhang, L. M. Peng, F. Ding, Z. F. Liu and J. Zhang, *Nat. Commun.*, 2013, **4**, 2205–2210.
- 12 Q. Qing, D. A. Nezich, J. Kong, Z. Y. Wu and Z. F. Liu, *Nano Lett.*, 2010, **10**, 4715–4720.
- 13 Z. F. Liu, L. Y. Jiao, Y. G. Yao, X. J. Xian and J. Zhang, *Adv. Mater.*, 2010, **22**, 2285–2310.
- 14 D. Jariwala, V. K. Sangwan, L. J. Lauhon, T. J. Marks and M. C. Hersam, *Chem. Soc. Rev.*, 2013, **42**, 2824–2860.
- 15 W. Li, L. S. Zhang, Q. Wang, Y. Yu, Z. Chen, C. Y. Cao and W. G. Song, *J. Mater. Chem.*, 2012, **22**, 15342–15347.
- 16 L. Matlock-Colangelo and A. Baeumner, *Lab Chip*, 2012, **12**, 2612–2620.
- 17 H. Q. Hou and D. H. Reneker, *Adv. Mater.*, 2004, **16**, 69–73.
- 18 A. Greiner and J. H. Wendorff, *Angew. Chem., Int. Ed.*, 2007, **46**, 5670–5703.
- 19 I. Zafropoulou, M. S. Katsiotis, N. Boukos, M. A. Karakassides, S. Stephen, V. Tzitzios, M. Fardis, R. V. Vladea, S. M. Alhassan and G. Papavassiliou, *J. Phys. Chem. C*, 2013, **117**, 10135–10142.
- 20 K. Chang and W. X. Chen, *ACS Nano*, 2011, **5**, 4720–4728.
- 21 Y. M. Shi, Y. Wang, J. I. Wong, A. Y. S. Tan, C. L. Hsu, L. J. Li, Y. C. Lu and H. Y. Yang, *Sci. Rep.*, 2013, **3**, 2169–2176.
- 22 X. S. Wang, H. B. Feng, Y. M. Wu and L. Y. Jiao, *J. Am. Chem. Soc.*, 2013, **135**, 5304–5307.
- 23 K. K. Liu, W. J. Zhang, Y. H. Lee, Y. C. Lin, M. T. Chang, C. Y. Su, C. S. Chang, H. Li, Y. M. Shi, H. Zhang, C. S. Lai and L. J. Li, *Nano Lett.*, 2012, **12**, 1538–1544.
- 24 X. W. Mao, F. Simeon, G. C. Rutledge and T. A. Hatton, *Adv. Mater.*, 2013, **25**, 1309–1314.
- 25 M. Chhowalla, H. S. Shin, G. Eda, L. J. Li, K. P. Loh and H. Zhang, *Nat. Chem.*, 2013, **5**, 263–275.
- 26 S. B. Lee, S. B. Son, K. M. Park, G. Lee, K. H. Oh, S. H. Lee and W. R. Yu, *ACS Appl. Mater. Interfaces*, 2012, **4**, 6702–6710.
- 27 Y. M. Shi, W. Zhou, A. Y. Lu, W. J. Fang, Y. H. Lee, A. L. Hsu, S. M. Kim, K. K. Kim, H. Y. Yang, L. J. Li, J. C. Idrobo and J. Kong, *Nano Lett.*, 2012, **12**, 2784–2791.



Self-assembly of various Au nanocrystals on functionalized water-stable PVA/PEI nanofibers: A highly efficient surface-enhanced Raman scattering substrates with high density of “hot” spots

Han Zhu^a, MingLiang Du^{a,b,*}, Ming Zhang^{a,b}, Pan Wang^a, ShiYong Bao^a, Meiling Zou^a, YaQin Fu^{a,b}, JuMing Yao^{a,b}

^a Department of Materials Engineering, College of Materials and Textile, Zhejiang Sci-Tech University, Hangzhou 310018, PR China

^b Key Laboratory of Advanced Textile Materials and Manufacturing Technology, Zhejiang Sci-Tech University, Ministry of Education, Hangzhou 310018, PR China

ARTICLE INFO

Article history:

Received 17 August 2013

Received in revised form

8 October 2013

Accepted 22 October 2013

Available online 31 October 2013

Keywords:

Self-assembly

Au nanocrystals

Nanofibers

SERS

ABSTRACT

We have demonstrated a facile approach for the fabrication of flexible and reliable sulfhydryl functionalized PVA/PEI nanofibers with excellent water stability for the self-assembly of Au nanocrystals, such as Au nanoparticles (AuNPs), Au nanoflowers (AuNFs) and Au nanorods (AuNRs), used as the highly efficient surface-enhanced Raman scattering (SERS) substrates for the detection of rhodamine B (RhB). Various methods were employed to cross-link the PVA nanofibers with better morphology and porous structures after immersing in water for desired times. Various SERS-active Au nanocrystals, such as AuNPs, AuNFs, and AuNRs have been successfully synthesized. After the grafting of MPTES on the cross-linked PVA/PEI nanofibers, the Au nanocrystals can easily be self-assembled on the surfaces of the nanofibers because of the strong interactions of the Au–S chemical bondings. The Au nanocrystals self-assembled throughout the PVA/PEI nanofibers used as SERS substrates all exhibit enhanced SERS signals of RhB compared with their individual nanocrystals. It is mainly due to the close interparticle distance, mutual orientation and high density of “hot” spots, that can strongly affect the overall optical response and the SERS enhancement. By changing the amounts of the self-assembled AuNFs on the nanofibers, we can control the density of the “hot” spots. With the increased amounts of the AuNFs throughout the nanofibers, the SERS substrates show enhanced Raman signals of the RhB, indicating that the increased density of “hot” spots can directly lead to the SERS enhancement. The AuNFs/(PVA/PEI) SERS substrates show good sensitivity, reliability and low detection limit (10^{-9} M). The presented approach can be broadly applicable to the assembly of different types of plasmonic nanostructures and these novel materials with strong SERS enhancement can be applied in bioanalysis and biosensors.

© 2013 Elsevier B.V. All rights reserved.

1. Introduction

Surface-enhanced Raman scattering (SERS) is a powerful technique for the trace level detection of various biological and chemical species and would promise to make a huge impact in life sciences, environmental monitoring, and homeland security (Wang et al., 2013, 2012b; Gong et al., 2012; Fan et al., 2013; Kim et al., 2011; Lee et al., 2011). This is not only due to its high sensitivity but also because SERS provides vibrational (fingerprint) information of target molecules. Recently, due to the versatility in surface modification, bio-inertness, and remarkable optical

properties known as localized surface plasmon resonance (LSPR), Au nanostructures have created a great promise for their use in a variety of electronic, optical, and biomedical applications, catalysts and SERS substrates (Vigderman et al., 2012; Engel et al., 2012; Saha et al., 2012b; Aragay et al., 2012; Xiao et al., 2010; Personick et al., 2011; Perez-Juste et al., 2005; Xie et al., 2011). One of the most active research fields in SERS substrates is related to the quest for new substrates with improved enhancement efficiency and reproducibility. These efforts include several approaches, such as the development of new nanomaterials by top-down methods and the self-assembly of nanoparticles (NPs) in planar platforms (Fan et al., 2013; Anker et al., 2008; Fan and Brolo, 2009).

Assembly of individual NPs into a nanostructured hierarchy is emerging as a crucial step toward their integration within devices, which is a frontier area of research in modern chemistry and materials science (Zhang et al., 2012a; Kotov 2011; Sanchez-Iglesias et al., 2010).

* Corresponding author at: Department of Materials Engineering, College of Materials and Textile, Zhejiang Sci-Tech University, Hangzhou 310018, PR China. Tel.: +86 571 86843763.

E-mail addresses: du@zstu.edu.cn, psdum1@gmail.com (M. Du).

For example, even though the individual NPs are shown to exhibit a modest SERS effect, and while the metal nanostructures assembled in an organized manner with extremely small (typically less than 5 nm) interparticle spacing, it would result in significantly large SERS enhancement due to the strong capacitive coupling (Lee et al., 2011; Liu et al., 2013; Xie and Schlucker, 2013; Rycenga et al., 2011). This effect is largely influenced by the polarization of incident light relative to different interparticle vectors, with the polarization parallel to interparticle axis resulting in the largest SERS enhancement (Lee et al., 2011; Moskovits, 2005). When the analyte molecules are trapped in the interstitial sites, the “hot spots” formed between the assembled nanostructures and experienced enormous localized electromagnetic field, which effectively results in large SERS enhancement. It is well-known that the “hot” spots make a major contribution to SERS, and the enhancement due to the assembled NPs is about six orders of magnitude higher than for isolated NPs (Liu et al., 2013; Qian et al., 2012; Saha et al., 2012a). Although self-assembly has been widely studied, the fabrication of controllable and reproducible “hot” spots is still a major challenge.

Up to date, support-assisted self-assembly of nanostructures has drawn more attention because of their high densities and reproducible “hot” spot structures. Silica, carbon nanotubes, and inorganic nanowires are commonly used as support materials for depositing metal NPs (Peng et al., 2011; Schmit et al., 2012; Yoon et al., 2009; Yuan et al., 2009). For example, Schmit et al. described a new class of materials for SERS consisting of gold NPs coated onto hollow, buoyant silica microspheres and these SERS-active nanomaterials exhibit a low detection limit of ~ 170 ppt for cyanide (Schmit et al., 2012). As one of the 1-D substrates, electrospun polymer nanofibers gradually attracted the attention of many researchers because of the associated advantages of the synthesizing technique and the obtained product. There are several remarkable characteristics such as extremely large surface area to volume ratio, flexibility in surface functionalities, high porosity and superior mechanical performance, compared with the carbon nanotubes, metal and metal oxide nanowires, making the polymer nanofibers optimal candidates for self-assembly of nanocrystals (Destaye et al., 2013; Wang et al., 2012a; Peng et al., 2012; Liu et al., 2011; Zhu et al., 2013b, 2013c). Recently, Yu et al. have demonstrated a facile way for the fabrication of arranged Ag nanoparticles (AgNPs) and Au nanorods (AuNRs) embedded in poly(vinyl alcohol) (PVA) nanofibrous mats by electrospinning, both exhibiting high SERS enhancement (Zhang et al., 2012a; He et al., 2009). Meanwhile, Schlucker et al. have reported that the SERS enhancement also has a strong analyte distance-dependence feature – only molecules on or very close to the metal surface experience the enormous field enhancement (Wang et al., 2013; Schlucker, 2009). However, the metal nanocrystals embedded in the PVA nanofibers may restrict the close distance between the analyte molecules and the nanocrystals, resulting in weak SERS enhancement. In addition, in Yu's studies, the substrates PVA nanofibers were water-soluble and cannot be applied in water environment, which may impose restrictions on their practical applications.

In our previous studies, our groups have shown that uniform and well-dispersed Au and AgNPs can be immobilized on the amino-functionalized halloysite nanotubes via in situ reduction and these novel materials exhibit high catalytic activity and strong SERS enhancement (Zhu et al., 2012b; 2012c). In addition, we also fabricated the sulfhydryl functionalized water-stable PVA nanofibers to serve as a nanoreactor for the in situ growth of AgNPs, and the fabricated AgNPs/PVA nanofibers have been demonstrated to be a highly active biosensor for the detection of glutathione and glucose (Zhu et al., 2013b, 2013c). The previous studies lead us to develop a combined self-assembly and templating technique to construct various nanostructured arrays of metal nanocrystals.

The combination of hybrid aggregated nanostructures displays distinct optical and electrical properties compared with their individual components. Such hybrid structures show promise for applications in SERS substrates, electronics, optics, and photovoltaic cells (Huang et al., 2010; Zhang et al., 2010; Song et al., 2010).

Here, we reported flexible and reliable sulfhydryl functionalized PVA/PEI nanofibers with excellent water stability for the self-assembly of Au nanocrystals, such as AuNPs, Au nanoflowers (AuNFs), AuNRs, using the highly efficient SERS substrates for the detection of rhodamine B (RhB). For the aim of practical applications, various methods were employed to cross-link the PVA nanofibers with better morphology and porous structures after immersing in water for the desired time. Fourier transform infrared spectra (FTIR) and X-ray photoelectron spectrometer verified the linkage bondings of the cross-linked nanofibers. Various SERS-active Au nanocrystals, such as AuNPs, AuNFs, and AuNRs have been successfully synthesized. After the grafting of 3-mercaptopropyl-trimethoxysilane (MPTES) on the cross-linked PVA/PEI nanofibers, the Au nanocrystals can easily be self-assembled on the surfaces of the nanofibers because of the strong interactions of the Au–S chemical bondings. The amount of the Au nanocrystals on the nanofibers can be adjusted by changing the concentration of the nanocrystals solution. Therefore, with the fine formation of nanocrystal junctions, aggregates can produce intense Raman signatures of reporters with high reproducibility. The AuNFs with multibranch nanostructures exhibit higher SERS enhancement for the detection of RhB, due to more surface roughness and extremely small radii of curvature, resulting in strong electric field enhancement and subsequently large SERS enhancement factors per surface molecule, which is referred to as a “sharp tip effect”. The Au nanocrystals self-assembled throughout the PVA/PEI nanofibers as SERS substrates all exhibit enhanced SERS signals of RhB compared with their individual nanocrystals. It is mainly the close interparticle distance, mutual orientation and high density of “hot” spots, that can strongly affect the overall optical response and the SERS enhancement. By changing the amounts of the self-assembled AuNFs on the nanofibers, we can control the density of the “hot” spots and with the increased amounts of the AuNFs throughout the nanofibers, the SERS substrates show enhanced Raman signals of the RhB, indicating that the increased density of “hot” spots can directly lead to the SERS enhancement. The AuNFs/(PVA/PEI) SERS substrates show good sensitivity, reliability and low detection limit (10^{-9} M). The presented approach can be broadly applicable to different types of plasmonic nanostructures and these novel materials with strong SERS enhancement can be applied in bioanalysis and biosensors.

2. Material and methods

2.1. Materials

The materials information used in this paper is shown in [Supporting information](#).

2.2. Fabrication of the water-stable PVA nanofibrous mats

In the fabrication of PVA/GA nanofibers, the GA solution (30 wt%) was mixed with the PVA aqueous solution (10 wt%) under vigorous stirring to achieve a homogeneous solution, in which the mass ratio of PVA and GA was 4:1. The as-prepared PVA/GA electrospun precursor solution was collected in a 10 mL syringe equipped with a 24 gage stainless steel needle tip. The syringe was fixed on an electric syringe pump set to maintain constant feed rate of 0.01 mL min^{-1} for PVA/GA nanofibers. The voltage was

12 kV and the distance between the needle tip and the collector were 12 cm.

In the fabrication of the cross-linked PVA nanofibers via GA vapor, the PVA precursor solution (10 wt%) was firstly electrospun into the PVA nanofibers, and then treated via the GA vapor in a vacuum oven at 60 °C for 24 h.

For the preparation of cross-linked PVA/PEI electrospun precursor solution, PEI (50 wt%) and PVA (12 wt%) solutions were mixed together under magnetic stirring overnight with a PEI/PVA mass ratio of 1:3 to achieve a homogeneous solution. The electrospun procedure of PVA/PEI precursor was similar to PVA/GA nanofibers. The constant of the feed rate, voltage and distance are 0.005 mL min⁻¹, 20 kV and 20 cm respectively. The freshly prepared PEI/PVA nanofibers were then cross-linked by GA vapor to render the nanofibers with water stability. The diameters and distribution of all the prepared nanofibers were measured by Image-Pro Plus6.2 software (200 nanofibers were randomly selected for the measurement).

2.3. Facile synthesis of the various Au nanocrystals

A green and facile approach was used to synthesize the AuNPs. In brief, 10 mL Au (III) solution (5.0 mmol L⁻¹) and 90 mL water were first injected into a 3-neck flask (fitted with a reflux condenser and a Teflon-coated stir bar) under vigorous stirring by magnetic force at 65 °C. Then, 0.025 g EGCG dissolved in 5 mL water were injected into the above Au (III) solution and the mixture was kept refluxing for 3 h to form homogeneous AuNPs in aqueous solution. The obtained AuNPs aqueous solution was transferred into a beaker after cooling to room temperature and stored at 4 °C in a refrigerator before use.

In a typical experiment to synthesize AuNFs, 1 mL of 100 mM HEPEs (pH 7.4) was mixed with 9 mL of water, followed by the addition of 500 µL of 20 mM HAuCl₄ solution. The color of solution changed from light yellow to pink and finally to turbid blue under ambient environment within 30 min without disturbing.

The AuNRs were prepared according to the seed growth method with a slight adjustment (Park et al., 2013). Briefly, the seed solution was made by adding a freshly prepared, ice-cold NaBH₄ solution (0.6 mL, 0.01 M) into a solution composed of HAuCl₄ (0.025 mL, 0.1 M) and CTAB (10 mL, 0.1 M). The growth solution was prepared separately by mixing HAuCl₄ (500 µL, 0.1 M), AgNO₃ (100 µL, 0.1 M), and CTAB (100 mL, 0.1 M), at room temperature. Next, ascorbic acid (600 µL, 0.1 M) was added to the growth solution as a mild reducing agent. Finally, 100 µL of the seed solution aged for 5 min was added into the growth solution.

2.4. Self-assembly of the Au nanocrystals on the MPTEs functionalized PVA/PEI nanofibers

For the functionalization of the PVA/PEI nanofibers by MPTEs, the water-stable nanofibrous mats were immersed into the MPTEs ethanol solution (10 vol%) by vigorous shaking in an incubator shaker at 40 °C for 12 h and then rinsed with DIW and ethanol three times. The freshly washed nanofibrous mats were immersed into the desired volume of Au nanocrystals aqueous solution (AuNPs, 10 mL; AuNFs 12 mL, AuNRs, 8 mL) followed by vigorous shaking in an incubator shaker at 40 °C for 3 h until the Au nanocrystals aqueous solution changed to colorless. The fabricated nanofibrous mats were rinsed with DIW three times, followed by drying at room temperature. The diameters and distributions of the Au nanocrystals were measured by Image-Pro Plus6.2 software (200 particles were randomly selected for the measurement).

2.5. SERS experiments

RhB was chosen as a model analyte to investigate the performance of the Au nanocrystals assembled on the PVA/PEI nanofibers as a substrate for SERS detection. The AuNPs, AuNFs, and AuNRs solution was mixed with the RhB solution (1 mL, 10⁻⁵ M) for 12 h to make the adsorption equilibrium of RhB on the Au nanocrystals. Similarly, the SERS measurements were performed by dropping 1 mL of RhB solution (10⁻⁵ M) onto the PVA/PEI nanofibers with Au nanocrystals assembled substrates. Then, the nanofibers substrates mat was washed thoroughly with water to remove unbound RhB molecules and finally dried at room temperature to evaporate all of the water.

2.6. Instrumentation

Transmission electron microscopy (TEM) images were obtained with a JSM-2100 transmission electron microscopy (JEOL, Japan) at an acceleration voltage of 200 kV. The EDS spectrum of the AuNFs/(PVA/PEI) nanofibers was also recorded by the TEM. The morphologies of all the electrospun nanofibers were observed by a JSM-6700F field-emission scanning electron microscope (FE-SEM, JEOL, Japan) at an acceleration voltage of 1 kV. X-ray Diffraction (XRD) patterns of the PVA/PEI nanofibers with and without Au nanocrystals were characterized with a SIEMENS Diffraktometer D5000 X-ray diffractometer using Cu Kα radiation source at 35 kV, with a scan rate of 0.02° 2θ s⁻¹ in the 2θ range of 10–80°. Fourier transform infrared (FTIR) spectra were recorded on a Nicolet 5700 FTIR spectrometer in transmittance mode at a resolution of 4 cm⁻¹ and 32 scans in the range from 4000 nm to 400 nm. The as-prepared AuNPs, AuNFs and AuNRs aqueous solution were examined by a Lambda 900 UV–vis spectrophotometer (Perkin Elmer, USA). All the spectra were collected over a wavelength range of 200–800 nm. Thermogravimetric analysis (TGA; Pyris 1) was carried out from 298 to 1073 K at a heating rate of 5 K/min in N₂ atmosphere. X-ray photoelectron spectra of cross-linked PVA/PEI nanofibers, MPTEs functionalized PVA/PEI nanofibers and AuNFs/(PVA/PEI) nanofibers were recorded using an X-ray Photoelectron Spectrometer (Kratos Axis Ultra DLD) with an aluminum (mono) Kα source (1486.6 eV). The aluminum Kα source was operated at 15 kV and 10 mA. Raman spectra of all the samples were recorded by a Renishaw inVia Raman microscope using a 785 nm laser excitation source. The excitation light intensity in front of the objective was 10 mW with a spectral collection time of 1 s for SERS experiments. The integration time for our measurements was set to 10 s.

3. Results and discussion

The polymer nanofibers substrate with good morphology, water stability and porous structures for the self-assembly of Au nanocrystals is a prerequisite factor for the fabrication of reliable and reproducible SERS substrates. To retain their water stability, three different methods were utilized to cross-link the PVA nanofibers. The PVA/GA nanofibers were firstly prepared from the PVA/GA solution and, as shown in Fig. 1a, uniform and smooth nanofibers without any adhesion can be obtained. The average diameter of the PVA/GA nanofibers is 260 ± 42 nm (Fig. S1). However, when the obtained PVA/GA nanofibrous mats were immersed in water, it was found to instantaneously dissolve in water and swell considerably. As shown in Fig. 1d, the nanofibers start to fuse with each other and destroy porous openings of the nanofibrous mats.

It should be noted that maintaining the nanofiber morphology and porous structure of nanofibers mats is important for the

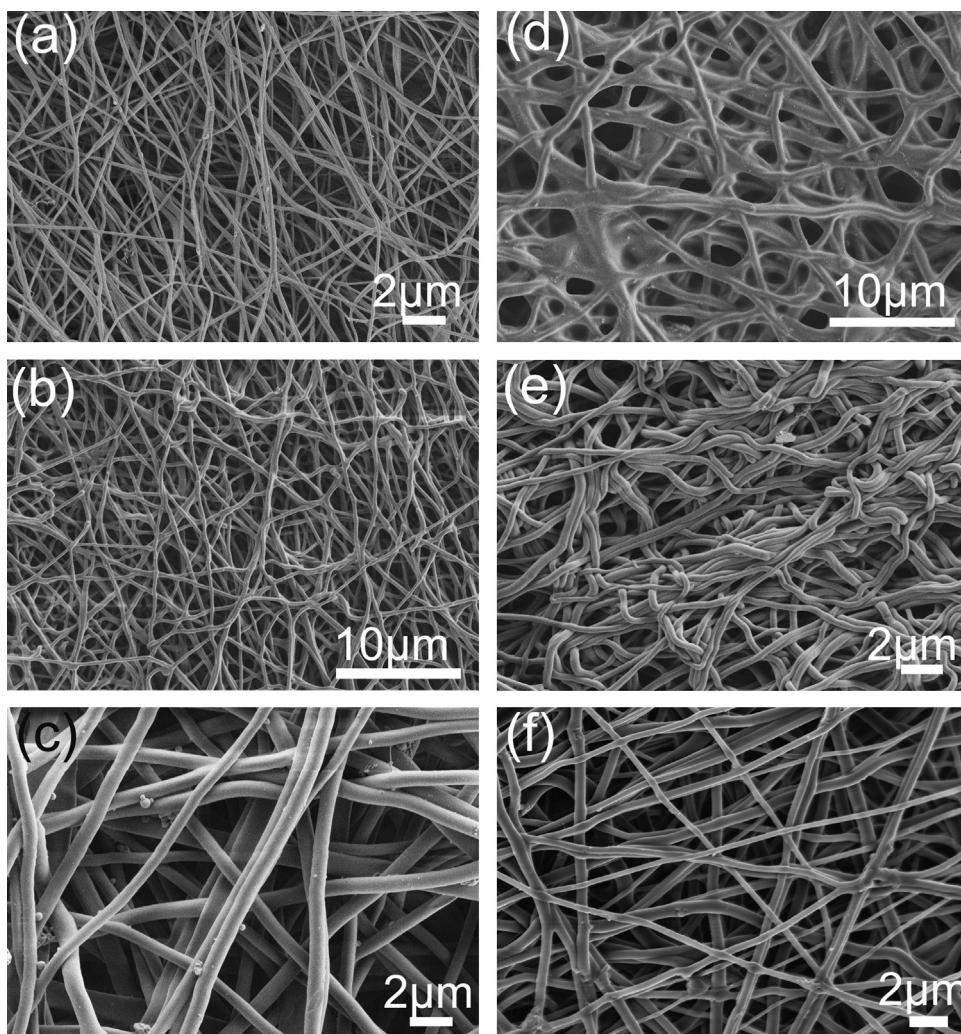


Fig. 1. FE-SEM images of the (a) fresh PVA/GA nanofibers, (b) cross-linked PVA nanofibers via GA vapor, and the (c) cross-linked PVA/PEI nanofibers via GA vapor. The FE-SEM images of the corresponding nanofibers immersed in water for (d) 30 min, (e) 24 h, and (f) 72 h.

practical applications where a high surface-area-to-volume ratio is considered advantageous (Destaye et al., 2013). After the treatment by GA vapor, as shown in Fig. 1b, the originally straight nanofibers become merged and entangled among each other and form interfiber bonding/fused mostly at the intersection points. It is because the GA vapor contains water vapor and it could soften and swell the surfaces of the nanofibers, leading to the direct contact with nearby nanofibers at intersection points and then the formation of interfiber bondings. When the GA vapor cross-linked PVA nanofibrous mats were immersed in water for 24 h, as shown in Fig. 1e, the phenomena of the merged and entangled nanofibers become serious and compared with Fig. 1b, the porous structures were destroyed. Through the GA vapor treatment, the water stability of the nanofibers can be improved; however, the porous structures cannot withstand the water. Fig. 1c shows the cross-linked PVA/PEI nanofibers via GA vapor, smooth and uniform PVA/PEI nanofibers with random orientation were obtained with an average diameter of 510 ± 50 nm (Fig. S2). There are no significant merged and entangled nanofibers instead of interfiber bonding/fused nanofibers at the intersection points with excellent porous nanofibers. After immersing in water for 72 h, as shown in Fig. 1f, the water-insoluble PVA/PEI nanofibrous mats were still well preserved and kept excellent porous fiber structure, suggesting the successful cross-linking reaction to form aldimine linkages between the free amino groups of PEI and the GA (Destaye et al.,

2013; Zhu et al., 2013c). The cross-linkages of the PVA/GA and PVA/PEI nanofibers are characterized by FTIR spectra, and the information and discussion are shown in Supporting information (Fig. S3).

Three different morphologies of the Au nanocrystals with SERS activity have been successfully synthesized, which are AuNPs, AuNRs, and AuNFs. For the synthesis of AuNPs, unlike the most widely used sodium citrate methods, our groups have introduced the natural tea polyphenols (TP) to act both as reducer and stabilizer to synthesize Au and AgNPs (Zhu et al., 2012c; Zou et al., 2013). In the present investigation, we use the main ingredient of TP, epigallocatechin gallate (EGCG), both as the reducer and stabilizer to synthesize AuNPs. As shown in Fig. 2a, relatively uniform AuNPs with an average diameter about 20.2 ± 2.6 nm (Fig. S4) are well-dispersed in water without any aggregations, indicating the reliable stabilization of the EGCG.

Fig. 2d exhibits that the AuNPs are mainly composed of (111) planes with a d-spacing of 0.23 nm, which could be indexed by the face-centered cubic (fcc) structure of Au crystals (Zhu et al., 2012a, 2013a). The selected-area electron diffraction (SAED) of the AuNPs reveals diffraction rings indexed to the (111), (200), (222), and (311) planes of fcc gold, respectively, indicating the polycrystallinity of AuNPs (Du and He, 2010). The AuNRs were prepared using a seed-mediated growth method in aqueous solutions and are stabilized with CTAB. As shown in Fig. 2b, the shapes and sizes of

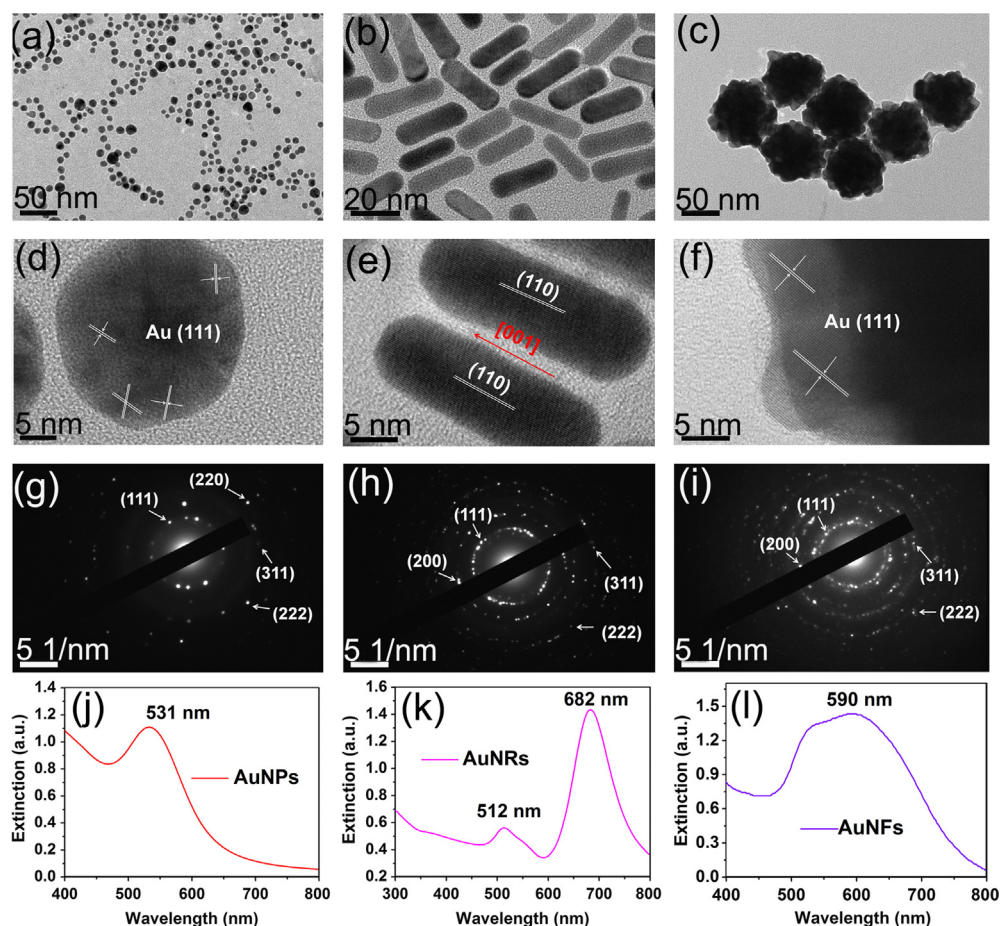


Fig. 2. TEM and HRTEM images of the (a) and (d) AuNPs, (b) and (e) AuNRs, and (c) and (f) AuNFs. The corresponding SAED patterns of the (g) AuNPs, (h) AuNRs, and (i) AuNFs. The UV-vis spectra of the (j) AuNPs, (k) AuNRs and (l) AuNFs solution.

the nanorods samples are relatively uniform with an average radius of $r_{\text{rod}} = 7$ nm and an average length of $l_{\text{rod}} = 35$ nm.

Fig. 2e shows that the AuNRs are single-crystalline, growing along the [001] direction. The SAED of the AuNRs indicates diffraction rings indexed to the (111), (220), (222), and (311) planes of fcc gold (Singh et al., 2013). For the synthesis of AuNFs, a common Good's buffer in chemistry and biochemistry, HEPES, could be used as a weak reducing agent in AuNFs synthesis. Fig. 2c shows the typical TEM image of the AuNFs synthesized in 10 mM HEPES solution. The as-synthesized AuNFs are quasi-spherical, consisting of a solid Au core with many short, irregular, and obtuse Au nanocrystals. The diameter of the quasi-spherical AuNFs varies from 50 to 80 nm, and the Au nanocrystals around the Au cores have a variety of shapes and sizes. The HRTEM image (Fig. 2f) shows that the short, irregular, and obtuse Au nanocrystals which protruded from the core of the nanoflowers are single-crystalline and the distinct lattice fringes with a d-spacing of 0.23 nm correspond to the (111) planes of fcc gold. The SAED pattern shows that the AuNFs are crystalline and randomly oriented (He et al., 2012; Zhang et al., 2011; Xie et al., 2008).

Fig. 2j shows a sharp absorption peak located at the 531 nm, which is believed to be a consequence of photoexcitation of the free conduction electrons on the surface of AuNPs (Zhu et al., 2012c; Zou et al., 2013). The characteristic surface plasmonic resonance (SPR) band of AuNPs is relatively narrow, suggesting a good dispersion and narrow size distribution of AuNPs. As for AuNRs, Fig. 2k shows a longitudinal SPR peak at 682 nm and a transverse one at 512 nm (Ye et al., 2012; Jiang et al., 2012; Qiao et al., 2011). Similarly, the extinction spectrum of AuNFs indicates

a broad SPR peak located around 590 nm, which is shown in Fig. 2l. All the extinction spectra can confirm the successful synthesis of the Au nanocrystals.

The cross-linked PVA/PEI nanofibers were firstly functionalized by MPTES, and then used as the substrates for the self-assembly of the Au nanocrystals, which are AuNPs, AuNRs, and AuNFs. As shown in Fig. 3a and b, uniform AuNPs are evenly dispersed throughout the PVA/PEI nanofibers. The AuNPs are attached to the surfaces of the nanofibers and there are no obvious aggregated AuNPs, indicating the strong chemical bonding between the AuNPs and the -SH groups. For the self-assembly of the AuNFs, large amount of the AuNFs were densely immobilized on the surfaces of the PVA/PEI nanofibers, which are shown in Fig. 3c and d. As shown in Fig. 3e and f, a portion of the independent AuNRs can be observed immobilized on the PVA/PEI nanofibers. However, relatively serious aggregated AuNRs are emerged on the PVA/PEI nanofibers. It is because in the synthesis of AuNPs and AuNFs, EGCG and HEPES are both used as the reducer and the capping agents, and they are weak capping agents, while the CTAB is a strong capping agents.

There is a competition between these capping agents and thiol groups on the nanofibers surface. When different processes of bindings compete, the binding leading to the maximum decrease in the surface energy prevails. Therefore, the good dispersion of Au nanocrystals on the nanofibers surface strongly depends on the ability of the thiol groups modified surface to displace the stabilizer at the surface of Au nanocrystals. As for the weak capping agents, the AuNPs and AuNFs showed a homogeneous distribution over the MPTES functionalized nanofibers due to the

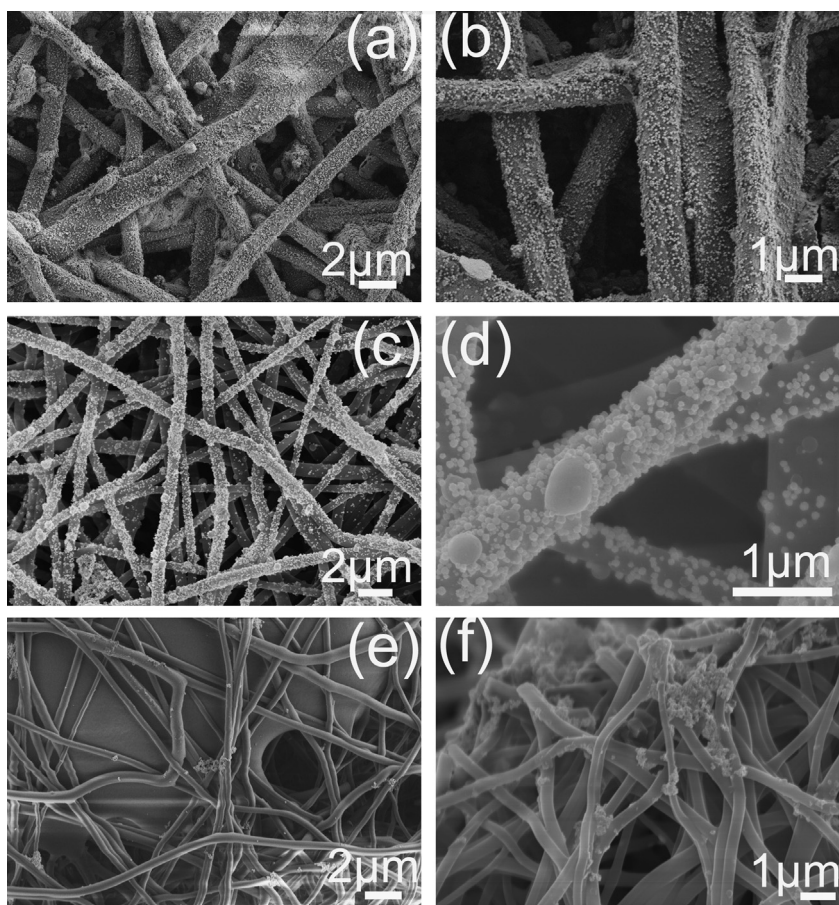


Fig. 3. FE-SEM images of the self-assembly of the (a) and (b) AuNPs, (c) and (d) AuNRs, and (e) and (f) AuNFs on the MPTES functionalized PVA/PEI nanofibers.

strong Au–S bondings. The CTAB-stabilized AuNRs showed a poor adsorption and aggregated AuNRs on MPTES functionalized PVA/PEI nanofibers. This is probably because of the high stability of the CTAB bilayers around the particles and the combined effect of charge repulsion between thiol groups and quaternary ammonium (Tamoto et al., 2012).

The FTIR spectra, XRD patterns and TG curves of the fabricated Au nanocrystals self-assembled on the MPTES functionalized PVA/PEI nanofibers are discussed in Supporting information (Figs. S5 and S6).

XPS spectra were used to study the chemical bondings and illustrate the chemical changes between the MPTES grafting and the self-assembly process. Fig. 4a and b show the C 1s XPS spectra of the cross-linked PVA/PEI and MPTES functionalized PVA/PEI nanofibers. As shown in Fig. 4a, four distinct XPS peaks are observed, indicating four different binding energies (BEs) of C 1s. The primary C1s peak, located at 284.7 eV, was ascribed to the C–C backbone of the PVA/PEI (Chen et al., 2011; He et al., 2011; Khatri et al., 2008). The 286.6 eV peak was mainly attributed to the carbon atoms of the carbonyl group (C=O) as well as the carbon atoms adjacent to the amide bond (C–NH₂) (Tamoto et al., 2012). The fitted peak at 287.5 eV was also attributed to carbon atoms adjacent to the amide bond (C–NHR) in PEI. In addition, the C peak with BE at 289.7 eV is attributed to the carbon atoms of aldimine groups as well as the ester group (Chen et al., 2011; He et al., 2011). The XPS results can demonstrate the formation of the aldimine groups, indicating the successful cross-linkages of the PVA/PEI nanofibers. Comparing Fig. 4b with a, similar C 1s peaks can be observed and the peaks are located at 284.7, 285.9, 287.8, and 289.0 eV, respectively. The C 1s XPS spectrum of the MPTES functionalized PVA/PEI nanofibers shows a new emerged peak

with BE at 290.7 eV which is attributed to the carbon atoms of C–O–Si groups in MPTES, indicating the successful grafting of MPTES on PVA/PEI nanofibers (He et al., 2011; Khatri et al., 2008). As shown in Fig. 4c and d, the O 1s spectra of the PVA/PEI nanofibers with and without MPTES both exhibit a strong peak with BE at 532.4 eV, belonging to the C–OH groups in PVA.

Fig. 4d exhibits two chemical states of the O 1s, and the weaker O 1s peak located at 533.8 eV is ascribed to the Si–O groups, confirming the grafting of MPTES on nanofibers. As shown in Fig. 4e, the appearance of characteristic Si 2p peaks at 102.1 eV, Si 2p_{1/2} at 98.0 eV, and Si 2p_{3/2} at 96.9 eV, which are ascribed to the Si–O, Si–C and Si–Si bondings (Selegard et al., 2010; Wang et al., 2004). The presence of Si–O bondings can successfully confirm the grafting between –OH groups in PVA and Si–C groups in MPTES. The above XPS results can strongly support the successfully cross-linkages of the PVA/PEI nanofibers and the grafting reaction between the MPTES and the –OH groups. The Au–S bondings generated between the –SH groups in MPTES and the Au nanocrystals and the formation of the Au–S bondings are the key factor for the self-assembly process. The S 2p XPS spectra of the MPTES functionalized PVA/PEI nanofibers before and after the self-assembly of Au nanocrystals were used to study the Au–S bondings.

As shown in Fig. 4f, the XPS S 2p core level spectrum of MPTES functionalized PVA/PEI nanofibers exhibits a pair of peaks, which are ascribed to the spin–orbit-splitting doublet with the S 2p_{3/2} and S 2p_{1/2} BE positions at 163.8 and 164.8 eV, respectively (Selegard et al., 2010; Wang et al., 2004). This is consistent with the binding energy of unbound thiol (–SH) groups, which is in accord with the previously reported literatures (Zhu et al., 2013b; Selegard et al., 2010). As for the analysis of the AuNFs/(PVA/PEI)

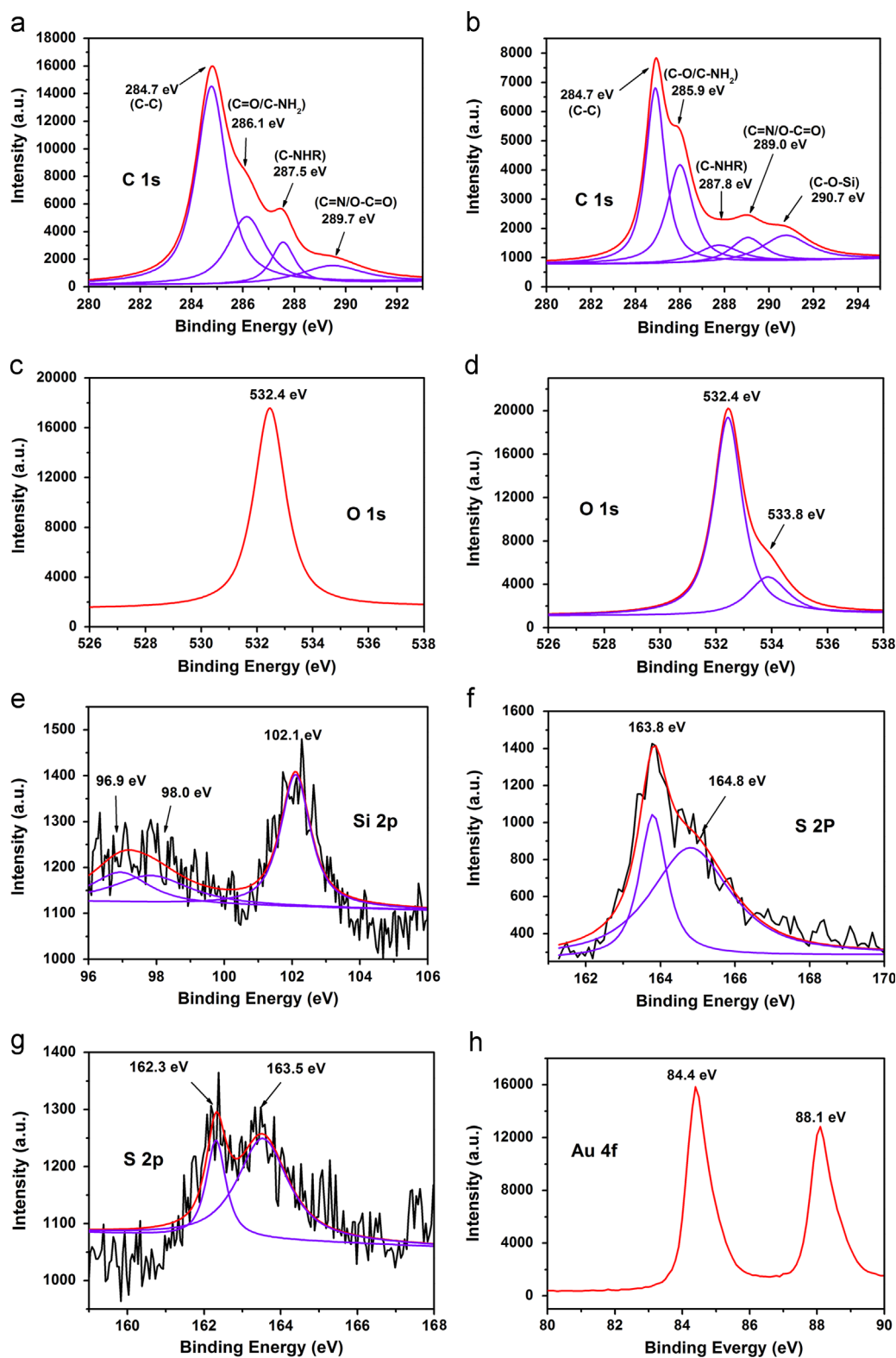


Fig. 4. C 1s XPS spectra of the (a) cross-linked PVA/PEI and (b) MP TES functionalized PVA/PEI nanofibers. O 1s XPS spectra of the (c) cross-linked PVA/PEI and (d) MP TES functionalized PVA/PEI nanofibers. Si 2p XPS spectra of the (e) MP TES functionalized PVA/PEI nanofibers. S 2p XPS spectra of the (f) MP TES functionalized PVA/PEI and (g) AuNFs/(PVA/PEI) nanofibers. (h) Au 4f XPS spectra of the AuNFs/(PVA/PEI) nanofibers.

nanofibers sample, the observed doublet peaks of S 2p_{3/2} and S 2p_{1/2} with the BEs at 162.3 eV and 163.5 eV, respectively, are corresponding to thiolate species, confirming the formation of the Au–S bondings (Zhu et al., 2013b; Selegard et al., 2010). In addition, the Au 4f XPS spectrum of the AuNFs/(PVA/PEI)

nanofibers shown in Fig. 4h exhibits two sharp and distinct peaks located at 88.1 eV and 84.4 eV and they are in agreement with the binding energies of Au 4f_{7/2} and Au 4f_{5/2}, respectively (Zhu et al., 2012c, 2013a). Compared with the BEs of Au⁰ (87.7 eV and 84.0 eV), the shifts in the BE indicate the strong Au–S bondings

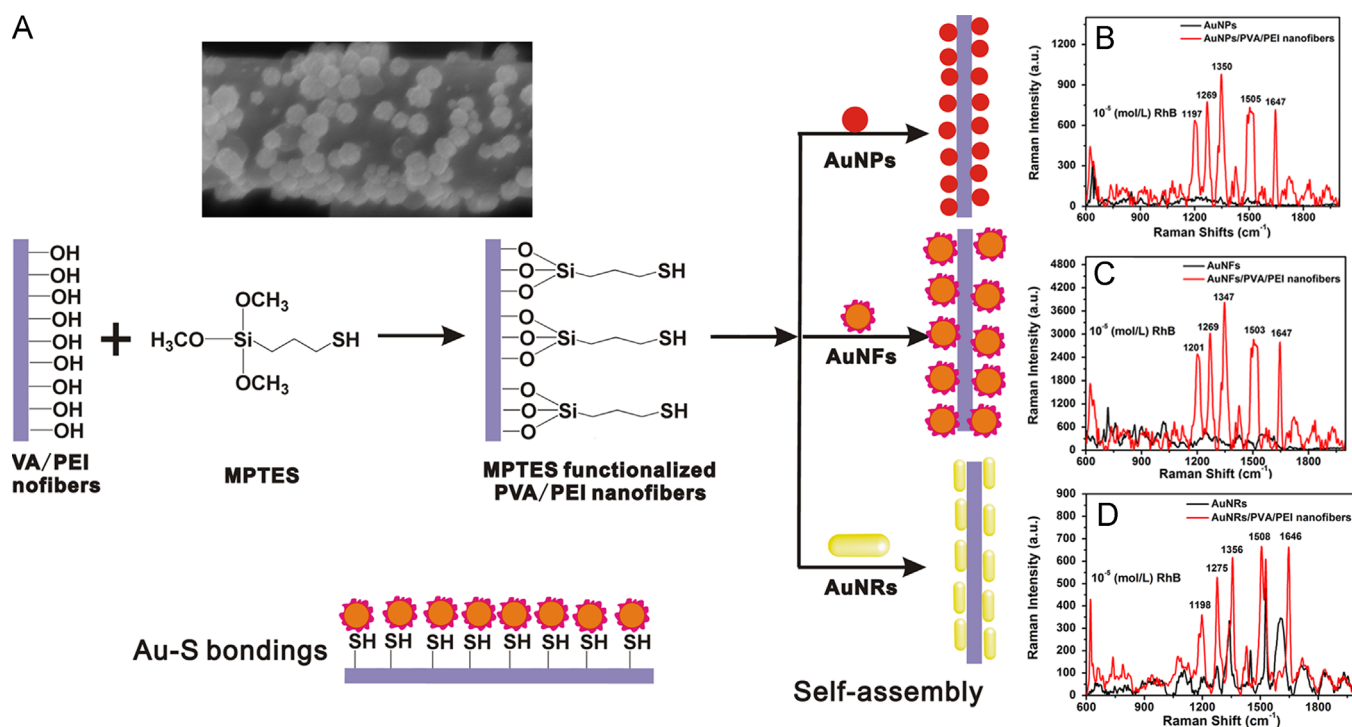


Fig. 5. (A) Schematic illustrations of the MPTES functionalization procedure of PVA/PEI nanofibers and the self-assembly process of the Au nanocrystals. SERS spectra of RhB (10^{-5} M) molecules collected on independent Au nanocrystals and the PVA/PEI nanofibers self-assembled with (B) AuNPs, (C) AuNFs, and (D) AuNRs. The inset is the FE-SEM image of AuNFs/PVA/PEI nanofiber.

effects between the AuNFs and $-\text{SH}$ (Saha et al., 2012a; Zhu et al., 2013a). In addition, Tanaka et al. (2003) and Negishi et al. (2005) have also reported that the relatively high BEs of Au 4f was due to the binding of surface Au atoms in AuNPs with the stabilizer or passive molecules surrounding the NPs, which led to a substantial electron donation from AuNPs to the stabilizer molecules. Thus, based on the above XPS results and analysis, we can conclude that the MPTES molecules have been successfully grafted on the PVA/PEI nanofibers and a considerably larger fraction of the thiol groups coordinate to the surface of the AuNFs, indicating the formation of the strong Au-S bondings.

The schematic illustrations of the MPTES functionalization procedure of PVA/PEI nanofibers and the self-assembly process of the Au nanocrystals on MPTES functionalized PVA/PEI nanofibers are shown in Fig. 5A. In the SERS studies, a typical analyte rhodamine B (RhB) was selected as a model to demonstrate the SERS performance of these substrates. Due to the complex surface morphology of the AuNFs/(PVA/PEI) nanofibers, it is difficult to calculate an accurate enhancement factor. Fig. 5B–D shows the SERS spectra of 10^{-5} M RhB collected on different samples based on the Au nanocrystals and Au nanocrystals assembled on the PVA/PEI nanofibers, respectively. The SERS spectra of RhB based on AuNPs, AuNFs, and AuNRs all exhibit relative weaker Raman signals. After the self-assembly of the Au nanocrystals on the nanofibers, dramatic increase in Raman signals can be observed. The strong Raman signals of RhB located at 615, 1201, 1269, 1347, 1503, 1647 cm^{-1} are assigned to the C–C ring in-plane bending, C–H in-plane bending, C–O–C stretching and C–C stretching of aromatic rings (1347, 1503 and 1647 cm^{-1}), respectively, which are associated with the literatures (Zhang et al., 2005; Ahamad and Ianoul, 2011; Liu et al., 2012). Careful comparison of the SERS spectra based on different substrates, show that the Raman peaks of the RhB indicate slightly differences. It is known that there are two primary mechanisms of SERS enhancement which should be responsible for the SERS enhancements, which are electromagnetic field enhancement (EM) and chemical

enhancement (CM) (Zhang et al., 2005; Ahamad and Ianoul, 2011; Liu et al., 2012). When the RhB molecules adsorbed on the Au nanocrystals, the charge transfer between the metallic nanoparticles and adsorbed molecules can make a weak contribution for the SERS enhancements, resulting in the slight differences in Raman peaks of RhB (Gabudean et al., 2012). It should be noted that compared with the Raman intensities of the AuNPs/(PVA/PEI) and AuNRs/(PVA/PEI) nanofibers, the AuNFs/(PVA/PEI) SERS substrate demonstrates the higher Raman enhancement. According to previous studies, there are two primary mechanisms of SERS enhancement that should be responsible for the results (Qian et al., 2012; Saha et al., 2012a).

The electromagnetic effect is mostly caused on the presence of metal surfaces' roughness featured, and for a SERS substrate, the SERS-active sites ("hot" spots) are critical for the effect of SERS. It is noticeable that systems of interacting particles can produce the largest enhancements, which was recognized in early SERS research (Rycenga et al., 2011; Qian et al., 2012; Saha et al., 2012a). Compared with the single particle-based SERS substrates (AuNPs, AuNFs, and AuNRs), the Au nanocrystals assembled on nanofibers have more surface roughness than do single particles of similar size, and that means that the high densities of the assembled Au nanocrystals can create more "hot spots" at the junction positions, resulting in the intense Raman signatures of reporters. The Raman intensities of RhB based on AuNFs are higher than that on AuNPs and AuNRs, it is because compared with the AuNPs and AuNRs with smooth surfaces, the as-synthesized AuNFs possess many tips of the nanoscale bumps or the tiny cavities on the AuNFs surfaces and larger total surface area because of the roughness of the AuNFs surface, which are potential "hot" spots for the electromagnetic enhancement effects (Xie et al., 2008; Liu et al., 2012). The electromagnetic fields generated by surface plasmons depend quite intricately on the shape of the NPs, their spatial arrangement, and their environment. Combining the advantages of the AuNFs and the high densities of the "hot" spots caused by the self-assembly, it is not surprising to observe that the

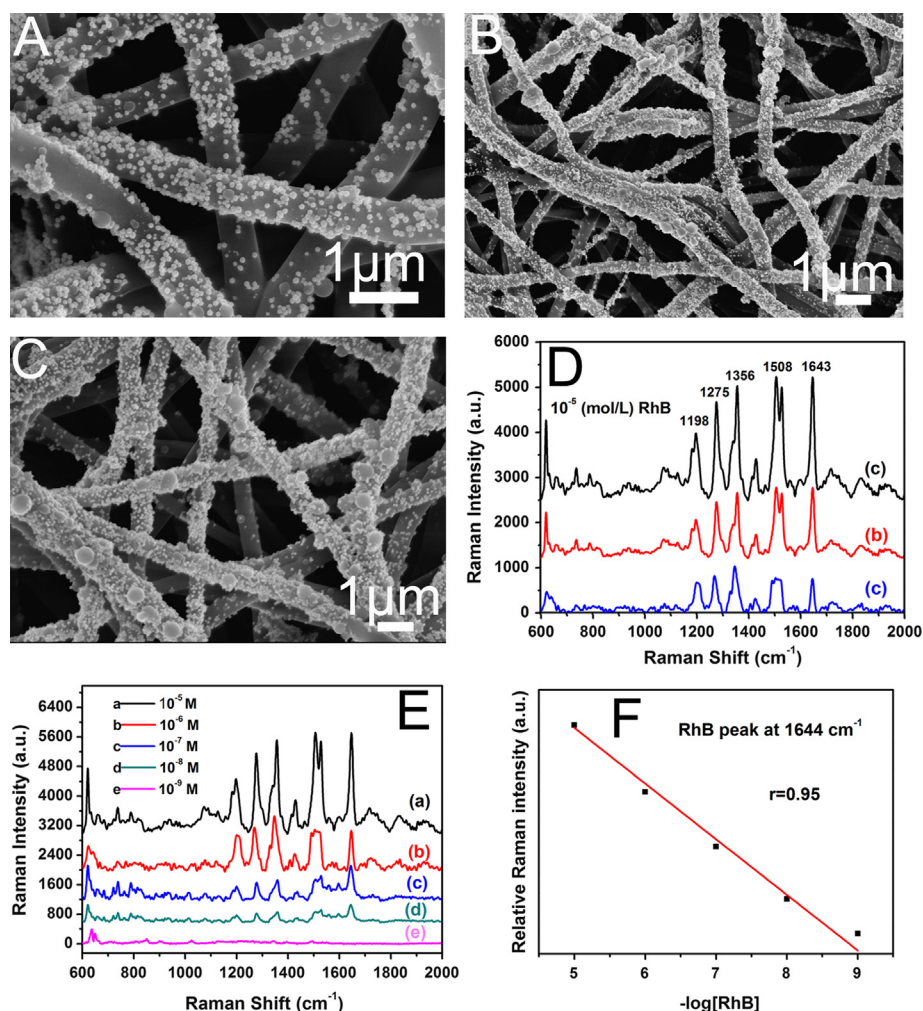


Fig. 6. FE-SEM images of the AuNFs assembled on the PVA/PEI nanofibers with increasing amounts of AuNFs solutions: (A) 5 mL, (B) 10 mL and (C) 15 mL. (D) The corresponding SERS spectra of RhB (10^{-5} M) based on the AuNFs/(PVA/PEI) nanofibers with increasing amounts of AuNFs solutions: (a) 15 mL, (b) 10 mL and (c) 5 mL. (E) SERS spectra obtained from different concentrations of RhB from 10^{-5} M to 10^{-9} M using AuNFs/(PVA/PEI) nanofibers as substrates. (F) Logarithmic plot of [RhB] versus SERS intensity accompanied with linear fitting.

AuNFs/(PVA/PEI) nanofibers exhibits the highest SERS signals for RhB among the samples in our present investigations.

The above SERS results indicate that the densities of the assembled Au nanocrystals throughout the nanofibers are the key factor for the creation of “hot” spots and the SERS enhancement effects. However, Zhang et al. (2012b) have reported that the intensity of the Raman signal of rhodamine 6G would decreased with the increased aggregation of AgNPs on the polyacrylonitrile nanofibers, that is, with the increase of concentration of NPs, the aggregation phenomenon of NPs will increase, which would result in the decrease of SERS signal. Therefore, an optimum concentration of AuNFs assembled on the PVA/PEI nanofibers should be considered for the preparation of reliable SERS substrates.

According to the previously studies (He et al., 2009; Schlucker, 2009) the AuNFs/(PVA/PEI) nanofibers with reasonable amounts of AuNFs from 5 mL to 15 mL were used as the SERS substrates for the detection of RhB. As shown in Fig. 6A, at the low concentration of AuNFs solution, the AuNFs are evenly assembled throughout the PVA/PEI nanofibers, and seldom coupling AuNFs can be observed. With the increased concentration of AuNFs solution, more and more AuNFs are assembled around the nanofibers and many adjacent AuNFs start to form coupling AuNFs. When the nanofibers were nearly completely covered by the AuNFs, the AuNFs are right next to each other and create highest density “hot” spots, which are beneficial for the SERS detection efficiency. At this level of AuNFs, the nanofibers

were almost completely covered by AuNFs, and the distances between neighboring NPs are less than 10 nm, which are called “hot” spots rather than the aggregation of the AuNFs. Therefore, below 15 mL of the AuNFs, few aggregation of AuNFs can be found and the SERS intensity will not decrease.

The corresponding SERS spectra of RhB (10^{-5} M) based on the AuNFs/(PVA/PEI) substrates are shown in Fig. 6D, and as expected, from curve c to curve a, the Raman signals intensities increased with the increased densities of the AuNFs and the “hot” spots. Therefore, when excited by incident light, the hot spots can contribute to larger SERS enhancement. According to the previous literatures, Zhu et al. (2004) have reported that the SERS intensities should depend on both size and population (i.e. interparticle distance) of NPs, and they showed that there is a threshold particle density where the interaction between the particles becomes significant (Lee and Park, 2011; Fan and Brolo, 2009; Wang et al., 2006). When the population is lower than this threshold, the SERS intensity increased slowly with the particle density. However, the SERS intensity will increase rapidly due to the surface plasmons coupling after the threshold value is reached (Lee and Park, 2011). The LSPR of metallic nanoparticles is the result of the collective oscillation of conduction electrons within the particles upon interaction with light (Kundu, 2013). In our present investigation, the close distance of two AuNFs leads to the interaction of their LSPR and result in the strong SERS enhancement effects.

To prove the sensitivity and reliability of AuNFs/(PVA/PEI) SERS substrates, SERS spectra of RhB were collected by varying its concentration from 10^{-5} to 10^{-9} M. As shown in Fig. 6E, from curve a to curve e, the intensities of the Raman signals of RhB decreased with the increased RhB concentrations from 10^{-5} to 10^{-9} M and 10^{-8} M RhB can still be detected with this substrate. However, the intensity of 10^{-9} M RhB is very weak, indicating the lowest detection limit of RhB. In this study, the concentration of RhB is varied and the SERS signal is decreased. It is because the decrease of RhB molecules results in the decrease of RhB molecules bound to the Au nanocrystals, and therefore, the Raman signals collected from the Au nanocrystals bonded with RhB molecules decreased. The low detection limits obtained in our SERS substrates are lower than our reported studies and the recently published literatures (Zhu et al., 2012b; Zhang et al., 2012b; Wu et al., 2010).

Fig. 6F illustrated the corresponding plot of I_{SERS} versus $-\log [R6G]$, in which I_{SERS} is the SERS intensity recorded for the band at 1644 cm^{-1} , which are the strongest bands in the R6G spectrum. The results show that the data can be fitted by a linear plot and the correlation coefficient is 0.95. The detection limit of RhB is about 10^{-9} M, which is considered as the lowest concentration leading the SERS intensity of the marker band at 1644 cm^{-1} . These SERS substrates based on PVA/PEI nanofibers with self-assembled Au nanocrystals exhibit highly efficient SERS enhancement. The Raman intensities of the detection can be easily adjusted by changing the densities of the AuNFs throughout the nanofibers. With the increased particle density of AuNFs on the nanofibers, the interparticle distances become shorter, together with the increased “hot” spots, leading to strong SERS enhancement effects. In practical applications, the water-stable SERS substrate is feasible to use as a recyclable SERS substrate.

4. Conclusions

In summary, we demonstrated a facile approach for the fabrication of flexible and reliable sulfhydryl functionalized PVA/PEI nanofibers with excellent water stability for the self-assembly of Au nanocrystals, such as AuNPs, Au nanoflowers (AuNFs), Au nanorods (AuNRs), as the highly efficient SERS substrates for the detection of RhB. Various methods were employed to cross-link the PVA nanofibers with better morphology and porous structures after immersing in water for the desired time. Various SERS-active Au nanocrystals, such as AuNPs, AuNFs, and AuNRs have been successfully synthesized. After the grafting of MPTES on the cross-linked PVA/PEI nanofibers, the Au nanocrystals can easily be self-assembled on the surfaces of the nanofibers because of the strong interactions of the Au–S chemical bondings. The amount of the AuNFs on the nanofibers can be adjusted by changing the concentration of the nanocrystals solution. Therefore, with the finely formed nanocrystals junctions, aggregates can produce intense Raman signatures of reporters with high reproducibility. The Au nanocrystals self-assembled throughout the PVA/PEI nanofibers using as SERS substrates both indicate enhanced SERS signals of RhB compared with their individual nanocrystals. It is mainly due to the close interparticle distance, mutual orientation and high density of “hot” spots, that can strongly affect the overall optical response and the SERS enhancement. By changing the amounts of the self-assembled AuNFs on the nanofibers, we can control the density of the “hot” spots and with the increased amounts of the AuNFs throughout the nanofibers, the SERS substrates show enhanced Raman signals of the RhB, indicating that the increased density of “hot” spots can directly lead to the SERS enhancement. The AuNFs/(PVA/PEI) nanofibers SERS substrates show good sensitivity, reliability and low detection limit

(10^{-9} M). The presented approach can be broadly applicable to different types of plasmonic nanostructures and these novel materials with strong SERS enhancement can be applied in bioanalysis and biosensors.

Acknowledgments

We acknowledge the support of the project of the National Natural Science Foundation of China (NSFC) (51243001 and 51373154), and the 521 Talent Project of Zhejiang Sci-Tech University.

Appendix. Supporting information

Supporting information associated with this article can be found in the online version at <http://dx.doi.org/10.1016/j.bios.2013.10.047>.

References

- Ahamad, N., Ianoul, A., 2011. *J. Phys. Chem. C* 115, 3587–3594.
- Anker, J.N., Hall, W.P., Lyandres, O., Shah, N.C., Zhao, J., Van Duyne, R.P., 2008. *Nat. Mater.* 7, 442–453.
- Aragay, G., Pino, F., Merkoci, A., 2012. *Chem. Rev.* 112, 5317–5338.
- Chen, J.J., Struk, K.N., Brennan, A.B., 2011. *Langmuir* 27, 13754–13761.
- Destaye, A.G., Lin, C.K., Lee, C.K., 2013. *ACS Appl. Mater. Interfaces* 5, 4745–4752.
- Du, X., He, J.H., 2010. *Dalton Trans.* 39, 9063–9072.
- Engel, Y., Schiffman, J.D., Goddard, J.M., Rotello, V.M., 2012. *Mater. Today* 15, 478–485.
- Fan, M.K., Brolo, A.G., 2009. *Phys. Chem. Chem. Phys.* 11, 7381–7389.
- Fan, M.K., Lai, F.J., Chou, H.L., Lu, W.T., Hwang, B.J., Brolo, A.G., 2013. *Chem. Sci.* 2013 (4), 509–515.
- Gabudean, A.M., Focsan, M., Astilean, S., 2012. *J. Phys. Chem. C* 116, 12240–12249.
- Gong, X., Bao, Y., Qiu, C., Jiang, C.Y., 2012. *Chem. Commun.* 48, 7003–7018.
- He, D., Hu, B., Yao, Q.F., Wang, K., Yu, S.H., 2009. *ACS Nano* 3, 3993–4002.
- He, F.A., Fan, J.T., Song, F., Zhang, L.M., Chan, H.L.W., 2011. *Nanoscale* 3, 1182–1188.
- He, J., Perez, M.T., Zhang, P., Liu, Y.J., Babu, T., Gong, J.H., Nie, Z.H., 2012. *J. Am. Chem. Soc.* 134, 3639–3642.
- Huang, J., Zhang, L.M., Chen, B., Ji, N., Chen, F.H., Zhang, Y., Zhang, Z.J., 2010. *Nanoscale* 2, 2733–2738.
- Jiang, G.Q., Hore, M.J.A., Gam, S., Composto, R.J., 2012. *ACS Nano* 6, 1578–1588.
- Khatri, O.P., Adachi, K., Murase, K., Okazaki, K.I., Torimoto, T., Tanaka, N., Kuwabata, S., Sugimura, H., 2008. *Langmuir* 24, 7785–7792.
- Kim, D.Y., Yu, T., Cho, E.C., Ma, Y.Y., Park, O.O., Xia, Y.N., 2011. *Angew. Chem. Int. Ed.* 50, 6328–6331.
- Kotov, N.A., 2011. *J. Mater. Chem.*, 16673–16674.
- Kundu, S., 2013. *J. Mater. Chem. C* 1, 831–842.
- Lee, C.H., Tian, L.M., Abbas, A., Kattumenu, R., Singamaneni, S., 2011. *Nanotechnology* 22, 275311–275318.
- Lee, Y.H., Park, T.G., 2011. *Langmuir* 27, 2965–2971.
- Liu, J.Y., Cai, H.B., Yu, X.X., Zhang, K., Li, X.J., Li, J.W., Pan, N., Shi, Q.W., Luo, Y., Wang, X.P., 2012. *J. Phys. Chem. C* 116, 15741–15746.
- Liu, Y.Y., Zhang, Y.X., Ding, H.L., Xu, S.C., Li, M., Kong, F.Y., Luo, Y.Y., Li, G.H., 2013. *J. Mater. Chem. A* 1, 3362–3371.
- Liu, Z., Zhou, C.S., Zheng, B.Z., Qian, L., Mo, Y., Luo, F.L., Shi, Y.L., Choi, M.M.F., Xiao, D., 2011. *Analyst* 136, 4545–4551.
- Moskovits, M., 2005. *J. Raman Spectrosc.* 36, 485–496.
- Negishi, Y., Nobusada, K., Tsukuda, T., 2005. *J. Am. Chem. Soc.* 127, 5261–5270.
- Park, K., Drummy, L.F., Wadams, R.C., Koerner, H., Nepal, D., Fabris, L., Vaia, R.A., 2013. *Chem. Mater.* 25, 555–563.
- Peng, M.F., Gao, J., Zhang, P.P., Li, Y., Sun, X.H., Lee, S.T., 2011. *Chem. Mater.* 23, 3296–3301.
- Peng, X.H., Santulli, A.C., Sutter, E., Wong, S.S., 2012. *Chem. Sci.* 3, 1262–1272.
- Perez-Juste, J., Rodriguez-Gonzalez, B., Mulvaney, P., Liz-Marzan, L.M., 2005. *Adv. Funct. Mater.* 15, 1065–1071.
- Personick, M.L., Langille, M.R., Zhang, J., Harris, N., Schatz, G.C., Mirkin, C.A., 2011. *J. Am. Chem. Soc.* 133, 6170–6173.
- Qian, K., Liu, H.L., Yang, L.B., Liu, J.H., 2012. *Nanoscale* 4, 6449–6454.
- Qiao, Y., Chen, H., Lin, Y.Y., Huang, J.B., 2011. *Langmuir* 27, 11090–11097.
- Rycenga, M., Xia, X.H., Moran, C.H., Zhou, F., Qin, D., Li, Z.Y., Xia, Y.N., 2011. *Angew. Chem. Int. Ed.* 50, 5473–5477.
- Saha, A., Palmal, S., Jana, N.R., 2012a. *Nanoscale* 4, 6649–6657.
- Saha, K., Agasti, S.S., Kim, C., Li, X.N., Rotello, V.M., 2012b. *Chem. Rev.* 112, 2739–2779.
- Sanchez-Iglesias, A., Grzelczak, M., Perez-Juste, J., Liz-Marzan, L.M., 2010. *Angew. Chem. Int. Ed.* 49, 9985–9989.
- Schlucker, S., 2009. *Chem. Phys. Chem.* 10, 1344.
- Schmit, V.L., Martoglio, R., Scott, B., Strickland, A.D., Carron, K.T., 2012. *J. Am. Chem. Soc.* 134, 59–62.

- Selegard, L., Khranovskyy, V., Soderlind, F., Vahlberg, C., Ahren, M., Kall, P.O., Yakimova, R., Uvdal, K., 2010. *ACS Appl. Mater. Interfaces* 2, 2128–2135.
- Singh, D.K., Jagannathan, R., Khandelwal, P., Abraham, P.M., Poddar, P., 2013. *Nanoscale* 5, 1882–1893.
- Song, S.P., Qin, Y., He, Y., Huang, Q., Fan, C.H., Chen, H.Y., 2010. *Chem. Soc. Rev.* 39, 4234–4243.
- Tamato, R., Lecomte, S., Si, S., Moldovan, S., Ersen, O., Delville, M.H., Oda, R., 2012. *J. Phys. Chem. C* 116, 23143–23152.
- Tanaka, A., Takeda, Y., Imamura, M., Sato, S., 2003. *Phys. Rev. B: Condens. Matter* 68, 195415.
- Vigderman, L., Khanal, B.P., Zubarev, E.R., 2012. *Adv. Mater.* 24, 4811–4841.
- Wang, H.H., Liu, C.Y., Wu, S.B., Liu, N.W., Peng, C.Y., Chan, T.H., Hsu, C.F., Wang, J.K., Wang, Y.L., 2006. *Adv. Mater.* 18, 491–495.
- Wang, J., Yao, H.B., He, D., Zhang, C.L., Yu, S.H., 2012a. *ACS Appl. Mater. Interfaces* 4, 1963–1971.
- Wang, Y., Tang, Z.Y., Liang, X.R., Liz-Marzan, L.M., Kotov, N.A., 2004. *Nano Lett.* 4, 225–231.
- Wang, Y.Q., Yan, B., Chen, L.X., 2013. *Chem. Rev.* 113, 1391–1428.
- Wang, Z.Y., Zong, S.F., Li, W., Wang, C.L., Xu, S.H., Chen, H., Cui, Y.P., 2012b. *J. Am. Chem. Soc.* 134, 2993–3000.
- Wu, H., Lin, D.D., Pan, W., 2010. *Langmuir* 26, 6865–6868.
- Xiao, M.D., Chen, H.J., Ming, T., Shao, L., Wang, J.F., 2010. *ACS Nano* 4, 6565–6572.
- Xie, J.P., Zhang, Q.B., Lee, J.Y., Wang, D.I.C., 2008. *ACS Nano* 2, 2473–2480.
- Xie, W., Schlucker, S., 2013. *Phys. Chem. Chem. Phys.* 15, 5329–5344.
- Xie, W., Herrmann, C., Kompe, K., Haase, M., Schlucker, S., 2011. *J. Am. Chem. Soc.* 133, 19302–19305.
- Ye, X.C., Jin, L.H., Caglayan, H., Chen, J., Xing, G.Z., Zheng, C., Doan-Nguyen, V., Kang, Y.J., Engheta, N., Kagan, C.R., Murray, C.B., 2012. *ACS Nano* 6, 2804–2817.
- Yoon, I., Kang, T., Choi, W., Kim, J., Yoo, Y., Joo, S.W., Park, Q.H., Ihee, H., Kim, B., 2009. *J. Am. Chem. Soc.* 131, 758–762.
- Yuan, J.Y., Gao, H.T., Schacher, F., Xu, Y.Y., Richter, R., Tremel, W., Muller, A.H.E., 2009. *ACS Nano* 3, 1441–1450.
- Zhang, C.L., Lv, K.P., Cong, H.P., Yu, S.H., 2012a. *Small* 8, 648–653.
- Zhang, F.Z., Zhao, X.F., Feng, C.H., Li, B., Chen, T., Lu, W., Lei, X.D., Xu, S.L., 2011. *ACS Catal.* 1, 232–237.
- Zhang, J.T., Li, X.L., Sun, X.M., Li, Y.D., 2005. *J. Phys. Chem. B* 109, 12544–12548.
- Zhang, L.F., Gong, X., Bao, Y., Zhao, Y., Xi, M., Jiang, C.Y., Fong, H., 2012b. *Langmuir* 28, 14433–14440.
- Zhang, T.J., Wang, W., Zhang, D.Y., Zhang, X.X., Ma, Y.R., Zhou, Y.L., Qi, L.M., 2010. *Adv. Funct. Mater.* 20, 1152–1160.
- Zhu, H., Du, M.L., Yu, D.L., Wang, Y., Zou, M.L., Xu, C.S., Fu, Y.Q., 2012a. *Dalton Trans.* 41, 13795–13799.
- Zhu, H., Du, M.L., Zou, M.L., Xu, C.S., Fu, Y.Q., 2012b. *Dalton Trans.* 41, 10465–10471.
- Zhu, H., Du, M.L., Zou, M.L., Xu, C.S., Li, N., Fu, Y.Q., 2012c. *J. Mater. Chem.* 22, 9301–9307.
- Zhu, H., Du, M.L., Yu, D.L., Wang, Y., Wang, L.N., Zou, M.L., Zhang, M., Fu, Y.Q., 2013a. *J. Mater. Chem. A* 1, 919–929.
- Zhu, H., Du, M.L., Zhang, M., Wang, P., Bao, S.Y., Wang, L.N., Fu, Y.Q., Yao, J.M., 2013b. *Biosens. Bioelectron.* 43, 210–215.
- Zhu, H., Du, M.L., Zhang, M., Wang, P., Bao, S.Y., Fu, Y.Q., Yao, J.M., 2013c. *Sensor. Actuat. B – Chem.* 185, 608–619.
- Zhu, Z.H., Zhu, T., Liu, Z.F., 2004. *Nanotechnology* 15, 357–364.
- Zou, M.L., Du, M.L., Zhu, H., Xu, C.X., Fu, Y.Q., 2012. *J. Phys. D: Appl. Phys.* 45, 325302–325308.
- Zou, M.L., Du, M.L., Zhu, H., Xu, C.S., Li, N., Fu, Y.Q., 2013. *Polym. Eng. Sci.* 53, 1099–1108.

Cite this: *RSC Adv.*, 2014, 4, 794

In situ growth of Rh nanoparticles with controlled sizes and dispersions on the cross-linked PVA–PEI nanofibers and their electrocatalytic properties towards H_2O_2 †

Han Zhu,^a Ming Zhang,^{*ab} ShengYing Cai,^a YingTing Cai,^a Pan Wang,^a ShiYong Bao,^a Meiling Zou^a and MingLiang Du^{ab}

A facile approach for the synthesis of uniform, small size and well-dispersed rhodium nanoparticles (RhNPs) on cross-linked polyvinyl alcohol–polyethyleneimine (PVA–PEI) nanofibers has been demonstrated. Various methods were firstly employed to cross-link PVA nanofibers and the cross-linked PVA–PEI nanofibers exhibited good water stability and porous structures after immersing in water for 72 h. Because of the strong chelate effects among the amine groups, hydroxyl groups and Rh^{3+} ions, uniform RhNPs with an average diameter of about 2.5 ± 0.2 nm can evenly and densely grow throughout the PVA–PEI nanofibers *via* an *in situ* reduction. Meanwhile, the better dispersion and smaller size of the RhNPs grown on the nanofibers in comparison with the pre-synthesized RhNPs directly deposited on the nanofibers exhibit the advantages of *in situ* reduction for size and dispersion control. The successful fabrication of the RhNPs(PVA–PEI) nanofibers with various densities of well-dispersed RhNPs demonstrates that the strong chelate effects and stabilization of the PVA–PEI nanofibers also play an essential role in the size and dispersion control of RhNPs. The crystal structures, chemical bonding and interactions of the prepared nanofibers were verified using XPS and FTIR spectra and XRD patterns. These novel nanomaterials were fabricated as non-enzymatic electrochemical sensors and exhibit highly electrocatalytic activity towards H_2O_2 .

Received 2nd September 2013
Accepted 8th November 2013

DOI: 10.1039/c3ra44834g

www.rsc.org/advances

Introduction

The rational design of new generation catalysts with excellent performance requires control over their architecture at the nanoscale. The size, shape and dispersion control of nanostructures determines their catalytic behavior through the adjustment of the number and geometric structure of the active sites.^{1–3} Recently, noble metal nanoparticles (NPs) with sizes below 10 nm have been extensively studied in catalysis due to their high surface to volume ratios, unique electronic property and catalytic activity that are significantly different from their bulk forms.^{4,5} To date, various noble metals, such as gold, silver, palladium, and platinum have been studied extensively in catalysis reactions.^{6,7} However, compared to other noble metals, the synthesis of size-controlled and well-dispersed rhodium nanoparticles (RhNPs) is a challenging task and there are few

reports on the size and dispersion control of RhNPs.^{1,7} Rh is a choice metal for this study not only because of the lack of structural control but also because of its versatility, activity, and selectivity over so many chemical transformations, such as NO reduction, CO oxidation, hydrogenations, electro-oxidations, and hydroformylations.^{8–12}

Previously literature has reported that the electrocatalytic activity of metal NPs is extremely sensitive to their sizes, shapes and dispersion.^{13–15} Small size usually can dramatically affect their physical and chemical properties arise from their large surface-area-to-volume ratio and the spatial confinement of electrons, phonons, and electric fields in and around these particles.^{16–19} However, along with the exciting properties caused by the small size, and due to the high surface energy and large surface curvature of NPs, significant challenges are still remain for the preparation and isolation of NPs with controlled sizes and dispersion.^{1,2,20} The lack of the structural control for Rh could be attributed to the small number of suitable surfactants or adsorbate additives which can stabilize the growing Rh surface.¹ Therefore, the metal precursors are reduced in the presence of the surface stabilizer, which prevent aggregation and may also impact the control in the growth process. In addition, because of the growing environmental concerns and increasingly stringent regulations governing auto emissions,

^aDepartment of Materials Engineering, College of Materials and Textile, Zhejiang Sci-Tech University, Hangzhou 310018, P. R. China

^bKey Laboratory of Advanced Textile Materials and Manufacturing Technology, Zhejiang Sci-Tech University, Ministry of Education, Hangzhou 310018, P. R. China. E-mail: du@zstu.edu.cn; Tel: +86-571-86843255

† Electronic supplementary information (ESI) available. See DOI: 10.1039/c3ra44834g

more efficient, reproducible, stable catalysts are needed and based on the demands, more and more noble metal NPs are intend to load on the substrates.^{15,21}

As a kind of 1-D substrates, polymer nanofibers prepared by the electrospinning process gradually attracted the attention of many researchers because of the associated advantages of the synthesizing technique and the obtained products.^{22–25} Compared with the widely used 1-D substrates, such as carbon nanotubes, metal and metal oxide nanowires, the electrospun nanofibers possess several remarkable characteristics such as flexibility in surface functionalities, high specific surface area, high porosity and superior mechanical performance.^{23–27} Meanwhile, the surfaces of the polymer nanofibers possess abundant chemical groups, making the polymer nanofibers to be optimal substrates for the immobilization of metal NPs. Among a wide series of electrospun polymers, poly(vinyl alcohol) (PVA) attracted particular attention due to its plenty advantageous properties such as water solubility, hydrophilicity, chemical and thermal stability, and biocompatibility.^{24,28,29} However, the water soluble PVA nanofibers cannot stay in water, which impose restrictions on the widely practical applications. Various methods were employed to cross-linked PVA nanofibers using physical methods such as heat and radiation or chemical agents including glutaraldehyde (GA), glyoxal, and boric acid.^{28,29} It should be noted that the cross-linkage of the PVA nanofibers usually results in the formation of merged and entangled nanofibers and the damages of the porous structures of the nanofibers.^{20,30} Therefore, how to obtain the cross-linked PVA nanofibers with good water stability and porous structures still remain challenge.

Recent studies in our groups have shown that small, uniform and well-dispersed Au and AgNPs can be synthesized in polyacrylonitrile nanofibers or immobilized on the halloysite nanotubes *via in situ* reduction and these novel materials exhibit high catalytic activity and antibacterial property.^{31–34} In addition, we also fabricated the sulfhydryl functionalized water-stable PVA nanofibers to served as a nanoreactor for the *in situ* formation of AgNPs, and the fabricated AgNP-immobilized PVA nanofibers have been demonstrated to be a highly active biosensor for the detection of glutathione and glucose.^{20,30} These successes in the fabrication of Au, Ag and PtNPs embedded in or immobilized on the electrospun polymer nanofibers lead us to develop a facile approach to synthesis small, uniform and well-dispersed RhNPs on the surfaces of cross-linked PVA nanofibers for the electrochemical detection of H₂O₂.

In the present investigations, various methods were firstly employed to cross-linked PVA nanofibers with good water stability and porous structures. The morphologies of cross-linked nanofibers immersed in water for the desired times help us to obtain a best substrates for the growth of RhNPs. The cross-linking reaction of PVA–PEI nanofibers is due to the formation of acetal bridges generated between PVA–GA, and aldimine linkages generated between the GA–PEI.^{24,28–30} The chemical bondings informations were verified by the FTIR and XPS characterizations. The cross-linked PVA–PEI nanofibers with good water stability and porous structures were immersed in RhCl₃ solution to complex the Rh³⁺ ions with the amine and

hydroxyl groups of the PEI–PVA nanofibers because of the chelate effects. Through the reduction by NaBH₄, small, uniform and well-dispersed RhNPs were grown on the surfaces of PVA–PEI nanofibers *via in situ* reduction. The pre-synthesized RhNPs in water directly deposited on the PVA–PEI nanofibers exhibit larger size and aggregated RhNPs clusters, indicating the advantages of the *in situ* reduction and the stabilization of the PVA–PEI nanofibers in the control of the size and dispersion of the RhNPs. A series of RhNPs/(PVA–PEI) nanofibers mats with various densities of RhNPs were prepared and the RhNPs can also show uniform size and well dispersion. The fabricated non-enzymatic RhNPs/(PVA–PEI) nanofibrous mats electrochemical sensors exhibit highly electrocatalytic activity towards H₂O₂, which would be the promising nanomaterials for the widely application in the biosensors and bioelectrocatalysis.

Experimental method

Materials

Rhodium (III) chloride hydrate (RhCl₃·3H₂O, 99.9%), polyvinyl alcohol (88% hydrolyzed, *M_w* = 88 000), and polyethyleneimine (PEI, branched, *M_w* = 750 000, 50 wt% in water) were acquired from Shanghai Civi Chemical Technology Co., Ltd. Glutaraldehyde (GA) aqueous solution (30 wt%) and hydrochloric acid were obtained from Aladdin Chemistry Co., Ltd. Epigallocatechin gallate (EGCG) was purchased from Xuancheng Baicao Plant Industry and Trade Co., Ltd. Nafion aqueous solution (5 wt%) was obtained by Aldrich Chemistry Co., Ltd. All the chemicals were used as received without further purification. Deionized water (DIW, 18.2 MΩ) was used for all solution preparations.

Fabrication of the water-stable PVA nanofibrous mats *via* various methods

For the preparation of PVA solution (10 wt%), a certain amount of PVA powder was firstly dissolved in DIW at 85 °C overnight under magnetic stirring to get homogeneous solution, and then the solution was cooled down to room temperature naturally. (1) In the fabrication of PVA–GA nanofibers, the GA solution (30 wt%) was mixed with the PVA aqueous solution under vigorous stirring to achieve a homogeneous solution, in which the mass ratio of PVA and GA was 4 : 1. The prepared PVA–GA electrospun precursor solution was collected in a 10 mL syringe equipped with a 24 gauge stainless steel needle tip. The syringe was fixed on an electric syringe pump set to maintain constant feed rate of 0.01 mL min^{−1} for PVA–GA nanofibers. The voltage was 12 kV and the distance between the needle tip and the collector were 12 cm. (2) In the fabrication of the cross-linked PVA nanofibers, the PVA precursor solution (10 wt%) was firstly electrospun into the PVA nanofibers, and then treatment *via* the GA vapor in a vacuum oven at 60 °C for 24 h. (3) For the preparation of the acid promoted cross-linked PVA–GA nanofibers, the above prepared PVA–GA nanofibers were immersed in a mixed solution containing 10 vol% of HCl aqueous solution (37 wt%) and 90 vol% methanol for 24 h to produce water-stable nanofibrous mats. (4) For the preparation of PVA–PEI

electrospun precursor solution, PEI (50 wt%) and PVA (12 wt%) solutions were mixed together under magnetic stirring overnight with a PEI–PVA mass ratio of 1 : 3 to achieve a homogeneous solution. The electrospun procedure of PVA–PEI precursor was the same as PVA nanofibers. The constant of the feed rate, voltage and distance are $0.005 \text{ mL min}^{-1}$, 20 kV and 20 cm. The freshly prepared PEI–PVA nanofibers were then cross-linked by GA vapor to render the nanofibers with water stability. The diameters and distribution of all the prepared nanofibers were measured by Image-Pro Plus6.2 software (200 particles of nanofibers were randomly selected for the measurement).

Facile preparation of the RhNPs immobilized on cross-linked PVA–PEI nanofibers via an *in situ* reduction approach

0.110 g of the freshly prepared cross-linked PVA–PEI nanofibrous mats were immersed into the desired volume of RhCl_3 solution (5 mL, 10 mM) by vigorous shaking in an incubator shaker at room temperatures for 3 h to reach the adsorption equilibrium of the Rh^{3+} ions. Then the PVA–PEI nanofibers chelated with Rh^{3+} ions were rinsed with DIW and ethanol three times, respectively. After that, the prepared $\text{Rh}^{3+}/(\text{PVA-PEI})$ nanofibers mats were immersed into NaBH_4 solution followed by vigorous shaking in an incubator shaker at room temperatures for 1 h. The as-produced $\text{RhNPs}/(\text{PVA-PEI})$ nanofibers mats were rinsed with DIW three times, followed by drying at room temperature for 2 h, and stored under ambient conditions. The diameters and distribution of the RhNPs and nanofibers were measured by Image-Pro Plus6.2 software (200 particles of RhNPs were randomly selected for the measurement).

Fabrication of the RhNPs deposited on the cross-linked PVA–PEI nanofibrous mats

The RhNPs (5 mL, 10 mM) were firstly synthesized in DIW (45 mL) using NaBH_4 as the reductant and the EGCG as the stabilizer. Then, 0.110 g of the freshly prepared cross-linked PVA–PEI nanofibrous mats were immersed into the desired volume of RhNPs (50 mL) solution by vigorous shaking in an incubator shaker at room temperatures for 3 h to reach the adsorption equilibrium of the RhNPs. The as-produced $\text{RhNPs}/(\text{PVA-PEI})$ nanofibers mats were rinsed with DIW three times, followed by drying at room temperature for 2 h, and stored under ambient conditions. The diameters and distribution of the RhNPs and nanofibers were measured by Image-Pro Plus6.2 software (200 particles of RhNPs were randomly selected for the measurement).

Facile preparation of the $\text{RhNPs}/(\text{PVA-PEI})$ nanofibers with various loading of the RhNPs via an *in situ* reduction approach

A similar approach was used for the preparation of $\text{RhNPs}/(\text{PVA-PEI})$ nanofibers with various loading of the RhNPs. The PVA–PEI nanofibrous mats with same weight were immersed into DIW solution containing 1, 2.5, 5, 7.5 mL RhCl_3 solution, respectively, to reach the adsorption equilibrium of the Rh^{3+}

ions. Then, the prepared $\text{Rh}^{3+}/(\text{PVA-PEI})$ nanofibers mats were immersed into NaBH_4 solution followed by vigorous shaking in an incubator shaker at room temperatures for 1 h. The as-produced $\text{RhNPs}/(\text{PVA-PEI})$ nanofibrous mats were rinsed with DIW three times, followed by drying at room temperature for 2 h, and stored under ambient conditions. The diameters and distribution of the RhNPs and nanofibers were measured by Image-Pro Plus6.2 software (200 particles of RhNPs were randomly selected for the measurement).

Electrocatalytic experiments

Electrocatalytic experiments were conducted with a CHI660C workstation (Shanghai Chenhua, Shanghai). All experiments were carried out using a conventional three-electrode system in 0.1 M phosphate buffered saline (PBS), where PVA–PEI/GCE and $\text{RhNPs}/\text{PVA-PEI}/\text{GCE}$ was used as the working electrode, a platinum foil as the auxiliary electrode and a saturated Ag/AgCl electrode as the reference electrode. The buffer was purged with high-purity nitrogen for at least 30 min prior to each experiment, and the nitrogen environment was then kept over the solution to protect the solution from oxygen. Electrochemical performances of the fabricated electrodes were tested using a three-electrode system by cyclic voltammetry (CV).

Instrumentation

Transmission electron microscopy (TEM) images were obtained with a JSM-2100 transmission electron microscopy (JEOL, Japan) at an acceleration voltage of 200 kV. The EDS spectrum of the $\text{RhNPs}/(\text{PVA-PEI})$ nanofibers was also recorded by the TEM. The morphologies of all the electrospun nanofibers were observed by a JSM-6700F field-emission scanning electron microscope (FE-SEM, JEOL, Japan) at an acceleration voltage of 1 kV. X-ray Diffraction (XRD) patterns of the PVA–PEI nanofibers and $\text{RhNPs}/(\text{PVA-PEI})$ nanofibers were characterized with a SIEMENS D5000 X-ray diffractometer using Cu K_α radiation source at 35 kV, with a scan rate of $0.02^\circ 2\theta \text{ s}^{-1}$ in the 2θ range of $10\text{--}80^\circ$. Fourier transform infrared (FTIR) spectra were recorded on a Nicolet 5700 FTIR spectrometer in transmittance mode at a resolution of 4 cm^{-1} and 32 scans in the range from 4000 nm to 400 nm. Thermogravimetric analysis (TGA; Pyris 1) was carried out from 298 to 1073 K at a heating rate of 5 K min^{-1} in N_2 atmosphere. X-ray photoelectron spectra of cross-linked PVA–PEI nanofibers and $\text{RhNPs}/(\text{PVA-PEI})$ nanofibers were recorded using an X-ray Photoelectron Spectrometer (Kratos Axis Ultra DLD) with an aluminium (mono) K_α source (1486.6 eV). The aluminium K_α source was operated at 15 kV and 10 mA.

Result and discussion

A better substrate for the growth of RhNPs should be taken into account firstly. It is well-known that the PVA is one of the water-solubility polymer, and in the widely application, much attentions should be drawn to promote the water-stability of the PVA. In this paper, we used four different methods to prepare the cross-linked PVA nanofibers and the morphologies of the PVA

nanofibrous mats *via* different treatments before and after soaked in the water are shown in Fig. 1. Fig. 1a shows the PVA–GA nanofibrous mats prepared from the PVA–GA solution and smooth and uniform nanofibers with random orientation were obtained with an average diameter of 250 ± 38 nm (Fig. S1†). However, after soaking in water for 1 h, the reserved PVA nanofibers swell considerably and the nanofibers start to fuse with each other and destroy the porous structures. The control of the morphology and the porous structures of the nanofibrous mats is essential for the practical applications where a high surface-area-to-volume ratio is considered advantageous.^{20,29} As shown in Fig. 1b, the cross-linked PVA nanofibers treated by GA vapor show distinct nanofibers with average diameter of 460 ± 54 nm (Fig. S2†). It can be observed from Fig. 2f that after soaking in the water for 24 h, the cross-linked PVA nanofibers were swollen, became soft, and intertwined together. Meanwhile, except for the destroyed porous structures, the morphology of the nanofibers still maintained in these mats, indicating that the GA vapor can indeed improve their water stability.

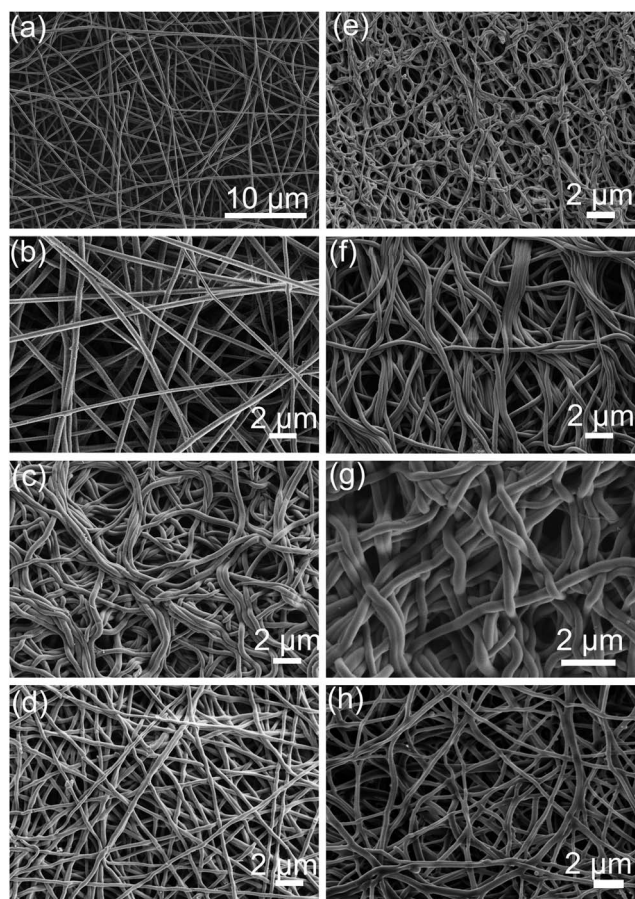


Fig. 1 FE-SEM images of the as-electrospun PVA–GA nanofibrous mats prepared from the PVA–GA mixed solution, (b) cross-linked PVA nanofibrous mats *via* GA vapor, (c) acid promoted GA cross-linked PVA–GA nanofibrous mats and (d) cross-linked PVA–PEI nanofibrous mats *via* GA vapor; FE-SEM images of the corresponding cross-linked PVA nanofibrous mats *via* different treatments immersed in water for (e) 1, (f) 24, (g) 48, and (h) 72 h, respectively.

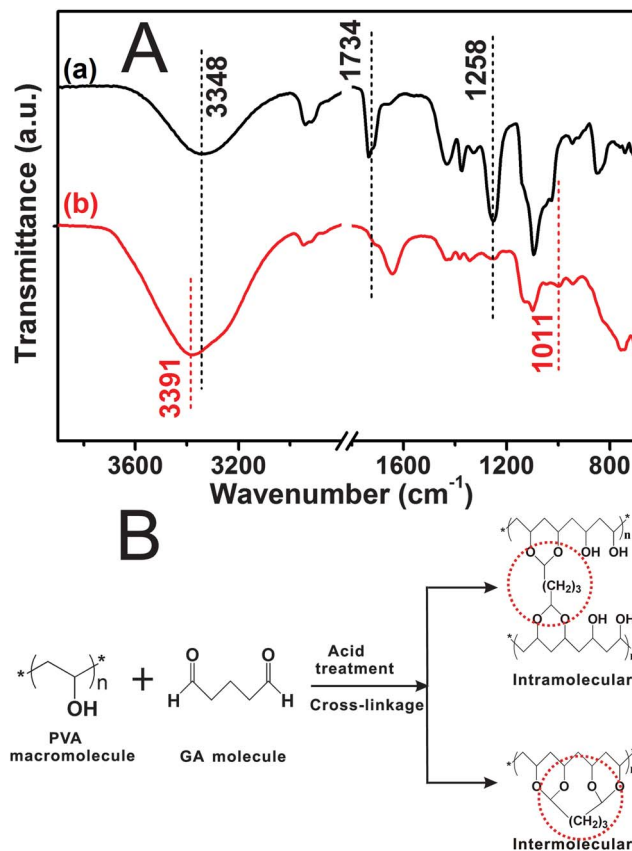


Fig. 2 (A) FTIR spectra of the (a) PVA–GA and (b) acid promoted cross-linked PVA nanofibrous mats; (B) schematic illustration of the cross-linkages between the hydroxyl groups of PVA and aldehyde groups of GA.

Fig. 1c shows the morphology of the acid promoted cross-linked PVA–GA nanofibrous mats. In a prepared procedure, the solution containing both PVA and GA was firstly electrospun into homogeneous nanofibers, and then the PVA–GA nanofibers were immersed into acidic solution to promote the cross-linking generated between hydroxyl groups of the PVA and the aldehyde groups of GA.^{28,29} The morphology of the nanofibrous mats before and after immersing in water for 48 h did not change so much, indicating the enhanced water resistant compared with the freshly prepared PVA–GA nanofibers (Fig. 1a and b). However, the nanofibers before and after soaking in water were both merged and entangled among each other. Based on the above results, the simply mixed PVA with GA, GA vapor and acid promoted cross-linkage are not able to prepare the water-stable PVA nanofibers with uniform and distinct nanofibers, porous structures and high surface-area-to-volume ratio. Therefore, in order to keep the water stability along with the porous structures, another approach should be considered. In biomaterials and bioscience, the PEI polymer with perfect biocompatibility is widely used for the gene and drug delivery, gamma scintigraphy imaging agent, gene therapy and so on.^{35–37} In the present investigation, we use the hyperbranched PEI polymer as the second component to promote the water-stability and morphology of the PVA nanofibers. The mixed PVA

and PEI solution were firstly electrospun into homogeneous nanofibers, and then treat *via* GA vapor for 24 h to improve the water-stability. As shown in Fig. 1d, uniform and distinct nanofibers with average diameter about 460 ± 52 nm (Fig. S3†) are observed, and the nanofibers only formed interfiber bonding/fused mostly at the intersection points because of the GA vapor. It is because that during the GA vapor procedure, the GA vapor contains water vapor and it can swell and soften the surface of the nanofibers, leading to the directly contact with nearby nanofibers at intersection points to form interfiber bonding.²⁹ After immersing in water for 72 h, there is almost no significant merged and entangled nanofibers and the porous structures still remains, indicating the reliable cross-linkage and good water-stability of PVA-PEI nanofibers. Compare the freshly cross-linked PVA-PEI nanofibers with the immersed nanofibers (480 ± 78 nm, Fig. S4†) for 72 h, the average diameters also did not change much.

The chemical bondings of the cross-linked PVA nanofibrous mats were confirmed by FTIR spectra. As shown in Fig. 2A, curve a shows the electrospun PVA-GA nanofibers prepared from the mixed PVA-GA solution, and the morphology of the nanofibers is corresponding to Fig. 1a. The broad band centered at 3348 cm^{-1} are associated with the stretching vibration of hydroxyl ($-\text{OH}$) groups from intermolecular and intramolecular hydrogen bonds.^{20,28–30} The strong peaks located at 1734 and 1258 cm^{-1} are assigned to the $\text{C}=\text{O}$ stretching vibration of free GA aldehyde groups and $\text{C}-\text{O}$ stretching vibration of hydroxyl groups in PVA, respectively. The schematic illustration of the cross-linkages process between PVA and GA is shown in Fig. 2B. Compared with curve a, after the acid promoted cross-linkage of PVA-GA nanofibers, the intensities of the peaks at 1734 cm^{-1} and 1258 cm^{-1} decreased significantly. This means that the acid promoted the cross-linking of the aldehyde groups of GA and the hydroxyl groups of PVA, leading to the formation of ether linkages.²⁵ In addition, a new peak emerged at 1011 cm^{-1} is attributed to the formed ether linkages, indicating the formation of acetal bridges between the aldehyde and the hydroxyl groups. The cross-linkage both in intramolecular and/or intermolecular occurred within and at the point of contact nanofibers, leading to the phenomena of the merged and entangled nanofibers (Fig. 1c). The band became relative broad and moved to 3391 cm^{-1} , which also implied the involvement of the $-\text{OH}$ groups in the cross-linkages, resulting in the partial destruction of hydrogen bonds.³⁰ The chemical bondings of the cross-linked PVA-PEI nanofibrous mats would discuss later.

Based on the above results, the cross-linked PVA-PEI nanofibers were used as the substrates for the growth of RhNPs. As shown in Fig. 3a, the FE-SEM image shows the distinct RhNPs/(PVA-PEI) nanofibers with uniformly average diameter of 540 ± 80 nm (Fig. S5†). The surfaces of the nanofibers are covered by large amounts of small RhNPs, which can also be observed by the TEM image (Fig. 3b). From Fig. 3c, a mass of RhNPs are evenly and densely distributed on the surface of the PVA-PEI nanofibers and there is nearly no aggregated RhNPs, indicating the strong stabilization of the amino and hydroxyl groups. A narrow diameter distribution of the RhNPs has been observed with an average size of 2.5 ± 0.2 nm (Fig. S6†) and the particle

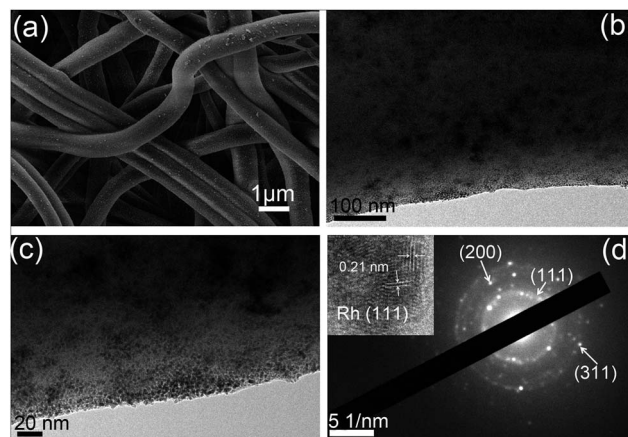


Fig. 3 FE-TEM (a) and TEM (b and c) images of the RhNPs/(PVA-PEI) nanofibers; SAED pattern of the RhNPs/PVA-PEI nanofibers and the inset is the HRTEM of the small RhNPs.

sizes were measured by 200 particles from enlarged TEM images using imaging analysis software, Image-Pro Plus6.2 software (Media Cybernetics Ltd). The size distribution diagram is shown in Fig. S6.† The inset in Fig. 3d exhibits a HRTEM image of RhNPs, showing lattice fringes of the (111) plane with an interplanar distance of 0.21 nm, which is according with the XRD results.^{38–40} Fig. 3d shows the selected area electron diffraction (SAED) pattern of the RhNPs/(PVA-PEI) nanofibers and it reveals the polycrystal rings indexed to the (111), (200), and (311) planes of fcc Rh crystal, respectively, indicating the polycrystallinity of RhNPs.^{39,41,42}

Because of the strong chelate effects among the $-\text{NH}$ groups, $-\text{OH}$ groups and Rh^{3+} ions, the small RhNPs can evenly grow on the surfaces of PVA-PEI nanofibers *via in situ* reduction, and the stabilization of PVA and PEI can impose restrictions on the size and distribution of RhNPs, leading to the formation of the uniform and well-dispersed RhNPs.^{28,33,34} In order to show the advantages of the PVA-PEI assistant *in situ* reduction for the controlled size and distribution of RhNPs, we firstly synthesized the RhNPs by NaBH_4 in water and then the as-synthesized RhNPs were directly deposited on the PVA-PEI nanofibers. Fig. 4a shows the small and uniform RhNPs with average diameter of about 2.8 ± 0.3 nm (Fig. S7†), which is almost the same size as the RhNPs grown on PVA-PEI nanofibers (Fig. 3b). It is well known that because of the high surface energy, the RhNPs are easily aggregated to form larger sizes.^{1,20} In our previously reports, a green compound, EGCG, was used both as reducer and stabilizer for the synthesis of AuNPs, PtNPs and AgNPs.^{20,30,31}

In the present studies, with the assistant of the stabilization of the EGCG, there is no aggregated RhNPs in water (Fig. 4a and b). Fig. 4b shows the HRTEM image of RhNPs, the lattice fringes of an interplanar spacing of 0.21 nm is according with the (111) plane of RhNPs.^{38–40} Compared with the *in situ* growth of RhNPs on PVA-PEI nanofibers (Fig. 3a), large size RhNPs clusters were deposited on the nanofibers, and the aggregated phenomena were relatively serious. As shown in Fig. 4d and e, the large size RhNPs clusters varied from 50 nm to 200 nm, are consist of

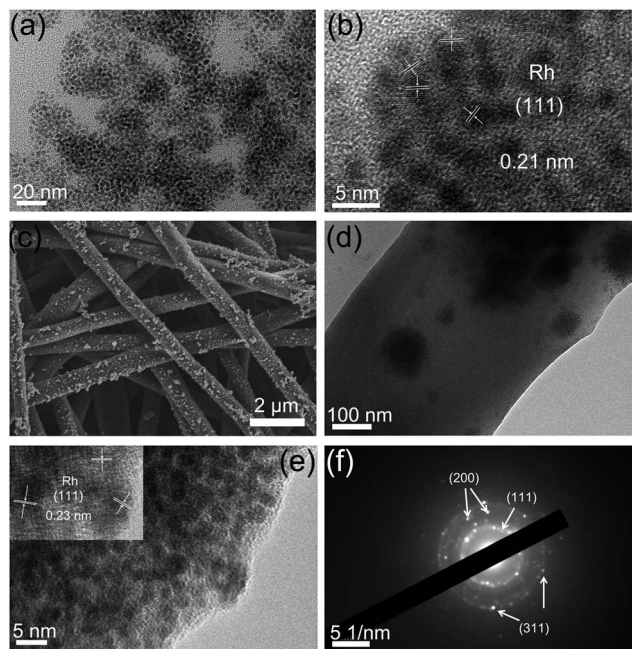


Fig. 4 (a) TEM and (b) HRTEM images of the synthesized RhNPs in water by NaBH_4 with the stabilization of EGCG; (c) FE-SEM and (d and e) TEM image and (f) SAED pattern of the PVA-PEI nanofibers deposited with RhNPs; the inset in the HRTEM image of the RhNPs deposited on PVA-PEI nanofibers.

many small RhNPs. Small RhNPs are united to form Rh clusters, indicating that the $-\text{NH}$ groups can not catch the small RhNPs to get a better distribution through the whole nanofibers. Therefore, the chelate effects between the NH groups and RhNPs is very weak, it cannot afford the enough stabilization for the RhNPs to prevent the aggregated RhNPs clusters. The inset in Fig. 4e show the lattice fringes of the $\text{Rh}(111)$ planes, and the SAED pattern also reveals the polycrystal rings indexed to the (111), (200), and (311) planes of fcc Rh crystal, respectively, which are according with the XRD results.^{39,41,42}

The results of thermogravimetric analysis (TGA) are displayed in Fig. 5A. The weight losses of 8.57 wt% for the cross-linked PVA-PEI and RhNPs/(PVA-PEI) nanofibers, are nearly both observed up to 55 °C, which can be attributed to the loss of free water molecular. The TGA curve of original cross-linked PVA-PEI nanofibers (curve a) shows that a great weight loss of 84.45 wt% occurred between 55 and 570 °C, which is caused by the decomposition of the PVA-PEI nanofibrous mats. Upon the temperature 570 °C, the polymer component of PVA-PEI nanofibrous mats was burned out. Compared with the curve a, the weight losses of 75.53 wt% for RhNPs/(PVA-PEI) nanofibrous mats is observed up to 450 °C, and the component of PVA-PEI nanofibrous mats have almost decomposed, while the Rh residues remains. With the comparison between the RhNPs/(PVA-PEI) nanofibrous mats and PVA-PEI nanofibrous mats, the loading capacity of RhNPs within the nanofibrous mats was estimated to be 8.92 wt%. Fig. 5B presents the results obtained from the energy dispersive X-ray spectroscopic (EDS) analysis. The EDS analysis was mostly used for the determination of

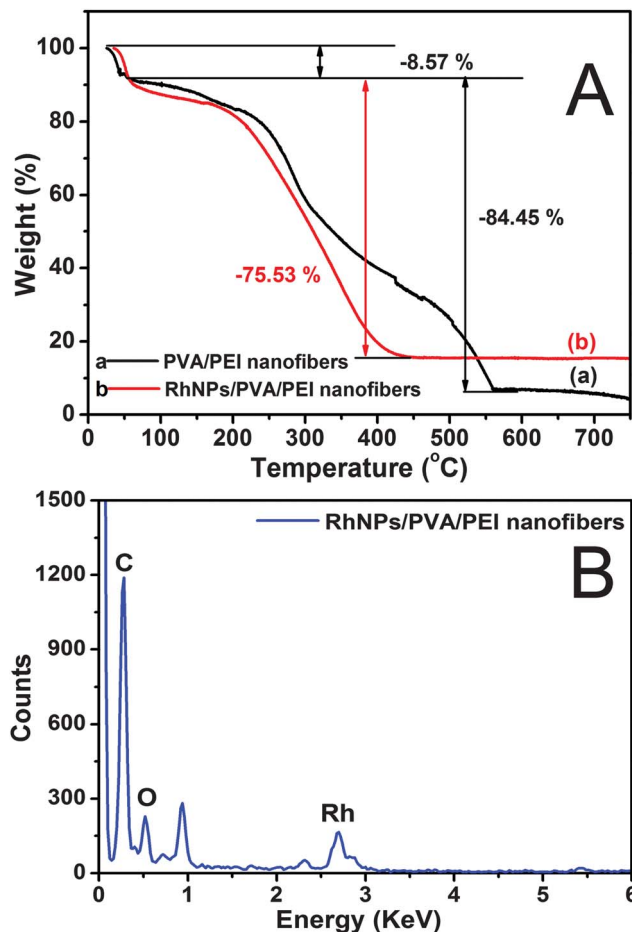


Fig. 5 (A) TGA curves of the cross-linked (a) PVA-PEI and (b) RhNPs/(PVA-PEI) nanofibers; (B) EDS spectra of the RhNPs/(PVA-PEI) nanofibers.

elements present in the products. The EDS spectrum consisted of different peaks for Rh, C, and O. The large intense Rh peak came from the RhNPs, and the C and O peak came from the PVA, PEI and GA.

Fig. 6 shows the FTIR spectra of the pure PVA-PEI nanofibers and cross-linked PVA-PEI nanofibers with and without the growth of RhNPs. In the above discussion, the process and chemical bondings of cross-linkage between PVA and GA have been demonstrated. In this part, the hyperbranched PEI polymer possess large amounts of primary amine and imine groups with high activity and were used as the second component to crosslink the PVA nanofibers.^{28,43,44} As shown in curve a and b, the peak located at 1650 cm^{-1} is ascribed to the bending vibrations of the primary amine groups in the pure and cross-linked PVA-PEI nanofibers, which is essential for the complexation of Rh^{3+} ions.²⁸ The strong peaks located at 1740 cm^{-1} and 1253 cm^{-1} are assigned to the $\text{C}=\text{O}$ stretching vibration of aldehyde groups and the $\text{C}-\text{O}$ stretching vibration of hydroxyl groups in PVA.^{20,28,29} The peak located at the 1582 cm^{-1} is attributed to the bending vibration of imine groups in PEI.^{45,46} After the treatment by GA vapor, some peaks have changed, which can identify the cross-linkage of the

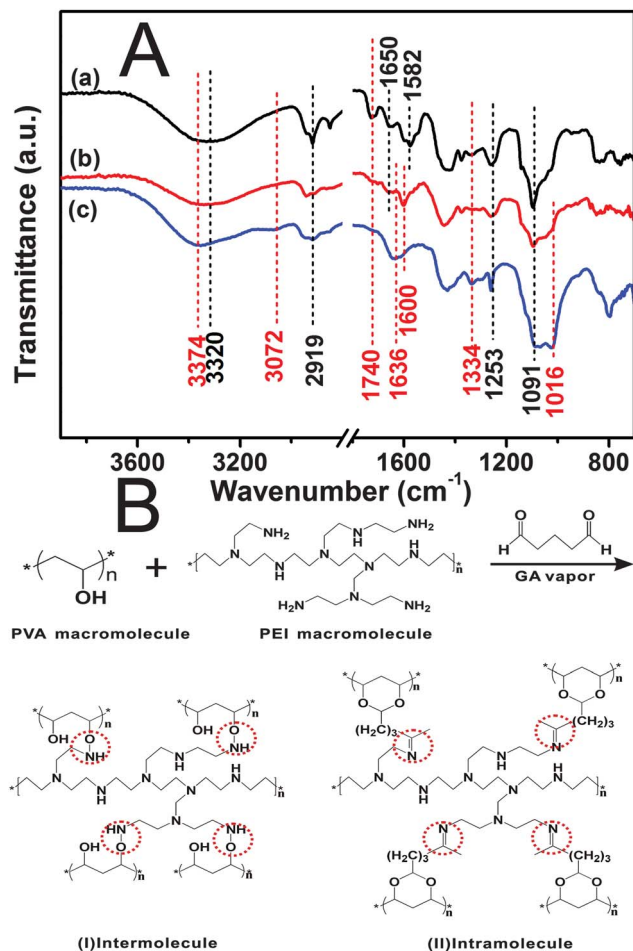


Fig. 6 FTIR spectra of the pure PVA-PEI (a), cross-linked PVA-PEI (b) and RhNPs/(PVA-PEI) (c) nanofibers; (B) schematic illustration of the cross-linkages between the PVA and PEI via the GA vapor.

PEI-PVA nanofibers. The peak ascribed to the $\text{C}=\text{O}$ groups (1740 cm^{-1}) become weaker and a new peak emerged at 1600 cm^{-1} are indicative of the aldimine linkages generated between the GA-PEI.^{28,29}

The chemical bondings among PVA, PEI and GA are shown in Fig. 6B. In addition, compared with curve a, another new peak located at 1016 cm^{-1} are emerged in curve b and c, and it belongs to the ether linkages generated between the GA-PVA. The above information can confirm the successful cross-linkage of the PVA-PEI nanofibers. The followed several evidences can support the chemical interactions among the amino groups, hydroxyls groups and RhNPs. After the growth of RhNPs on cross-linked PVA-PEI nanofibers, the peak location of primary amine groups (1650 cm^{-1}) moves to 1636 cm^{-1} , indicating the chemical interactions between the RhNPs and $-\text{NH}$ groups. In addition, the peak ascribed to the bending vibration of amine groups becomes strong also can support the chelate effects. The broad band centered at 3320 cm^{-1} in curve a and b are attributed to the stretching vibrations of $-\text{NH}$ and $-\text{OH}$ groups, and with the growths of RhNPs, the peak moves to 3374 cm^{-1} and become relatively sharp, which is presumably due to the interaction between the amino/hydroxyl groups of the PEI-PVA

polymers and the immobilized RhNPs.^{30,31} Furthermore, as shown in curve c, two new peaks emerged at 3072 cm^{-1} and 1334 cm^{-1} , are attributed to the stretching and bending vibrations of associated $-\text{NH}$ groups, respectively, which is caused by the hydrogen bonds and chelate effects.

Fig. 7 shows the morphology evolutions of the RhNPs/(PVA-PEI) nanofibers with various amounts of RhNPs. As shown in Fig. 7a, at the low concentration of RhCl_3 , the as-formed RhNPs were well dispersed around the PVA-PEI nanofibers. With the increasing concentration of RhCl_3 , more RhNPs were grown on the surfaces of the nanofibers and no obviously aggregated RhNPs clusters were observed, indicating the perfect stabilization of the PVA and PEI (Fig. 7b). When the amounts of RhCl_3 are further increased to 5 mL, more and more RhNPs formed on the surfaces of nanofibers until the nanofibers are completely encapsulated by a thin layer of RhNPs shells. In addition, there are still no significant aggregated RhNPs clusters. When 7.5 mL RhCl_3 adopted, large amounts of RhNPs are densely grown on the whole nanofibers, which are shown in Fig. 7d. Beyond the minimum loading of RhNPs, the RhNPs start to grow on the previously formed thin layer of RhNPs and join together to form a thicker solid RhNPs shells. Therefore, without the stabilization of the $-\text{NH}$ and $-\text{OH}$ groups of PVA-PEI nanofibers, more and more aggregated RhNPs clusters formed.

XRD patterns of the above RhNPs/(PVA-PEI) nanomaterials are shown in Fig. 8. As shown in Fig. 8, the curve a shows the XRD pattern of the pure PVA-PEI nanofibers and a broad peak centered at 20.8° is attributed to the (101) plane of semi-crystalline PVA.^{47,48} XRD patterns of the RhNPs/(PVA-PEI) nanofibers with various amounts of RhCl_3 ranged from 1 mL to 7.5 mL are shown from curve b to curve e. When 1 mL RhCl_3 adopted, the as-prepared RhNPs/(PVA-PEI) nanofibers mats show very weak characteristic peaks of Rh crystal. With the amounts of RhCl_3 increase to 5 mL, three relatively distinct characteristic peaks of Rh crystal located at 40.2° , 49.7° and 70.0° can be observed, which are according with the (111), (200), and (220) planes ascribed to the face-centered cubic (fcc) Rh

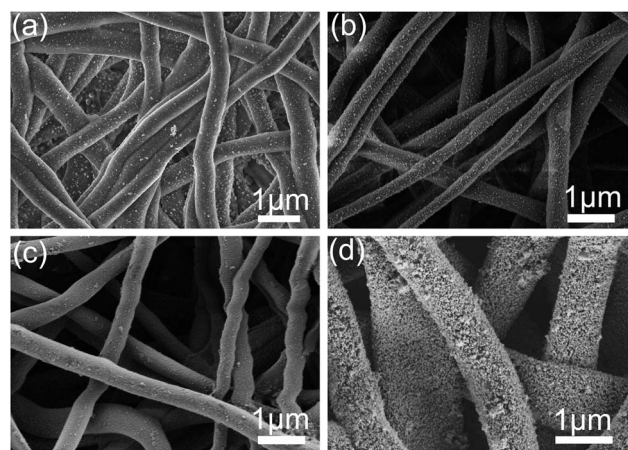


Fig. 7 FE-SEM images of the RhNPs/(PVA-PEI) nanofibers *via in situ* reduction with various amounts of RhCl_3 solution: (a) 1 mL, (b) 2.5 mL, (c) 5 mL and (d) 7.5 mL.

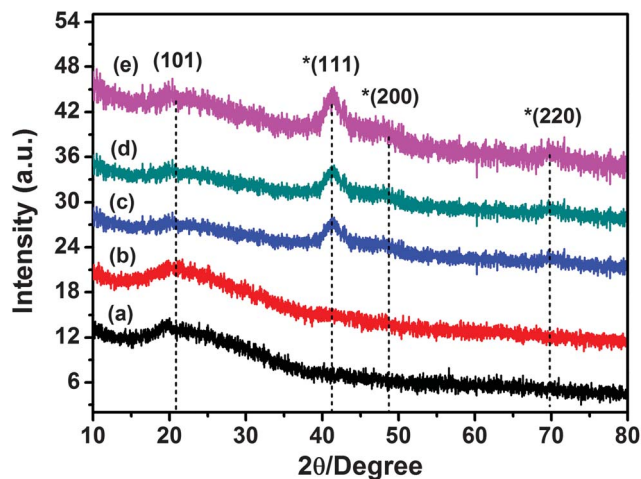


Fig. 8 XRD Patterns of the as-synthesized (a) PVA-PEI and RhNPs/(PVA-PEI) nanofibers with various amounts of RhCl_3 solution: (b) 1 mL, (c) 2.5 mL, (d) 5 mL and (e) 7.5 mL.

metal (JCPDS: 050685).^{49–51} Although the XRD patterns of the PVA-PEI and RhNPs/(PVA-PEI) nanofibers look similar, close examination shows that because of the increased loading of RhNPs on PVA-PEI nanofibers, the relatively intensity of (101) plane peaks become weak, and while the intensity of the Rh plane peaks become strong. There is no other impurity peaks could be detected, such as Rh oxide, indicating the pure phase of the Rh nanocrystals. The XRD results also can show several evidences for the stabilization effects to control the size of RhNPs. It is previously reported that the larger well faceted particles (>5 nm) have predominately exposed (111) crystal planes.⁴⁹ Grass *et al.* have prepared size-controlled RhNPs with average diameter ranged from 1.9 to 11.3 nm and study the size-dependent XRD patterns.⁴⁹ If the size of RhNPs is lower than 5 nm, the (200) and (220) planes peaks are very weak, which are similar with the curve b, c and d. Therefore, based on the FE-SEM images and XRD patterns, the sizes of the major RhNPs grown on PVA-PEI nanofibers can be changed in the range from 2 to 6 nm (below 5 mL of the RhCl_3). The relative strong (111), (200) and (220) peaks (curve e) can also indicate the larger size of the RhNPs, which are due to the aggregated RhNPs clusters.

XPS spectra were used to testify the chemical states and chemical interactions of the prepared nanomaterials and help us to understand the growth process of the RhNPs on nanofibers. The whole XPS spectra of the PVA-PEI and RhNPs/(PVA-PEI) nanofibers are shown in Fig. S8.† Fig. 9A shows the Rh 3d core-level XPS spectra of the RhNPs/(PVA-PEI) nanofibers, and two peaks with binding energy (BE) at 307.5 eV and 312.2 eV are consistent with the literature data for the BE of core levels Rh 3d_{5/2} and Rh 3d_{3/2}, respectively, for the zero-valent Rh.^{52–54} According to the literatures, the metallic Rh(0) shows 3d_{5/2} XPS signal at 307.2 eV, and the relative higher BE of RhNPs in PVA-PEI nanofibers are mainly attributed to the strong chemical bindings among the surface Rh atoms, NH groups and OH groups. The previously literatures have reported that the relatively high BE of metal NPs was due to the binding of

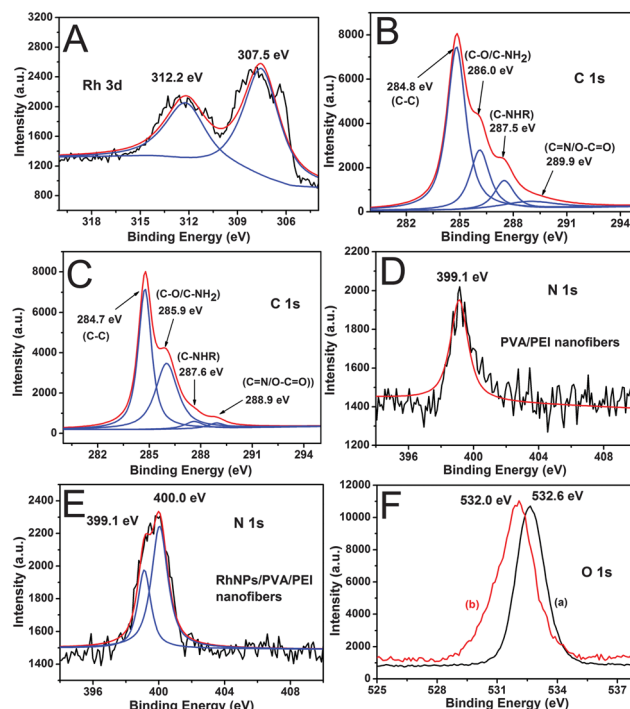


Fig. 9 (A) Rh 3d XPS spectra of the RhNPs/(PVA-PEI) nanofibrous mats; C 1s XPS spectra of the (B) cross-linked PVA-PEI nanofibers and (C) RhNPs/(PVA-PEI) nanofibers; N 1s XPS spectra of the (D) cross-linked PVA-PEI nanofibers and (E) RhNPs/(PVA-PEI) nanofibers; (F) O 1s XPS of the (a) cross-linked PVA-PEI nanofibers and (b) RhNPs/(PVA-PEI) nanofibers.

surface metal atoms with the stabilizer or passive molecules surrounding the NPs, which lead to a substantial electron donation from metal NPs to the stabilizer molecules.³¹ In addition, there are no additional peaks such as Rh(I) and Rh(III) appeared, suggesting that metallic Rh(0) is obviously the predominant species in the RhNPs.

As shown in Fig. 9B and C 1s XPS spectra of the cross-linked PVA-PEI nanofibers shows four significant peaks located at 284.8, 286.0, 287.5 and 289.9 eV, which are according with the carbon atoms in different functional groups: the C-C, the C in C-O and/or C-NH₂ bonds, the C in C-NHR bonds and the C in C=N (aldimine groups) and/or O-C=O bonds.^{55–57} The existence of the aldimine groups indicate the cross-linkage of PVA-PEI nanofibers, which is according with the FTIR results. Compared with Fig. 9B, the C 1s XPS of the RhNPs/(PVA-PEI) nanofibers also shows four similar peaks, which are located at 284.7, 285.9, 287.6 and 288.9 eV, respectively. However, the intensity of the XPS peak of C-NHR bonds has a significant decrease after the growth of RhNPs, indicating the strong interactions between the NH groups and RhNPs. The N 1s XPS spectra of the PVA-PEI nanofibers shows a peak located at 399.1 eV (Fig. 9D), and after the growth of RhNPs, two obvious peaks are appeared in the N 1s XPS spectra of the RhNPs/(PVA-PEI) nanofibers (Fig. 9E). One of the peaks located at 399.1 eV belongs to the unchelated NH groups, while the BE of the other one moves to 400.0 eV because of the strong interactions between the NH groups and RhNPs.^{33,57}

Meanwhile, the O 1s XPS spectra of the PVA-PEI nanofibers before and after the growth of RhNPs show two significant peaks, which are located at the 532.6 and 532.0 eV, respectively. The shift of the BE of O 1s can also indicate the strong interactions between the OH groups and RhNPs. Based on the XPS results for the O, N, C and Rh elements, it can be concluded that the chelating effects among the NH groups, OH groups and Rh^{3+} ions are the keys for the synthesis of uniform, small size and well dispersion RhNPs on PVA-PEI nanofibers. The schematic illustration of the growth process of the RhNPs on PVA-PEI nanofibers is shown in Scheme 1.

As shown in Scheme 1, the PVA-PEI nanofibers were firstly cross-linked by the GA vapor to improve the water stability of the nanofibrous mats. The surfaces of the PVA-PEI nanofibers possess abundant amino (NH) and hydroxyl (OH) groups and these groups can catch the Rh^{3+} ions to form chelate complex because of the chelate effects among the amino groups, hydroxyl groups and Rh^{3+} ions.^{29–33} Then, the $\text{Rh}^{3+}/(\text{PVA-PEI})$ chelated nanofibers were immersed in the NaBH_4 solution, and because of the stabilization of the functional groups, the as-formed Rh chelate complexes were reduced to the small RhNPs immediately *via* the *in situ* reduction. The formed small RhNPs were immobilized on the surfaces of the nanofibers without any collision with other RhNPs. It means that the sizes and distributions of the RhNPs can be controlled through the chelate effects.

RhNPs possess distinct physical and chemical attributes that make them excellent scaffolds for the potential applications in electrocatalysis, electrochemical sensor, bioelectrocatalysis and so on.^{58–60} The detection of H_2O_2 plays a significant role in many fields including clinic, food, pharmaceutical and environmental analyses.^{20,28,61–63} The detection of H_2O_2 based on electrochemical sensors is one of the most used methods because of its low detection limit as well as low costs. However, most sensors based on enzymes or proteins may result in limited lifetime,

stability problem and complex procedures in the fabrication process. Therefore, in the present investigation, the novel nanomaterials were used as a non-enzymatic electrochemical sensor for the electrocatalytic towards H_2O_2 . The electrocatalytic activity of the as-prepared RhNPs/(PVA-PEI) nanofibers was studied with electrochemical cyclic voltammetry. Fig. 10A shows the cyclic voltammograms (CVs) of the (PVA-PEI)/GCE and RhNPs/(PVA-PEI)/GCE electrochemical sensors. Aqueous solutions with 1.0 mM of HQ in 0.1 M of sodium phosphate buffer (PB) at pH 6.8 were used for the electrochemical measurement. As shown in Fig. 10A, well-defined CVs of (PVA-PEI)/GCE (curve a) are observed, and the redox peak currents of HQ are about 28.6 and $-16.6 \mu\text{A}$, with potentials at 0.48 and 0.06 V, respectively.

For the RhNPs/(PVA-PEI)/GCE sensors (curve b and c), the intensities of redox peaks have an obvious increase, and the currents of HQ are about 52.7 and $-28.4 \mu\text{A}$, with potential at 0.48 and 0.00 V, respectively. The growth of RhNPs on PVA-PEI

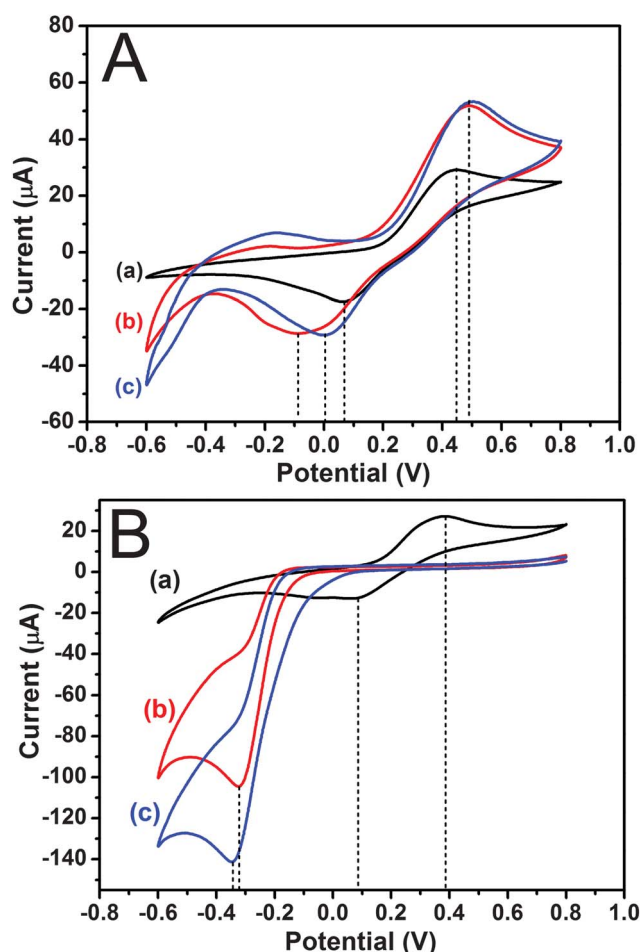
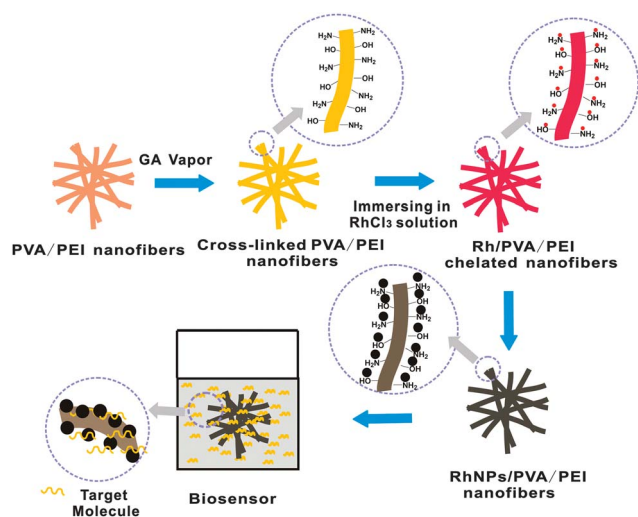


Fig. 10 (A) CVs of (a) PVA-PEI, (b) RhNPs/(PVA-PEI) (2.5 mL RhCl_3), and (c) RhNPs/(PVA-PEI) (5 mL RhCl_3) nanofibrous mats functionalized GCE with 1.0 mM HQ in 0.1 M PB (pH 6.8) (scan rate, 50 mV s^{-1}). (B) CVs of (a) PVA-PEI, (b) RhNPs/(PVA-PEI) (2.5 mL RhCl_3), and (c) RhNPs/(PVA-PEI) (5 mL RhCl_3) nanofibrous mats functionalized GCE with 1.0 mM HQ and 5.0 mM H_2O_2 in 0.1 M PB (pH 6.8) (scan rate, 50 mV s^{-1}).



Scheme 1 Schematic illustration of the growth process of the RhNPs on PVA-PEI nanofibers and their application in electrochemical sensors for the electrocatalytic of H_2O_2 .

nanofibers can improve the interfacial electron-transfer kinetics of HQ at the electrode interface, resulting in the increase of the currents.^{20,28} As shown in Fig. 10B, with the addition of H₂O₂, the redox peak currents are about 27.5 and −12.4 μA, with potentials at 0.08 and 0.38 V. Compared with the currents of HQ obtained in Fig. 10A (curve a, 28.6 and −16.6 μA), the presence of H₂O₂ had little effects on the reduction peak currents (16.6 μA) and the potential of HQ (0.08 V), suggesting the weak reactions between HQ and H₂O₂. However, while for the RhNPs/(PVA-PEI) nanofibrous mats with various loading of RhNPs, with the addition of H₂O₂, the reduction peak currents (104 and 141 μA) caused by HQ both increased significantly accompanying with the disappearance of the oxidation current peak (Fig. 10B, curve b and c), indicating the strong reactions between H₂O₂ and HQ. In addition, compare curve b with curve c, the reduction peak currents increased from 104 μA to 141 μA with the increased loading of the RhNPs. The results indicate that the RhNPs/(PVA-PEI)/GCE electrochemical sensors exhibit remarkable electrochemical catalysis toward H₂O₂, indicating the fast direct electron transfer. Obviously, the presence of the small and well-dispersed RhNPs on PVA-PEI nanofibers is the key factor for the direct electron transfer, that is, the H₂O₂ molecule can fast and easily reach the surfaces of the RhNPs. Meanwhile, excellent electrocatalytic activity of the biosensors can also benefit from the highly porous fibrous structure and increased surface area of nanofibers mats. According to the previously studies,^{20,30} the good peak currents can lead to the good current response towards the H₂O₂ and the peak currents obtained in this study are higher than our previously works at the same experimental conditions. The fabricated non-enzymatic RhNPs/(PVA-PEI) nanofibrous mats electrochemical sensor exhibit highly electrocatalytic activity towards H₂O₂, which would be the promising nanomaterials for the widely application in the biosensors and bioelectrocatalysis.

Conclusions

In summary, a facile approach to the synthesis of uniform, small sized and well-dispersed RhNPs on cross-linked PVA-PEI nanofibers has been demonstrated. In order to get a perfect substrate for the growth of RhNPs, various methods were firstly employed to cross-linked PVA nanofibers and the cross-linked PVA-PEI nanofibers show good water stability and porous structures after immersing in water for 72 h. The chemical bonding of the cross-linked PVA nanofibers was discussed and confirmed by XPS and FTIR spectra. Because of the strong chelate effects among the amine groups, hydroxyl groups and Rh³⁺ ions, uniform RhNPs with an average diameter of about 2.5 ± 0.2 nm can evenly and densely grow throughout the PVA-PEI nanofibers *via* an *in situ* reduction. Meanwhile, the better dispersion and smaller size of the RhNPs grown on the nanofibers in comparison with the pre-synthesized RhNPs directly deposited on the nanofibers exhibit the advantage of *in situ* reduction for the size and dispersion control. The successful fabrication of the RhNPs/(PVA-PEI) nanofibers with various densities of well-dispersed RhNPs (average diameter ranged from 2–6 nm) demonstrated

that the strong chelate effects and stabilization of the PVA-PEI nanofibers play an essential factor for the size and dispersion control of RhNPs. The crystal structures and chemical interactions of the RhNPs/(PVA-PEI) nanofibers were verified by XPS spectra and XRD patterns. These novel nanomaterials were fabricated as non-enzymatic electrochemical sensors and exhibit highly electrocatalytic activity towards H₂O₂, which would be promising nanomaterials for wide application in biosensors and bioelectrocatalysis.

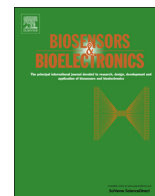
Acknowledgements

We acknowledge the support of the project of the National Natural Science Foundation of China (NSFC) (51243001, 51373154), the 521 Talent Project of Zhejiang Sci-Tech University, and Research Project of Department of Education of Zhejiang Province (Grant number: Y201122268).

Notes and references

- 1 B. T. Sneed, C. H. Kuo, C. N. Brodsky and C. K. Tsung, *J. Am. Chem. Soc.*, 2012, **134**, 18417.
- 2 D. A. J. M. Ligthart, R. A. Santen and E. J. M. Hensen, *Angew. Chem., Int. Ed.*, 2011, **50**, 5306–5310.
- 3 Z. L. Cheng, A. A. Zaki, J. Z. Hui, V. R. Muzykantov and A. Tsourkas, *Science*, 2012, **338**, 903–910.
- 4 J. A. Scholl, A. L. Koh and J. A. Dionne, *Nature*, 2012, **483**, 421–427.
- 5 S. B. Kim, R. D. Pike and D. A. Sweigart, *Acc. Chem. Res.*, 2013, **46**, DOI: 10.1021/ar300353n.
- 6 M. S. Hegde, G. Madras and K. C. Patil, *Acc. Chem. Res.*, 2009, **42**, 704–712.
- 7 H. B. Pan and C. M. Wai, *New J. Chem.*, 2011, **35**, 1649–1660.
- 8 H. Kobayashi, H. Morita, M. Yamauchi, R. Ikeda, H. Kitagawa, Y. Kubota, K. Kato, M. Takata, S. Toh and S. Matsumura, *J. Am. Chem. Soc.*, 2012, **134**, 12390.
- 9 H. Kobayashi, H. Morita, M. Yamauchi, R. Ikeda, H. Kitagawa, Y. Kubota, K. Kato and M. Takat, *J. Am. Chem. Soc.*, 2011, **133**, 11034.
- 10 S. Poorahong, P. Santhosh, G. V. Ramirez, T. F. Tseng, J. I. Wong, P. Kanatharana, P. Thavarungkul and J. Wang, *Biosens. Bioelectron.*, 2011, **26**, 3670–3673.
- 11 T. Ayvali, M. Zahmakiran and S. Ozkar, *Dalton Trans.*, 2011, **40**, 3584–3591.
- 12 H. Zhang, W. Y. Li, M. S. Jin, J. Zeng, T. Yu, D. Yang and Y. N. Xia, *Nano Lett.*, 2011, **11**, 898–903.
- 13 A. Fihri, M. Bouhrara, B. Nekoueshahraki, J. M. Basset and V. Polshettiwar, *Chem. Soc. Rev.*, 2011, **40**, 5181–5203.
- 14 N. T. Khi, J. S. Yoon, H. J. Kim, S. M. Lee, B. Kim, H. Baik, S. J. Kwon and K. Lee, *Nanoscale*, 2013, **5**, 5738–5742.
- 15 J. J. Hirner, Y. Shi and S. A. Blum, *Acc. Chem. Res.*, 2011, **44**, 603–613.
- 16 Y. Z. Lu and W. Chen, *ACS Catal.*, 2012, **2**, 84–90.
- 17 N. Dahal, S. Garcia, J. P. Zhou and S. M. Humphrey, *ACS Nano*, 2012, **6**, 9433–9446.

- 18 W. Y. Huang, J. N. Kuhn, C. K. Tsung, Y. W. Zhang, S. E. Habas, P. D. Yang and G. A. Somorjai, *Nano Lett.*, 2008, **8**, 2027–2034.
- 19 S. M. Humphrey, M. E. Grass, S. E. Habas, K. Niesz, G. A. Somorjai and T. Don Tilley, *Nano Lett.*, 2007, **7**, 785–790.
- 20 H. Zhu, M. L. Du, M. Zhang, P. Wang, S. Y. Bao, Y. Q. Fu and J. M. Yao, *Sens. Actuators, B*, 2013, **185**, 608–619.
- 21 B. Yoon and C. M. Wai, *J. Am. Chem. Soc.*, 2005, **127**, 17174–17175.
- 22 R. Sahay, P. S. Kumar, R. Sridhar, J. Sundaramurthy, J. Venugopal, S. G. Mhaisalkar and S. Ramakrishna, *J. Mater. Chem.*, 2012, **22**, 12953–12971.
- 23 D. Li and Y. N. Xia, *Adv. Mater.*, 2004, **16**, 1151–1170.
- 24 W. Y. Liu, S. Thomopoulos and Y. N. Xia, *Adv. Healthcare Mater.*, 2012, **1**, 10–25.
- 25 J. Wang, H. B. Yao, D. He, C. L. Zhang and S. H. Yu, *ACS Appl. Mater. Interfaces*, 2012, **4**, 1963–1971.
- 26 X. Fang, H. Ma, S. L. Xiao, M. W. Shen, R. Guo, X. Y. Cao and X. Y. Shi, *J. Mater. Chem.*, 2011, **21**, 4493–4501.
- 27 A. G. El-Deen, N. A. M. Barakat, K. A. Khalil and H. Y. Kim, *J. Mater. Chem. A*, 2013, **1**, 11001–11010.
- 28 Y. P. Huang, H. Ma, S. G. Wang, M. W. Shen, R. Guo, X. Y. Cao, M. F. Zhu and X. Y. Shi, *ACS Appl. Mater. Interfaces*, 2012, **4**, 3054–3061.
- 29 A. G. Destaye, C. K. Lin and C. K. Lee, *ACS Appl. Mater. Interfaces*, 2013, **5**, 4745–4752.
- 30 H. Zhu, M. L. Du, M. Zhang, P. Wang, S. Y. Bao, L. N. Wang, Y. Q. Fu and J. M. Yao, *Biosens. Bioelectron.*, 2013, **49**, 210–215.
- 31 H. Zhu, M. L. Du, M. L. Zou, C. S. Xu, N. Li and Y. Q. Fu, *J. Mater. Chem.*, 2012, **22**, 9301–9307.
- 32 M. L. Zou, M. L. Du, H. Zhu, C. S. Xu, N. Li and Y. Q. Fu, *Polym. Eng. Sci.*, 2013, **53**, 1099–1108.
- 33 H. Zhu, M. L. Du, M. L. Zou, C. S. Xu and Y. Q. Fu, *Dalton Trans.*, 2012, **41**, 10465–10471.
- 34 M. L. Zou, M. L. Du, H. Zhu, C. X. Xu and Y. Q. Fu, *J. Phys. D: Appl. Phys.*, 2012, **45**, 325302–325308.
- 35 T. B. Ren, L. Li, X. J. Cai, H. Q. Dong, S. M. Liu and Y. Y. Li, *Polym. Chem.*, 2012, **3**, 2561–2569.
- 36 H. Petersen, P. M. Fechner, D. Fischer and T. Kissel, *Macromolecules*, 2002, **35**, 6867–6874.
- 37 W. Y. Yuan, Z. S. Lu and C. M. Li, *J. Mater. Chem.*, 2012, **22**, 9351–9357.
- 38 S. Kundu, K. Wang and H. Liang, *J. Phys. Chem. C*, 2009, **113**, 18570–18577.
- 39 M. Pradhan, S. Sarkar, A. K. Sinha, M. Basu and T. Pal, *J. Phys. Chem. C*, 2010, **114**, 16129–16142.
- 40 Q. Yuan, Z. Y. Zhou, J. Zhuang and X. Wang, *Chem. Mater.*, 2010, **22**, 2395–2402.
- 41 J. Walter, S. Wakita, W. Boonchuduang and S. Hara, *J. Phys. Chem. B*, 2002, **106**, 8547–8554.
- 42 B. A. Kakade, S. Sahoo, S. B. Halligudi and V. K. Pillai, *J. Phys. Chem. C*, 2008, **112**, 13317–13319.
- 43 A. F. Thunemann, *Macromolecules*, 2000, **33**, 6878–6885.
- 44 M. S. A. Rahaman, L. Zhang, L. H. Cheng, X. H. Xu and H. L. Chen, *RSC Adv.*, 2012, **2**, 9165–9172.
- 45 Y. Zhang, J. M. Liu and X. P. Yan, *Anal. Chem.*, 2013, **85**, 228–234.
- 46 A. Lopez-Marzo, J. Pons and A. Merkoç, *J. Mater. Chem.*, 2012, **22**, 15326–15335.
- 47 J. S. Lin, Y. Liu, D. Y. Wang, Q. Qin and Y. Z. Wang, *Ind. Eng. Chem. Res.*, 2011, **50**, 9998–10005.
- 48 K. Das, D. Ray, N. R. Bandyopadhyay, A. Gupta, S. Sengupta, S. Sahoo, A. Mohanty and M. Misra, *Ind. Eng. Chem. Res.*, 2010, **49**, 2176–2185.
- 49 M. E. Grass, S. H. Joo, Y. W. Zhang and G. A. Somorjai, *J. Phys. Chem. C*, 2009, **113**, 8616–8623.
- 50 T. Ikeda, A. K. Xiong, T. Yoshinaga, K. Maeda, K. Domen and T. Teranishi, *J. Phys. Chem. C*, 2013, **117**, 2467–2473.
- 51 Y. W. Zhang, M. E. Grass, W. Y. Huang and G. A. Somorjai, *Langmuir*, 2010, **26**, 16463–16468.
- 52 I. Pis, V. Stetsovych, J. Mysliveček, M. Kettner, M. Vondracek, F. Dvorak, D. Mazur, V. Matolin and V. Nehasil, *J. Phys. Chem. C*, 2013, **117**, 12679–12688.
- 53 A. Iordan, M. Zaki, C. Kappenstein and C. Geron, *Phys. Chem. Chem. Phys.*, 2003, **5**, 1708–1715.
- 54 Y. Wang, Y. G. Nie, J. S. Pan, L. K. Pan, Z. Sun, L. L. Wang and C. Q. Sun, *Phys. Chem. Chem. Phys.*, 2010, **12**, 2177–2182.
- 55 J. J. Yuan and R. H. Jin, *J. Mater. Chem.*, 2011, **21**, 10720–10729.
- 56 H. Y. Liu, T. Kuila, N. H. Kim, B. C. Ku and J. H. Lee, *J. Mater. Chem. A*, 2013, **1**, 3739–3746.
- 57 E. P. Dillon, C. A. Crouse and A. R. Barron, *ACS Nano*, 2008, **2**, 156–164.
- 58 D. Astruc, E. Boisselier and C. Ornelas, *Chem. Rev.*, 2010, **110**, 1857–1959.
- 59 D. J. M. Snelders, N. Yan, W. J. Gan, G. Laurenczy and P. J. Dyson, *ACS Catal.*, 2012, **2**, 201–207.
- 60 J. Satija, V. V. R. Sai and S. Mukherji, *J. Mater. Chem.*, 2011, **21**, 14367–14386.
- 61 Y. Li, J. J. Zhang, J. Xuan, L. P. Jiang and J. J. Zhu, *Electrochem. Commun.*, 2010, **12**, 777–780.
- 62 K. J. Chen, K. C. Pillai, J. Rick, C. J. Pan, S. H. Wang, C. C. Liu and B. J. Hwang, *Biosens. Bioelectron.*, 2012, **33**, 120–127.
- 63 J. J. Wang, D. X. Han, X. H. Wang, B. Qi and M. S. Zhao, *Biosens. Bioelectron.*, 2012, **36**, 18–21.



Short communication

Facile fabrication of AgNPs/(PVA/PEI) nanofibers: High electrochemical efficiency and durability for biosensors



Han Zhu^b, MingLiang Du^{a,b,*}, Ming Zhang^{a,b}, Pan Wang^b, ShiYong Bao^b, LiNa Wang^a,
YaQin Fu^{a,b}, JuMing Yao^{a,b}

^a Key Laboratory of Advanced Textile Materials and Manufacturing Technology, Zhejiang Sci-Tech University, Ministry of Education, Hangzhou 310018, PR China

^b Department of Materials Engineering, College of Materials and Textile, Zhejiang Sci-Tech University, Hangzhou 310018, PR China

ARTICLE INFO

Article history:

Received 19 February 2013

Received in revised form

2 April 2013

Accepted 15 April 2013

Available online 15 May 2013

Keywords:

Biosensor

Nanofiber

Ag nanoparticles

Electrochemical

ABSTRACT

A novel, facile and green approach for the fabrication of H₂O₂, glutathione (GSH) and glucose detection biosensor using water-stable PVA and PVA/PEI nanofibers decorated with AgNPs by combining an in situ reduction approach and electrospinning technique has been demonstrated. Small, uniform and well-dispersed AgNPs embedded in the PVA nanofibers and immobilized on functionalized PVA/PEI nanofibers indicate the highly sensitive detection of H₂O₂ with a detection limit of 5 μM and exhibit a fast response, broad linear range, low detection limit and excellent stability and reusability.

© 2013 Elsevier B.V. All rights reserved.

1. Introduction

The development of materials science has brought great impetus to applied electrochemical fields and many efforts always have been made in finding new materials with good properties to improve electrochemical performances (Feng et al., 2011; Lin and Yan, 2012; Mao et al., 2010; Wang et al., 2012; Trefry et al., 2010). Electrochemical biosensors using various nanomaterials achieve the direct electron transfer between the enzyme and the electrode, which is very important for the fundamental studies and the construction of biosensors (Feng et al., 2011; Wang et al., 2012). However, enzymes often exhibit sluggish electron transfer at conventional electrodes because of unfavorable orientation on the electrode surface or the adsorption of impurities that cause denaturation. (Feng et al., 2011; Myung et al., 2011; Ishikawa et al., 2010; Cella et al., 2010) Therefore, appropriate promoters should be employed to facilitate the electron transfer and retain the bioactivity of immobilized enzymes. With the rapid development of nanotechnology, metal nanoparticles (MNPs) have been extensively used in electroanalysis due to their unique capabilities to enhance mass transport, facilitate catalysis, increase surface area,

and control an electrode's microenvironment (Wang et al., 2003; Jin 2012; Sau et al., 2010; Lu et al., 2008; Zhang et al., 2013).

A common challenge in MNPs-based biosensors is controlling the size, dispersion, stability, electrocatalytic activity of the MNPs and finding a convenient synthesis procedure. Recently, nanofibers are intensively applied as substrate materials in the fabrication of advanced intelligent biosensors due to their flexibilities, high specific surface area, high porosity, and good mechanical strength (Wang et al., 2012; Li and Xia 2004; Zhu et al., 2012a, 2012b). Compared with the traditional materials used for biosensors, the combined advantages of biocompatible nanofibers and MNPs would lead to high sensitivity and stability for the biosensing (Yang et al., 2012; Zhong et al., 2012; Huang et al., 2012; Zhu et al., 2012a,b).

Here, we reported a novel strategy for the fabrication of well-dispersed small Ag nanoparticles (AgNPs) embedded in water-stable poly(vinyl alcohol) (PVA) nanofibers and immobilized on the functionalized water-stable PVA/poly(ethyleneimine) (PEI) nanofibers by combining an in situ reduction approach and electrospinning technique, and these novel materials exhibit a highly sensitive detection of H₂O₂, GSH and glucose and possess good stability and repeatability.

2. Material and methods

Details of the materials and methods are given in the [Supporting information](#).

* Corresponding author at: Key Laboratory of Advanced Textile Materials and Manufacturing Technology, Zhejiang Sci-Tech University, Ministry of Education, Hangzhou 310018, PR China. Tel.: +86 571 86843255.

E-mail addresses: psdumli@yahoo.com.cn, du@zstu.edu.cn (M. Du).

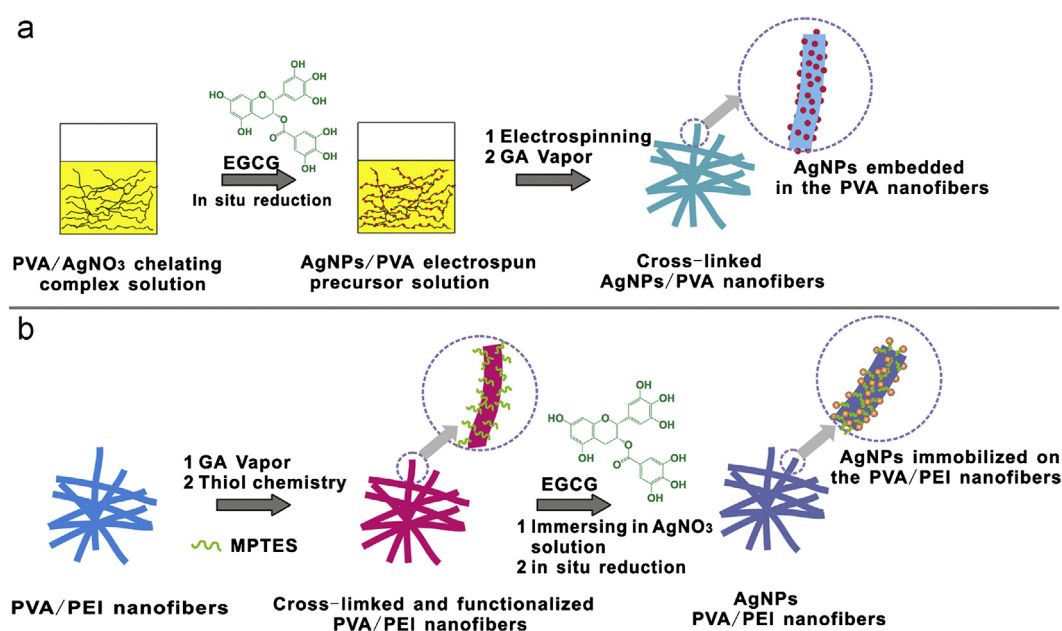
3. Results

A schematic of the fabrication process of AgNPs/PVA and AgNPs/(PVA/PEI) nanofibers is shown in Scheme 1. In the typical experiments for fabricating AgNPs/PVA water-stable nanofibers, PVA solution were firstly mixed with AgNO₃ solution, and because of the chelating effect between hydroxyl groups and Ag⁺ ions, the abundant hydroxyl groups of the PVA molecular chains could “anchor” Ag⁺ ions to form chelate complex. After the addition of the green reductant, epigallocatechin gallate (EGCG), the Ag⁺ ions in the chelate complex would grow to AgNPs (Zhu et al., 2012; Zhu et al., 2012). The AgNPs/PVA nanofibers mats were obtained by electrospinning the above precursor and then crosslinked by glutaraldehyde (GA) vapor to gain water stability. As shown in Fig. 1a and b, well-dispersed small AgNPs embedded in PVA nanofibers with a uniformly average diameter of 3.3 ± 0.3 nm have been successfully prepared. Nearly no AgNPs aggregation are observed, indicating the effective protection of PVA molecular chains and EGCG (Zhu et al., 2012a, 2012b).

High-resolution transmission electron microscopy (HRTEM) image of the AgNPs shows the lattice spacing of the (1 1 1) planes of Ag with a spacing of about 0.23 nm (Gu et al., 2009; Metraux and Mirkin 2005; Sun and Xia 2002). The morphology of the water-stable AgNPs/PVA nanofibers is shown in Fig. 1c and d, and compared with the pristine nanofibers before cross-linking (Fig. S1 and S2, average diameter = 410 ± 60 nm), uniform and excellent porous fibrous structures are well-retained, except for an obvious increase in the mean fiber diameter (630 ± 73 nm). This can be ascribed to the swelling of the fibers during the GA vapor cross-linking process and the morphology of the as-prepared water-stable nanofibers is better than that the previously reported literatures (Wang et al., 2012; Huang et al., 2012). As shown in Fig. 1(d), small AgNPs can be observed on the surface of PVA nanofibers, and after the immersion in water for 12, 24, 48 and 64 h, the nanofibers still kept excellent porous fibrous structure and no adhesion phenomenon appeared (Fig. S3). In addition, large amount of the small AgNPs still can be observed, indicating the reliability of the water-stable nanofibers (Fig. S3). The UV–vis spectrum of the AgNPs/PVA nanofibers exhibit a strong and sharp surface plasmon resonance (SPR) peak at 419 nm, which is

attributed to the isolated spherical AgNPs (Metraux and Mirkin, 2005; Sun and Xia 2002). The sharp SPR peak of AgNPs can also indicate the relative uniformly NPs' size distribution.

It is well known that the smaller the size, the higher the activity of NPs could be. Through the in situ approach in polymer solution and electrospun technique, small and well dispersed AgNPs can be obtained. However, most of the AgNPs are embedded in the PVA nanofibers so that the activity of the AgNPs may be restrained. In order to maximize the opportunity to use the higher activity caused by the small size, another approach for the fabrication of small AgNPs with well dispersion immobilized on the surface of nanofibers has been demonstrated, which is shown in Scheme 1b. In the typical process, the as-prepared PVA/PEI water-stable nanofibers were firstly functionalized with 3-mercaptopropyl-trimethoxysilane (MPTES) to provide sulfhydryl groups, which can chelate with Ag⁺ ions and will “anchor” the small AgNPs (Wang et al., 2012; Zhu et al., 2012b). Then the prepared Ag⁺/PVA/PEI nanofibers mats were immersed into EGCG solution, after a certain time, the AgNPs/(PVA/PEI) nanofibers were obtained. Fig. 1e and f shows the TEM images of the AgNPs immobilized on the surface of functionalized PVA/PEI nanofibers with a narrow size distribution of about 7.3 ± 0.4 nm. The small AgNPs are uniformly distributed on the surface of nanofibers, except for a few aggregation NPs, which are corresponded with the FE-SEM images in Fig. 1g and h. As shown in Fig. 1g, uniform nanofibers with random orientation and porous fibrous structure were generated with a mean diameter of 508 ± 48 nm (inset in Fig. 1g). The aim of the introduction of PEI is to improve the morphology of the nanofibers and the water stability. At the same condition, after the cross-linking of PVA/PEI nanofibers, the diameter is smaller than cross-linked PVA nanofibers, it is because that the aldehyde groups of GA is able to interact with the amine groups of PEI and the hydroxyl groups of PVA Huang et al. (2012). HRTEM images shown in Fig. 1f were visible with a spacing of about 0.23 nm, which corresponded to the lattice spacing of the (1 1 1) planes of Ag (Gu et al., 2009; Metraux and Mirkin, 2005; Sun and Xia, 2002). Compared with the UV–vis spectrum of AgNPs/PVA nanofibers, the SPR peak has a red-shift and move to 436 nm, indicating the relative bigger size of AgNPs (Metraux and Mirkin, 2005; Sun and Xia 2002).



Scheme 1. Schematic of the fabrication process of the (a) AgNPs embedded in the PVA water-stable nanofibers and (b) AgNPs immobilized on the functionalized PVA/PEI water-stable nanofibers.

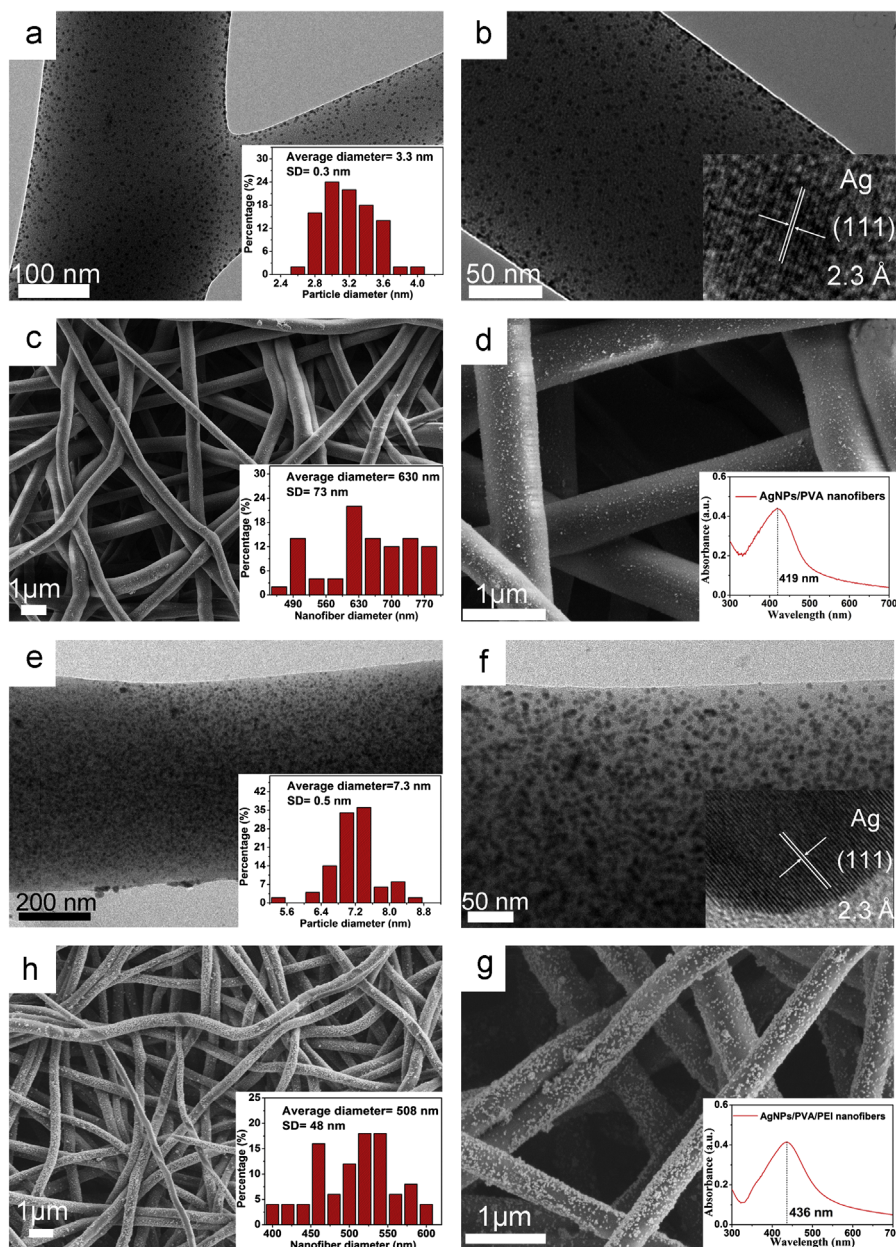


Fig. 1. TEM images of the (a, b) AgNPs/PVA and (e, f) AgNPs/(PVA/PEI) nanofibers. The insets are the corresponding size distribution and HRTEM images of AgNPs. FE-SEM images of (c, d) the AgNPs/PVA and (g, h) AgNPs/(PVA/PEI) nanofibers. The insets are the size distribution of the AgNPs/PVA and AgNPs/(PVA/PEI) nanofibers, and the UV-vis spectra of AgNPs/PVA and AgNPs/(PVA/PEI) nanofibers, respectively.

As shown in Fig. S4F, curve a shows the X-ray diffraction (XRD) spectrum of AgNPs/PVA nanofibers, a broad peak around $2\theta = 19.2^\circ$, corresponding to the (1 0 1) plane of semicrystalline PVA [Zhao et al. \(2010\)](#). The weak diffraction peak located at 37.8° can be indexed as Ag nanocrystal, which correspond to the (1 1 1) planes. It is important to note that compared with curve a, the diffraction peak of Ag (1 1 1) planes become more sharp and the PVA peak become relatively weak. In addition, three new emerging peaks located at 44.4° , 64.7° and 77.3° can also be indexed to the Ag crystal (JCPDS: 04-0783), which correspond to the (2 0 0), (2 2 0) and (3 1 1) planes of face-center cubic silver ([Gu et al., 2009](#); [Zhao et al., 2010](#)). The strong peaks of AgNPs indicate the higher ratio of exposed AgNPs than that embedded in PVA nanofibers.

X-ray photoemission spectroscopy (XPS) measurements were performed to reveal the chemical bond formation during the fabrication of AgNPs/PVA and AgNPs/(PVA/PEI) nanofibers.

The O 1s chemical states in PVA nanofibers show a strong peak located at 530.3 eV and after the formation of AgNPs, the peak move to 530.0 eV, indicating the chelating effect between the hydroxyls and the AgNPs (Fig. S4A) ([Zhu et al., 2012a](#); [Chen et al., 2011](#)). The Ag 3d spectra (Fig. S4B and C) of AgNPs/(PVA/PEI) and AgNPs/PVA nanofibers both demonstrate two significant peaks, located at 371.5, 365.6, 374.0 and 368.0 eV, which are in agreement with the binding energies of Ag 3d_{5/2} and Ag 3d_{3/2}, respectively [Zhu et al. \(2012b\)](#). Compared with the standard binding energy of Ag 3d_{5/2} and Ag 3d_{3/2}, the binding energies of the two kind of nanofibers are lower than bulk Ag (368.2 and 374.2 eV), indicating the strong interaction among the AgNPs, hydroxyls and sulfhydryl groups ([Wang et al., 2012](#); [Zhu et al., 2012a](#)). The core level S 2p and Si 2p spectra of AgNPs/(PVA/PEI) nanofibers are shown in Fig. S4D and E. A peak fit is included below the experimental spectrum, presenting two S 2p spin-orbit coupled doublets. The double peak

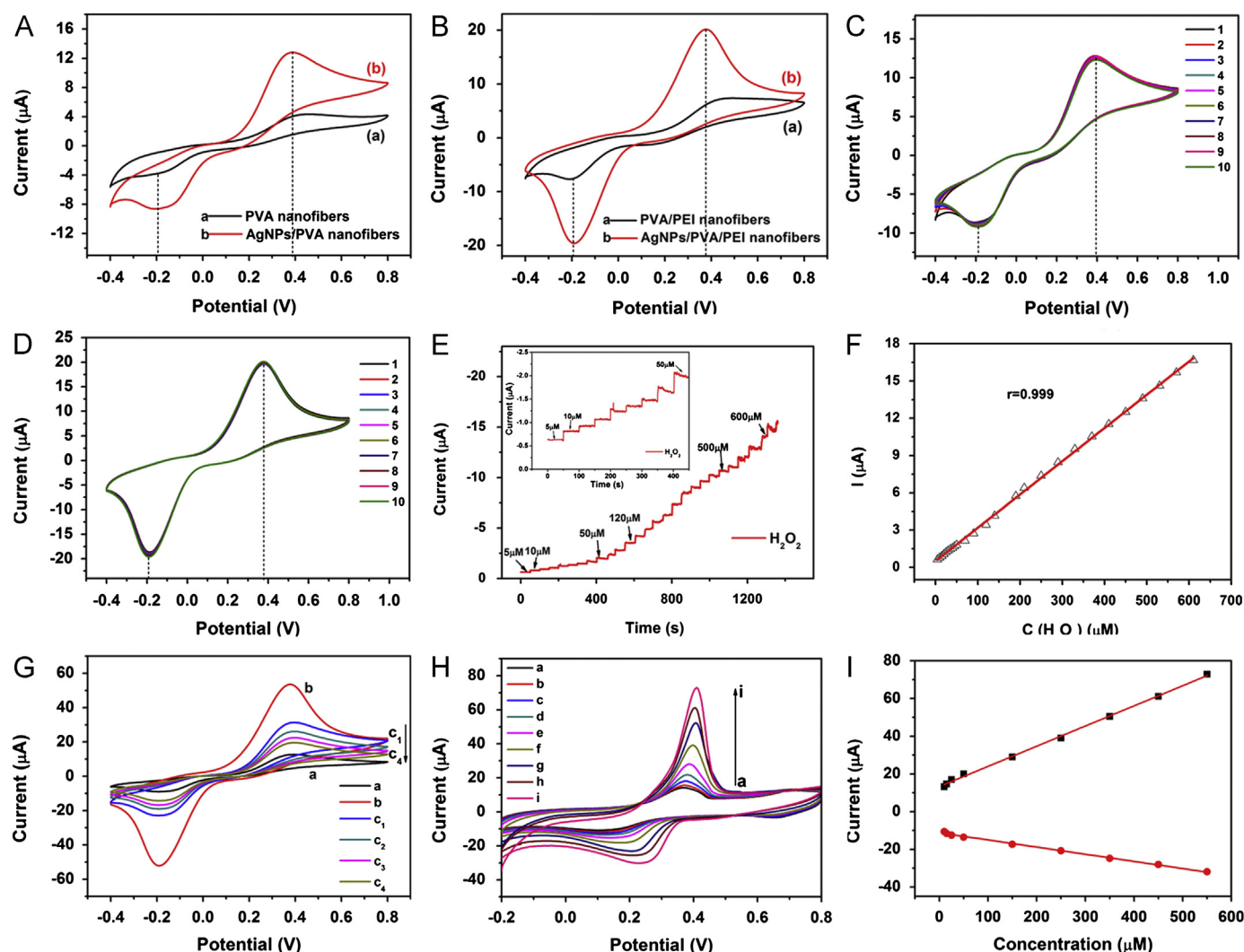


Fig. 2. CVs obtained with (A) AgNPs/PVA and (B) AgNPs/(PVA/PEI) nanofibers functionalized GCE immersed in 1.0 mM HQ in 0.1 M PB (pH 6.8) in the presence of 5.0 mM H_2O_2 (scan rate, 50 mV s^{-1}); The CVs cycles of the prepared (C) AgNPs/PVA/GCE and (D) AgNPs/(PVA/PEI)/GCE at the same conditions; (E) amperometric response of the fabricated HRP/AgNPs/(PVA/PEI)/GCE biosensor to successive addition of different concentrations of H_2O_2 to 1.0 M phosphate buffer (PB) at -0.22 V . Inset shows the response of the biosensor to $5 \mu\text{M}$ H_2O_2 ; (F) relationship of calibration curve and linear fitting curve between the current and the H_2O_2 concentration. (G) CVs obtained with AgNPs/(PVA/PEI)/GCE immersed in 1.0 mM HQ in 0.1 M PB (pH 6.8) in the absence of H_2O_2 (a) and in the presence of 10 mM H_2O_2 (scan rate, 50 mV s^{-1}); (c1–c4) same as (b) with 50, 100, 150, 200 μM GSH, respectively; (scan rate, 50 mV s^{-1}). (H) CVs of AgNPs/(PVA/PEI)/GCE electrode in the presence of different concentrations of glucose (5, 10, 15, 25, 50, 150, 250, 350, 450 and 550 μM) at the scan rate of 50 mV s^{-1} . (I) The redox peak currents in CV versus glucose concentration.

is an energy doublet with the $2p_{3/2}$ and $2p_{1/2}$ binding energy peaks positioned at about 162.2 and 163.3 eV, demonstrating the presence of thiolate species (Chen et al., 2011; Selegard et al., 2010; Khatri et al., 2008).

The formation of thiolate is attributed to interact between sulfur and Ag at the AgNPs. The appearance of characteristic Si 2p peaks at 102.1 eV, Si $2p_{1/2}$ at 97.9 eV, and Si $2p_{3/2}$ at 96.9 eV, which are ascribed to the Si–O, Si–C and Si–Si bondings (Khatri et al., 2008; Wang et al., 2004; Cheung et al., 2003). The presence of Si–O bondings successfully confirmed the grafting between PVA/PEI nanofibers and MPES. The Schematic picture of the chemical bondings of AgNPs/(PVA/PEI) and AgNPs/PVA nanofibers is shown in Fig. S5.

In this communication, such small, uniform and well-dispersed AgNPs possess high ratio of surface atoms with free valences to the cluster of total atoms and can provide electrochemical reversibility for redox reactions, which is not possible on the bulk metal electrode. The electrochemical behavior of horseradish peroxidase (HRP)/PVA/glassy carbon electrodes (GCE) and HRP/AgNPs/PVA/GCE in the presence of 5.0 mM of H_2O_2 was revealed by the cyclic voltammograms (CVs) (Fig. 2A). Well-defined CVs were obtained in biosensors based on both the HRP/PVA/GCE and HRP/AgNPs/PVA/GCE (Fig. 2A). The redox peak

currents of hydroquinone (HQ) (curve a) are about 4.1 and $3.7 \mu\text{A}$, with potentials at (0.42 and -0.19 V) and the other redox peak currents (curve b) are about 8.5 and $12.5 \mu\text{A}$, with potentials at (0.38 and -0.20 V), respectively. An obvious increase of the peak-to-peak separation was observed, indicating that the AgNPs can successfully promote the HRP embedded in the AgNPs/PVA nanofibers. In the same condition, compared with the redox peak currents in PVA/PEI nanofibers electrode (7.2 and $-7.4 \mu\text{A}$), the AgNPs/(PVA/PEI) nanofibers electrode obtain a significant increase (20.3 and $-20.1 \mu\text{A}$), which is ascribed to the relative higher content of exposed AgNPs. It should be noted that even the AgNPs embedded in PVA nanofibers possess the smaller size and higher specific surface area, but the AgNPs on PVA/PEI nanofibers have higher ratio of exposed AgNPs, which also can be demonstrated by XRD characterization (Fig. S4A).

Therefore, much more AgNPs could take part in the reactions, leading to the relative higher electrocatalytic activity. The reusability and recyclability are crucial issues for practical applications, especially for the costly rare and noble metals. The fabricated AgNPs/PVA and AgNPs/(PVA/PEI) nanofibers electrodes used for 10 times were compared by the CV curves (Fig. 2C and D). The reproducibility of the same electrode in the measurements,

expressed as the relative standard deviation (RSD), was less than 3.3% for 10 successive experiments in the presence of 5.0 mM of H_2O_2 . The redox peaks are almost the same, indicating the excellent stability and reusability of fabricated AgNPs/PVA and AgNPs/(PVA/PEI) nanofibers electrodes. Considering the good reduction current (20.1 μA) caused by HQ in the presence of H_2O_2 , we choose the AgNPs/(PVA/PEI) nanofibers mats as the electrode to accurately determine the concentration of H_2O_2 . Fig. 2E shows the amperometry response and calibration curve of steady state current vs. concentration of H_2O_2 . Stepped increases of the amperometric reduction currents were observed with the addition of H_2O_2 at a constant potential of -0.22 V . The current response of the sensors was rapidly enhanced and approached about 98% of its steady state current within 1 s, which is much shorter than that in the previous reports (Chen et al., 2008; Zhu et al., 2006; Lei et al., 2004). The rapid electrode response to the change of the H_2O_2 concentration is attributed to the fast diffusion of the H_2O_2 into the AgNPs/PVA/PEI nanofibers network structures and the surface of small AgNPs. Fig. 2F shows a linear relationship with the concentration of H_2O_2 (5–0.6 mM) with the correlation coefficient of 0.999. The detection limit of 0.6 mM was estimated at a signal-to-noise ratio of 3. The results indicated the HRP/AgNPs/(PVA/PEI)/GCE has much higher catalytic ability for the reduction of H_2O_2 than that in the previous reports (Chen et al., 2008; Zhu et al., 2006; Lei et al., 2004), and the high sensitivity may result in the excellent biocompatible microenvironment of the AgNPs/(PVA/PEI) nanofibers around the enzyme.

Beside H_2O_2 , glutathione (GSH) and glucose are widely found in all forms of life and play essential roles in the health of organisms, and therefore, they were also used as model compounds in our experiments to testify the electrochemical activity and flexibility of the biosensor. Fig. 2G shows the CVs of GSH using HRP/AgNPs/(PVA/PEI)/GCE as electrode and in the presence of 1 mM HQ, there appears a pair of redox peaks (curve a). After the addition of 5 mM H_2O_2 , the amperometric reduction currents increase (curve b) and upon addition of 50 μM GSH, the reduction current decreases dramatically (curve c1). With the further increase of the concentration of GSH (curve c1 to curve c2) the decrease is enhanced. It is well-known that with the assists of H_2O_2 , the HRP can easily convert HQ to benzoquinone (BQ), and then the benzoquinone is subsequently reduced back to HQ by a rapid reaction involving the acceptance of two electrons from the electrode (Taraban et al., 1997; Liu et al., 2009). The model compound, GSH, is an inhibitor (reduced thiols, R-SH), and it may react with BQ to produce a reduced adduct (quinoid–thiol) (Huang et al., 2002; Elyacoubi et al., 2006) and lead to less BQ derivatives reaching the electrode surface, which can decrease the reduced peak current of HQ. Because of the reduced thiols suppression of the mediator recycling process and inhibition of the activity of HRP, a reduced thiol biosensor can be obtained. Fig. 2H and I shows the electrochemical responses of different concentrations of glucose using HRP/AgNPs/(PVA/PEI)/GCE as an electrode. It can be observed that the redox peaks increase linearly with increasing glucose concentration from 5 μM to 550 μM . The AgNPs/(PVA/PEI) nanofibers modified electrodes exhibit superior performance in the detection of H_2O_2 as compared to the previously reported literatures (Chen et al., 2008; Zhu et al., 2006; Lei et al., 2004; Luo et al., 2009). After storage at 4 °C in a refrigerator for 3 months, the response of H_2O_2 and glucose decrease slightly compared with the fresh biosensor, indicating good durability and stability of the biosensor (Fig. S6).

4. Conclusions

In summary, we have demonstrated a novel, facile and green approach for the fabrication of H_2O_2 detection biosensor using water-stable PVA and PVA/PEI nanofibers decorated with AgNPs

by combining an in situ reduction approach and electrospinning technique. Two methods were used to synthesize small, uniform and well-dispersed AgNPs embedded in the PVA nanofibers and immobilized on functionalized PVA/PEI nanofibers. The fabricated HRP/AgNPs/(PVA/PEI) biosensor allowed the highly sensitive detection of H_2O_2 , GSH and glucose and exhibited a fast response, broad linear range, low detection limit and excellent stability and reusability. The response and redox peak currents increase with the increase of the ratio of exposed AuNPs. The feasible process and high detection sensitivity of the biosensor based on AgNPs decorated PVA/PEI nanofibers may pave the way in developing a new film support–enzyme hybrid substrate material for biosensors or bioelectrocatalysts.

Acknowledgment

We acknowledge the support of the project of the National Natural Science Foundation of China (NSFC) (51243001) and the 521 Project of Zhejiang Sci-Tech University.

Appendix A. Supporting information

Supplementary data associated with this article can be found in the online version at <http://dx.doi.org/10.1016/j.bios.2013.04.016>.

References

- Cella, L.N., Chen, W., Myung, N.V., Mulchandani, A., 2010. *Journal of the American Chemical Society* 132, 5024–5026.
- Chen, A., Kafi, A.K.M., Wu, G., 2008. *Biosensors and Bioelectronics* 24, 566–571.
- Chen, J.J., Struk, K.N., Brennan, A.B., 2011. *Langmuir* 27, 13754–13761.
- Cheung, M.K.L., Trau, D., Yeung, K.L., Carles, M., Sucher, N.J., 2003. *Langmuir* 19, 5846–5850.
- Elyacoubi, A., Zayed, S.I.M., Blankert, B., Kauffmann, J.M., 2006. *Electroanalysis* 18, 345–350.
- Feng, X.M., Li, R.M., Ma, Y.W., Chen, R.F., Shi, N.E., Fan, Q.L., Huang, W., 2011. *Advanced Functional Materials* 21, 2989–2996.
- Gu, C.D., Cheng, C., Huang, H.Y., Wong, T.L., Wang, N., Zhang, T.Y., 2009. *Crystal Growth and Design* 9, 3278–3285.
- Huang, T.H., Kuwana, T., Warsinke, A., 2002. *Biosensors and Bioelectronics* 17, 1107–1113.
- Huang, Y.P., Ma, H., Wang, S.G., Shen, M.W., Guo, R., Cao, X.Y., Zhu, M.F., Shi, X.Y., 2012. *ACS Applied Materials and Interfaces* 4, 3054–3061.
- Ishikawa, F.N., Curreli, M., Olson, C.A., Liao, H.I., Sun, R., Roberts, R.W., Cote, R.J., Thompson, M.E., Zhou, C.W., 2010. *ACS Nano* 4, 6914–6922.
- Jin, Y.D., 2012. *Advanced Materials* 24, 5153–5165.
- Khatir, O.P., Adachi, K., Murase, K., Okazaki, K., Torimoto, T., Tanaka, N., Kuwabata, S., Sugimura, H., 2008. *Langmuir* 24, 7785–7792.
- Lei, C.X., Hu, S.Q., Gao, N., Shen, G.L., Yu, R.Q., 2004. *Bioelectrochemistry* 65, 33–39.
- Li, D., Xia, Y.N., 2004. *Advanced Materials* 16, 1151–1170.
- Lin, P., Yan, F., 2012. *Advanced Materials* 24, 34–51.
- Liu, L.J., Xi, F.N., Zhang, Y.M., Chen, Z.C., Lin, X.F., 2009. *Sensors and Actuators B: Chemical* 135, 642–649.
- Lu, J., Do, I., Drzal, L.T., Worden, R.M., Lee, I., 2008. *ACS Nano* 2, 1825–1832.
- Luo, S.L., Zeng, X.D., Li, X.F., Liu, X.Y., Liu, Y., Kong, B., Yang, S.L., Wei, W.Z., 2009. *Biosensors and Bioelectronics* 25, 896–900.
- Mao, S., Lu, G.H., Yu, K.H., Bo, Z., Chen, J.H., 2010. *Advanced Materials* 22, 3521–3526.
- Metraux, G.S., Mirkin, C.A., 2005. *Advanced Materials* 17, 412–415.
- Myung, S., Solanki, A., Kim, C., Park, J., Kim, K.S., Lee, K.B., 2011. *Advanced Materials* 23, 2221–2225.
- Sau, T.K., Rogach, A.L., Jackel, F., Klar, T.A., Feldmann, J., 2010. *Advanced Materials* 22, 1805–1825.
- Selegard, L., Khranovskyy, V., Soderlind, F., Vahlberg, C., Ahren, M., Kall, P.O., Yakimova, R., Uvdal, K., 2010. *ACS Applied Materials and Interfaces* 2, 2128–2135.
- Sun, Y.G., Xia, Y.N., 2002. *Science* 298, 2176–2179.
- Taraban, M.B., Leshina, T.V., Anderson, M.A., Grissom, C.B., 1997. *Journal of the American Chemical Society* 119, 5768–5769.
- Trefry, J.C., Monahan, J.L., Weaver, K.M., Meyerhoefer, A.J., Markopolous, M.M., Arnold, Z.S., Wooley, D.P., Pavel, I.E., 2010. *Journal of the American Chemical Society* 132, 10970–10972.
- Wang, J., Musameh, M., Lin, Y.H., 2003. *Journal of the American Chemical Society* 125, 2408–2409.

- Wang, J., Yao, H.B., He, D., Zhang, C.L., Yu, S.H., 2012. ACS Applied Materials and Interfaces 4, 1963–1971.
- Wang, Y., Tang, Z.Y., Liang, X.R., Liz-Marzan, L.M., Kotov, N.A., 2004. Nano Letters 4, 225–231.
- Yang, S.Y., Liu, Y.M., Tan, H., Wu, C., Wu, Z.Y., Shen, G.L., Yu, R.Q., 2012. Chemical Communications 48, 2861–2863.
- Zhang, Z.H., Zhang, L.B., Hedhili, M.N., Zhang, H.N., Wang, P., 2013. Nano Letters 13, 14–20.
- Zhao, L.N., Yang, D.Y., Dong, M.D., Xu, T., Jin, Y., Xu, S.L., Zhang, F.Z., Evans, D.G., Jiang, X.Y., 2010. Industrial and Engineering Chemistry Research 49, 5610–5615.
- Zhong, X., Yuan, R., Chai, Y.Q., 2012. Chemical Communications 48, 597–599.
- Zhu, H., Du, M.L., Zou, M.L., Xu, C.S., Li, N., Fu, Y.Q., 2012a. Journal of Materials Chemistry 22, 9301–9307.
- Zhu, H., Du, M.L., Zou, M.L., Xu, C.S., Fu, Y.Q., 2012b. Dalton Transactions 41, 10465–10471.
- Zhu, J.H., Cai, W.Y., Xu, Q., Zhao, X.N., Chen, H.Y., 2006. Chemistry of Materials 18, 279–284.



Facile and green fabrication of small, mono-disperse and size-controlled noble metal nanoparticles embedded in water-stable polyvinyl alcohol nanofibers: High sensitive, flexible and reliable materials for biosensors

Han Zhu^b, MingLiang Du^{a,b,*}, Ming Zhang^{a,b}, Pan Wang^b, ShiYong Bao^b, YaQin Fu^{a,b}, JuMing Yao^{a,b}

^a Key Laboratory of Advanced Textile Materials and Manufacturing Technology, Zhejiang Sci-Tech University, Ministry of Education, Hangzhou 310018, PR China

^b Department of Materials Engineering, College of Materials and Textile, Zhejiang Sci-Tech University, Hangzhou 310018, PR China

ARTICLE INFO

Article history:

Received 16 February 2013

Received in revised form 12 May 2013

Accepted 16 May 2013

Available online 25 May 2013

Keywords:

Biosensor

Electrospin

Nanofiber

Nanoparticle

ABSTRACT

A facile and green approach has been demonstrated for the fabrication of highly uniform and monodisperse noble metal (Ag, Au, Pt) nanoparticles (NMNPs) in polyvinyl alcohol (PVA) nanofibers by combining an in situ reduction and electrospinning technique, which are used as efficient biosensor for the detection of H_2O_2 . The small and stable NMNPs can be easily obtained in aqueous solution using EGCG as both reductant and stabilizer. Through electrospinning technique, uniform and smooth nanofibers can be obtained and the NMNPs with narrow size distributions are well dispersed in PVA nanofibers. The investigation indicates that the viscosity of the PVA solution play an important role in controlling the size of NMNPs. The fabricated AgNPs/PVA nanofibers functionalized electrodes exhibits remarkable increased electrochemical catalysis toward H_2O_2 and excellent stability and reusability. The biosensor allows the highly sensitive detection of H_2O_2 with a broad linear range span of the concentration of H_2O_2 from $10 \mu M$ to $560 \mu M$. The rapid electrode response to the change of the H_2O_2 concentration is attributed to the fast diffusion of the H_2O_2 onto the surface of small AgNPs through the porous nanofibers structures.

© 2013 Elsevier B.V. All rights reserved.

1. Introduction

Noble metal nanostructures have received intensive research interests in recent decades due to their unique structure-dependent properties and potential applications in numerous fundamental and applied fields, such as catalysis, sensors, energy conversion, antibacterial, biology and biomedicine [1–4]. Recent years have witnessed tremendous efforts devoted to the design and synthesis of noble metal nanoparticles (NMNPs) in the application of electrochemical biosensors [5–7]. Electrochemical biosensors, a subclass of chemical sensors, possess high specificity of biological recognition processes [8,9]. These devices contain a biological recognition element (enzymes, proteins, antibodies, nucleic acids, cells, tissues or receptors) that selectively reacts with the target analyte and produces an electrical signal that is related to the concentration of the analyte [9,10]. Electrochemical detection of biomolecules using nanomaterials can often achieve high sensitivity because nanomaterials are extremely sensitive to electronic perturbations in the surrounding environment [11,12]. For example, Mao et al. prepared

reduced graphene oxide sheet decorated with gold nanoparticles using as biosensors for the detection of protein, suggesting a lower detection limit and rapid current response [6].

It is well-known that the electrocatalytic activity of metal nanoparticles is extremely sensitive to their sizes, sharp and dispersion [13–16]. Small size usually can dramatically affect their physical and chemical properties arising from their large surface-area-to-volume ratio and the spatial confinement of electrons, phonons, and electric fields in and around these particles [17–20]. However, along with the exciting properties caused by the small size, significant challenges still remain for the preparation and isolation of nanoparticles with controlled polydispersity, toxicity, and aggregation, which are due to the high surface energy and large surface curvature of nanoparticles.

A high dispersion of NMNPs is basically important to present high catalytic activity, and unfortunately, the associated tendency of NMNPs to aggregate would lower their catalytic activity and reuse life-time [21–23]. Therefore, how to design and prepare NMNPs with long-term dispersion stability and high catalytic efficiency is a primary challenge for the widely applications. Recently, one-dimensional (1-D) nanostructures such as nanowires, nanobelts and nanotubes were used as supports to protect NMNPs against aggregating and facilitate their recovery [24,25]. Chauhan et al. fabricated Au nanoparticles/multiwalled carbon nanotubes/polymers modified Au electrodes used as lysine

* Corresponding author at: Key Laboratory of Advanced Textile Materials and Manufacturing Technology, Zhejiang Sci-Tech University, Ministry of Education, Hangzhou 310018, PR China. Tel.: +86 571 86843255.

E-mail addresses: du@zstu.edu.cn, psdum1@gmail.com (M. Du).

biosensors, demonstrating an improved analytical performance with higher stability and low limit of detection and response time [26]. However, conventional deposition precipitation method is unlikely to produce highly dispersed NPs.

Organic polymer nanofibers have been recently recognized as a new kind of 1-D supports and besides the stabilizing and protecting effects for NMNPs, polymers can offer unique possibilities for modifying both the environment around NMNPs and access to the catalytic sites [21,22]. Through electrospinning technique, various morphologies nanofibrous mats with high specific surface area, porosity, flexibility and stability can be easily achieved [27–30]. Polyvinyl alcohol (PVA) is a water soluble polymer with good biocompatibility. Combining the flexibility, good biocompatibility and porous structures of PVA nanofibers, we use the PVA solution to prepare the uniform, well-dispersion and small size of NMNPs.

In modern life, from the viewpoint of practical applications, it would be of great value to explore a facile and green approach for the synthesis of NMNPs in nanoscience [21,31]. In our previous reports, a green reductant, tea polyphenols (TP) was used to synthesize small and uniform Au nanoparticles (AuNPs) and the TP can also act as a stabilizer for protecting the AuNPs from aggregations [31–34]. In this paper, a group of water-soluble polyphenols richly deposited in plants, epigallocatechin gallate (EGCG), was used as reductant for the synthesis of NMNPs in PVA and aqueous solution via an *in situ* reduction. It is easy to achieve small, highly dispersion, reliable, stable, and uniform NMNPs using this method. Through electrospinning technique, uniform and smooth nanofibers can be obtained and the NMNPs with narrow size distributions are well dispersed in PVA nanofibers. The size of AgNPs embedded in PVA nanofibers and the morphology and diameter of the nanofibers can be adjusted by changing the concentration of PVA. In order to obtain AgNPs/PVA nanofibrous mats with performance porous structures and water stability, GA vapor was used to crosslink the nanofibers. After the immersion in water for 12, 24, 48 h, respectively, the porous nanofibers structure was still well preserved, suggesting the successful crosslinkage. The functional AgNPs/PVA nanofibrous mats were used as electrochemical biosensors for the detection of H_2O_2 .

2. Experiment

2.1. Materials

Silver nitrate (AgNO_3) was acquired from Changzhou GuoYu Environmental S&T Co., Ltd. Chloroplatinic acid ($\text{H}_2\text{PtCl}_6 \cdot 6\text{H}_2\text{O}$, 99.9%) and chloroauric acid ($\text{HAuCl}_4 \cdot 4\text{H}_2\text{O}$, 99.9%) were acquired from Shanghai Civi Chemical Technology Co., Ltd. Polyvinyl alcohol (88% hydrolyzed, Mw = 88 000), horseradish peroxidase (HRP, RZ ~ 3, activity ≥ 300 units mg^{-1}), hydroquinone (HQ) and H_2O_2 (30 wt%) were obtained from Aladdin Chemistry Co., Ltd. Epigallocatechin gallate (EGCG) was purchased from Xuancheng Baicao Plant Industry and Trade Co., Ltd. Glutaraldehyde (GA) aqueous solution (30 wt%) and phosphate buffer (PB) were obtained from Hangzhou Gaojing Fine Chemical Co., Ltd. Nafion aqueous solution (5 wt%) was obtained by Aldrich Chemistry Co., Ltd. All the chemicals were used as received without further purification. Deionized water (DIW) was used for all solution preparations.

2.2. Green synthesis of noble metal (Ag, Au, Pt) nanoparticles (NMNPs) in aqueous solution using EGCG as reductant

For the synthesis of NMNPs, 2 mL Ag (I) solution (5 mmol L^{-1}), 2 mL Au (III) solution (5.0 mmol L^{-1}) and 3 mL Pt (VI) solution (10.0 mmol L^{-1}) were firstly dissolved in 25 mL DIW under moderate stirring to get a homogeneous solution. Then, the mixture

were injected into a 3-neck flask (fitted with a reflux condenser and a Teflon-coated stir bar) and heated to 65°C with vigorously stirring by magnetic force. After a few minutes, 0.0125 g, 0.0125 g, and 0.025 g EGCG dissolved in 5 mL DIW, were injected into the above Ag (I), Au (III), and Pt (VI) solution, respectively. Samples were taken over a period time and then refrigerated at 4°C for the following characterizations. The reaction times of each sample were 1 min, 5 min, 15 min, 30 min, 60 min, 120 and 180 min, respectively. The diameters and distribution of the NMNPs were measured by Image-Pro Plus6.2 software (200 particles of NMNPs were randomly selected for the measurement).

2.3. Preparation of NMNPs in PVA electrospun precursor solution using EGCG as reductant

5 g PVA powder was dissolved in 45 mL DIW to get a concentration of 10 wt% solution and was stirred at 80°C for 5 h to obtain a transparent homogeneous solution. The solution was then cooled to room temperature and 10 mL 10 wt% PVA solution were injected into three 3-neck flask, respectively. The calculated amounts of AgNO_3 (0.0375 g), $\text{HAuCl}_4 \cdot 3\text{H}_2\text{O}$ (0.0462 g) and $\text{H}_2\text{PtCl}_6 \cdot 6\text{H}_2\text{O}$ (0.0642 g) were added into the flasks, respectively. 0.025 g EGCG dissolved in 2 mL DIW was injected into the above solutions, respectively. The solutions were kept at 65°C under vigorously stirring for 3 h to ensure the complete reduction. After that, the precursor solutions for electrospinning were refrigerated at 4°C for the further characterizations.

2.4. Electrospinning of NMNPs embedded in PVA nanofibers

Each of the noble-metal-PVA electrospun precursor solution was collected in a 10 mL syringe equipped with a 24 gauge stainless steel needle tip. The syringe was fixed on an electric syringe pump set to maintain a constant feed rate of 0.01 mL min^{-1} . The high voltage power supplier was connected to the needle by a high-voltage insulating wire with two clamps at the end. A grounded metal plate covered with aluminum foil served as the collector. The voltage used for electrospinning was 12 kV. The distance between the needle tip and the collector was 12 cm. All experiments were performed at room temperature. Finally, after 4 h, the NMNPs/PVA nanofibrous mats were peeled off from the aluminum foil and kept in polyethylene sealing bags. The diameters and distribution of the NMNPs and nanofibers were measured by Image-Pro Plus6.2 software (200 particles of NMNPs were randomly selected for the measurement).

2.5. Preparation of size-controlled AgNPs embedded in PVA nanofibers

1.2, 1.5 and 1.8 g PVA powder were dissolved in 13.8, 13.5 and 13.2 mL DIW to get a series concentration of 8, 10, and 12 wt%, respectively. 0.0375 g AgNO_3 was added into the PVA solutions, respectively, and the solutions were vigorously stirred at 65°C for 0.5 h to obtain a homogeneous solution. Then, 0.025 g EGCG dissolved in 2 mL DIW was injected into the above solutions, respectively. The solutions were kept at 65°C under vigorously stirring for 3 h to ensure the complete reduction. After that, the precursor AgNPs/PVA solutions were used to prepare a non-woven mat via electrospinning technique. The electrospun time of the precursor solutions are 3 h and then, the AgNPs/PVA nanofiber mats were peeled off from the aluminum foil and kept in polyethylene sealing bags. The diameters and distribution of the nanofibers were measured by Image-Pro Plus6.2 software (200 nanofibers were randomly selected for the measurement).

2.6. Fabrication of the water-stable AgNPs/PVA nanofibers biosensors for H_2O_2 detection

The AgNPs/PVA nanofibers mats were firstly treated by GA vapor under vacuum oven at 80 °C for overnight to achieve the water stable nanofibers. For the fabricating procedure of the biosensor, the glassy carbon electrode (GCE) with a diameter of 3 mm was polished carefully using alumina slurry as a polisher to get a mirror-like surface, followed by rinsing with DIW and ethanol and then drying by nitrogen. The water stable AgNPs/PVA nanofibers mat was immersed in 3 mg mL⁻¹ of HRP solution (1 mL) at 4 °C overnight in a humidity chamber. Then, the HRP modified AgNPs/PVA fibrous mat was glued by Nafion aqueous solution (1 wt%) on the pre-treated GCE and left to dry by N₂ at room temperature. The modified electrode was washed gently with DIW and then soaked in PB at 4 °C. This modified electrode is denoted as HRP/(AgNPs/PVA)/GCE. The control sample, HRP/PVA/GCE was fabricated using similar procedures for the preparation of HRP/(AgNPs/PVA)/GCE. All the modified electrodes were stored at 4 °C in a refrigerator before further characterizations.

2.7. Biosensing experiments

Amperometric experiments were conducted with a CHI660 C workstation (Shanghai Chenhua, Shanghai). All experiments were carried out using a conventional three-electrode system in 0.1 M PB, where HRP/AgNPs/PVA/GCE was used as the working electrode, a platinum foil as the auxiliary electrode and a saturated Ag/AgCl electrode as the reference electrode. The buffer was purged with high-purity nitrogen for at least 30 min prior to each amperometric

experiment, and the nitrogen environment was then kept over the solution to protect the solution from oxygen. Electrochemical performances of the fabricated electrodes were tested using a three-electrode system by cyclic voltammetry (CV).

2.8. Instrumentation

Transmission electron microscopy (TEM) images were obtained with a JSM-2100 transmission electron microscopy (JEOL, Japan) at an acceleration voltage of 200 kV. The morphologies of the electrosynthesized NMNPs/PVA nanofibers were observed by a JSM-6700F field-emission scanning electron microscope (FE-SEM, JEOL, Japan) at an acceleration voltage of 1 kV. Fourier transform infrared (FTIR) spectra were recorded on a Nicolet 5700 FTIR spectrometer in transmittance mode at a resolution of 4 cm⁻¹ and 32 scans. Ultraviolet–visible (UV–vis) spectra were obtained at 25 °C with a Lambda 900 UV-Vis spectrophotometer (Perkin Elmer, USA). X-ray photoelectron spectra of pure PVA and AgNPs/PVA nanofibers were recorded using an X-ray Photoelectron Spectrometer (Kratos Axis Ultra DLD) with an aluminum (mono) Ka source (1486.6 eV). The aluminum Ka source was operated at 15 kV and 10 mA.

3. Result and discussion

3.1. Synthesis of well-dispersed noble metal nanoparticles (NMNPs) in aqueous using EGCG as a green reductant

Due to the potential widely application of NMNPs in catalysis, sensor, bioscience, imaging and optical devices, a simple, green and stable preparation approach should draw considerable attention. In

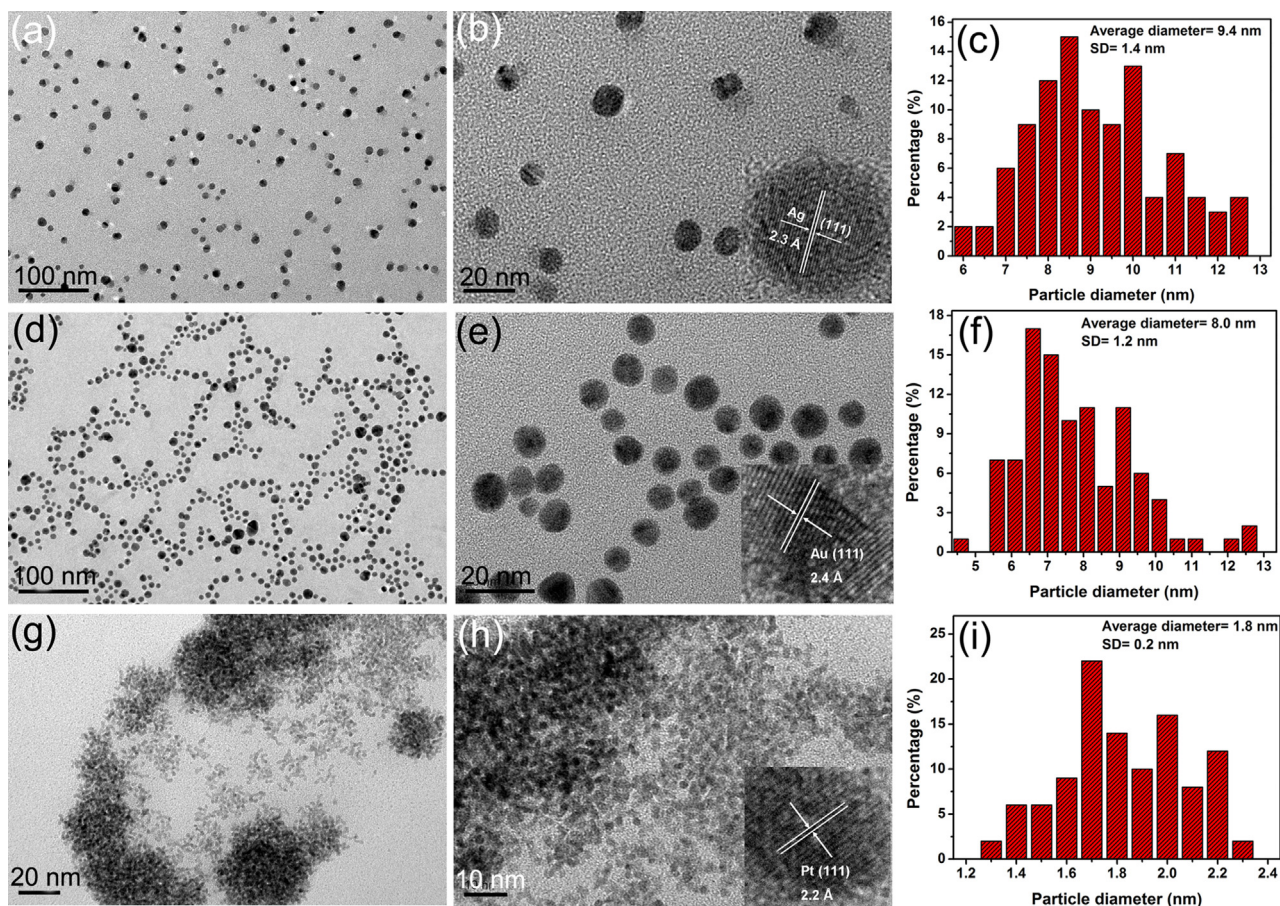


Fig. 1. TEM images of (A, B) AgNPs, (D, E) AuNPs and (G, H) PtNPs synthesized in aqueous solutions using EGCG as reductant. The corresponding diameter distributions of the (C) AgNPs, (F) AuNPs and (I) PtNPs.

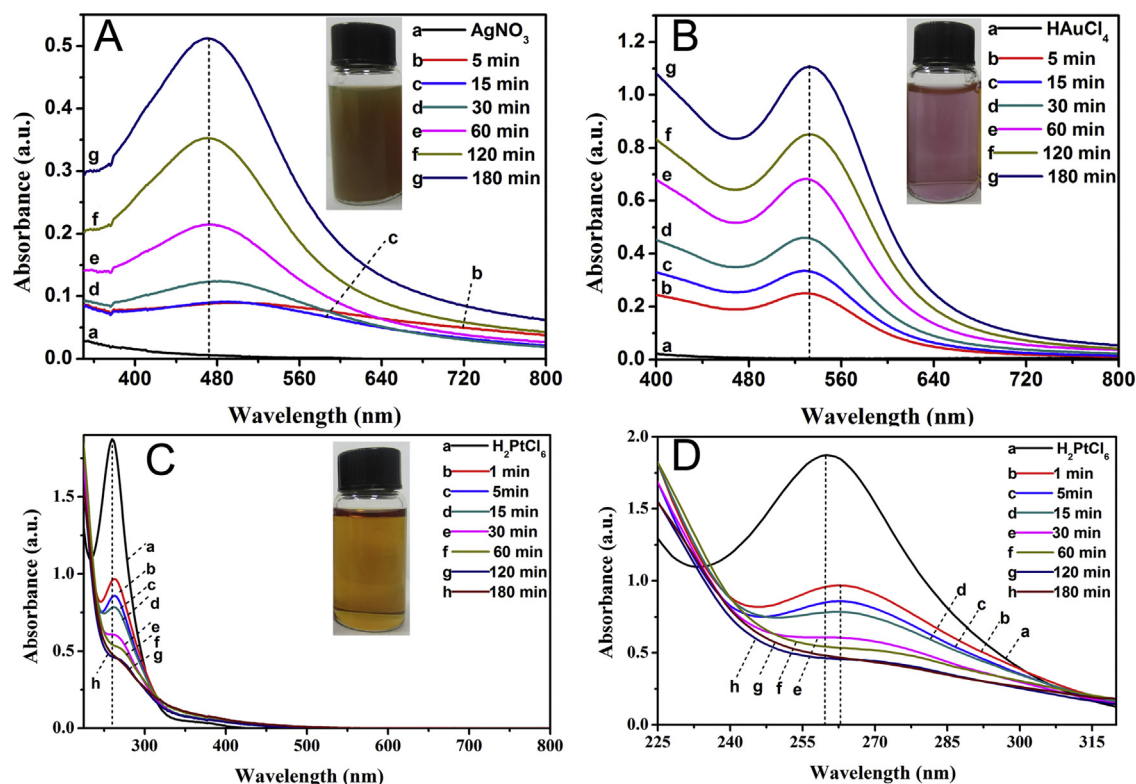


Fig. 2. UV-vis spectra of (A) AgNPs, (B) AuNPs and (C, D) PtNPs in aqueous solution and the insets are the photographs of the corresponding NMNPs solution.

the present investigation, well-dispersed and relative uniformly Ag, Au and Pt nanoparticles were obtained through a facile and green method. Fig. 1 shows the TEM and HRTEM images of the NMNPs and the corresponding diameter distributions. As exemplified in Fig. 1A and B, spherical and well-separated AgNPs are obtained and the HRTEM images shown in Fig. 1B were visible with a spacing of about 0.23 nm, which corresponded to the lattice spacing of the (1 1 1) planes of Ag [33,34]. Fig. 1C shows that the average diameter of AgNPs is 9.4 ± 1.4 nm, indicating the relative uniform diameter distribution. Meanwhile, similar phenomena are showed that there is nearly not aggregated AuNPs and PtNPs in aqueous solution, indicating the stabilization effect of polyphenols [21,33,34]. The AuNPs possess an average diameter of 8.0 ± 1.2 nm and exhibit a uniformly spherical morphology. HRTEM images exhibit the clear lattice fringes that can be assigned to Au (1 1 1) planes [35,36]. Fig. 1G and H shows the small PtNPs with a uniform diameter distribution of 1.8 ± 0.2 nm and the HRTEM images exhibit the clear lattice fringes of Pt (1 1 1) planes [23]. Based on the above results, the green reductant, EGCG, can effectively serve as a reductant and stabilizer for the synthesis of NMNPs [21,31–34].

The UV-vis spectra of the NMNPs in aqueous solution grown with increasing reaction time and the photographs of the corresponding NMNPs solution are shown in Fig. 2. The insets in Fig. 2 show that the colors of the AgNPs, AuNPs and PtNPs are brown, wine red and yellow, respectively. The color evolutions of these NMNPs solution with increasing reaction time are shown in Figs. S1, S2 and S3. Two strong surface plasmon resonance (SPR) bands corresponding to the AgNPs and AuNPs are observed, respectively, which are shown in Fig. 2A and B. They become stronger with the increasing reaction time. As shown in Fig. 2A, after the addition of EGCG, a broad band emerged around 520 nm and with the reaction time further increases, the SPR peaks of AgNPs move to 470 nm and become sharper, indicating the blue-shift of SPR peaks. As exemplified in Fig. 2B, a series of strong and sharp SPR peaks of AuNPs are observed at 525 nm, which can be considered as a superposition of

the contribution from intraband transitions, and it is believed to be a consequence of photoexcitation of the free conduction electrons on the surface of AuNPs [31–34,37]. According to the literatures, the sharp SPR peaks of AgNPs and AuNPs can also indicate the relative uniformly NPs' size distribution [31–33]. Fig. 2C shows the corresponding UV-vis absorption spectra of PtNPs solution and indicates that the solution of Pt NPs has no absorption band in the visible range, which is consistent with previous reports [23]. On the other hand, Fig. 2D shows the spectra of PtNPs in the range from 225 to 315 nm. The absorption peak located at 264 nm in curve a is ascribed to PtCl_6^{2-} anions and when the EGCG were added into the H_2PtCl_6 solution, the peak moves to 266 nm, which is caused by the electrostatic interactions between the PtCl_6^{2-} anions and phenolic hydroxyl groups [23]. With the increasing reaction time, the peaks of PtCl_6^{2-} become weak and after 3 h, the peaks are vanished, indicating the complete formation of PtNPs.

Fig. 3a shows the FTIR spectrum of EGCG, and the absorption bands at 1340 cm^{-1} and 1145 cm^{-1} are ascribed to the O–H in-plane bending vibration and to O–H aromatic, which are the characteristic peaks of EGCG. After the redox reactions in synthesizing NMNPs, the peaks at 1340 cm^{-1} and 1145 cm^{-1} become weak or vanished. Meanwhile, the absorption band around 3364 cm^{-1} shifted to 3410 cm^{-1} , 3433 cm^{-1} and 3404 cm^{-1} , respectively, and became relatively narrow, which also implied the involvement of the O–H groups in the reduction of NM ions, resulting in the partial destruction of hydrogen bonds among EGCG molecules [32–34,38]. The synthesis procedure of the NMNPs in aqueous solution is shown in Fig. S4.

3.2. Preparation of mono-dispersed NMNPs in PVA nanofibers using EGCG as a green reductant

In the above works, small NMNPs have been successfully synthesized using a green reducer, EGCG. However, the size control, dispersion in substrates and effective applications of these NMNPs

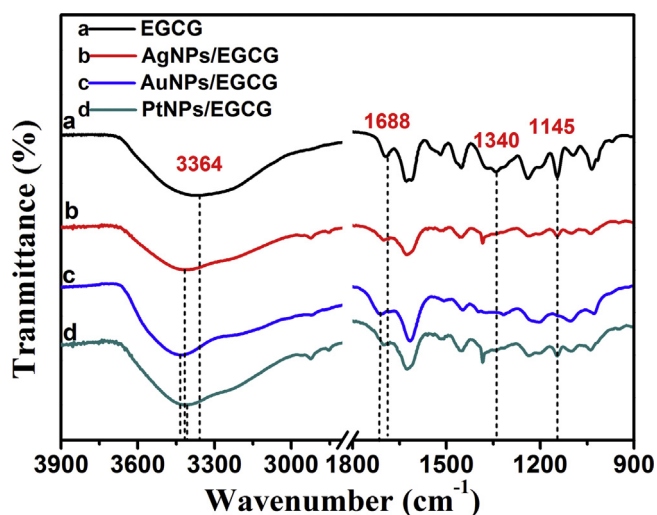


Fig. 3. FTIR spectra of (a) EGCG, (b) AgNPs/EGCG solution, (c) AuNPs/EGCG solution and (d) PtNPs/EGCG solution.

are still crucial challenges. Here, we synthesized well dispersion and stable NMNPs embedded in the PVA nanofibers by combining an in situ reduction and electrospinning technique. As shown in Fig. 4A and B, small AgNPs with an average diameter about 5.9 ± 0.5 nm are well dispersed in the PVA nanofibers. Similarly, the AuNPs and PtNPs with average diameters about 4.8 ± 0.6 and 2.6 ± 0.2 nm, respectively, are uniformly embedded in the PVA nanofibers. Compared with Fig. 1, the NMNPs embedded in PVA

nanofibers had a narrow distribution and better dispersion than those in aqueous solution. Therefore, it is concluded that the PVA polymer might play a crucial role of stabilizer and direct the particular arrangements of NMNPs during the reduction and electrospinning process.

The morphologies and the diameter distributions of the NMNPs/PVA nanofibers are shown in Fig. 5. Uniform and smooth nanofibers with random orientation are obtained and the average diameters of AgNPs/PVA, AuNPs/PVA and PtNPs/PVA nanofibers are about 340 ± 45 nm, 315 ± 40 nm, and 310 ± 50 nm, respectively. A higher magnification FE-SEM image indicates that some of the NMNPs can be seen on the surface of PVA nanofibers (Fig. S5). Meanwhile, the NMNPs/PVA nanofibers indicate highly porous structure, and the porous structure can improve the adsorption of the nanofibers. The UV-vis spectra of the NMNPs/PVA solution are shown in Fig. 6A and two sharp absorption peaks located at 440 and 550 nm are the SPR bands. Compared with Fig. 2, the SPR bands of AgNPs has a hypsochromic shift from 470 nm to 440 nm, while the AuNPs has a bathochromic shift from 525 nm to 550 nm. It is well known that such hypsochromic and bathochromic shifts in the UV-vis spectra are related to chemical changes in the environment [31,39]. The UV-vis absorption spectra of PtNPs/PVA solution still have no absorption band in the visible range solution, which is consistent with Fig. 2. The FTIR spectra of PVA and NMNPs/PVA nanofibers are shown in Fig. 6B. The broaden band located around 3404 cm^{-1} are attributed to the stretching vibration of $-\text{OH}$ groups, while the two sharp peaks at 1736 cm^{-1} and 1254 cm^{-1} are assigned to the $\text{C}=\text{O}$ stretching vibration and $\text{C}-\text{O}$ stretching vibration of hydroxyl groups in PVA [22,40,41]. After the fabricating of NMNPs/PVA nanofibers, the broaden band move to

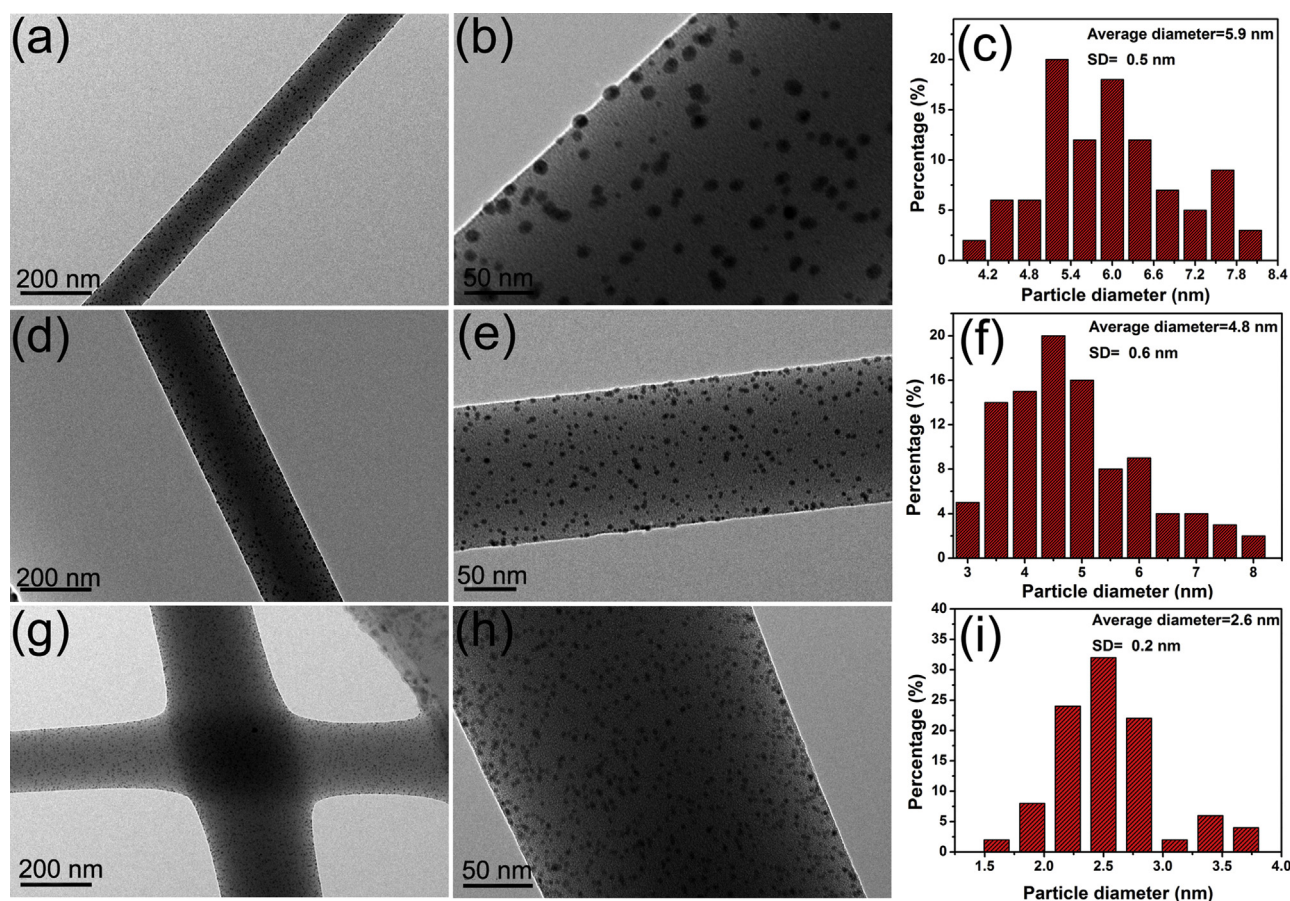


Fig. 4. TEM images of the (A, B) AgNPs/PVA, (D, E) AuNPs/PVA and (G, H) PtNPs/PVA nanofibers. The corresponding diameter distributions of (C) AgNPs, (F) AuNPs and (I) PtNPs.

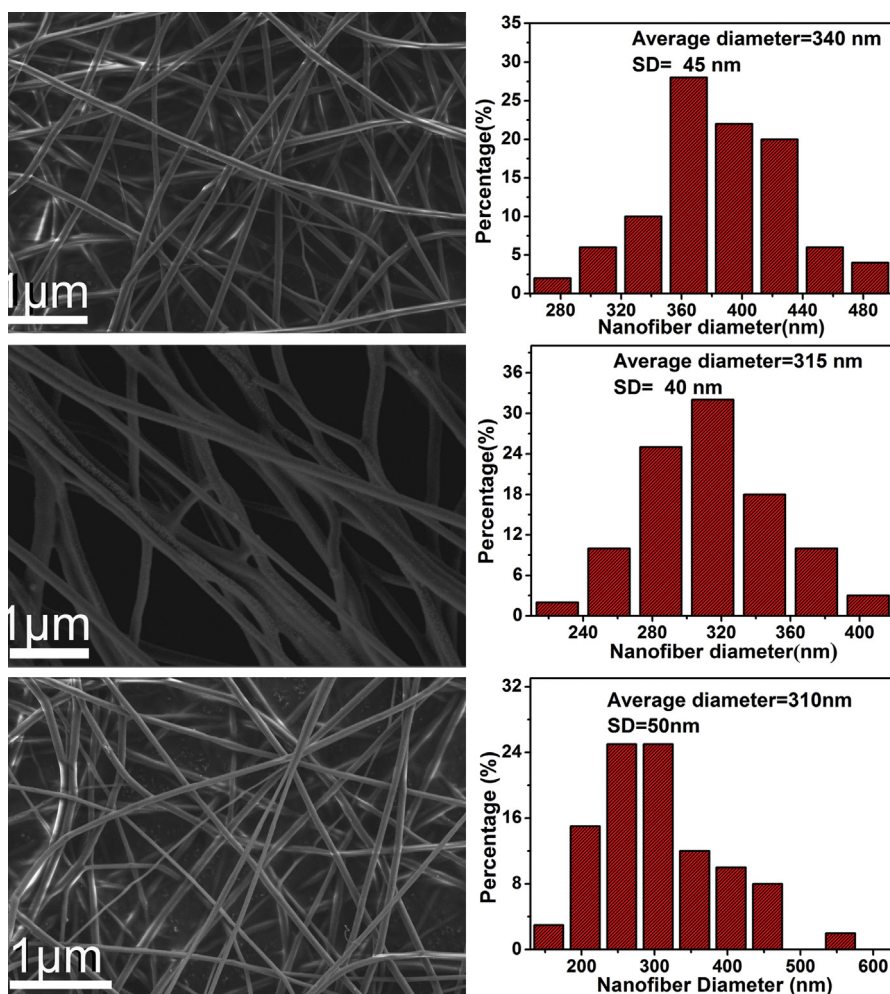


Fig. 5. FE-SEM images of the (A) AgNPs/PVA, (B) AuNPs/PVA and (C) PtNPs/PVA nanofibers with a concentration of PVA at 10 wt%. The corresponding diagrams of the average diameter of (D) AgNPs/PVA, (E) AuNPs/PVA and (F) PtNPs/PVA nanofibers.

3328 cm^{-1} , 3335 cm^{-1} and 3322 cm^{-1} respectively, suggesting the chelating effects between hydroxyls groups of PVA and NMNPs.

Based on the above studies, these novel NMNPs/PVA nanofibers have been successfully fabricated and in the following works, we will focus on the study of the growth mechanism, size control of NPs, morphologies of nanofibers, water-stability and biosensor applications. We chose AgNPs/PVA nanofibers as the example for the mentioned study. XPS was used to further probe the surface chemical compositions and chemical oxidation state of the as-prepared PVA and AgNPs/PVA nanofibers. The binding energies obtained in the XPS analysis were corrected for specimen charging by referencing the C1s to 284.6 eV. As shown in Fig. 7A, the binding energy shift of O 1s from 530.4 eV to 530.0 eV in PVA

and AgNPs/PVA nanofibers was a result of the strong coordination between AgNPs and oxygen [31–34]. The XPS spectra of Ag 3d in AgNPs/PVA nanofibers demonstrates two significant peaks, locating at 371.4 and 365.7 eV, which are in agreement with the binding energies of Ag 3d_{5/2} and Ag 3d_{3/2}, respectively [34,42–44]. Compared with the standard binding energy of Ag 3d_{5/2} and Ag 3d_{3/2}, the binding energies of the two kind of nanofibers are lower than bulk Ag (368.2 and 374.2 eV), indicating the strong interactions among the AgNPs and hydroxyls groups. The XPS experimental data are in a good agreement with what have been reported in the reference for both Ag⁺ to Ag⁰ [42].

Based on the above results, the growth mechanism of these novel materials are portrayed in Scheme 1 and the AgNPs/PVA nanofibers were taken as an example. Recently, the PVA, organic polymer, is regarded as a new class of supports for stabilizing NMNPs because in addition to stabilizing and protecting these particles, polymers can offer unique possibilities for modifying both the environment around NPs and access to the catalytic sites [21]. As illustrated in Scheme 1, the PVA molecular chains possess large amounts of hydroxyls groups, which had been proven to be excellently bonded with Ag ions by forming a stable Ag–OH chelate complex [31–34]. Because of the high viscosity of the polymer solution and the stabilization of PVA, the synthesis of AgNPs of different sizes was a kinetically driven process. After the complete formation of Ag–OH chelate complex, and with the addition of the reducer, EGCG, the pre-formed Ag–OH chelate complex were reduced to

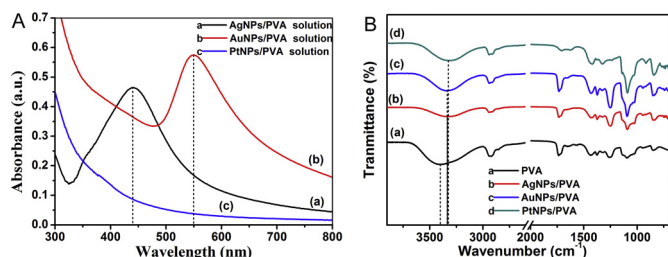


Fig. 6. (A) UV-vis spectra and (B) FTIR spectra of the AgNPs/PVA, AuNPs/PVA and PtNPs/PVA solutions.

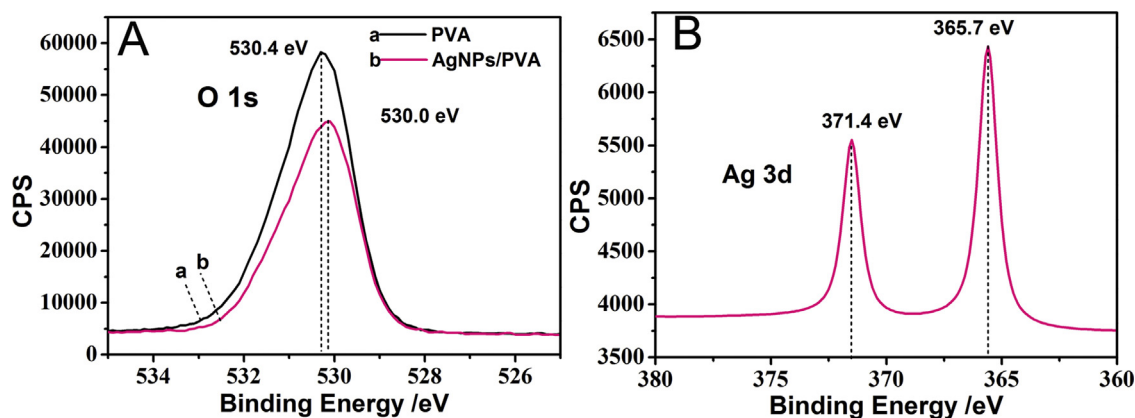


Fig. 7. XPS spectra of the PVA and AgNPs/PVA nanofibers: (A) O 1s and (B) Ag 3d spectra of PVA and AgNPs/PVA nanofibers.

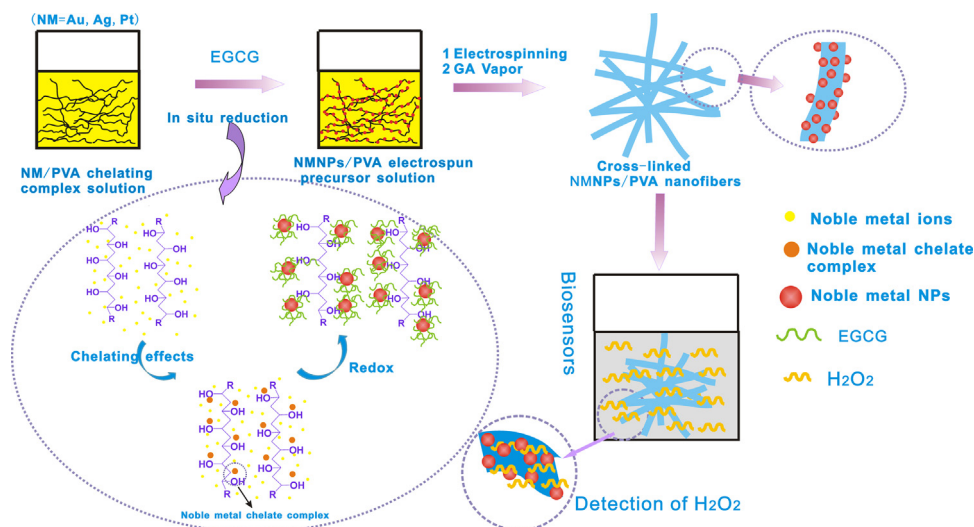
the original Ag nuclei (Ag^0) in situ. Due to the high viscosity of PVA solution, the EGCG is not fast chelated with the Ag nuclei. At a relative low dosage of EGCG, the nucleation rate is relatively faster than the growth rate and more and more Ag nuclei are formed. Due to the chelating effect between the Ag ions and hydroxyls groups in PVA molecular chains, the formed Ag nuclei can be confined and cannot collide with each other to aggregate easily. When the diffusion equilibrium of EGCG is achieved, the unchelated Ag ions were coated on the surface of Ag nuclei with EGCG molecular and grown into large-sized AgNPs. Then, the synthesized AgNPs/PVA precursor solutions were electrospun into nanofibers.

3.3. Synthesis of the size-controlled AgNPs embedded in PVA nanofibers using EGCG as a green reductant

As discussed above, the viscosity of the PVA solution may play an important role in controlling the size of AgNPs, and therefore, we studied the effectiveness of PVA concentration on the sizes of AgNPs. The AgNPs/PVA nanofibers with different sizes of AgNPs are shown in Fig. 8. The AgNPs with various diameters are well dispersed in PVA nanofibers, indicating the reliability of this facile and green approach. With the increasing of the mass fraction of PVA from 8 wt% to 12 wt%, the average diameters of AgNPs decreased from 3.9 nm to 2.4 nm, indicating the significant effects of the viscosity on the size control. Both AgNPs achieved at different PVA's mass fractions possess narrow size distribution, and the standard

deviations (SD) are 0.3, 0.3 and 0.4 nm, respectively, which are smaller than that in aqueous solution (Fig. 1).

It is well known that the uniformity of electrospun nanofibers is greatly influenced by the polymer solution properties and the electrospinning processing parameters. The morphologies of these AgNPs/PVA nanofibers with different polymer concentration (8 wt%, 10 wt%, and 12 wt%) are shown in Fig. 9. As shown in Fig. 9A, at the concentration of 8 wt%, the nanofibers possess high porous fibrous structure and the average diameter is about 260 ± 80 nm, along with some adhesion phenomenon among nanofibers. With the increasing of polymer concentration, the diameters increase from 380 nm to 410 nm. What's more, smooth and uniform nanofibers are obtained at the polymer concentration of 12 wt% (Fig. 9E). Meanwhile, the AgNPs/PVA nanofibers retain their excellent porous fiber structure and almost no adhesion phenomena occurred. The UV–vis spectra of these AgNPs/PVA precursor solutions can also provide evidences for the size-controlled AgNPs, which are shown in Fig. 10. At the same conditions, except for the polymer concentrations, a hypsochromic shifts can be obtained with the increased PVA concentration. The absorption peaks move from 438 nm to 419 nm and according to the literatures, the smaller size of NMNPs could lead to hypsochromic shifts [31–34]. The UV–vis results are according with the TEM images, which are shown in Fig. 8, indicating that the size-controlled AgNPs embedded in PVA nanofibers have been successfully fabricated by changing the polymer concentrations.



Scheme 1. A schematic illustration of the fabrication procedure of NMNPs/PVA nanofibers.

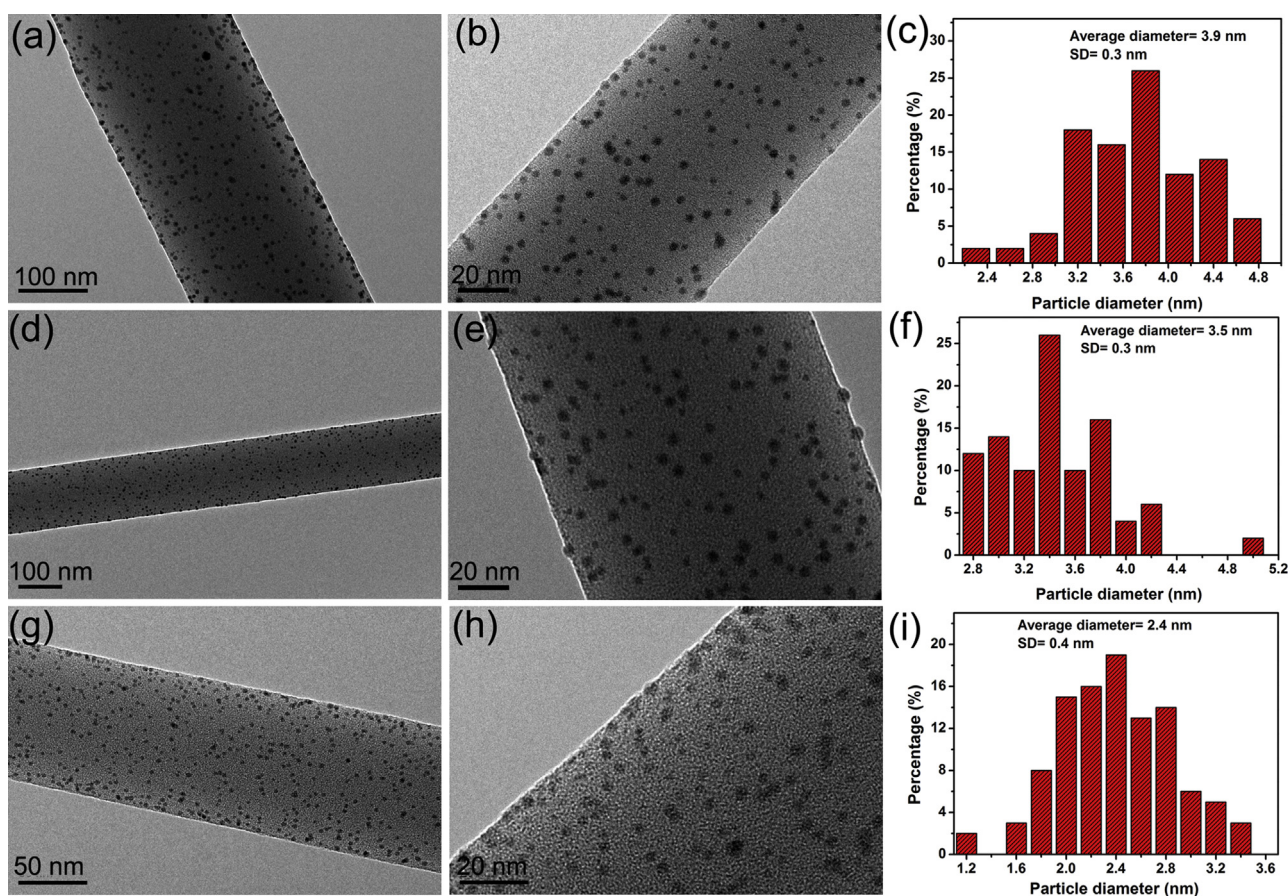


Fig. 8. TEM images of the AgNPs/PVA nanofibers with different average sizes of AgNPs by changing the mass fraction of PVA in the precursor solution: (A, B) 8 wt%, (D, E) 10 wt% and (G, H) 12 wt%. (C, F, I) The corresponding average diameters of AgNPs embedded in PVA nanofibers.

3.4. Fabrication of AgNPs/PVA nanofibers functionalized electrodes using as biosensors for the detection of H_2O_2

In the past decades, NMNPs are widely used in many areas, such as catalysis, surface enhanced Raman scattering, and antibacterial. In this paper, combining the flexibility, good biocompatibility and porous structures of PVA nanofibers with the small size, uniform and well-dispersion of NMNPs, we used these fabricated AgNPs/PVA nanofibers hybrid membranes as efficient substrate materials integrated in biosensors. As we know, the PVA used for electrospun is a kind of water-soluble polymers, and therefore, a critical problem should be solved to retain the nanofibers' water stability. In order to obtain AgNPs/PVA nanofibers with performance porous structures and water stability, GA vapor was used to crosslink the nanofibers. As shown in Fig. 11A and S5a, after the treatments with GA vapor, the nanofibers mats became water-stable and still kept excellent porous fiber structures. The average diameter of the crosslinked nanofibers (505 ± 55 nm, Fig. S5b) was larger than that of the non-crosslinked nanofibers (415 ± 40 nm, Fig. 9F), possibly due to the swelling of the nanofibers during the GA vapor crosslinking [41]. After the immersion in water for 12, 24, 48 h, respectively, the porous nanofibers structure was still well preserved (Fig. 11) and the AgNPs can clearly be seen embedded in PVA nanofibers, suggesting the successful crosslinking.

In order to broaden the application of these novel materials, the AgNPs/PVA nanofibers were used as biosensors for the detection of H_2O_2 . Due to the practical applications in various fields such as food, clinical, pharmaceutical, industrial, biological,

or environmental research areas, H_2O_2 detection is essential for our life and the high concentration of H_2O_2 will cause a negative effect on human health [21]. Various materials have been used as biosensors, for example, Feng et al. synthesized graphene/polyaniline composite film and the biosensor showed a good linear response over a wide range of concentrations from $1 \mu\text{M}$ to $160 \mu\text{M}$, and a low detection limit of $0.8 \mu\text{M}$ [45]. Meanwhile, Zhong et al. prepared spherical Pd@Cys- C_{60} nanoparticles using as electrochemical biosensor for the detection of glucose [46]. Li et al. fabricated Se/Pt nanocomposites as nonenzymatic hydrogen peroxide sensor have a linear relationship with the concentration of H_2O_2 from $10 \mu\text{M}$ up to 15 mM with a correlation coefficient of 0.9991 [47]. In addition, our previous report also indicates the highly sensitive detection of H_2O_2 with a detection limit of $5 \mu\text{M}$ and exhibits a fast response, broad linear range, low detection limit and excellent stability and reusability based on the AgNPs functionalized PVA/PEI nanofibers biosensor [48]. In this paper, combining the flexibility, good biocompatibility and porous structures of PVA nanofibers with the small size, uniform and well-dispersion of NMNPs, we used these fabricated AgNPs/PVA nanofibers hybrid membranes as efficient substrate materials integrated in biosensors. For the application of enzyme-based biosensors, the electron transfer between the enzyme and the electrode is very important for the fundamental studies and the construction of biosensors [45]. Therefore, appropriate promoters should be employed to facilitate the electron transfer and retain the bioactivity of immobilized enzymes. Based on the large specific area, high conductivity, and good biocompatibility of AgNPs and porosity of the nanofibers, the horseradish peroxidase (HRP) can be easily entrapped tightly

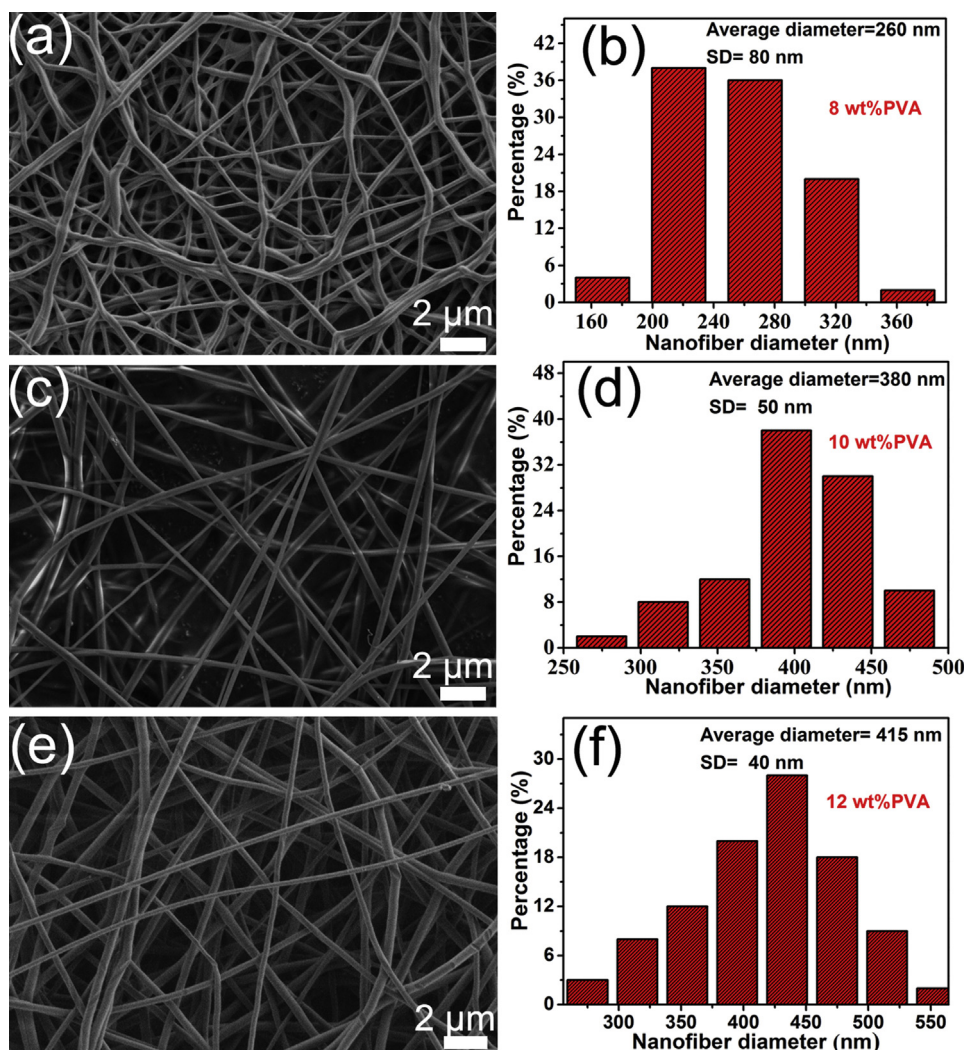


Fig. 9. FE-SEM images of AgNPs/PVA nanofibers with different PVA concentrations: (A) 8 wt%, (C) 10 wt%, and (D) 12 wt%. (B, D, F) The corresponding average diameters of the nanofibers.

onto the negatively charged AgNPs through electrostatic attraction due to its positive charge at pH values below its isoelectric point (the pH value at the isoelectric point is 8.9) [21,45]. Furthermore, hydroquinone (HQ) is used to detect hydrogen peroxide as an excellent electron mediator. The electrochemical properties of these fabricated HRP/(AgNPs/PVA)/GCE are investigated in detail, which are shown in Fig. 12. Well-defined cyclic voltammograms (CVs) of the HRP/PVA/GCE and HRP/(AgNPs/PVA)/GCE are observed with a certain concentration of H_2O_2 . As shown in Fig. 12A, the HRP/PVA/GCE shows weak redox peaks with currents of HQ at 2.3 and $-3.1 \mu A$ and potentials at 0.47 and $-0.23 V$, respectively, indicating that the PVA is not electroactive in this potential range. From Fig. 12B, the CV of HRP/(AgNPs/PVA)/GCE shows a pair of well-defined redox peaks at with currents 15.3 and $-11.5 \mu A$ and potentials at 0.39 and $-0.19 V$, respectively. Compared with the HRP/PVA/GCE, HRP/(AgNPs/PVA)/GCE exhibits remarkable increased electrochemical catalysis toward H_2O_2 , indicating the fast direct electron transfer between the redox-active site of HRP and GCE [49,50].

Apparently, the presence of the small and well-dispersed AgNPs is an important factor for the direct electron transfer of HRP [45,51,52]. Furthermore, the highly porous fibrous structure and increased surface area of AgNPs/PVA nanofibers mats also promote the electrochemical catalytic activity. As promising functional materials, the reusability and recyclability are crucial

issues for practical applications, especially for the costly rare and noble metals. The fabricated AgNPs/PVA nanofibers functionalized electrodes used for 10 times were compared by the CV curves (Fig. 12B) and the redox peaks are almost the same, suggesting the

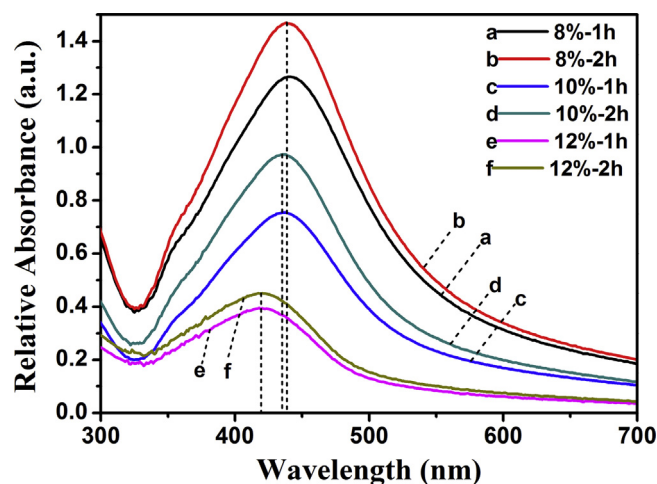


Fig. 10. UV-vis spectra of the AgNPs/PVA solutions at different PVA concentrations of 8 wt%, 10 wt% and 12 wt%.

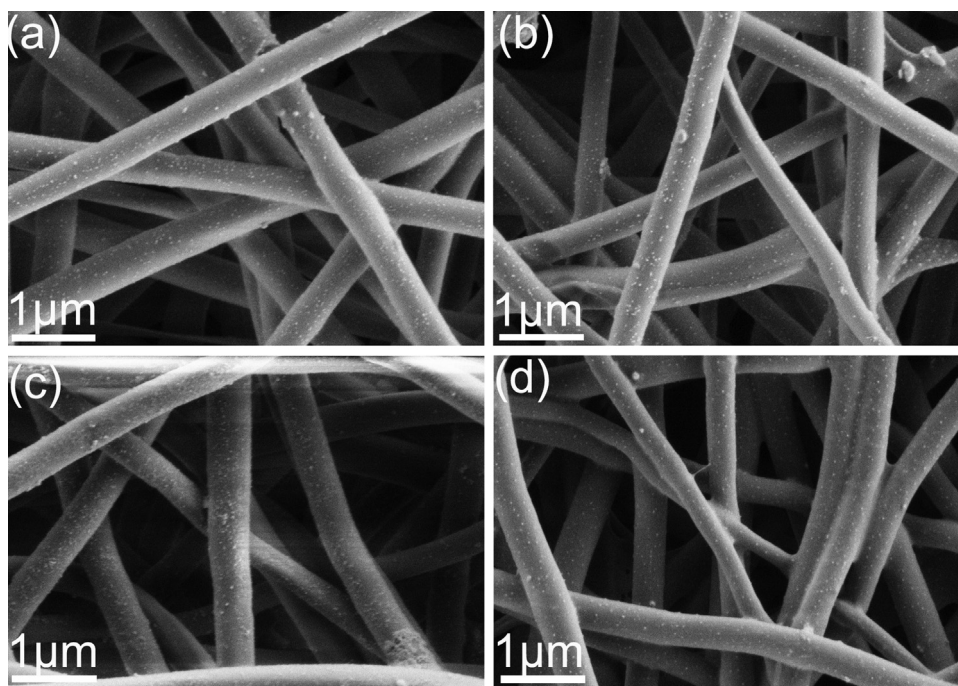


Fig. 11. FE-SEM images of (A) the cross-linked AgNPs/PVA nanofibers and different immersion time in water: (B) 12 h, (C) 24 h, and (D) 48 h.

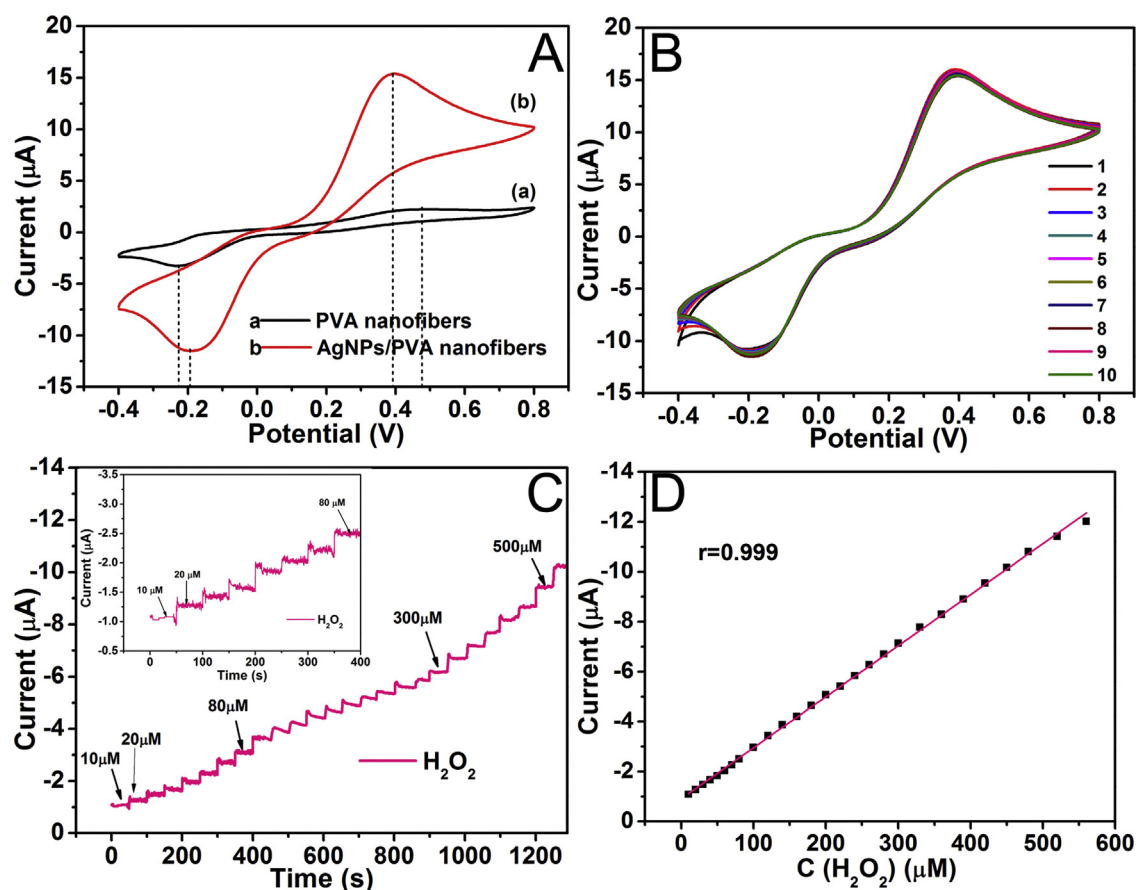


Fig. 12. (A) CVs obtained with AgNPs/PVA and nanofibers functionalized GCE immersed in 1.0 mM HQ in 0.1 M PBS (pH 6.8) in the presence of 5.0 mM H_2O_2 (scan rate, 50 mV s^{-1}); (B) the CVs cycles of the prepared AgNPs/PVA/GCE at the same conditions; (C) amperometric response of the fabricated HRP/(AgNPs/PVA)/GCE biosensor to successive addition of different concentrations of H_2O_2 to 1.0 M phosphate buffer (PB) at -0.19 V . Inset shows the response of the biosensor from $10 \text{ } \mu\text{M}$ to $80 \text{ } \mu\text{M}$ H_2O_2 ; (D) relationship of the calibration curve and linear fitting curve between the currents and the H_2O_2 concentration.

excellent stability and reusability of fabricated AgNPs/PVA nanofibers functionalized electrodes. As shown in Fig. 12C and D, a typical current–time response of the sensor with successive additions of H_2O_2 and the calibration plots of the currents versus the concentration of H_2O_2 , respectively. The AgNPs/PVA nanofibers biosensor responded rapidly and approached about 98% of its steady state current less than 2 s. The rapid electrode response to the change of the H_2O_2 concentration is attributed to the fast diffusion of the H_2O_2 onto the surface of small AgNPs through the porous nanofibers structures. The linear range spans the concentration of H_2O_2 from $10\ \mu\text{M}$ to $560\ \mu\text{M}$, with the correlation coefficient of 0.999. The detection limit of $0.56\ \text{mM}$ was estimated at a signal-to-noise ratio of 3. The high sensitivity may result in the excellent biocompatible microenvironment of the AgNPs/PVA nanofibers around the enzyme.

4. Conclusion

In summary, a facile and green approach has been demonstrated for the fabrication of highly uniform and mono-disperse NMNPs in PVA nanofibers by combining an in situ reduction and electrospinning technique, which are used as efficient biosensor for the detection of H_2O_2 . The small and stable AgNPs, AuNPs and PtNPs with average diameters about 9.4 ± 1.4 , 8.0 ± 1.2 and $1.8 \pm 0.2\ \text{nm}$, respectively, can be easily obtained in aqueous solution using EGCG as both reductant and stabilizer. Meanwhile, the similar process was used for the preparation of NMNPs/PVA electrospun precursor solution. Through electrospinning technique, uniform and smooth nanofibers can be obtained and the NMNPs with narrow size distributions are well dispersed in PVA nanofibers, which are confirmed by TEM and FE-SEM. UV–vis, FTIR and XPS were used to investigate the growth mechanism of these novel materials. After elaborative studies, it is proposed that the viscosity of the PVA solution play an important role in controlling the size of NMNPs and size-controlled AgNPs are obtained. Based on the large specific area, high conductivity, and good biocompatibility of AgNPs and porosity of the nanofibers, the AgNPs/PVA nanofibers were used as biosensor for the detection of H_2O_2 . The fabricated AgNPs/PVA nanofibers functionalized electrodes exhibit remarkable increased electrochemical catalysis toward H_2O_2 and excellent stability and reusability. The fabricated HRP biosensor allowed the highly sensitive detection of H_2O_2 with a broad linear range span of the concentration of H_2O_2 from $10\ \mu\text{M}$ to $560\ \mu\text{M}$. The rapid electrode response to the change of the H_2O_2 concentration is attributed to the fast diffusion of the H_2O_2 onto the surface of small AgNPs through the porous nanofibers structures. The AgNPs/PVA nanofibrous mats could be further applied to immobilize many other enzymes, and the resulting enzyme/AgNPs/PVA nanofibrous mats may find wide applications in bioelectroanalysis and bioelectrocatalysis.

Acknowledgements

We acknowledge the support of the project of the National Natural Science Foundation of China (NSFC) (Grant number: 51243001), the 521 Project of Zhejiang Sci-Tech University and The Young Researchers Foundation of Key Laboratory of Advanced Textile Materials and Manufacturing Technology, Ministry of Education, Zhejiang Sci-Tech University (Grant number: 2011QN02).

Appendix A. Supplementary data

Supplementary data associated with this article can be found, in the online version, at <http://dx.doi.org/10.1016/j.snb.2013.05.062>.

References

- [1] I. Choi, H.D. Song, S. Lee, Y.I. Yang, T. Kang, J. Yi, Core-satellites assembly of silver nanoparticles on a single gold nanoparticle via metal ion-mediated complex, *Journal of the American Chemical Society* 134 (2012) 12083–12090.
- [2] Y.G. Sun, Y.N. Xia, Shape-controlled synthesis of gold and silver nanoparticles, *Science* 298 (2002) 2176–2179.
- [3] J.E. Millstone, S.J. Hurst, G.S. Metraux, J.I. Cutler, C.A. Mirkin, Colloidal gold and silver triangular nanoprisms, *Small* 5 (2009) 646–664.
- [4] T.K. Sau, A.L. Rogach, Nonspherical noble metal nanoparticles: colloidal-chemical synthesis and morphology control, *Advanced Materials* 22 (2010) 1781–1804.
- [5] Y.D. Jin, Engineering plasmonic gold nanostructures and metamaterials for biosensing and nanomedicine, *Advanced Materials* 24 (2012) 5153–5165.
- [6] S. Mao, G.H. Lu, K.H. Yu, Z. Bo, J.H. Chen, Specific protein detection using thermally reduced graphene oxide sheet decorated with gold nanoparticle-antibody conjugates, *Advanced Materials* 22 (2010) 3521–3526.
- [7] J. Lu, I. Do, L.T. Drzal, R.M. Worden, I. Lee, Nanometal-decorated exfoliated graphite nanoplatelet based glucose biosensors with high sensitivity and fast response, *ACS Nano* 2 (2008) 1825–1832.
- [8] N.J. Ronkainen, H.B. Halsall, W.R. Heineman, Electrochemical biosensors, *Chemical Society Reviews* 39 (2010) 1747–1763.
- [9] L.N. Cella, W. Chen, N.V. Myung, A. Mulchandani, Single-walled carbon nanotube-based chemiresistive affinity biosensors for small molecules: ultrasensitive glucose detection, *Journal of the American Chemical Society* 132 (2010) 5024–5026.
- [10] Q. Li, K. Cheng, W.J. Weng, P.Y. Du, G.R. Han, Highly sensitive hydrogen peroxide biosensors based on TiO_2 nanodots/ITO electrodes, *Journal of Materials Chemistry* 22 (2012) 9019–9026.
- [11] Y.H. Sun, R.M. Kong, D.Q. Lu, X.B. Zhang, H.M. Meng, W.H. Tan, G.L. Shen, R.Q. Yu, A nanoscale DNA–Au dendrimer as a signal amplifier for the universal design of functional DNA-based SERS biosensors, *Chemical Communications* 47 (2011) 3840–3842.
- [12] S.Y. Yang, Y.M. Liu, H. Tan, C. Wu, Z.Y. Wu, G.L. Shen, R.Q. Yu, Gold nanoparticle based signal enhancement liquid crystal biosensors for DNA hybridization assays, *Chemical Communications* 48 (2012) 2861–2863.
- [13] C. Wang, H.F. Yin, S. Dai, S.H. Sun, A general approach to noble metal-metal oxide dumbbell nanoparticles and their catalytic application for CO oxidation, *Chemistry of Materials* 22 (2010) 3277–3282.
- [14] A.S. Thakor, J. Jokerst, C. Zavaleta, T.F. Massoud, S.S. Gambhir, Gold nanoparticles: a revival in precious metal administration to patients, *Nano Letters* 11 (2011) 4029–4036.
- [15] Y.N. Xia, Y.J. Xiong, B. Lim, S.E. Skrabalak, Shape-controlled synthesis of metal nanocrystals: simple chemistry meets complex physics? *Angewandte Chemie International Edition* 47 (2008) 2–46.
- [16] M. Roca, A.J. Haes, Silica-void-gold nanoparticles temporally stable surf ace-enhanced Raman scattering substrates, *Journal of the American Chemical Society* 130 (2008) 14273–14279.
- [17] J. Zeng, X.H. Xia, M. Rycenga, P. Hennehan, Q.G. Li, Y.N. Xia, Successive deposition of silver on silver nanoplates: lateral versus vertical growth, *Angewandte Chemie International Edition* 50 (2011) 244–249.
- [18] Y.X. Li, J.T. Cox, B. Zhang, Electrochemical responses and electrocatalysis at single Au nanoparticles, *Journal of the American Chemical Society* 132 (2010) 3047–3054.
- [19] C. Zhu, J. Zeng, J. Tao, M.C. Johnson, I. Schmidt-Krey, L. Blubaugh, Y.M. Zhu, Z.Z. Gu, Y.N. Xia, Kinetically controlled overgrowth of Ag or Au on Pd nanocrystal seeds: from hybrid dimers to nonconcentric and concentric bimetallic nanocrystals, *Journal of the American Chemical Society* 134 (2012) 15822–15831.
- [20] M.R. Langille, M.L. Personick, J. Zhang, C.A. Mirkin, Defining rules for the shape evolution of gold nanoparticles, *Journal of the American Chemical Society* 134 (2012) 14542–14554.
- [21] H. Wu, X. Huang, M.M. Gao, X.P. Lia, B. Shi, Polyphenol-grafted collagen fiber as reductant and stabilizer for one-step synthesis of size-controlled gold nanoparticles and their catalytic application to 4-nitrophenol reduction, *Green Chemistry* 13 (2011) 651–658.
- [22] J. Wang, H.B. Yao, D. He, C.L. Zhang, S.H. Yu, Facile fabrication of gold nanoparticles-poly(vinyl alcohol) electrospun water-stable nanofibrous mats: efficient substrate materials for biosensors, *ACS Applied Materials & Interfaces* 4 (2012) 1963–1971.
- [23] H. Dong, D. Wang, G. Sun, J.P. Hinestroza, Assembly of metal nanoparticles on electrospun nylon 6 nanofibers by control of interfacial hydrogen-bonding interactions, *Chemistry of Materials* 20 (2008) 6627–6632.
- [24] J. Wang, M. Musameh, Y.H. Lin, Solubilization of carbon nanotubes by nafion-toward the preparation of amperometric biosensors, *Journal of the American Chemical Society* 125 (2003) 2408–2409.
- [25] T.J. Zhang, W. Wang, D.Y. Zhang, X.X. Zhang, Y.R. Ma, Y.L. Zhou, L.M. Qi, Biotemplated synthesis of gold nanoparticle-bacteria cellulose nanofiber nanocomposites and their application in biosensing, *Advanced Functional Materials* 20 (2010) 1152–1160.
- [26] N. Chauhan, A. Singh, J. Narang, S. Dahiya, C.S. Pundir, Development of amperometric lysine biosensors based on Au nanoparticles/multiwalled carbon nanotubes/polymers modified Au electrodes, *Analyst* 137 (2012) 5113–5122.
- [27] D. Li, Y.N. Xia, Electrospinning of nanofibers: reinventing the wheels? *Advanced Materials* 16 (2004) 1151–1170.

- [28] D. Li, Y.N. Xia, Electrospinning of polymeric and ceramic nanofibers as uniaxially aligned arrays, *Nano Letters* 3 (2003) 555–560.
- [29] H. Wu, R. Zhang, X.X. Liu, D.D. Lin, W. Pan, Electrospinning of Fe, Co, and Ni nanofibers: synthesis, assembly, and magnetic properties, *Chemistry of Materials* 19 (2007) 3506–3511.
- [30] A.C. Kamps, M. Fryd, S.J. Park, Hierarchical self-assembly of amphiphilic semi-conducting polymers into isolated, bundled, and branched nanofibers, *ACS Nano* 6 (2012) 2844–2852.
- [31] H. Zhu, M.L. Du, M.L. Zou, C.S. Xu, N. Li, Y.Q. Fu, Facile and green synthesis of well-dispersed Au nanoparticles in PAN nanofibers by tea polyphenols, *Journal of Materials Chemistry* 22 (2012) 9301–9307.
- [32] H. Zhu, M.L. Du, M.L. Zou, C.S. Xu, Y.Q. Fu, Green synthesis of Au nanoparticles immobilized on halloysite nanotubes for surface-enhanced Raman scattering substrates, *Dalton Transactions* 41 (2012) 10465–10471.
- [33] M.L. Zou, M.L. Du, H. Zhu, C.S. Xu, Y.Q. Fu, Green synthesis of halloysite nanotubes supported Ag nanoparticles for photocatalytic decomposition of methylene Blue, *Journal of Physics D: Applied Physics* 45 (2012) 325302–325308.
- [34] M.L. Zou, M.L. Du, H. Zhu, C.S. Xu, N. Li, Y.Q. Fu, Synthesis of silver nanoparticles in electrospun polyacrylonitrile nanofibers using tea polyphenols as the reductant, *Polymer Engineering & Science* (2012), DOI 10.1002/pen.23358.
- [35] H. Zhu, M.L. Du, D.L. Yu, Y. Wang, L.N. Wang, M.L. Zou, M. Zhang, Y.Q. Fu, A new strategy for the surface-free-energy-distribution induced selective growth and controlled formation of Cu₂O–Au hierarchical heterostructures with a series of morphological evolutions, *Journal of Materials Chemistry A* 1 (2013) 919–929.
- [36] H. Zhu, M.L. Du, D.L. Yu, Y. Wang, M.L. Zou, C.S. Xu, Y.Q. Fu, Selective growth of Au nanograins on specific positions (tips, edges and facets) of Cu₂O octahedrons to form Cu₂O–Au hierarchical heterostructures, *Dalton Transactions* 41 (2012) 13795–13799.
- [37] M.F. Peng, J. Gao, P.P. Zhang, Y. Li, X.H. Sun, S.T. Lee, Reductive self-assembly of Ag nanoparticles on germanium nanowires and their application in ultrasensitive surface-enhanced Raman spectroscopy, *Chemistry of Materials* 23 (2011) 3296–3301.
- [38] R.J. Liao, Z.H. Tang, Y.D. Lei, B.C. Guo, Sodium deoxycholate functionalized graphene and its composites with polyvinyl alcohol, *Journal of Physical Chemistry C* 115 (2011) 20740–20746.
- [39] X. Huang, H. Wu, X.P. Liao, B. Shi, One-step, size-controlled synthesis of gold nanoparticles at room temperature using plant tannin, *Green Chemistry* 12 (2010) 395–399.
- [40] A.S. Asran, K. Razghandi, N. Aggarwal, G.H. Michler, T. Groth, Nanofibers from blends of polyvinyl alcohol and polyhydroxy butyrate as potential scaffold material for tissue engineering of skin, *Biomacromolecules* 11 (2010) 3413–3421.
- [41] Y.P. Huang, H. Ma, S.G. Wang, M.W. Shen, R. Guo, X.Y. Cao, M.F. Zhu, X.Y. Shi, Efficient catalytic reduction of hexavalent chromium using palladium nanoparticle-immobilized electrospun polymer nanofibers, *ACS Applied Materials & Interfaces* 4 (2012) 3054–3061.
- [42] Y. Ding, Y. Wang, L. Su, H. Zhang, Y. Lei, Preparation and characterization of NiO–Ag nanofibers, NiO nanofibers, and porous Ag: towards the development of a highly sensitive and selective non-enzymatic glucose sensor, *Journal of Materials Chemistry* 20 (2010) 9918–9926.
- [43] P.R. Selvakannan, A. Swami, D. Srisathiyarayanan, P.S. Shirude, R. Pasricha, A.B. Mandale, M. Sastry, Synthesis of aqueous Au core-Ag shell nanoparticles using tyrosine as a pH-dependent reducing agent and assembling phase-transferred silver nanoparticles at the air–water interface, *Langmuir* 20 (2004) 7825–7836.
- [44] P. Jiang, S.Y. Li, S.S. Xie, Y. Gao, L. Song, Double-stranded helices and molecular zippers assembled from single-stranded coordination polymers directed by supramolecular interactions, *Chemistry – A European Journal* 10 (2004) 4817–4821.
- [45] X.M. Feng, R.M. Li, Y.W. Ma, R.F. Chen, N.E. Shi, Q.L. Fan, W. Huang, One-step electrochemical synthesis of graphene/polyaniline composite film and its applications, *Advanced Functional Materials* 21 (2011) 2989–2996.
- [46] X. Zhong, R. Yuan, Y.Q. Chai, In situ spontaneous reduction synthesis of spherical Pd@Cys–C-60 nanoparticles and its application in nonenzymatic glucose biosensors, *Chemical Communications* 48 (2012) 597–599.
- [47] Y. Li, J.J. Zhang, J. Xuan, L.P. Jiang, J.J. Zhu, Fabrication of a novel nonenzymatic hydrogen peroxide sensor based on Se/Pt nanocomposites, *Electrochemistry Communications* 12 (2010) 777–780.
- [48] H. Zhu, M.L. Du, M. Zhang, P. Wang, S.Y. Bao, L.N. Wang, Y.Q. Fu, J.M. Yao, Facile fabrication of AgNPs/(PVA/PEI) nanofibers: high electrochemical efficiency and durability for biosensors, *Biosensors and Bioelectronics* (2013), <http://dx.doi.org/10.1016/j.bios.2013.04.016>.
- [49] S. Myung, A. Solanki, C.J. Kim, J. Park, K.S. Kim, K.B. Lee, Graphene-encapsulated nanoparticle-based biosensor for the selective detection of cancer biomarkers, *Advanced Materials* 23 (2011) 2221–2225.
- [50] I.M. Feigel, H. Vedala, A. Star, Biosensors based on one-dimensional nanostructures, *Journal of Materials Chemistry* 21 (2011) 8940–8954.
- [51] O. Akhavan, E. Ghaderi, Copper oxide nanoflakes as highly sensitive and fast response self-sterilizing biosensors, *Journal of Materials Chemistry* 21 (2011) 12935–12940.
- [52] Y. Ding, Y. Wang, L.C. Zhang, H. Zhang, C.M. Li, Y. Lei, Preparation of TiO₂–Pt hybrid nanofibers and their application for sensitive hydrazine detection, *Nanoscale* 3 (2011) 1149–1157.

Biographies

Han Zhu received his bachelor's degree in 2011 from Nanjing University of Technology. He is a PhD candidate in materials science in Zhejiang Sci-Tech University. His research areas include nanomaterials, electrospinning and biosensors.

MingLiang Du received his PhD in materials science and engineering from South China University of Technology in 2007. He is now an associate professor in faculty of Materials and Textiles in the Zhejiang Sci-Tech University. His research interests are in field of polymer functional materials and nanomaterials.

Ming Zhang obtained her PhD in 2005 from Jilin University, and joined Professor ZhongFan Liu's group as a postdoctoral fellow at Peking University in 2005. She is now worked in faculty of Materials and Textiles in the Zhejiang Sci-Tech University. Her research interests are in field of miniemulsion polymerization.

Pan Wang received her bachelor's degree in 2012 from Zhong Yuan University of Technology. She is a graduate student in materials science in Zhejiang Sci-Tech University. Her research areas include nanomaterials and electrospinning.

Shiyong Bao received his bachelor's degree in 2012 from Zhejiang Sci-Tech University. He is a graduate student in materials science in Zhejiang Sci-Tech University. His research areas include nanomaterials and electrospinning.

Yaqin Fu received her PhD degree from Kyoto institute of technology in 2004. She is now a professor in Faculty of Materials and Textiles in Zhejiang Sci-Tech University. Her research interests are in field of the functional fiber and composite materials.

Ju ming Yao received his PhD degree in 2003 from Tokyo University of Agriculture and Technology. He is now a professor and doctoral supervisor in faculty of Materials and Textiles in Zhejiang Sci-Tech University. His research interests are in field of biopolymer materials.

See discussions, stats, and author profiles for this publication at: <https://www.researchgate.net/publication/258157487>

Organic–inorganic hybrid network constructed in polypropylene matrix and its reinforcing effects on polypropylene composites

Article in *Journal of Reinforced Plastics and Composites* · February 2013

DOI: 10.1177/0731684412467841

CITATION

1

READS

40

5 authors, including:



Han Zhu

Jiangnan University

53 PUBLICATIONS 548 CITATIONS

[SEE PROFILE](#)



Mingliang Du

Zhejiang Sci-Tech University

76 PUBLICATIONS 2,044 CITATIONS

[SEE PROFILE](#)



Xianming Zhang

Zhejiang Sci-Tech University

26 PUBLICATIONS 131 CITATIONS

[SEE PROFILE](#)

Some of the authors of this publication are also working on these related projects:



Designed nanoarchitectures for electrocatalytic water splitting [View project](#)

Organic-inorganic hybrid network constructed in polypropylene matrix and its reinforcing effects on polypropylene composites

Han Zhu¹, MingLiang Du^{1,2}, CongSheng Xu¹,
XianMing Zhang^{1,2} and YaQin Fu^{1,2}

Abstract

A facile approach was proposed to improve the mechanical properties of the polymer composites by organic-inorganic hybrid networks assembled via hydrogen bonding between halloysite nanotubes and organic hydrogen bonding coupler. Organic hydrogen bonding couplers were incorporated to the polypropylene composites and the hybrid networks were *in situ* constructed in the process of the fabricating of the composites. The investigations suggest that the formation of hybrid network can remarkably improve the mechanical properties of the composites, mainly including the tensile strength, flexural properties. In addition, the hydrogen bonds between organic hydrogen bonding coupler and halloysite nanotubes and the constructed organic-inorganic hybrid networks were characterized by Fourier transform infrared spectroscopy and X-ray photoelectron spectroscopy. The results show that the absorption of Si-O of the Fourier transform infrared spectroscopy spectra and the binding energy of the Si and Al atoms of the X-ray photoelectron spectroscopy spectra changed to some extent, indicating the existence of hydrogen bonds between organic hydrogen bonding coupler and halloysite nanotubes. Dynamic mechanical studies suggest the existence of the hybrid networks in the polypropylene matrix.

Keywords

Hydrogen bond, hybrid networks, polypropylene, composites, mechanical properties

Introduction

In recent years, preparing all kinds of excellent performance polymer composites with polymer and fillers (mainly inorganic fillers) has become a very convenient and favored strategy in polymer science for their advantages such as more easily to be processed, higher thermal stability, lower cost and so on.^{1,2} However, the compatibility between polymer and fillers may lead to the unsatisfied performance, which impedes the further application of the polymer/filler composites.^{3,4} As a consequence, how to reinforce the polymer materials is always the emphasis in polymer science.^{5–7}

In the present, many approaches have been taken for the reinforcement of polymer materials, such as fiber-reinforced composites, chemical modifications, reinforcement of composites with whiskers, hydrogen bonding bridged inorganics and so on.^{8–12} Compared

with the conventional method such as utilizing coupling agents to improve the compatibility of the polymer/inorganic filler composites, hydrogen bonding bridged inorganics is a method irrespective of the low compatibility between inorganics and polymer materials.⁸

¹Department of Polymer Materials and Engineering, Zhejiang Sci-Tech University, China

²Key Laboratory of Advanced Textile Materials and Manufacturing Technology, Ministry of Education, China

Corresponding author:

MingLiang Du, Key Laboratory of Advanced Textile Materials and Manufacturing Technology, Ministry of Education, Hangzhou 310018, China.

Email: du@zstu.edu.cn

So far, the formation of filler network in polymer matrix have been reported by numerous researchers.^{13,14} Although the reinforcing effects of inorganics on plastics are widely reported, the reinforcement of polypropylene (PP) via inorganics network has not been fully recognized and the development of the reinforcing strategy irrespective of the polarity discrepancy is highly desirable. Traditionally, the interface and compatibility play a crucial role in improving the mechanical properties of plastics/inorganic filler composites. Recently, another new strategy was proposed irrespective of the low compatibility between inorganics and thermoplastics.^{15–17} Compared with the conventional method to improve the compatibility of the plastics/inorganic filler composites, this method exhibits much effective reinforcing effects and the process is much facile.

In present work, we intend to further verify the effectiveness of the strategy in reinforcing PP through hybrid network assembly of HNTs during the process. Three hydrogen bonding coupler (HBC), tea polyphenols (TP), Zein and polylactic acid (PLA), were incorporated to form hybrid networks with halloysite nanotubes (HNTs) through hydrogen bonds. The effectiveness of this strategy to PP was also examined.

Experimental

Materials

PP granules were purchased from Basel Company. The melt flow index was determined as 2.84 g/10 min (after ISO-1133: 1997(E)). HNTs were collected from Hubei Province, China. The Brunauer-Emmett-Teller (BET) surface area of the HNTs was determined as 50.45 m²/g with a specific surface area and porosity analyzer, ASAP 2020 of Micromeritics. TP, Zein and PLA were employed as HBC for the construction of organic-inorganic hybrid networks. TP was provided by Xuancheng Baicao Plant Industry and Trade Co., Ltd. TP are a group of water-soluble polyphenols richly deposited in plants, belonging to the flavonoid family, and mainly consist of epicatechin, epicatechin gallate, epigallocatechin and epigallocatechin gallate, in which the epigallocatechin gallate makes up about 45% of the total TP. Zein (F4000), with a molecular weight of 35 kDa, was purchased from Shanghai Jinhui Biotechnology Co., Ltd. PLA was a commercial product (Zhejiang Haisheng biological materials Co., Ltd., China) with high optical purity with about 98% L-lactide content, density 1.24 g/cm³, weight-average molecular weight (M_w) 250 kDa, polydispersity 1.70 and the glass transition temperature and melting point of 60.48 and 166.40°C, respectively. In the

manuscript, TP, Zein and PLA all consist of multiple hydroxyl groups and the hydroxyl groups can form hydrogen bonds with the surface hydroxyl groups of HNTs to construct hybrid networks.

Preparation of the PP/HNTs composites

In the present investigation, all raw materials were mixed with a twin-screw extruder. The screw diameter of the twin-screw-extruder is 35 mm and the screw speed was 100 r/min. The temperatures profile from the barrel to the die were 175/185/195/200/200/200/200/200/200/230°C, respectively, which are shown in Table 1.

The pelletized granules were dried in vacuum oven under 80°C for 6 h. Then the granules were injection molded to the specimens for characterizations at 200°C. The composition of the PP/HNTs/HBC composites is shown in Table 2.

Characterizations

Transmission electron microscopy. The HNTs were dissolved in diluted water solution and respectively dropped on the ultra-thin carbon-coated copper grid and dried under an infrared lamp for 5 min. The images were acquired using a JSM-2100 transmission electron microscopy (TEM, JEOL, Japan) at an accelerating voltage of 200 kV.

Scanning electron microscopy. The HNTs powders were spread on the conducting adhesive and the images were acquired using a LEO 1530 VP scanning electron microscopy (SEM) machine.

Mechanical properties determinations. Instron 3367 universal testing machine was used to perform the tensile, flexural and impact testing of PP/HNTs composites according to the standards of ISO 527-93, ISO 178-93 and ISO 180-93, respectively.

Dynamic mechanical measurements. Dynamic mechanical behavior measurements of all the PP, PP/HNTs and PP/HNTs/TP composites were performed on a DMA 242 dynamic analyser provided by Netzsch Company. The PP/HNTs composites were heated from –60 to 100°C at a ramping rate of 5°C/min in stretching mode.

Attenuated total refraction-Fourier transform infrared spectroscopy. HNTs powder, the organic HBC and the model mixtures of HNTs and the organic HBC were sheet-molded to small discs (about 2 mm thick and diameter about 10 mm). Then the little discs were analyzed by a Bruker Vector 33 spectrometer with the spectra changing from 4000 to 400 cm^{–1} wave numbers.

Table 1. The temperatures profile from the barrel to the die

Heating position	I	II	III	IV	V	VI	VII	VIII	IX	X	die
Set temperature, °C	175	185	195	200	200	200	200	200	200	200	230
Actual temperature, °C	175 ± 3	185 ± 3	195 ± 3	200 ± 3	200 ± 3	200 ± 3	200 ± 3	200 ± 3	200 ± 3	200 ± 3	230 ± 3

HBC: hydrogen bonding coupler; HNTs: halloysite nanotubes; PP: polypropylene.

Table 2. The composition of the PP/HNTs/HBC composites. (HBC is TP, Zein and PLA, respectively)

Sample	PP content (phr)	HNTs content (phr)	HBC content (phr)
Pure PP	100	0	0
PP/HNTs	100	30	0
PP/HNTs/HBC	100	30	1
PP/HNTs/HBC	100	30	2.5
PP/HNTs/HBC	100	30	5
PP/HNTs/HBC	100	30	7.5
PP/HNTs/HBC	100	30	10

HBC: hydrogen bonding coupler; HNTs: halloysite nanotubes; PP: polypropylene; TP: tea polyphenols; PLA: polylactic acid.

X-ray photoelectron spectroscopy. X-ray photoelectron spectroscopy (XPS) spectra of HNTs, organic HBC and PP/HNTs/organic HBC composites were recorded by using an X-ray photoelectron spectrometer (Kratos Axis Ultra DLD) with an Aluminum (mono) Ka source (1486.6 eV). The Aluminum Ka source was operated at 15 kV and 10 mA. The vacuum degree was 10^{-8} to 10^{-7} , and the analysis area was about 0.7×0.3 mm. For all the samples, a low-resolution survey run (0–1100 eV, pass energy = 160 eV) was performed. In order to obtain more information about the formation of hydrogen bonding, a high-resolution survey (pass energy = 48 eV) was performed at spectral regions relating to Si and Al.

Results and discussion

The reinforcing effects of HNTs hybrid network assembly on polypropylene composites

Figure 1(a) displays the TEM image of naturally occurring HNTs with abounded hydroxyls and the predominant form is a hollow tubular structure in the submicrometer range. The size of the inner and outer diameter of the halloysite tubules are approximately 15–20 and 40–50 nm, respectively, depending on the deposit condition.^{10,12–14} As shown in Figure 1(b), the lumen length of the natural HNTs range from 500 to 2000 nm, and the high aspect ratio could afford more opportunities for the formation of hybrid networks. As reported previously, the typical crystal structure of HNTs consists of two types of hydroxyl groups with aluminol (Al-OH) groups in the internal surface and

Si-OH groups on the external surface.^{10,14,18} Due to their outstanding properties, such as good dispersion in polymer matrix, larger ratio length, high strength, high modulus etc, HNTs have been disclosed as a new kind of ideal inorganic modifier to improve the mechanical and thermal properties of polymers.^{18,19}

Figure 2 shows the different contents of HBC constructed hybrid networks with HNTs and the effect of various PP/HNTs/HBC ratios on mechanical properties of the PP/HNTs composites. It can be seen from Figure 2(a)–(e) that the flexural modulus, flexural strength and young's modulus of PP/HNTs composite both significantly increase to the maximum value and then decrease slowly with the increase of HBC contents. Compared with neat PP, the increment of the flexural modulus of PP/HNTs composites with 7.5 phr TP, Zeins and PLA adopted are 83%, 80% and 123%, respectively. Meanwhile, the increment of the flexural strength of PP/HNTs composite are 32%, 26% and 47%, respectively, with the content of TP, Zeins and PLA increasing to 5 phr. The increment of the young's modulus of PP/HNTs composite are 43%, 41% and 49%, respectively, with the content of TP, Zeins and PLA increasing to 7.5 phr. It is clear that PLA has a remarkable influence on the flexural modulus, young's modulus and flexural strength of PP/HNTs composite. Compared with TP and Zein, PLA possess longer molecular chains and more amounts of hydroxyls, which can offer more opportunity for the construction of hybrid networks via hydrogen bondings and the entanglement between HNTs and PP segments.^{20–22} As previously reported, HBC possess multiple hydroxyls and the hydroxyls can be incorporated with HNTs

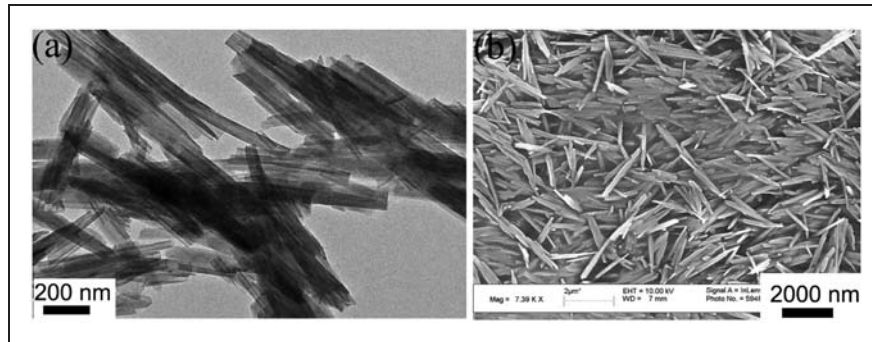


Figure 1. TEM and SEM images of the HNTs. TEM: Transmission electron microscopy; SEM: scanning electron microscopy; HNTs: halloysite nanotubes.

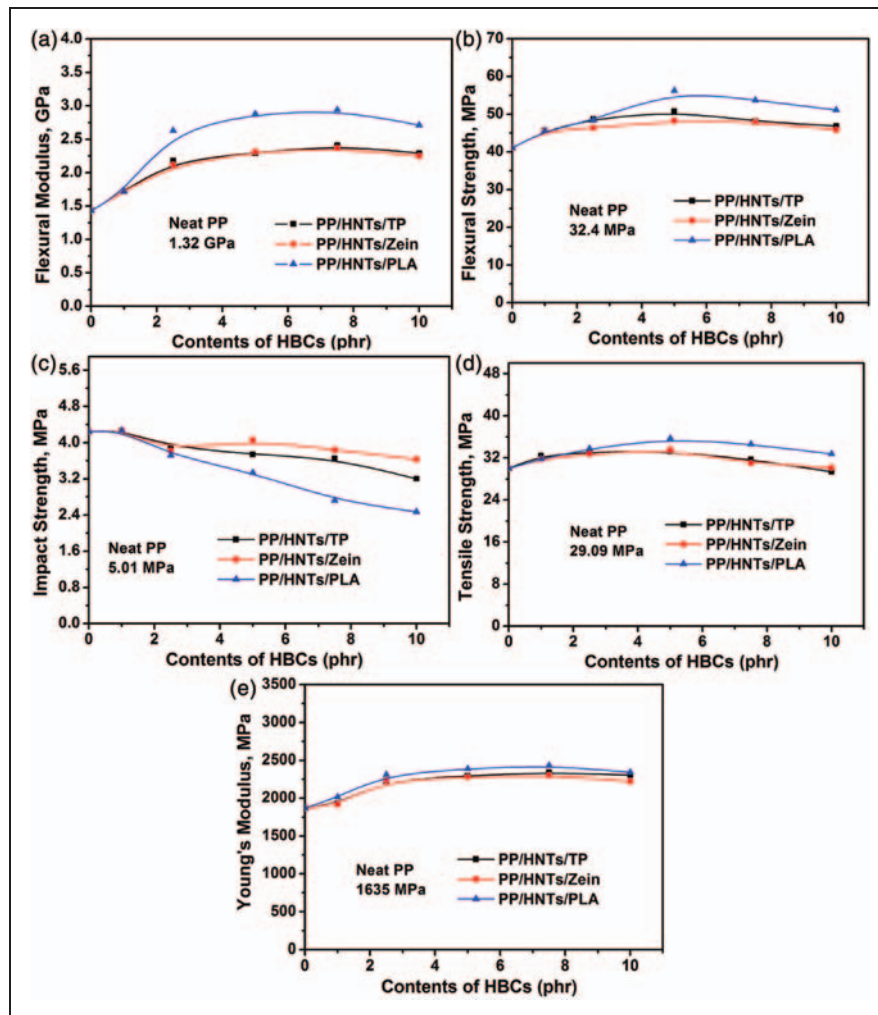


Figure 2. (a)–(e) Effects of the HBCs on mechanical properties of PP/HNTs (100/30) composite. HBC: hydrogen bonding coupler; PP: polypropylene; HNTs: halloysite nanotubes.

to form organic-inorganic hybrid networks through hydrogen bonds, which restricts the movement of HNTs and PP chains and then effectively increases the stiffness of PP/HNTs composite.¹⁹ With the

incorporation of the HBC, the HNTs could be bridged via the hydrogen bonding between the hydroxyl groups on the surfaces of HNTs and functionalities of the organics. Once the organic-inorganic hybrid network

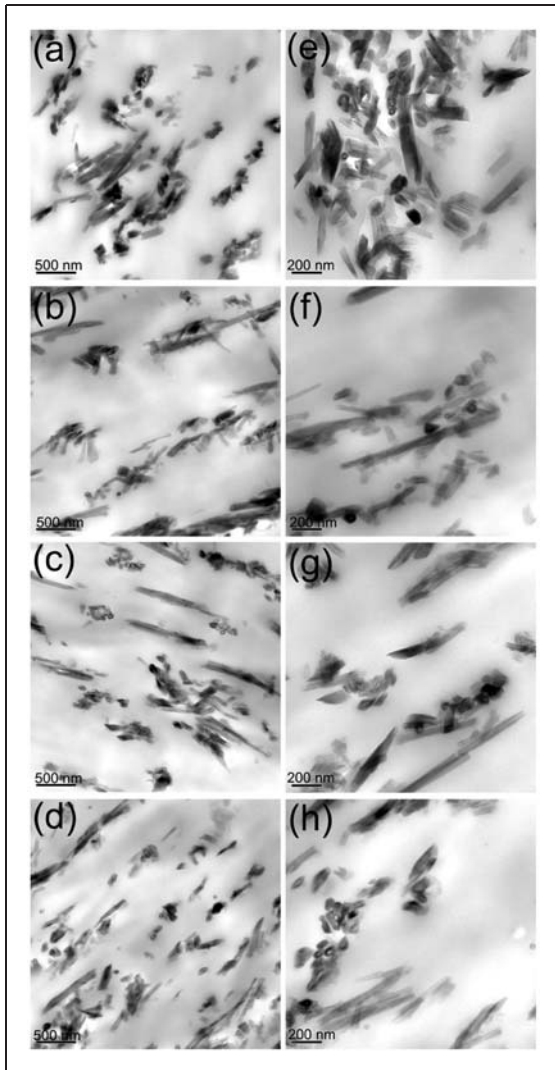


Figure 3. Morphology of ((a) and (e)) PP/HNTs (100/30) composites, ((b) and (f)) PP/HNTs/TP (100/30/5), ((c) and (g)) PP/HNTs/Zein (100/30/5) and ((d) and (h)) PP/HNTs/PLA (100/30/5). HBC: hydrogen bonding coupler; PP: polypropylene; HNTs: halloysite nanotubes; TP: tea polyphenols; PLA: polylactic acid.

constructed, the mobility of the PP chains at the interface will be therefore substantially restricted and consequently the composites show much higher rigidity. In addition, the hybrid network structure would be beneficial to the transfer of the loaded stress, which also should be responsible for the improved flexural properties and tensile strength. Figure 2(c) shows the effects of HBC on tensile strength of PP/HNTs composite. It is clear that the tensile strength also increases to the maximum value and then decreases slowly with the increase of HBC contents. It may due to the well dispersion of HNTs, the nano effect and the organic-inorganic hybrid networks formed by hydrogen bond between the HBC and HNTs. Figure 2(d) shows the effects of HBC on the impact strength of the PP/HNTs

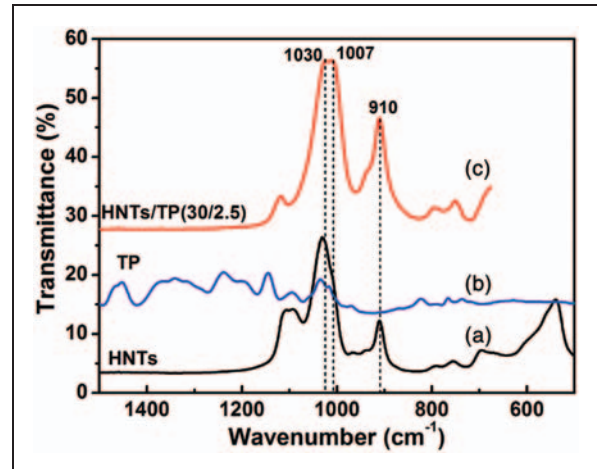


Figure 4. ATR-FTIR spectra of (a) HNTs, (b) TP and (c) HNTs/TP (HNTs:TP = 30/2.5). ATR-FTIR: attenuated total reflection-Fourier transform infrared spectroscopy; HNTs: halloysite nanotubes; TP: tea polyphenols.

composite. When 30 phr HNTs is incorporated, small decrease on the impact strength of the composite was obtained and with the inclusion of the increased amount of HBC, the impact strength decreased significantly. It may due to the formation of organic-inorganic hybrid networks and the hybrid networks can limit the free movement of PP chain, resulting in the reducing of the free volume of the PP chain segment. As discussed above, once the organic-inorganic hybrid networks constructed through hydrogen bonds, the movement of HNTs and PP chains were confined. When the composites are impacted, the dissipation of impact energy is less effective, leading to the deteriorated impact properties for all the composites. As a consequence, all the composites with the formation of hybrid networks show lower toughness.

The morphologies of the PP/HNTs composites and PP/HNTs/HBC composites are shown in Figure 3. Figure 3(a) and (e) show that the HNTs are dispersed disorderly in the PP matrix. The rings in the photos are the cross-sections of the tubes which are perpendicular to the observation direction. After the incorporation of TP, Zein and PLA, as indicated from Figure 3(b) to (h), the dispersion of HNTs in the composite is more uniform than the one without HBC. Compared with Figure 3(e)–(f), a close examination shows that for the PP/HNTs composites, the HNTs tend to self-aggregate via hydrogen bonding in the PP matrix because of the presence of surface hydroxyl groups of HNTs. Once the organics HBC containing hydrogen bonding functionalities are added, the hydroxyl groups on the surface of HNTs would combine with the HBC via hydrogen bonding, avoiding the self-aggregation of HNTs and consequently improving the dispersion of HNTs in PP matrix.

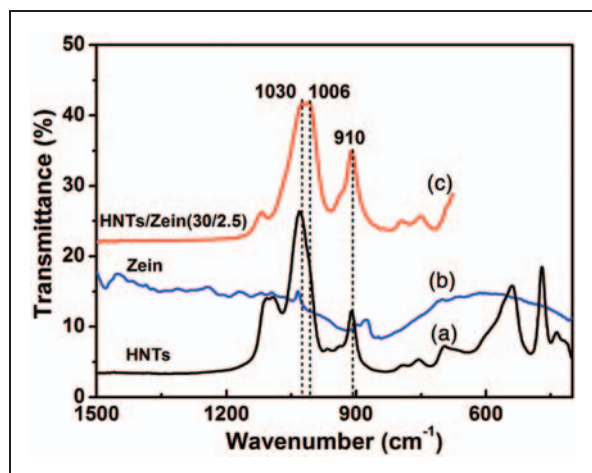


Figure 5. ATR-FTIR spectra of (a) HNTs, (b) Zein and (c) HNTs/Zein (HNTs/Zein = 30/2.5). ATR-FTIR: attenuated total reflection-Fourier transform infrared spectroscopy; HNTs: halloysite nanotubes.

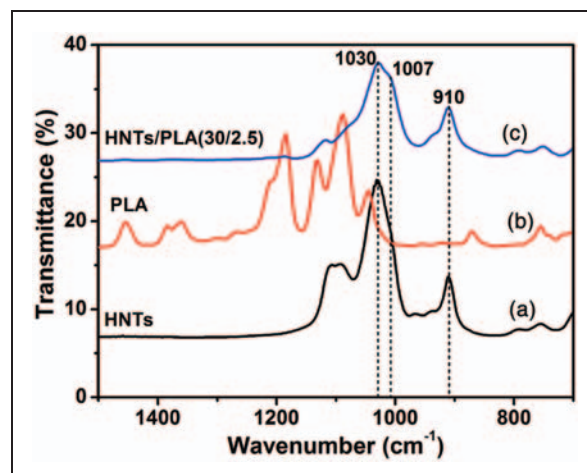


Figure 6. ATR-FTIR spectra of (a) HNTs, (b) PLA and (c) HNTs/PLA (HNTs/PLA = 30/2.5). ATR-FTIR: attenuated total reflection-Fourier transform infrared spectroscopy; HNTs: halloysite nanotubes; PLA: polylactic acid.

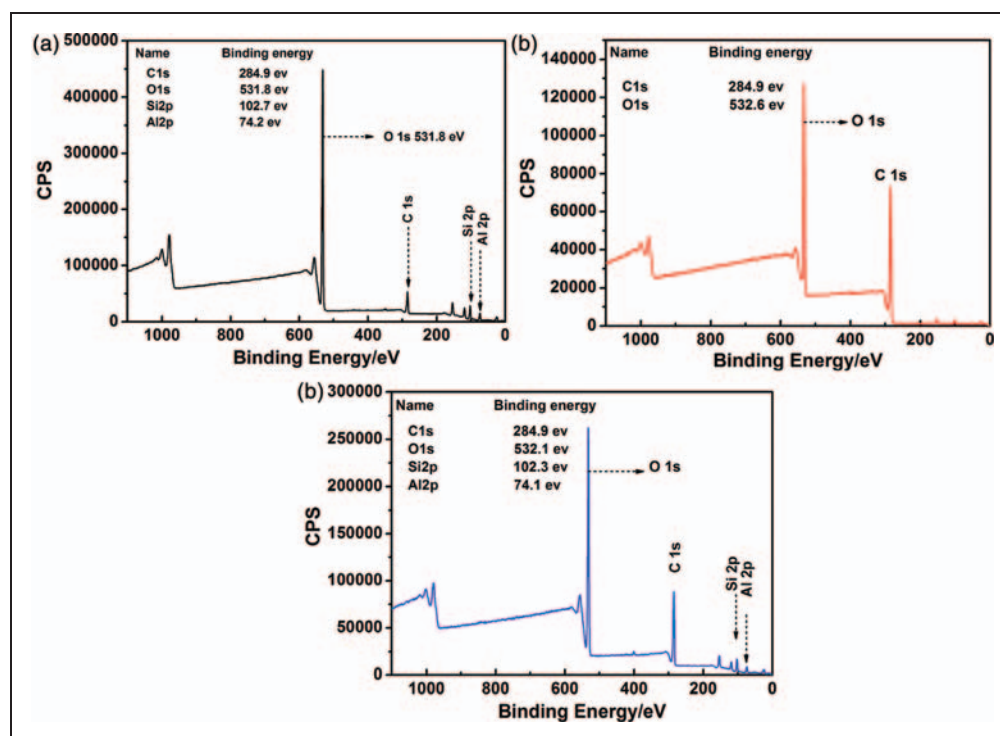


Figure 7. Low-resolution XPS spectra of (a) HNTs, (b) TP and (c) HNTs/TP. XPS: X-ray photoelectron spectroscopy; HNTs: halloysite nanotubes; TP: tea polyphenols.

Characterizations of the formation of hybrid network between HNTs and TP

In the present work, we attempted to form organic-inorganic hybrid network constructed by hydrogen bonding interaction between HNTs and organic HBC. For this reason, all organic HBC used to form the hybrid network is required to contain hydrogen

bonding functionalities. In the present study, TP, Zein and PLA possessing large amount of hydroxyls (hydrogen bonding functionalities) were chosen to serve as organic HBC.

Figure 4–6 reveal the infrared spectra of several organic hydrogen ligands, HNTs and model compounds, respectively. Figure 4 shows the attenuated total reflection-Fourier transform infrared

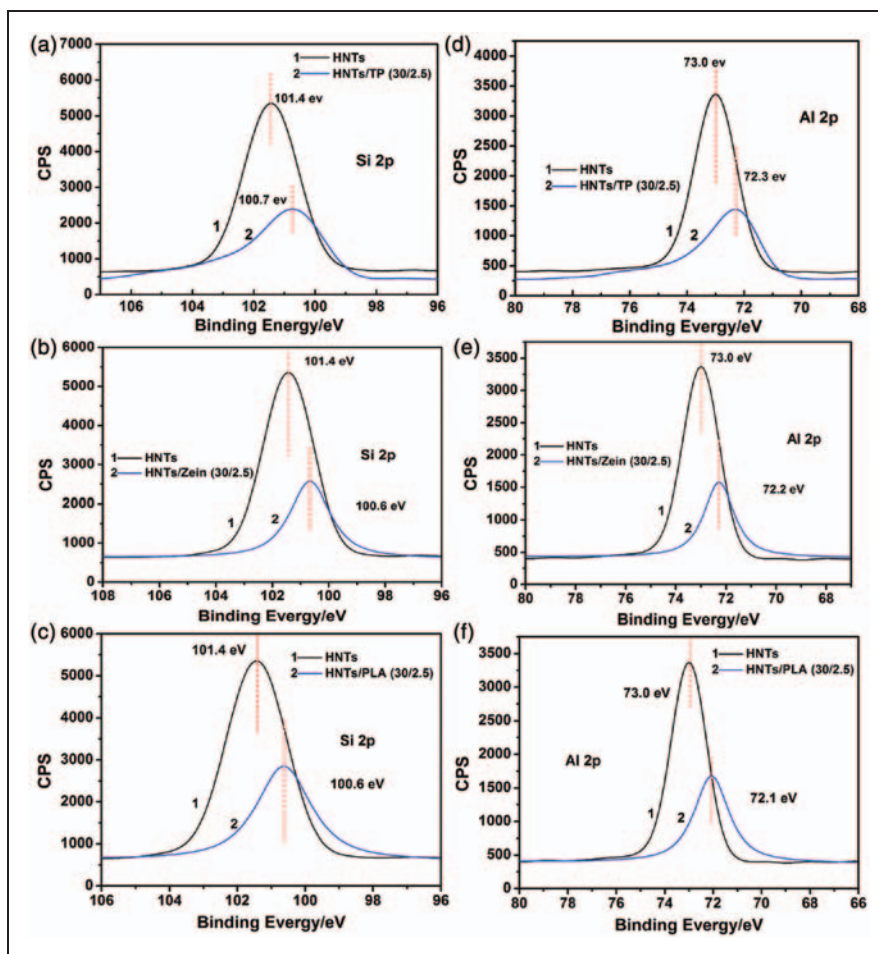


Figure 8. High-resolution Si 2p XPS spectra of (a) HNTs/TP, (b) HNTs/Zein and (c) HNTs/PLA. High-resolution Al 2p XPS spectra of (a) HNTs/TP, (b) HNTs/Zein and (c) HNTs/PLA. XPS: X-ray photoelectron spectroscopy; HNTs: halloysite nanotubes; TP: tea polyphenols; PLA: polylactic acid.

spectroscopy (ATR-FTIR) spectra of pure HNTs powders (curve a), TP powder (curve b) and the HNTs/TP composites (curve c). The characteristic peaks of HNTs that occurred at 1030 cm^{-1} and 910 cm^{-1} are ascribed to in-plane stretching of Si-O and the internal and external hydroxyls on the layered structure, which is caused by silicate and aluminum oxide octahedral. After the addition of TP, a new peak emerged at 1007 cm^{-1} , which is attributed to the formation of hybrid networks through hydrogen bondings between HNTs and TP.

The similar results can also be obtained from the ATR-FTIR spectra of HNTs/Zein composites. From Figure 5, the Si-O and internal and external hydroxyls absorption peaks of HNTs are located at 1030 cm^{-1} and 910 cm^{-1} , respectively. Meanwhile, a new absorption peak located at 1006 cm^{-1} in the HNTs/Zein composites indicates that the hydrogen bonding is presented in the HNTs/Zein compounds.

As shown in Figure 6, similarly, in the ATR-FTIR spectra of HNTs/PLA, a new peak emerged at 1007 cm^{-1} is attributed to the formation of hybrid networks through hydrogen bondings between HNTs and PLA. In addition, the Si-O and internal and external hydroxyls absorption peaks of HNTs are located at 1030 cm^{-1} and 910 cm^{-1} , respectively. In conclusion, the FTIR characterizations confirm the formation of hybrid networks through hydrogen bonding between HNTs and HBCs.

XPS was further used to probe the surface chemical compositions and chemical state of the HNTs, TP and HNTs/HBC composites to confirm the formation of hydrogen bonding between HNTs and TP. As shown in Figure 7(a) and (b), the bonding energy of O 1s of the HNTs and TP are 531.8 eV and 532.6 eV, respectively. However, the O 1s spectra of HNTs/TP shown in Figure 7(c) indicates that the binding energy of O 1s have moved to 532.1 eV.

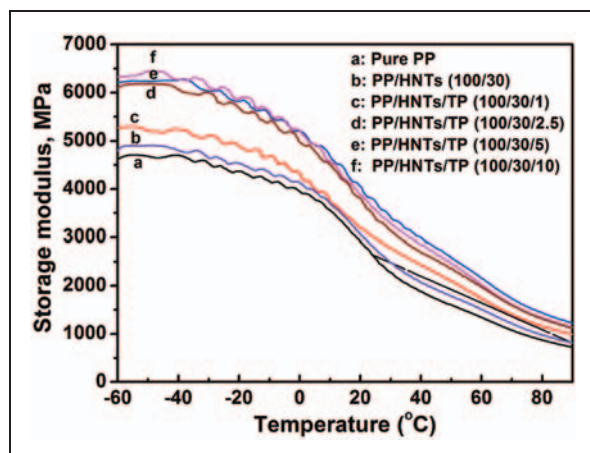


Figure 9. Effects of TP on storage modulus of PP/HNTs composites.

In order to further study the hydrogen bonding interaction between HNTs and HBC, high-resolution XPS spectra of Si and Al are obtained. As shown in Figure 8(a) and (d), compared with the binding energy of Si 2p and Al 2p in HNTs, respectively, there is a significant shift of 0.3 eV and 0.7 eV in HNTs/TP compounds, respectively, indicating that both Si and Al atoms are involved in the hydrogen bonding interaction between TP and HNTs.²³ Meanwhile, as shown in Figure 8, the bonding energy of Si 2p are 100.6 and 100.6 eV in HNTs/Zein and HNTs/PLA composites, respectively, while 101.4 eV in HNTs. In addition, the Al 2p spectra of HNTs/Zein and HNTs/PLA composites are 72.2 and 72.3 eV, respectively, while the Al 2p spectrum are 73.0 eV in HNTs. Both of the results reveal obvious shifts, indicating that the atom chemical environments of O and Si have obvious changes, indicating the formation of hydrogen bonds.^{24,25}

It has been extensively investigated by many researchers that the formation of network structure in polymer matrix would lead to the variation of moduli.^{26–28} Therefore, to further testify the existence of hydrogen bonding in the PP/HNTs matrix, the dynamic mechanical measurements of the composites were performed. In the present manuscript, TP is a kind of typical HBC, which possess many phenolic hydroxyl groups and offer much more opportunities for the construction of hybrid networks. In addition, the formation mechanism of hybrid networks among TP, Zein, PLA and HNTs is similar. Therefore, the PP/HNTs/TP composites were used to characterize the formation of the hybrid networks. Figure 9 shows the effects of TP on the storage modulus of PP/HNTs composite. Figure 9 reveals that the storage modulus increases to a certain extent when 1 phr, 2.5 phr and 5 phr TP are added to the PP/HNTs composite,

respectively. Furthermore, it can be seen that with the increase of the TP content from 1 phr to 2.5 phr, a sharp increase in the storage modulus of the composites is obtained. With the increasing of TP contents to 10 phr, a smaller improvement of the storage modulus of the composite is obtained. PP/HNTs composites with a series content of the TP show much higher storage modulus compared with neat PP/HNTs, which ascribe this phenomenon to the hydrogen bonding interaction between TP and HNTs in the PP matrix. Once the organic-inorganic hybrid network constructed via hydrogen bonding, the constitutive mobility of PP segments would significantly be restricted due to the entanglement between HNTs and PP segments. As a consequence, the storage modulus of PP/HNTs/TP composites is considerably increased. It is speculated that the formation of hybrid networks will effectively limit the free movement of PP chain, resulting in the increasing of the stiffness of the composite and storage modulus.

Conclusions

Through the incorporation of certain organic HBC, PP/HNTs/HBC composites were prepared. In the composites, organic-inorganic hybrid networks were constructed by hydrogen bonding between HBC and HNTs, resulting in the significant increasing of the mechanical properties, such as flexural modulus, flexural strength and tensile strength. However, the impact strength gradually reduces with the inclusion of the increasing amounts of organic HBC, which is due to the formation of organic-inorganic hybrid networks. The formation of the organic-inorganic hybrid networks limits the free movement of PP chain, making the reducing free volume of the PP chain segment. The results of ATR-FTIR and XPS results demonstrate the strong hydrogen bonding interactions between HNTs and HBC. The dynamic mechanical behavior of composite materials indicates the formation of hybrid networks between HBC and HNTs with the incorporation of HBC.

Funding

This research is funded by the National Natural Science Foundation of China (NSFC) (grant no. 50903072, 51243001) and Zhejiang Province Natural Science Foundation (grant no. Y4100197, Y4100534).

References

- Porter D, Metcalfe E and Thomas MJK. Nanocomposite fire retardants-A review. *Fire Mater* 2000; 24: 45–52.
- Utracki LA and Kamal MR. Clay-containing polymeric nanocomposites. *Arab J Sci Eng* 2002; 27: 43–67.

3. Kim DH, Fasulo PD, Rodgers WR, et al. Structure and properties of polypropylene-based nanocomposites: Effect of PP-g-MA to organoclay ratio. *Polymer* 2007; 48: 5308–5323.
4. Molnara S, Pukanszky B, Hammer CO, et al. Impact fracture study of multicomponent polypropylene composites. *Polymer* 2000; 41: 1529–1539.
5. Costache MC, Wang DY, Heidecker MJ, et al. The thermal degradation of poly(methyl methacrylate) nanocomposites with montmorillonite, layered double hydroxides and carbon nanotubes. *Polym Advan Technol* 2006; 17: 272–280.
6. Miyagawa H, Misra M and Mohanty AK. Mechanical properties of carbon nanotubes and their polymer nanocomposites. *J Nanosci Nanotechnol* 2005; 5: 1593–1615.
7. Xia ZP, Yu JY, Cheng LD, et al. Scale effect on jute/cotton fibres and their blended yarns. *Fibers Text East Eur* 2009; 17: 43–45.
8. Du ML, Guo BC, Liu MX, et al. Reinforcing thermoplastics with hydrogen bonding bridged inorganics. *Physica B* 2010; 405: 655–662.
9. Jacob S, Suma KK, Mendez JM, et al. Reinforcing effect of nanosilica on polypropylene-nylon fibre composite. *Mat Sci Eng B* 2010; 168: 245–249.
10. Zhu H, Du ML, Zou ML, et al. Green synthesis of Au nanoparticles immobilized on halloysite nanotubes for surface-enhanced Raman scattering substrates. *Dalton Trans* 2012; 41: 10465–10471.
11. Xing DM, He GH, Hou ZJ, et al. Preparation and characterization of a modified montmorillonite/sulfonated polyphenylether sulfone/PTFE composite membrane. *Int J Hydrogen Energ* 2011; 36: 2177–2183.
12. Xu HHK, Quinn JB, Smith DT, et al. Effects of different whiskers on the reinforcement of dental resin composites. *Dent Mater* 2003; 19: 359–367.
13. Kashiwagi T, Du FM, Douglas JF, et al. Nanoparticle network reduced the flammability of polymer nanocomposites. *Nat Mater* 2005; 4: 928–933.
14. Dalmas F, Chazeau L, Gauthier C, et al. Large deformation mechanical behavior of flexible nanofiber filled polymer nanocomposites. *Polymer* 2006; 47: 2802–2812.
15. Du ML, Guo BC, Liu MX, et al. Formation of reinforcing inorganic network in polymer via hydrogen bonding self-assembly process. *Polym J* 2007; 39: 208–212.
16. Khalili SMR, Eslami Farsani R and Rafiezadeh S. An experimental study on the behavior of PP/EPDM/JUTE composites in impact, tensile and bending loadings. *J Reinf Plast Comp* 2011; 30: 1341–1347.
17. Bera M, Alagirusamy R and Das A. A study on interfacial properties of jute-PP composites. *J Reinf Plast Comp* 2010; 29: 3155–3161.
18. Liu MX, Guo BC, Zou QL, et al. Interactions between halloysite nanotubes and 2,5-bis(2-benzoxazolyl) thiophene and their effects on reinforcement of polypropylene/halloysite nanocomposites. 2008; 19: 205709–205718.
19. Du ML, Guo BC, Liu MX, et al. Preparation and Characterization of polypropylene grafted halloysite and their compatibility effect to polypropylene/halloysite composite. *Polym J* 2006; 38: 1198–1204.
20. Baltazar-y-Jimenez A, Seviaryna I, Sain M, et al. Acoustic, tomographic, and morphological properties of bismaleimide-modified PLA green composites. *J Reinf Plast Comp* 2011; 30: 1329–1340.
21. Kucharczyk P, Sedlarik V, Miskolczi N, et al. Properties enhancement of partially biodegradable polyamide/poly-lactide blends through compatibilization with novel poly-alkenyl-poly-maleic-anhydride-amide/imide-based additives. *J Reinf Plast Comp* 2012; 31: 189–202.
22. Jiang AJ, Xi JL and Wu HW. Effect of surface treatment on the morphology of sisal fibers in sisal/poly(lactic acid) composites. *J Reinf Plast Comp* 2012; 31: 621–630.
23. Li L, Chan CM and Weng LT. The effects of specific interactions on the surface structure and composition of miscible blends of poly(vinyl alcohol) and poly(N-vinyl-2-pyrrolidone). *Polymer* 1998; 39: 2355–2360.
24. Zhu H, Du ML, Zou ML, et al. Facile and green synthesis of well-dispersed Au nanoparticles in PAN nanofibers by tea polyphenols. *J Mater Chem* 2012; 22: 9301–9307.
25. Liu SY, Chan CM, Weng LT, et al. Surface segregation in polymer blends and interpolymer complexes with increasing hydrogen bonding interactions. *Polym Sci B* 2005; 43: 1924–1930.
26. Kharchenko SB, Douglas JF, Obrzut J, et al. Flow-induced properties of nanotube-filled polymer materials. *Nat Mater* 2004; 3: 564–568.
27. Kashiwagi T, Du FM, Douglas JF, et al. Nanoparticle networks reduce the flammability of polymer nanocomposites. *Nat Mater* 2005; 4: 928–933.
28. Payne AR and Whittaker RE. Low strain dynamic properties of filled rubbers. *Rubber Chem Technol* 1971; 44: 440–478.

Facile and green synthesis of well-dispersed Au nanoparticles in PAN nanofibers by tea polyphenols†

Han Zhu,^b MingLiang Du,^{*ab} MeiLing Zou,^b CongSheng Xu,^b Ni Li^{ab} and YaQin Fu^{ab}

Received 13th December 2011, Accepted 7th March 2012

DOI: 10.1039/c2jm16569d

The green natural compounds, tea polyphenols (TP), were introduced to synthesize well-dispersed Au nanoparticles (AuNPs) in polyacrylonitrile (PAN) nanofibers by combining an *in situ* reduction approach and electrospinning technique. The AuNPs were firstly synthesized in aqueous solution to test the reducibility of the TP. Then, the well-dispersed AuNPs in PAN nanofibers were obtained by an *in situ* reduction approach and electrospinning technique. Fourier transform infrared spectroscopy (FTIR) was utilized to confirm the reducibility of TP. The transmission electron microscopy (TEM) and the ultraviolet-visible spectroscopy (UV-Vis) demonstrated the formation of AuNPs and their morphology. Surprisingly, compared with the AuNPs in aqueous solution, the AuNPs in PAN nanofibers *via* electrospinning were much smaller and well-dispersed and it was attributed to the stabilization effect of PAN through the chelating effect between gold and cyano groups. Apart from the reducibility effect, TP also served as a stabilizer together with PAN to prevent the aggregation of AuNPs effectively, which were testified by X-ray photoelectron spectroscopy (XPS) results.

Introduction

Nanostructured noble metals are widely used in various technological applications due to their unique optical, electronic, imaging, magnetic and catalytic properties.^{1–5} Haruta *et al.* have found that the Au nanoparticles as small as 2 nm showed an excellent catalytic property for total oxidation of CO.⁶ Meanwhile, gold-based nanotechnology is becoming more and more significant in modern science and various kinds of applications of Au nanoparticles (AuNPs) have been explored both in chemical and biological research.^{7,8} Highly dispersed AuNPs have been discovered to be exceptionally active for a number of chemical reactions, such as oxidation and reduction.⁹ A particular attraction is the use of functional AuNPs in pharmaceutical and biological fields, such as drug delivery, photothermal ablation therapy and molecular diagnostics, because AuNPs have excellent biological biocompatibility and low toxicity.^{10–15}

There are already many methods for the synthesis of AuNPs, however, most are either complex, time-consuming, or require strict synthetic conditions.^{12–20} From the viewpoint of practical applications, it would be of great value to explore a facile approach for the synthesis of uniform AuNPs with small particle

sizes. The previous widely adopted methods of synthesizing AuNPs often involve a chemical reductant, such as sodium borohydride and hydrazine, *etc.* These reducing agents are highly active and have potential environmental risks, which might be an issue for wide application. In the present investigation, we proposed a facile and environmental friendly approach to synthesize AuNPs with a small size and narrow distribution using tea polyphenols (TP) as the reductant.¹⁵ TP compounds, which are a group of water-soluble polyphenols richly deposited in plants, belonging to the flavonoid family, mainly consist of epicatechin (EC), epicatechin gallate (ECG), epigallocatechin (EGC) and epigallocatechin gallate (EGCG), in which the EGCG makes up about 45% of the total TP.^{21–23} Studies have shown that such compounds possess many properties, such as reducibility, chelating with metal ions, antibacterial activity, *etc.*^{24–27} However, until now, no reports are found on the synthesis of gold nanoparticles using TP.

Electrospinning technique is an effective method to obtain fibers with nanoscale diameter and nanofibers that are prepared in the form of a non-woven mat possess high specific surface area and high porosity and, subsequently, are ideal substances for tissue engineering scaffolds, catalytic carriers and filter materials.^{28–31,34} Xia *et al.* have studied electrospun TiO₂ nanofibers with Pt nanoparticles and nanowires for catalytic applications, showing us a great prospect for catalysis.³² It is well-recognized that AuNPs exhibit high catalytic activities for certain chemical reactions, moreover, the particle size of AuNPs is often essential to the catalytic activities. Shao's group showed that AuNPs of 3–5 nm in silica nanotubes exhibited a good catalytic activity for reducing 4-nitrophenol.³⁴ Shi's group synthesized collagen

^aKey Laboratory of Advanced Textile Materials and Manufacturing Technology, Zhejiang Sci-Tech University, Ministry of Education, Hangzhou 310018, P. R. China. E-mail: du@zstu.edu.cn; Tel: +86-571-86843255

^bDepartment of Materials Engineering, College of Materials and Textile, Zhejiang Sci-Tech University, Hangzhou 310018, P. R. China

† Electronic supplementary information (ESI) available. See DOI: 10.1039/c2jm16569d

fiber-supported AuNPs with an effective size control in the range 5–18 nm and found that the catalytic behaviors depended on the nanoparticle size and the AuNPs of 5.2 ± 1.6 nm showed the best activity for the reduction of 4-nitrophenol.⁹

In this paper, we reported a facile and green route to synthesize AuNPs/PAN nanofibers *via* an *in situ* reduction approach by TP and electrospinning technique. At first, we confirmed the availability of synthesizing AuNPs using TP as the reductant in aqueous solution. Then, we combined the electrospinning method and the green reducibility of the TP to fabricate AuNPs/PAN nanofibers containing well-dispersed AuNPs. The availability of the reducing method and the fabrication approach were tested, meanwhile, the morphology and structure of the synthesized AuNPs were characterized and discussed.

Experimental

Materials

Chloroauric acid ($\text{HAuCl}_4 \cdot 4\text{H}_2\text{O}$, 99.9%) was acquired from Shanghai Civi Chemical Technology Co., Ltd. Polyacrylonitrile (PAN, $M_w \approx 1.4 \times 10^5$, copolymerized with 10 wt% methyl acrylate) was manufactured by Sinopec Shanghai Petrochemical Co., Ltd. Tea polyphenols (TP) were purchased from Xuancheng BaiCao Plant Industry and Trade Co., Ltd. and the main ingredients are tabulated in Table 1. Dimethyl formamide (DMF, 99.5%) was obtained from Hangzhou Gaojing Fine Chemical Co., Ltd.

Synthesis of AuNPs in aqueous solution using TP as reductant

The AuNPs were synthesized using TP as the reducing agent. 1 mmol $\text{HAuCl}_4 \cdot 4\text{H}_2\text{O}$ was dissolved in 100 mL deionized water to get a 10.0 mmol L^{-1} Au(III) solution. Then, 3 mL Au(III) solution (0.03 mmol Au(III)) was added to 40 mL deionized water. The mixture was heated to 65°C and vigorously stirred by magnetic force and then 0.012 g TP dissolved in 7 mL deionized water was added to the mixture. Samples were taken at different reaction times and then refrigerated at 4°C . The reaction times of each sample were 1 min, 15 min, 30 min, 60 min and 120 min.

Synthesis of AuNPs in PAN/DMF solution with TP

0.067 mmol PAN powder was dissolved in 60 mL DMF under magnetic stirring at 65°C and 0.6 mmol $\text{HAuCl}_4 \cdot 4\text{H}_2\text{O}$ dissolved in 30 mL DMF were dropped into the PAN/DMF

solution. 0.025 g TP were dissolved in 10 mL DMF at room temperature and then immediately added drop-wise to the above PAN/DMF solution. Therefore, the mass fraction of PAN in the DMF solution was 10 wt% and the mass ratio of $\text{HAuCl}_4 \cdot 4\text{H}_2\text{O}$ and the PAN powder was 2.5 wt%. The mixture was stirred by magnetic agitator for 300 min. Samples were taken at different reaction times and the samples were refrigerated at 4°C . The reaction times of each sample were 30 min, 60 min, 120 min, 200 min, 300 min and 400 min.

Electrospinning of AuNPs/PAN nanofibers

The above mixture solution with a reaction time of 60 min and mass ratio of 2.5 wt% ($\text{HAuCl}_4 \cdot 4\text{H}_2\text{O}$ to PAN) was used to prepare a non-woven mat *via* electrospinning technique. The solution was transferred into a syringe with a stainless copper needle at the tip. The needle was connected to a high voltage power supply. The applied voltage was 12 kV, the needle to collector distance was 12 cm and the flow rate of the solution was 0.01 mL min^{-1} . All experiments were performed at room temperature. The electrospun nanofibers were collected onto a piece of aluminum foil. Finally, the nanofiber mats were peeled off from the aluminum foil and kept in polyethylene sealing bags.

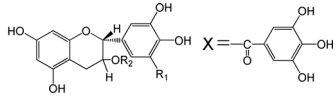
Characterization

Fourier transform infrared spectroscopy (FTIR). A thin layer of the prepared solutions obtained from various aged reaction times was spread on KBr pellets individually and then dried at room temperature. The FTIR analysis was conducted by an Image-Pro Nicolet 5700 FTIR spectrometer.

Ultraviolet-visible spectroscopy (UV-Vis). The as-prepared AuNPs in the aqueous solution and the AuNPs in PAN/DMF solution were examined by a Lambda 900 UV-Vis spectrophotometer (Perkin Elmer, USA), and the reference solutions were treated with deionized water and DMF, respectively. To confirm the reducibility of TP for Au(III) ions, the UV-Vis spectra of TP heated for different times at 65°C were also tested. All the spectra were collected over a wavelength range of 200–800 nm.

Transmission electron microscopy (TEM) and high resolution transmission electron microscopy (HRTEM). The diluted AuNPs in aqueous solution were dropped on the ultra-thin carbon-coated copper grid and dried under an infrared lamp for 5 min.

Table 1 The main ingredients of TP

Ingredients	Percentage	Structural Formula
Epigallocatechin (EGC)	12.3%	 <p> $R_1 = \text{OH}, R_2 = \text{H}$, EGC $R_1 = \text{OH}, R_2 = \text{X}$, EGCG $R_1 = R_2 = \text{H}$, EC $R_1 = \text{H}, R_2 = \text{X}$, ECG </p>
Catechin gallate (EGCG)	45.3%	
Catechin (EC)	4.3%	
Epicatechin gallate (ECG)	9.1%	

The electrospun nanofibers were placed on the ultra-thin carbon-coated copper grid and dried under an infrared lamp for 5 min. The images were acquired using JSM-2100 transmission electron microscopy (TEM, JEOL, Japan) at an accelerating voltage of 200 kV. The sizes of AuNPs (200 counts) were measured with Image-Pro Plus 6.2 software.

Field emission scanning electron microscopy (FE-SEM). The nanofiber mats were plated with a thin layer of gold before observations. The morphology of the electrospun AuNPs/PAN nanofibers was observed by a JSM-6700F field-emission scanning electron microscope (FE-SEM, JEOL, Japan). The diameters of AuNPs/PAN nanofibers (100 counts) were measured with Image-Pro Plus 6.2 software.

X-ray photoelectron spectroscopy (XPS). X-ray photoelectron spectra of pure PAN powder, TP and AuNPs/PAN nanofibers were recorded using an X-ray Photoelectron Spectrometer (Kratos Axis Ultra DLD) with an aluminum (mono) K_{α} source (1486.6 eV). The aluminum K_{α} source was operated at 15 kV and 10 mA. For all of the samples, a low-resolution survey run (0–1100 eV, pass energy = 160 eV) was performed. In order to obtain more information about the chelating effect, a high-resolution survey (pass energy = 48 eV) was performed at spectral regions relating to gold, oxygen and nitrogen.

Results and discussion

Synthesis of well-separated AuNPs in the aqueous reduced by TP

The TEM images of AuNPs in the aqueous solution are shown in Fig. 1. Fig. 1A, with the corresponding insets, portrays the morphology of the AuNPs with a reducing time of 60 min. The average diameter of AuNPs shown in Fig. 1C was about 23.8 ± 6.1 nm. As mentioned above, TP was a mixture of different polyphenols, therefore the synthesized AuNPs exhibited a relatively wide size distribution. The insets located in the lower right corner of Fig. 1A and D indicate that the AuNPs were spherical and well-separated in aqueous solution. Fig. 1D showed that the

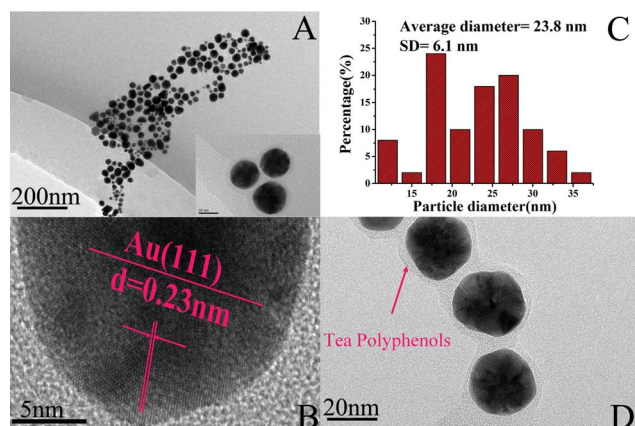


Fig. 1 (A, D) TEM images of the morphology of the AuNPs and (C) the corresponding particle size distribution of AuNPs. (B) The HRTEM image of AuNPs. The inset in (A) shows the well-separated AuNPs. The reduction time of the sample is 60 min.

AuNPs were coated with a layer of TP (with thickness of 2–3 nm, as shown in Fig. S1, see ESI†) and separated well, suggesting a stabilization effect of TP for AuNPs, which will be discussed later. The lattice fringes shown in Fig. 1B were visible with a spacing of about 0.23 nm, which corresponded to the lattice spacing of the (111) planes of Au.

Fig. 2 shows the UV-Vis absorption spectra taken at different intervals after mixing HAuCl_4 aqueous solution with TP aqueous solution. The mixture solutions were transparent and the color changed from golden yellow to deep purple with the increasing reaction time. In Fig. 2, the TP solution (curve a) and TP solution heated for 120 min at 65°C (curve h) both showed an absorption peak around 275 nm. In addition, as shown in Fig. 2S (see ESI†), all of the samples heated at 65°C for different times also showed the same absorption peak around 275 nm. There's no evolution for the UV-Vis spectra curves of the TP and all of the heated samples, indicating that the heating (65°C) was not sufficient to oxidize TP. An absorption peak at 290 nm appeared in curve b and is a result of the charge transfer between the gold and chloro ligands.^{14,37} When TP was added to the chloroauric acid solution, the absorption peak at 290 nm vanished because of the reduction of Au(III) by TP. In addition, a new peak emerged at 580 nm and the absorption peak of AuNPs can be considered as a superposition of the contribution from intraband transitions, which is believed to be a consequence of photoexcitation of the free conduction electrons on the surface of AuNPs.^{33,36} According to the literature,^{14,33} a strong and sharp peak around 275 nm also corresponds to Au clusters or small NPs due to the inter-band transitions, which may be overlaid with the absorption of TP in the present investigations. The broad band around 580 nm was assigned to the surface plasma resonance of larger Au nanoparticles.

The broad band indicated a relatively high polydispersity of the AuNPs, both in size and shape. Very interestingly, a comparison of the spectra showed that with a reaction time increase from 1 min to 120 min, the surface plasmon resonance band had a hypsochromic shift from 580 nm to 560 nm. It is

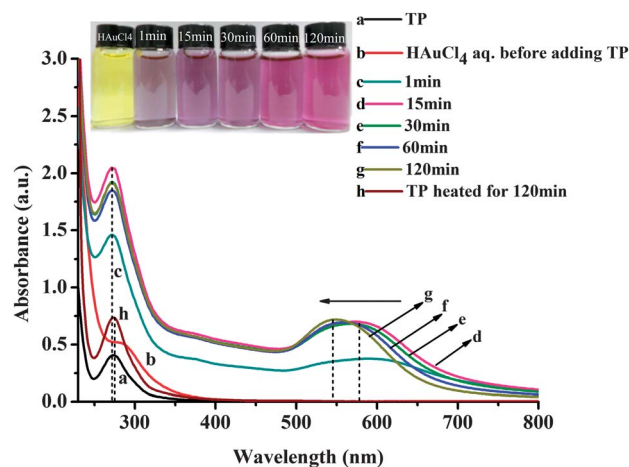
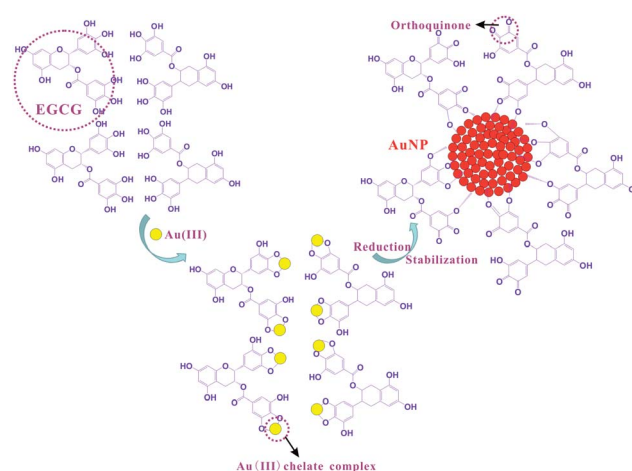


Fig. 2 UV-Vis absorption spectra of (a) TP, (h) TP heated for 120 min, (b) HAuCl_4 aq. before adding TP and (c–g) AuNPs in aqueous solution at different reaction times. The insets are the color of the corresponding samples at different reaction times.

well-established that such hypsochromic shifts in the UV-Vis spectrum are related to chemical changes in the environment.^{33,36} Thus, the observed shifts here would be in accordance with the reduction of Au ions through TP, followed by structural changes in the TP molecules. All of the above information confirmed the reducing and protective actions of the green compounds and it shows a great perspective for reducing other noble metal without introducing any hazardous substances.

Further research was done to test the reducibility of TP for synthesizing AuNPs. The FTIR spectra of TP and the oxidized TP and the chemical changes before and after oxidation are indicated in Fig. 3. The absorption peaks at 1455 cm⁻¹ and 1096 cm⁻¹ assigned to C–H alkanes in aromatic rings and C–O–C stretching vibration did not change during the reaction process. Based on the comparison spectrum of oxidized TP, the emerging absorption band at 2367 cm⁻¹ in oxidized TP was ascribed to the stretching vibration of C=O, suggesting the formation of the orthoquinone structure in TP. The obvious weak absorption peaks at 1344 cm⁻¹ and 1037 cm⁻¹ belong to the O–H in-plane bending vibration and C–O–H stretching vibration of phenolic hydroxyls in TP, respectively, which were results of the oxidation. The absorption band around 3371 cm⁻¹ shifted to 3414 cm⁻¹ and became relatively narrow, which also implied the involvement of the O–H groups in the reduction of Au ions, resulting in the partial destruction of hydrogen bonds among TP molecules. In addition, the damping absorption peak at 1147 cm⁻¹ assigned to O–H aromatic further indicated that the reduction of Au ions could be coupled to orthoquinone groups of oxidized TP.^{9,14,25,35} All of the above data further confirmed the reducibility of TP and indicated that the phenolic hydroxyls were oxidized to orthoquinone.

The reaction mechanism for the formation of AuNPs in aqueous solution by TP reduction is illustrated in Scheme 1. As a typical plant polyphenol, TP was a mixture of different polyphenols with multiple orthophenolic hydroxyls, which could have various reducing capabilities. As the main ingredients of TP, EGCG was employed for the mechanisms instead of TP. As reported in the literature, EGCG has been proven to be an



Scheme 1 A schematic illustration of the mechanism for the formation and stabilization of AuNPs in aqueous solution reduced by EGCG (the main ingredients of TP).

excellent bidentate ligand to bond with Au(III) ions by forming a stable five-member chelating ring.^{9,14} The orthophenolic hydroxyls can chelate with the Au(III) ions, leading to the formation of a Au(III) chelate complex. Then, the chelated Au(III) ions were reduced into Au⁰ atoms *in situ*, while a part of the phenolic hydroxyls of EGCG are simultaneously oxidized to the corresponding carbonyl groups, orthoquinone.^{9,14} According to Tripathy's research,²⁶ both the formed carbonyls and free hydroxyls are able to stabilize AuNPs by the interaction between the surface Au atoms of AuNPs and oxygen atoms of EGCG molecules.

Preparation of AuNPs/PAN nanofibers by electrospinning technique

In the above work, we confirmed the availability of the reducibility of TP in synthesizing AuNPs in aqueous solution and obtained well-separated AuNPs with an average diameter of about 23.8 ± 6.1 nm successfully. In the following work, we described an effective facile route to fabricate AuNPs/PAN nanofibers with a well-dispersed distribution of small AuNPs, which would be used potentially for catalytic applications. It was obviously seen in Fig. 4A and C that the AuNPs were spherical and well-dispersed in the PAN nanofibers. The average diameter of the AuNPs embedded in PAN nanofibers was 4.8 ± 1.1 nm. The morphology of the AuNPs in PAN/DMF precursor solution before electrospinning was shown in Figs 3S and 4S (see ESI†). In Fig. 4D, the latter fringe spacing of AuNPs was about 0.23 nm, which corresponded to the (111) plane.⁴² Compared with the AuNPs in the aqueous solution, the diameter of AuNPs embedded in PAN nanofibers was one order of magnitude smaller than these in aqueous solution and had a narrow distribution of diameter. Therefore, it is concluded that the PAN polymer might play a crucial role of stabilizer and direct the particular arrangements of Au nanoparticles during the reduction and electrospinning process.

The UV-Vis absorption spectra of the AuNPs/PAN nanofiber precursor solution with different reaction times are shown in Fig. 5. With an increase of reaction time, the solution colors

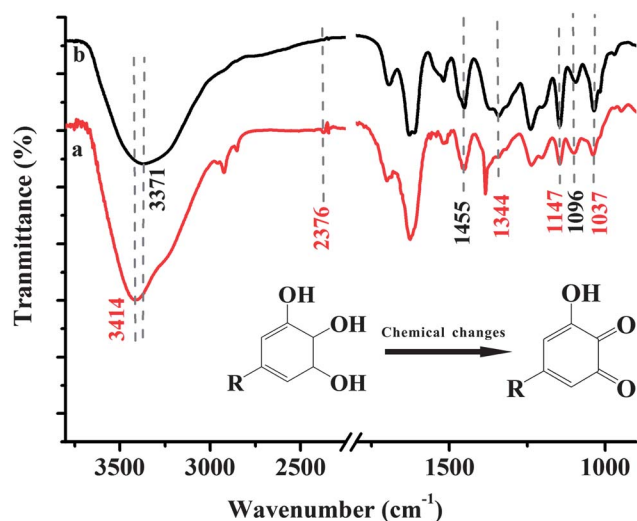


Fig. 3 The FTIR spectra of (a) TP and (b) TP after oxidation.

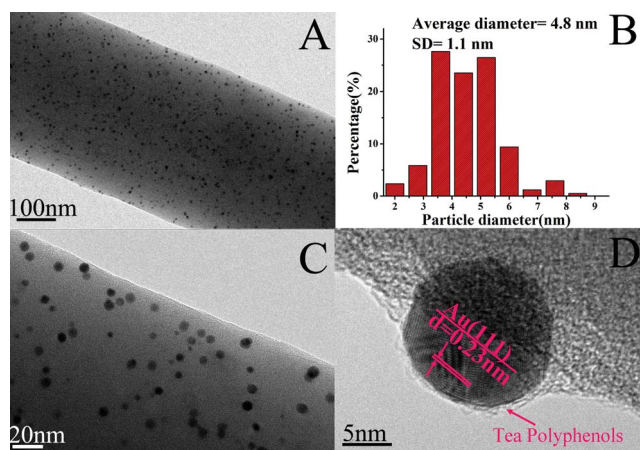


Fig. 4 (A, C) TEM images of the AuNPs/PAN nanofibers, (B) the corresponding particle size distribution of the AuNPs. (D) The HRTEM image of the AuNP embedded in PAN nanofibers.

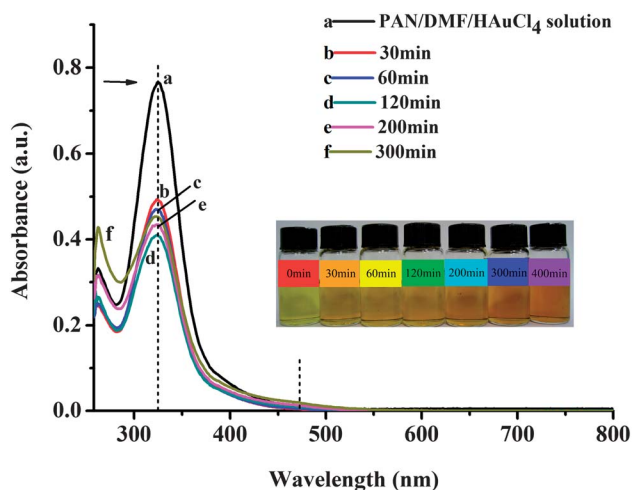
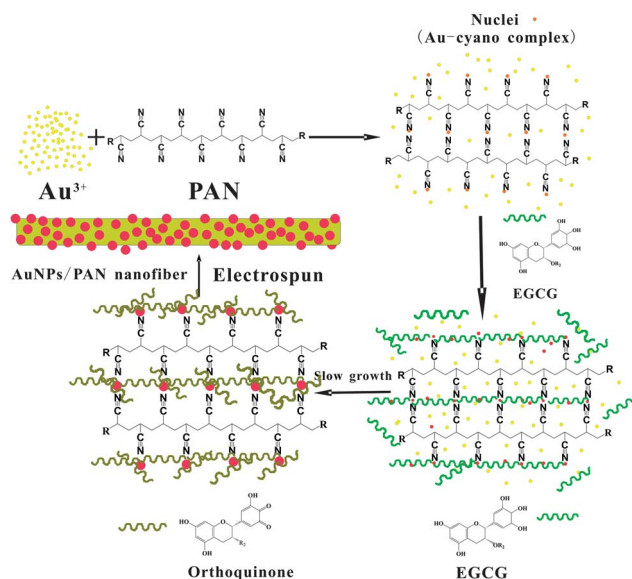


Fig. 5 Temporal evolution of UV-Vis absorption spectra after addition of TP into HAuCl₄/PAN/DMF solution. The insets show the corresponding samples at different reaction times.

changed from gold-yellow to orange-red. However, there was no dramatic UV peak shift. The two narrow UV peaks remained at around 261 nm and 323 nm. The absorption peak around 261 nm was assigned to the characteristic peak of the AuNPs in the nanofibers precursor solution. With the increase of the reducing time from 30 min to 300 min, the peak around 261 nm exhibited a red-shift from 261 nm to 263 nm (from curve b to curve f) and becomes more intense, which is attributed to the decrease of the particle size.^{18,33} Another absorption peak at 323 nm was assigned as the characteristic for PAN.^{30,45,46} Comparing with the UV-Vis absorption spectra in Fig. 5 and Fig. 2, we found that the absorption around 580 nm hypsochromic shifts to about 470 nm and became relatively weak, suggesting the nearly disappearance of larger size of AuNPs, which was in accordance with the results of TEM images in Fig. 4 and Fig. 1.

The present process of fabrication of the AuNPs/PAN nanofibers is schematically illustrated in Scheme 2. It has been known that the main chains of PAN polymer possess a large number of



Scheme 2 A schematic illustration of the mechanism for the fabrication of AuNPs/PAN nanofibers.

cyano groups that have one lone electron pair and can form a chelate complex with the Au ions.^{9,38,44} The functional groups can effectively catch the Au ions, leading to the formation of Au-cyano complexes through the chelating effect.^{9,30} The synthesis of AuNPs of different sizes was a kinetically driven process.^{38,39}

At the beginning of the process, the PAN polymer firstly seized the Au ions through chelating effect, and then formed a Au-cyano nucleus. Due to the chelating effect between the Au ion and cyano in PAN, the nuclei cannot collide with each other to aggregate easily. In addition, because of the high viscosity of the solution, the diffusion of the Au ions was slow and resulted in the nucleus growing at a relatively low rate. When the TP solution is added to the precursor solution, the Au ions can also chelate with the phenolic hydroxyls of TP. Thus the Au ions were further diffused to the Au nucleus region and reduced on the surface of Au nuclei by TP with the oxidation of the phenolic hydroxyls to orthoquinone. As a consequence, the synthesized AuNPs were wrapped with a layer of TP (with a thickness of 0.5–1 nm, as shown in Fig. S1 in ESI†), which can be seen in Figs 1D and 4D. FTIR spectra of the AuNPs synthesized with TP in the presence of PAN and embedded in the PAN nanofibers are shown in Figs 5S and 6S (see ESI†). These FTIR spectra also confirmed that the AuNPs reduced by TP were coupled with orthoquinone groups of oxidized TP. The cooperation between the chelating effect of cyano in PAN and the phenolic hydroxyls of TP with gold meant that the size and morphology of the as-synthesized AuNPs were small, well-dispersed and possessed a narrow diameter distribution, as demonstrated in Fig. 4.

In a word, the PAN polymer acted as a chelating agent and the TP served as both a reductant and stabilizer during our facile and green approach to synthesize the well-dispersed small AuNPs.

The chelating effects of Au ions with cyano groups in PAN molecules and hydroxyl groups in TP molecules were tested by XPS. Fig. 6A showed the XPS spectrum in the Au 4f region of the AuNPs/PAN nanofibers. It can be seen from the spectrum that the two XPS peaks at 88.0 eV and 84.5 eV were in agreement

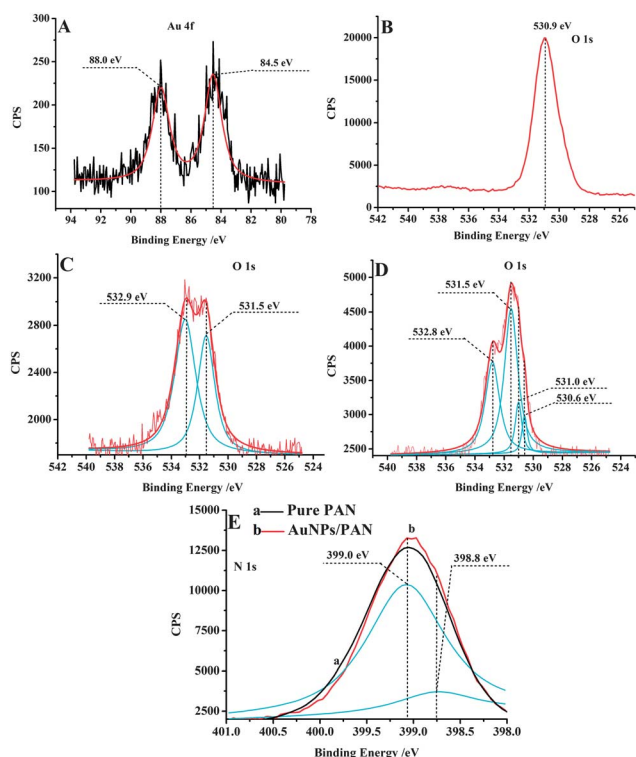


Fig. 6 XPS spectra of the electrospun nanofibers, pure PAN and TP: (A) Au 4f of PAN/AuNPs nanofibers; (B) O 1s of TP; (C) O 1s of the pure PAN; (D) O 1s of PAN/AuNPs nanofibers; (E) N 1s of the comparison between pure PAN powder and AuNPs/PAN nanofibers.

with the binding energies of Au 4f_{7/2} and Au 4f_{5/2}, respectively. Compared with Au⁰ (87.7 eV and 84.0 eV),^{9,26} the changes in the binding energy indicated the chelating effects between Au ions and PAN molecules. The oxygen 1s XPS spectra of TP, pure PAN and AuNPs/PAN nanofibers are shown in Fig. 6B, C and D. TP showed a single O 1s XPS peak at 530.9 eV, while pure PAN had two O 1s peaks at 531.5 eV and 532.9 eV, which was due to the two different chemical environments of oxygen in methyl acrylate (PAN contains 10 wt% of methyl acrylate). As for the O 1s XPS spectra of AuNPs/PAN nanofibers in Fig. 6D, after the peak separation with Origin 8.0 software, there were mainly three peaks at 530.9 eV, 531.5 eV and 532.8 eV, which were thought to be from TP and methyl acrylate in PAN, respectively. It is believed that the new emerging peak at 531.0 eV was a result of the strong coordination between AuNPs and oxygen.^{9,39,43} From Figs 1D and 4D, it can be seen that the AuNPs were encapsulated with a layer of TP molecules, which could restrain the AuNPs from aggregation during the synthesis process. In addition, there was a binding energy shift of oxygen 1s from 530.9 eV to 530.6 eV in TP before and after reduction, while there was nearly no shift for the oxygen 1s in methyl acrylate. Tanaka and Negishi have found that the relatively high binding energy of Au 4f was due to the binding of surface Au atoms in AuNPs with the stabilizer or passive molecules surrounding the nanoparticles, which led to a substantial electron donation from AuNPs to the stabilizer molecules.^{40,41}

The XPS spectra of the nitrogen 1s in pure PAN and AuNPs/PAN nanofibers are shown in Fig. 6E. The strong peak at 399.1 eV exists both in pure PAN (curve a) and AuNPs/PAN

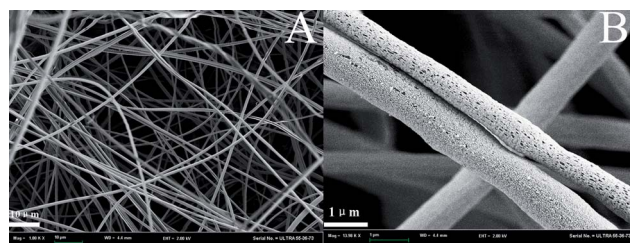


Fig. 7 (A) FE-SEM image of a non-woven mat of AuNPs/PAN nanofibers. (B) A highly magnified FE-SEM image of the AuNPs/nanofibers.

nanofibers (curve b), suggesting nearly no change of the chemical environment for most of the nitrogen in PAN molecular chains. However, a relatively weak peak of nitrogen 1s was occurred at 398.8 eV and it is concluded that the C≡N groups on the surface of PAN nanofibers may be involved in the interaction with AuNPs.⁴⁴ In other words, there was coordination between AuNPs and nitrogen, which was helpful for the synthesis of AuNPs with a smaller size and good distribution. Based on the above effects, the AuNPs with a diameter around 5 nm were formed and well-dispersed in PAN nanofibers. On the basis of all of the above data, we confirmed that the green TP can serve both as a reductant and stabilizer during the reaction process, and the PAN polymer can also be used as a stabilizing agent to prevent aggregation due to the chelating effect between the cyano groups and Au ions.

Fig. 7 shows the FE-SEM images of the non-woven mat of AuNPs/PAN nanofibers *via* electrospinning technique. As illustrated in Fig. 7A, there is a three-dimensional network structure consisting of a large quantity of randomly deposited nanofibers and the average diameter of AuNPs/PAN nanofibers was about 780 ± 170 nm, which is shown in Fig. 8S (see ESI†). More FE-SEM images are shown in Fig. 7S (see ESI†). Fig. 7B indicates that the surface of the nanofibers was relatively rough and porous, which can provide a high specific surface area. As previously discussed, the AuNPs were synthesized and well-dispersed in the PAN nanofibers, which was promising for the potential catalytic application. Due to the rough and porous surface of the nanofibers, we will explore the synthesis of noble nanoparticles on the surface and in the pores of the nanofibers, which would possess more catalytic activity.

Conclusion

In this study, we showed a green and facile synthesis of well-dispersed small AuNPs embedded in the electrospun PAN nanofibers by combining an electrospinning technique and *in situ* reduction approach. The UV-Vis spectra of the AuNPs synthesized in the aqueous and PAN/DMF solutions confirmed the reduction of TP and the formation of AuNPs. The morphology of the formed AuNPs were characterized by TEM. In our synthetic route, the PAN worked as a stabilizer to catch the Au ions through the chelating effect and formed an Au-cyano nucleus and then the Au ions were reduced by TP. The results of FTIR and XPS confirmed the reducibility of TP and indicated the interaction between the AuNPs with TP and PAN. The FE-SEM indicated that the as-prepared AuNPs/PAN nanofibers exhibited a relatively rough and porous surface, which might

provide a bright prospect for the catalytic activity. This new route provides a useful approach for the fabrication of nano-catalysts based on a noble metal.

Acknowledgements

This work is supported by the project of National Natural Science Foundation of China (NSFC) (Grant number: 50903072, 10902099), Zhejiang Province Natural Science Foundation (Grant number: Y4100197) and Science Foundation of Zhejiang Sci-Tech University (ZSTU) under No. 0901803-Y.

References

- 1 H. Tsunoyama, H. Sakurai, N. Ichikuni, Y. Negishi and T. Tsukuda, *Langmuir*, 2004, **20**, 11293–11296.
- 2 P. Migowski and J. Dupont, *Chem.–Eur. J.*, 2007, **13**, 33–39.
- 3 R. C. Jin, Y. W. Cao, C. A. Mirkin, K. L. Kelly, G. C. Schatz and J. G. Zheng, *Science*, 2001, **294**, 1901–1903.
- 4 A. S. K. Hashmi and G. J. Hutchings, *Angew. Chem.*, 2006, **118**, 8064–8105.
- 5 X. Fang, H. Ma, S. L. Xiao, M. W. Shen, R. Guo, X. Y. Cao and X. Y. Shi, *J. Mater. Chem.*, 2011, **21**, 4493–4501.
- 6 M. Haruta, M. Yamata, T. Kobayashi and S. Lijima, *J. Catal.*, 1989, **115**, 301–309.
- 7 A. Rai, A. Prabhune and C. C. Perry, *J. Mater. Chem.*, 2010, **20**, 6789–6798.
- 8 Y. W. Cao, R. Jin and C. A. Mirkin, *J. Am. Chem. Soc.*, 2001, **123**, 7961–7962.
- 9 H. Wu, X. Huang, M. M. Gao, X. P. Liao and B. Shi, *Green Chem.*, 2011, **13**, 651–658.
- 10 J. J. Zhang, M. M. Gu, T. T. Zheng and J. J. Zhu, *Anal. Chem.*, 2009, **81**, 6641–6648.
- 11 S. Liu, G. Y. Chen, P. N. Prasad and M. T. Swihart, *Chem. Mater.*, 2011, **23**, 4098–4101.
- 12 E. Thimsen, *Chem. Mater.*, 2011, **23**, 4612–4617.
- 13 Z. C. Xu, Y. L. Hou and S. H. Sun, *J. Am. Chem. Soc.*, 2007, **129**, 8698–8699.
- 14 X. Huang, H. Wu, X. P. Liao and B. Shi, *Green Chem.*, 2010, **12**, 395–399.
- 15 M. C. Moulton, L. K. Braydich-Stolle, M. N. Nadagouda, S. Kunzelman, S. M. Hussain and R. S. Varma, *Nanoscale*, 2010, **2**, 763–770.
- 16 M. Schulz-Dobrick, K. V. Sarathy and M. Jansen, *J. Am. Chem. Soc.*, 2005, **127**, 12816–12817.
- 17 A. Rai, A. Prabhune and C. C. Perry, *J. Mater. Chem.*, 2010, **20**, 6789–6798.
- 18 J. Garcia-Serrano, U. Pal, A. M. Herrera, P. Salas and C. Angeles-Chavez, *Chem. Mater.*, 2008, **20**, 5146–5153.
- 19 C. Kruger, S. Agarwal and A. Greiner, *J. Am. Chem. Soc.*, 2008, **130**, 2710–2711.
- 20 A. N. Shipway, M. Lahav and I. Willner, *Adv. Mater.*, 2000, **12**, 993–997.
- 21 S. Tsubaki, H. Iida, M. Sakamoto and J. Azuma, *J. Agric. Food Chem.*, 2008, **56**, 11293–11299.
- 22 Y. Wang, Z. X. Shi and J. Yin, *ACS Appl. Mater. Interfaces*, 2011, **3**, 1127–1133.
- 23 Y. N. Chen, Y. D. Lee, H. Vedala, B. L. Allen and A. Star, *ACS Nano*, 2010, **4**, 6854–6862.
- 24 A. Yella, H. W. Lee, H. N. Tsao, C. Y. Yi, A. K. Chandiran, M. K. Nazeeruddin, E. W. G. Diau, C. Y. Yeh, S. M. Zakeeruddin and M. Grätzel, *Science*, 2011, **334**, 629–633.
- 25 Y. S. Park, M. K. Lee, B. G. Heo, K. S. Ham, S. G. Kang, J. Y. Cho and S. Gorinstein, *Plant Foods Hum. Nutr.*, 2010, **65**, 186–191.
- 26 P. Tripathy, A. Mishra, S. Ram, H.-J. Fecht, J. Bansmann and R. J. Behm, *Nanotechnology*, 2009, **20**, 075701.
- 27 L. L. Song, R. Liang, D. D. Li, Y. D. Xing, R. M. Han, J. P. Zhang and L. H. Skibsted, *J. Agric. Food Chem.*, 2011, **59**(23), 12643–12651.
- 28 D. He, B. Hu, Q. F. Yao, K. Wang and S. H. Yu, *ACS Nano*, 2009, **3**, 3993–4002.
- 29 G. M. Kim, A. Wutzler, H. J. Radusch, G. H. Michler, P. Simon, R. A. Sperling and W. J. Parak, *Chem. Mater.*, 2005, **17**, 4949–4957.
- 30 J. Bai, Y. X. Li, M. Y. Li, S. G. Wang, C. Q. Zhang and Q. B. Yang, *Appl. Surf. Sci.*, 2008, **254**, 4520–4523.
- 31 X. H. Li, C. L. Shao and Y. C. Liu, *Langmuir*, 2007, **23**, 10920–10923.
- 32 E. Formo, E. Lee, D. Campbell and Y. N. Xia, *Nano Lett.*, 2008, **8**, 668–672.
- 33 S. Pocovi-Martínez, M. Parreno-Romero, S. Agouram and J. Perez-Prieto, *Langmuir*, 2011, **27**, 5234–5241.
- 34 Z. Y. Zhang, C. L. Shao, P. Zou, P. Zhang, M. Y. Zhang, J. B. Mu, Z. C. Guo, X. H. Li, C. H. Wang and Y. C. Liu, *Chem. Commun.*, 2011, **47**, 3906–3908.
- 35 R. J. Liao, Z. H. Tang, Y. D. Lei and B. C. Guo, *J. Phys. Chem. C*, 2011, **115**, 20740–20746.
- 36 J. Guan, L. Jiang, J. Li and W. S. Yang, *J. Phys. Chem. C*, 2008, **112**, 3267–3271.
- 37 P. D. Cozzoli, M. L. Curri, C. Giannini and Angela Agostiano, *Small*, 2006, **2**, 413–421.
- 38 C. Q. Zhang, Q. B. Yang, N. Q. Zhan, L. Sun, H. G. Wang, Y. Song and Y. X. Li, *Colloids Surf., A*, 2010, **362**, 58–64.
- 39 S. G. Gholap, M. V. Badiger and C. S. Gopinath, *J. Phys. Chem. B*, 2005, **109**, 13941–13947.
- 40 Y. Negishi, K. Nobusada and T. Tsukuda, *J. Am. Chem. Soc.*, 2005, **127**, 5261–5270.
- 41 A. Tanaka, Y. Takeda, M. Imamura and S. Sato, *Phys. Rev. B: Condens. Matter*, 2003, **68**, 195415.
- 42 D. Baranov, L. Manna and A. G. Kanaras, *J. Mater. Chem.*, 2011, **21**, 16694–16703.
- 43 Z. H. Tang, C. F. Zeng, Y. D. Lei, B. C. Guo, L. Q. Zhang and D. M. Jia, *J. Mater. Chem.*, 2011, **21**, 17111–17118.
- 44 Z. R. Yue, K. R. Benak, J. W. Wang, C. L. Mangun and J. Economy, *J. Mater. Chem.*, 2005, **15**, 3142–3148.
- 45 Z. P. Zhang and M. Y. Han, *J. Mater. Chem.*, 2003, **13**, 641–643.
- 46 K. J. Lee, W. K. Oh, J. Y. Song, S. J. Kim, J. W. Lee and J. Jang, *Chem. Commun.*, 2010, **46**, 5229–5231.

Green synthesis of Au nanoparticles immobilized on halloysite nanotubes for surface-enhanced Raman scattering substrates†

Han Zhu,^a MingLiang Du,^{*a,b} MeiLing Zou,^a CongSheng Xu^a and YaQin Fu^{a,b}

Received 8th May 2012, Accepted 11th June 2012

DOI: 10.1039/c2dt30998j

A facile and green route was introduced to synthesize Au nanoparticles immobilized on halloysite nanotubes (AuNPs/HNTs) used for surface-enhanced Raman scattering substrates. The naturally occurring HNTs were firstly functionalized with a large amount of $-NH_2$ groups by *N*-(β -aminoethyl)- γ -aminopropyl trimethoxysilane (AEAPTES), which possesses one lone electron pair and will “anchor” Au ions to form a chelate complex. Then, with the addition of tea polyphenols (TP), the Au ions were reduced on the surface of the previously formed Au– NH_2 chelate complex to form AuNPs. Transmission electron microscopy (TEM) and field emission scanning electron microscopy (FE-SEM) observations indicate that a large amount of AuNPs were synthesized on HNTs. The AuNPs are irregularly spherical and densely dispersed on HNTs and the diameter of the nanoparticles varies from 20 to 40 nm. The interactions between AuNPs and $-NH_2$ groups were verified by X-ray photoelectron spectroscopy (XPS) and the results showed that the functional groups can “anchor” AuNPs through the chelating effect. The as-prepared AuNPs/HNTs nanomaterials with several nanometers gaps among nanoparticles were used as a unique surface-enhanced Raman scattering substrate, which possessed strong and distinctive Raman signals for R6G, indicating the remarkable enhancement effect of the AuNPs/HNTs.

1. Introduction

The current exciting cutting edge research in the field of nanotubular materials, such as carbon nanotubes (CNTs) and boron nitride nanotubes (BNNTs), has recently been attracting interest.^{1–3} Compared with the above mentioned nanotubes, halloysite nanotubes (HNTs) are readily obtainable, much cheaper and possess a special structure and large reserves in many countries, such as China, New Zealand, Australia, *etc.*^{4–7} A mass of researchers have studied the applications of HNTs, such as in catalysis carriers, nanoreactors, entrapment systems for loading, dye or heavy metal adsorbents, storage and controlled release of drugs, anticorrosion agents, biocides and reinforcement of polymers.^{4,6–10} HNTs ($Al_2Si_2O_5(OH)_4 \times nH_2O$) possess a hollow tubular structure with an approximately 15 nm lumen, 50 nm external diameter and length of 1000–200 nm. It is a two-layered (1 : 1) aluminosilicate chemically similar to kaolin, with aluminol (Al–OH) groups in the internal surface and Si–OH groups on the external surface, which are potential anchoring sites for nanoparticles.^{9,10} Recently, HNTs used as a substrate for the organization of noble metal nanoparticles excitingly attract

interest for many potential applications such as catalysis for CO_x -free hydrogen, Cr(vi) removal and photocatalytic degradation of CO_2 , owing to their unique optical, electronic, imaging, magnetic and catalytic properties.^{5,9,11–14} Meanwhile, gold nanostructures have been the focus of intense research owing to their fascinating optical, electronic, and chemical properties and promising applications in catalysis, nanoelectronics, biomedicine and surface-enhanced Raman scattering (SERS).^{14–20} SERS is one of the most powerful probing tools for biochemical applications and trace detection of organic chemicals because it enables ultrasensitive, low-cost and real-time detection.^{21–24} A large amount of research works have demonstrated that the giant signal amplification in SERS arises from the electromagnetic enhancement at so-called ‘hot spots’, which may be in either interstitial voids of metal nanoparticles or metal structures with intersections, bifurcations and high radii of curvature. Although SERS effects can be achieved simply by exploiting the electromagnetic resonance properties of roughened surfaces or nanoparticles of Au or Ag, the fabrication of reliable SERS substrates with uniformly high enhancement factors remains the focus of much research.

There are various methods for the synthesis of AuNPs, however, most are either complex or time-consuming, or require strict synthetic conditions.^{24–26} The previous widely employed reducing agents for synthesizing AuNPs, such as sodium borohydride, *N,N*-dimethylformamide (DMF) and hydrazine, *etc.*, are highly active or have potential environmental risk for wide applications. There are three main criteria for a “green” synthesis of nanoparticles: an environmentally compatible solvent system, an

^aDepartment of Materials Engineering, College of Materials and Textile, Zhejiang Sci-Tech University, Hangzhou 310018, P.R. China

^bKey Laboratory of Advanced Textile Materials and Manufacturing Technology, Zhejiang Sci-Tech University, Ministry of Education, Hangzhou 310018, P. R. China. E-mail: du@zstu.edu.cn; Tel: +86-571-86843255

†Electronic supplementary information (ESI) available. See DOI: 10.1039/c2dt30998j

eco-friendly reducing agent and a non-hazardous capping agent for stabilizing the nanoparticles.^{27–31} Nowadays, there has been an increased emphasis on the greener production of environmentally benign and renewable materials as the respective reducing and stabilizing agents. In our previous work,³² we have firstly introduced the green natural compounds, tea polyphenols (TP) both serving as a reducer and stabilizer, to synthesize AuNPs successfully. The green TP are groups of water-soluble polyphenol compounds richly deposited in plants, belonging to the flavonoid family, and mainly include epicatechin (EC), epicatechin gallate (ECG), epigallocatechin (EGC) and epigallocatechin gallate (EGCG), in which the EGCG makes up about 46% of the total TP.^{30–35} Wang *et al.* have successfully synthesized TiO₂ nanoparticles/HNTs nanostructure *via* depositing the TiO₂ nanoparticles onto HNTs and Zhu *et al.* have reported the preparation of HNTs-supported Ru nanoparticles.^{5,9} However, there are no reports about the application of AuNPs immobilized on HNTs for SERS substrates. Meanwhile, it remains challenging to obtain a cheap, reliable, stable and uniform SERS signal spanning a wide dynamical range.

In the present investigation, due to the advantages of HNTs, such as the special nanotubular structure, high specific area and high absorption ability, we immobilized AuNPs onto the surface of HNTs to create more ‘hot spots’ for the enhancement of SERS signals. *N*-β-Aminoethyl-γ-aminopropyl trimethoxysilane (AEAPTES) is composed of a large number of primary and secondary amino groups in a molecule. As reported, the amino groups possess lone electron pairs, which can catch the noble metal ions to form a chelate complex through the chelating effect and exhibit good stability for immobilizing nanoparticles onto HNTs.^{11,36} In our present study, we introduce a two-step method to synthesize AuNPs immobilized on HNTs (AuNPs/HNTs). Firstly, HNTs were functionalized by grafting AEAPTES onto HNTs and then, we used TP as a reducing agent and stabilizer to synthesize AuNPs/HNTs through an *in situ* approach. A series of characterizations were made to test and confirm the present investigations. The as-prepared AuNPs/HNTs nanomaterials have been used as a surface-enhanced Raman scattering substrate, which possessed strong and distinctive Raman signals for R6G, indicating the remarkable enhancement effect.

2. Experiment section

2.1 Materials

The halloysite nanotubes (HNTs) were collected from Hubei Province, China. The Brunauer–Emmett–Teller (BET) specific surface area was determined as 50.45 m² g^{−1}. Chloroauric acid (HAuCl₄·3H₂O, 99.9%) was acquired from Shanghai Civi Chemical Technology Co., Ltd, China. Tea polyphenols (TP) were purchased from Xuancheng BaiCao Plant Industry and Trade Co., Ltd, China. *N*-(β-Aminoethyl)-γ-aminopropyl trimethoxysilane (AEAPTES, NH₂CH₂CH₂NHCH₂CH₂CH₂ Si(OCH₃)₃) was purchased from Sinopharm Chemical Reagent Co., Ltd, China.

2.2 Functionalization of HNTs using AEAPTES

The HNTs were firstly purified *via* a repeated washing/centrifugation process and then dried at 80 °C in a vacuum oven for

12 hours. 5 g AEAPTES was dissolved in 95 g 95% ethanol and then an appropriate amount of acetic acid was drop into the mixture to make the pH reach a constant value of about 4. The mixture was stirred vigorously at room temperature for 1.5 hours. Next, 5 g HNTs were added to the as-prepared solution and the mixture was kept under refluxing conditions for 6 hours at 80 °C. The functionalized HNTs were purified *via* a repeated washing/centrifugation process with ethanol to remove ungrafted AEAPTES and possible products of hydrolysis. Then, the functionalized HNTs were dried for 12 hours in an oven under vacuum at 80 °C and used for further experiments.

2.3 Synthesis of the Au nanoparticles immobilized on HNTs

HAuCl₄·3H₂O was dissolved in deionized water to get a 10.0 mmol L^{−1} Au³⁺ solution. 15 mL Au³⁺ solution was dropped in 30 mL HNTs solution (dissolved 0.5 g functionalized HNTs in 30 mL deionized water) and then the mixture was heated to 45 °C and stirred vigorously for 1 h. At last, 0.034 g TP dissolved in 5 mL deionized water were added to the mixture. After 15 minutes, the as-prepared powder was purified *via* repeated washing/centrifugation process with ethanol and then dried in vacuum oven at 80 °C and used for further experiments and characterizations.

2.4 SERS measurements

For SERS studies, a Thermo Scientific Nicolet NXR Fourier Transform Raman was used to carry out the SERS measurement and the as-synthesized AuNPs/HNTs were used as SERS substrates. R6G has been extensively studied and well-characterized by SERS, and in this study it was chosen as a model analyte to investigate the performance of the as-prepared AuNPs/HNTs substrate for SERS detection. 0.005 g HNTs and AuNPs/HNTs were dipped in 1 mL R6G (from 10^{−3} M to 10^{−6} M) aqueous solution for 30 min and then were dropped onto the Si substrate and dried under an infrared lamp. 1 mL AuNPs in aqueous solution were mixed with 1 mL R6G solution and then dropped in NMR tube for SERS measurements, which was used as a control.

2.5 Characterization

2.5.1 X-ray diffraction (XRD). The crystal structure of HNTs and AuNPs/HNTs were characterized with a SIEMENS Diffraktometer D5000 X-ray diffractometer using a Cu Kα radiation source at 35 kV, with a scan rate of 0.02° 2θ s^{−1} in the 2θ range of 10–80°.

2.5.2 Fourier transform infrared spectroscopy (FTIR). The pure HNTs powder and the as-synthesized functionalized HNTs powder were spread on KBr pellets individually and then dried under an infrared lamp. The FTIR analysis was conducted by a Nicolet 5700 FTIR spectrometer.

2.5.3 Transmission electron microscopy (TEM). The HNTs and the as-synthesized AuNPs/HNTs were dissolved in diluted water solution and respectively dropped on the ultra-thin carbon-coated copper grid and dried under an infrared lamp for

5 minutes. The images were acquired using a JSM-2100 transmission electron microscopy (TEM, JEOL, Japan) at an accelerating voltage of 200 kV.

2.5.4 Scanning electron microscopy (SEM). The HNTs powders were spread on the conducting adhesive and the images were acquired using a LEO 1530 VP SEM machine.

2.5.5 Field emission scanning electron microscopy (FE-SEM). The morphology of the AuNPs/HNTs powder was observed by a ULTRA-55 field-emission scanning electron microscope (FE-SEM, JEOL, Japan).

2.5.6 X-ray photoelectron spectroscopy (XPS). X-ray photoelectron spectra of pure HNTs powder and AuNPs/HNTs powder were recorded by using an X-ray photoelectron spectrometer (Kratos Axis Ultra DLD) with an aluminum (mono) $K\alpha$ source (1486.6 eV). The aluminum $K\alpha$ source was operated at 15 kV and 10 mA. For all of the samples, in order to obtain more information about the chelating effect, a high-resolution survey (pass energy = 48 eV) was performed at spectral regions relating to gold and nitrogen.

2.5.7 Fourier Transform Raman (FT-Raman). A Thermo Scientific Nicolet NXR Fourier Transform Raman spectrometer was used to carry out the SERS measurement. An argon ion laser of 1064 nm at a spectral resolution of 4 cm^{-1} and a spot size of 1 μm was used for excitation. The laser power on the specimens was measured at 0.3 mW. The recorded spectra were raw data without any background subtraction or processing.

2.5.8 Ultraviolet-visible spectroscopy (UV-Vis). The spectra of pure HNTs and as-prepared AuNPs/HNTs powder were collected by a Lambda 900 UV-Vis spectrophotometer (Perkin Elmer, USA). All of the spectra were collected over a wavelength range of 200–800 nm.

3 Results and discussion

3.1 Morphology of HNTs and functionalization of HNTs using AEAPTES

The structure and morphology of the HNTs were observed by TEM and SEM. Fig. 1a displays the TEM image of naturally occurring HNTs and the predominant form is a hollow tubular structure in the submicrometer range. The size of the inner and outer diameters of the halloysite tubules are about 15–20 and 40–50 nm, respectively, depending on the deposit condition. The lumen length of the natural HNTs ranging 500–2000 nm is shown in Fig. 1b, indicating the polydispersity of HNTs in length.

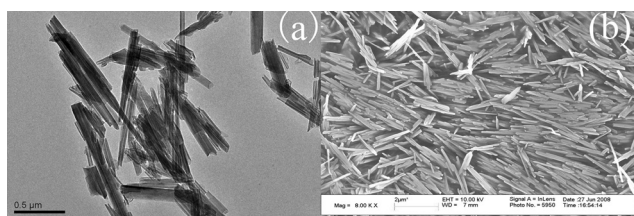


Fig. 1 The TEM (a) and SEM (b) images of HNTs.

FTIR analysis was conducted to investigate the chemical changes during the reaction process and testify the grafted AEAPTES onto HNTs. The photographs of pure HNTs powder, functionalized HNTs powder and AuNPs/HNTs powder are shown in Fig. 1S (see ESI†). Fig. 2 shows the FTIR spectra of pure HNTs powders (curve a) and the functionalized HNTs powders (curve b). The characteristic peaks of HNTs that occurred at 3698 cm^{-1} , 3623 cm^{-1} and 1634 cm^{-1} are attributed to O–H stretching of inner-surface hydroxyl groups, O–H stretching of inner hydroxyl groups and deformation of water, respectively. These absorption peaks have no change after modification, suggesting that the basic structure of HNTs and functionalized HNTs remain constant.^{5,7,9–11} However, several absorption peaks at 2927 cm^{-1} , 2860 cm^{-1} and 1381 cm^{-1} are newly emerged, which are attributed to C–H asymmetric and symmetric stretching vibrations of AEAPTES, respectively.¹¹ The band at 3452 cm^{-1} is assigned to the stretching vibration of N–H. The intensity of the peaks observed at 1109 cm^{-1} and 1034 cm^{-1} ascribed to in-plane stretching of Si–O increase and become relatively narrow, which can also imply the existence of AEAPTES grafted on the HNTs.^{37–39} The above results can demonstrate that AEAPTES, the sole source for C–H and N–H, has successfully been grafted onto the HNTs.

To prove that the AEAPTES were chemically bonded onto HNTs, the XPS spectra of the pure HNTs powder and functionalized HNTs powder are investigated and the spectra of O 1s are presented in Fig. 3. As observed in Fig. 3a, the intense characteristic peak that emerged at 531.7 eV corresponds well with O 1s of pure HNTs powder binding energy. After the functionalization of HNTs by AEAPTES, the binding energy of O 1s is increased to 532.5 eV, indicating that the AEAPTES has successfully grafted on the HNTs. The chemical changes during the reaction process are shown in Fig. 2S (see ESI†).

3.2 Synthesis of the AuNPs immobilized on HNTs

A facile and green approach was introduced to synthesize AuNPs/HNTs using tea polyphenols (TP) as the reductant. The

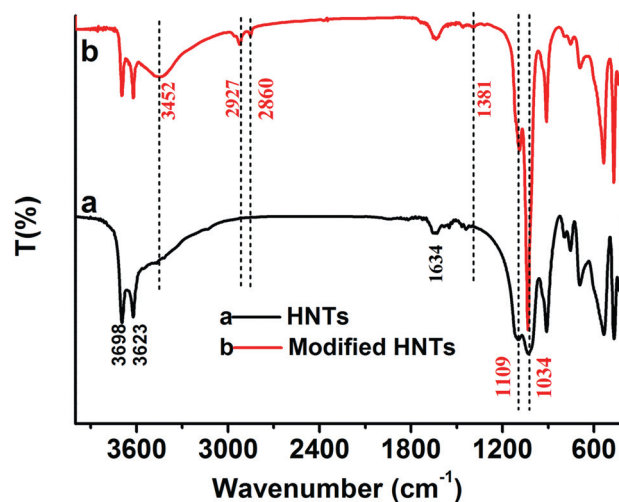


Fig. 2 FTIR spectra of HNTs (curve a) and functionalized HNTs using AEAPTES (curve b).

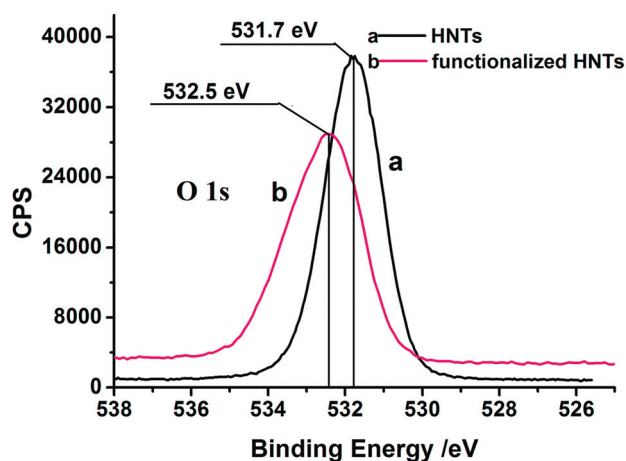


Fig. 3 The XPS spectra of the HNTs before and after surface functionalization by AEAPTES: (a) O 1s of pure HNTs powder (b) O 1s of functionalized HNTs by AEAPTES.

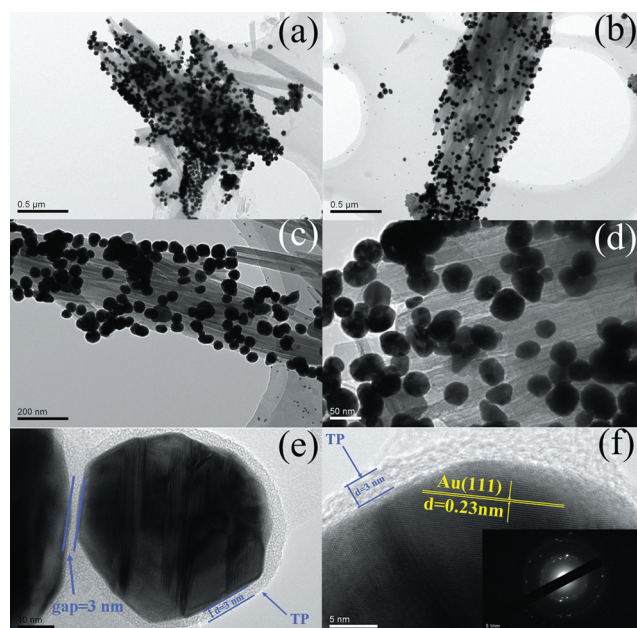


Fig. 4 (a–e) TEM images of AuNPs/HNTs; (f) a HRTEM image of the AuNP and the insert is the corresponding selected area electron diffraction pattern.

morphology and structure of the as-synthesized AuNPs/HNTs are shown in Fig. 4.

As shown in Fig. 4a and b, a large amount of AuNPs were immobilized on the HNTs. The AuNPs are irregularly spherical and densely dispersed on the HNTs and the diameter of the nanoparticles varies from 20 to 40 nm, which can be seen in Fig. 4c and d. Fig. 4e shows that the AuNPs are surrounded by a layer of TP and the thickness of the layer is about 3 nm.

Due to the stabilization of TP,^{31,32} the AuNPs separated well and nearly no aggregations are observed. The high resolution TEM image (Fig. 4f) shows that the lattice fringes are visible with a spacing of about 0.23 nm, which corresponds to the lattice spacing of the (111) planes of Au.^{30–32} As shown in Fig. 4f, the electron diffraction pattern of the corresponding

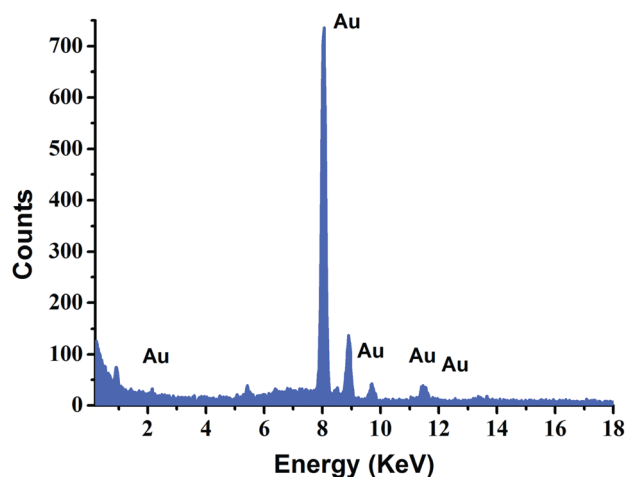


Fig. 5 The EDX spectrum of the AuNPs immobilized on HNTs.

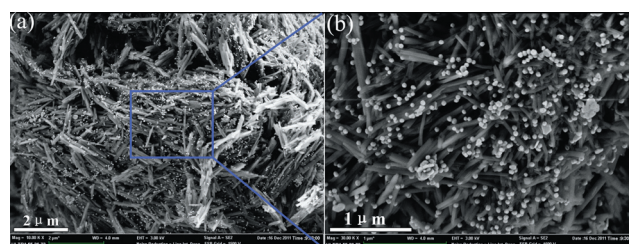


Fig. 6 (a, b) FE-SEM images of the AuNPs/HNTs.

selected area of AuNPs indicate the polycrystallinity of AuNPs and the diffuse ring confirm the existence of TP.

The EDX spectrum of the AuNPs immobilized on HNTs is shown in Fig. 5. The EDX spectrum only exhibits the characteristic peaks of Au, suggesting that the obtained product is composed of pure Au and confirming the existence of AuNPs immobilized on HNTs. Besides, the UV-Vis spectra of HNTs and AuNPs also indicate that the surface plasmon resonance absorption peak of AuNPs is 537 nm, as shown in Fig. 3S (see ESI†).

From the FE-SEM images shown in Fig. 6, quantities of well-dispersed AuNPs were immobilized on the surface of HNTs, which is in accordance with the TEM results (Fig. 4). Notably, the AuNPs were irregularly dispersed on the surface of the HNTs, which indicates that the AuNPs were synthesized and immobilized on the surface of HNTs and it was believed that this will display a promising and potential prospect for SERS detection.

To further confirm the presence of the AuNPs, the HNTs and AuNPs/HNTs powder were characterized by XRD and the diffraction patterns of HNTs before and after the immobilization of AuNPs are shown in Fig. 7. According to the literature,^{5,9} all of the observed peaks mainly can be indexed to the characteristic peaks of HNTs, as shown in curve A. Some of the characteristic peaks reduced after the immobilization of AuNPs. However, four new peaks emerged, a new stronger peak at $2\theta = 38.1^\circ$ and three relatively weak peaks at $2\theta = 44.4^\circ$, 64.6° and 77.6° , which exactly match with the reference values for the Au (111), Au (200), Au (200) and Au (311) lattice planes, respectively.^{20,31,37} All of the peaks are characteristic of face-centered cubic (fcc)

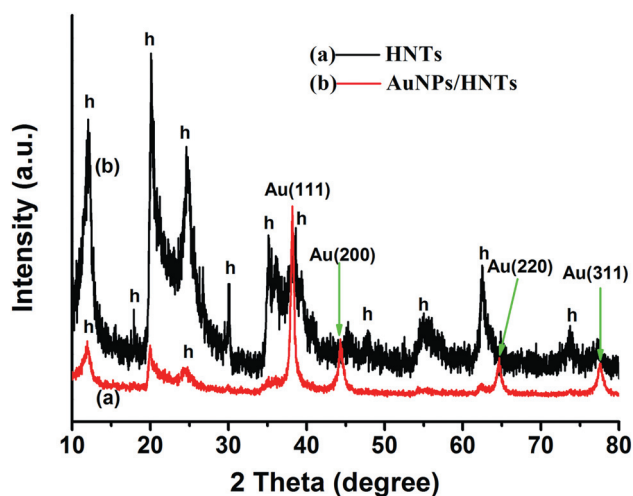
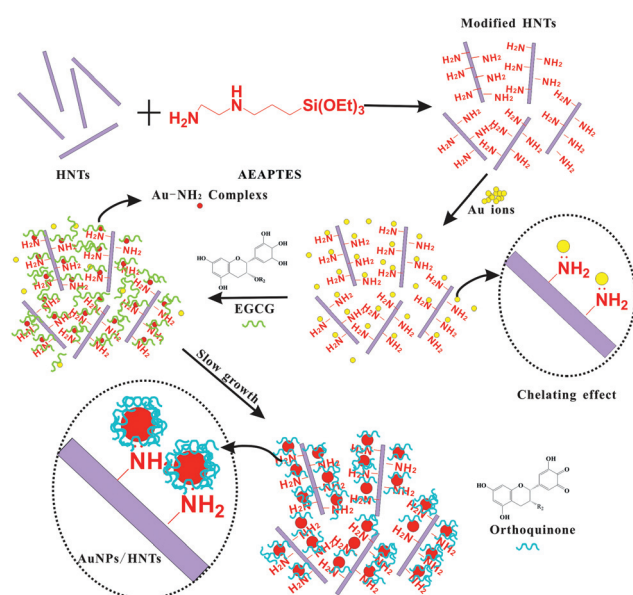


Fig. 7 The XRD patterns of HNTs powder (curve a) and AuNPs/HNTs powder (curve b). (h: HNTs).



Scheme 1 A schematic illustration of the synthesis of the AuNPs immobilized on HNTs.

gold (JCPDS-4748).^{31,32} From the above results, it can be further confirmed that the AuNPs/HNTs were successfully synthesized.

The present process is schematically illustrated in Scheme 1. Firstly, the surface of HNTs are functionalized with -NH_2 by AEAPTES. As is well-known, the functionalized HNTs possess a large amount of -NH_2 groups, which have one lone electron pair and can form a chelating complex with Au ions.^{11,30,32} Due to the chelating effects between Au ions and -NH_2 groups, most of the Au ions were “anchored” by the -NH_2 groups, resulting in the formation of Au- NH_2 complexes. Then, with the addition of TP, the previously formed Au- NH_2 complexes can also chelate with the phenolic hydroxyls of TP and, meanwhile, the Au ions were reduced by TP. Consequently, besides the chelating effects, the TP can also used as a stabilizer to protect the AuNPs from aggregation. As the reaction proceeded, other Au ions were

further diffused to the Au- NH_2 complexes region and reduced on the surface of Au- NH_2 complexes by TP with the oxidation of the phenolic hydroxyls to orthoquinone.^{30–33} As a consequence, the synthesized AuNPs were wrapped with a layer of TP, which can be observed in Fig. 4e and f. The chelating effect between Au ions and -NH_2 groups will be testified later.

The chelating effects of AuNPs with -NH_2 groups were testified by XPS analysis. The chemical state of the AuNPs immobilized on the functionalized HNTs is presented in Fig. 8. As observed in Fig. 8a, the intense doublets that emerged at 88.3 eV and 84.6 eV correspond well with Au 4f₇ and Au 4f₅ binding energies, respectively. Compared with zero valent Au⁰ (87.7 eV and 84.0 eV), the changes of the binding energy indicate the interaction between AuNPs and -NH_2 groups.^{31,32} Negishi *et al.* have also pointed out that the Au 4f peaks occurring at relatively higher binding energy can be attributed to the surface Au atoms of AuNPs bonded to the surface surrounding the stabilizer or passive molecules, suggesting that a substantial electron donation from AuNPs to stabilizer molecules is present.⁴⁰ Fig. 8b shows the nitrogen 1s XPS spectrum of the functionalized HNTs; two peaks occurred at 399.5 eV and 401.6 eV, standing for two chemical states of nitrogen in HNTs. However, the binding energies of nitrogen 1s observed in Fig. 8c shift to 400.2 eV and 402.1 eV, demonstrating the strong interaction between AuNPs and -NH_2 groups. In conclusion, all of the above results can confirm the chelating effects between the AuNPs and -NH_2 groups and the functional groups can “anchor” AuNPs through the chelating effect, which shows an exciting prospect for immobilization of AuNPs.

SERS has become a powerful technique to detect chemical and biological molecules toward single-molecule detection sensitivity. AuNPs have been widely used as the SERS source due to their intriguing and strong SERS activity.^{41–44} As reported, AuNPs with different morphologies, such as gold nanoparticles, nanorods and nanoflowers have been used as the SERS substrate. Here, AuNPs immobilized on HNTs were used as SERS substrates to detect Rhodamine 6G (R6G), a typical model analyte for SERS performance evaluation.^{42–45}

As exemplified by Fig. 9, curve a displays very weak Raman signals for a 10^{-3} M R6G aqueous solution enhanced by AuNPs and there is nearly no enhancement effect of R6G on the HNTs without AuNPs (curve b). Notably, the AuNPs/HNTs SERS substrates (curve c) show strong and distinctive Raman signals for R6G, indicating the remarkable enhancement effect on the AuNPs immobilized on HNTs. Three different concentrations of R6G aqueous solution (from 10^{-3} M to 10^{-6} M) were applied in the SERS test using AuNPs/HNTs as the SERS substrates and the results are shown in Fig. 10. Prominent Raman bands of R6G at 1650, 1505, 1362, 1305 and 1181 cm^{-1} are observed in Fig. 9 and 10. The peak at 1180 cm^{-1} is associated with C–C in-plane bend modes, and the signals between 1306 and 1650 cm^{-1} are due to aromatic C–C stretching vibrations.^{41,46} When the amount of R6G on the AuNPs/HNTs substrate was reduced to 10^{-6} M (1 mL aqueous solution), some peaks of R6G molecules were still observed, as shown in curve c, which contains the same characteristic Raman peaks of R6G in common with curves a and b. These indicated that the AuNPs/HNTs substrate possessed a relatively high surface enhancement efficiency and showed a promising prospect for application as SERS substrates.

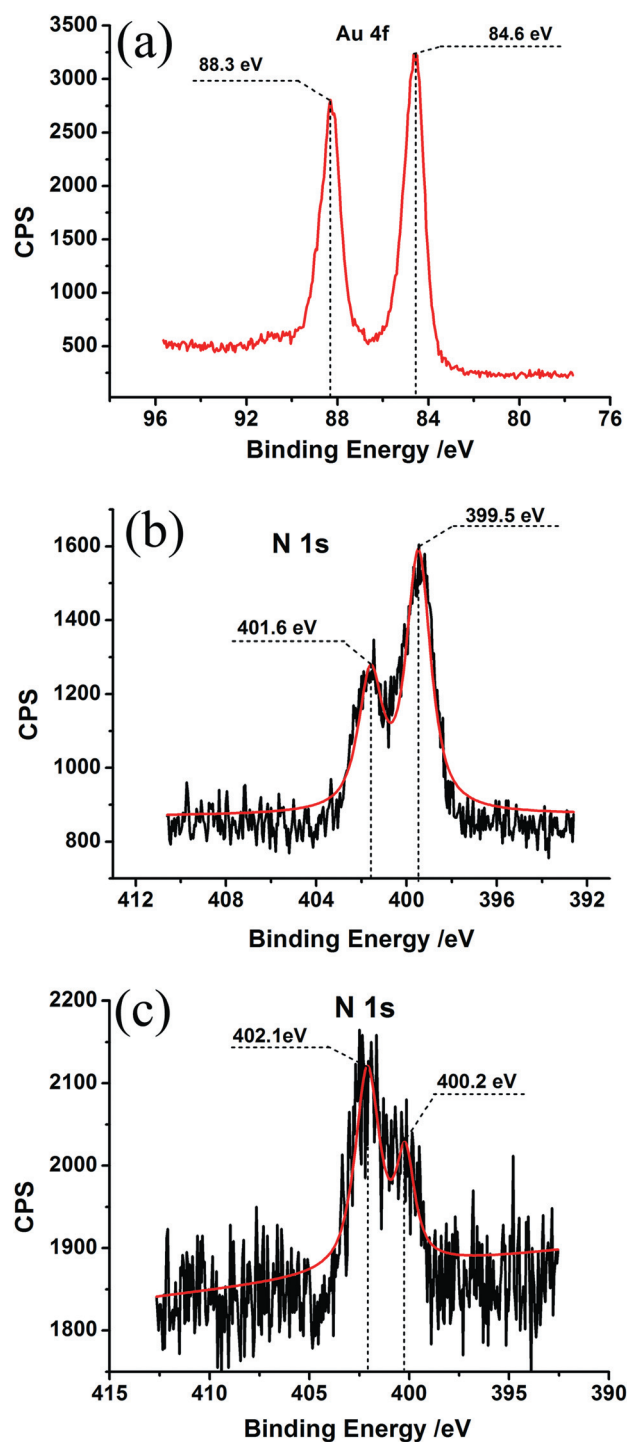


Fig. 8 XPS spectra of the functionalized HNTs before and after surface functionalization with AuNPs (a) Au 4f of AuNPs/HNTs; (b) N 1s of functionalized HNTs; (c) N 1s of AuNPs/HNTs.

According to the electromagnetic theory of SERS, the size, shape and proximity of nanostructures all affect the frequency and magnitude of the localized surface plasmons, *i.e.*, the degree of Raman enhancement.⁴³ The widely accepted SERS enhancement theory is electromagnetic enhancement at so-called 'hot spots' and several theoretical groups have investigated field enhancement for SERS from metal nanoparticle arrays. Garcia-Vidal and Pendry reported that very localized plasmon modes,⁴³

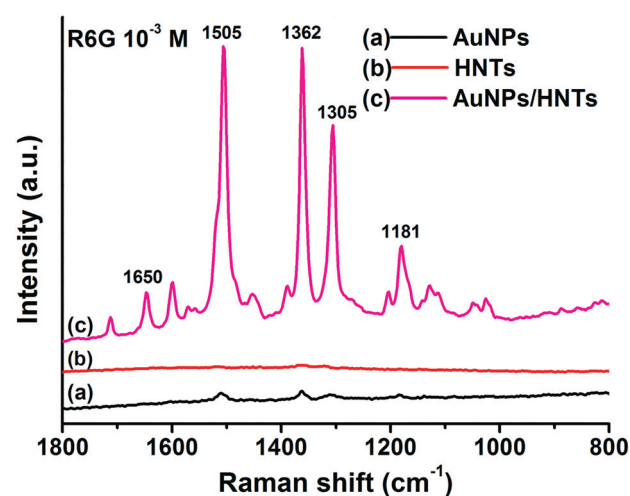


Fig. 9 SERS spectra of 1 mL 10^{-3} M R6G collected on (a) AuNPs in aqueous solution, (b) pure HNTs powder, (c) AuNPs/HNTs powder.

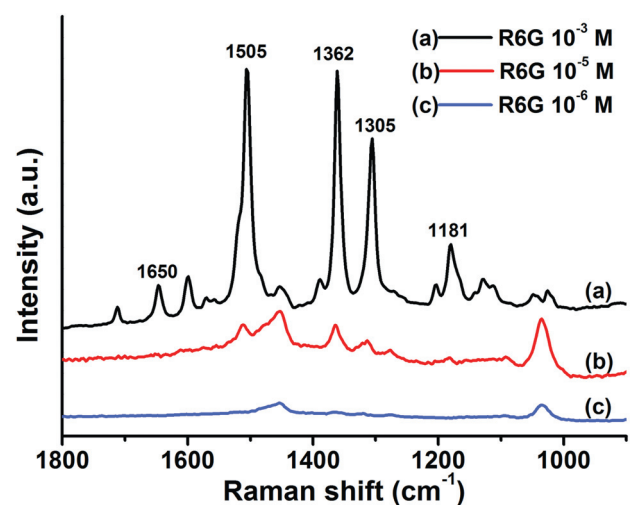


Fig. 10 SERS spectra obtained from AuNPs/HNTs with 1 mL of R6G solution of different concentrations: (a) 10^{-3} M R6G, (b) 10^{-5} M R6G and (c) 10^{-6} M R6G.

created by strong electromagnetic coupling between two adjacent metallic objects, dominate the SERS response in an array of nanostructures. In our present investigation, a large amount of AuNPs were densely dispersed on HNTs and the gaps among nanoparticles were about several nanometers, which can be seen in Fig. 4. According to the literatures,^{44,47–49} the interparticle-coupling-induced enhancement was attributed to the broadening of the plasmon resonance peak because the probability of the resonance covering both the excitation wavelength and the Raman peak increases with its width. Wang *et al.* have studied highly Raman-enhancing substrates based on silver nanoparticle arrays with tunable sub-10 nm gaps and pointed out the great SERS enhancement effect on a substrate with precisely controlled 'hot junctions' in the sub-10 nm region, which also confirmed the theoretical prediction of interparticle-coupling-induced Raman enhancement.⁴⁴ To investigate the localized surface plasmon resonance effect in the AuNPs/HNTs substrate, the UV-Vis spectra of AuNPs/HNTs was recorded by UV-Vis spectroscopy, as shown in Fig. 3S (see ESI†). Generally, the

peak shape and position of SPR in UV-Vis spectra are dependent on the size, shape, arrangement (*e.g.*, density and interparticle spacing) and the surrounding dielectric constant of AuNPs.^{32,41,50} In our present work, the AuNPs immobilized on HNTs with high density and close gaps between two nanoparticles, and the dipoles induced by plasmon resonance would couple and transmit on the whole substrate. Consequently, the plasmon resonance absorption of our substrate is broad and strong, which is evidence for the high enhancement effect of the AuNPs/HNTs substrate. Consequently, the roughness of AuNPs/HNTs and the characteristics of AuNPs, *i.e.*, size, low gaps, separation and high density, immobilized on HNTs may provide an optimum environment for the enhancement in Raman signals. The above results indicated that the AuNPs/HNTs substrate possessed a relatively high surface enhancement efficiency and showed a promising prospect for application as SERS substrates.

4. Conclusion

In the present investigation, a facile and green route was proposed to synthesise AuNPs/HNTs used for surface-enhanced Raman scattering substrates. HNTs were firstly functionalized with -NH_2 by *N*-(β -aminoethyl)- γ -aminopropyl trimethoxysilane (AEAPTES), which “anchors” Au ions to form a chelate complex. Then, with the addition of TP, the Au- NH_2 complexes can also chelate with the phenolic hydroxyls of TP and, meanwhile, the Au ions were reduced by TP. Besides the chelating effects, the TP can also be used as stabilizer to protect the AuNPs from aggregation. TEM, SEM and FE-SEM observations indicate that a large amount of Au nanoparticles were immobilized on HNTs. The AuNPs are irregularly spherical and densely dispersed on HNTs and the diameter of the nanoparticles varies from 20 to 40 nm. The chelating interactions between AuNPs and -NH_2 groups were verified by XPS spectra. The as-prepared AuNPs/HNTs nanomaterials with several nanometers gaps among nanoparticles were used as a unique surface-enhanced Raman scattering substrate, which possessed strong and distinctive Raman signals for R6G, indicating the remarkable enhancement effect of the AuNPs/HNTs.

Acknowledgements

This work is supported by the project of National Natural Science Foundation of China (NSFC) (Grant number: 50903072), Zhejiang Province Natural Science Foundation (Grant number: Y4100197) and Science Foundation of Zhejiang Sci-Tech University (ZSTU) under No. 0901803-Y.

References

- 1 P. Serp and E. Castillejos, *ChemCatChem*, 2010, **2**, 41–47.
- 2 X. L. Pan and X. H. Bao, *Chem. Commun.*, 2008, 6271–6281.
- 3 S. J. Guo, J. Li, W. Ren, D. Wen, S. J. Dong and E. K. Wang, *Chem. Mater.*, 2009, **21**, 2247–2257.
- 4 Y. M. Lvov, D. G. Shchukin, H. Mohwald and R. R. Price, *ACS Nano*, 2008, **2**, 814–820.
- 5 R. J. Wang, G. H. Jiang, Y. W. Ding, Y. Wang, X. K. Sun, X. H. Wang and W. X. Chen, *ACS Appl. Mater. Interfaces*, 2011, **3**, 4154–4158.
- 6 M. L. Du, B. C. Guo and D. M. Jia, *Polym. Int.*, 2010, **59**, 574–582.
- 7 M. L. Du, B. C. Guo, M. X. Liu, X. J. Cai and D. M. Jia, *Physica B*, 2010, **405**, 655–662.
- 8 C. Y. Wan, M. Li, X. Bai and Y. Zhang, *J. Phys. Chem. C*, 2009, **113**, 16238–16246.
- 9 L. Wang, J. L. Chen, L. Ge, Z. H. Zhu and V. Rudolph, *Energy Fuels*, 2011, **25**, 3408–3416.
- 10 M. X. Liu, B. C. Guo, M. L. Du, F. Chen and D. M. Jia, *Polymer*, 2009, **50**, 3022–3030.
- 11 P. Luo, J. S. Zhang, B. Zhang, J. H. Wang, Y. H. Zhao and J. D. Liu, *Ind. Eng. Chem. Res.*, 2011, **50**, 10246–10252.
- 12 X. Zhang, H. Wang and B. Q. Xu, *J. Phys. Chem. B*, 2005, **109**, 9678–9683.
- 13 D. Astruc, *Inorg. Chem.*, 2007, **46**, 1884–1894.
- 14 S. L. Smitha, K. G. Gopchandran, T. R. Ravindran and V. S. Prasad, *Nanotechnology*, 2011, **22**, 265705–265711.
- 15 Y. Qin, A. L. Pan, L. F. Liu, O. Moutanabbir, R. B. Yang and M. Knez, *ACS Nano*, 2011, **5**, 788–794.
- 16 R. M. Finch, N. A. Hodge, G. J. Hutchings, A. Meagher, Q. A. Pankhurst, M. R. H. Siddiqui, F. E. Wagner and R. Whyman, *Phys. Chem. Chem. Phys.*, 1999, **1**, 485–489.
- 17 F. Cardenas-Lizana, S. Gomez-Quero, N. Perret and M. A. Keane, *Catal. Sci. Technol.*, 2011, **1**, 652–661.
- 18 S. G. Jang, A. Khan, M. D. Dimitriou, B. J. Kim, N. A. Lynd, E. J. Kramer and C. J. Hawker, *Soft Matter*, 2011, **7**, 6255–6263.
- 19 S. Murru, A. A. Gallo and R. S. Srivastava, *ACS Catal.*, 2011, **1**, 29–31.
- 20 M. N. Nadagouda, G. Hoag, J. Collins and R. S. Varma, *Cryst. Growth Des.*, 2009, **9**, 4979–4983.
- 21 Y. Y. Jiang, X. J. Wu, Q. Li, J. J. Li and D. S. Xu, *Nanotechnology*, 2011, **22**, 385601–385607.
- 22 Y. J. Chen, G. H. Tian, K. Pan, C. G. Tian, J. Zhou, W. Zhou, Z. Y. Ren and H. G. Fu, *Dalton Trans.*, 2012, **41**, 1020–1026.
- 23 C. H. Lee, L. M. Tian, A. Abbas, R. Kattumenu and S. Singamaneni, *Nanotechnology*, 2011, **22**, 275311–275318.
- 24 J. Yin, T. Wu, J. B. Song, Q. Zhang, S. Y. Liu, R. Xu and H. W. Duan, *Chem. Mater.*, 2011, **23**, 4756–4764.
- 25 G. M. Kim, A. Wutzler, H. J. Radusch, G. H. Michler, P. Simon, R. A. Sperling and W. J. Parak, *Chem. Mater.*, 2005, **17**, 4949–4957.
- 26 M. C. Daniel and D. Astruc, *Chem. Rev.*, 2004, **104**, 293–346.
- 27 S. J. Guo and E. Wang, *Nano Today*, 2011, **6**, 240–264.
- 28 M. N. Nadagouda and R. S. Varma, *Green Chem.*, 2008, **10**, 859–862.
- 29 E. Gonzalez, J. Arbiol and V. F. Puntes, *Science*, 2011, **334**, 1377–1380.
- 30 W. J. Parak, *Science*, 2011, **334**, 1359–1360.
- 31 H. Wu, X. Huang, M. M. Gao, X. P. Liao and B. Shi, *Green Chem.*, 2011, **13**, 651–658.
- 32 H. Zhu, M. L. Du, M. L. Zou, C. S. Xu, N. Li and Y. Q. Fu, *J. Mater. Chem.*, 2012, **22**, 9301–9307.
- 33 M. C. Moulton, L. K. Braydich-Stolle, M. N. Nadagouda, S. Kunzelman, S. M. Hussain and R. S. Varma, *Nanoscale*, 2010, **2**, 763–770.
- 34 L. Peng, X. X. Wang, X. G. Shi, C. G. Li, C. G. Ye and X. H. Song, *Food Chem.*, 2011, **129**, 1475–1482.
- 35 H. Y. Jiang, T. Shii, Y. Matsuo, T. Tanaka, Z. H. Jiang and I. Kouno, *Food Chem.*, 2011, **129**, 830–836.
- 36 C. Deng, N. Yao, X. Lu, S. X. Qu, B. Feng, J. Weng and X. B. Yang, *J. Mater. Sci.*, 2009, **44**, 4394–4398.
- 37 I. Gorelikov and N. Matsuura, *Nano Lett.*, 2008, **8**, 369–373.
- 38 J. M. Pan, H. Yao, L. C. Xu, H. X. Ou, P. W. Huo, X. X. Li and Y. S. Yan, *J. Phys. Chem. C*, 2011, **115**, 5440–5449.
- 39 G. Ma, X. G. Yue, S. L. Zhang, C. R. Rong, L. F. Wang, G. B. Wang and H. L. Wang, *Polym. Eng. Sci.*, 2011, **51**, 1051–1058.
- 40 Y. Negishi, K. Nobusada and T. Tsukuda, *J. Am. Chem. Soc.*, 2005, **127**, 5261.
- 41 M. F. Peng, J. Gao, P. P. Zhang, Y. Li, X. H. Sun and S. T. Lee, *Chem. Mater.*, 2011, **23**, 3296–3301.
- 42 J. X. Fang, S. Y. Du, S. G. Lebedkin, Z. Y. Li, R. Kruk, M. Kappes and H. Hahn, *Nano Lett.*, 2010, **10**, 5006–5013.
- 43 H. H. Wang, C. Y. Liu, S. B. Wu, N. W. Liu, C. Y. Peng, T. H. Chan, C. F. Hsu, J. K. Wang and Y. L. Wang, *Adv. Mater.*, 2006, **18**, 491–495.
- 44 H. Wang and J. N. Halas, *Adv. Mater.*, 2008, **20**, 820–825.
- 45 D. He, B. Hu, Q. F. Yao, K. Wang and S. H. Yu, *ACS Nano*, 2009, **12**, 3993–4002.
- 46 P. Hildebrandt and M. J. Stockburger, *Phys. Chem.*, 1984, **88**, 5935–5944.
- 47 C. F. Tian, *et al.*, *Nanotechnology*, 2012, **23**, 165604–165610.
- 48 Y. H. Feng, S. X. Xing, J. Xu, H. Wang, J. W. Lim and H. Y. Chen, *Dalton Trans.*, 2010, **39**, 349–351.
- 49 C. Q. Chen, Y. H. Zheng, Y. Y. Zhan, X. Y. Lin, Q. Zheng and K. M. Wei, *Dalton Trans.*, 2011, **40**, 9566–9570.
- 50 J. He, P. Zhang, J. L. Gong and Z. H. Nie, *Chem. Commun.*, 2012, DOI: 10.1039/c2cc32070c.

Selective growth of Au nanograins on specific positions (tips, edges and facets) of Cu₂O octahedrons to form Cu₂O–Au hierarchical heterostructures†Han Zhu,^a MingLiang Du,^{*a,b} DongLiang Yu,^a Yin Wang,^c MeiLing Zou,^a CongSheng Xu^a and YaQin Fu^{a,b}

Received 6th July 2012, Accepted 30th July 2012

DOI: 10.1039/c2dt31487h

This communication demonstrates a novel strategy for the selective growth of Au nanograins (AuNGs) on specific positions (tips, edges and facets) of Cu₂O octahedrons to form Cu₂O–Au hierarchical heterostructures. The surface energy distribution of the octahedrons generally follows the order of $\gamma_{\text{(facets)}} < \gamma_{\text{(edges)}} < \gamma_{\text{(tips)}}$ and leads to the preferential growth and evolution of the heterostructures. These novel Cu₂O–Au hierarchical heterostructures show fascinating degradations of methylene blue (MB), due to the suppressed electron/hole recombination phenomena and the highly efficient light harvesting.

The rational growth of heterostructure nanocrystals with multiple components and tailored geometries is of significant interest because of their multifunctional properties and new features arising from the effective coupling of their different domains.^{1,2} The attraction of multicomponent nanostructures is that multiple functions can be incorporated into one system for specific applications and for fascinating new properties induced by the hetero-interfaces.^{3,4} In such systems, each component usually retains its original properties while modifications are confined to the interfacial region, which is much smaller than the entire system. In nanomaterials, however, new properties can be attained by combining several materials in the same nanosystem, where, due to the small size, the effect of synergetic properties of the separate components may become a dominant factor.^{4–6} For example, Kong *et al.* prepared size-controlled Au@Cu₂O octahedral structures that exhibited excellent photocatalytic activity toward organic degradation.⁷ Therefore, understanding and manipulating the semiconductor/metal interfacial structures is not only critical to enhance the desired properties of the composite materials, but also offers a new opportunity for discovering multifunctional materials with potentially exciting and unique properties.

Cu₂O as a p-type semiconductor with a direct band gap of 2.17 eV, is a material with prospective applications in photocatalysis,^{7,8} solar energy conversion,⁹ gas sensors,¹⁰ negative electrode material for lithium-ion batteries,¹¹ templates,^{6,12,13} antibacterial activity,¹⁴ solar-driven water splitting,¹⁵ and metal-insulator-metal resistive switching memory.¹⁴ In the past decade, noble metal–Cu₂O heterostructures have been attracting much attention to understand the structure–property relationships. Qin *et al.* prepared micro-sized Au cubic cages with hierarchical structures using Cu₂O cubes as the starting material and these showed great microwave absorption capability.¹³ Liu *et al.* have studied the selective growth of Au nanoparticles on different facets of Cu₂O microcrystals with enhanced electrocatalytic properties, indicating that the Au nanoparticles were preferentially deposited on the {111} facets because of the different surface energy between the {111} and {100} planes of Cu₂O crystals.⁵ Meanwhile, Gao *et al.* reported that with the activated and shaped tips on Au petals, secondary metal structures of silver were directionally constructed on the Au flowers to generate the subsequent Au–Ag bimetallic heterostructured flowers.⁴ For Cu₂O–Au heterostructures, an interesting question is whether the Au nanoparticles could also selectively grow on the same facets but in different positions such as tips or edges. However, so far, it is still a challenge to achieve selective growth only on specific positions of the seed surface, especially only on the edges or facets, and to prepare nanoparticles with edges or facets selectively coated by other substances.^{16,17} This kind of selective growth is significant to the nanoscaled adjustments (structures and properties) and the preparation of novel nanostructures.

In this work, a novel Cu₂O–Au hierarchical heterostructure is reported in which Au nanograins (AuNGs) can preferentially grow on the activated and sharpened tips and edges of Cu₂O octahedrons. Unexpectedly, after the octahedrons were completely encapsulated by AuNGs layers, an unimagined nanostructure, Au nanowhiskers (AuNWs), were homogeneously formed on the AuNGs layers. In this growth process, small Au nanoparticles (AuNPs) acted as the nucleation centres of the AuNWs and with the catalysis of the pre-formed small AuNPs, the new Au nuclei continued to grow, aligned along the growth direction of the {111} axes, to form AuNWs. In the present work, we firstly prepared octahedron shaped Cu₂O crystals without any surfactants to eliminate the influence of surfactants for the selective growth of AuNGs. The procedure used to synthesize the octahedron shaped Cu₂O crystals and Cu₂O–Au heterostructures with various morphologies were shown in Scheme 1S and

^aDepartment of Materials Engineering, College of Materials and Textile, Zhejiang Sci-Tech University, Hangzhou 310018, P. R. China

^bKey Laboratory of Advanced Textile Materials and Manufacturing Technology, Zhejiang Sci-Tech University, Ministry of Education, Hangzhou 310018, P. R. China. E-mail: du@zstu.edu.cn; Tel: +86-571-86843255

^cMOE Key Laboratory of Macromolecular Synthesis and Functionalization, Department of Polymer Science and Engineering, Zhejiang University, Hangzhou 310027, China

†Electronic supplementary information (ESI) available. See DOI: 10.1039/c2dt31487h

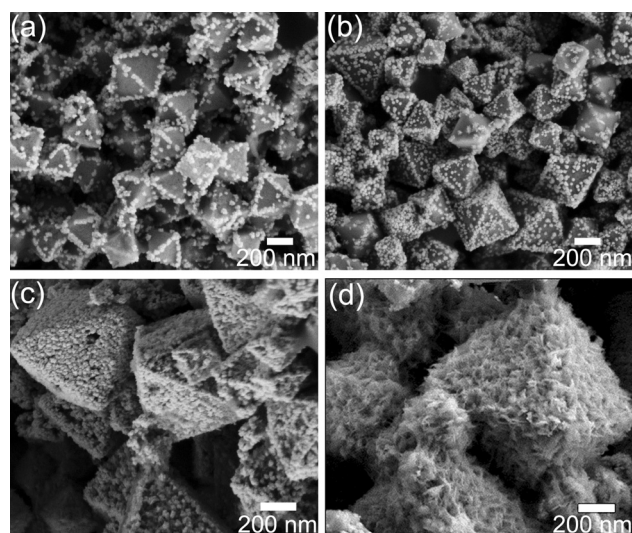


Fig. 1 (a)–(d) FE-SEM images of the AuNGs selectively grown on Cu_2O octahedron shaped crystals with different HAuCl_4 volumes: (a) 0.25 mL, (b) 0.50 mL, (c) 0.75 mL and (d) 1.00 mL. The concentration of the HAuCl_4 aqueous solution is 5 mM.

Table 1S (see ESI†). Through a galvanic reaction, AuCl_4^- ions can be reduced by Cu_2O crystals directly at room temperature. With the increasing amount of AuCl_4^- , four novel architectures are obtained, and there are AuNGs grown along the crystal edges of Cu_2O octahedrons, AuNGs grown on the crystal facets of the Cu_2O octahedrons, Cu_2O octahedrons encapsulated by a layer of AuNGs and the AuNWs grown on AuNGs layers. Detailed experiments can be found in the ESI.†

As exemplified in Fig. 1a, it was found that most of the AuNGs with an average diameter of 27.4 ± 4.2 nm (Fig. S1, see ESI†) selectively grow on the crystal edges of the Cu_2O octahedron shaped crystals, and energy-dispersive X-ray (EDS) analysis confirms the existence of Au (Fig. 3c). From Fig. 1b, following an increasing volume of AuCl_4^- , not only the crystal edges are covered by AuNGs, but also the $\{111\}$ facets of the Cu_2O octahedron shaped crystals. After preferentially growing on the crystal edges, numerous AuNGs are then homogeneously formed on the surface of the Cu_2O octahedrons, which is shown in Fig. 1c. With a further increase of the number of formed AuNGs, the surfaces of the Cu_2O octahedrons become rough as these AuNGs have joined together to form a solid facet, resulting in the Cu_2O octahedrons being completely encapsulated by a layer of irregular arranged AuNGs. In addition, there are some pores and splits on the AuNG layers, indicating that the AuNG layers were fabricated by etching out Cu_2O portions, which can confirm the galvanic reaction between Cu_2O and AuCl_4^- (Fig. S2, see ESI†). When the volume of AuCl_4^- increases to 1 mL, as seen in Fig. 1d, a large amount of AuNWs are homogeneously fabricated on the surface of AuNG layers. The AuNWs produced using this method range from 20 to 60 nm in length (Fig. S3, see ESI†).

Further studies were contemplated to understand the growth mechanism, we monitored the concentration-dependent Cu_2O –Au hierarchical heterostructures using transmission electron microscopy (TEM) and X-ray diffraction pattern (XRD) analyses. Fig. 2a–f show the TEM images of the structures

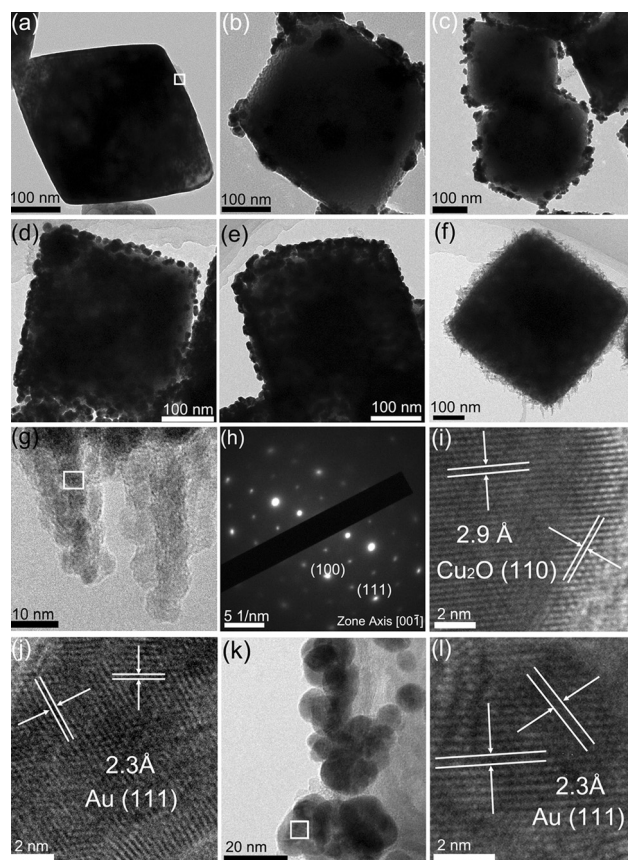


Fig. 2 TEM images of the process of the selective growth of AuNGs on Cu_2O octahedron shaped crystals with different volumes of HAuCl_4 : (a) 0.00 mL, (b) 0.15 mL, (c) 0.25 mL, (d) 0.50 mL, (e) 0.75 mL and (f) 1.00 mL. Higher-magnification TEM image of (g) the AuNWs and (k) the AuNGs. (h) Selected area electron diffraction (SAED) pattern and (i) HRTEM image of the square region of the octahedron shaped Cu_2O crystals. HRTEM images of the square regions of (j) AuNWs and (l) AuNGs.

obtained from different volumes (0.00, 0.15, 0.25, 0.5, 0.75 and 1 mL, respectively) of HAuCl_4 . The Cu_2O octahedrons ranging from 200 nm to 300 nm (Fig. S5, see ESI†) with smooth edges and $\{111\}$ facets are shown in Fig. 2a and the SAED pattern shows the diffraction spots of Cu_2O , confirming the single crystal structure of the Cu_2O octahedron, which is shown in Fig. 2h. More TEM and FE-SEM images are shown in Fig. S4.† The HRTEM images taken near the particle edges reveal distinct lattice fringes with d spacings of 2.9 Å, which correspond to the $\{110\}$ lattice planes of Cu_2O . As shown in Fig. 2b, only the tips of the octahedron are overgrown with AuNGs, and upon increasing the volume of HAuCl_4 to 0.25 mL, the AuNGs start to form on the crystal edges, which are shown in Fig. 2c. Fig. 2k shows the higher-magnification TEM image of the AuNGs, and these AuNGs are comprised of several small nanoparticles ranging from 5 to 10 nm in diameter. From Fig. 2d, after the AuNGs are completely arrayed along the crystal edges, the AuNGs begin to grow on the $\{111\}$ facets of the octahedrons. Due to the continuous growth of AuNGs on the $\{111\}$ facets, the AuNGs are packed densely on the surface of the Cu_2O octahedrons until they completely cover the octahedrons, which can be seen in

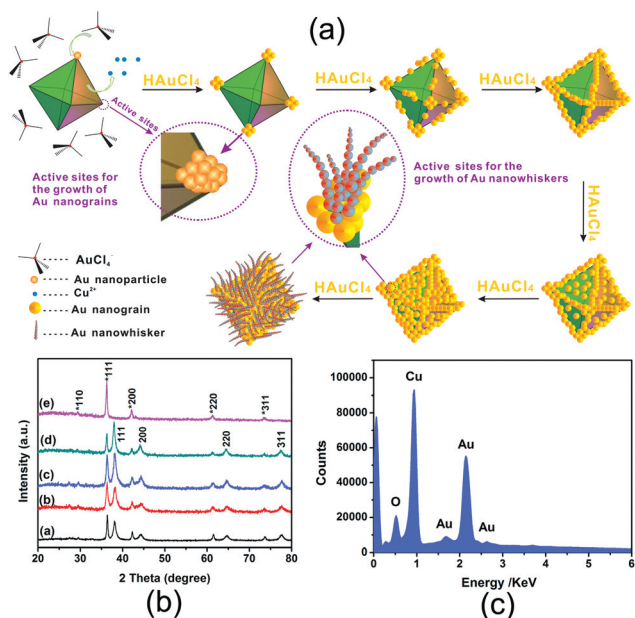


Fig. 3 (a) Schematic illustration of the selective growth process of the AuNGs on Cu₂O octahedrons. (b) XRD patterns of the intermediate products obtained at different concentrations of Au³⁺ ions during the transformation process of the octahedron Cu₂O crystals to the Cu₂O–Au hierarchical heterostructures. The volumes of HAuCl₄ (5 mM) are (a) 0.25 mL, (b) 0.5 mL, (c) 0.75 mL, (d) 1 mL, and (e) 0.00 mL, respectively. (c) EDS spectrum of the AuNGs grown on the edges of Cu₂O octahedrons (0.25 mL HAuCl₄).

Fig. 2e. When the volume of HAuCl₄ is further increased to 1 mL, a large amount of vimineous AuNWs are uniformly formed on the AuNGs layers with lengths ranging from 30 to 60 nm. Fig. 2g shows that small AuNPs accumulated along the growth direction to form the AuNWs. In addition, the HRTEM images (Fig. 2j and 2l) of the square regions of the AuNWs and AuNGs show fringe spacings of 2.3 Å that correspond to interplanar separation between the {111} planes, indicating that the growth direction of the AuNWs was along the {111} axes.

The present selective growth process is schematically illustrated in Fig. 3a. The driving force for the *in situ* reduction of AuCl₄⁻ on the Cu₂O octahedrons is ascribed to the standard reduction potential difference between AuCl₄⁻/Au (0.99 V vs. standard hydrogen electrode (SHE)) and Cu⁺/Cu₂O (0.203 V vs. SHE) pairs; that is, AuCl₄⁻ injected into the Cu₂O colloid solution can be immediately reduced by Cu₂O at room temperature.^{3,4,12} The different positions of the facets of the Cu₂O octahedrons possess different surface energy, and the surface energy distribution of the octahedrons generally follows the order of $\gamma_{\text{facets}} < \gamma_{\text{edges}} < \gamma_{\text{tips}}$.^{17–20} Therefore, the diversity of the surface energy of the same facets of the Cu₂O crystals at different positions, such as tips and edges, would lead to the preferential growth of the metal nanoparticles. As illustrated in Fig. 3a, the AuCl₄⁻ ions were preferentially adsorbed on the tips (active sites) of the octahedrons because of their highest surface energy, and then they formed Au nuclei through a galvanic reaction.^{16–18,21} More and more AuNPs formed and developed into AuNGs directly in order to reduce the surface energy of the octahedrons. These AuNGs were formed by small Au

nanoparticles through coalescence and continuous growth in some regions on the surface of the octahedrons.

After the preferential growth on the tips, the AuNGs continued to grow along the edges (these possess the next-highest surface energy) of the octahedrons and further reduced the surface energy. When the surface energy of the tips and edges were reduced to the same level as that of the {111} facets of the octahedrons, the AuNGs were no longer grown on the tips and edges instead of the {111} facets. With further growth, the Cu₂O octahedrons were completely covered by AuNG layers. When the volume of the Au precursors was increased further, due to the porous structure of the AuNG layers, AuCl₄⁻ ions can diffuse into the shell and react with the inner Cu₂O crystals. The previously formed small AuNPs can serve as nucleation centers in the growth of AuNWs. At the catalysis of the small AuNPs,^{18,22,23} new Au nuclei grew continuously, aligned along the growth direction of the {111} axes to form AuNWs.

The identity and detailed crystal structure of the as-prepared Cu₂O–Au hierarchical heterostructures were analyzed using XRD characterization. The curve e (in Fig. 3(b)) shows the XRD pattern of Cu₂O crystals and all the diffraction peaks located at 29.55°, 36.42°, 42.30°, 61.34° and 73.53° (as shown in Fig. 3(b), labelled with *) can be indexed as the octahedron phases of the Cu₂O crystal (JCPDS:05-0677).^{24,25} No other impurity peaks could be detected, confirming the formation of phase-pure Cu₂O. From Fig. 3(b) (from curve a to curve d), the XRD patterns of the obtained Cu₂O–Au hierarchical heterostructures suggest that the products consist of both Cu₂O and Au crystals. All the new emerging peaks, located at 38.19°, 44.39°, 64.58° and 81.72°, can be indexed as crystalline Au (JCPDS: 65-2870),^{26,27} indicating that the AuNGs were successfully formed, that is, AuCl₄⁻ can be spontaneously reduced onto the surfaces of Cu₂O without additional reductive agents at room temperature. With the increasing concentration of Au³⁺ ions from 0.25 mL to 1 mL (Fig. 3(b), from curve a to curve d), the intensity of the Au crystal peaks ({111}, {200}, {220}, {311}) became stronger, while the peaks of the Cu₂O signal (*111, *200, *220, *311) became weaker. This is consistent with the evolution processes of AuNGs grown on the surfaces of Cu₂O octahedrons. Meanwhile, it is speculated that the decreasing intensity of the Cu₂O crystal peaks was mainly caused by the etching of Cu₂O during the transformation process.

As previous research reported, Cu₂O has been used as a photocatalyst for hydrogen production and for the degradation of organic pollutants under visible light irradiation.^{5,7,13} We investigated the photocatalytic performance of Cu₂O octahedrons and the as-prepared Cu₂O–Au hierarchical heterostructures towards the degradation of an organic reagent, methylene blue (MB) under a fluorescent lamp for 3 h. Fig. 4 shows the degradation (C/C₀) of MB at different reaction times and the final degradations and photographs of the MB solution after irradiation for 3 h using various photocatalysts. In a control experiment, when MB was exposed to the fluorescent lamp in the presence of H₂O₂, this led to ca. 25% degradation of MB (see Fig. S6 and S7 in the ESI† for detailed information). As expected, the presence of Cu₂O octahedrons led to obvious increases in the photodegradation of MB to ca. 68%, indicating that these Cu₂O octahedrons were photoactive and had the ability to facilitate the degradation of MB. With the selective growth of AuNGs on the

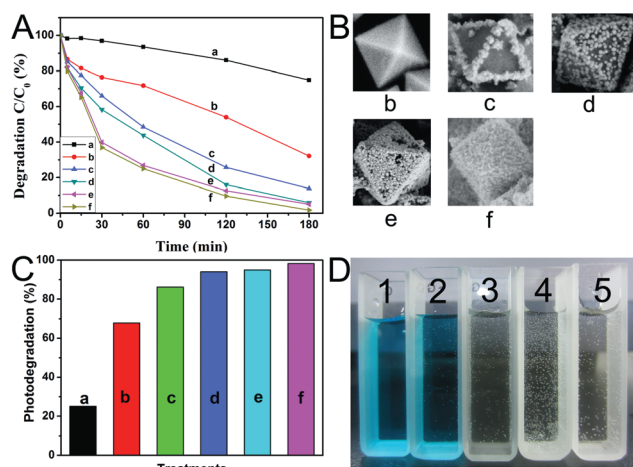


Fig. 4 (A) Degradations of MB expressed as a reduction in the intensity of absorbance of 664 nm at different irradiation times with different photocatalysts: (a) H_2O_2 , (b) Cu_2O octahedrons and AuNGs grown on Cu_2O octahedrons with different volumes of HAuCl_4 : (c) 0.25 mL, (d) 0.50 mL, (e) 0.75 mL and (f) 1.00 mL. (B) The morphologies of the corresponding photocatalysts (b–f). (C) The final percentage of photodegradation of MB as a reduction in the intensity of absorbance at 664 nm and all the samples (a–f) were under a irradiated under a fluorescent lamp (25 W, $\lambda > 400$ nm) for 3 h. (D) Photographs of the MB solution after irradiation for 3 h in the absence of H_2O_2 (1) and the presence of H_2O_2 (300 μL) (2), and in the presence of Cu_2O –Au hierarchical heterostructures (samples 3–5 are in accordance with c, e and f).

Cu_2O octahedrons, these Cu_2O –Au hierarchical heterostructures show a considerably enhanced photocatalytic activity for the degradation of MB, from *ca.* 86% to *ca.* 95%. In our metal–semiconductor systems, during the photoexcitation, electrons can migrate from the semiconductor to the metal across the Schottky barrier, where they are trapped and the electron/hole recombination phenomena are suppressed. Therefore, the hole is free to diffuse through Cu_2O to the surface where it can be used to oxidize the MB molecules. The AuNGs growth along the crystal edges of the Cu_2O octahedrons allowed *ca.* 86% degradation of MB, and with the increasing AuNGs formed on the {111} crystal facets of the Cu_2O octahedrons, the degradations improved to 94%. When the Cu_2O octahedrons were completely encapsulated by a AuNG layer, 95% degradation of MB was obtained, and the indistinctive enhanced photocatalytic activity may be partially ascribed to the relatively higher Au loading in this architecture, which might decrease the total effective Cu_2O surface area during the photocatalytic degradation of MB. Compared with the above materials' photocatalytic degradations, the AuNGs obtained the highest degradation of MB at *ca.* 98%. The AuNGs grown on the surface of AuNG layers could afford more active surface area, which can offset the negative effects of photocatalytic activity caused by higher Au loading, and this enhanced photocatalytic activity was mainly attributed to the enlarged active surface area of the AuNGs. In addition, the UV-Vis spectra of the Cu_2O octahedrons and Cu_2O –AuNGs heterostructures before and after photocatalysis were investigated, which are shown in Fig. 8S.† A weak absorption band, centered at 543 nm, was caused by the Cu_2O octahedrons (Fig. 8SA, see ESI†) and, after the photocatalysis, there is nearly

no change of the Cu_2O absorption band, indicating that the surface optical properties of the material remain the same. Meanwhile, as shown in Fig. 8SB, after the growth of the AuNGs, the Cu_2O –AuNGs display obvious visible light absorption ranging from 450 to 900 nm because of the localized surface plasmon resonance of the AuNGs, presenting highly efficient light harvesting. After the photocatalysis, the absorption band centered at 545 increases to 574 nm, indicating that the noble-metal cocatalysts enhance the quantum yield of the photoinduced electron-transfer processes.^{28,29}

Conclusions

In summary, we have demonstrated a novel approach for the selective growth of AuNGs on specific positions of Cu_2O octahedrons to form Cu_2O –Au hierarchical heterostructures with various Au nanostructures. FE-SEM, TEM, and XRD were used to study the morphologies, microstructures and crystal structures of these Cu_2O –Au hierarchical heterostructures, clearly indicating the selective growth process as a result of the diversity of surface energy of the facets of Cu_2O crystals at different positions such as tips and edges. In photocatalytic experiments, these Cu_2O –Au hierarchical heterostructures show fascinating degradations of MB, due to the suppressed electron/hole recombination phenomena. Due to this, the hole is free to diffuse through Cu_2O to the surface where it can be used to oxidize MB molecules. This strategy offers a new opportunity for discovering multifunctional materials with potentially exciting and unique properties.

Acknowledgements

We acknowledge the support of the project of National Natural Science Foundation of China (NSFC) (grant number: 50903072), Zhejiang Province Natural Science Foundation (grant number: Y4100197) and Science Foundation of Zhejiang Sci-Tech University (ZSTU) under number 0901803-Y.

Notes and references

- 1 L. Q. Mai, F. Yang, Y. L. Zhao, X. Xu, L. Xu and Y. Z. Luo, *Nat. Commun.*, 2011, **2**, 381.
- 2 H. G. Yang, C. H. Sun, S. Z. Qiao, J. Zou, G. Liu, S. C. Smith, H. M. Cheng and G. Q. Lu, *Nature*, 2008, **453**, 638–641.
- 3 C. H. Kuo, Y. C. Yang, S. J. Gwo and M. H. Huang, *J. Am. Chem. Soc.*, 2011, **133**, 1052–1057.
- 4 L. Gao, L. Z. Fan and J. Zhang, *Langmuir*, 2009, **25**, 11844–11848.
- 5 X. W. Liu, *Langmuir*, 2011, **27**, 9100–9104.
- 6 X. W. Liu, *RSC Adv.*, 2011, **1**, 1119–1125.
- 7 L. N. Kong, W. Chen, D. K. Ma, Y. Yang, S. S. Liu and S. M. Huang, *J. Mater. Chem.*, 2012, **22**, 719–724.
- 8 Y. H. Liang, L. Shang, T. Bian, C. Zhou, D. H. Zhang, H. J. Yu, H. T. Xu, Z. Shi, T. R. Zhang, L. Z. Wu and C. H. Tung, *CrystEngComm*, 2012, **14**, 4431–4436.
- 9 L. Suljo, C. Phillip and B. I. David, *Nat. Mater.*, 2011, **10**, 911–921.
- 10 L. L. Duan, F. Bozoglian, S. Mandal, B. Stewart, T. Privalov, A. Llobet and L. C. Sun, *Nat. Chem.*, 2012, **4**, 418–423.
- 11 J. Liu, S. Z. Qiao, J. S. Chen, X. W. Lou, X. R. Xing and G. Q. Lu, *Chem. Commun.*, 2011, **47**, 12578–12591.
- 12 F. Hong, S. D. Sun, H. J. You, S. C. Yang, J. X. Fang, S. W. Guo, Z. M. Yang, B. J. Ding and X. P. Song, *Cryst. Growth Des.*, 2011, **11**, 3694–3697.

- 13 Y. Qin, R. C. Che, C. Y. Liang, J. Zhang and Z. W. Wen, *J. Mater. Chem.*, 2011, **21**, 3960–3965.
- 14 S. D. Sun, X. P. Song, Y. X. Sun, D. C. Deng and Z. M. Yang, *Catal. Sci. Technol.*, 2012, **2**, 925–930.
- 15 S. Fukuzumi, T. Kishi, H. Kotani, Y. M. Lee and W. W. Nam, *Nat. Chem.*, 2011, **3**, 38–41.
- 16 N. N. Fan, Y. Yang, W. F. Wang, L. J. Zhang, W. Chen, C. Zou and S. M. Huang, *ACS Nano*, 2012, **6**, 4072–4082.
- 17 T. T. Tran and X. M. Lu, *J. Phys. Chem. C*, 2011, **115**, 3638–3645.
- 18 S. A. Dayeh, E. T. Yu and D. L. Wang, *J. Phys. Chem. C*, 2007, **111**, 13331–13336.
- 19 Z. C. Xu, E. Lai, S. H. Yang and H. S. Kimberly, *Chem. Commun.*, 2012, **48**, 5626–5628.
- 20 G. R. Zhang, D. Zhao, Y. Y. Feng, B. S. Zhang, D. S. Su, G. Liu and B. Q. Xu, *ACS Nano*, 2012, **6**, 2226–2236.
- 21 C. G. Read, E. M. P. Steinmiller and K. S. Choi, *J. Am. Chem. Soc.*, 2009, **131**, 12040–12041.
- 22 M. A. Mahmoud, W. Qian and M. A. El-Sayed, *Nano Lett.*, 2011, **11**, 3285–3289.
- 23 C. H. Kuo, T. E. Hua and M. H. Huang, *J. Am. Chem. Soc.*, 2009, **131**, 17871–17878.
- 24 P. Lignier, R. Bellabarba and R. T. P. Tooze, *Chem. Soc. Rev.*, 2012, **41**, 1708–1720.
- 25 W. C. Huang, L. M. Lyu, Y. Ch. Yang and M. H. Huang, *J. Am. Chem. Soc.*, 2012, **134**, 1261–1267.
- 26 H. Zhu, M. L. Du, M. L. Zou, C. S. Xu, N. Li and Y. Q. Fu, *J. Mater. Chem.*, 2012, **22**, 9301–9307.
- 27 H. Zhu, M. L. Du, M. L. Zou, C. S. Xu and Y. Q. Fu, *Dalton Trans.*, 2012, DOI: 10.1039/c2dt30998j.
- 28 P. V. Kamat, *J. Phys. Chem. Lett.*, 2012, **3**, 663–672.
- 29 M. Achermann, *J. Phys. Chem. Lett.*, 2010, **1**, 2837–2843.

AgNPs/PVA and AgNPs/(PVA/PEI) hybrids: preparation, morphology and antibacterial activity

This article has been downloaded from IOPscience. Please scroll down to see the full text article.

2013 J. Phys. D: Appl. Phys. 46 345303

(<http://iopscience.iop.org/0022-3727/46/34/345303>)

View [the table of contents for this issue](#), or go to the [journal homepage](#) for more

Download details:

IP Address: 130.240.43.43

The article was downloaded on 14/08/2013 at 10:37

Please note that [terms and conditions apply](#).

AgNPs/PVA and AgNPs/(PVA/PEI) hybrids: preparation, morphology and antibacterial activity

Pan Wang², Han Zhu², Shiyong Bao², MingLiang Du^{1,2} and Ming Zhang^{1,2}

¹ Key Laboratory of Advanced Textile Materials and Manufacturing Technology, Zhejiang Sci-Tech University, Ministry of Education, Hangzhou 310018, People's Republic of China

² Department of Materials Engineering, College of Materials and Textile, Zhejiang Sci-Tech University, Hangzhou 310018, People's Republic of China

E-mail: du@zstu.edu.cn

Received 9 April 2013

Published 6 August 2013

Online at stacks.iop.org/JPhysD/46/345303

Abstract

Two strategies are demonstrated to fabricate AgNPs/PVA and AgNPs/(PVA/PEI) nanofibre hybrids. In the first approach, we synthesized AgNPs in poly(vinylalcohol) (PVA) solution and then electrospun the AgNPs/PVA solution into the AgNPs/PVA nanofibres. In the other one, the polyethylenimine (PEI) was introduced to improve the water-stability of PVA and then the AgNPs were immobilized on electrospun PVA/PEI nanofibres to fabricate the AgNPs/(PVA/PEI) nanofibres. Field-emission scanning electron microscopy, transmission electron microscopy, ultraviolet–visible spectroscopy and x-ray photoelectron spectroscopy (XPS) were utilized to investigate the morphology and the growth mechanism of the hybrids. The investigations demonstrate that both of the obtained AgNPs/PVA hybrids and AgNPs/(PVA/PEI) hybrids exhibit good water-stability and good antibacterial activity against *E. coli* and *S. aureus*.

(Some figures may appear in colour only in the online journal)

1. Introduction

In recent years, with the steady and fast-growing field of nanoscience and nanotechnology, nanosized noble metal particles have attracted plenty of attention because of their tempting properties in physics (such as electronic and optical devices), biotechnology (such as biosensing and antimicrobial agents), chemistry (such as catalyst and initiator) and so on [1–3]. Among them, Ag nanoparticles (AgNPs) are efficient and cost-effective noble metal nanoparticles; their special structure makes them possess particle effect, surface effect, quantum size effect and macroscopic quantum tunnelling effect, all of which allow AgNPs to have wide applications in many fields. Due to the marked interaction with biopolymer (such as enzyme, DNA, cell wall and cell membrane) effectively in bacteria, AgNPs exhibit excellent applications especially in biotechnology, such as antimicrobial agent. Weiss and Kriegel *et al* have already demonstrated a number of applications of the antibacterial activity of AgNPs [4, 5].

However, naked AgNPs are easily oxidized during storage and tend to aggregate due to their high surface energy [6, 7], resulting in a remarkable reduction in their antibacterial activity. Therefore, much attention has been focused on the synthesis of small-size and highly dispersed AgNPs [8]. As we know, essentially, there are two strategies that have been used to obtain small-size AgNPs with high dispersion: one is the introduction of AgNPs on/into solid supports (including polymeric membrane, metal oxide, carbon and so forth) [8–11] with different nanostructures (such as nanotubes, fibres, spheres and so on) [8, 12–17] to form composite structure. The other strategy is to put the small-size AgNPs into colloidal solutions containing complexes or surfactants with polymer ligands [8, 18, 19]. However, this process can cause loss in the activity of AgNPs. Meanwhile, the small-size AgNPs can lead to difficulty in sedimentation from the solution, so their recycling is not satisfactory for large-scale applications. Therefore, the first method seems to be better. Nanostructures materials, such as nanotubes and spheres are time-consuming and costly, which make them unsuitable for

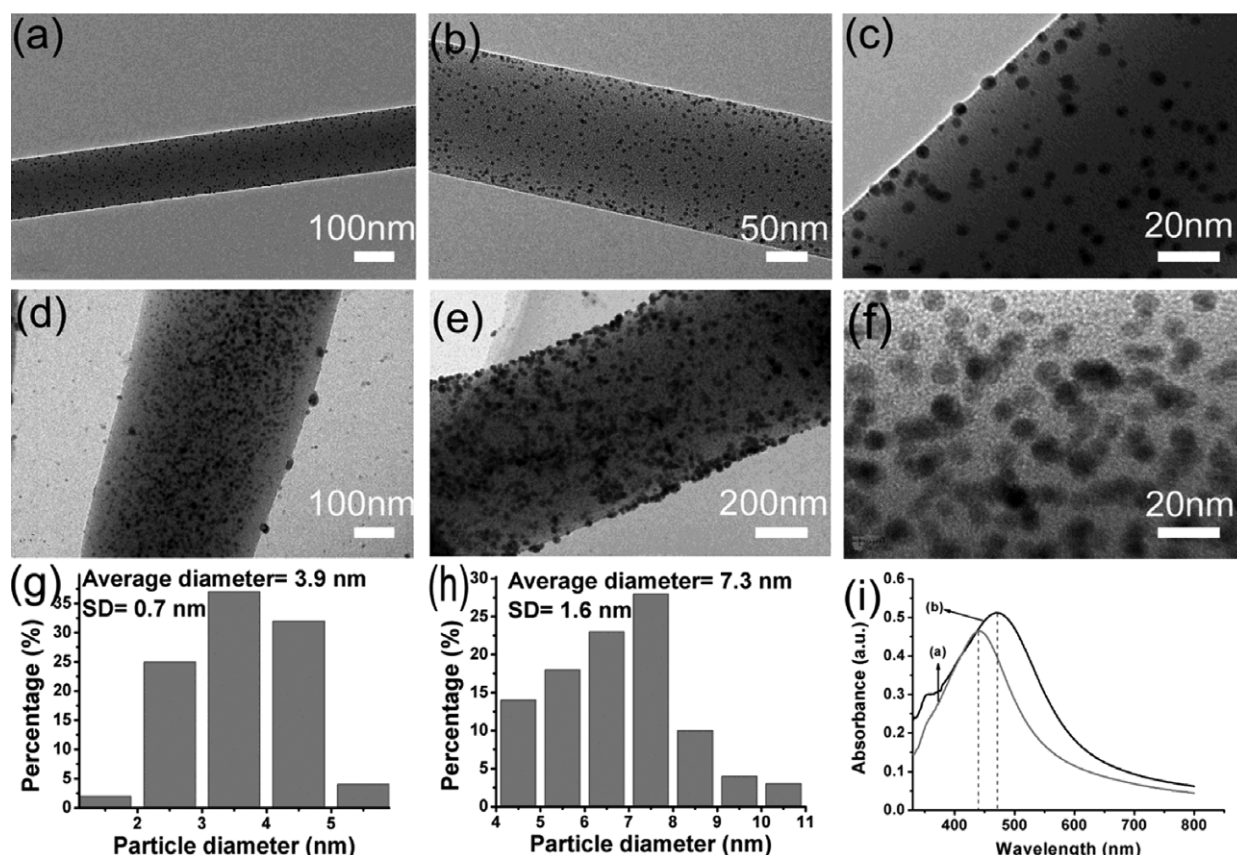


Figure 1. (a), (b), (c) TEM images of the AgNPs/PVA hybrids and (g) the corresponding particle distribution of AgNPs; (d), (e), (f) TEM images of the AgNPs/(PVA/PEI) hybrids and (h) the corresponding particle distribution of AgNPs; (i) The UV-Vis spectra of (a) AgNPs/PVA hybrids and (b) AgNPs/(PVA/PEI) hybrids.

practical application. From the relevant research, we know polymeric membrane is not only easy to obtain, but can also control AgNPs to release effectively. Therefore, the fabrication of Ag-based membraniform antibacterial agents might be very promising in antibiofilm.

During the last few decades, electrospinning has been developed to be a remarkably simple, efficient and versatile technique, which has been exploited to process polymer, metal oxide materials and gelation into 1D nanofibres [20]. The resulting nanofibres have high surface area that make them potential candidates for a variety of fields, such as membrane technology [21, 22], drug delivery system [23], enzyme immobilization [24], electronics [25] and sensors [26]. Obviously, this method provides an approach to bridge the dimensional and property gap between macroscale engineering materials and nanoscale materials [8]. Through the wonderful technology, 2D membraniform nanostructure could be easily fabricated. Poly(vinylalcohol) (PVA) is an easily electrospun polymer that can be used as the solid support of AgNPs. Its high polar, water-soluble, biocompatibility, processability and hydrophilicity [22, 27–29] have led to its industrious use in areas such as membranes [30], adhesives [31], paints and coating [22, 31].

Based on the advantages of electrospun PVA nanofibres, we adopted the nanofibres mat to support AgNPs. To improve the water-stability of PVA, we selected glutaraldehyde [32–34] as chemical cross-linkers to reduce its water solubility.

We modified PVA with polyethylenimine (PEI), which has abundant amine groups on the molecular chains, and they should be an ideal polymer for the fabrication of a polycationic nanofibre reactor [35].

In the present investigations, two procedures are employed to fabricate AgNPs/PVA and AgNPs/(PVA/PEI) nanofibre hybrids. In the first approach, we synthesized AgNPs in the PVA solution and then electrospun the AgNPs/PVA solution into the AgNPs/PVA nanofibres. In the other one, PEI was introduced to improve the water-stability of PVA and then the PVA/PEI nanofibres were functionalized by thiols groups to fabricate the AgNPs/(PVA/PEI) nanofibres. Our investigations indicate that the two kinds of obtained hybrids exhibited pretty good antibacterial activity.

2. Experimental sections

2.1. Chemicals and materials

Polyvinylalcohol (PVA, 88% hydrolyzed, $M_w = 88\,000$) was supplied by Sigma Aldrich. Silver nitrate (AgNO_3 , 99.8%) was obtained from Shanghai Reagent Factory. PEI (50%, $M_w = 70\,000$) was acquired from Aladdin Chemistry Co., Ltd. Epigallocatechin gallate (EGCG, 98%) was collected from Xuancheng BaiCao Plant Industry and Trade Co., Ltd. Glutaraldehyde (GA, 25%) was bought from Kermel, Tianjin Chemical Reagent Co., Ltd (3-Mercaptopropyl)

triethoxysilane (MPTES, $C_9H_{22}O_3SSi$, 95%) was gained from TCI (Shanghai) Development Co., Ltd. Absolute ethyl alcohol (C_2H_5OH) was from Hangzhou Gaojing Fine Chemical Industry. Deionized water was prepared by an ultra-pure water purifier system. All chemicals were used as received without further purification.

2.2. Synthesis of AgNPs embedded in PVA nanofibres by an *in situ* reduction method

10 ml 12 wt% PVA was put in a breaker at 65 °C and stirred by magnetic force for 30 min. 0.027 g $AgNO_3$ dissolved in 4 ml deionized water was added to the mixture, and after 1 h, 0.003 g EGCG dissolved in 1 ml purified water was dropped into the above mixture for 2 h. Thus, the solution with 0.024 wt% Ag was obtained. The solutions with 0.030 wt% Ag and 0.040 wt% Ag were acquired through the same method. The above solutions were electrospun under a fixed voltage of 15 kV, the products were collected for 5 h on a piece of aluminum foil at a distance of 12 cm, meanwhile, the velocity of flow was set at 0.3 ml h⁻¹. The mat was cross-linked by GA vapour at 60 °C for 24 h.

2.3. Synthesis of AgNPs immobilized on PVA/PEI nanofibres

14 g 12 wt% PVA and 1.12 g PEI were placed in a breaker and then stirred for 12 h at a proper rate. The mixture was electrospun for 5 h to acquire a piece of mat with the following related parameters: 18.6 kV, 15 cm, 0.3 ml h⁻¹. Then the nanofibre mat was cross-linked by the above-mentioned method. The cross-linked nanofibre mat was functionalized by the mixture of 3 ml MPTES and 45 ml ethanol in a immersion oscillator at 40 °C for 12 h, followed by being placed in a beaker containing silver nitrate solution for 1 h and put into EGCG solution for 2 h in sequence. The mass fraction of Ag was in correspondence with the AgNPs embedded in PVA nanofibres, respectively.

2.4. Antibacterial activity evaluation

The antibacterial activity of the hybrids was appraised against the bacteria of Gram-negative *Escherichia coli* (*E. coli*) ATCC 25922 and Gram-positive *Staphylococcus aureus* (*S. aureus*) ATCC 6538 by the nonwoven fabric attachment method [40–42]. The two kinds of microorganism were cultivated in sterilized Luria–Bertain (LB) broth and then incubated overnight at 37 °C with shaking before use. 100 μ l bacterial suspensions were spread uniformly over the agar plates. The two kinds of prepared hybrids were cut into small pieces with a diameter of 2 cm. After that, these circular pieces of AgNPs/PVA and AgNPs/(PVA/PEI) hybrids were placed over the solidified agar gel in different Petri dishes. In the end, the inoculated agars in the Petri plates were kept for incubation at 37 °C, and after 12 h and 20 h, the breadth of inhibition zone was recorded, respectively.

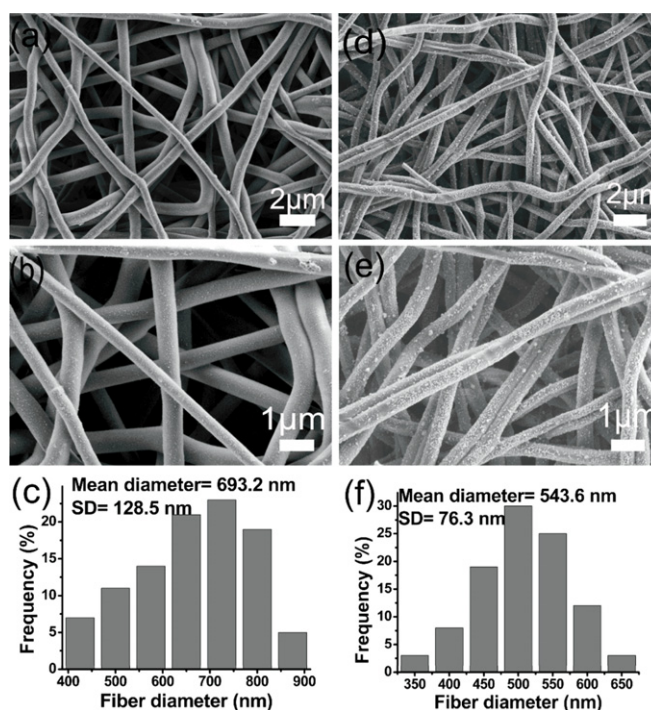


Figure 2. (a), (b) FE-SEM images of AgNPs/PVA hybrids and (c) the corresponding diameter distribution of nanofibres; (d), (e) FE-SEM images of AgNPs/(PVA/PEI) hybrids and (f) the corresponding diameter distribution of nanofibres.

2.5. Characterization

Two pieces of the two kinds of hybrids were placed in absolute ethyl alcohol, then ultrasonified for about ten minutes, dropped on the ultra-thin carbon-coated copper grid and dried under infrared lamp for five minutes, respectively. The images were acquired using a JSM-2100 transmission electron microscopy (TEM, JEOL, Japan) at an accelerating voltage of 200 kV. The spectra of AgNPs/PVA and AgNPs/(PVA/PEI) hybrids were collected by a Lambda 900 ultraviolet–visible (UV–Vis) spectrophotometer (Perkin Elmer, USA). All the spectra were collected over a wave length range of 200–800 nm. The morphology of the AgNPs/PVA and AgNPs/(PVA/PEI) hybrids were observed by an ULTRA-55 field-emission scanning electron microscope (FE-SEM, JOEL, Japan). X-ray photoelectron spectra of PVA nanofibres, AgNPs/PVA hybrids, PVA/PEI nanofibres and AgNPs/(PVA/PEI) hybrids were recorded by using an x-ray photoelectron spectrometer (Kratos Axis Ultra DLD) with aluminum (mono) K_{α} source (1486.6 eV). The aluminum K_{α} source was operated at 15 kV and 10 mA. The high-resolution survey (pass energy = 48 eV) was performed at spectral regions relating to silver, oxygen and sulfur.

3. Results and discussion

3.1. Morphology and structure of AgNPs/PVA and AgNPs/(PVA/PEI) hybrids

TEM images of the AgNPs/PVA hybrids are shown in figures 1(a)–(c). As described in the figure, the AgNPs

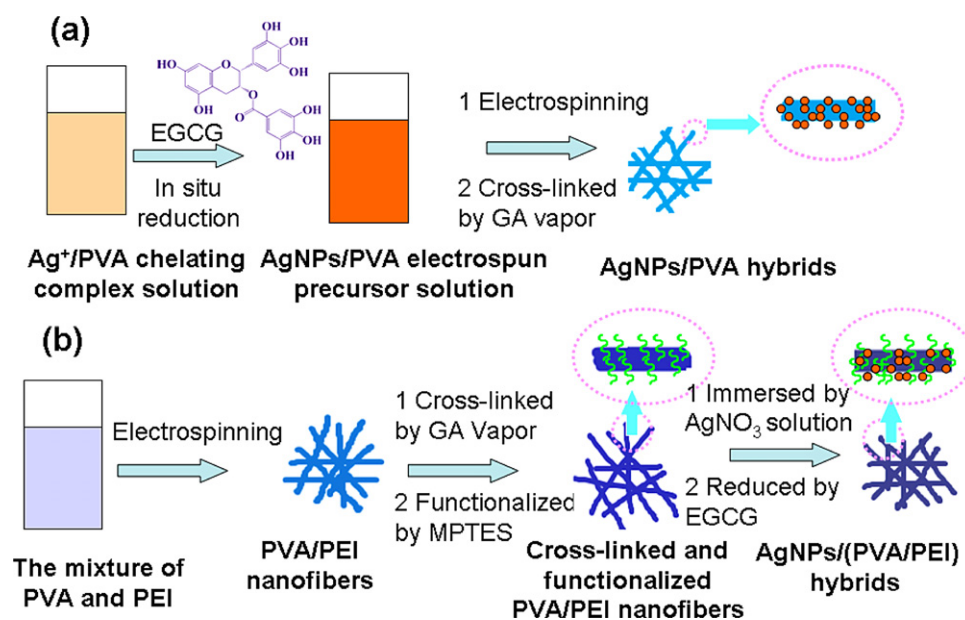


Figure 3. A schematic illustration of the procedure for the fabrication of (a) the AgNPs/PVA hybrids and (b) AgNPs/(PVA/PEI) hybrids.

are uniformly dispersed in PVA nanofibres and have a relatively narrow particle diameter distribution about 3.9 nm (figure 1(g)). The morphology of the AgNPs immobilized on PVA/PEI nanofibres are shown in figures 1(d)–(f), and it can be seen that the AgNPs with an average diameter of 7.3 nm (figure 1(h)) distributed on PVA/PEI nanofibres evenly. Compared with the AgNPs embedded in PVA nanofibres, the average diameter of the AgNPs on PVA/PEI nanofibres is much larger and the diameter distribution of AgNPs is broader. The UV–Vis absorption spectra of the AgNPs/PVA hybrids and AgNPs/(PVA/PEI) hybrids are shown in figure 1(i). Obviously, the band in curve (b) around 467 nm is broader than the band in curve (a) around 437 nm, indicating that the AgNPs on PVA/PEI nanofibres are larger than the AgNPs in PVA nanofibres and have a relatively higher polydispersity, which corresponds well with the TEM results. Typically, the intensive surface plasma resonance (SPR) band of AgNPs has a hypsochromic shift from 415 to 386 nm. The shift of SPR is attributed to the competition between the growth of AgNP size (which leads to the bathochromic shift) and electron transfer (which results in a change in free electron concentration of Ag and may cause bathochromic shift or hypsochromic shift of SPR peak) [39, 42].

Figure 2 shows the FE-SEM images of the hybrids via electrospinning technique. As can be seen from figures 2(a) and (b), a large quantity of AgNPs are well-dispersed in PVA nanofibres, which have a mean diameter of 693.2 nm and possess a relatively smooth surface. Obviously, through the *in situ* approach, AgNPs can be generated in PVA by the reduction of Ag⁺ which is dissolved in the electrospun precursor solution [4, 36–38]. As illustrated in figures 2(d)–(f), it is apparent that quite a number of AgNPs grow on the outside of modified PVA nanofibres. Evidently, most of the AgNPs have good dispersion, apart from a few of them stuck together. Thus, AgNPs can be homogeneously immobilized on the mat through a silver–sulfur bonding

interaction after the introduction of thiol groups from MPTES [43]. As can be seen from the chart (figure 2(f)), the mean diameter of the PVA/PEI nanofibres is 543.6 nm, which is much smaller compared with that of PVA nanofibres. What's more, the former has a narrow distribution of diameter.

Figure 3(a) summarizes the procedure for the preparation of AgNPs/PVA hybrids. AgNO₃, which was selected as the source of Ag ions, was added to the PVA solution first, and then the Ag⁺ was *in situ* reduced by EGCG. Thus, the AgNPs/PVA electrospun precursor solution was obtained. Afterward, the above solution was electrospun and subsequently cross-linked by the vapour of GA, during which the reaction between the hydroxyl groups of PVA and the aldehyde groups of GA happened, so as to enhance the water-stability of PVA [32, 43]. With the above procedures, the AgNPs/PVA hybrids were acquired. It is believed that the concentration of PVA polymer is higher than water and it may restrict the free growth of AgNPs and direct the particular arrangements of AgNPs. Therefore, in the fabrication process of the AgNPs, the polymer solution may play a crucial role for the diameter and distribution of the AgNPs. In figure 3(b), the PVA/PEI nanofibres were achieved through the process of electrospinning. After this, the PVA/PEI nanofibres were cross-linked by the GA vapour and then functionalized by MPTES, during which high-density -SH groups were introduced onto the surface of the PVA/PEI nanofibres, allowing a number of Ag⁺ to be immobilized via the interaction between Ag ions and SH groups [43]. Then, the SH groups functionalized PVA/PEI nanofibres were immersed in AgNO₃ solution, followed by reducing with EGCG and then the AgNPs/(PVA/PEI) hybrids were obtained. According to the literature, EGCG is an excellent bidentate ligand to bond with Ag⁺ by forming a stable five-member chelating ring. Afterward, the chelated Ag ions were reduced into Ag element as well as a part of the phenolic hydroxyls of EGCG being oxidized to the corresponding orthoquinone and

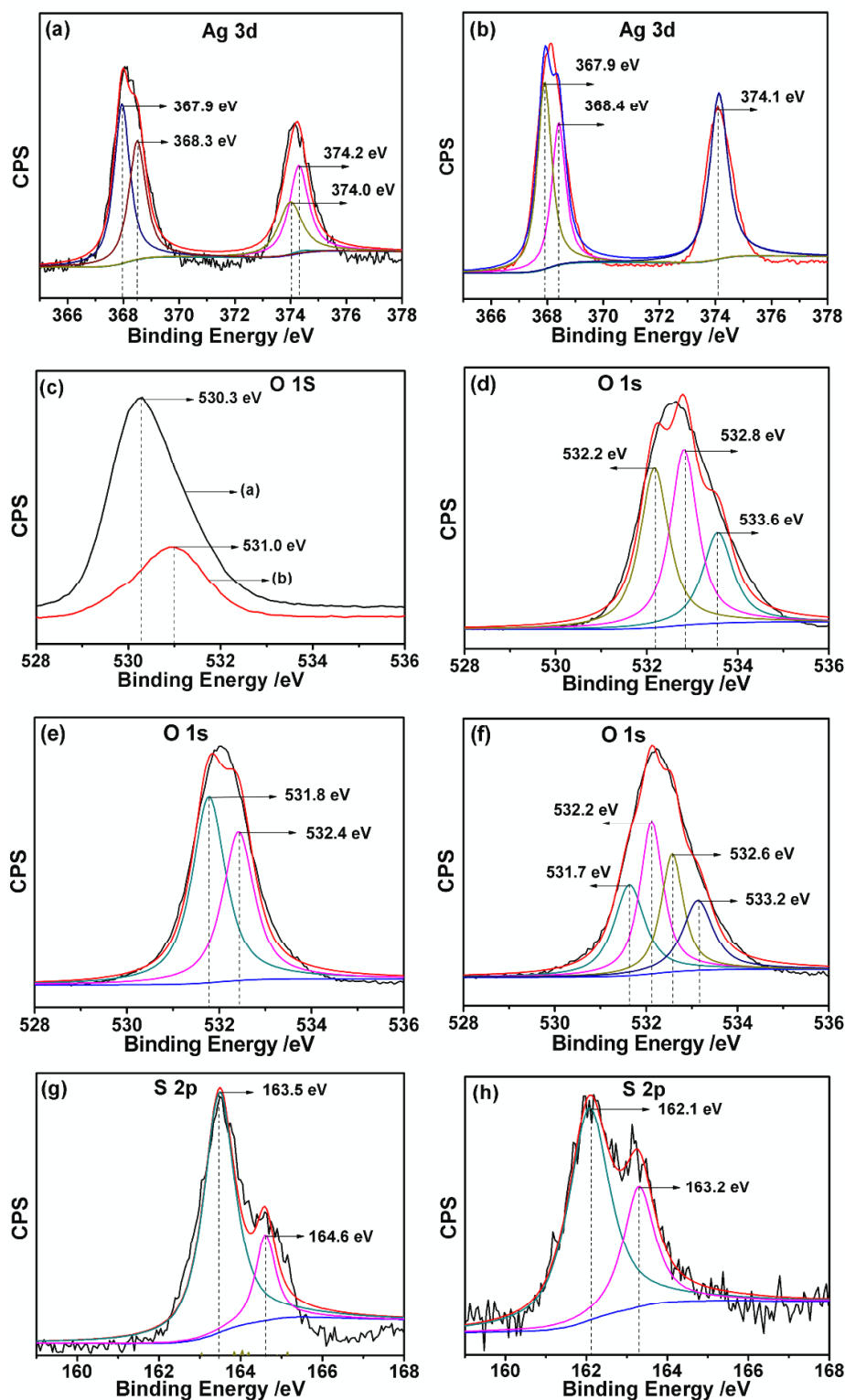


Figure 4. XPS spectra of Ag, oxygen, and sulfur atoms. (a) Ag 3d of AgNPs/PVA hybrids; (b) Ag 3d of AgNPs/(PVA/PEI) hybrids; (c) (a) O 1s in pure PVA; (b) O 1s in EGCG; (d) O 1s in AgNPs/PVA hybrids; (e) O 1s in PVA/PEI nanofibres; (f) O 1s in AgNPs/(PVA/PEI) hybrids; (g) S 2p of PVA/PEI nanofibres; (h) S 2p of AgNPs/(PVA/PEI) hybrids.

carbonyl groups. The formed carbonyls and free hydroxyls are both able to stabilize AgNPs by the interaction between the surface Ag atoms of AgNPs and oxygen atoms of EGCG [39, 44, 45, 48, 49]. Hence, it is concluded that chelating

effects of AgNPs with hydroxyls in PVA and sulfhydryls in MPES play an important role in the formation of AgNPs/PVA and AgNPs/(PVA/PEI) hybrids, which will be demonstrated by x-ray photoelectron spectroscopy (XPS).

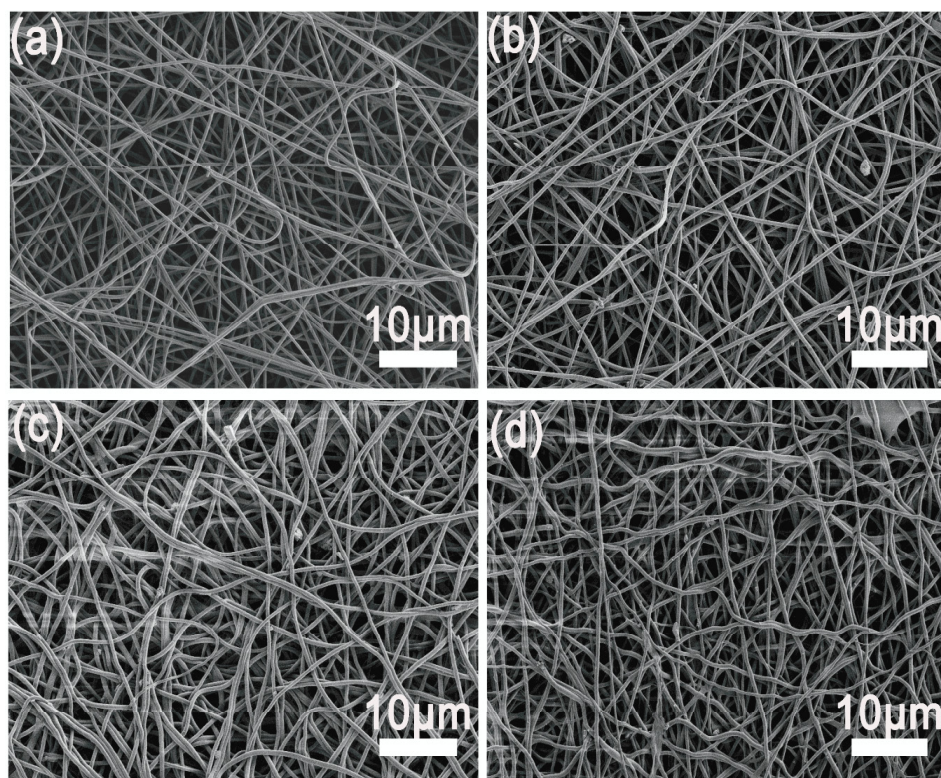


Figure 5. FE-SEM images of the AgNPs/PVA hybrids immersing in water for different times (a) 0 h (b) 12 h (c) 24 h (d) 48 h.

The XPS characterization was used to further characterize the fabrication process of the hybrids. Figure 4(a) shows the XPS spectrum in the Ag 3d region of the AgNPs/PVA hybrids. These peaks observed at 368.3 eV and 374.2 eV are ascribed to Ag 3d_{5/2} and Ag 3d_{3/2} of the bulk Ag, respectively. The other two peaks located at 367.9 and 374.0 eV are attributed to the chelating effects of Ag with hydroxyls in PVA. As can be seen in figure 4(b), the binding energy of Ag 3d_{5/2} shifts to 368.4 eV, while the binding energy of Ag 3d_{3/2} shifts to 374.1 eV, which is assigned to the interaction between AgNPs and hydroxyls [45, 47]. The peak located at 367.9 eV is ascribed to the interactions between AgNPs and sulfhydryl group.

As shown in figure 4(c), the peak at 530.3 eV and 531.0 eV are assigned to the O 1s in PVA and EGCG molecules, respectively. After the addition of EGCG and the formation of AgNPs, as can be seen in figure 4(d), the O 1s peak in AgNPs/PVA hybrids possesses three peaks at 532.2, 532.8 and 533.6 eV, which are mainly attributed to the involvement of hydroxyls in PVA and the vibration of phenolic hydroxyls in EGCG. In figure 4(e), the peaks at 531.8 eV and 532.4 eV are ascribed to the O 1s in PVA and MPTES molecules, respectively. The binding energy of O 1s in PVA shifts to a higher value, indicating the chemical changes in the environment. After being immersed in AgNO₃ solution and reduced by EGCG, as shown in figure 4(f), the O 1s peak in AgNPs/(PVA/PEI) hybrids are divided into four peaks. The peaks at 531.7 and 532.6 eV are assigned to the involvement of hydroxyls in PVA, which is the result of the chelating effects between AgNPs and hydroxyls. The peak at 532.2 eV is ascribed to the O 1s in MPTES, the variation indicates the

change of its existing chemical environment. The peak at 533.2 eV also implies the vibration of phenolic hydroxyls in EGCG [39, 42].

The XPS spectra of the S 2p in PVA/PEI nanofibres and AgNPs/(PVA/PEI) hybrids are shown in figures 4(g) and (h). It can be clearly seen that S 2p spectra have an S 2p_{3/2,1/2} doublet structure. The peaks located at 163.5 eV and 164.6 eV shift to 162.1 eV and 163.2 eV, respectively, which may result from the chemical bond formation between sulfur and Ag. As is known from the literature, the sulfur attached to metal would lead to lower electronegativity, and the decrease of binding energy of S 2p [46, 50]. Based on the above data, it can be concluded that the interactions among AgNPs, hydroxyls and sulfhydryls play a significant role in the formation process of AgNPs/PVA and AgNPs/(PVA/PEI) hybrids.

As we know, the PVA is a kind of water-soluble polymer, and it is important to improve the water-stability of PVA for widely practical applications. To testify the water-stability of the obtained AgNPs/PVA hybrids, the nanofibres mats immersed in water for different times are provided. As shown in figure 5, with the increase of the soak time, there are nearly no changes of the morphology of the nanofibres, indicating that the cross-linking of the hybrids by the GA vapour is effective way to improve the water-stability of the nanofibres.

3.2. Antibacterial activity

Traditionally, the antibacterial effects of the materials could be qualitatively determined by the length of the inhibition zones. Figures 6 and 7 show the experimental results of the antibacterial tests for the AgNPs/PVA and AgNPs/(PVA/PEI)

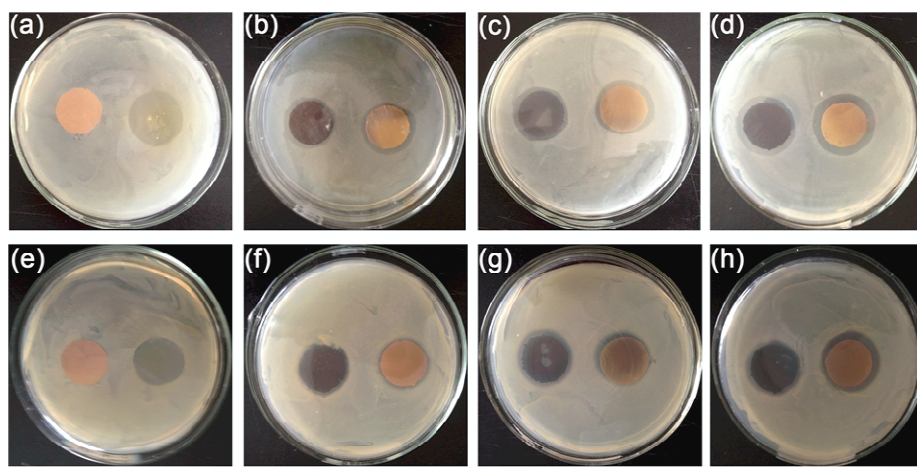


Figure 6. Pictures of inhibition zone test of hybrids after 12 h.

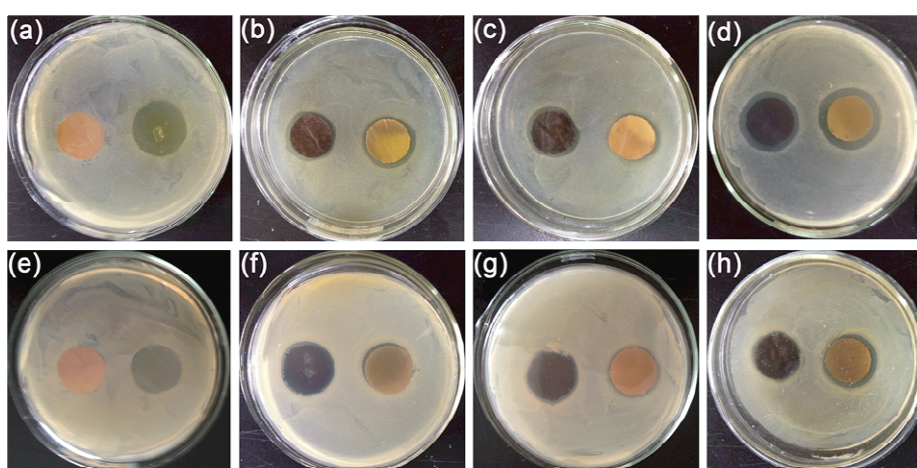


Figure 7. Pictures of inhibition zone test of hybrids after 20 h.

hybrids. As observed clearly from figures 6 and 7, the pure PVA nanofibre mat and pure PVA/PEI nanofibre mat exhibit no bacterial properties against *E. coli* and *S. aureus* at all. On the other hand, for the AgNPs/PVA hybrids and AgNPs/(PVA/PEI) hybrids, with the increase of AgNPs, the length of the inhibition zones become bigger. Meanwhile, there was no significant difference between the two different kinds of hybrids, indicating that both AgNPs/PVA hybrids and AgNPs/(PVA/PEI) hybrids can control AgNPs to release effectively. What's more, the two kinds of hybrids contained low content of AgNPs, implying that the two kinds of methods are both facile and effective.

The hybrids in the first line are against *E. coli*, in the second line are against *S. aureus*: (a) pure PVA, pure AgNPs/(PVA/PEI); (b) 0.024 wt% AgNPs/PVA, 0.024 wt% AgNPs/(PVA/PEI); (c) 0.030 wt% AgNPs/PVA, 0.030 wt% AgNPs/(PVA/PEI); (d) 0.040 wt% AgNPs/PVA, 0.040 wt% AgNPs/(PVA/PEI).

4. Conclusion

In summary, two strategies are demonstrated to fabricate AgNPs/PVA and AgNPs/(PVA/PEI) nanofibre hybrids. In the

first approach, we synthesized AgNPs in the PVA solution and then electrospun the AgNPs/PVA solution into the AgNPs/PVA nanofibres. In the other one, the PEI were introduced to improve the water-stability of PVA and then the PVA/PEI nanofibres were functionalized by thiols groups to fabricate the AgNPs/(PVA/PEI) nanofibres. The experimental results demonstrated that both of the as-prepared AgNPs/PVA hybrids and AgNPs/(PVA/PEI) hybrids exhibited good water-stability and good antibacterial activity against *E. coli* and *S. Aureus*. Moreover, these strategies are significant with respect to the synthesis of nanocomposites that have potential applications in catalysts, sensors and so forth.

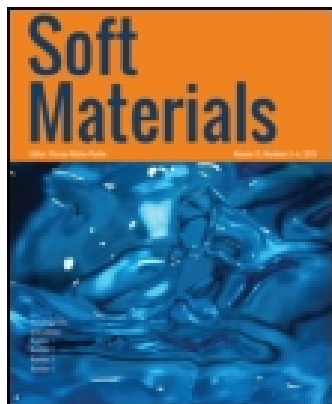
Acknowledgments

This work is supported by the project of National Natural Science Foundation of China (NSFC) (Grant No: 51243001) and the 521 Talent Project of Zhejiang Sci-Tech University.

References

- [1] Zhang C Q, Yang Q B, Zhan N Q, Sun L, Wang H G, Song Y and Li Y X 2010 *Colloids Surf. A* **362** 58

- [2] Kong H and Jang J 2006 *Chem. Commun.* **3010**
- [3] Zhang Z Y, Shao C L, Zou P, Zhang P, Zhang M Y, Mu J B, Guo Z C, Li X H, Wang C H and Liu Y C 2011 *Chem. Commun.* **47** 3906
- [4] Kriegel C, Kit K M, McClements D J and Weiss J 2009 *Langmuir* **25** 1154
- [5] Weiss J, McClements J and Takhistov P 2007 *Food Aust.* **59** 274
- [6] Wu H, Wu C, He Q and Liao X P 2010 *Mater. Sci. Eng. C* **30** 770
- [7] Sharma V K, Yngard R A and Lin Y 2009 *Adv. Colloid. Interface Sci.* **145** 83
- [8] Zhang Z Y, Shao C L, Sun Y Y, Mu J B, Zhang M Y, Zhang P, Guo Z C, Liang P P, Wang C H and Liu Y C 2012 *J. Mater. Chem.* **22** 1387
- [9] Wunder S, Polzer F, Lu Y, Mei Y and Ballauff M J 2010 *J. Phys. Chem. C* **114** 8814
- [10] Sun X and Li Y 2004 *Angew. Chem. Int. Edn Engl.* **43** 597
- [11] Zhang H, Li X and Chen G 2009 *J. Mater. Chem.* **19** 8223
- [12] Patel A C, Li S, Wang C and Wei Y 2007 *Chem. Mater.* **19** 1231
- [13] Wang Z, Chen X, Chen M and Wu L 2009 *Langmuir* **25** 7646
- [14] Tang S, Vongehr S and Meng X 2010 *J. Mater. Chem.* **20** 5436
- [15] Tang S, Vongehr S and Meng X 2010 *J. Phys. Chem. C* **114** 977
- [16] Huang X, Dong W, Wang G, Yang M, Tan L, Feng Y and Zhang X J 2011 *J. Colloid Interface Sci.* **359** 40
- [17] Jiang H, Akita T, Ishida T, Haruta M and Xu Q 2009 *J. Am. Chem. Soc.* **131** 11302
- [18] Lewis L N 1993 *Chem. Rev.* **93** 2693
- [19] Schmid G 1992 *Chem. Rev.* **92** 1709
- [20] Li D and Xia Y 2004 *Adv. Mater.* **16** 1151
- [21] Gopal R, Kaur S, Ma Z W, Chan C, Ramakrishna S and Matsuura T 2006 *J. Membr. Sci.* **281** 581
- [22] Pirzada T, Arvidson S A, Saquing C D, Shah S S and Khan S A 2012 *Langmuir* **28** 5834
- [23] Qi H, Hu P, Xu J and Wang A 2006 *Biomacromolecules* **7** 2327
- [24] Bhardwaj N and Kundu S C 2010 *Biotechnol. Adv.* **28** 325
- [25] Wu Y, Dong Z, Wilson S and Clark R L 2010 *Polymer* **51** 3244
- [26] Cheng C, Chen J, Chen F, Hu P, Wu X F, Reneker D H and Hou H 2010 *J. Appl. Phys. Sci.* **116** 1581
- [27] Hassan C M and Peppas N A 2011 *Adv. Polym. Sci.* **289** 1253
- [28] Wang X, Fang D, Yoon K, Hsiao B S and Chu B 2006 *J. Membr. Sci.* **278** 261
- [29] Kubo S and Kadla J F 2003 *Biomacromolecules* **4** 561
- [30] Xiao S, Feng X and Huang R Y 2007 *J. Membr. Sci.* **302** 36
- [31] Jenni A, Holzer L, Zurbriggen R and Herwegh M 2005 *Cement Concrete Res.* **35** 35
- [32] Tang C, Saquing C D, Harding J R and Khan S A 2010 *Macromolecules* **43** 630
- [33] Kurkuri M D and Aminabhavi T M 2004 *J. Control. Release* **96** 9
- [34] Yuan J, Mo H, Wang M, Li L, Zhang J and Shen J 2012 *J. Appl. Polym. Sci.* **124** 1067
- [35] Fang X, Ma H, Xiao S L, Shen M W, Guo R, Cao X Y and Shi X Y 2011 *J. Mater. Chem.* **21** 4493
- [36] Porel S, Singh S, Harsha S S, Rao D N and Radhakrishnam T P 2005 *Chem. Mater.* **17** 9
- [37] Li Z, Huang H, Shang T, Yang F, Zheng W, Wang C and Manohar S K 2006 *Nanotechnology* **17** 917
- [38] Rifai S, Breen C A, Solis D J and Swager T M 2006 *Chem. Mater.* **18** 21
- [39] Zhu H, Du M L, Zou M L, Xu C S, Li N and Fu Y Q 2012 *J. Mater. Chem.* **22** 9301
- [40] An J, Zhang H, Zhang J T and Zhao Y H 2009 *Colloid Polym. Sci.* **287** 1425
- [41] Min K D, Youk J H, Kwark Y J and Park W H 2007 *Fiber Polym.* **8** 591
- [42] Zou M L, Du M L, Zhu H, Xu C S, Li N and Fu Y Q 2012 *Polym. Sci.* **53** 1099–108
- [43] Wang J, Yao H B, He D, Zhang C L and Yu S H 2012 *ACS Appl. Mater. Interfaces* **4** 1963
- [44] Wu H, Huang X, Gao M M, Liao X P and Shi B 2011 *Green Chem.* **13** 651
- [45] Du J M, Zhang J L, Liu Z M, Han B X, Jiang T and Huang Y 2006 *Langmuir* **22** 1307
- [46] Yang D Q, Hennequin B and Sacher E 2006 *Chem. Mater.* **18** 5033
- [47] Uzayisenga V, Lin X D, Li L M, Anema J R, Yang Z L, Huang Y F, Lin H X, Li S B, Li J F and Tian Z Q 2012 *Langmuir* **28** 9140
- [48] Huang X, Wu H, Liao X P and Shi B 2010 *Green Chem.* **12** 395
- [49] Tripathy P, Mishra A, Ram S, Fecht H J, Bansmann J and Behm R J 2009 *Nanotechnology* **20** 075701
- [50] Yang Y W and Fan L J 2002 *Langmuir* **18** 1157



Soft Materials

Publication details, including instructions for authors and subscription information:

<http://www.tandfonline.com/loi/lsfm20>

Facile Fabrication of Palladium Nanoparticles Immobilized on the Water-Stable Polyvinyl Alcohol/Polyethyleneimine Nanofibers Via In-Situ Reduction and Their High Electrochemical Activity

Pan Wang^b, Ming Zhang^{ab}, YingTing Cai^b, ShengYing Cai^b, MingLiang Du^{ab}, Han Zhu^b, ShiYong Bao^b & Qin Xie^c

^a Key Laboratory of Advanced Textile Materials and Manufacturing Technology, Zhejiang Sci-Tech University, Ministry of Education, Hangzhou, P. R. China

^b Department of Materials Engineering, College of Materials and Textiles, Zhejiang Sci-Tech University, Hangzhou, P. R. China

^c Center for Nanochemistry, Beijing National Laboratory for Molecular Sciences, State Key Laboratory for Structural Chemistry of Unstable and Stable Species, College of Chemistry & Molecular Engineering, Peking University, Beijing, P. R. China

Accepted author version posted online: 28 Jul 2014.

To cite this article: Pan Wang, Ming Zhang, YingTing Cai, ShengYing Cai, MingLiang Du, Han Zhu, ShiYong Bao & Qin Xie (2014) Facile Fabrication of Palladium Nanoparticles Immobilized on the Water-Stable Polyvinyl Alcohol/Polyethyleneimine Nanofibers Via In-Situ Reduction and Their High Electrochemical Activity, *Soft Materials*, 12:4, 387-395, DOI: [10.1080/1539445X.2014.937493](https://doi.org/10.1080/1539445X.2014.937493)

To link to this article: <http://dx.doi.org/10.1080/1539445X.2014.937493>

PLEASE SCROLL DOWN FOR ARTICLE

Taylor & Francis makes every effort to ensure the accuracy of all the information (the "Content") contained in the publications on our platform. However, Taylor & Francis, our agents, and our licensors make no representations or warranties whatsoever as to the accuracy, completeness, or suitability for any purpose of the Content. Any opinions and views expressed in this publication are the opinions and views of the authors, and are not the views of or endorsed by Taylor & Francis. The accuracy of the Content should not be relied upon and should be independently verified with primary sources of information. Taylor and Francis shall not be liable for any losses, actions, claims, proceedings, demands, costs, expenses, damages, and other liabilities whatsoever or howsoever caused arising directly or indirectly in connection with, in relation to or arising out of the use of the Content.

This article may be used for research, teaching, and private study purposes. Any substantial or systematic reproduction, redistribution, reselling, loan, sub-licensing, systematic supply, or distribution in any form to anyone is expressly forbidden. Terms & Conditions of access and use can be found at <http://www.tandfonline.com/page/terms-and-conditions>

Facile Fabrication of Palladium Nanoparticles Immobilized on the Water-Stable Polyvinyl Alcohol/Polyethyleneimine Nanofibers Via *In-Situ* Reduction and Their High Electrochemical Activity

PAN WANG², MING ZHANG^{1,2*}, YINGTING CAI², SHENGYING CAI², MINGLIANG DU^{1,2}, HAN ZHU², SHIYONG BAO², and QIN XIE³

¹Key Laboratory of Advanced Textile Materials and Manufacturing Technology, Zhejiang Sci-Tech University, Ministry of Education, Hangzhou, P. R. China

²Department of Materials Engineering, College of Materials and Textiles, Zhejiang Sci-Tech University, Hangzhou, P. R. China

³Center for Nanochemistry, Beijing National Laboratory for Molecular Sciences, State Key Laboratory for Structural Chemistry of Unstable and Stable Species, College of Chemistry & Molecular Engineering, Peking University, Beijing, P. R. China

Received August 11, 2013; Accepted June 17, 2014

A facile strategy for the fabrication of electrochemical biosensors by immobilizing well-dispersed palladium nanoparticles (PdNPs) on the water-stable polyvinyl alcohol/polyethyleneimine (PVA/PEI) nanofibers through the combination of electrospinning technique and the process of *in-situ* reduction has been demonstrated. The synthesized PdNPs/(PVA/PEI) nanocomposites were characterized by field-emission scanning electron microscopy (FE-SEM), transmission electron microscopy (TEM), X-ray diffraction (XRD), and X-ray photoelectron spectroscopy (XPS). The experimental results confirmed that the PdNPs immobilized on the electrospun PVA/PEI nanofibers with an average diameter of 3.4 nm were well-dispersed, which could be ascribed to the complexation between Pd(II) and the free amine groups of PEI. Further investigations suggested that the PdNPs/(PVA/PEI) nanocomposites with well-separated PdNPs and large surface area exhibited high performance as electrochemical biosensors to detect hydrogen peroxide (H₂O₂).

Keywords: Electrochemical activity, Electrospinning, H₂O₂, PdNPs/(PVA/PEI) nanocomposites

Introduction

With the progress of time and the improvement of living standards, the demands for more sensitive sensors for global environmental monitoring, food inspection, and medical diagnostics have become urgent, leading to an upsurge of interest in the exploration of efficient sensors (1). The past several decades have witnessed the significant development in preparing sensitive sensors for accurate detection of NH₃, HCHO, H₂O₂, and so on. Varied nanostructures, such as hierarchical mesoporous SnO₂ structures (2), PANI/PEO nanowires (3), and LiCl-doped TiO₂ nanofibers (4) have been employed as gas sensors or humidity sensors. Nanostructured materials have been widely used as sensing materials, which may be attributed to their high surface-to-volume ratios, high porosity, and low cross-section areas. Consequently, better performances of electrochemical detectors,

such as mass transport and electric charge transport, have been reported (1, 5–7).

In response to the extensive need for electrochemical detectors, tremendous efforts have been focused on the development of the nanostructured materials. Electrospinning is a noticeable technique that provides a relatively inexpensive strategy to acquire continuous fibrous mats with higher surface area to volume ratio through the action of an external electric field (8–13). The easily-acquired nanomaterials with remarkable specific surface area and high porosity make them potential candidates in the fields of drug delivery systems, enzyme immobilization, and electrochemical biosensors (14).

Noble metal nanoparticles have received immense attention due to their unique structure-dependent properties and potential applications in numerous areas, such as electronics, catalysis, and sensor-technology (15–17). Among the many investigated metal nanoparticles, PdNPs have proven to be of great importance in the fields of catalysis (18), hydrogen storage (19), and electrochemical biosensors (20, 21) because of their large surface area-to-volume ratio. However, the PdNPs are easy to aggregate, difficult to recycle, and quickly consumed. Therefore, it is necessary to load PdNPs on the surface of supporting nanomaterials with high surface area, desired recovery, low cost, and longevity (14, 20). PVA is a type of biocompatible synthetic polymer

*Address correspondence to: Ming Zhang, Key Laboratory of Advanced Textile Materials and Manufacturing Technology, Zhejiang Sci-Tech University, Ministry of Education, 928 Second Street, Hangzhou 310018, P. R. China. Email: zhangming@zstu.edu.cn

Color versions of one or more of the figures in the article can be found online at www.tandfonline.com/lsmf.

with high-temperature-resistance and mechanical-stability (10) and its nanofibrous mats can be conveniently obtained by electrospinning the aqueous solution (22). However, the prepared nanofibrous mats are rapidly dissolved in water, which limits their practical applications. PEI is a cationic branched weak polyelectrolyte with high concentration of secondary amine functional groups, making it an ideal polymeric ligand for complexing heavy metal ions (23, 24). Over the past several years, intensive research has been conducted to develop PVA/PEI nanofibrous mats that are cross-linked by glutaraldehyde (GA) as supporting nanomaterials (25). Based on a previous study (26), we successfully prepared well-separated PdNPs functionalized PVA/PEI nanofibrous mats for electrochemical biosensors.

In the present work, we acquired PVA/PEI nanofibers by the process of electrospinning and then cross-linked them with GA vapor to render the fibrous mats water-stable, followed by the immobilization of PdNPs on PVA/PEI nanofibers. Subsequently, the PdNPs/(PVA/PEI) nanocomposites were obtained through *in-situ* reduction of the Pd(II) complexed with the water-stable nanofibrous mats. TEM, FE-SEM, XRD, FT-IR, EDS, TGA, and XPS were employed to characterize the morphology and investigate the PdNPs/(PVA/PEI) nanocomposites. The electrochemical activity of the PdNPs/(PVA/PEI) nanocomposites were investigated by the detection of H_2O_2 . The results suggested that the PdNPs immobilized on the PVA/PEI nanofibers were well-dispersed and the PdNPs/(PVA/PEI) nanocomposites exhibited high sensitivity as electrochemical biosensors for the detection of H_2O_2 .

Experimental Section

Materials

Palladium chloride (PdCl_2 , 99.9%) was obtained from Shanghai Civi Chemical Technology Co., Ltd. Sodium borohydride (NaBH_4) was bought from Tianjin Yongda Chemical Reagent Co., Ltd. Epigallocatechingallate (EGCG, 98%) was supplied by Xuancheng BaiCao Plant Industry and Trade Co., Ltd. Polyethylenimine (PEI, 50%, $M_w = 70000$) and Nafion aqueous solution (5 wt%) were acquired from Aladdin Chemistry Co., Ltd. Polyvinylalcohol (PVA, 88% hydrolyzed, $M_w = 88000$) was from Sigma Aldrich. Glutaraldehyde (GA, 25%) was purchased from Kermel, Tianjin Chemical Reagent Co., Ltd. Ethanol ($\text{C}_2\text{H}_5\text{OH}$) and phosphate buffer (PBS) was gained from Hangzhou Gaojing Fine Chemical Industry. Hydroquinone (HQ), horseradish peroxidase (HRP, RZ \sim 3, activity \geq 250 units mg^{-1}) and H_2O_2 (30 wt%) were obtained from Aladdin Chemistry Co., Ltd. All chemicals were analytical grade and used as received without further purification. Deionized water used in all experiments was purified using a Milli-Q Plus 185 water purification system (Millipore, Bedford, MA).

Methods

Synthesis of Well-Separated PdNPs in the Aqueous Solution

The well-separated PdNPs in the aqueous solution were synthesized as follows: i) 2 mL of 4 g/L EGCG was slowly added into

5 mL of 4 mM PdCl_2 solution under continued stirring at room temperature over a period of 5 min; ii) after thorough mixing, 0.04 mol/L NaBH_4 with a volume of 10 mL was dripped into the aforementioned solution; iii) entire solution was maintained under mechanical stirring for an hour; and iv) the PdNPs were obtained and kept for further observations.

Preparation of PdNP/(PVA/PEI) Nanocomposites

In a typical synthesis, the electrospun PVA/PEI nanofibers were prepared as follows: 14 g PVA (12 wt%) and 1.12 g PEI (50 wt%) were mixed together under appropriate stirring for 12 h to acquire homogeneous solution. The obtained mixture was electrospun under a fixed voltage of 18.6 kV; the products were collected for 6 h on a piece of aluminum foil at a distance of 15 cm, and the velocity of flow was set at 0.3 mL/h. The freshly prepared nanofibrous mats were detached from the aluminum foil and cross-linked by GA vapor at 60°C for 24 h. Three pieces of the cross-linked PVA/PEI nanofibrous mats (C0) with a weight of 10 mg were immersed into 2.5 mL, 7.5 mL, and 12.5 mL of PdCl_2 solution (4 mM), respectively, and labeled C1, C2, and C3, respectively. After the absorption equilibrium, the mats were removed and washed with deionized water to remove excess Pd(II). Then, the PdNPs/(PVA/PEI) nanocomposites were synthesized by reducing the Pd(II) that are absorbed on the PVA/PEI nanofibers into PdNPs with NaBH_4 .

Electrochemical Evaluation of PdNP/(PVA/PEI) Nanocomposites

The electrochemical experiments were conducted with a CHI660E workstation (Shanghai Chenhua, Shanghai, China). The whole process was carried out using a conventional three-electrode system in 0.1 mol/L PBS (pH = 6.8). Herein, a saturated Ag/AgCl electrode and a platinum foil electrode were selected as the reference electrode and the auxiliary electrode, respectively. The PdNP/(PVA/PEI) nanocomposites (C1 and C3) and PVA/PEI nanofibrous mats (C0) were immersed in 2.5 mg/mL HRP solution (2 mL) at 4°C overnight in a humidity chamber. Then, the HRP modified nanocomposites were obtained. The HRP/(PdNPs/[PVA/PEI])/GCE and HRP/(PVA/PEI)/GCE were both employed as the working electrodes. Prior to the surface coating, the GC electrode was polished carefully with 1.0, 0.3, and 0.05 μm alumina powder and rinsed with deionized water, followed by sonication in acetone, ethanol, and distilled water, respectively. Afterward, the electrode was allowed to dry under nitrogen. Then, 2 μL of Nafion (0.2%) and HRP/(PdNP/[PVA/PEI]) and HRP/(PVA/PEI) nanocomposites were placed on the surface of the GC electrode, successively. Eventually, the electrodes were dried with an infrared lamp for further electrochemical experiments. The PBS was purged with nitrogen for 1 h prior to each experiment to maintain the solution from oxygen exposure.

Instrumentation

The obtained PdNPs in aqueous solution and the PdNP/(PVA/PEI) nanocomposites were both placed on the ultra-thin carbon-coated copper grid and dried under infrared

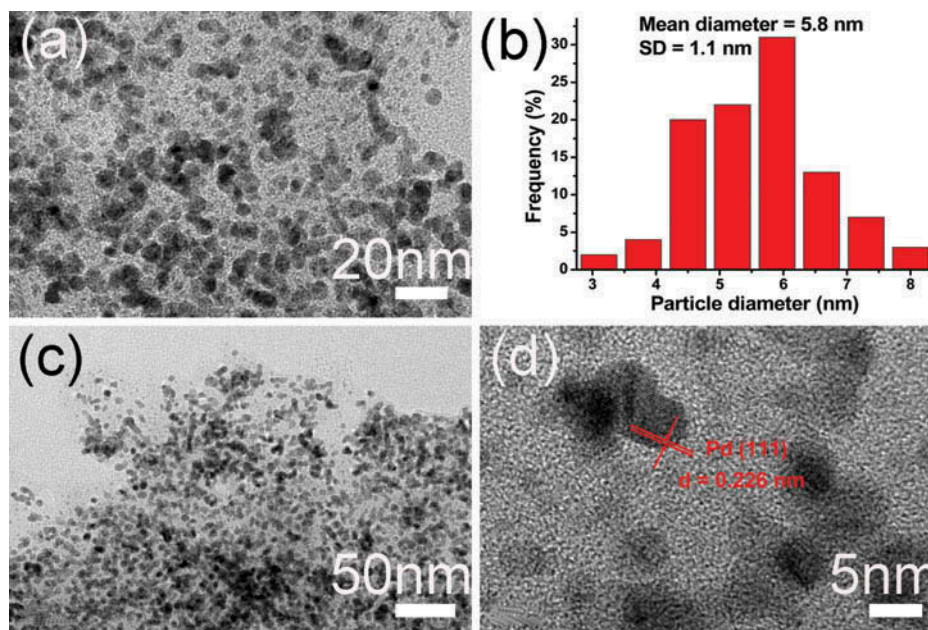


Fig. 1. (a) and (c) TEM images of the PdNPs and (b) the corresponding particle size distribution of PdNPs. (d) The HRTEM image of the PdNPs.

lamp for ten minutes, respectively, and the samples were performed on a JSM-2100 transmission electron microscopy (TEM, JEOL, Japan) at an accelerating voltage of 200 kV. The surface morphologies of the PdNP/(PVA/PEI) nanocomposites were characterized by a field emission scanning electron microscope (FE-SEM, JEOL ULTRA-55) with an energy dispersive spectrometer (EDS). The composition and crystal phase of the obtained samples were checked by a X-ray diffractometer (XRD, Thermo ARL X'TRA) using a Cu $K\alpha$ radiation source at 35 kV, with a scan rate of $0.02^\circ 2\theta \text{ s}^{-1}$ in the 2θ range 10 – 80° . The Fourier transform infrared spectroscopy (FT-IR) spectra of PVA/PEI nanofibers and PdNP/(PVA/PEI) nanocomposites were recorded on a Thermo Scientific Nicolet 5700 FTIR spectrometer in the wavenumber of 500 – 4000 cm^{-1} under ambient conditions. The X-ray photoelectron spectra (XPS) of the PVA/PEI nanofibers and PdNP/(PVA/PEI) nanocomposites were recorded by using an X-ray photoelectron spectrometer (Kratos Axis Ultra DLD) with Aluminum (mono) $K\alpha$ source (1486.6 eV). The high-resolution survey (pass energy = 48 eV) was performed at spectral regions relating to carbon, oxygen, nitrogen, and palladium. The aluminum $K\alpha$ source was operated at 15 kV and 10 mA . The thermal properties of PVA/PEI nanofibers and PdNP/(PVA/PEI) nanocomposites were carried out on a Perkin-Elmer Pyris 1 Thermogravimetric Analyzer (TGA) with a heating rate of $5^\circ\text{C}/\text{min}$ between 30°C and 800°C in a nitrogen atmosphere. The sizes of PdNPs and the fiber diameters of PdNP/(PVA/PEI) nanocomposites were both measured with Image-Pro Plus 6.2 software, and at least 100 randomly selected nanoparticles or nanocomposites in different FE-SEM or TEM images were analyzed for each sample in order to acquire the average diameter or size distribution histograms.

Results and Discussion

Fig. 1 illustrates the morphology and particle size distribution of the obtained PdNPs in the aqueous solution. As observed in the figure, the synthesized PdNPs were well-separated, which is attributed to the fact that EGCG served as both dispersant and stabilizer during the process of synthesizing well-dispersed PdNPs (16). It is evident that the PdNPs exhibited a relatively narrow size distribution, and the average diameter of the PdNPs was in the range 4.7 – 6.9 nm . The indicated lattice spacing of 0.226 nm , as shown in Fig. 1(d), along a certain direction can be assigned to the interplanar spacing of Pd (111), which also echoed the later XRD analysis.

The morphologies and microstructures of the as-prepared PdNP/(PVA/PEI) nanocomposites were investigated via TEM combined with selected area electron diffraction (SAED), which are shown in Fig. 2. In our present work, the PVA/PEI nanofibrous mats, which provide many “sites” for Pd(II), were immersed into different volumes of PdCl_2 solution, followed by the reduction of NaBH_4 after the end of the absorption process. Apparently, compared with that of the PdNPs in the aqueous, the mean diameter PdNPs immobilized on the PVA/PEI nanofibers was much smaller, ranging from 2.3 nm to 4.5 nm . On the other hand, it is clearly seen that some of the PdNPs were aggregated, which may be assigned to the following reasons. First, the Pd (II), which was not absorbed on the PVA/PEI nanofibrous mats in the aqueous, was reduced and then attached to the surface of the nanocomposites; and secondly, the small particle diameter of the PdNPs leads to higher surface energy, which is also of great significance to the aggregations (25, 27, 28). In the meantime, the SAED investigation also indicated the polycrystalline structure of the

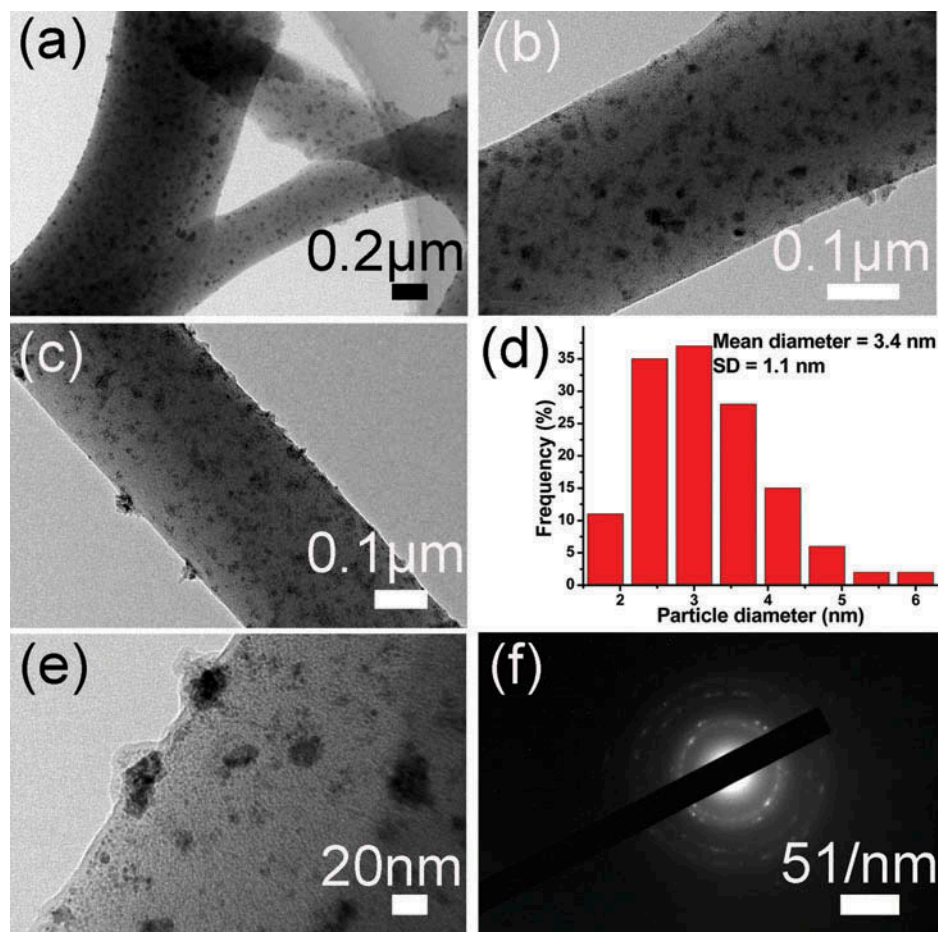


Fig. 2. The TEM images of the PdNPs/(PVA/PEI) nanocomposites (a), (b), (c) and (e); and (d) the corresponding particle size distribution of PdNPs. (f) The SAED pattern of PdNPs.

synthesized PdNPs immobilized on the PVA/PEI nanofibrous mats (29, 30).

In order to observe the macroscopic morphology of the acquired PdNP/(PVA/PEI) nanocomposites, the FE-SEM images were taken. As presented in Fig. 3, there is a three-dimensional network structure consisting of a large quantity of randomly deposited nanofibers and the average diameter of the PdNP/(PVA/PEI) nanocomposites was approximately 588 ± 130 nm. Evidently, with the increase of the contents of Pd(II), the quantity of PdNPs which were immobilized on the PVA/PEI nanofibers was increased. Additionally, the PdNPs were well-dispersed and did not exhibit obvious aggregation, which could be ascribed to the effective “sites” provided by PVA/PEI nanofibers. From the EDS spectrum, as demonstrated in Fig. 3(e), the existence of the Pd element further demonstrates the successful immobilization of PdNPs on the nanofibers.

The typical X-ray diffraction (XRD) patterns of PVA/PEI nanofibers, together with those of the PdNP/(PVA/PEI) nanocomposites that possessed different levels of PdNPs, are shown in Fig. 4. Fig. 4 shows the broad diffraction pattern detected at 2θ between 17° and 23° , which is caused by the scattering from the PVA/PEI nanofibers (18). As depicted in Fig. 4, there were more diffraction peaks detected in the nanocomposites with the increase of the content of PdNPs. Characteristic Pd

peaks at 40.1° , 46.3° , and 67.5° corresponds to the (111), (200), and (220) plane of a typical Pd crystal structure, respectively (31, 32). According to the standard pattern of Pd (JCPDS NO. 05-0681), all of the peaks can be indexed to the face-centered cubic (fcc) of Pd, suggesting a good crystallinity of the supported PdNPs in the nanocomposites (33–35).

The FT-IR analysis was used to verify the chemical changes during the reaction process. As illustrated in Fig. 5, the broad absorption band around 3338 cm^{-1} in curve (a) shifts to 3363 cm^{-1} , implying the involvement of O-H groups and N-H groups during the formation process of PdNPs, which is presumably attributed to the interaction between the hydroxyl/amino groups of the PVA/PEI nanofibers and the obtained PdNPs. The peak at 1720 cm^{-1} and 1440 cm^{-1} are ascribed to the C=O and -CH₂- of GA, respectively, and the intensity in curve (b) is relatively lower than that of in curve (a), which may be caused by the immersion of PdCl₂ solution, leading to the dissolution of partial GA. The absorption peaks centered at 850 cm^{-1} , which are assigned to the stretch vibrations of C-O in curve (a) become weaker in curve (b), confirming the variation of O-H groups in the reduction of Pd ions (36, 37). The peaks at 1096 cm^{-1} and 1599 cm^{-1} are indicative of the ether linkages and aldimine generated between GA/PVA and GA/PEI after cross-linking (26).

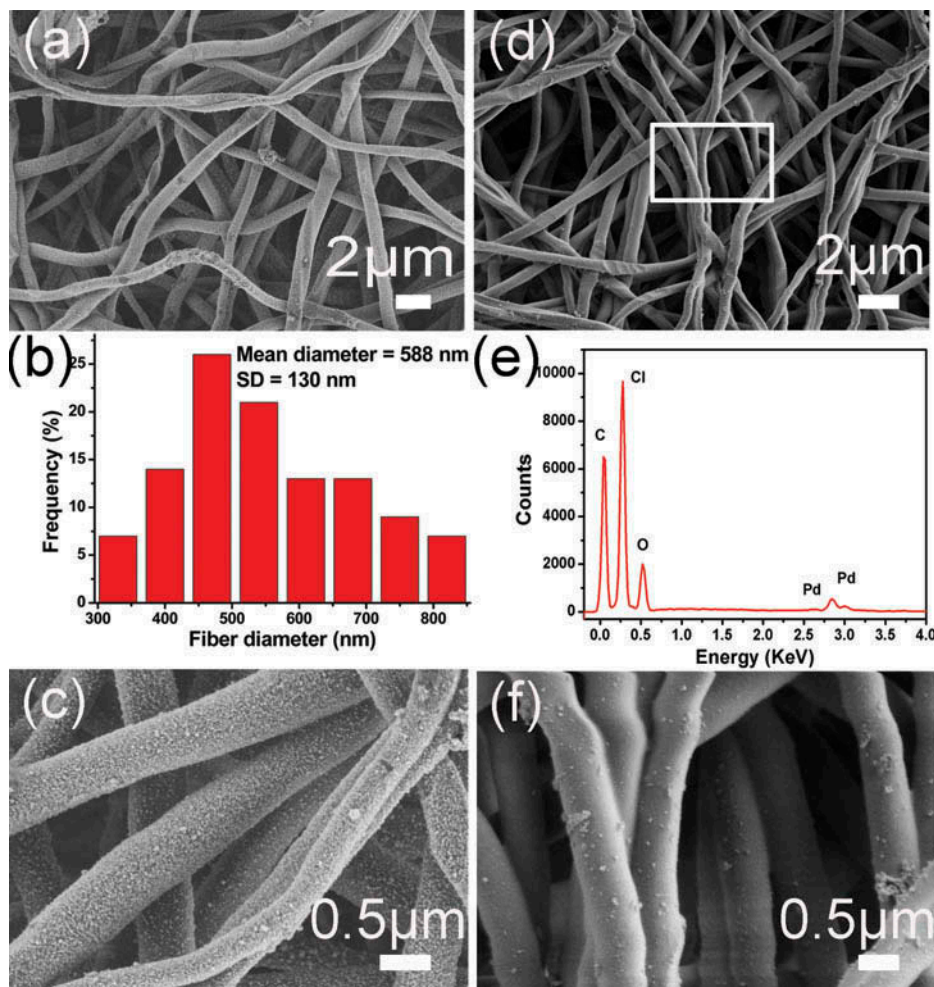


Fig. 3. The FE-SEM images of the PdNPs/(PVA/PEI) nanocomposites (a) and (c) are corresponding to C3; (d) and (f) are corresponding to C1; (b) the corresponding fiber diameter distribution of PdNPs/(PVA/PEI) nanocomposites; and (e) EDS spectrum of the PdNPs/(PVA/PEI) nanocomposites (C1).

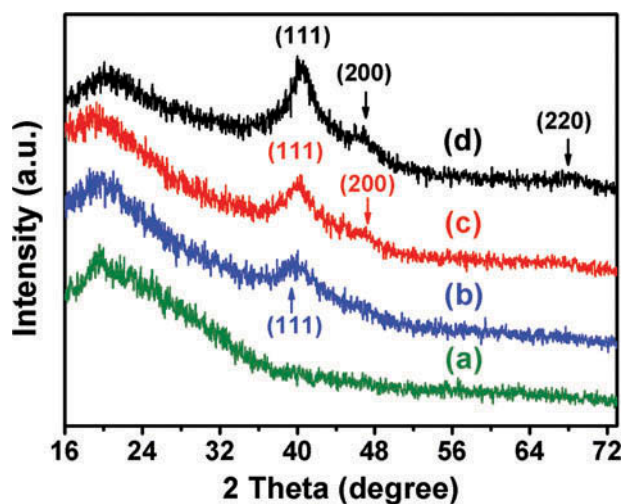


Fig. 4. XRD patterns of (a) PVA/PEI nanofibers (C0); (b)–(d) PdNPs/(PVA/PEI) nanocomposites (corresponding to C1, C2, and C3, respectively).

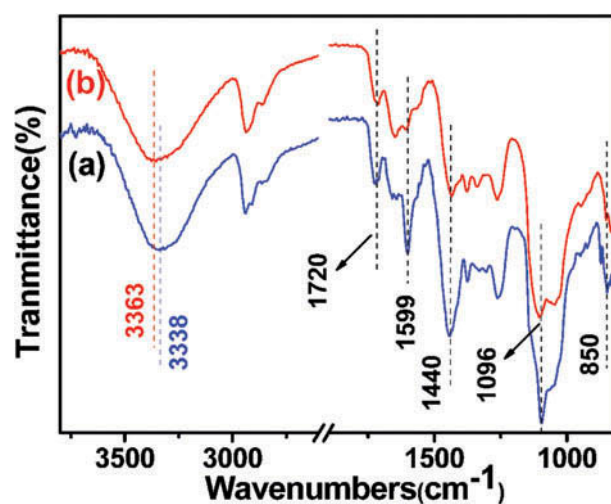


Fig. 5. The FT-IR spectra of (a) PVA/PEI nanofibers and (b) PdNPs/(PVA/PEI) nanocomposites.

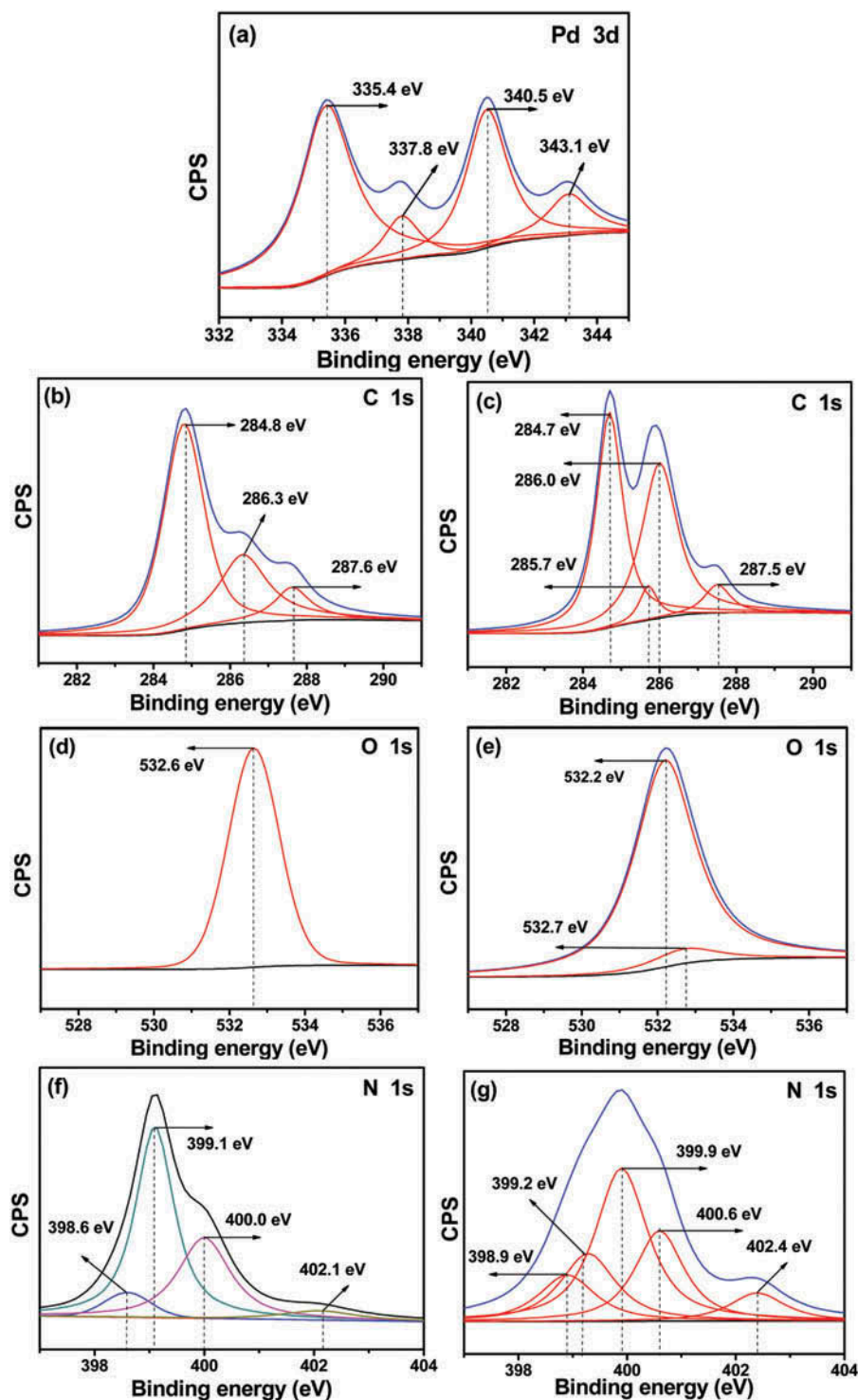


Fig. 6. XPS spectra of (b, d, f) PVA/PEI nanofibers and (a, c, e, g) PdNPs/(PVA/PEI) nanocomposites.

The surface elemental composition was acquired by X-Ray photoelectron spectroscopy (XPS) measurements. As observed in Fig. 6(a), the splitting pattern of the Pd 3d band of the resulting PdNP/(PVA/PEI) nanocomposites consists of two doublets: the more intensive doublet with the binding energy at 335.4 eV and 340.5 eV are ascribed to the Pd 3d_{5/2} and Pd 3d_{3/2} for metallic Pd, whereas the other doublet with binding energy at 337.8 eV and

343.1 eV belongs to the oxidation state of Pd (38–40). The clear difference in the intensity of these two doublets indicated that a small portion of PdNPs was oxidized into PdO, which might be due to that the external PdNPs were easily oxidized to the form of Pd oxide under ambient conditions (41, 42). The XPS spectra in the C 1s binding energy range were also obtained on PVA/PEI nanofibers and PdNP/(PVA/PEI) nanocomposites. In Fig. 6(b),

the deconvoluted XPS peaks of C 1s centered at the binding energies of 284.8, 286.3, and 287.6 eV correspond to sp^2 -hybridized C-C & C-H, C-OH, and C=O groups, respectively (38, 43, 44). However, the peaks of sp^2 -hybridized for C-OH were divided into two peaks, suggesting the hydroxyl groups were changed during the formation process of PdNPs. The binding energy shift of O 1s from 532.6 eV [in Fig. 6(d)] to 532.2 eV and 532.7 eV [in Fig. 6(e)] was due to the strong coordination between the surface hydroxyl group and PdNPs (45). The binding energy between 398.6 eV and 399.1 eV belong to the N 1s peak for the tertiary amine moieties, and the binding energy at 400.0 eV is attributed to the primary amine groups (46).

Additionally, the N 1s at a higher binding energy of 402.1 eV originated from quaternary ammonium bonds (47, 48), as demonstrated in Fig. 6(f). However, as seen in Fig. 6(g), many intermediate values appeared, implying the formation of different chemical states of nitrogen in PEI and the strong interaction between PdNPs and PEI during the reduction of Pd(II) (46, 48, 49).

TGA was employed to characterize the thermal stability of the nanofibrous mats and the loading capacity of PdNPs immobilized on the PVA/PEI nanofibers. As shown in Fig. 7, the PVA/PEI nanofibers exhibit two main degradation stages (A1A2 and A2A3), whereas the PVA/PEI nanofibers with PdNPs show a single-step sharp degradation curve (B1B2) (36). In the case of

the pristine PVA/PEI nanofibers, the degradation process was fast after 185°C as observed in Fig. 7(a), and showed a decomposition of 51.9% in step-1. At the temperature above 750°C, the PVA/PEI nanofibers are burned out (50). In contrast, the PdNP/(PVA/PEI) nanocomposites reflected an improvement in its thermal stability of about 25°C (onset point 210°C) when compared with the pristine PVA/PEI nanofibers. Additionally, based on the TGA data, the loading of the PdNPs on the nanofibrous mats was estimated to be 18.3% (51).

Concentrated efforts have been focused on the detection of H_2O_2 , considering its extensive applications in various fields such as biological, chemical, environmental, clinical, food, and industrial analysis (5, 25). The majority of the research methods for measuring H_2O_2 have been investigated, such as colorimetric, chromatographic, and photometric methods, which are time-consuming and low-efficient. Therefore, exploring a high-efficiency analytic technique is of vital significance. Among these, the electrochemical method is attracting increasing attention because of its high sensitivity, simplicity, and precision (52). The horseradish peroxidase (HRP), which is an important peroxidase that can catalyze the oxidation of substrates when activated by hydrogen peroxide or other peroxides, could be attached tightly onto the negatively charged PdNPs through electrostatic attraction (10, 27). Herein, taking advantages of the porous structures of PVA/PEI nanofibers and the well-dispersed PdNPs, we selected these prepared HRP/(PdNP/(PVA/PEI) nanocomposites as substrate materials in electrochemical biosensors, and the HRP/(PVA/PEI nanofibers) were used as a control. Furthermore, hydroquinone (HQ) was employed to detect H_2O_2 as an excellent electron mediator (25).

As shown in Fig. 8(a), (b), and (c), well-defined cyclic voltammograms (CVs) of the HRP/(PVA/PEI nanofibers)/GCE and HRP/(PdNP/[PVA/PEI] nanocomposites)/GCE are observed. In the presence of 0.5 μ M, 1 μ M, and 10 μ M H_2O_2 , the redox peak potential obtained at the HRP/(PdNP/(PVA/PEI) nanocomposites)/GCE (C1) was (-0.18 and 0.42 V), suggesting the strong reactions among HRP, H_2O_2 , and HQ. Whereas, for the HRP/(PVA/PEI nanofibers)/GCE (C0), with the inexistence of PdNPs, the change of the cathodic peak current and the anodic peak current are both extremely remarkable, indicating that the PdNPs play a key role in the electron transfer between the redox-active site of H_2O_2 and GCE. However, with an evident increase of the PdNPs, there was a minimal obvious difference for the electrochemical activity toward the HQ, indicating that the fabricated HRP biosensor allowed the highly sensitive detection of H_2O_2 . Only the mass concentrations of

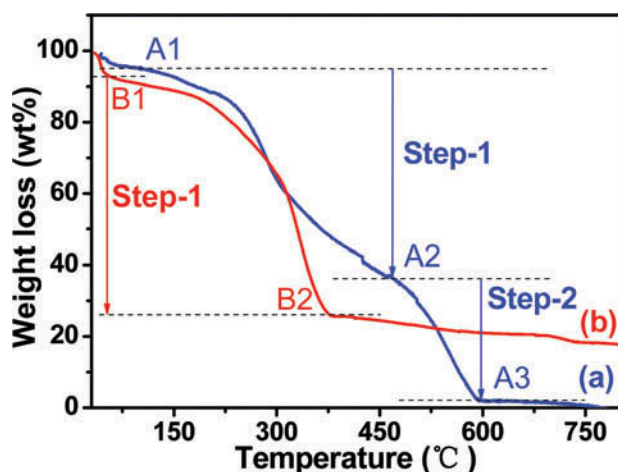


Fig. 7. TGA curves of the PVA/PEI nanofibers [curve (a)] and PdNPs/(PVA/PEI) nanocomposites [curve (b)].

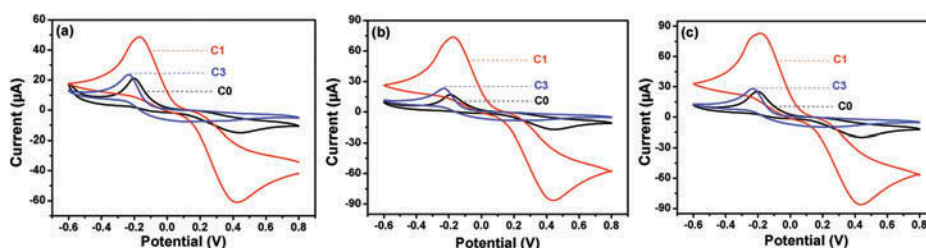


Fig. 8. Cyclic voltammograms of (C0) HRP/(PVA/PEI nanofibers)/GCE, (C1) HRP/(PdNPs/(PVA/PEI) nanocomposites)/GCE (2.5 mL $PdCl_2$), and (C3) HRP/(PdNPs/(PVA/PEI) nanocomposites)/GCE (12.5 mL $PdCl_2$). The functionalized GCE in (a), (b) and (c) were immersed in 10.0 mM HQ in 0.1 M PBS (pH = 6.8) containing 0.5 μ M, 1 μ M, and 10 μ M H_2O_2 , respectively (scan rate, 50 mV s^{-1}).

PdNPs immobilized on the PVA/PEI nanofibrous mats were kept in a suitable range, which may be as a result of the active sites being blocked due to the agglomeration of PdNPs (20). Taking into consideration the sensitive response to H_2O_2 of the as-prepared HRP/(PdNP/(PVA/PEI) nanocomposites, it is believed that the highly porous fibrous structure of the PdNP/(PVA/PEI) nanocomposites were a facile substrate material for the development of enzyme-based electrochemical biosensors for H_2O_2 detection (53, 54).

Conclusions

In summary, the PdNP/(PVA/PEI) nanocomposites, which took advantage of the large surface area of PVA/PEI nanofibers and the high catalytic activity of PdNPs, were successfully fabricated by employing the electrospinning technique and the *in-situ* reduction. Further research demonstrated that the PdNP/(PVA/PEI) nanocomposites showed high performance as electrochemical biosensors for the detection of H_2O_2 , and the electron transfer between the redox-active site of H_2O_2 and GCE were greatly enhanced. We hope that this approach to fabricating the PdNP/(PVA/PEI) nanocomposites and the resulting sensing behaviors will aid in the design of nanosensors functionalized by noble metal nanoparticles and has clear implications for the future environmental pollution monitoring devices.

Funding

We acknowledge the support of the project from the National Natural Science Foundation of China (NSFC) (Grant number: 51373154) and the 521 Project of Zhejiang Sci-Tech University.

References

- Ding, B., Wang, M. R., Wang, X. F., Yu, J. Y., and Sun, G. (2010) *Mater. Today*, 13:16–27.
- Zhang, G., and Liu, M. L. (2000) *Sens. Actuators, B*, 69:144–152.
- Liu, H. Q., David, J. K., Czaplowski, A., and Craighead, H. G. (2004) *Nano Lett.*, 4:671–675.
- Li, Z. Y., Zhang, H. N., Zheng, W., Wang, W., Huang, H. M., Wang, C., MacDiarmid, A. G., and Wei, Y. (2008) *J. Am. Chem. Soc.*, 130:5036–5037.
- Tan, S. W., Tan, X. C., Xu, J., Zhao, D. D., Zhang, J. L., and Liu, L. (2011) *Anal. Methods*, 3:110–115.
- Tang, C., Ozcam, A. E., Stout, B., and Khan, S. A. (2012) *Biomacromolecules*, 13:1269–278.
- Li, D., and Xia, Y. N. (2004) *Adv. Mater.*, 16:1151–1170.
- Fang, X., Ma, H., Xiao, S. L., Shen, M. W., Guo, R., Cao, X. Y., and Shi, X. Y. (2011) *J. Mater. Chem.*, 21:4493–4501.
- Reneker, D. H., and Chun, I. (1996) *Nanotechnology*, 7:216–223.
- Wang, J., Yao, H. B., He, D., Zhang, C. L., and Yu, S. H. (2012) *ACS Appl. Mater. Interfaces*, 4:1963–1971.
- Ding, B., Kim, H. Y., Lee, S. C., Shao, C. L., Lee, D. R., Park, S. J., Kwag, G. B., and Choi, K. J. (2002) *J. Polym. Sci., Part B*, 40:1261–1268.
- Hang, A. T., Tae, B., and Park, J. S. (2010) *Carbohydr. Polym.*, 82:472–479.
- Wang, X., Chen, X., Yoon, K., Fang, D., Hsiao, B. S., and Chu, B. (2005) *Environ. Sci. Technol.*, 39:7684–7691.
- Pirzada, T., Arvidson, S. A., Saquing, C. D., Shah, S. S., and Khan, S. A. (2012) *Langmuir*, 28:5834–5844.
- Sun, Y. G., and Xia, Y. N. (2002) *Science*, 298:2176–2179.
- Choi, I., Song, H. D., Lee, S., Yang, Y. I., Kang, T., and Yi, J. (2012) *J. Am. Chem. Soc.*, 134:12083–12090.
- Sau, T. K., and Rogach, A. L. (2010) *Adv. Mater.*, 20:1781–1804.
- Shao, M. H., Sasaki, K., and Adzic, R. R. (2006) *J. Am. Chem. Soc.*, 128:3526–3527.
- Rose, A., Maniguet, S., Mathew, R. J., Slater, C., Yao, J., and Russell, A. E. (2003) *Phys. Chem. Chem. Phys.*, 5:3220–3225.
- Zhu, X. H., and Lin, X. Q. (2007) *Anal. Sci.*, 23:981–990.
- Sun, Y., and Wang, H. H. (2007) *Adv. Mater.*, 19:2818–2823.
- Praptowidodo, V. S. (2005) *J. Mol. Struct.*, 739:207–212.
- Chanda, M., and Rempel, G. L. (2001) *Ind. Eng. Chem. Res.*, 40:1624–1632.
- Hu, C. H., Zhang, L., Wu, D. Q., Cheng, S. X., Zhang, X. Z., and Zhuo, R. X. (2009) *J. Mater. Chem.*, 19:3189–3197.
- Zhu, H., Du, M. L., Zhang, M., Wang, P., Bao, S. Y., Wang, L. N., Fu, Y. Q., and Yao, J. M. (2013) *Biosens. Bioelectron.*, 49:210–215.
- Fang, X., Ma, H., Xiao, S. L., Shen, M. W., Guo, R., Cao, X. Y., and Shi, X. Y. (2011) *J. Mater. Chem.*, 21:4493–4501.
- Zhu, H., Du, M. L., Zhang, M., Wang, P., Bao, S. Y., Fu, Y. Q., and Yao, J. M. (2013) *Sens. Actuators, B*, 185:608–619.
- Guo, S. J., Dong, S. J., and Wang, E. K. (2010) *ACS Nano*, 4:547–555.
- Huang, J. F., Vongehr, S., Tang, S. C., Lu, H. M., and Meng, X. K. (2010) *J. Phys. Chem. C*, 114:15005–15010.
- Fu, G. T., Wu, K., Lin, J., Tang, Y. W., Chen, Y., Zhou, Y. M., and Lu, T. H. (2013) *J. Phys. Chem. C*, 117:9826–9834.
- Song, Y. J., Kim, J. Y., and Park, K. W. (2009) *Cryst. Grow. Design*, 9:505–507.
- Huang, Y. P., Ma, H., Wang, S. G., Shen, M. W., Guo, R., Cao, X. Y., Zhu, M. F., and Shi, X. Y. (2012) *ACS Appl. Mater. Interfaces*, 4:3054–3061.
- Joshi, R. K., Yoshimura, M., Chiu, C. C., Tung, F. K., and Ueda, K. (2008) *J. Phys. Chem. C*, 112:1857–1864.
- Zhang, Y., Xiang, Q., Xu, J. Q., Xu, P. C., Pan, Q. Y., and Li, F. (2009) *J. Mater. Chem.*, 19:4701–4706.
- Fan, F. R., Attia, A., Sur, U. K., Chen, J. B., Xie, Z. X., Li, J. F., Ren, B., and Tian, Z. Q. (2009) *Cryst. Grow. Design*, 9:2335–2340.
- Zhao, L. N., Yang, D. Y., Dong, M. D., Xu, T., Jin, Y., Xu, S. L., Zhang, F. Z., Evans, D. G., and Jiang, X. Y. (2010) *Ind. Eng. Chem. Res.*, 49:5610–5615.
- Kim, J. H., Min, B. R., Lee, K. B., Won, J., and Kang, Y. S. (2002) *Chem. Commun.*, 2732–2733.
- Huang, H. J., and Wang, X. (2013) *Phys. Chem. Chem. Phys.*, 15:10367–10375.
- Feng, Y. Y., Zhang, G. R., and Xu, B. Q. (2013) *RSC Adv.*, 3:1748–1752.
- Hu, B., Wu, T., Ding, K., Zhou, X., Jiang, T., and Han, B. (2010) *J. Phys. Chem. C*, 114:3396–3400.
- Ohashi, M., Beard, K. D., Ma, S., Blom, D. A., St-Pierre, J., Van Zee, J. W., and Monnier, J. R. (2010) *Electrochim. Acta*, 55:7376–7384.
- Feng, L., Si, F., Yao, S., Cai, W., Xing, W., and Liu, C. (2011) *Catal. Commun.*, 12:772–775.
- Guo, Y., Sun, X., Liu, Y., Wang, W., Qiu, H., and Gao, J. (2012) *Carbon*, 50:2513–2523.
- Zhang, Y., Zhang, N., Tang, Z. R., and Xu, Y. J. (2012) *ACS Nano*, 6:9777–9789.
- Guin, D., Manorama, S. V., Latha, J. N. L., and Singh, S. (2007) *J. Phys. Chem. C*, 111:13393–13397.
- Zhu, H., Du, M. L., Zou, M. L., Xu, C. S., and Fu, Y. Q. (2012) *Dalton Trans.*, 41:10465–10471.
- Ira, Y. F., Nurit, B., Abraham, N., Ervin, I. W., Jacob, G., and Abraham, J. D. (2008) *Biomacromolecules*, 9:3044–3050.
- Jeong, E. H., Yang, J., and Youk, J. H. (2007) *Mater. Lett.*, 61:3991–3994.

49. Hughes, K. J., Dube, A., Sharma, M., and Engstrom, J. R. (2012) *J. Phys. Chem. C*, 116:21948–21960.
50. Li, R., Hu, F. P., Bao, Q. L., Qiao, Y., Yu, S. C., Guo, J., and Li, C. M. (2010) *Chem. Commun.*, 46:689–691.
51. Yang, J. H., and Lee, Y. D. (2012) *J. Mater. Chem.*, 22: 8512–8517.
52. Xu, X., Tian, B. Z., Zhang, S., Kong, J. L., Zhao, D. Y., and Liu, B. H. (2004) *Anal. Chem. Acta*, 519:31–38.
53. Pan, W., Zhang, X. K., Ma, H. Y., and Zhang, J. T. (2008) *J. Phys. Chem. C*, 112:2456–2461.
54. Lang, X. Y., Guo, H., Chen, L. Y., Kudo, A., Yu, J. S., Zhang, W., Inoue, A., and Chen, M. W. (2010) *J. Phys. Chem. C*, 114:2600–2603

The preparation of tubular heterostructures based on titanium dioxide and silica nanotubes and their photocatalytic activity†

Cite this: *Dalton Trans.*, 2014, **43**, 1846

Pan Wang,^a Mingliang Du,^{*a} Ming Zhang,^a Han Zhu^a and Shiyong Bao^{a,b}

Tubular heterostructures based on titanium dioxide (TiO₂) and silica nanotubes (SNTs) with high photocatalytic activity have been successfully obtained by a simple combination of an electrospinning technique and a solvothermal process. The as-prepared products were characterized by field-emission scanning electron microscopy (FE-SEM), transmission electron microscopy (TEM), X-ray diffraction (XRD), Fourier transform infrared spectroscopy (FT-IR), and N₂ absorption-desorption experiments. The results confirmed that SNTs with high specific surface area were obtained by efficiently controlling the phase separation and solvent evaporation during the process of electrospinning and calcination, and TiO₂ was successfully grown on the SNT substrates. The obtained titanium dioxide/silica nanotubes (TiO₂/SNTs) heterostructures showed high photocatalytic activities to degrade Rhodamine 6G because of the formation of heterostructures, which might improve the separation of photogenerated electrons and holes. Furthermore, the TiO₂/SNTs heterostructures could be easily recycled without an evident decrease in photocatalytic activity.

Received 19th July 2013,
Accepted 25th October 2013

DOI: 10.1039/c3dt51959g

www.rsc.org/dalton

1. Introduction

In the past few decades, with the development of technology and the progress of society, various advanced technologies have been developed for environmental remediation. Among these strategies, photocatalytic reaction based on heterostructures has attracted extensive attention, and is regarded as a potential solution to the recent severe problems of environmental crises.^{1–3} Heterostructured nanomaterials based on engineered oxide-oxide or metal-oxide multimaterial junctions offer to enhance the functional performance by combining individual material characteristics, which had shown significant advantages when compared with their single-component counterparts.⁴ Hence, it is timely and necessary to search for novel heterostructured nanomaterials with low cost and high performance.

Since Fujishima and Honda's first reports of UV-light-induced redox chemistry on TiO₂, the study of photocatalysts with the fascinating properties of nontoxicity and high chemical stability has drawn significant attention from the research and development communities.^{5–7} Extraordinarily, photocatalytic

reactions on TiO₂ nanoparticles have been attracting much interest from the viewpoint of their possible applications for dealing with environmental problems, that is, purification of air as well as polluted wastewater with dilute organic compounds.^{8,9} However, TiO₂ nanoparticles are prone to aggregate and become consumed quickly, resulting in a remarkable reduction in their photocatalytic activity and enormous waste. To overcome the disadvantages, a great deal of effort has been made, for instance, putting TiO₂ nanoparticles into colloidal solutions containing surfactants or complexes with polymer ligands (coating method), the introduction of TiO₂ nanoparticles on/into catalysis carriers (supported technology), and so on.^{10–14}

In recent years, the preparation of catalysis carriers has attracted tremendous attention, considering that the strategy could efficiently avoid the aggregation of TiO₂ nanoparticles without a decrease of their catalytic activity. It is well known that a large amount of solid supports (such as carbon, organic composite, polymer, metal oxide and so forth) with different nanostructures (including nanotubes, spheres, microporous metal-organic framework (MMOF), fibers, and so on) are of great importance for broad applications in catalyst carriers.^{15–17} Among the material family, SNTs have always attracted interest because of their easy processing, facile surface modification, large specific surface area, and excellent mechanical performance and stability.^{18,19} As a novel class of inorganic structures, SNTs are particularly significant for fundamental

^aZhejiang Sci-Tech University, Hangzhou, China. E-mail: psduml@163.com

^bDepartment of Materials Engineering, Zhejiang Sci-Tech University, Hangzhou, Zhejiang, China

†Electronic supplementary information (ESI) available. See DOI: 10.1039/c3dt51959g

science and potential applications such as catalysis carriers, bioseparation, drug delivery, and controlled release.^{20,21}

Up to now, various synthesis strategies for SNTs have been reported. As the most common and conventional routes, template methods have been extensively studied as an alternative route to prepare SNTs. Various templates, such as polycarbonate (PC) membrane, polyvinylpyrrolidone (PVP) fibers, surfactants, and gel systems,^{22,23} have been used. However, template strategies will not only bring many impurities into the resulting SNTs, but also show low efficiencies and high cost. Therefore, it remains a challenge to fabricate SNTs by template methods, and it is also necessary and important to develop a simple and direct method to obtain highly purified silica nanotubes.

During the past decade, electrospinning has emerged as a convenient, versatile and cost-effective technique for generating extremely long continuous fibers with diameters ranging from several micrometers down to a few nanometers by applying a high voltage to a polymer solution or melt.²⁴ By employing this method, one-dimensional tubular nanostructures could be fabricated, usually through a spinneret with two coaxial capillaries to produce core/shell nanofibers, followed by selective removal of the core section.²⁵ Herein, based on solvent evaporation and phase separation, we present an effective and facile route to fabricate polyvinylpyrrolidone/tetraethyl orthosilicate (PVP/TEOS) microtubes (MTs) *via* the traditional single-nozzle electrospinning technique. Further investigations found that SNTs could be acquired through heat treatment of the above NTs. The as-prepared SNTs might be one of the most promising supports for the fabrication of TiO₂-based tubular heterostructures due to their high specific surface area, availability, and chemical stability.^{10,26,27}

In this report, we highlight our work on the facile preparation of SNTs and TiO₂/SNTs. The SNTs were obtained by combining the sol-gel method, the electrospinning technique and the process of calcination. Then, a one-step solvothermal method was applied to prepare TiO₂/SNTs heterostructures. As-prepared TiO₂/SNTs tubular heterostructures with high specific surface area exhibited excellent photocatalytic activity and recyclability in the degradation of organic pollutants. The processes might provide a new insight into the fabrication of tubular materials and various heterostructures.

2. Experiment section

2.1 Materials

Tetraethyl orthosilicate (Si(OC₂H₅)₄, TEOS, 98%), polyvinylpyrrolidone ((C₆H₉NO)_n, PVP, *M_n* = 1 300 000), titanium butoxide (Ti(OC₄H₉)₄, 99%) and dimethylpyridine N-oxide (DMPO) were purchased from Aladdin Chemical Reagent Co., Ltd (Shanghai, China). Absolute ethanol (C₂H₅OH) was acquired from Hangzhou Gaojing Fine Chemical Industry Co., Ltd (Hangzhou, China). Isopropyl alcohol ((CH₃)₂CHOH, reagent grade) was supplied by Tianjin Yongda Chemical Reagent Co., Ltd (Tianjin, China). Hydrochloric acid (HCl, 36–38%) was obtained

from Zhejiang Three Eagle Chemical Reagent Co., Ltd (Jinhua, China). Rhodamine 6G (C₂₈H₃₁ClN₂O₃, 99%) was bought from ACROS Organics (New Jersey, USA). Deionized water was prepared using a Barnstead from Thermo Scientific (Shanghai, China). All chemicals were of analytical grade and used as received without further purification.

2.2 The preparation of SNTs

In a typical preparation, PVP powder with the mass of 1.5 g was completely dissolved in 16 mL of absolute ethanol. Then, 3.2 mL of TEOS was slowly added into the above PVP solution. After being stirred for 3 h, the precursor was transferred into a plastic syringe for electrospinning under the voltage of 10 kV and the flow rate of 1.2 mL h⁻¹. The resulting products were collected at a distance of about 14 cm to the syringe tip. Afterwards, the acquired PVP/TEOS microfibers were calcined at the rate of 8 °C min⁻¹ until a temperature of 600 °C was reached and held for 3 h. Accordingly, SNTs were obtained, and kept for further characterizations and experiments.

2.3 The synthesis of TiO₂/SNTs heterostructures

TiO₂/SNTs heterostructures were synthesized by a facile solvothermal method. In a typical synthesis, 0.3 mL of butyl titanate was dissolved in 6 mL of isopropanol to obtain the precursor solution. Then SNTs with the mass of 150 mg were added into the above solution under vigorous magnetic stirring, and the pH of the mixture was adjusted to 4 using hydrochloric acid (0.3 M) at room temperature. The mixture solution was then transferred into a Teflon-lined tube reactor and was kept at 160 °C for 24 h. Once cooled to room temperature, the resultant was centrifuged, washed with distilled water, and dried at 60 °C under vacuum for 24 h.

2.4 Photocatalytic activity measurements

The photocatalytic activity of the samples was evaluated by degradation of Rhodamine 6G under irradiation with a 500 W high-pressure mercury lamp with a characteristic wavelength of 365 nm in an XPA-7 Photoreaction Spectrometer (Nanjing xujiang). The temperature of the reactant solution was maintained below 283 K by the flow of cold water during the reaction. In each experiment, 30 mg of the photocatalyst was added into 60 mL of Rhodamine 6G aqueous solution with a concentration of 10 mg L⁻¹ in a reaction cell with a Pyrex jacket. Prior to irradiation, the suspension was magnetically stirred in the dark for 1 h to reach adsorption-desorption equilibrium of Rhodamine 6G on the surface of the photocatalyst. After given time intervals, 2 mL of the suspension solution was taken out and then centrifuged (11 000 rpm, 5 min) to remove the photocatalyst particles for UV-Vis absorption measurements. As a control, another sample was evaluated without irradiation (in order to test the adsorption ability of the catalyst), and then investigated by the aforementioned method. The percentage of degradation is reported as *C/C₀*, where *C* is the maximum peak of the absorption spectra of Rhodamine 6G for each irradiated time interval at a wavelength of 525 nm, and *C₀* is the absorption of the starting concentration.

2.5 Characterizations

2.5.1 Field emission scanning electron microscopy (FE-SEM). The morphologies of the PVP/TEOS microfibers and SNTs were characterized by a field emission scanning electron microscope (FE-SEM, JEOL ULTRA-55) operated at an accelerating voltage of 1 kV.

2.5.2 Transmission electron microscopy (TEM). The samples for transmission electron microscopy (TEM) and high-resolution transmission electron microscopy (HRTEM) measurements were evaluated using a JEOL JSM-2010 (acceleration voltage of 200 kV).

2.5.3 X-ray diffraction (XRD). The compositions of the powders (SNTs and TiO_2/SNTs) were analyzed with an X-ray diffractometer (XRD, Thermo ARL X'TRA) using a $\text{Cu K}\alpha$ radiation source at 35 kV with a scan rate of $0.02^\circ 2\theta \text{ s}^{-1}$ in the 2θ range of $10\text{--}80^\circ$.

2.5.4 Fourier transform infrared spectroscopy (FT-IR). SNTs powder and as-prepared TiO_2/SNTs heterostructures were spread on KBr pellets and then dried under an infrared lamp. FT-IR measurements were recorded on a Thermo Scientific Nicolet 5700 FT-IR spectrometer in the wavenumber range of $500\text{--}4000 \text{ cm}^{-1}$.

2.5.5 Ultraviolet-visible spectroscopy (UV-Vis). UV-Vis spectra of the as-synthesized TiO_2/SNTs heterostructures were collected using a Perkin Elmer Lambda 900 UV-Vis spectrophotometer over a wavelength range of $200\text{--}800 \text{ nm}$.

2.5.6 Electron spin resonance (ESR). ESR spectra were acquired with a Bruker A3000 electron paramagnetic resonance spectrometer. The settings were as follows: center field, 3478.00 G ; microwave frequency, 9.88 GHz ; and power, $20 \text{ }\mu\text{W}$.

2.5.7 Energy dispersive spectrometer (EDS). The elementary compositions of the TiO_2/SNTs heterostructures were obtained on an Oxford Inca-6587 spectrometer.

2.5.8 N_2 absorption-desorption experiments. The process was carried out at -193°C using a BeiShiDe Instruments S&T 3H-2000 PS1 specific surface and pore size analysis instrument. The samples were subjected to outgassing for 3 h at 200°C before the experiment. The surface area was evaluated using the BET (Brunauer-Emmett-Teller) method.

3. Results and discussion

Fig. 1 shows the FE-SEM and TEM images of PVP/TEOS microfibers prepared by electrospinning the PVP/ $\text{C}_2\text{H}_5\text{OH}$ /TEOS precursor. It was obviously seen that large quantities of microfibers with a smooth outer surface and homogeneous diameters were synthesized *via* the electrospinning technique. The typical average diameter of the fibers was about $1 \text{ }\mu\text{m}$ and the standard deviation was 99.6 nm . TEM images indicated that the hollow structures had already formed within the samples after electrospinning. The hollow PVP/TEOS microfibers were $250\text{--}300 \text{ nm}$ in wall thickness and $300\text{--}350 \text{ nm}$ in inner diameter, which was consistent with the corresponding FE-SEM images.

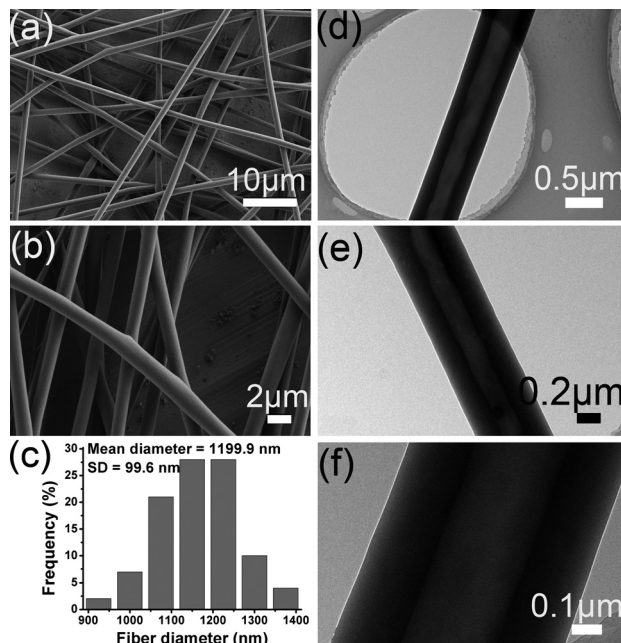


Fig. 1 FE-SEM (a and b) and TEM (d, e and f) images of PVP/TEOS microfibers; (c) the corresponding diameter distribution of PVP/TEOS microfibers.

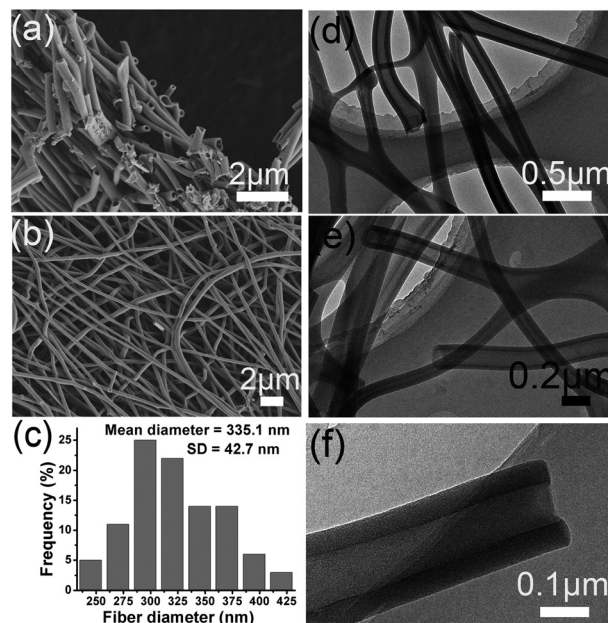
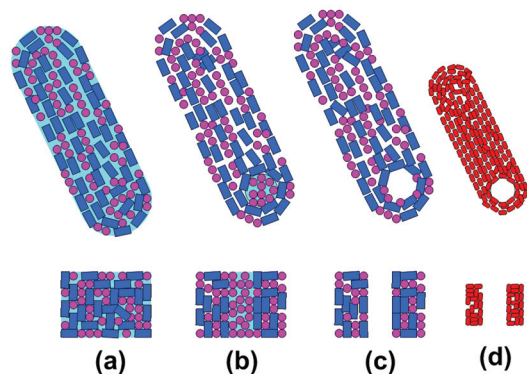


Fig. 2 FE-SEM (a and b) and TEM (d, e and f) images of SNTs; (c) the corresponding diameter distribution of SNTs.

In order to obtain pure SNTs, electrospun hollow PVP/TEOS microfibers were calcined so as to remove the PVP and promote the formation of silica. The morphologies and the diameter distribution of the obtained samples were investigated with FE-SEM, as shown in Fig. 2(a)–(c). It was clearly seen that these consistent tubular products have the average diameter of 335 nm . Meanwhile, it could be observed that

pure SNTs aligned in a random orientation because of the bending instability associated with the spinning jet.²⁸ In the meantime, TEM images of the SNTs further confirmed the hollow structure, as can be seen in Fig. 2(d)–(f). Fig. 2(f) exhibits a cross-section of the nanotubes, and the result reveals that our obtained products are comprised of tubular microfibers with the wall thickness of 40–60 nm and the mean diameter of 300 nm, which is in accordance with the FE-SEM observations. Evidently, the diameter of the hollow fibers decreases to less than half that of the PVP/TEOS microfibers shown in Fig. 1. The distinct contrast might be assigned to two reasons. First, PVP was completely decomposed during the high temperature annealing treatments, leaving many vacancies in the tube walls, accordingly resulting in shrinkage of the nanotubes during the calcination process.^{26,27} On the other hand, silica molecules could be reconstructed in the tube walls at high temperature, which might also lead to the diameter decrease of the nanotubes.

As is known, organic–inorganic composite fibers can be acquired by combining the sol–gel method and the electrospinning technique. Also, inorganic fibers could be obtained through calcination of the above composite fibers so as to remove the polymer binder. In our experiments, once the electrospinning process began, fibers (in Scheme 1(a)) were spun out from the nozzle, and the ethanol solvent in the precursor will evaporate rapidly from the fibers. Then, a concentration gradient of ethanol would form along the radial direction of the fibers. Obviously, the ethanol concentration at the center of the fibers is higher compared to that at the edge of the fibers, and the concentration gradient would eventually push the system into unstable phase states and a phase separation happens. As a result, TEOS would inevitably diffuse along the concentration gradient of ethanol. Meanwhile, it is well known that TEOS shows a high solubility in ethanol but is incompatible with PVP; therefore, TEOS would concentrate at the center of microfibers and PVP would be forced to migrate from the core of the fibers to the outer surface. The PVP/TEOS microtubes are filled with TEOS at this moment, as illustrated in Scheme 1(b). Moreover, as a volatile liquid, TEOS might evaporate through the wall of the microtubes



Scheme 1 Schematic diagram of the formation mechanism of silica nanotubes. ●, ethanol; ■, PVP; ●, TEOS; ■, silica nanotubes.

easily. Therefore, based on the above results and discussions, it is considered that the morphologies of the fibers in a way depend on the competition between the evaporation rate and the process of phase separation; when the former plays a leading role, hollow PVP/TEOS fibers are formed, as shown in Scheme 1(c).^{33–35} As the calcination process proceeds, PVP molecules would become decomposed gradually and removed completely from the composite fibers. In the meantime, pure SNTs (as can be seen in Scheme 1(d)) were obtained through the interaction of TEOS and oxygen in the air. It is evident that the nanotubes show rough walls with porous structures, which is also evidence of a rapid phase separation during the electrospinning process and drastic chemical reactions.

Successful preparation of TiO_2 /SNTs heterostructures was confirmed by their corresponding TEM images and the EDS spectrum. TEM images of the samples shown in Fig. 3 indicated that there was essentially no change of the nanofibers' external morphology during the growth of TiO_2 nanoparticles. It is evident that a large amount of nanoparticles deposited on the SNTs can be found in Fig. 3. Compared with the TEM images of pure TiO_2 (Fig. S1†), TiO_2 nanoparticles loaded on the SNTs were significantly smaller in particle size. Furthermore, in Fig. 3(f), the latter fringe spacing of TiO_2 nanoparticles was 0.24 and 0.35 nm, which correspond to the (004) and (101) planes, respectively.^{35–38} The chemical elemental component of the resulting samples was characterized by the EDS spectrum, which indicates that TiO_2 /SNTs are composed of the elements Si, Ti, and O.

To evaluate the pore structure and specific surface area, N_2 adsorption–desorption isotherms of the heterostructures were performed before and after the deposition of TiO_2 nanoparticles. Typical isotherms of the SNTs and TiO_2 /SNTs

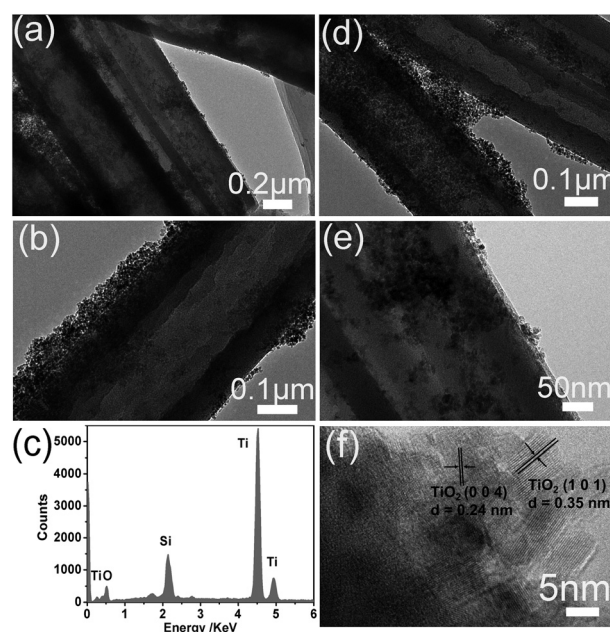


Fig. 3 The TEM images of TiO_2 /SNTs heterostructures (a, b, d and e); (c) the EDS spectrum of TiO_2 /SNTs; (f) the HRTEM image of TiO_2 nanoparticles.

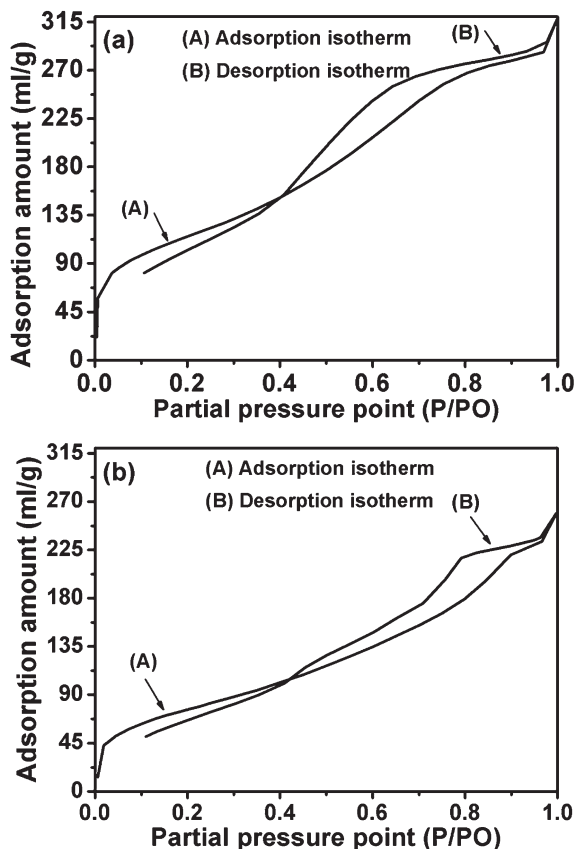


Fig. 4 Adsorption-desorption isotherms of SNTs (a) and TiO₂/SNTs heterostructures (b).

samples is shown in Fig. 4. Evidently, with the loading of TiO₂ nanoparticles, the hysteresis loop became shorter, indicating a reduction of the pore volume. This seems to be logical as the loading of TiO₂ nanoparticles was dispersed and deposited on the surface of SNTs, decreasing the diameter of SNTs and thus diminishing the surface area. The BET surface areas of SNTs and TiO₂/SNTs were determined to be around 411.58 and 279.31 m² g⁻¹, respectively. The reduction of the BET surface area of TiO₂/SNTs can be attributed to the deposition of TiO₂ nanoparticles.

The FT-IR spectra of the SNTs and TiO₂/SNTs heterostructures were used to investigate the compositions and structures of the resulting samples. As shown in Fig. 5, the absorption peak at 3481 cm⁻¹ belongs to the asymmetrical stretching vibration of -OH groups, which are related to the bound water and free water that may absorb on the surface of the SNTs. The peak at 1633 cm⁻¹ is attributed to the bending vibration absorption peak of H-O-H which is derived from the pore water and surface absorbed water. The characteristic peaks of silica at 1090 cm⁻¹ and 802 cm⁻¹ are assigned to the asymmetrical stretching and symmetric stretching of Si-O-Si bonds, respectively.²⁹⁻³¹ Compared to SNTs, no other characteristic signals are detected in TiO₂/SNTs, but the intensity of the peaks shows distinct changes, which may be attributed to the fact that the SNTs were coated by the acquired TiO₂ nanoparticles;

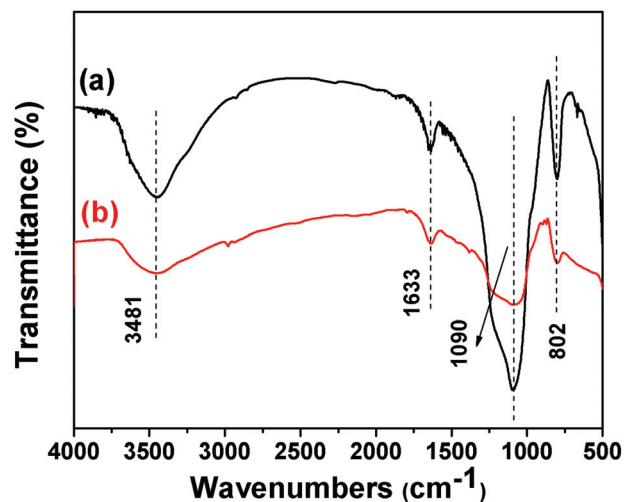


Fig. 5 FT-IR spectra of SNTs (curve a) and TiO₂/SNTs heterostructures (curve b).

accordingly, the characteristic absorption peaks of SNTs are becoming much weaker.

To further verify the formation of TiO₂/SNTs heterostructures and the presence of TiO₂ nanoparticles, the SNTs and TiO₂/SNTs powder were characterized by XRD. As shown in Fig. 6, according to the literature, the strong and broad diffractions in curve a in the 2θ range between 23 and 25 degrees are assigned to amorphous silica.³²⁻³⁴ On the basis of JCPDS 21-1272, as observed in curve b, all the characteristic signals of TiO₂ can be ascribed to the (101), (004), (200), (105), (211), and (204) planes of anatase structure TiO₂,³⁵⁻³⁸ which is in good accordance with pure TiO₂ (Fig. S2†). From the above results, it can be further confirmed that the TiO₂/SNTs were successfully synthesized. However, the peak of amorphous silica appeared to be narrower and weaker in curve b compared to that of the pure SNTs, probably because of coating of TiO₂ nanoparticles, which might weaken the diffraction of amorphous silica.

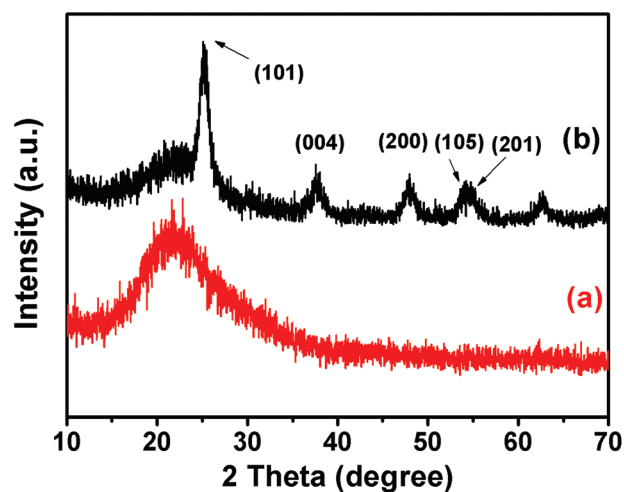


Fig. 6 The XRD patterns of SNTs (curve a) and TiO₂/SNTs heterostructures (curve b).

To demonstrate the photocatalytic activity of the as-obtained TiO_2/SNTs heterostructures for the degradation of organic pollutants, we carried out experiments on the photocatalytic degradation of Rhodamine 6G as a test reaction. Furthermore, in the comparative experiments, pure TiO_2 (Fig. S1 and S2†) was used as a photocatalytic reference to understand the photocatalytic activity of the TiO_2/SNTs heterostructures. As is well known, the band gap of pure TiO_2 is 3.2 eV, which greatly limits its photoresponse to the solar energy. In order to investigate the degradation ability of the heterostructures based on TiO_2 and SNTs, UV irradiation was selected as the light source. In Fig. 7, control experiments were performed under different conditions: (a) with UV irradiation but in the absence of the photocatalyst; (b) in the presence of photocatalysts but in the dark. After UV light irradiation for 90 min, the degradation efficiency of Rhodamine 6G was about 90% and 55% for the TiO_2/SNTs heterostructures and pure TiO_2 , respectively. Obviously, the TiO_2/SNTs heterostructures showed much higher photocatalytic activities than pure TiO_2 . Also, there was no appreciable degradation of Rhodamine 6G in the absence of photocatalysts and in the presence of photocatalysts but in the dark. Therefore, Rhodamine 6G could be degraded efficiently when UV light was used as the light source in the presence of TiO_2/SNTs heterostructure photocatalysts. More importantly, it was indicated that these heterostructures could be easily separated and recovered by sedimentation without decreasing their photocatalytic activities distinctly and would greatly promote their practical application to eliminate organic pollutants

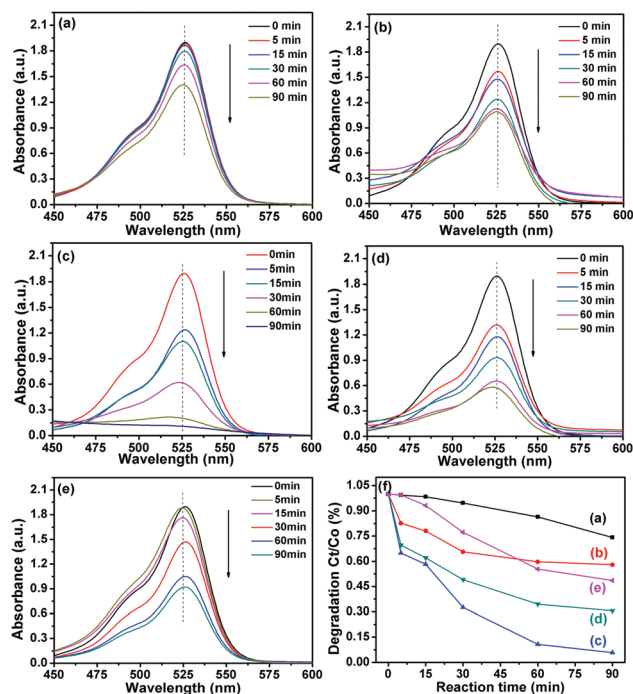


Fig. 7 Photocatalytic activity of TiO_2/SNTs heterostructures to Rhodamine 6G: (a) no catalyst; (b) TiO_2/SNTs under dark conditions; (c) TiO_2/SNTs ; (d) TiO_2/SNTs for the second time; (e) pure TiO_2 ; (f) photocatalytic decomposition curves of Rhodamine 6G.

from waste water. In order to probe the effect of absorbance and identify whether there is Rhodamine 6G over the surface of the obtained heterostructure, FT-IR measurement (Fig. S3†) was employed to illustrate them. It could be seen clearly that the characteristic peaks of Rhodamine 6G almost disappeared after the degradation process. Zhang *et al.* have already studied the photocatalytic capability of silica/titania nanotubes composite membrane.⁴⁴ Compared with their work, we emphasized the facile preparation process of TiO_2/SNTs by electrospinning and put forward the heterostructures to explain why TiO_2/SNTs exhibited higher photocatalytic activity than pure TiO_2 , which would be demonstrated by our later analysis.

The generation of a large amount of $\text{O}_2^{\cdot-}$ and OH^{\cdot} radicals from the tubular TiO_2/SNTs heterostructures during the degradation of Rhodamine 6G was demonstrated by ESR with dimethylpyridine N-oxide (DMPO) as a spin-trapping reagent. As described in Fig. 8(a), four characteristic peaks for DMPO-OH^{\cdot} with an intensity ratio of 1:2:2:1 were obviously observed when the TiO_2/SNTs heterostructures were illuminated with UV irradiation. On the other hand, pure TiO_2 exhibits no characteristic peaks under the same conditions,

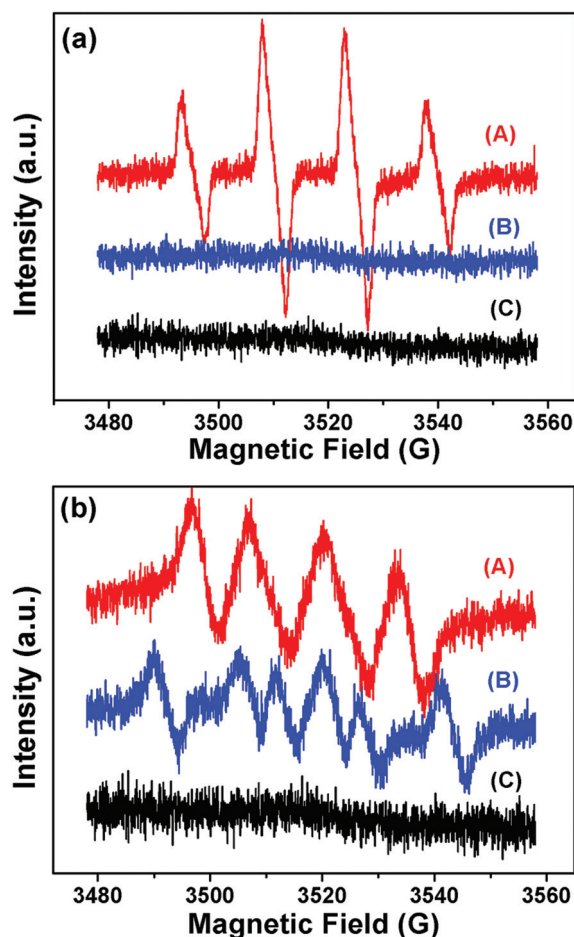
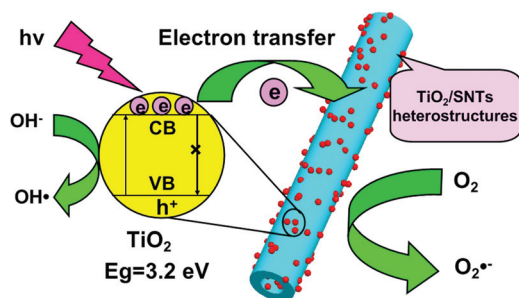


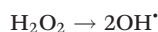
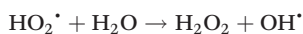
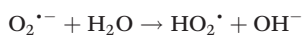
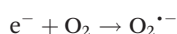
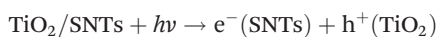
Fig. 8 The ESR spectra for (A) TiO_2/SNTs heterostructures, (B) pure TiO_2 , (C) no catalyst at ambient temperature: (a) in aqueous dispersion for DMPO-OH^{\cdot} ; (b) in methanol dispersion for $\text{DMPO-O}_2^{\cdot-}$.



Scheme 2 Proposed mechanisms for the photocatalysis of TiO₂/SNTs heterostructures.

suggesting that there are almost no OH[•] radicals during the degradation process. In addition, it could be seen clearly in Fig. 8(b) that six characteristic peaks for DMPO–O₂^{•-} were detected in methanol. The above experimental results further verify the reason why our obtained TiO₂/SNTs heterostructures display higher photocatalytic activity than the pure TiO₂.^{45–47}

In order to explain the difference between the TiO₂/SNTs heterostructures and pure TiO₂ in photocatalytic degradation of Rhodamine 6G, on the basis of earlier reports on the photocatalytic degradation of pollutants, a proposed mechanism of photodegradation of Rhodamine 6G with TiO₂/SNTs heterostructures is illustrated schematically in Scheme 2. The mechanism was that SNTs supported catalysts were believed to exhibit cooperative effects between SNTs and TiO₂ nanoparticles. Here, a high-energy photon excites an electron from the valence band to the conduction band of TiO₂, photogenerated electrons in TiO₂ may move freely toward the surface of the SNTs and excess of valence band holes were left in the TiO₂ to migrate to the surface and react with H₂O or OH⁻ to produce active species such as OH[•],^{1,28,39} suggesting that the photogenerated electrons and holes were efficiently separated. Because SNTs exhibit the characteristic properties of a p-type semiconductor⁴⁰ while TiO₂ is an n-type semiconductor,⁴¹ we can conclude that the p–n junction is formed between SNTs and TiO₂ and then reduces the recombination of electron–hole pairs, leading to enhanced photocatalytic activity. The mechanism of the photocatalytic degradation of Rhodamine 6G in our experiment was proposed to be the following:



Upon UV light irradiation, photogenerated electrons in TiO₂ moved freely to the surface of the SNTs; meanwhile, the photogenerated holes were left in the valence band of TiO₂. Subsequent to the above process, the holes (h⁺) were ultimately trapped by surface hydroxyl groups (or H₂O) at the catalyst surface to yield OH[•] radicals; at the same time, the dissolved oxygen molecules react with the surface of the SNTs electrons (e⁻) to yield superoxide radical anions (O₂^{•-}), which generate hydroperoxy (HO₂[•]) and hydroxyl ions. Then the hydroxyl radical (OH[•]) was produced, which is a strong oxidizing agent to decompose the organic dye.^{42,43}

4. Conclusions

In summary, SNTs with high specific area surface were acquired through calcination of hollow PVP/TEOS microfibers, which could be generated by effectively controlling the phase separation and solvent evaporation in the process of electrospinning. Further research showed that SNTs were excellent carriers for TiO₂ nanoparticles, and as-prepared TiO₂/SNTs heterostructures exhibited higher photocatalytic activities than pure TiO₂ for the degradation of Rhodamine 6G under UV light irradiation. Moreover, TiO₂/SNTs heterostructures could be easily recycled without a distinct decrease of the photocatalytic activity. The study also suggests that tubular TiO₂/SNTs heterostructures are an outstanding type of UV-light-driven photocatalysts for environmental remediation applications.

Notes and references

- 1 X. Zhang, L. Z. Zhang, T. F. Xie and D. J. Wang, *J. Phys. Chem. C*, 2009, **113**, 7371.
- 2 R. Asahi, T. Morikawa, T. Ohwaki, K. Aoki and Y. Taga, *Science*, 2001, **293**, 269.
- 3 A. Fujishima and K. Honda, *Nature*, 1972, **238**, 37.
- 4 R. Fiz, F. Hernandez-Ramirez, T. Fischer, L. Lopez-Conesa, S. Estrade, F. Peiro and S. Mathur, *J. Phys. Chem. C*, 2013, **117**, 10086.
- 5 H. G. Yang and H. C. Zeng, *J. Am. Chem. Soc.*, 2005, **127**, 270.
- 6 A. Kudo and Y. Miseki, *Chem. Soc. Rev.*, 2009, **38**, 253.
- 7 D. C. Daniela, R. Fabrizio, S. Santucci and L. Luca, *J. Phys. Chem. C*, 2012, **116**, 18427.
- 8 J. Du, X. Y. Lai, N. L. Yang, J. Zhai, D. Kisailus, F. B. Su, D. Wang and L. Jiang, *ACS Nano*, 2011, **5**, 590.
- 9 K. Takashi, Y. Daiki and Y. Hiromi, *J. Phys. Chem. C*, 2010, **114**, 15049.
- 10 Z. Y. Zhang, C. L. Shao, Y. Y. Sun, J. B. Mu, M. Y. Zhang, P. Zhang, Z. C. Guo, P. P. Liang, C. H. Wang and Y. C. Liu, *J. Mater. Chem.*, 2012, **22**, 1387.
- 11 A. C. Patel, S. Li, C. Wang, W. Zhang and Y. Wei, *Chem. Mater.*, 2007, **19**, 1231.

- 12 S. Wunder, F. Polzer, Y. Lu, Y. Mei and M. Ballauff, *J. Phys. Chem. C*, 2010, **114**, 8814.
- 13 X. Sun and Y. Li, *Angew. Chem., Int. Ed.*, 2004, **43**, 597.
- 14 H. Zhang, X. Li and G. Chen, *J. Mater. Chem.*, 2009, **19**, 8223.
- 15 S. K. Li, F. Z. Huang, Y. Wang, Y. H. Shen, L. G. Qiu, A. J. Xie and S. J. Xu, *J. Mater. Chem.*, 2011, **21**, 7459.
- 16 S. H. Xuan, W. Q. Jiang, X. L. Gong, Y. Hu and Z. Y. Chen, *J. Phys. Chem. C*, 2009, **113**, 553.
- 17 Q. Li, B. D. Guo, J. G. Yu, J. R. Ran, B. H. Zhang, H. J. Yan and J. R. Gong, *J. Am. Chem. Soc.*, 2011, **133**, 10878.
- 18 G. L. Li, Z. L. Zheng, H. Mohwald and D. G. Shchukin, *ACS Nano*, 2013, **7**, 2470.
- 19 F. Hoffmann, M. Cornelius, J. Morell and M. Froba, *Angew. Chem., Int. Ed.*, 2006, **45**, 3216.
- 20 A. J. Nan, X. Bai, S. J. Son, S. B. Lee and H. Ghandehari, *ACS Nano*, 2008, **8**, 2150.
- 21 S. J. Son, J. Reichel, B. He, M. Schuchman and S. B. Lee, *J. Am. Chem. Soc.*, 2005, **127**, 7316.
- 22 S. W. Bian, Z. Ma, L. S. Zhang, F. Niu and W. G. Song, *Chem. Commun.*, 2009, 1261.
- 23 M. Adachi, T. Harada and M. Harada, *Langmuir*, 2000, **16**, 2376.
- 24 M. Yamanaka, Y. Miyake, S. Akita and K. Nakano, *Chem. Mater.*, 2008, **20**, 2072.
- 25 J. H. Jung, M. Park and S. Shinkai, *Chem. Soc. Rev.*, 2010, **39**, 4286.
- 26 D. Li and Y. Xia, *Adv. Mater.*, 2004, **16**, 1168.
- 27 X. H. Li, C. L. Shao and Y. C. Liu, *Langmuir*, 2007, **23**, 10920.
- 28 J. B. Mu, C. L. Shao, Z. C. Guo, Z. Y. Zhang, M. Y. Zhang, P. Zhang, B. Chen and Y. C. Liu, *ACS Appl. Mater. Interfaces*, 2011, **3**, 590.
- 29 T. Pirzada, S. A. Arvidson, C. D. Saquing, S. S. Shah and S. A. Khan, *Langmuir*, 2012, **28**, 5834.
- 30 D. Srinivasan, R. Rao and A. Zribi, *J. Electron. Mater.*, 2006, **35**, 504.
- 31 G. I. Andrade, E. F. Barbosa-Stancioli, A. A. P. Mansur, W. L. Vasconcelos and H. S. Mansur, *J. Mater. Sci.*, 2008, **43**, 450.
- 32 H. Yu, R. Sheikholeslami and W. O. S. Doherty, *Ind. Eng. Chem. Res.*, 2002, **41**, 3379.
- 33 Z. W. Huang, F. Cui, H. X. Kang, J. Chen, X. Z. Zhang and C. G. Xia, *Chem. Mater.*, 2008, **20**, 5090.
- 34 C. H. Bartholomew and R. J. Farrauto, *J. Catal.*, 1976, **45**, 41.
- 35 W. Y. Dong, Y. J. Sun, C. W. Lee, W. M. Hua, X. C. Lu, Y. F. Shi, S. C. Zhang, J. M. Chen and D. Y. Zhao, *J. Am. Chem. Soc.*, 2007, **129**, 13894.
- 36 P. D. Yang, D. Y. Zhao, D. I. Margolese, B. F. Chmelka and G. D. Stucky, *Nature*, 1998, **396**, 152.
- 37 D. L. Li, H. S. Zhou and I. Honma, *Nat. Mater.*, 2004, **3**, 65.
- 38 S. Y. Choi, M. Mamak, N. Coombs, N. Chopra and G. A. Ozin, *Adv. Funct. Mater.*, 2004, **14**, 335.
- 39 K. Woan, G. Pyrgiotakis and W. Sigmund, *Adv. Mater.*, 2009, **21**, 2233.
- 40 S. K. Poznyak and A. I. Kulak, *Electrochim. Acta*, 1990, **35**, 1941.
- 41 X. P. Lin, J. C. Xing, W. D. Wang, Z. C. Shan, F. F. Xu and F. Q. Huang, *J. Phys. Chem. C*, 2007, **111**, 18288.
- 42 T. Aarthi and G. Madras, *Ind. Eng. Chem. Res.*, 2007, **46**, 7.
- 43 K. Rajeshwar, M. Osugi, W. Chanmanee, C. Chenthamarakshan, M. Zanoni, P. Kajitvichyanukul and A. R. Krishnan, *J. Photochem. Photobiol., C*, 2008, **9**, 171.
- 44 H. M. Zhang, X. Quan, S. Chen and H. M. Zhao, *Environ. Sci. Technol.*, 2006, **40**, 6104.
- 45 Z. H. Li, Z. P. Xie, Y. F. Zhang, L. Wu, X. X. Wang and X. Z. Fu, *J. Phys. Chem. C*, 2007, **111**, 18348.
- 46 Y. F. Zhao, S. T. Zhang, B. Li, H. Yan, S. He, L. Tian, W. Y. Shi, J. Ma, M. Wei, D. G. Evans and X. Duan, *Chem.-Eur. J.*, 2011, **17**, 13175.
- 47 M. Ruzzi, E. Sartori, A. Moscatelli, I. V. Khudiyakov and N. J. Turro, *J. Phys. Chem. A*, 2013, **117**, 5232.



Facile fabrication of AuNPs/PANI/HNTs nanostructures for high-performance electrochemical sensors towards hydrogen peroxide

Pan Wang^b, Mingliang Du^{a,b,*}, Ming Zhang^{a,b}, Han Zhu^b, Shiyong Bao^b, Meiling Zou^b, Tingting Yang^b

^a Key Laboratory of Advanced Textile Materials and Manufacturing Technology, Zhejiang Sci-Tech University, Ministry of Education, Hangzhou 310018, PR China

^b Department of Materials Engineering, College of Materials and Textile, Zhejiang Sci-Tech University, Hangzhou 310018, PR China

HIGHLIGHTS

- H₂O₂ detection biosensor using AuNPs/PANI/HNTs nanostructures was fabricated.
- *In situ* polymerization and reduction were employed.
- The biosensor exhibited high electrochemical performance.

ARTICLE INFO

Article history:

Received 10 January 2014

Received in revised form 7 March 2014

Accepted 12 March 2014

Available online 22 March 2014

Keywords:

Electrochemical sensors

Hydrogen peroxide

Polyaniline

Halloysite nanotubes

Gold nanoparticles

ABSTRACT

Here we proposed a facile strategy to synthesize multi-layered gold nanoparticles/polyaniline/halloysite nanotubes (AuNPs/PANI/HNTs) nanostructures used for electrochemical sensors. The PANI/HNTs were firstly obtained by making use of the *in situ* polymerization as well as employing the thioglycolic acid (TA) as the dopant, thereafter, Au ions were anchored to TA and then reduced by PANI. Field emission scanning electron microscopy (FE-SEM) and transmission electron microscopy (TEM) observations implied that a large amount of uniform AuNPs were immobilized on the PANI/HNTs. The as-prepared AuNPs/PANI/HNTs nanostructures were also characterized by Fourier transform infrared spectroscopy (FTIR), X-ray diffraction (XRD) and X-ray photoelectron spectroscopy (XPS), and the results confirmed the successful synthesis of AuNPs/PANI/HNTs nanostructures and explained the reactions in depth as well. Further investigations suggested that the AuNPs/PANI/HNTs nanostructures with well-separated AuNPs exhibited high electrochemical performance as sensors to detect hydrogen peroxide (H₂O₂).

© 2014 Elsevier B.V. All rights reserved.

1. Introduction

Electrochemical sensors have been drawing tremendous attention due to their great promise in a wide range of fields, such as industry and environmental monitoring, food inspection and medical diagnosis, since the initial development of glucose enzyme electrodes by Lyons and Clark in 1962 [1–3]. Recent years, with the increasingly serious environmental problems and peoples' close concerning to health, concentrated efforts have been focused on the detection of H₂O₂, considering its extensive applications in various fields such as biological, environmental, clinical, and food analysis [4], leading to an upsurge of interests to explore various

H₂O₂ detectors. Recently, we synthesized AgNPs/(PVA/PEI) nanofibers and found that the nanofibers could be used as high electrochemical efficiency and durability for H₂O₂ electrochemical sensors [5]. Feng et al. have synthesized graphene/polyaniline composite film to detect H₂O₂ and the electrochemical sensor showed a good linear response over a manifold range of concentrations [6]. Apparently, multi-layered nanostructured materials have been extensively used as sensing materials, attributing to their high surface-to-volume ratios, high porosity and low cross-section.

Most recently, as far as representative conducting polymers, polyaniline has caught the eyes of researchers, considering its wide applications in actuators, gas sensors, electrochemical capacitors and memory devices [7,8]. In order to facilitate the electron transfer, metal nanoparticles have been widely employed to enhance electrocatalytic activity [9]. Therefore, metal nanoparticles combined with polyaniline have demonstrated functionality in a variety of fields [10]. Meanwhile, one of the important factors in

* Corresponding author at: Key Laboratory of Advanced Textile Materials and Manufacturing Technology, Zhejiang Sci-Tech University, Ministry of Education, Hangzhou 310018, PR China. Tel./fax: +86 571 86843255.

E-mail address: du@zstu.edu.cn (M. Du).

optimizing the properties of their applications is the stable and uniform size of the metal nanoparticles. Highly dispersed gold nanoparticles (AuNPs) have been discovered to be exceptionally active for a number of chemical reactions, such as oxidation and reduction [10,11]. However, the mechanical properties and long-term stability of the AuNPs/PANI remain a significant issue which deserves our attention and further exploration.

Halloysite nanotubes (HNTs, $\text{Al}_2\text{Si}_2\text{O}_5(\text{OH})_4 \cdot n\text{H}_2\text{O}$), an abundant deposited natural silicate resource with nanotubular structures, are easily obtainable and much cheaper, which could be collected from many parts of our country [12,13]. HNTs, a naturally occurred silicate with good chemical stability and large specific surface area, possess hollow structures with Al–OH groups in the internal surface and Si–OH groups on the external surface, making them easy to functionalize and perfect to be used as substrates. Recent years, HNTs were selected as reliable substrates in many scopes, such as, the organization of noble metal nanoparticles and many other materials with lower mechanical stability [14]. Inspired by their specific structure and wide applications, we also chose HNTs as dependent substrates to support our AuNPs/PANI nanofibers.

In the present investigation, we prepared PANI/HNTs nanostructures through a simple one-step *in situ* polymerization by using HNTs as templates and aniline as reactant. Additionally, we also introduced TA to dope the PANI and act as stabilizers as well to synthesis uniform and monodisperse AuNPs. Consequently, the AuNPs/PANI/HNTs were acquired. In another aspect, a series of characterizations were employed to detect and confirm the samples. The electrochemical performance of the as-obtained nanocomposites was also investigated in detail, and according to our results, the sensors based on the nanostructured AuNPs/PANI/HNTs composites exhibit high sensitivity towards H_2O_2 .

2. Experimental section

2.1. Chemicals and materials

The HNTs were obtained from Hubei Province, China. Aniline ($\text{C}_6\text{H}_7\text{N}$, 99.9%), hydroquinone (HQ), H_2O_2 (30 wt%), horseradish peroxidase (HRP, RZ ~ 3 , activity ≥ 250 units mg^{-1}), and thioglycolic acid ($\text{C}_2\text{H}_4\text{O}_2\text{S}$, TA, 98%) were supplied by Aladdin Chemistry Co., Ltd. Ammonium persulfate ($(\text{NH}_4)_2\text{S}_2\text{O}_8$, APS, 98%), glucose and ammonium hydroxide ($\text{NH}_3 \cdot \text{H}_2\text{O}$, 27%) were acquired from Hangzhou Gaojing Fine Chemical Industry, and aniline was distilled under reduced pressure. Hydrochloric acid (HCl, 36%) was bought from Shanghai Three-eagles Chemical Reagent Co., Ltd. Chloroauric acid ($\text{HAuCl}_4 \cdot 4\text{H}_2\text{O}$, 99.9%) was collected from Shanghai Civi Chemical Technology Co., Ltd. Deionized water (DIW, 18.2 M Ω) was used for all solution preparations. All chemicals were analytical grade.

2.2. The fabrication of AuNPs/PANI/HNTs nanostructures

The PANI/HNTs nanostructures were synthesized by the one-step *in situ* polymerization of aniline in the presence of HNTs. A description of the synthesis method is given as follows. A solution of 75 mL of 1 M HCl containing 150 mg of HNTs was stirred and sonicated at room temperature for 1 h, successively. Then, 0.75 mL of aniline monomer was added to the above suspension and then was stirred for 1 h. After that, 0.45 g of APS dissolved in 2 mL of 1 M HCl solution was added into to the reaction mixture drop by drop slowly. When the suspension turned to dark green, the polymerization of aniline occurred. The solutions were kept at room temperature and left at rest to polymerize for 6 h. Followed by an excess of $\text{NH}_3 \cdot \text{H}_2\text{O}$ (0.1 M) was used for dedoping and 3.5 mL of TA (1.0 M) was employed as a dopant. Then the PANI/HNTs nanostructures were collected using a centrifuge (at

12,000 rpm for 20 min) after being washed two times with DIW and alcohol and then dried under vacuum at 60 °C for 24 h.

The AuNPs were deposited onto the PANI/HNTs nanostructures via the reduction of Au ions. Typically, 20 mg of PANI/HNTs nanostructures were dispersed in 20 mL DIW by vigorous stirring for 2 h, then 1.44 mL of fresh prepared $\text{HAuCl}_4 \cdot 4\text{H}_2\text{O}$ (10 mM) was dropped into the suspensions. Several hours later, the AuNPs/PANI/HNTs nanostructures were obtained through the process of centrifuging, washing and drying, as described above.

2.3. The electrochemical measurement of AuNPs/PANI/HNTs nanostructures

The electrochemical experiments were conducted with a CHI660E workstation (Shanghai Chenhua, Shanghai). A three-electrode cell was employed for electrochemical evaluation in the PBS (pH = 6.8), where the Pt wire and a saturated Ag/AgCl electrode were used as the counter and reference electrodes, respectively. In the meantime, the HRP/(AuNPs/PANI/HNTs)/GCE was used as the working electrode, and the pure HNTs and the blank GCE were also selected as controls. Prior to the surface coating, the GC electrode was polished carefully with 1.0, 0.3, and 0.05 μm alumina powder and rinsed with DIW, followed by sonication in acetone and ethanol, successively. Appropriate amount of AuNPs/PANI/HNTs nanostructures and pure HNTs were mixed with Nafion (0.2%), respectively, and then were coated on the surface of the GCE. After that, the electrodes were allowed to dry under nitrogen and the PBS was also purged with nitrogen for 1 h prior to each experiment, so as to keep over the solution from oxygen.

2.4. Characterization

2.4.1. Field emission scanning electron microscopy (FE-SEM) and energy dispersive spectrometer (EDS)

The morphologies and the elementary composition of the pure HNTs, PANI/HNTs nanostructures and the AuNPs/PANI/HNTs nanostructures were recorded by a field emission scanning electron microscope (FE-SEM, JEOL ULTRA-55), attaching with an energy dispersive spectrometer (EDS).

2.4.2. Transmission electron microscopy (TEM)

For TEM imaging, the synthesized samples were dispersed in ethanol and drop cast onto the ultra-thin carbon-coated copper grid and dried under infrared lamp for ten minutes, respectively.

2.4.3. Fourier transform infrared spectroscopy (FTIR)

A Thermo Scientific Nicolet 5700 FTIR spectrometer was employed to characterize the FTIR spectra of pure HNTs, PANI/HNTs nanostructures and the AuNPs/PANI/HNTs nanostructures during the wave number of 500–4000 cm^{-1} under ambient conditions.

2.4.4. X-ray diffraction (XRD)

The crystal phase of the acquired samples were checked by a X-ray diffractometer (XRD, Thermo ARL X'TRA) using a Cu K α radiation source at 35 kV, with a scan rate of 0.02° 2 θ s^{-1} in the 2 θ range of 10–90°.

2.4.5. X-ray photoelectron spectroscopy (XPS)

The X-ray photoelectron spectra of the obtained examples were testified with an X-ray photoelectron spectrometer (K-Alpha, USA) with Al K X-ray source (1486.6 eV). The high-resolution survey (pass energy = 48 eV) was performed at spectral regions relating to oxygen, nitrogen, gold and sulfur.

3. Results and discussion

Fig. 1 displays the systematic sketch of the fabrication process of AuNPs/PANI/HNTs nanostructures and the obtained FE-SEM images of the obtained samples. As shown in Fig. 1(B1 and B2), the FE-SEM images of naturally occurring HNTs is in the micrometer range, and presents cylinder-shaped and polydisperse. After the *in situ* polymerization of aniline in the suspensions of HNTs, it is clearly that the vast majority of HNTs were coated with PANI (in Fig. 1(D1 and D2)). Fig. 1(F1) illustrated the structures and morphologies of the AuNPs/PANI/HNTs nanostructures, and it is difficult to make the AuNPs out in this magnification. However, from the EDS spectrum, as observed in Fig. 1(F2), the existence of the Au element further demonstrated the successful immobilization of AuNPs on the PANI/HNTs nanostructures.

TEM imaging was used to further determine the detailed micro-structure of the samples. As shown in Fig. 2(A and B), the HNTs are about 70 nm in diameter and present obvious hollow structure. After the *in situ* polymerization of aniline, it can be seen in Fig. 2(C and D) that a bundle of HNTs were coated and bounded by short fibrous PANI, as well as the PANI/HNTs nanostructures showed well-dispersion. Along the length direction of the HNTs, most parts of the surface are tightly coated by PANI, and almost no parts of the HNTs are naked, implying the strong binding between HNTs and PANI. There is no obvious change in size and morphology of the PANI nanofibers after the loading of AuNPs on them, and large amounts of AuNPs in uniform and small size are detected in Fig. 2(E and F). Herein, the nitrogens along the polyaniline chain provide physical stabilization for the autoreduced AuNPs, and thiol groups (–SH) can also function as stabilizers for the synthesis of small, stable, monodisperse AuNPs [15,16], which will be further confirmed by the XPS analysis.

The structure and composition of the AuNPs/PANI/HNTs nanostructures were further explored by spectroscopy measurement.

In the FTIR characterization, as described in Fig. 3(A and a), the characteristic peaks of HNTs that observed at 1630 cm^{-1} , 3621 cm^{-1} and 3696 cm^{-1} are attributed to the deformation of water, O–H stretching of inner hydroxyl groups and O–H stretching of inner-surface hydroxyl groups, respectively. The obvious absorption peaks emerged at 1106 cm^{-1} and 1029 cm^{-1} are in accordance with the in-plane stretching of Si–O [17,18]. On the other hand, it cannot be ignored that there is a significant shift of the two peaks of Si–O, which also implies the successful polymerization of aniline and the reduction of Au ions. The new peaks detected at 1301 cm^{-1} , 1486 cm^{-1} , and 1562 cm^{-1} in Fig. 3(A and b) are ascribed to the vibration of C–C, C=C, and C=N, respectively. Obviously, the intensity of the peaks in Fig. 3(A and c), when compared with that in Fig. 3(A and b) and (A and c), became relatively weak, indicating the strong interaction between HAuCl_4 and PANI during the synthesis of AuNPs. It is evident that the strong absorption peak around 1697 cm^{-1} is the characteristic peak of C=O in TA.

The PANI loaded on the HNTs could be further confirmed by XRD. According to the literature, all of the detected peaks can be indexed to the characteristic peaks of HNTs, as primarily shown in Fig. 3(B and a) and (B and b). After the loading of PANI and the formation of AuNPs, it can be seen that the diffraction peaks of HNTs were difficult to observe. At the same time, in the case of AuNPs/PANI/HNTs nanostructures, two new peaks centered at $2\theta = 20.1^\circ$ and 25.2° are the characteristic Bragg diffraction peaks of PANI, suggesting that they have partly crystalline structures, according to previous reports [19,20]. It is also noteworthy that four broad peaks centered at $2\theta = 38.1^\circ$, 44.4° , 64.6° and 77.6° which were observed in Fig. 3(B and c), matching exactly well with the reference values for the Au (111), Au (200), Au (220) and Au (311) lattice planes, respectively [21,22]. The above results can demonstrate that the AuNPs/PANI/HNTs nanostructures with fibrous PANI and well-dispersed AuNPs were successfully fabricated.

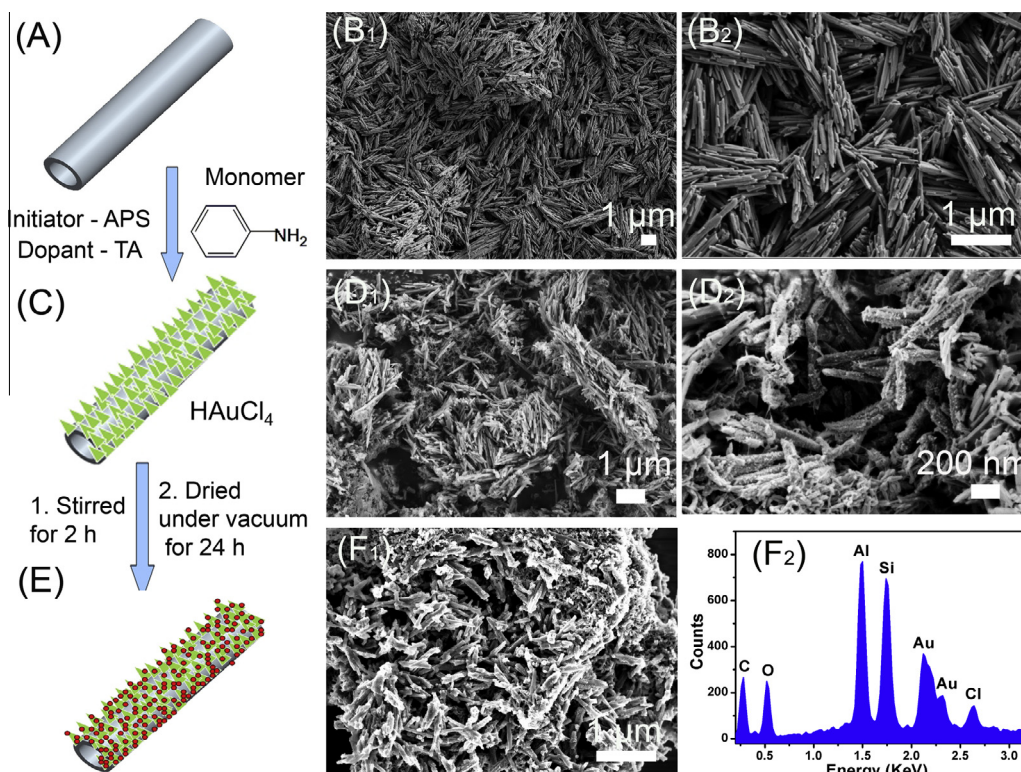


Fig. 1. The schematic illustration of the AuNPs/PANI/HNTs nanostructures (A. HNTs; C. PANI/HNTs; E. the AuNPs/PANI/HNTs nanostructures); the FE-SEM images of the HNTs (B1 and B2), PANI/HNTs (D1 and D2) and AuNPs/PANI/HNTs nanostructures (F1); EDS spectrum of the AuNPs/PANI/HNTs nanostructures (F2).

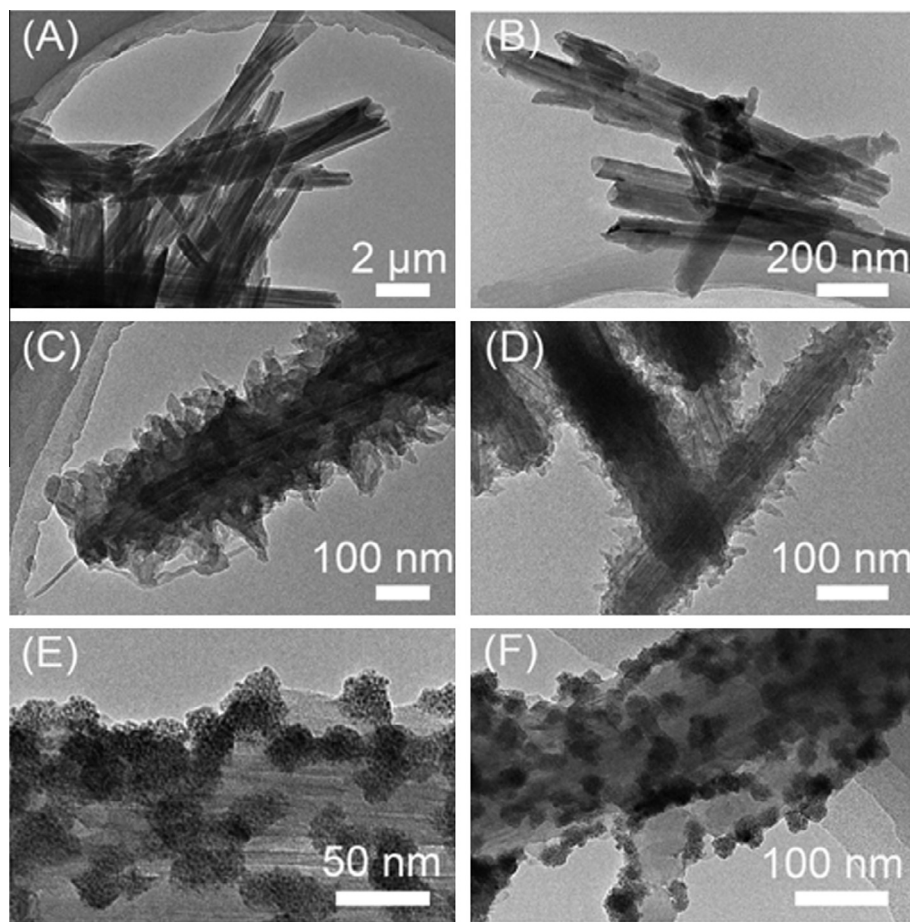


Fig. 2. The TEM images of the HNTs (A and B), PANI/HNTs (C and D) and AuNPs/PANI/HNTs nanostructures (E and F).

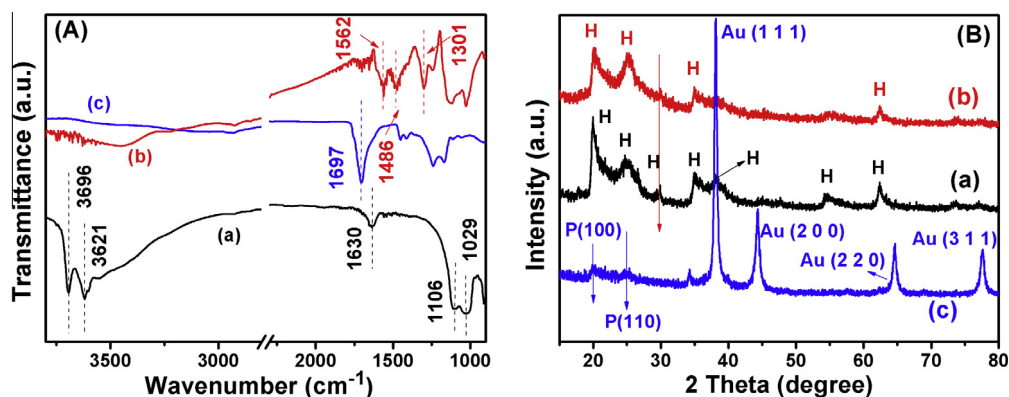


Fig. 3. (A) FTIR spectra and (B) XRD patterns of HNTs (a), PANI/HNTs (b) and AuNPs/PANI/HNTs nanostructures (c). (H: HNTs, P: PANI).

The XPS measurements were used to detect the surface elemental composition and study the chemical process in depth. As depicted in Fig. 4(A), the XPS N 1s spectrum of PANI/HNTs exhibits a peak at 399.2 eV, which is ascribed to the quinonoid imine (=N⁺) in PANI [23], in the meantime, the other two peaks with binding energy at 399.9 eV and 400.9 eV, which are assigned to the benzenoid amine (—NH—), and positively charged nitrogen (N⁺), respectively [24]. After the fabrication of AuNPs/PANI/HNTs nanostructures, the binding energy of the three different states shifts to 399.3, 400.1 and 401.0 eV, which can be observed in Fig. 4(B), respectively. It is apparent that there were significant changes in their relatively intensity between benzenoid amine

and quinonoid imine, implying that the benzenoid amine were oxidized to quinonoid imine and it is mainly the nitrogen lone electron pair that interacts with the metal matrix during the redox reaction between PANI and HAuCl₄, which were consistent with the theoretical prediction [25]. It can be obviously seen that S 2p spectra have an S 2p_{3/2}, 1/2 doublet structure. The peaks located at 163.7 and 164.8 eV (in Fig. 4(C)) shift to 162.4 and 163.4 eV (in Fig. 4(D)), respectively, which can be attributed to the formation of chemical bond between sulfhydryl (—SH) and AuNPs [26]. When the HAuCl₄ was dropped into the suspension, the —SH groups could capture Au ions to form SH—Au chelating complex first, and then the SH—Au chelating complex were reduced to Au atoms

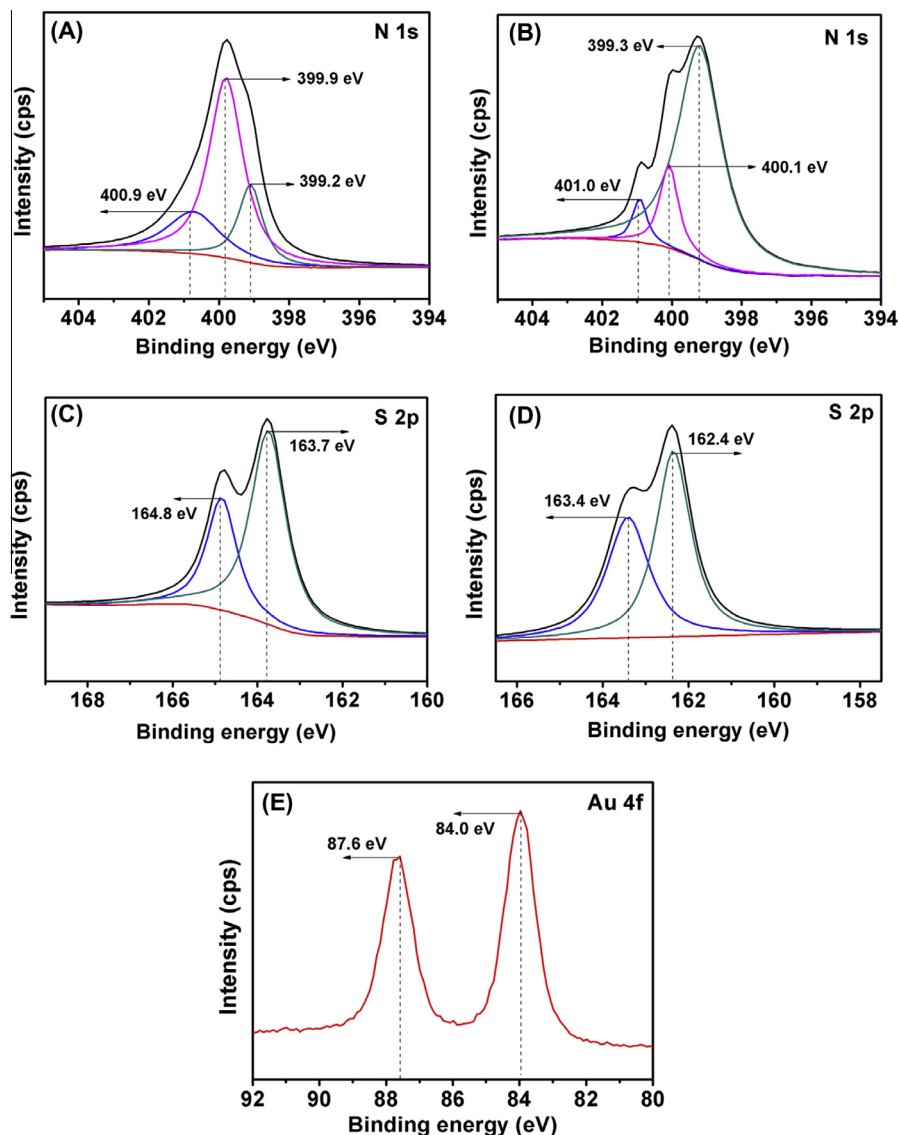


Fig. 4. XPS spectra of N 1s in (A) PANI/HNTs and (B) AuNPs/PANI/HNTs nanostructures, S 2p in (C) PANI/HNTs and (D) AuNPs/PANI/HNTs nanostructures, Au 4f in AuNPs/PANI/HNTs nanostructures (E).

nuclei and grow into nanoparticles gradually, avoiding the aggregation of AuNPs. Yang et al. [27] reported that lower electronegativity and the decrease of binding energy of S 2p would happen when the sulfur attached to metal. As observed in Fig. 4(E), the Au 4f XPS spectrum of Au/PANI/HNTs nanostructures located at 84.0 eV and 87.6 eV correspond well to the standard binding energy of Au⁰ (84.0 and 87.6 eV), which suggests that large quantities of Au ions were reduced to AuNPs. Meanwhile, the binding energy at 87.6 eV implied that there were strong interactions between the small portion of AuNPs and the Au/PANI/HNTs nanostructures [28,29]. Depended on the aforementioned analysis, we can draw conclusions that the AuNPs could be achieved through direct reduction of H₂AuCl₄ by PANI and the TA plays a crucial role in the process of obtaining stable, small and well-dispersed AuNPs [30,31].

As described above, we have fabricated the nanostructured AuNPs/PANI/HNTs composites through a facile route. Considering the good mechanical stability of HNTs and the excellent electrochemical activity of AuNPs and PANI, we hold the view that the AuNPs/PANI/HNTs nanocomposites can be exploited as remarkable electrochemical sensors for the detection of H₂O₂. A 0.1 M phos-

phate buffer at pH 6.8 was used as a probe to investigate performance of the fabricated H₂O₂ electrode. HRP was employed for the determination of H₂O₂, and HQ was used to detect H₂O₂ as an excellent electron mediator.

For the experiments, cyclic voltammetry (CV) was used to study the electrochemical signal transduction ability of the nanocomposites. The pure HNTs and the blank GCE were used as references in Fig. 5(A and B). Well-defined CV curves were observed in H₂O₂-sensing based on the HRP/(AuNPs/PANI/HNTs)/GCE. The redox peak currents of HQ are about 150 and 30 μ A and potentials at -0.3 and 0.45 V, respectively, as depicted in Fig. 5(A and c). On the other hand, as for the HRP/(AuNPs/PANI/HNTs)/GCE, the reduction current (110 μ A) caused by HQ decreased to some extent accompanying with the disappearance of the oxidation current peak with the addition of 5.0 mM H₂O₂ in Fig. 5(B and c), implying the existence of strong reactions among HQ, H₂O₂, and HRP [32]. The large distinguishable response toward the detection of H₂O₂ indicates that the charge transport within the AuNPs/PANI/HNTs nanocomposites is relatively fast, indicative of their remarkable electrochemical activity. At the same time, it should be noted that the pure HNTs exhibited relatively poor electrochemical activity in

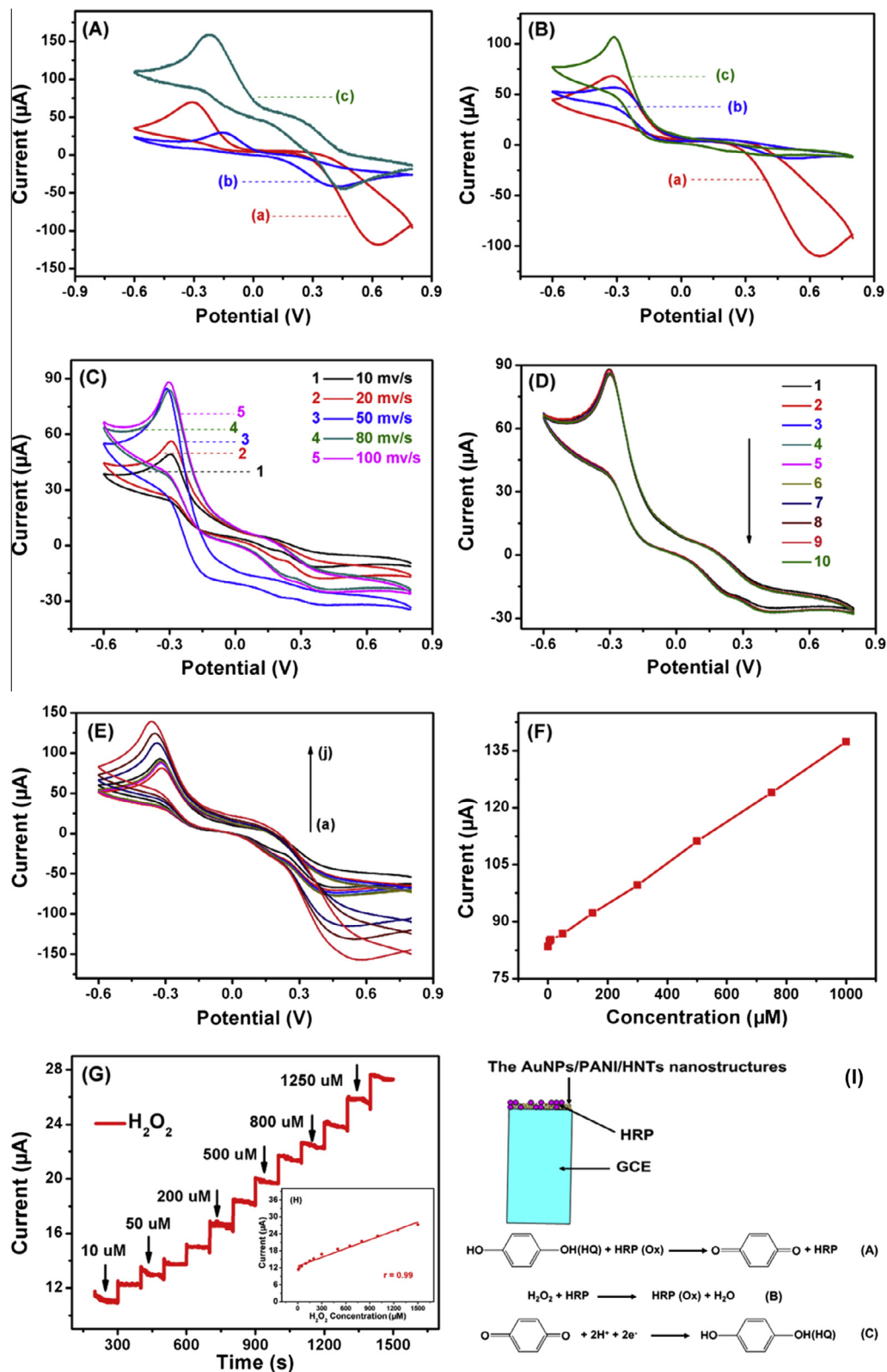


Fig. 5. (A) (In the absence of H₂O₂) and (B) (in the presence of 5.0 mM H₂O₂) are the cyclic voltammograms (CVs) of the blank GCE (a), HRP/pure HNTs/GCE (b) and HRP/(AuNPs/PANI/HNTs)/GCE (c) immersed in 10.0 mM HQ in 0.1 M PBS (pH = 6.8), respectively; (C) the CVs of HRP/(AuNPs/PANI/HNTs)/GCE in the presence of 5.0 mM H₂O₂ in the same conditions at different scan rates; (D) The CVs cycles of HRP/(AuNPs/PANI/HNTs)/GCE in the presence of 5.0 mM H₂O₂ in the same conditions at the scan rate of 100 mV/s; (E) the CVs of HRP/(AuNPs/PANI/HNTs)/GCE in the presence of different concentrations of H₂O₂ (1, 5, 10, 50, 300, 500, 750 and 1000 μM) at the scan rate of 100 mV/s; (F) the reduction peak currents in CV versus H₂O₂ concentration; (G) amperometric response of the fabricated HRP/(AuNPs/PANI/HNTs)/GCE to successive addition of different concentrations of H₂O₂ to 0.1 M PBS; (H) the relationship between the current and the H₂O₂ concentration; (I) schematic presentation of the H₂O₂ sensor based on the HRP/(AuNPs/PANI/HNTs)/GCE and reaction process.

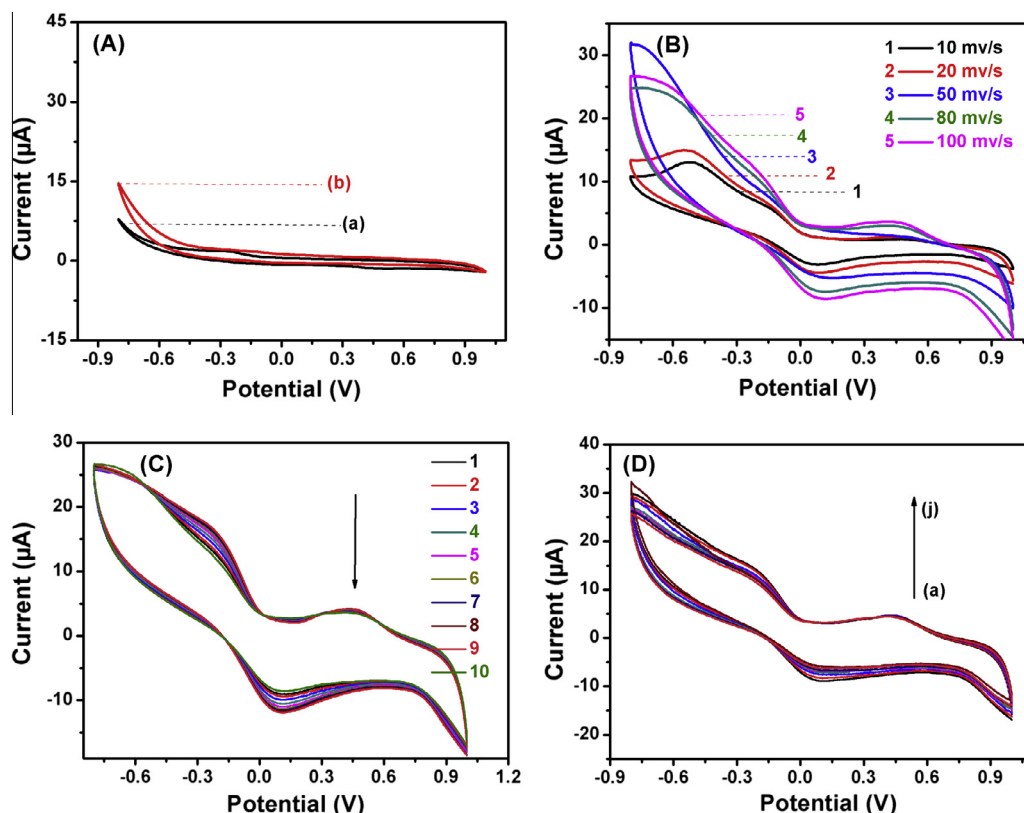


Fig. 6. (A) The cyclic voltammograms (CVs) of the blank GCE (a), and pure HNTs/GCE (b) immersed in 10.0 mM potassium ferricyanide in 0.1 M PBS (pH = 6.8) in the presence of 5.0 mM glucose, respectively; (B) the CVs of (AuNPs/PANI/HNTs)/GCE in the same conditions at different scan rates; (C) the CVs cycles of (AuNPs/PANI/HNTs)/GCE in the same conditions at the scan rate of 100 mV/s; (D) the CVs of (AuNPs/PANI/HNTs)/GCE in the presence of different concentrations of glucose (1, 5, 20, 50, 100, 200, 300, 500, 750, and 1000 μM) at the scan rate of 100 mV/s.

this potential range, as well as the blank GCE showed almost no sensitivity towards H_2O_2 , when compared to the HRP/(AuNPs/PANI/HNTs)/GCE, which excluded the interferences effectively. In Fig. 5(C), with the change of the scan rates, the HRP/(AuNPs/PANI/HNTs)/GCE also showed corresponding response, and these phenomena indicated the AuNPs/PANI/HNTs had a good adaptability. As illustrated in Fig. 5(D), the CVs were almost the same and did not shown distinct change. From these facts, we could draw the conclusion that the AuNPs/PANI/HNTs nanocomposites revealed good mechanical stability and reusability and the samples can be acted as excellent electrode material and the HNTs are also employed as reliable supports.

Fig. 5(E and F) shows the electrochemical responses of different concentrations of H_2O_2 solution using HRP/(AuNPs/PANI/HNTs)/GCE as an electrode. It can be observed that an occurrence of reduction current is clearly observed at each period of H_2O_2 injection from 1 μM to 1000 μM at a scan rate of 100 mV/s. We also measured the amperometric response for the HRP/(AuNPs/PANI/HNTs)/GCE to monitor the operational stability and sensitivity of the corresponding electrochemical sensors in the presence of different concentrations of H_2O_2 . In Fig. 5(G), stepped increases of the amperometric reduction currents were observed with the addition of H_2O_2 . The current response of the sensors was rapidly enhanced and then reached its steady state current, which due to the fast diffusion ratio of the H_2O_2 into the nanostructured AuNPs/PANI/HNTs composites [33–37]. Fig. 5(H) shows a linear relationship with the concentration of H_2O_2 (0.01–1.5 mM) with the correlation coefficient of 0.99, and the detection limit is 0.972 μM at a signal-to-noise ratio of 3.

In addition, we also investigated glucose as model compounds in our experiments to testify the electrochemical activity and flex-

ibility of the sensor. Ramanaviciene et al. [38,39] have already studied glucose biosensor based on polyaniline and AuNPs in the presence of glucose oxidase (GOx) comprehensively. Compared to their research, our study was conducted without the existence of GOx. Fig. 6 showed the CVs of glucose using AuNPs/PANI/HNTs nanocomposites as the working electrode, it is obvious that there were weak redox peaks and successive additions of glucose lead to an increase of the current, suggesting the flexibility and reliability of the AuNPs/PANI/HNTs nanocomposites when acted as electrochemical sensors. Apart from H_2O_2 and glucose, we also anticipated that the prepared nanocomposites could be used to detect glutathione (GSH), ascorbic acid and so forth [40–42].

4. Conclusion

In summary, AuNPs/PANI/HNTs nanostructures had been successfully fabricated through the combination of the *in situ* polymerization of aniline and the facile reduction process of Au ions. The FE-SEM and TEM images demonstrated that the PANI nanofibers were immobilized on the surface of HNTs and great amounts of AuNPs in well-dispersion were implanted into the PANI nanofibers. Further characterizations indicated that the doped PANI nanofibers were preferable reducing agents and stabilizer in the fabrication of AuNPs. Our further experimental results also revealed that the acquired nanostructured AuNPs/PANI/HNTs composites can be acted as reliable electrochemical sensors and exhibited high-sensitivity and well-durability towards the detection of H_2O_2 , as well as made further exploration and outlook of its wide applications. Finally, we believe that this type of high-performance nanostructured sensors, combined with a low-cost and

scalable technique shows great potential for use in applications relating to environmental monitoring, beverage industry, and the medical diagnosis.

Acknowledgements

We acknowledge the support of the project of the National Natural Science Foundation of China (NSFC) (51373154), the 521 Talent Project of Zhejiang Sci-Tech University.

References

- [1] D.Y. Zhai, B.R. Liu, Y. Shi, L.J. Pan, Y.Q. Wang, W.B. Li, R. Zhang, G.H. Yu, *ACS Nano*. **7** (2013) 4.
- [2] C. Dhand, M. Das, M. Datta, B.D. Malhotra, *Biosens. Bioelectron.* **26** (2011) 6.
- [3] A. Kausaite-Minkstiniene, V. Mazeiko, A. Ramanaviciene, A. Ramanavicius, *Biosens. Bioelectron.* **26** (2010) 12.
- [4] X.C. Tan, J.L. Zhang, S.W. Tan, D.D. Zhao, Z.W. Huang, Y. Mi, Z.Y. Huang, *Sensors* **9** (2009) 8.
- [5] H. Zhu, M.L. Du, M. Zhang, P. Wang, S.Y. Bao, L.N. Wang, Y.Q. Fu, J.M. Yao, *Biosens. Bioelectron.* **49** (2013) 54.
- [6] X.M. Feng, R.M. Li, Y.W. Ma, R.F. Chen, N.E. Shi, Q.L. Fan, W. Huang, *Adv. Funct. Mater.* **21** (2011) 15.
- [7] Y.F. Lin, C.H. Chen, W.J. Xie, S.H. Yang, C.S. Hsu, M.T. Lin, W.B. Jian, *ACS Nano*. **5** (2011) 2.
- [8] C.O. Baker, B. Shedd, P.C. Innis, P.G. Whitten, G.M. Spinks, G.G. Wallace, R.B. Kaner, *Adv. Mater.* **20** (2008) 1.
- [9] Z.C. Xu, Y.L. Hou, S.H. Sun, *J. Am. Chem. Soc.* **129** (2007) 28.
- [10] A. Kumar, L. Joshi, R. Prakash, *Ind. Eng. Chem. Res.* **52** (2013) 27.
- [11] L. Wang, J.L. Chen, L. Ge, Z.H. Zhu, V. Rudolph, *Energy Fuels* **25** (2011) 8.
- [12] Y.M. Lvov, D.G. Shchukin, H. Mohwald, R.R. Price, *ACS Nano*. **2** (2008) 5.
- [13] M.L. Du, B.C. Guo, M.X. Liu, X.J. Cai, D.M. Jia, *Phys. B: Condens. Matter*. **405** (2010) 2.
- [14] X. Zhang, H. Wang, B.Q. Xu, *J. Phys. Chem. B* **109** (2005) 19.
- [15] O.B. Christina, S. Brian, J.T. Ricky, A.M.-M. Alfredo, S.O. Cengiz, O. Mihri, Y. Yang, B.K. Richard, *ACS Nano*. **5** (2011) 5.
- [16] R.J. Tseng, J. Huang, J. Ouyang, R.B. Kaner, Y. Yang, *Nano Lett.* **5** (2005) 6.
- [17] R.J. Wang, G.H. Jiang, Y.W. Ding, Y. Wang, X.K. Sun, X.H. Wang, W.X. Chen, *ACS Appl. Mater. Interfaces* **3** (2011) 10.
- [18] H. Zhu, M.L. Du, M.L. Zou, C.S. Xu, Y.Q. Fu, *Dalton Trans.* **41** (2012) 34.
- [19] H.W. Park, T. Kim, J.J. Huh, M.J. Kang, J.E. Lee, H. Yoon, *ACS Nano*. **6** (2012) 9.
- [20] J.J. Xu, K. Wang, S.Z. Zu, B.H. Han, Z.X. Wei, *ACS Nano*. **4** (2010) 9.
- [21] M.N. Nadagouda, G. Hoag, J. Collins, R.S. Varma, *Cryst. Growth Des.* **9** (2009) 11.
- [22] I. Gorelikov, N. Matsuura, *Nano Lett.* **8** (2008) 1.
- [23] J.R. Pels, F. Kapteijn, J.A. Moulijn, Q. Zhu, K.A. Thomas, *Carbon* **33** (2005) 11.
- [24] R. Ohta, K.H. Lee, N. Saito, Y. Inoue, H. Sugimura, O. Takai, *Thin Solid Films* **434** (2003) 1.
- [25] G. Neshet, G. Marom, D. Avnir, *Chem. Mater.* **20** (2008) 13.
- [26] P. Wang, H. Zhu, S.Y. Bao, M.L. Du, M. Zhang, *J. Phys. D: Appl. Phys.* **46** (2013) 34.
- [27] D.Q. Yang, B. Hennequin, E. Sacher, *Chem. Mater.* **18** (2006) 21.
- [28] Y. Negishi, K. Nobusada, T. Tsukuda, *J. Am. Chem. Soc.* **127** (2005) 14.
- [29] J.A. Larsson, M. Nolan, J.C. Greer, *J. Phys. Chem. B* **106** (2002) 23.
- [30] H. Zhu, M.L. Du, D.L. Yu, Y. Wang, L.N. Wang, M.L. Zou, M. Zhang, Y.Q. Fu, *J. Mater. Chem. A* **1** (2013) 3.
- [31] Y. Jin, H.Y. Chen, M.H. Chen, N. Liu, Q.W. Li, *ACS Appl. Mater. Interfaces* **5** (2013) 8.
- [32] J. Wang, H.B. Yao, D. He, C.L. Zhang, S.H. Yu, *ACS Appl. Mater. Interfaces* **4** (2012) 4.
- [33] Q. Yao, L.D. Chen, W.Q. Zhang, H.C. Liufu, X.H. Chen, *ACS Nano*. **4** (2010) 4.
- [34] M.N. Hyder, S.W. Lee, F.C. Cebeci, D.J. Schmidt, Y. Shao-Horn, P.T. Hammond, *ACS Nano*. **5** (2011) 11.
- [35] W. Pan, X.K. Zhang, H.Y. Ma, J.T. Zhang, *J. Phys. Chem. C* **112** (2008) 7.
- [36] X.Y. Lang, H. Guo, L.Y. Chen, A. Kudo, J.S. Yu, W. Zhang, A. Inoue, M.W. Chen, *J. Phys. Chem. C* **114** (2010) 6.
- [37] S.P. Zhou, H.M. Zhang, X.H. Wang, J. Li, F.S. Wang, *RSC Adv.* **3** (2013) 6.
- [38] N. German, A. Ramanavicius, J. Voronovic, A. Ramanaviciene, *Colloids and Surf. A: Physicochem. Eng. Aspects* **413** (2012) 5.
- [39] V. Mazeiko, A. Kausaite-Minkstiniene, A. Ramanaviciene, Z. Balevicius, A. Ramanavicius, *Sens. Actuators B: Chem.* **189** (2013).
- [40] A. Kausaite-Minkstiniene, V. Mazeiko, A. Ramanaviciene, A. Ramanavicius, *Sens. Actuators B: Chem.* **158** (2011).
- [41] F. Chai, C. Wang, T. Wang, L. Li, Z.M. Su, *ACS Appl. Mater. Interfaces* **2** (2010) 5.
- [42] Y.Y. Liu, Q.X. Zhou, Z.H. Zeng, R. Qiao, X.S. Wang, B.W. Zhang, *J. Phys. Chem. B* **112** (2008) 32.

Accepted Manuscript

Title: Structure regulation of silica nanotubes and their adsorption behaviors for heavy metal ions: PH effect, kinetics, isotherms and mechanism<!--<query id="Q1"> “Your article is registered as a regular item and is being processed for inclusion in a regular issue of the journal. If this is NOT correct and your article belongs to a Special Issue/Collection please contact p.d.thangavelu@elsevier.com immediately prior to returning your corrections.”</query>-->



Author: Pan Wang Mingliang Du Han Zhu Shiyong Bao
Tingting Yang Meiling Zou

PII: S0304-3894(14)01018-8
DOI: <http://dx.doi.org/doi:10.1016/j.jhazmat.2014.12.034>
Reference: HAZMAT 16469

To appear in: *Journal of Hazardous Materials*

Received date: 26-9-2014
Revised date: 10-12-2014
Accepted date: 18-12-2014

Please cite this article as: Pan Wang, Mingliang Du, Han Zhu, Shiyong Bao, Tingting Yang, Meiling Zou, Structure regulation of silica nanotubes and their adsorption behaviors for heavy metal ions: PH effect, kinetics, isotherms and mechanism, Journal of Hazardous Materials <http://dx.doi.org/10.1016/j.jhazmat.2014.12.034>

This is a PDF file of an unedited manuscript that has been accepted for publication. As a service to our customers we are providing this early version of the manuscript. The manuscript will undergo copyediting, typesetting, and review of the resulting proof before it is published in its final form. Please note that during the production process errors may be discovered which could affect the content, and all legal disclaimers that apply to the journal pertain.

Structure regulation of silica nanotubes and their adsorption behaviors for heavy metal ions: pH effect, kinetics, isotherms and mechanism

Pan Wang¹, Mingliang Du^{*1,2}, Han Zhu¹, Shiyong Bao¹, Tingting Yang¹, and Meiling Zou¹

¹ College of Materials and Textiles, Zhejiang Sci-Tech University, Hangzhou 310018, P. R. China

² Key Laboratory of Advanced Textile Materials and Manufacturing Technology, Zhejiang Sci-Tech University, Ministry of Education, Hangzhou 310018, P. R. China

Corresponding Author: * E-mail: du@zstu.edu.cn Tel.: 0086-0571-86843255

Highlights

1. SNTs were synthesized via an electrospinning and calcination process.
2. The structure of SNTs could be regulated by altering process parameters.
3. SNTs exhibit excellent adsorption capacity and efficiency for heavy metal ions.

Graphical abstract: Silica nanotubes were synthesized *via* an electrospinning technique and exhibited excellent adsorption capacity and efficiency for heavy metal ions from wastewater.

Abstract

Silica nanotubes (SNTs) with controlled nanotubular structure were synthesized *via* an electrospinning and calcination process. In this regard, SNTs were found to be ideal adsorbents for Pb(II) removal with a higher adsorption capacity, and surface modification of the SNTs by sym-Diphenylcarbazine (SD-SNTs) markedly enhanced the adsorption ability due to the chelating interaction between imino groups and Pb(II). The pH effect, kinetics, isotherms and adsorption mechanism of SNTs and SD-SNTs on Pb(II) adsorption were investigated and discussed detailedly. The adsorption capacity for Pb(II) removal was found to be significantly improved with the decrease of pH value. The Langmuir adsorption model agreed well with the experimental data.

As for kinetic study, the adsorption onto SNTs and SD-SNTs could be fitted to pseudo-first-order and pseudo-second-order model, respectively. In addition, the as-prepared SNTs and SD-SNTs also exhibit high adsorption ability for Cd(II) and Co(II). The experimental results demonstrate that the SNTs and SD-SNTs are potential adsorbents and can be used effectively for the treatment of heavy-metal-ions-containing wastewater.

Keywords: Silica nanotubes (SNTs), Structure regulation, Adsorption, Heavy metal ions, Pb(II).

1. Introduction

With the accelerated process of modernization, over-use of industrial chemicals, organic compounds and fossil fuels have attracted intensive attention [1,2]. Abundant existence of heavy metals (for instance, Ba^{2+} , Pb^{2+} , Cd^{2+} , Cr^{3+} , Co^{2+} , Cu^{2+} , Ni^{2+} , Zn^{2+} , and Hg^{2+}) in water has become a topic of worldwide concern as it brings many severe challenges to the public health and environmental ecosystems [3]. Especially, the exorbitant usage and indiscriminate disposal of these metals in the metallurgical industry and chemical manufacturing have resulted in serious consequences. Pb(II) is a common water pollutant with high toxicity as it is a kind of easily accumulated, nondegradable heavy metal. Accumulation of high levels of Pb(II) can cause a series of adverse damages to humans, such as poor muscle coordination, retardation of mental and physical development, and irreversible brain damage [4,5].

Taking into account of the rapid population growth, increasing demands for clean water, along with the continued environmental destruction, it is imperative to remove these heavy metal contaminants from wastewater before being released into environmental ecosystems. Tremendous efforts have been proposed in response to heavy metal contamination, such as membrane filtration technology, adsorption, ion exchange, biological treatment and chemical precipitation [6,7]. Among the present technologies, adsorption is regarded as one of the most convenient, low-cost and relatively promising approaches for water decontamination and has been widely used in practical applications [8]. Plenty of traditional adsorbents have been fabricated for the removal of heavy metals, including the nanofibrous membranes, ion exchangers, hollow spherical structures and inorganic nanotubes (carbon nanotubes, halloysite nanotubes and so on) [9]. Nevertheless, these materials have some inherent disadvantages such as low adsorption capacities or high costs, which place urgent needs for the development of new adsorbent materials aimed at protecting our water and ensuring widespread access to clean and

affordable potable water.

In the past couple decades, nanomaterials, with their fascinating physiochemical properties, have received considerable interests for various applications such as nanotransistors, energy storage devices, sensors, biomaterial delivery tools, adsorption materials and electrode materials [10,11]. Hollow inorganic nanoparticles have recently attracted an increasing number of attentions because of their distinct characteristics that are advantageous for a variety of adsorption applications, such as their ability to carry the high payload of functional molecules and ions on their large surface area [12]. Among these different types of inorganic nanomaterials, silica nanomaterials have aroused great interests due to their distinct optical, electrical, and mechanical properties and a number of favorable structural features, for instance, facile surface functionalization, easy incorporation with other nanomaterials, uniform and tunable particle and pore size, high surface area and pore volume, and so forth [13,14].

The preferable one-dimensional (1D) silica nanomaterials, silica nanotubes (SNTs), considering their large pore volume and outstanding properties, have gradually been demonstrated to play significant roles in bioseparation, drug targeting, enzyme immobilization, and waste-water treatment [15]. As a consequence, the facile preparation and the research of potential attractive applications of SNTs have been a hot topic since their discovery. For the acquisition of SNTs, Guo *et al* [16] and Guler *et al* [17] have already fabricated SNTs by the traditional templating method. Shao *et al* [18], Jan *et al* [19], and Zhang *et al* [20] have employed the SNTs as the catalyst carriers. Herein, we conveniently acquired large amounts of randomly oriented SNTs primarily relied on the technique of electrospinning by effectively controlling the process of solvent evaporation, phase separation and calcination, which can be seen in our previous reports [21]. Additionally, to the best of our knowledge, for the first time, we introduce SNTs as adsorbents for heavy metals based on their intriguing properties in the present studies.

In this manuscript, we proposed to investigate the structure regulation of SNTs and the feasibility of applying them as novel adsorbents for the removal of Pb(II) from aqueous solutions. Meanwhile, to increase the adsorption capacity of SNTs, it is essential to decorate them with compounds containing heteroatoms or other functional groups which initiate chemical reactions during the adsorption process. Adsorbent dosage and pH were analyzed to investigate the adsorption behaviors through equilibrium and kinetic studies. In addition, Langmuir and Freundlich isotherms were applied to evaluate the adsorption models and the parameters of these adsorbents. The adsorption mechanism of Pb(II) on the SNTs and SD-SNTs were illustrated and discussed comprehensively. Besides, cobalt (Co(II)) and cadmium (Cd(II)) were also employed to evaluate the developed adsorbents. This work not only provides useful new adsorbent materials for environmental protection, but also offers a class of practical application of SNTs in water/wastewater treatment that could be used in the future.

2. Experimental

2.1. Materials

Lead(II) nitrate ($\text{Pb}(\text{NO}_3)_2$, 99.999%), Cadmium nitrate tetrahydrate ($\text{Cd}(\text{NO}_3)_2$, 99.999%), and sym-Diphenylcarbazine ($\text{C}_{13}\text{H}_{14}\text{N}_4\text{O}$, SD) were purchased from Aladdin Chemical Reagent Co., Ltd (Shanghai, China). Stock solutions of Pb(II), Cd(II) and Co(II) were prepared by dissolving $\text{Pb}(\text{NO}_3)_2$, $\text{Cd}(\text{NO}_3)_2$ and $\text{Co}(\text{NO}_3)_2 \cdot 6\text{H}_2\text{O}$ into ultrapure water, respectively. For pH adjustment, sodium hydroxide (NaOH) and hydrochloric acid (HCl) were obtained from Tianjin Yongda Chemical Reagent Co., Ltd (Tianjin, China) and Zhejiang Three Eagle Chemical Reagent Co., Ltd (Jinhua, China), respectively. Acetone ($\text{C}_3\text{H}_6\text{O}$) was acquired from Hangzhou Gaojing Fine Chemical Industry Co., Ltd (Hangzhou, China). The SNTs are obtained by self-regulation, which can be seen in our previous reports [21]. All chemicals were of analytical grade and used in the current study without further purification.

2.2. Surface modification of SNTs

In our experiment, for the comparative study and exploration of the maximum adsorption capacity of the SNTs, the pure SNTs were modified by SD *via* employing the Solvent-Nonsolvent Method [8,22,23] according to the following procedure. For surface modification, a predetermined amount of SD was mixed with appropriate amount of acetone for 30 minutes to form a clear solution. Next, a specified amount of SNTs were immersed into the acquired mixtures for several hours with stirring at 30 °C, and the rotational speed was set at 150 rpm in a SHA-CA shaker bed (Jiangnan Instrument Factory of Jintan, Jiangsu Province, China). Finally, the supernatant was removed and the precipitates were dried in a vacuum oven at 60 °C for 12 hours to obtain SD-SNTs.

2.3. Batch adsorption experiments

Batch adsorption experiments were conducted by taking advantage of the traditional bottle-point method in the above mentioned constant temperature water oscillator at 30 °C and a 100 rpm agitation. 10 mg of the adsorbent samples (SNTs or SD-SNTs) were equilibrated in 50 mL glass vials with 40 mL of aqueous solutions containing Pb(II), Cd(II) or Co(II) at designed levels. In order to study the effect of pH values similar to those presented in typical heavy-metal-polluted rivers [24] and to evaluate its effect on the adsorption process, the initial concentration of Pb(II), Cd(II) and Co(II) was set to 50 ppm, and the pH of the solutions was varied between 3 and 10 (adding HCl or NaOH as needed). Adsorption kinetics were performed by mixing an 80 mL solution containing 50 ppm Pb(II), Cd(II) or Co(II) and 20 mg of SNTs or SD-SNTs and determined by sampling 0.5 mL aliquots at various time intervals. In the isothermal study, the initial concentration

of Pb(II), Cd(II) or Co(II) ranged from 5 ppm to 175 ppm. Additional details about batch adsorption are described at length in the related figure and table captions.

Prior to the test, the sorbents were filtered from the solution through 0.45 μm filters and the filtrate was collected for future analysis. The concentration of Pb(II), Cd(II) and Co(II) in solution was determined by a Solaar M6 atomic absorption/emission spectrometer equipped with a FS95 graphite furnace atomizer and deuterium background correction.

The adsorption capacity of the adsorbents for Pb(II) at equilibrium (q_e , mg/g) and the amount of metal adsorbed per unit mass of adsorbent at time t (q_t , mg/g) was calculated according to the following equation:

$$q_t = \frac{(C_0 - C_t)V}{W} \quad (1)$$

$$q_e = \frac{(C_0 - C_e)V}{W} \quad (2)$$

where C_0 (mg/L) is the initial metal concentration, C_t (mg/L) and C_e (mg/L) are the metal concentrations at time t and the equilibrium liquid-phase metal concentration, respectively; V is the volume of the metal ion solution (mL), and W is the amount of adsorbent (mg).

2.4. Characterization and analysis

The morphology evolution of the SNTs was observed with a JSM-2100 transmission electron microscopy (TEM, JEOL, Japan) at an acceleration voltage of 200 kV and a JSM-6700F field emission scanning electron microscopy (FE-SEM, JEOL, Japan) at an acceleration voltage of 3 kV. HAADF-STEM images and STEM-EDS mapping images of a select area of Pb-SNTs and Pb-SD-SNTs were recorded by a STEM (Tecnai G2 F30 S-Twin, Philips-FEI) at an acceleration voltage of 300 kV. Fourier transform infrared (FTIR) absorption spectra were obtained on a Thermo Scientific Nicolet 5700 FTIR spectrometer in the wavenumber range of 500-4000 cm^{-1} using the KBr tableting method. X-ray photoelectron spectra of the Pb-SNTs and Pb-SD-SNTs were recorded with an X-ray photoelectron spectrometer (Kratos Axis Ultra DLD) attached with an aluminum (mono) $K\alpha$ source (1486.6 eV), the aluminum $K\alpha$ source was operated at 15 kV and 10 mA, and the high-resolution survey (pass energy = 48 eV) was performed at spectral regions relating to oxygen, lead and nitrogen.

3. Results and discussion

3.1. The Characterization and structure regulation of SNTs

The SNTs were acquired by calcining the PVP-TEOS- $\text{C}_2\text{H}_5\text{OH}$ composite fibers obtained by electrospinning technique, theoretical analysis and simulations have been

contributed by our previous report [21]. Before being used for further investigations and applications, the local structure and morphology of the prepared SNTs were examined by FE-SEM and high magnification TEM measurements. As shown in **Fig. 1 a and b**, the FE-SEM images of the product clearly show a well-grown, fibrous silica nanostructure with open cavities at the tube edges. Additionally, the TEM images (**c and d**) reveal a straightforward hollow structure. The porous nature of the SNTs with mesopores perforating the wall are confirmed by nitrogen sorption measurements, as illustrates in our previous reports. The BET surface areas of SNTs were determined to be $411 \text{ m}^2/\text{g}$, which is rather larger when compared with other inorganic hollow nanomaterials [21]. These characterizations suggest that large number of SNTs have been successfully fabricated and are suitable for adsorption studies.

Herein, based on the previous results and discussions, we further explored the effects on silica nanofibers caused by changing the TEOS content and calcinations rate. PVP-TEOS- $\text{C}_2\text{H}_5\text{OH}$ composite fibers (**Fig. 2a**), and the porous structured silica nanofibers (**Fig. 2b**) treated by the calcinations process of the previously mentioned PVP-TEOS- $\text{C}_2\text{H}_5\text{OH}$ composite fibers, are shown in **Fig. 2**. Hollow-shaped PVP-TEOS- $\text{C}_2\text{H}_5\text{OH}$ composite fibers in **Fig. 2 (c and e)** were successfully prepared by electrospinning with a certain amount of TEOS mixed into a proper concentration of PVP- $\text{C}_2\text{H}_5\text{OH}$ solution, after calcinations treatment, silica nanofibers with well-defined hollow structure (**Fig. 2 (d and f)**) are successfully prepared. Phase separation and solvent evaporation could be strictly controlled by altering the ratios of TEOS to PVP solution due to the volatility of TEOS and its compatibility with PVP. Accordingly, SNTs with different inner diameters could be produced, which attributed to the difference of TEOS content that congregates at the center line of the nanofibers when phase separation occurs [18,21].

The effect of the calcination rates of the hollow PVP-TEOS- $\text{C}_2\text{H}_5\text{OH}$ composite fibers on the morphology and structure of SNTs was also explored. As shown in **Fig. 3**, with the altering of the calcinations rates, the ratios of the nanotube diameter to the thickness of the nanotube wall (D/T) gradually changed. At lower calcinations rate, the reaction temperature achieves at higher temperature slowly, hence, the hollow PVP-TEOS- $\text{C}_2\text{H}_5\text{OH}$ composite fibers can experience lower temperatures for a longer period of time. Consequently, there is enough time for the rapid decomposition of PVP molecules and sufficient formation of silica molecules [18,53]. Accordingly, it's noted that the nanotubes have thicker tube walls and smaller D/T value with the increase of calcinations rates.

3.2. Surface modification and adsorption behaviors of Pb(II)

With the objective of increasing the adsorption capacity of the SNTs, it is necessary to decorate them with functional materials. It is well-documented that materials functionalized with sulfur, nitrogen and oxygen have shown high binding affinity to metals ions [22,23]. It's well known that SD is widely used to form stable chelates with metal ions because of its abundant imino groups, which are well recognized to have good affinity with the metal ions, immobilization of SD on different supporting materials for adsorption purpose has received widespread attention. In this work, the FTIR was used to demonstrate that the SNTs were successfully modified by SD. From the previous reports, the evident peaks in curve (a) (**Fig. 4**) detected at 801 and 1090 cm^{-1} belong to the symmetrical stretching and asymmetric stretching of Si-O-Si bonds, respectively. The broad strong absorption peak at 3480 cm^{-1} was attributed to the asymmetrical stretching vibration of the -OH groups, which are from the free water and bound water on the SNTs, while the characteristic peak at 1636 cm^{-1} is assigned to the bending vibration of H-O-H derived from the pore water and surface absorbed water [24,25,26]. As presented in curve (b), the absorption peak centered at 3321 cm^{-1} is owed to the overlapping and involvement of the stretching vibration of the O-H and N-H groups. While the peaks measured at 1596 cm^{-1} and 1493 cm^{-1} are ascribed to the in-plane bending vibration of aromatic ring and C-H groups, and the peaks at 691 cm^{-1} and 752 cm^{-1} are due to the out-plane bending vibration of C-H groups [27]. Obviously, the distinct absorption peak at 1662 cm^{-1} was the result of the stretching vibration of C=O groups [28]. These results confirm that the SNTs have been successfully functionalized with SD.

Herein, Pb(II) was selected to study the adsorption behaviors of SNTs and SD-SNTs. Meanwhile, the SNTs with the calcinations rate of 5 $^{\circ}\text{C}/\text{min}$ were chosen as the adsorbents. In order to in-depth characterize the morphology of SNTs and confirm that the Pb(II) was successfully absorbed by SNTs and SD-SNTs, high-angle annular dark field scanning TEM (HAADF-STEM) imaging and high resolution element mappings were performed and the results are shown in **Fig. 5**. As described in **Fig. 5 (a) and (c)**, the HAADF-STEM images of the Pb-SNTs and Pb-SD-SNTs exhibit an obviously and definitely hollow tubular structure. The STEM-EDS mapping observed in **Fig. 5 (b)** displays three elements, the orange and the red correspond to Si and O elements, respectively, while the yellow and green regions are corresponding to Pb elements. After the process of functionalization, the eventually acquired SD-SNTs still retain their well-defined tubular structure, apart from the relatively rough surface (in **Fig. 5 (c)**), which may be attributed to the affinity behavior and successful modification of the SD on SNTs. It can be observed apparently that N element (shown in red in the high resolution element

mappings in **Fig. 5 (d)** is detected, implying that the functional groups (-NH-) from the SD have been effectively grafted onto the surface of the SNTs. Intuitively, we can also unearth the phenomenon that the amounts of Pb(II) in **Fig. 5 (d)** are improved significantly comparing with that in **Fig. 5 (b)**, which would be also confirmed by the subsequent analysis.

It is well-known that pH is the dominant parameter controlling the adsorption of heavy metal ions. The adsorption behaviors of Pb(II) on the SNTs (a) and SD-SNTs (b) as a function of contact time, at an initial concentration of $50 \text{ mg}\cdot\text{L}^{-1}$, at 303 K with pH values of 4.0, 7.0, and 9.0 are shown in **Fig. 6**. Initially, the quantity of the adsorbed Pb(II) increases quickly for both of the two absorbents. After reaching a certain time, the adsorption process of Pb(II) on SNTs and SD-SNTs gradually reaches equilibrium, and in the present work, the adsorption equilibrium time is set as 240 min and 180 min for SNTs and SD-SNTs, respectively. After reaching equilibrium, along with the extension of time, the adsorption percentage and efficiency changed negligibly. Apart from that, it was evident from the data presented in **Fig. 6** that the extent of Pb(II) adsorption onto SNTs was much less than the Pb(II) adsorption onto SD-SNTs under the identical conditions at all time intervals, which was consistent with the above STEM observations. The results suggest that the adsorption capacity can be significantly enhanced when SNTs is modified with SD.

Also worth mentioning was the observation that the higher the pH of the solution, the smaller the adsorption quantity. In light of data obtained from previous studies, silica surfaces display a negative surface charge at neutral pH due to the presence of deprotonated hydroxyl groups on the surface [29]. Apparently, a low pH value or high acidity would result in competition between protons (H^+) and Pb(II) ions for the adsorption sites of the sorbent, leading to the declination in electrostatic interaction to some extent. At higher pH values (pH 9), the observed lower uptake could be attributed to the severe precipitation reaction between Pb(II) ions and hydroxyl ions (OH^-). This result is distinct from the adsorption behavior of conventional sorbents, for instance, tourmaline, soy protein hollow microspheres, and so on, because their adsorption for heavy metals is decreased at lower pH [4,7,30]. These differences are attributed to the competition between Pb(II) ions and protons for the adsorption site, as previously mentioned. Such performance of SNTs and SD-SNTs is very attractive because heavy metals are usually present in acidic, contaminated wastewater, as previously reported [31,33].

Of note is that SD-SNTs still exhibited satisfactory retention of Pb(II) at all pH

values, implying the strong complexation between Pb(II) and the functional groups originated from SD. These results are also confirmed with the XPS analysis. The adsorption behavior will be explained at length in the mechanism exploration.

A comparison of the maximum adsorption capacity of Pb(II) with various adsorbents are listed in Table 1. It can be found that SNTs and SD-SNTs both have a relatively large adsorption capacity of 42.85 and 64.70 mg·g⁻¹ for Pb(II), respectively, indicating that SNTs and SD-SNTs are potential fairly good materials for the removal of Pb(II) from aqueous solutions.

3.3. Adsorption kinetic studies of Pb(II) adsorption onto SNTs and SD-SNTs at different initial pH

Kinetic models are a significant aspect of adsorption studies and define the efficiency of the adsorption process. Kinetic models are proposed for a better understanding of the mechanism of adsorption. In order to convincingly investigate the adsorption behaviors of Pb(II) with the adsorbents, two kinetic models (pseudo-first-order kinetic model and pseudo-second-order kinetic model) have been employed to simulate the experimental data, as described hereinafter as eqs. (3)-(4).

The equation for pseudo-first-order kinetics is presented as follows:

$$\log(q_e - q_t) = \log q_e - \frac{k_1 \cdot t}{2.303} \quad (3)$$

where q_t and q_e are the amounts of Pb(II) adsorbed at time t and at equilibrium (mg·g⁻¹), and k_1 is the rate constant of the pseudo-first-order adsorption process (min⁻¹). The values of k_1 and q_e can be determined from the slope and intercept of plots of $\log(q_e - q_t)$ versus t (**Fig. 7**).

The pseudo-second-order model illustrates adsorption rate relationship with the difference of adsorption capacities at equilibrium and at different contact times, the pseudo-second-order kinetic model can be expressed as:

$$\frac{t}{q_t} = \frac{1}{k_2(q_e)^2} + \frac{t}{q_e} \quad (4)$$

where k_2 is the rate constant of the pseudo-second-order sorption (g·mg⁻¹·min⁻¹) and q_e is the amount of Pb(II) adsorbed (mg·g⁻¹) at equilibrium and q_t is the amount of the adsorption (mg·g⁻¹) at any time t . The values of k_1 and q_e can be calculated from a plot of t/q_t against t (**Fig. 7**).

For SNTs, as depicted in Table 2 and 3, according to the correlation coefficients (R^2), the pseudo-first-order equation fits the experimental kinetic data better than the pseudo-second-order equation. In addition, the comparison made between the experimental

adsorption capacity (experimental q_m) values and the calculated adsorption capacity (q_e) values shows that the calculated q_e values are comparable to the experimental q_m values for the pseudo-first-order kinetics. The above analysis indicate that the Pb(II) adsorption onto SNTs can be reasonably approximated by the pseudo-first-order model [32].

With regard to SD-SNTs, due to the modification by SD, their adsorption behavior differed from the SNTs. It was observed that the calculated q_e values obtained from the pseudo-second-order kinetics model are different from the experimental q_m values when compared with calculations from the pseudo-first-order equation, which possibly resulted from the imprecise sampling and inaccurate testing within the error range. More importantly, the correlation coefficient values for the pseudo-second-order model are much larger than that of pseudo-first-order model, suggesting that the adsorbent systems can be well-described by the pseudo-second-order kinetic model. The phenomenon also implies that the chelating reaction is the main adsorption mechanism of the adsorption process for SD-SNTs [31,34].

Additionally, the adsorption rate relating to the content of active adsorption sites on the matrix of the SD-SNTs adsorbent is almost always greater than that of SNTs, which suggests that SD-SNTs have higher adsorption efficiency than SNTs. Based on the above discussions and results, we can draw the conclusion that the capability and efficiency of Pb(II) adsorption are remarkably increased by the chemical functionalization with SD.

3.4. Adsorption isotherms of Pb(II) adsorption by SNTs and SD-SNTs

To examine the effect of Pb(II) concentration on the adsorption capacity, a comprehensive concentration study was carried out, and the isotherm studies were undertaken to simulate the metal uptake by adsorbents. The results shown in **Fig. 8** indicate that adsorption capacity increases with the increase in initial concentration of Pb(II) and achieves a maximum adsorption value gradually, which is noted as the maximum adsorption capacity.

The Langmuir and the Freundlich isotherms are the most frequently used models to describe and understand the equilibrium data of adsorption from aqueous solution. The Langmuir isotherm model is derived to model the assumptions of monolayer adsorption, a certain number of identical active sites, active sites distributed evenly on the surface of the adsorbent, and no interaction between adsorbents. The equation for the Langmuir isotherm is as follows:

$$\frac{C_e}{q_e} = \frac{1}{q_m K_L} + \frac{C_e}{q_m} \quad (5)$$

where q_e and C_e are the adsorption capacity ($\text{mg}\cdot\text{g}^{-1}$) and equilibrium concentration of the adsorbate ($\text{mg}\cdot\text{L}^{-1}$), respectively, while q_m and K_L represent the maximum adsorption capacity of adsorbents ($\text{mg}\cdot\text{g}^{-1}$) and the Langmuir adsorption constant ($\text{L}\cdot\text{mg}^{-1}$). The values of q_m and K_L are calculated from the slope and intercept of the linear plot of C_e/q_e against C_e .

The Freundlich isotherm is proposed based on multilayer adsorption and adsorption on heterogeneous surfaces, which can be illustrated as:

$$\log q_e = \log K_F + \frac{\log C_e}{n} \quad (6)$$

where K_F and n are the Freundlich constants, which represent the adsorption capacity and the adsorption strength, respectively. K_F and n can be obtained from the intercept and the slope of the linear plot of $\log q_e$ versus $\log C_e$.

Adsorption isotherms of Pb(II) onto SNTs and SD-SNTs are presented in **Fig. 9**, and in the corresponding Table 4. For the two adsorbents, the Langmuir equation shows a more significant correlation ($R^2 > 0.99$) with the experimental data than in the case of the Freundlich equation shows, which suggests a monolayer adsorption of Pb(II) onto SNTs and SD-SNTs [35,36]. On the other hand, the value of K_L (which is a relative indicator of adsorption capacity in the Langmuir theory) is larger for SD-SNTs than that for SNTs, implying that the Pb(II) adsorption capacity of SD-SNTs is higher than that of SNTs, which is consistent with the values of measured q_{max} , as compared with the values in Table 2 and 3. The experimental results imply that the Langmuir adsorption model is in well correspondence with the experimental data [2,4,6,31,38,39].

3.5. Adsorption mechanism of Pb(II) adsorption by SNTs and SD-SNTs

To further elucidate the adsorption mechanism, XPS analysis was performed on samples of SNTs, Pb-SNTs, SD-SNTs and Pb-SD-SNTs, the results are presented in **Fig. 10**. As shown in **Fig. 10 (a)**, the binding energy (BE) at 532.4 eV and 533.3 eV is assigned to the oxygen in silica and surface adsorbed oxygen in the form of OH^- from H_2O [39], respectively, which corresponds well with the FTIR results. The XPS spectra of O 1s obtained after Pb(II) adsorption on SNTs is described in **Fig. 10 (b)**. There are four O 1s signals at BE = 533.2 eV, 532.2 eV, 531.5 eV and 530.9 eV. The peak at 530.9 eV was ascribed to adsorbed oxygen (O^- or O_2^-) species, whereas the signal at BE = 531.5 eV corresponds to oxides lead [40-42,46], which indicates that Pb(II) adsorption is accompanied by a change in oxygen binding energy and the oxygen element takes part in Pb(II) adsorption.

In **Fig. 10 (c)**, the BE peaks for Pb(II) adsorbed by SNTs are centered at $144.2(\pm 0.3)$ eV for Pb 4f $5/2$ and $139.5 \text{ eV}(\pm 0.3)$ for Pb 4f $7/2$, which match the Pb(II) binding energy of $\text{Pb}(\text{NO}_3)_2$ in the reported literature [43]. The peak observed at 138.1 eV is due to the existence of PbO, while the BE at 142.1 eV implies the existence of electrostatic attraction between Pb(II) and SNTs [44,45]. Obviously, the BE at 144.1 eV and 139.4 eV of the Pb 4f-Pb-SD-SNTs in **Fig. 10 (d)** agrees well with the reported values for Pb 4f $5/2$ and 4f $7/2$, respectively. Interestingly, a remarkable shift to lower BE (142.0 eV and 137.1 eV) of Pb 4f was detected when Pb(II) was adsorbed onto SD-SNTs, implying that the interaction between Pb(II) and SD-SNTs is specific and much stronger than the electrostatic attraction between Pb(II) and SNTs. These results also provide the evidence of the formation of oxidation state lead (BE=137.9 eV).

The XPS spectra of N 1s-SD-SNTs are shown in **Fig. 10 (e)**. The BE at 399.9 eV is attributed to the amide groups, whereas the BE at 398.4 eV originated from the primary amine groups [47]. After the adsorption process, higher values of BE at 400.4 eV and 398.9 eV (**Fig. 10 (f)**) emerged due to the strong chelating interaction of SD and Pb(II) [43,44].

In light of data obtained from previous studies, the surfaces of silica display a negative surface charge at neutral pH due to the presence of deprotonated hydroxyl groups on the surface [29] and, as well known, the -NH- groups have been found to have high affinity for metal ions [40]. Consequently, as shown in **Scheme 1**, we propose the adsorption mechanism of Pb(II) by SNTs and SD-SNTs based on the above discussions. Obviously, the electrostatic interaction between positively charged heavy metal ions and the silica was found to play a major role in the adsorption of Pb(II) by SNTs. As for the SD-SNTs, from the extensive experimental and computational studies presented above, it can not be ignored that the -NH- groups functionalized onto the SNTs exhibit specific and strong chelating interactions with the target metals, while the electrostatic interactions also exist during the adsorption process. Therefore, we can draw the conclusion that the adsorption process is in fact the result of both electrostatic and non-electrostatic contributions, and the chelating interactions are the principal driving force for the adsorption of Pb(II) on SD-SNTs [29-31,38,46,48,49].

To further validate the extensive applications of SNTs and SD-SNTs on adsorption, a straightforward investigation was also carried out to analyze the adsorption performances of Cd(II) and Co(II) onto SNTs and SD-SNTs. As presented in **Fig. 11** and Table 5, the similar favorable results are observed in our previous study when compared with Pb(II). The fact is that at a low concentration the ratio of available adsorbents to the total heavy

metal ions is high and almost all ions could be bound to the adsorbents, whereas at high concentrations, the ratio is lower and consequently the adsorption capacity is dependent on the initial concentrations of heavy metal ions and content of adsorbents [7]. The excellent absorption capacity can be attributed to the hollow structure, good specific surface area and high-quality monodispersity. Kinetics and isotherms parameters for adsorption of Cd(II) and Co(II) at 303 K are given in the Supporting Information. The results of Table S1 and Table S2 imply that the Langmuir adsorption model is consistent with the experimental data [50]. The data from Table S3 and Table S4 support the general trend previously observed on the same substrate indicating that the Cd(II) and Co(II) adsorption onto SNTs is in accordance with the pseudo-first-order model, while the Cd(II) and Co(II) adsorption onto SD-SNTs is in well agreement with the pseudo-second-order kinetic model. The adsorption results confirmed that SNTs and SD-SNTs are good heavy metal ion absorbers with a high adsorption capacity under the described experimental conditions [51].

To further verify the stability and the possibility of regeneration of these materials, we calcined the SNTs after adsorbing Pb(II) at 600 °C in air for 3 h [52,53]. The as-prepared samples were imaged by TEM, and the corresponding results are presented in **Fig. S3**. As presented in the images, there is essentially no change in the structure and morphology of SNTs after the adsorption experiments and calcinations tests, which was indicative of the excellent stability and the potential recycling capability.

4. Conclusions

In summary, the structure of porous SNTs was successfully regulated by altering the content of TEOS in the precursor and controlling appropriate calcinations rates. Due to their prominent properties, new insights into the sorption of Pb(II) on the as-prepared SNTs at different pH levels were investigated. The results showed that the SNTs exhibited high adsorption ability for Pb(II) and the introduction of SD to the SNTs surface significantly enhanced the adsorption capacity and efficiency. The adsorption capacity for Pb(II) removal was found to be significantly improved with the decrease in pH value. The Langmuir adsorption model agrees well with the experimental data. A kinetic study was performed that suggests that the adsorption of Pb(II) onto SNTs and SD-SNTs can be fitted to pseudo-first-order and pseudo-second-order model, respectively. Moreover, the adsorption of Cd(II) and Co(II) onto SNTs and SD-SNTs further validated the excellent adsorption ability of these materials for heavy metal ions. The experimental results indicate that the SNTs and SD-SNTs are potential adsorbents and can be further applied to the treatment of wastewater contaminated with heavy metal ions.

Acknowledgments

We acknowledge the support of the project of the National Natural Science Foundation of China (NSFC) (Grant number: 51373154), and the 521 Talent Project of Zhejiang Sci-Tech University.

References

- [1] J. M. Gong, T. Liu, X. Q. Wang, X. L. Hu, L. Z. Zhang, Efficient removal of heavy metal ions from aqueous systems with the assembly of anisotropic layered double hydroxide nanocrystals@carbon nanosphere, *Environ. Sci. Technol.* 45 (2011) 6181–6187.
- [2] Y. Li, J. D. Wang, X. J. Wang, J. F. Wang, Adsorption–desorption of Cd(II) and Pb(II) on Ca-Montmorillonite, *Ind. Eng. Chem. Res.* 51 (2012) 6520–6528.
- [3] J. N. Dui, G. Y. Zhu, S. M. Zhou, Facile and economical synthesis of large hollow ferrites and their applications in adsorption for As(V) and Cr(VI), *ACS Appl. Mater. Interfaces* 5 (2013) 10081–10089.
- [4] C. P. Wang, J. Z. Wu, H. W. Sun, T. Wang, H. B. Liu, Y. Chang, Adsorption of Pb(II) ion from aqueous solutions by tourmaline as a novel adsorbent, *Ind. Eng. Chem. Res.* 50 (2011) 8515–8523.
- [5] C. Gao, X. Y. Yu, R. X. Xu, J. H. Liu, X. J. Huang, AlOOH-reduced graphene oxide nanocomposites: One-pot hydrothermal synthesis and their enhanced electrochemical activity for heavy metal ions, *ACS Appl. Mater. Interfaces* 4 (2012) 4672–4682.
- [6] C. J. Madadrang, H. Y. Kim, G. Gao, N. Wang, J. Zhu, H. Feng, M. Gorrington, M. L. Kasner, S. F. Hou, Adsorption behavior of EDTA-graphene oxide for Pb (II) removal, *ACS Appl. Mater. Interfaces* 4 (2012) 1186–1193.
- [7] D. G. Liu, Z. H. Li, W. Li, Z. R. Zhong, J. Q. Xu, J. J. Ren, Z. S. Ma, Adsorption behavior of heavy metal ions from aqueous solution by soy protein hollow microspheres, *Ind. Eng. Chem. Res.* 52 (2013) 11036–11044.
- [8] J. H. Chen, K. C. Hsu, Y. M. Chang, Surface modification of hydrophobic resin with tricaprilmethylammonium chloride for the removal of trace hexavalent chromium, *Ind. Eng. Chem. Res.* 52 (2013) 11685–11694.
- [9] J. Wang, L. Zhao, W. J. Duan, L. L. Han, Y. F. Chen, Adsorption of aqueous Cr(VI) by novel fibrous adsorbent with amino and quaternary ammonium groups, *Ind. Eng. Chem. Res.* 51 (2012) 13655–13662.
- [10] W. K. Oh, S. Kim, M. Choi, C. Kim, Y. S. Jeong, B. R. Cho, J. S. Hahn, J. Jang, Cellular uptake, cytotoxicity, and innate immune response of silica-titania hollow nanoparticles based on size and surface functionality, *ACS Nano*, 4 (2010) 5301–5313.

- [11] S. M. Kim, M. Jeon, K. W. Kim, J. Park, I. S. Lee, Postsynthetic functionalization of a hollow silica nanoreactor with manganese oxide-immobilized metal nanocrystals inside the cavity, *J. Am. Chem. Soc.* 135 (2013) 15714–15717.
- [12] K. G. Lee, R. Wi, M. Imran, T. J. Park, J. Lee, S. Y. Lee, D. H. Kim, Functionalization effects of single-walled carbon nanotubes as templates for the synthesis of silica nanorods and study of growing mechanism of silica, *ACS Nano*, 4 (2010) 3933–3942.
- [13] X. Y. Li, Q. J. He, J. L. Shi, Global gene expression analysis of cellular death mechanisms induced by mesoporous silica nanoparticle-based drug delivery system, *ACS Nano*, 8 (2014) 1309–1320.
- [14] N. Insin, J. B. Tracy, H. Lee, J. P. Zimmer, R. M. Westervelt, M. G. Bawendi, Incorporation of iron oxide nanoparticles and quantum dots into silica microspheres, *ACS Nano*, 2 (2008) 197–202.
- [15] M. H. Kim, H. K. Na, Y. K. Kim, S. R. Ryoo, H. S. Cho, K. E. Lee, H. Jeon, R. Ryoo, D. H. Min, Facile synthesis of monodispersed mesoporous silica nanoparticles with ultralarge pores and their application in gene delivery, *ACS Nano*, 5 (2011) 3568–3576.
- [16] A. F. Zhang, K. K. Hou, L. Gu, C. Y. Dai, M. Liu, C. S. Song, X. W. Guo, Synthesis of silica nanotubes with orientation controlled mesopores in porous membranes via interfacial growth, *Chem. Mater.* 24 (2012) 1005–1010.
- [17] A. Yildirim, H. Acar, T. S. Erkal, M. Bayindir, M. O. Guler, Template-directed synthesis of silica nanotubes for explosive detection, *ACS Appl. Mater. Interfaces* 3 (2011) 4159–4164.
- [18] Z. Y. Zhang, C. L. Shao, Y. Y. Sun, J. B. Mu, M. Y. Zhang, P. Zhang, Z. C. Guo, P. P. Liang, C. H. Wang, Y. C. Liu, Tubular nanocomposite catalysts based on size-controlled and highly dispersed silver nanoparticles assembled on electrospun silica nanotubes for catalytic reduction of 4-nitrophenol, *J. Mater. Chem.*, 22 (2012) 1387–1395.
- [19] J. S. Jan, T. H. Chuang, P. J. Chen, H. Teng, Layer-by-layer polypeptide macromolecular assemblies-mediated synthesis of mesoporous silica and gold nanoparticle/mesoporous silica tubular nanostructures, *Langmuir* 27 (2011) 2834–2843.
- [20] M. Zhang, W. Zhang, S. Wang, Synthesis of well-defined silica and Pd/silica nanotubes through a surface sol-gel process on a self-assembled chelate block copolymer, *J. Phys. Chem. C* 114 (2010) 15640–15644.

- [21] P. Wang, M. L. Du, M. Zhang, H. Zhu, S. Y. Bao, The preparation of tubular heterostructures based on titanium dioxide and silica nanotubes and their photocatalytic activity, *Dalton Trans.*, 43 (2014) 1846–1853.
- [22] J. H. Wang, X. Zhang, B. Zhang, Y. F. Zhao, R. Zhai, J. D. Liu, R. F. Chen, Rapid adsorption of Cr (VI) on modified halloysite nanotubes, *Desalination* 259 (2010) 22–28.
- [23] Q. Wen, J. C. Di, Y. Zhao, Y. Wang, L. Jiang, J. H. Yu, Flexible inorganic nanofibrous membranes with hierarchical porosity for efficient water purification, *Chem. Sci.*, 4 (2013) 4378–4382.
- [24] A. Samecka-Cymerman, A. J. Kempers, Heavy metals in aquatic macrophytes from two small agricultural and textile industry sewages SW Poland, *Arch. Environ. Contam. Toxicol.* 53 (2007) 198–206.
- [25] T. Pirzada, S. A. Arvidson, C. D. Saquing, S. S. Shah, S. A. Khan, Hybrid silica–PVA nanofibers via sol-gel electrospinning, *Langmuir*, 28 (2012) 5834–5844.
- [26] G. I. Andrade, E. F. Barbosa-Stancioli, A. A. P. Mansur, W. Vasconcelos, H. S. Mansur, Small-angle X-ray scattering and FTIR characterization of nanostructured poly(vinyl alcohol)/silicate hybrids for immunoassay applications, *J. Mater. Sci.*, 43 (2008) 450–463.
- [27] L. N. Chao, D. Y. Yang, M. D. Dong, T. Xu, Y. Jin, S. L. Xu, F. Z. Zhang, D. G. Evans, X. Y. Jiang, Fabrication and wettability of colloidal layered double hydroxide-containing PVA electrospun nanofibrous mats, *Ind. Eng. Chem. Res.*, 49 (2010) 5610–5615.
- [28] P. Wang, M. Zhang, Y. T. Cai, S. Y. Cai, M. L. Du, H. Zhu, S. Y. Bao, Facile fabrication of palladium nanoparticles immobilized on the water-stable polyvinyl alcohol/polyethyleneimine nanofibers via in situ reduction and their high electrochemical activity, *Soft Mater.*, 12, (2014) 387–395.
- [29] V. Puddu, C. C. Perry, Peptide adsorption on silica nanoparticles: Evidence of hydrophobic interactions, *ACS Nano*, 6 (2012) 6356–6363.
- [30] P. Luo, J. S. Zhang, B. Zhang, J. H. Wang, Y. F. Zhao, J. D. Liu, Preparation and characterization of silane coupling agent modified, halloysite for Cr(VI) removal, *Ind. Eng. Chem. Res.* 50 (2011) 10246–10252.
- [31] M. Hua, Y. N. Jiang, B. Wu, B. C. Pan, X. Zhao, Q. X. Zhang, Fabrication of a new hydrous Zr(IV) oxide-based nanocomposite for enhanced Pb(II) and Cd(II) removal from waters, *ACS Appl. Mater. Interfaces* 5 (2013) 12135–12142.

- [32] D. Xu, X. Tan, C. Chen, X. Wang, Removal of Pb(II) from aqueous solution by oxidized multiwalled carbon nanotubes, *J. Hazard. Mater.* 154 (2008) 407–416.
- [33] V. Chantawong, N. W. Harvey, V. N. Bashkin, Comparison of heavy metal adsorptions by thai kaolin and ballclay, *Water Air Soil Pollut.* 148 (2003) 111–125.
- [34] A. Sar, M. Tuzen, M. Soylak, Adsorption of Pb(II) and Cr(III) from aqueous solution on celtek clay, *J. Harzard. Mater.* 144 (2007) 41–46.
- [35] J. P. Wang, X. X. Ma, G. Z. Fang, M. F. Pan, X. K. Ye, S. Wang, Preparation of iminodiacetic acid functionalized multi-walled carbon nanotubes and its application as sorbent for separation and preconcentration of heavy metal ions, *J. Harzard. Mater.* 186 (2011) 1985–1992.
- [36] X. H. Zou, J. M. Pan, H. X. Ou, X. Wang, W. Guan, C. X. Li, Y. S. Yan, Y. Q. Duan, Adsorptive removal of Cr(III) and Fe(III) from aqueous solution by chitosan/attapulgitite composites: equilibrium, thermodynamics and kinetics, *Chem. Eng. J.* 167 (2011) 112–121.
- [37] X. Z. Zhao, B. Hu, J. J. Ye, Q. Jia, Preparation, characterization, and application of graphene-zinc oxide composites (G-ZnO) for the adsorption of Cu(II), Pb(II), and Cr(III), *J. Chem. Eng. Data* 58 (2013) 2395–2401.
- [38] H. Y. Shen, J. L. Chen, H. F. Dai, L. B. Wang, M. Q. Hu, New insights into the sorption and detoxification of chromium(VI) by tetraethylenepentamine functionalized nanosized magnetic polymer adsorbents: mechanism and pH effect. *Ind. Eng. Chem. Res.* 52 (2013) 12723–12732.
- [39] J. G. Deng, L. Zhang, H. G. Dai, H. He, C. T. Au, Strontium-doped lanthanum cobaltite and manganite: highly active catalysts for toluene complete oxidation, *Ind. Eng. Chem. Res.* 47 (2008) 8175–8183.
- [40] W. H. Zou, R. P. Han, Z. Z. Chen, J. Shi, H. M. Liu, Characterization and properties of manganese oxide coated zeolite as adsorbent for removal of copper(II) and lead(II) ions from solution, *J. Chem. Eng. Data* 51 (2006) 534–541.
- [41] M. S. Bootharaju, T. Pradeep, Uptake of toxic metal ions from water by naked and monolayer protected silver nanoparticles: an X-ray photoelectron spectroscopic investigation, *J. Phys. Chem. C* 114 (2010) 8328–8336.
- [42] A. S. Tselesh, Anodic behaviour of tin in citrate solutions: the IR and XPS study on the composition of the passive layer, *Thin Solid Films*, 516 (2008) 6253–6260.
- [43] J. N. Wang, C. Cheng, X. Yang, C. Chen, A. Li, A new porous chelating fiber: preparation, characterization, and adsorption behavior of Pb(II), *Ind. Eng. Chem. Res.* 52 (2013) 4072–4082.

- [44] A. Palermo, F. J. Williams, R. M. Lambert, In situ control of the composition and performance of a bimetallic alloy catalyst: the selective hydrogenation of acetylene over Pt/Pb, *J. Phys. Chem. B* 106 (2002) 10215–10219.
- [45] V. C. Taty-Costodes, H. Fauduet, C. Porte, A. Delacroix, Removal of Cd(II) and Pb(II) ions, from aqueous solutions, by adsorption onto sawdust of *pinus sylvestris*, *J. Hazard. Mater. B* 105 (2003) 121–142.
- [46] P. Wang, M. L. Du, M. Zhang, H. Zhu, S. Y. Bao, AgNPs/PVA and AgNPs/(PVA/PEI) hybrids: preparation, morphology and antibacterial activity, *J. Phys. D: Appl. Phys.*, 46 (2013) 345303–345310.
- [47] H. Zhu, M. L. Du, M. L. Zou, C. S. Xu, Y. Q. Fu, Green synthesis of Au nanoparticles immobilized on halloysite nanotubes for surface-enhanced raman scattering substrates. *Dalton Trans.* 41 (2012) 10465–10471.
- [48] Y. F. Yang, Y. L. Xie, L. C. Pang, M. Li, X. H. Song, J. G. Wen, H. Y. Zhao, Preparation of reduced graphene oxide/poly(acrylamide) nanocomposite and its adsorption of Pb(II) and methylene blue, *Langmuir* 29 (2013) 10727–10736.
- [49] L. Beqa, A. K. Singh, S. A. Khan, D. Senapati, S. R. Arumugam, P. C. Ray, Gold nanoparticle-based simple colorimetric and ultrasensitive dynamic light scattering assay for the selective detection of Pb(II) from paints, plastics, and water samples, *ACS Appl. Mater. Interfaces* 3 (2011) 668–673.
- [50] S. Joshi, I. Ghosh, S. Pokhrel, L. Madler, W. M. Nau, Interactions of amino acids and polypeptides with metal oxide nanoparticles probed by fluorescent indicator adsorption and displacement, *ACS Nano*, 6 (2012) 5668–5679.
- [51] M. Thirumavalavan, Y. T. Wang, L. C. Lin, J. F. Lee, Monitoring of the structure of mesoporous silica materials tailored using different organic templates and their effect on the adsorption of heavy metal ions, *J. Phys. Chem. C* 115 (2011) 8165–8174.
- [52] R. X. Jin, Y. Yang, Y. Xing, L. Chen, S. Y. Song, R. C. Jin, Facile synthesis and properties of hierarchical double-walled copper silicate hollow nanofibers assembled by nanotubes, *ACS Nano*, 8 (2014) 3664–3670.
- [53] Z. H. Zhang, X. H. Zhong, S. H. Liu, D. F. Li, M. Y. Han, Aminolysis route to monodisperse titania nanorods with tunable aspect ratio, *Angew. Chem. Int. Ed.*, 117 (2005) 3532–3536.

Figure Captions

Fig. 1. FE-SEM ((a) and (b)) images and TEM ((c) and (d)) images of SNTs.

Fig. 2. TEM images of electrospun PVP-TEOS-C₂H₅OH composite fibers (a, c, e) and their corresponding silica nanofibers or nanotubes after calcination (b, d, f) obtained by increasing the addition of TEOS (a, b: 2.5 mL of TEOS; c, d: 3.0 mL of TEOS; e, f: 3.5 mL of TEOS) to the PVP-C₂H₅OH solution, respectively.

Fig. 3. TEM images of SNTs which were obtained from the electrospun PVP-TEOS-C₂H₅OH composite fibers (in Fig. 2. (c) and (d)) with the increase of calcinations rates (a, b: 1 °C/min; c, d: 5 °C/min; e, f: 8 °C/min), respectively.

Fig. 4. The FTIR spectra of the SNTs (a) and SD-SNTs (b).

Fig. 5. HAADF-STEM images ((a) and (c)) and high resolution element mappings ((b) and (d)) taken on the Pb-SNTs ((a) and (b)) and Pb-SD-SNTs ((c) and (d)).

Fig. 6. Effect of contact time on the adsorption of Pb(II) onto the SNTs (a) and SD-SNTs (b) at an initial pH of 4.0, 7.0, and 9.0 ($C_0 = 50 \text{ mg} \cdot \text{L}^{-1}$, $T = 303 \text{ K}$).

Fig. 7. Pseudo-first-order kinetic plots for the adsorption of Pb(II) by SNTs (a) and SD-SNTs (c); pseudo-second-order kinetic plots for the adsorption of Pb(II) by SNTs (b) and SD-SNTs (d) ($T = 303 \text{ K}$).

Fig. 8. Effect of initial concentration of Pb(II) for adsorption capacity onto SNTs (a) and SD-SNTs (b); experimental conditions: initial concentration 5-175 mg/L, sample dose 20 mg/80 mL, pH 7.0, temperature $303 \pm 2 \text{ K}$, contact time 24 h.

Fig. 9. Langmuir isotherms for the adsorption of Pb(II) onto SNTs (a) and SD-SNTs (c); Freundlich isotherms for the adsorption of Pb(II) onto SNTs (b) and SD-SNTs (d); experimental conditions: initial concentration 5-175 mg/L, sample dose 20 mg/80 mL, pH 7.0, temperature $303 \pm 2 \text{ K}$, contact time 24 h.

Fig. 10. The XPS spectra of O 1s, Pb 4f and N 1s in SNTs, Pb-SNTs, SD-SNTs and Pb-SD-SNTs.

Fig. 11. Cd(II) and Co(II) adsorption as function of initial concentration and adsorbent.

Scheme 1. Schematic adsorption mechanism of Pb(II) by SNTs and SD-SNTs.

Table 1. Comparison of maximum adsorption capacities with various absorbents for Pb(II).

Table 2. Adsorption kinetic parameters of the pseudo-first-order model for Pb(II) on SNTs and SD-SNTs.

Table 3. Adsorption kinetic parameters of the pseudo-second-order model for Pb(II) on SNTs and SD-SNTs.

Table 4. Comparison of the Langmuir models and the Freundlich models for Pb(II) adsorption onto SNTs and SD-SNTs.

Table 5. Comparison of maximum adsorption capacities of various heavy metal ions by SNTs and SD-SNTs (The initial concentration of these heavy metal ions is between 5 and 175 mg/L; Conditions: pH = 7.0 and T = 303 K).

Table 1. Comparison of Maximum Adsorption Capacities with Various Absorbents for Pb(II)

adsorbent	adsorption capacity ($\text{mg} \cdot \text{g}^{-1}$)	ref
Oxidized MWCNTs	2.06	32
Kaolin	0.66	33
Celtek clay	18.08	34
Acid functionalized multiwalled carbon nanotubes	8.98	35
Activated carbon prepared from coconut shell	26.50	36
G-ZnO composites	23.42	37
SNTs	42.85	this work
SD-SNTs	64.70	this work

Table 2. Adsorption kinetic parameters of the pseudo-first-order model for Pb(II) on

SNTs and SD-SNTs

pH	k_1 (min^{-1})		q_e ($\text{mg} \cdot \text{g}^{-1}$)		R^2		experimental	
							q_m ($\text{mg} \cdot \text{g}^{-1}$)	
	SNTs	SD-SNTs	SNTs	SD-SNTs	SNTs	SD-SNTs	SNTs	SD-SNTs
4	0.00988	0.02298	39.78	67.50	0.990	0.898	47.85	72.34
7	0.01133	0.03185	38.61	72.31	0.972	0.855	42.85	64.70
9	0.00911	0.02411	36.98	67.81	0.958	0.772	41.17	61.88

Table 3. Adsorption kinetic parameters of the pseudo-second-order model for Pb(II) on SNTs and SD-SNTs

pH	k_2 ($\text{g} \cdot \text{mg}^{-1} \cdot \text{min}^{-1}$)		q_e ($\text{mg} \cdot \text{g}^{-1}$)		R^2		experimental	
							q_m ($\text{mg} \cdot \text{g}^{-1}$)	
	SNTs	SD-SNTs	SNTs	SD-SNTs	SNTs	SD-SNTs	SNTs	SD-SNTs
4	0.00037	0.00038	54.35	83.96	0.942	0.967	47.85	72.34
7	0.00035	0.00043	50.28	75.99	0.935	0.974	42.85	64.70
9	0.00030	0.00027	48.33	77.28	0.873	0.772	41.17	61.88

Table 4. Comparison of the Langmuir models and the Freundlich models for Pb(II) adsorption onto SNTs and SD-SNTs

Sample	Measured q_{max} ($\text{mg} \cdot \text{g}^{-1}$)	Langmuir			Freundlich		
		q_m ($\text{mg} \cdot \text{g}^{-1}$)	K_L ($\text{L} \cdot \text{mg}^{-1}$)	R^2	n	K_F ($\text{mg}^{1-n} \text{L}^n \text{g}^{-1}$)	R^2
SNTs	42.85	75.87	0.04442	0.992	2.17108	7.29055	0.948
SD-SNTs	64.70	112.36	0.05518	0.991	2.33798	13.10358	0.976

Table 5. Comparison of maximum adsorption capacities of various heavy metal ions by SNTs and SD-SNTs (The initial concentration of these heavy metal ions is between 5 and 175 mg/L; Conditions: pH = 7.0 and T = 303 K)

initial concentration (mg · L ⁻¹)	adsorption capacity (mg · g ⁻¹)					
	Pb(II)		Cd(II)		Co(II)	
	SNTs	SD-SNTs	SNTs	SD-SNTs	SNTs	SD-SNTs
5	9.86	14.17	9.14	13.98	9.14	13.94
35	40.76	54.05	35.52	55.71	36.96	56.54
50	42.02	66.76	42.44	63.96	43.86	67.86
150	66.13	98.27	67.33	98.41	68.06	103.97
175	66.30	101.21	68.61	99.54	70.34	104.43

Synthesis of Silver Nanoparticles in Electrospun Polyacrylonitrile Nanofibers Using Tea Polyphenols as the Reductant

MeiLing Zou,¹ MingLiang Du,^{1,2} Han Zhu,¹ CongSheng Xu,¹ Ni Li,^{1,2} YaQin Fu^{1,2}

¹ Department of Materials Engineering, College of Materials and Textile, Zhejiang Sci-Tech University, Hangzhou 310018, People's Republic of China

² Key Laboratory of Advanced Textile Materials and Manufacturing Technology, Zhejiang Sci-Tech University, Ministry of Education, Hangzhou 310018, People's Republic of China

Uniformly dispersed Ag nanoparticles (AgNPs) with diameter about 5 nm embedded in electrospun polyacrylonitrile (PAN) nanofibers were synthesized by using tea polyphenols (TP) as the reductant. The reducing ability of TP toward Ag ions was characterized by Fourier transform infrared spectroscopy and ultraviolet-visible spectra, and the results revealed that TP exhibit satisfied reducing ability in the synthesis process. Transmission electron microscopy observation showed that the synthesized spherical AgNPs with diameter about 5 nm were immobilized on the surface and in the interior of PAN nanofibers by electrospinning technology. The interactions of Ag with PAN and TP were investigated by X-ray photoelectron spectroscopy (XPS), and the results suggested that PAN polymer and TP both served as stabilizer during the synthesis of AgNPs because of the chelating interactions of Ag with cyano groups and phenolic hydroxyls. The synthesized AgNPs in PAN nanofibers exhibit good antibacterial property and may be used for antibacterial and catalytic applications. *POLYM. ENG. SCI.*, 53:1099–1108, 2013. © 2012 Society of Plastics Engineers

INTRODUCTION

Ag nanoparticles (AgNPs) have deserved special attention owing to their fascinating physical and chemical properties [1–4] and, so far, diverse applications of

AgNPs have been explored in chemical, catalytic, biological, and other fields [5–8]. Typically, AgNPs present high reactivity and selectivity in a broad range of catalytic reactions. As reported, Shen et al. developed highly monodispersed Cu- and Ag-based bimetallic nanocrystals for the efficient catalyst of CO oxidation [5]. Besides, AgNPs possess strong antimicrobial properties against various species of bacteria, low toxicity to human beings, and a long-term antibacterial efficiency, now that they have been applied in many related fields, such as pharmaceutical, silver-coated medical devices, textiles, food packaging, and so on [9–12].

It is well recognized that the size, shape, and surface properties of AgNPs are closely related to their properties; however, smaller AgNPs are easy to aggregate due to their high surface energy, so synthesis of AgNPs with small size and uniform dispersion has been devoted great efforts in recent years. During the application of AgNPs, they are often fastened to organic polymer or inorganic support to avoid aggregation [13–16]. Guo et al. have done much work on the synthesis of small and size-controlled AgNPs using tannin-grafted collagen fiber [6]. Jean et al. reported the synthesis of functionalized silica nanoparticles decorated by nanometallic Ag for optical sensing [1]. However, it should be mentioned that traditional chemical reductants, such as NaBH₄, dimethylhydrazine, hydrazine, and so forth, are environmental intolerance and will bring potential environment risk. Some green reducing agents have been reported to synthesize metallic nanoparticles, such as gold, platinum, and iron [17–19]. Consequently, it is meaningful to explore a facile approach for the synthesis of uniformly dispersed AgNPs with small particle size.

Plant polyphenols pervasively exist in the plant kingdom, like vegetables, fruits, beverages, and tea [20, 21]. Tea polyphenols (TP) are extracted from tea plants, and they are mixtures of polyphenol compounds belonging to the flavonoid family, mainly including catechin (EC),

Correspondence to: MingLiang Du; e-mail: du@zstu.edu.cn

Contract grant sponsor: National Natural Science Foundation of China (NSFC); contract grant numbers: 50903072 and 10902099; contract grant sponsor: Zhejiang Province Natural Science Foundation; contract grant number: Y4100197; contract grant sponsor: Science Foundation of Zhejiang Sci-Tech University (ZSTU); contract grant number: 0901803-Y; contract grant sponsor: The Young Researchers Foundation of Key Laboratory of Advanced Textile Materials and Manufacturing Technology, Ministry of Education, Zhejiang Sci-Tech University; contract grant number: 2011QN02.

DOI 10.1002/pen.23358

Published online in Wiley Online Library (wileyonlinelibrary.com).

© 2012 Society of Plastics Engineers

epigallocatechin (EGC), epicatechin gallate (ECG), and catechin gallate (EGCG). They have stimulated great interest due to their antimicrobial and antifungal properties and chelating of toxic heavy metals [22]. Previous studies have suggested that TP have functioned as both the “green” reductant and the capping agent for the synthesis of some metal nanospheres and no surfactant was used [23–26]. Inspired by their attractive properties, in this study, we chose TP as the green reducing agent to synthesize AgNPs.

In recent years, electrospinning technique has attracted great attention for it is the only method to produce fibers with nanosized diameter and high surface area [27, 28], and many kinds of the electrospun nanofibers have been chosen as the ideal support for nanoparticles [29–32]. PAN is an easy-electrospinning polymer, and more importantly, the $C\equiv N$ groups on the surface of PAN nanofibers could be involved in the interaction with Ag ions through chelating effect, which may contribute to synthesize smaller AgNPs [33–36]. Consequently, we chose PAN to electrospin the nanofibers in the present work.

Herein, we proposed a convenient method of introducing TP as the green reductant to synthesize AgNPs through an in situ reduction approach in PAN/dimethyl formamide (DMF) solution. In the synthesis process, uniformly dispersed AgNPs with narrow size distributions in PAN nanofibers were obtained by electrospinning technique. The synthesized AgNPs/PAN nanofibers membranes showed good antibacterial activity against *E. coli* and *S. aureus*.

EXPERIMENTAL

Chemicals and Materials

DMF (99.5%) was obtained from Hangzhou Gaojing Fine Chemical. Silver nitrate ($AgNO_3$, 99.8%) was acquired from Changzhou Guoyu Environmental Technology. Polyacrylonitrile powder (PAN, $M_w \approx 1.4 \times 10^5$, $\rho = 1.14$ – 1.15 g cm^{-3} , copolymerized with 10 wt% methyl acrylate) was manufactured by Sinopec Shanghai Petrochemical. TP, with bulk density of 0.5 g cm^{-3} , was purchased from Xuancheng BaiCao Plant Industry and Trade, and the main chemical compositions are listed as follows: 12.5% EGC, 45.3% EGCG, 4.3% EC, and 9.1% ECG.

Synthesis of AgNPs in DMF Solution Using TP as the Reductant

The AgNPs were synthesized using TP as the reducing agent. $AgNO_3$ (0.068 g) was added to 45-ml DMF solution. The mixture was heated to 60°C and stirred by magnetic force vigorously, then 0.01 g of TP was dissolved in 5 ml DMF by sonicating for 1 min, and the TP/DMF solution was dropped to the mixture; at last, the mixture was kept uninterruptedly stirring for 60 min at 60°C. The AgNPs were also synthesized without TP as the reducing agent. $AgNO_3$ (0.069 g) was added to 50-mL DMF

solution. The mixture was heated to 60°C and stirred by magnetic force vigorously for 60 min.

Synthesis of AgNPs in PAN/DMF Solution With and Without TP

The synthesis of AgNPs/PAN/DMF solution without extra reducing agent (DMF as the reductant) was carried out by the following procedure. The PAN solution was obtained by dissolving 6.371 g PAN powder into 45 ml DMF, stirring for 1 h at 60°C. $AgNO_3$ (0.159 g) powder was dissolved in 5 ml DMF at room temperature and added to the PAN/DMF solution dropwise within 2 min. Therefore, the mass fraction of PAN in the DMF solution was 12 wt% and the amount of $AgNO_3$ was 2.5 wt% (based on the weight of the PAN powder). The mixture was stirred for 60 min at 60°C.

The synthesis of AgNPs/PAN/DMF solution using TP as the reductant of $AgNO_3$ was similar as the above procedure. The only difference was that 0.012 g of TP was dissolved in 5-ml DMF solution and dropwise added to the system following on previous step. For contrast, another two samples with $AgNO_3$ content 1.0 and 7.5 wt% reduced by 0.005 and 0.036 g TP, respectively, were also prepared as the same procedure. All prepared samples were stored in liquid nitrogen.

Electrospinning of AgNPs/PAN Nanofibers

The above AgNPs/PAN/DMF solutions with $AgNO_3$ contents of 1.0, 2.5, and 7.5 wt% with reduction time of 60 min were fabricated into PAN nanofibers by electrospinning technique. The solutions were transferred into a syringe with a stainless copper needle at the tip and then electrospun under a fixed voltage of 12 kV and the needle to collector distance was 12 cm with the flow rate at 0.01 ml min^{-1} . The sie of syringe used for e-spinning was microinjection pump and the needle was + end. During e-spinning, the temperature was $25 \pm 2^\circ C$ and the humidity was 45%. The electrospun fibers were collected onto a piece of irrotational aluminum foil.

Characterization

Fourier Transform Infrared Spectroscopy. A thin layer of the prepared AgNPs/DMF/TP solution was spread on KBr pellets. The Fourier transform infrared spectroscopy (FTIR) analysis was conducted by a Nicolet 5700 FTIR spectrometer. The spectra were taken from 4000 to 400 cm^{-1} wavenumbers.

Ultraviolet–Visible Spectroscopy. The as-prepared AgNPs in the DMF and PAN/DMF solutions were examined by Lambda 900 Ultraviolet–visible spectroscopy (UV–vis) spectrophotometer (Perkin Elmer). The reference solution was DMF, and the spectra were collected over a wavelength range from 200 to 800 nm.

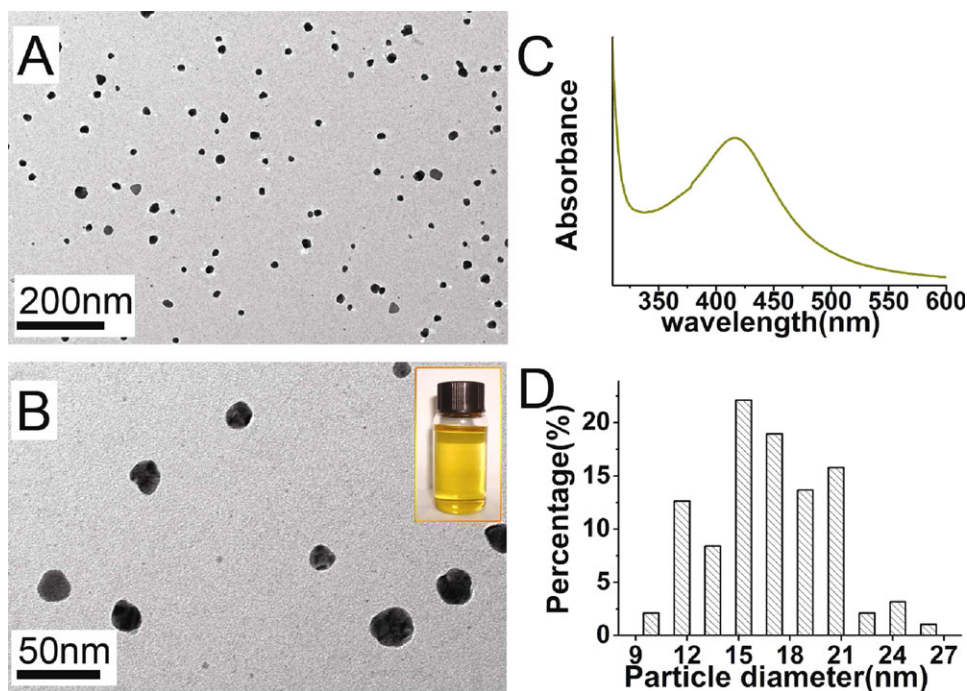


FIG. 1. TEM images of the AgNPs (A and B), particle diameter distribution, and UV-vis absorption spectrum of AgNPs. [Color figure can be viewed in the online issue, which is available at wileyonlinelibrary.com.]

Transmission Electron Microscopy and High-Resolution Transmission Electron Microscopy. The samples were prepared by dropping diluent AgNPs/DMF/TP solution onto a carbon-coated copper grid and dried under infrared lamp for 8 min. The AgNPs/PAN nanofibers samples were placed on ultrathin carbon-coated copper grids for observation. The images were acquired using JSM-2100 transmission electron microscope (JEOL, Japan) at an accelerating voltage of 200 kV.

Field-Emission Scanning Electron Microscopy (FE-SEM). The AgNPs/PAN nanofibers were plated with a thin layer of gold before observations. The morphology of electrospun AgNPs/PAN nanofibers were observed with a JSM-6700F field-emission scanning electron microscope (JEOL, Japan) under the voltage of 10.0 kV.

X-ray Photoelectron Spectroscopy. X-ray photoelectron spectra of pure PAN powder, TP, and AgNPs/PAN nanofibers were recorded by using an X-ray photoelectron spectrometer (Kratos Axis Ultra DLD) with an Aluminum (mono) K_{α} source (1486.6 eV). The high-resolution survey (pass energy = 48 eV) was performed at spectral regions relating to silver, oxygen, and nitrogen.

Antimicrobial Tests

The antibacterial activity of the AgNPs/PAN nanofiber membranes was assessed against bacterial strain Gram-negative bacteria *E. coli* ATCC 25922 and Gram-negative

bacteria *S. aureus* ATCC 6538. For qualitative measurement of antibacterial activity, a modified agar diffusion assay (disc test) (ISO 20645: 2004, Textile fabrics—Determination of antibacterial activity—Agar diffusion plate test) was carried out. The inhibition zone was measured as activity against above two microbial species. For a typical procedure, the bacterial strains were inoculated in the sterilized Luria-Bertani (LB) medium and incubated overnight at 37°C with shaking before using. Then from each bacterial suspension, 200 μ L volumes were withdrawn and spread uniformly over the agar plates. Small circular pieces of the AgNPs/PAN nanofiber membranes with the diameter of 2 cm were gently placed over the solidified agar gel in different petri dishes. Then the inoculated agars in the petri plates were kept for incubation at 37°C, after 18 h the lengths of inhibition zone were recorded.

RESULTS AND DISCUSSION

Synthesis of AgNPs Using TP as the Reductant

As observed in Fig. 1, AgNPs synthesized by using TP as the reductant in DMF solution with the reaction time of 60 min are obtained. Figure 1A and B reveals that most of the AgNPs are spherical and disperse uniformly, and the size distribution of the AgNPs is from about 10 to 26 nm. The inset in Fig. 1B shows that the prepared solution is transparent and the color is golden yellow. In addition, the intense absorption peak located at 416 nm in Fig. 1D is attributed to the surface plasma excitation of

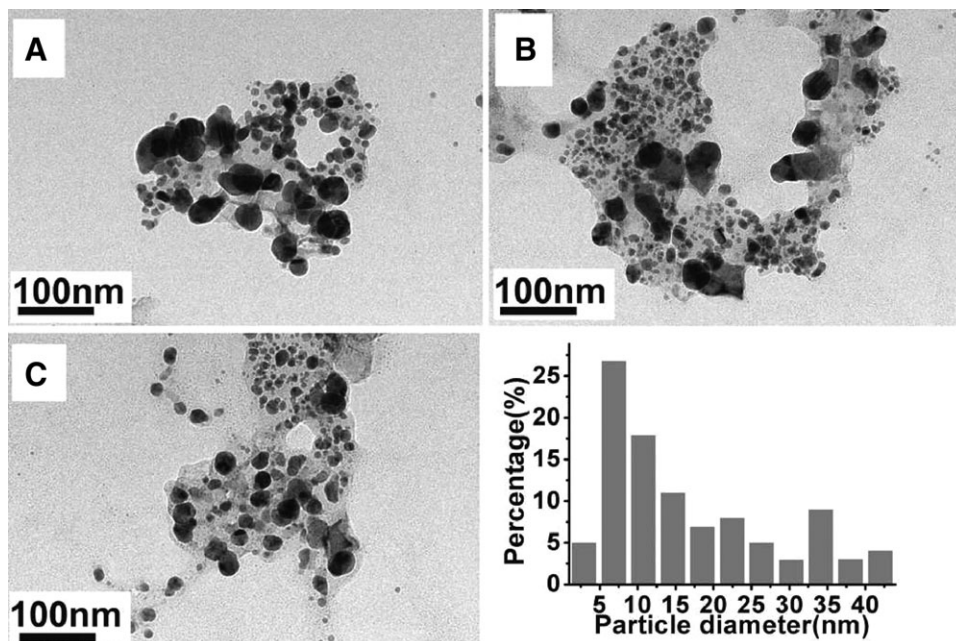


FIG. 2. TEM images of the AgNPs synthesized without TP and the corresponding size distribution.

AgNPs [37], so the UV–vis absorption spectrum of the prepared DMF solution can further confirm that the AgNPs were successfully synthesized.

Some previous studies have reported that the DMF also exhibits reducibility in the synthesis of AgNPs from AgNO_3 solution [38]. In the present work, the AgNPs synthesized using DMF as the reductant exhibit a relatively wide size distribution, and the average diameter is much bigger than that with the presence of TP (Fig. 2). Our previous work found that as consists of multiple hydroxyls, TP can chelate with the Ag ions and the chelated Ag ions can be reduced into Ag^0 atoms in situ, contributing to forming smaller and uniform AgNPs [39]. It is believed that the prepared AgNPs in the present approach were mainly reduced by TP, which will be discussed in the following work. The above data demonstrate that the green TP can serve as the reductant to synthesize AgNPs, suggesting a feasible procedure to produce AgNPs with narrow size distribution.

In the present approach, the supposed reaction between Ag ions and TP is illustrated in Fig. 3. FTIR analysis was used to testify the reducibility of TP toward Ag ions and investigate the chemical changes during the reaction process. The FTIR spectra of TP (A) and AgNPs/DMF/TP solution reacted for 60 min (B) are presented in Fig. 4.

The broad absorption peak at 3361 cm^{-1} is assigned to the O—H stretching vibration of phenolic hydroxyls, suggesting the existence of hydrogen bonds in TP. The absorption band between 1550 and 1480 cm^{-1} is ascribed to the aromatic rings. The absorption peaks at 1455 and 1096 cm^{-1} are assigned to C—H alkanes in aromatic rings and C—O stretching vibration, respectively. The typical absorption peaks of DMF can be assigned as follows: 2928 and 2860 cm^{-1} (C—H stretching vibration), 1387 cm^{-1} (C—H in-plane vibration), 1676 cm^{-1} (C=O stretching vibration), and 660 cm^{-1} (N—C=O flexural vibration). However, an obvious change is observed in the wide hydroxyl band $2820\text{--}3687\text{ cm}^{-1}$ region for curve b. The absorption peak at 3361 cm^{-1} gets relatively narrow and shifts to 3530 cm^{-1} , and it indicates that part of hydroxyls in TP participate in the redox reaction between TP and Ag ions. Furthermore, the peaks at 1344 , 1147 , and 1037 cm^{-1} ascribed to C—O—H stretching vibration, O—H damping vibration and C—O—H stretching vibration of phenolic hydroxyls in TP are nearly vanished, implying the involvement of the O—H groups in the reduction of Ag ions. Additionally, the peak at 1101 cm^{-1} in Fig. 4B is much stronger than that in Fig. 4A, and it is mainly attributed to the oxidation of part of aldehyde groups in DMF to carboxyl groups.

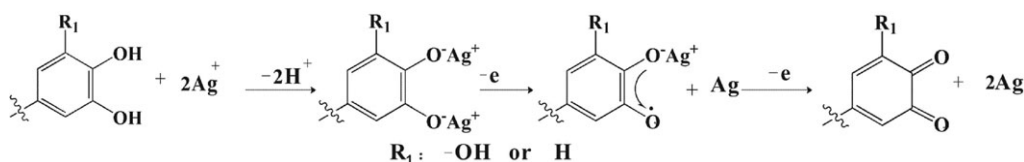


FIG. 3. Illustration of the reaction between Ag ions and TP.

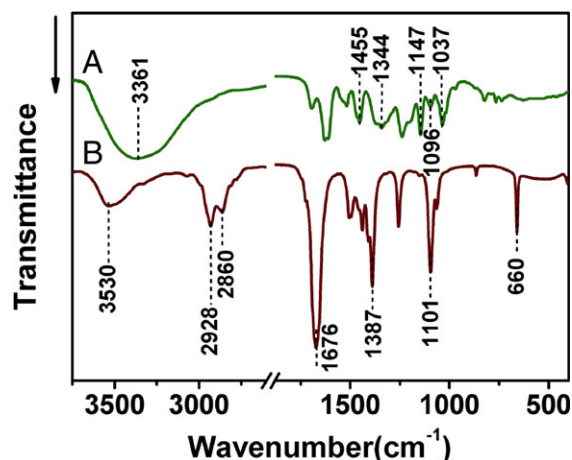


FIG. 4. The FTIR spectra of TP (A) and AgNPs/DMF/TP solution (B). [Color figure can be viewed in the online issue, which is available at wileyonlinelibrary.com.]

Fabrication of Electrospun PAN Nanofibers with AgNPs

In the above work, we successfully synthesized the well-dispersed AgNPs using TP as the effective reductant in DMF solution. Then, we propose a facile route to fabricate AgNPs/PAN nanofibers by combining the electrospinning technique and an in situ reduction approach. In the present investigations, we fabricated electrospun PAN nanofibers with uniformly dispersed AgNPs, which are shown in Fig. 5. From the figure, it can be seen that the AgNPs in PAN nanofibers exhibit very small diameter

and narrow size distribution. With the increasing concentration of AgNO₃, the amount of the AgNPs in PAN nanofibers increases gradually. As shown in the diameter distribution histogram, the average particle diameters of AgNPs in PAN nanofibers are about 2.8, 5.3, and 4.5 nm, corresponding to the AgNO₃ mass fractions of 1.0, 2.5, and 7.5 wt%, respectively. The size of AgNPs shown in Fig. 5B and C is much bigger than that in Fig. 5A, which may result from the different concentration of AgNO₃ and TP [37]. Surprisingly, in contrast to the AgNPs synthesized in DMF solution, as shown in Fig. 1, the AgNPs obtained by in situ approach in PAN nanofibers possess much smaller diameter, which indicates that the PAN polymer may act as a particular stabilizer and prevent the particle growth in the process of synthesis of AgNPs, and it will be discussed later. The high-resolution transmission electron microscopy (HRTEM) image of AgNPs is shown in Fig. 6. The AgNPs possess a well-resolved lattice planes, and the interplanar spacing is about 0.243 nm, corresponding to the (111) planes of fcc Ag.

In the present investigations, DMF was utilized as the solvent of PAN for electrospinning. However, DMF also can be used as a reductant for Ag ions; therefore, we compared the reducibility of DMF and TP by reducing AgNO₃ in PAN/DMF solutions. The UV-vis spectra, including AgNO₃/PAN/DMF solution reduced with and without TP, are shown in Fig. 7. Each curve has a typical and narrow absorption peak around 275 nm, which corresponds to AgNPs clusters or small AgNPs because of the interband transitions [40, 41]. With the increase of reac-

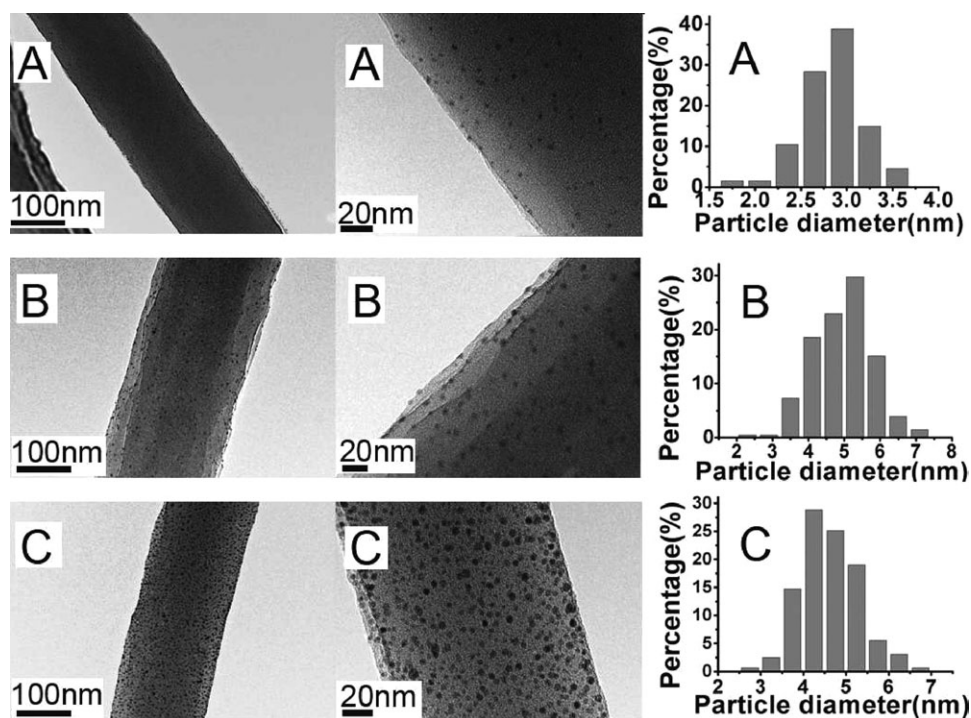


FIG. 5. TEM images of AgNPs/PAN nanofibers: (A) 1.0 wt%; (B) 2.5 wt%; (C) 7.5 wt%, with the corresponding diameter distribution histogram of the immobilized AgNPs.

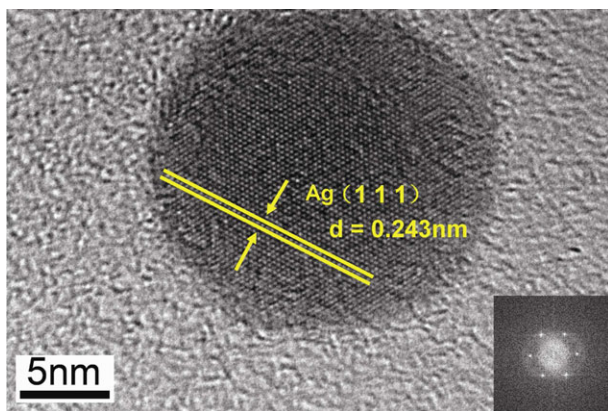


FIG. 6. HRTEM image of the AgNPs. [Color figure can be viewed in the online issue, which is available at wileyonlinelibrary.com.]

tion time from 1, 15, 30, and 45 to 60 min in both Fig. 7A and B, the absorption peaks exhibit redshifts from 277 to 281 nm. From Fig. 7A, it can be seen that the absorption peak around 275 nm become more intense with the increase of reaction time, indicating the reduction activity of DMF for Ag ions. However, with the addition of TP, the absorption of AgNPs appears much stronger even within very short reaction time, which indicates that TP display much higher reductive activity in terms of reducing Ag ions. With the introduction of TP as the reductant, the intensity of the absorption peak of AgNPs increase with reaction time going on, as shown in Fig. 7B. The inset photo portrays the color changes from colorless to yellow gradually. Typically, the intensive surface plasma resonance (SPR) band of AgNPs has a hypsochromic shift from 415 to 386 nm, and it is attributed to the free

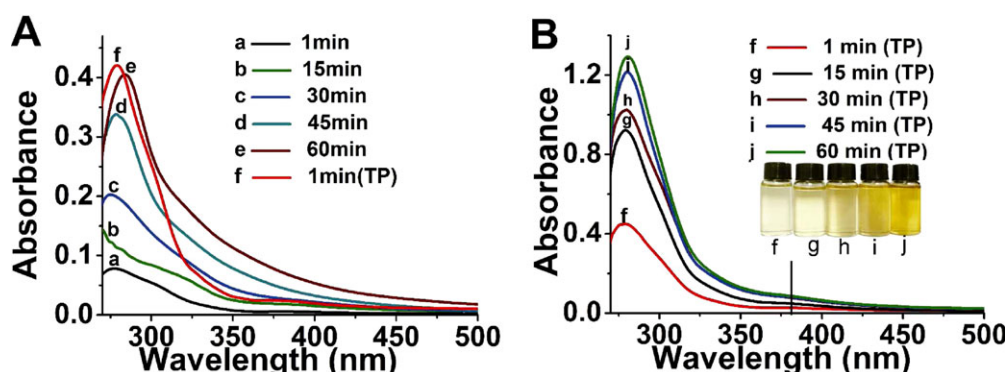


FIG. 7. UV-vis spectra of AgNO_3 (2.5 wt%)/DMF solution in the presence of PAN (12 wt%) with and without TP. [Color figure can be viewed in the online issue, which is available at wileyonlinelibrary.com.]

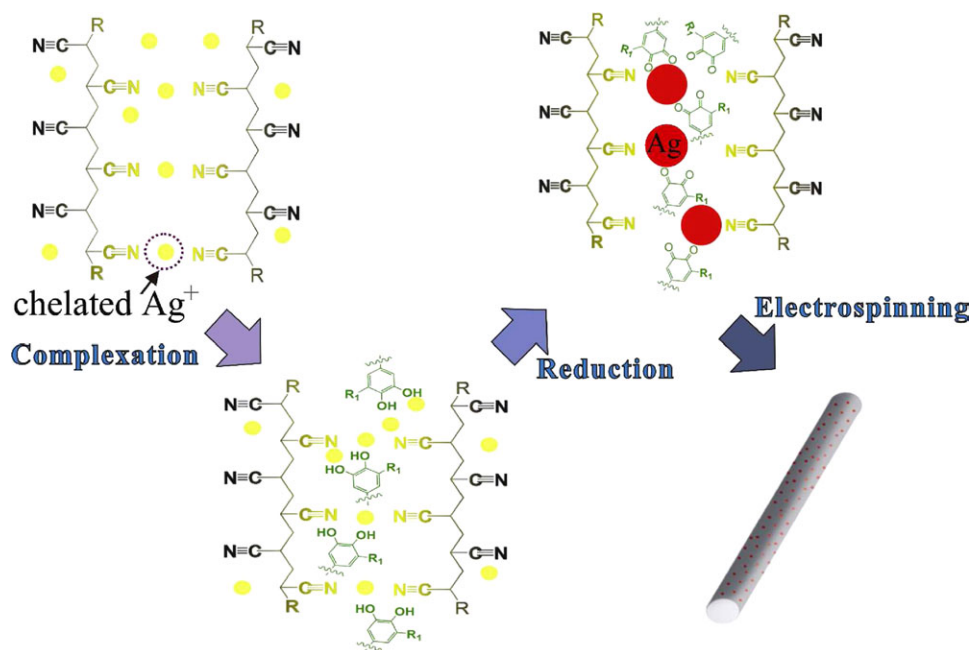


FIG. 8. Fabrication procedure of AgNPs immobilized in PAN nanofibers. [Color figure can be viewed in the online issue, which is available at wileyonlinelibrary.com.]

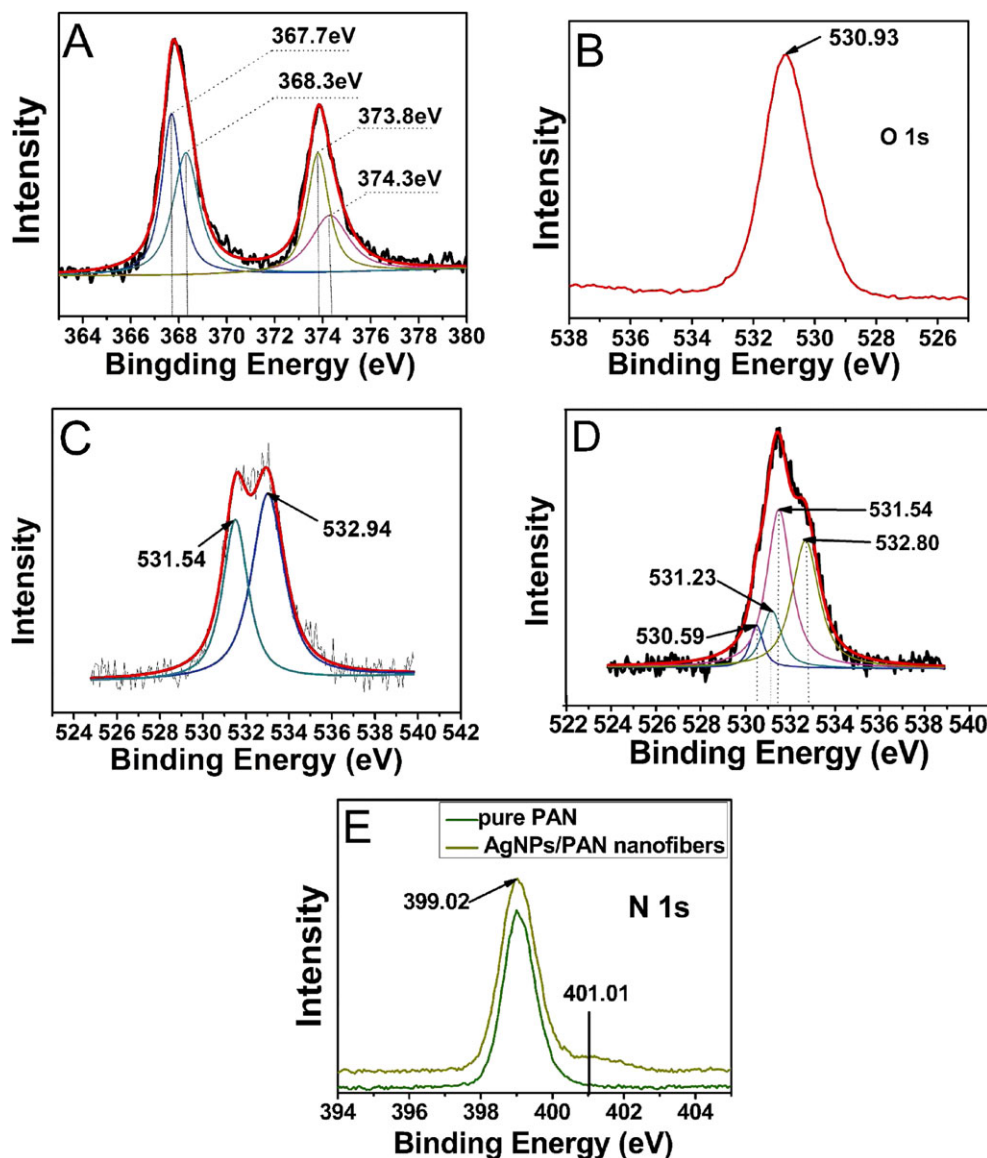


FIG. 9. XPS spectra of Ag, oxygen, and nitrogen atoms. (A) Ag 3d of AgNPs/PAN nanofibers; (B) O 1s of TP; (C) O 1s of the pure PAN; (D) O 1s of AgNPs/PAN nanofibers. (E) N 1s in pure PAN powder and AgNPs/PAN nanofibers. [Color figure can be viewed in the online issue, which is available at wileyonlinelibrary.com.]

conduction electrons on the surface of AgNPs (intraband excitation) [41]. And, the absorption strength appears relatively weak is due to the cyano group which is an effective extinction reagent.

Figure 8 summarized procedures for the typical preparation of AgNPs/PAN nanofibers. It is supposed that chelating effects of Ag ions and Ag nucleus with cyano groups in PAN polymer and phenolic hydroxyls in TP molecules play a crucial role in the synthesis of AgNPs in PAN nanofibers, which will be proved by X-ray photoelectron spectroscopy (XPS) results and discussed later. In the present procedure, the PAN polymer possesses a large amount of cyano groups, which can “anchor” Ag ions in the PAN/DMF solution through chelating effect. The addition of TP, introducing multiple phenolic hydrox-

yls to the reaction system, results in an increasing binding sites for Ag ions through chelating effect between Ag ions and the phenolic hydroxyls of TP molecules. The high density of functional groups (phenolic hydroxyls) in TP will reduce Ag ions to metallic Ag to form Ag nucleus accompanying the oxidation of phenolic hydroxyls to quinones. Then other Ag ions will gradually be reduced by TP and grow on the surface of the formed Ag nucleus. Because of the high viscosity of the solution and the chelating effect between Ag nucleus and phenolic hydroxyls in TP molecules, the Ag nucleus cannot easily collide with each other to coagulate. In addition, due to the chelating effects between cyano groups and Ag ions, the rate of Ag crystal growth is restrained, consequently, causing relatively smaller AgNPs compared with those

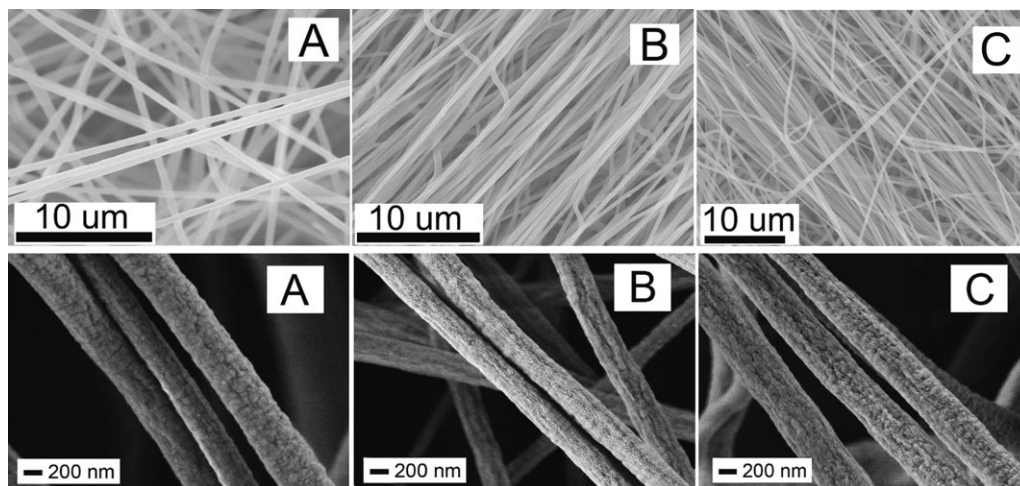


FIG. 10. SEM images of electrospun nanofibers with different concentration of AgNO_3 . (A) 1.0 wt%; (B) 2.5 wt%; (C) 7.5 wt%.

synthesized in DMF solution. At the same time, the formed quinones and free hydroxyls are able to stabilize AgNPs by interaction with the surface Ag atoms through electron donation and acceptance interaction, promoting the formation of spherical AgNPs with smaller sizes [6, 26]. The strong interactions between the reduced AgNPs and the functional groups from aromatic TP and PAN guarantee the good dispersion of the synthesized AgNPs in the electrospun PAN nanofibers. Overall, the PAN polymer act as a chelating agent and the TP serve as both the reductant and the protective agent, which plays a crucial role in preventing the particle growing to obtained smaller AgNPs.

To verify the above procedure and the chelating effects of Ag ions and Ag nucleus with cyano groups and phenolic hydroxyls, XPS characterization on Ag, oxygen, and nitrogen atoms in AgNPs/PAN nanofibers, pure PAN and TP were performed, and the results are shown in Fig. 9. As shown in Fig. 9A, a pair of doublets is observed in the Ag 3d region of AgNPs/PAN nanofibers, which is attributed to the spin-orbital splitting of $3d_{5/2}$ and $3d_{3/2}$ in Ag 3d core level, indicating the two kinds of chemical environments in the synthesized AgNPs. Compared with Ag^0 , the two peaks located at 368.3 and 374.3 eV are assigned to the Ag atoms of AgNPs [42], whereas two other new peaks located at 367.7 and 373.8 eV are observed, it is resulted from the chelating effects of Ag with cyano groups and phenolic hydroxyls [25, 43, 44]. The chelating effects of Ag with cyano groups and phenolic hydroxyls will induce an image dipole on the Ag atoms' surface, consequently a part of positive charges from the surface of AgNPs are donated to the stabilizer, causing a negative shift in Ag 3d core level.

The XPS spectra of oxygen for pure PAN and TP are shown in Fig. 9B and C, respectively. For pure PAN, the peaks at 531.54 and 532.94 eV are assigned to the two

types of oxygen atoms in the methyl acrylate copolymerized with acrylonitrile. There is only one peak at 530.93 eV in O 1s signal from TP, which is mainly attributed to C—OH in phenolichydroxyl. For AgNPs/PAN nanofibers, as shown in Fig. 9D, the O 1s signal peak can be divided into four peaks. Two peaks at 531.54 and 532.80 eV are accorded with that of pure PAN O 1s. As discussed above, after reaction with Ag ions, the O 1s peak corresponding to C—OH in TP is changed, oxidized from phenolic hydroxyls to quinones. Therefore, there is a shift of about 0.3 eV, from 531.23 to 530.93 eV, for the O 1s in TP. In addition, a new peak arises at 530.59 eV, attributing to the quinones from the oxidization of TP. In Fig. 9E, the peak located at 399.02 eV standing for N 1s is from cyano groups of PAN. However, another small peak arises at 401.01 eV, which may be attributed to the chelating interactions between nitrogen and Ag.

As discussed above, due to the chelating interactions of Ag ions with cyano groups and phenolic hydroxyls, PAN polymer and TP both serve as stabilizer during the synthesis of AgNPs in PAN nanofibers, preventing AgNPs from aggregation and obtaining AgNPs with relatively small size and uniform dispersion in PAN nanofibers.

Antibacterial Activity

Figure 10 shows the SEM images of electrospun nanofibers with different mass fraction of AgNO_3 . The majority diameter of the individual fibers obtained from these solutions is about 200–300 nm, which is identical with the values observed by transmission electron microscopy (TEM). Figure 11 shows the typical results of the antibacterial tests for the purpose of a qualitative evaluation. The lengths of the inhibition zones of the AgNPs/PAN nanofiber membranes were measured. It is observed from Fig. 11 that the pure PAN nanofiber membranes show nonbac-

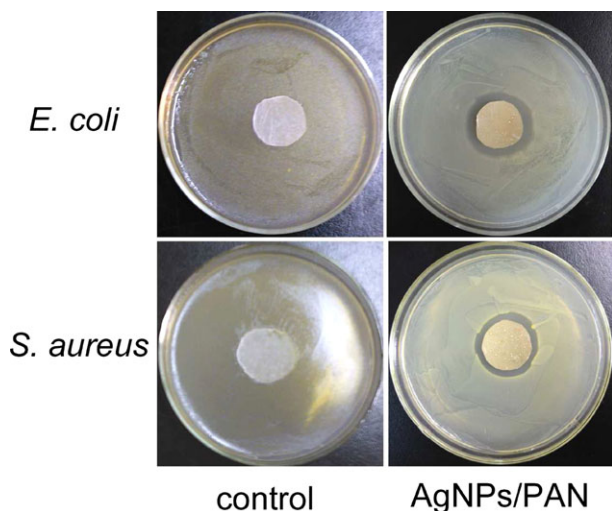


FIG. 11. Pictures of inhibition zone test of AgNPs/PAN nanofiber membranes with 7.5 wt% (based on the weight of PAN powder) concentration of AgNO_3 . [Color figure can be viewed in the online issue, which is available at wileyonlinelibrary.com.]

terial properties against either *E. coli* or *S. aureus* bacteria. However, the antibacterial activity of the AgNPs/PAN nanofiber membranes against both *E. coli* and *S. aureus* bacteria is proved by zones of bacterial growth inhibition around the circular pieces, and the lengths of inhibition zones are both about 5 mm, which indicates the good antibacterial property of AgNPs/PAN nanofiber membranes. In addition, as shown in Fig. 10, magnified images of electrospun AgNPs/PAN nanofibers exhibit relative rough surface, it is supposed that the synthesized AgNPs in PAN nanofibers possess potential and promising applications in antibacterial and catalytic areas.

CONCLUSIONS

AgNPs with uniform dispersion in PAN nanofibers were successfully synthesized using TP as the reductant and the stabilizer. The reducibility of TP was confirmed by UV-vis and FTIR. TEM results suggested that the spherical AgNPs with diameter about 5 nm were immobilized on the surface and in the interior of PAN nanofibers by electrospinning technology. The amount of AgNPs in nanofibers increased gradually with the increasing of AgNO_3 concentration in the original reaction system. The interactions of Ag with PAN and TP were investigated by XPS and the results suggested that PAN polymer and TP both served as stabilizer during the synthesis of AgNPs in PAN nanofibers, because of the chelating interactions of Ag with cyano groups and phenolic hydroxyls. The prepared AgNPs/PAN nanofiber membranes exhibited good antibacterial activity against *E. coli* and *S. aureus*. The synthesized AgNPs in PAN nanofibers exhibit good antibacterial property and may be used for antibacterial and catalytic applications.

REFERENCES

1. R.D. Jean, K.C. Chiu, T.H. Chen, C.H. Chen, and D.M. Liu, *J. Phys. Chem. C.*, **114**, 37 (2010).
2. S. Anandhakumar, S.P. Vijayalakshmi, G. Jagadeesh, and A.M. Raichur, *ACS Appl. Mater. Interfaces*, **3**, 9 (2011).
3. A. Serra, E. Filippo, M. Re, M. Palmisano, V.M. Antisari, A. Buccolieri, and D. Manno, *Nanotechnology*, **20**, 16 (2009).
4. P. Christopher and S. Linic, *J. Am. Chem. Soc.*, **130**, 34 (2008).
5. S.L. Shen, J. Zhuang, Y. Yang, and X. Wang, *Nanoscale*, **3**, 1 (2011).
6. J.L. Guo, H. Wu, X.P. Liao, and B.J. Shi, *Phys. Chem. C.*, **115**, 48 (2011).
7. C.L. Du, Y.M. You, X.J. Zhang, K. Johnson, and Z.X. Shen, *Plasmonics*, **4**, 3 (2009).
8. U.K. Parashar, V. Kumar, T. Bera, P.S. Saxena, G. Nath, S.K. Srivastava, and R. Giri, *Nanotechnology*, **22**, 41 (2011).
9. R. Nirmala, F.A. Sheikh, M.A. Kanjwal, J.H. Lee, S.J. Park, R. Navamathavan, and H.Y.J. Kim, *Nanopart. Res.*, **13**, 5 (2011).
10. E. Falletta, M. Bonini, E. Fratini, A.L. Nostro, G. Pesavento, A. Becheri, P.L. Nostro, P. Canton, and P. Baglioni, *J. Phys. Chem. C.*, **112**, 31 (2008).
11. F.M. Kelly and J.H. Johnston, *ACS Appl. Mater. Interfaces*, **3**, 4 (2011).
12. C. Zhao, G.P. Jin, L.L. Chen, and B. Yu, *Food Chem.*, **129**, 2 (2011).
13. S.H. Jeon, P. Xu, B. Zhang, N.H. Mack, H. Tsai, L.Y. Chiang, and H. Wang, *J. Mater. Chem.*, **21**, 8 (2011).
14. S. Porel, N. Venkatram, D.N. Rao, and T.P. Radhakrishnan, *J. Nanosci. Nanotechnol.*, **7**, 6 (2007).
15. B.S. Fu, M.N. Missaghi, C.M. Downing, M.C. Kung, H.H. Kung, and G.M. Xiao, *Chem. Mater.*, **22**, 7 (2010).
16. P.K. Rastogi, V. Ganesan, and S. Krishnamoorthi, *Mater. Sci. Eng., B*, **177**, 6 (2012).
17. S.K. Srivastava and M. Constanti, *J. Nanopart. Res.*, **14**, 831 (2012).
18. P. Raveendran, J. Fu, and S.L. Wallen, *Green Chem.*, **8**, 1 (2006).
19. T.H. Tsai, S. Thiagarajan, and S.M. Chen, *Electroanalysis*, **22**, 6 (2010).
20. Y.S. Lin, S.S. Wu, and J.K. Lin, *J. Agric. Food Chem.*, **51**, 4 (2003).
21. M. Daglia, A. Papetti, P. Grisoli, and C.J. Aceti, *Agric. Food Chem.*, **55**, 13 (2007).
22. C. Anesini, G.E. Ferraro, and R.J. Filip, *Agric. Food Chem.*, **56**, 19 (2008).
23. Y.N. Chen, Y.D. Lee, H. Vedala, B.L. Allen, and A. Star, *ACS Nano*, **4**, 11 (2010).
24. Y. Wang, Z.X. Shi, and J. Yin, *ACS Appl. Mater. Interfaces*, **3**, 4 (2011).
25. H. Wu, X. Huang, M.M. Gao, X.P. Liao, and B. Shi, *Green Chem.*, **13**, 3 (2011).

26. X. Huang, H. Wu, X.P. Liao, and B. Shi, *Green Chem.*, **12**, 3 (2010).
27. S.Y. Wei, J. Sampathi, Z.H. Guo, N. Anumandla, D. Rutman, A. Kucknoor, L. James, and A. Wang, *Polymer*, **52**, 25 (2011).
28. Y.L. Huang, A. Baji, H.W. Tien, Y.K. Yang, S.Y. Yang, C.C. Ma, H.Y. Liu, Y.W. Mai, and N.H. Wang, *Nanotechnology*, **22**, 47 (2011).
29. E. Formo, M.S. Yavuz, E.P. Lee, L. Lane, and Y.N. Xia, *J. Mater. Chem.*, **19**, 23 (2009).
30. G.M. Kim, A. Wutzler, H.J. Radusch, G.H. Michler, P. Simon, R.A. Sperling, and W.J. Parak, *Chem. Mater.*, **17**, 20 (2005).
31. P.O. Rujitanaroj, N. Pimpha, and P. Supaphol, *Polymer*, **49**, 21 (2008).
32. X. Fang, H. Ma, S. Xiao, M.W. Shen, R. Guo, X.Y. Cao, and X.Y. Shi, *J. Mater. Chem.*, **21**, 12 (2011).
33. X.G. Li, R. Liu, and M.R. Huang, *Chem. Mater.*, **17**, 22 (2005).
34. X.G. Li, X.L. Ma, J. Sun, and M.R. Huang, *Langmuir*, **25**, 3 (2009).
35. X.G. Li, H. Feng, and M.R. Huang, *Chem. Eur. J.*, **16**, 33 (2010).
36. X.G. Li, M.R. Huang, and S.X. Li, *Acta Mater.*, **52**, 18 (2004).
37. M.C. Moulton, L.K. Braydich-Stolle, M.N. Nadagouda, S. Kunzelman, S.M. Hussain, and R.S. Varma, *Nanoscale*, **43**, 6 (2010).
38. I. Pastoriza-Santos and L.M. Liz-Marzan, *Adv. Funct. Mater.*, **19**, 5 (2009).
39. H. Zhu, M.L. Du, M.L. Zou, C.S. Xu, N. Li, and YaQin Fu, *J. Mater. Chem.*, **22**, 18 (2012).
40. S. Pocovi-Martinez, M. Parreno-Romero, S. Agouram, and J. Perez-Prieto, *Langmuir*, **27**, 9 (2011).
41. K. Akhbari and A. Morsali, *Crystal Growth Design.*, **7**, 10 (2007).
42. J. Zhang, Y. Yuan, X.W. Xu, X.L. Wang, and X.R. Yang, *ACS Appl. Mater. Interfaces*, **3**, 10 (2011).
43. L.H. Jia, S. Zhang, F.N. Gu, Y. Ping, X.F. Guo, Z.Y. Zhong, and F.B. Su, *Micropor Mesopor Mat.*, **149**, 1 (2012).
44. X.Y. Yang, A. Wolcott, G. Wang, A. Sobo, R.C. Fitzmorris, F. Qian, J.Z. Zhang, and Y. Li, *Nano Lett.*, **9**, 6 (2009).

SYNTHESIS AND CHARACTERIZATION OF AU NANOPARTICLES/REDUCED GRAPHENE OXIDE NANOCOMPOSITE: A FACILE AND ECO-FRIENDLY APPROACH

MEILING ZOU, HAN ZHU, PAN WANG and SHIYONG BAO

*Faculty of Materials and Textiles
Zhejiang Sci-Tech University
310018 HangZhou, P. R. China*

MINGLIANG DU* and MING ZHANG

*Key Laboratory of Advanced Textile Materials and Manufacturing Technology
Zhejiang Sci-Tech University
Ministry of Education
Hangzhou 310018, P. R. China
du@zstu.edu.cn

Received 16 October 2013

Accepted 27 November 2013

Published 23 January 2014

In this paper, epigallocatechin gallate (EGCG) was used as a green reductant both for the fabrication of soluble reduced graphene oxide (rGO) and the synthesis of Au nanoparticles/rGO nanocomposite. Fourier transform infrared (FTIR) spectra confirmed the efficient removal of the oxygen-containing groups in graphene oxide (GO) through the reduction act of EGCG. Au nanoparticles (AuNPs) were anchored onto the rGO sheets by heating the mixed solution of rGO and chloroauric acid at 65°C using EGCG as reductant. Transmission electron microscopy (TEM), atomic force microscope (AFM) and X-ray photoelectron spectroscopy (XPS) were employed to characterize the resulting nanocomposite. Due to the chelating effect of polyhydroxy EGCG, AuNPs with diameters of ~20–50 nm were stably decorated onto both sides of the rGO sheets. Because this reduction method avoids the use of toxic reagents, AuNPs/rGO nanocomposite would be eco-friendly, and it might be useful not only for electronic devices but also for biocompatible materials in the future applications.

Keywords: Epigallocatechin gallate; soluble reduced graphene oxide; Au nanoparticles/reduced graphene oxide.

1. Introduction

Graphene sheets are of great significance in fundamental and applied science for their exceptional electronic, mechanical, plasma processes and thermal properties,^{1–6} leading to the development of

graphene-based strain sensors,⁷ molecular resolution sensor,⁸ electromechanical devices^{9–11} and surface enhanced Raman scattering substrates.¹² Currently, there is a great interest in functioning the graphene by chemical modification or doping nanosized noble

metals to enhance its electrical, sensing and interfacial properties.^{13–16} Decorating reduced graphene oxide (rGO) with Au nanoparticles (AuNPs) is a promising area for various applications, ranging from heterogeneous catalyst,¹⁷ electrochemical sensor¹⁸ to biochemical sensing application.¹⁹

Various methods have been reported for the synthesis of AuNPs/rGO nanocomposite, including solution chemical approach,^{20–22} electrochemical deposition of AuNPs onto rGO sheets,²³ microwave irradiation,²⁴ ultrasonication,²⁵ etc.

Chemical reduction of graphene oxide (GO) is considered to be one of the most eco-accessible and easy-controllable methods for preparing rGO on a large scale. The chemical reduction of GO typically involves highly toxic reducing agents which are harmful to human health and environment, and complicated surface modification is often needed to avoid aggregation of the rGO during reduction process.^{26,27} Typically, solution chemistry approach, toxic reducing agent NaBH_4 and hydrazine hydrate are always widely used for the reduction of HAuCl_4 and GO sheets.^{28,29} What is more, after reducing approach, rGO could not be dissolved in water again because of the removal of hydrophilic groups. To overcome these disadvantages, it is quite significant to find an efficient, green, eco-friendly way for the preparation of water-soluble AuNPs/rGO nanocomposite.

Epigallocatechin gallate (EGCG) is an environment-friendly reducing agent used in redox reaction recently, and it has been used as a green reducing agent for the synthesis of many noble nanoparticles in our previous research.^{30,31} In this work, rGO was considered as a support for the deposition of AuNPs. We presented the synthesis and characterization of AuNPs/rGO nanocomposite by using a simple and green synthesis method, based on the use of EGCG as a multiple role-play reagent, reductant and stabilizer, for the preparation of rGO and AuNPs. Uniform and extensive cover of AuNPs on rGO sheets can be obtained.

2. Experimental Section

2.1. Materials

Graphite powder (99.9995%) was obtained from Alfa-aesar Co., Ltd. Concentrated sulfuric acid (H_2SO_4 , 95–98%), potassium permanganate (KMnO_4), hydrogen peroxide (H_2O_2 , 30 wt.%), concentrated

hydrochloric acid (HCl , 0.1 mol/L) and Chloroauric acid ($\text{HAuCl}_4 \cdot 4\text{H}_2\text{O}$, 99.9%) were purchased from Aladdin Chemistry Co., Ltd. EGCG was purchased from Xuancheng BaiCao Plant Industry and Trade Company and used as received without further purification. Deionized water was used for all solution preparations.

2.2. Methods

2.2.1. Synthesis of EGCG–rGO

GO nanosheets was synthesized based on Hummers method.³² Hu's approach for the synthesis of GO is adopted through oxidizing the graphite powder in a mixture of concentrated sulfuric acid and KMnO_4 .²⁶ For the preparation of rGO, in a typical procedure, GO aqueous solution (1 mg/mL) was prepared by sonication of 150 mg GO nanosheets in deionized water, and the GO dispersion was brownish yellow [see Fig. 1(a)], then 300 mg EGCG (200 wt.% relative to GO) was added. The mixture was maintained at 80°C under vigorous stirring for 6 h. After being cooled to room temperature, the resulting mixture was centrifuged at 8000 rpm for 20 min and washed with ultrapure water five times to remove the residual EGCG. Finally, the product was dispersed in 150 mL ultrapure water and kept at room temperature.

2.2.2. Fabrication of rGO–AuNPs

Typically, 5 mL HAuCl_4 (10 mmol/L) was dropped tardily to 50 mL rGO solution and kept stirring for 30 min, and then the mixture was heated to 65°C. rGO — AuNPs was prepared by adding 5 mL EGCG (0.5 mg/mL) solution to the mixture

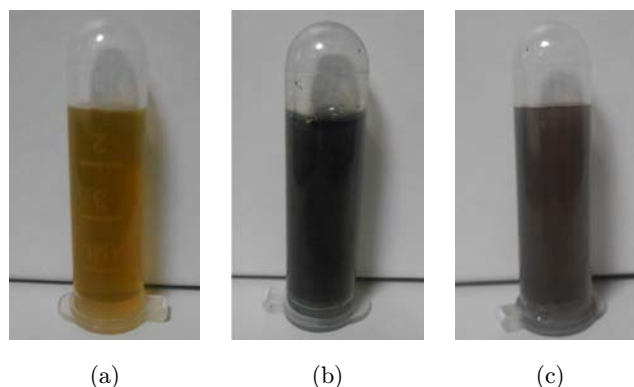


Fig. 1. Typical pictures of GO (a), brownish yellow, rGO (b), black and AuNPs/rGO (c), atropurpureus (color online).

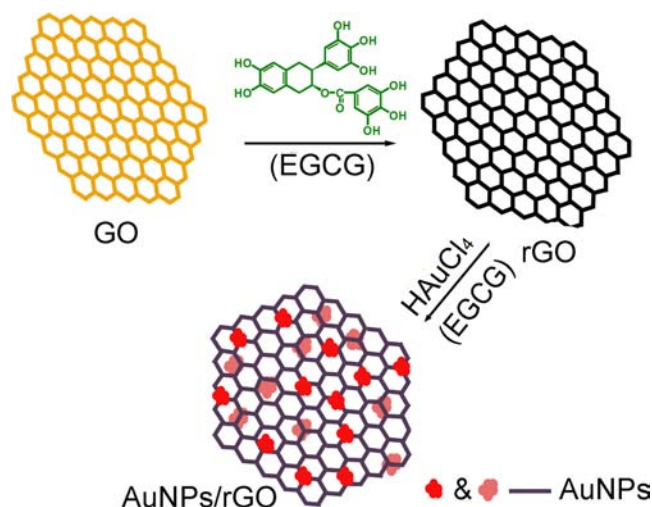


Fig. 2. Fabrication procedure of AuNPs/rGO (color online).

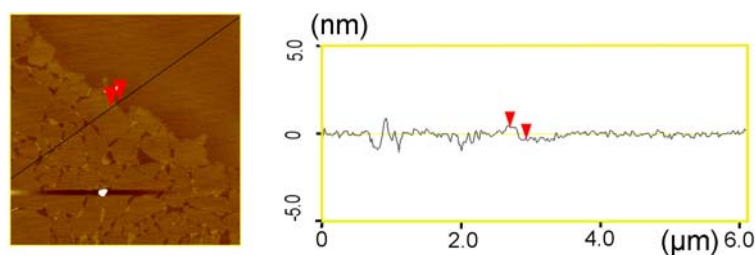
followed by vigorous stirring. The addition of EGCG solution was controlled drop-wise and the color of the mixture changed from black to atropurpureus [see Figs. 1(b) and 1(c)]. After 2 h, the mixture was centrifuged at 8000 rpm for 20 min and washed with ultrapure water for five times. Ultimately, the product was dispersed in 50 mL ultrapure water at room temperature. The whole fabrication procedure of AuNPs/rGO is presented in Fig. 2.

2.3. Characterization

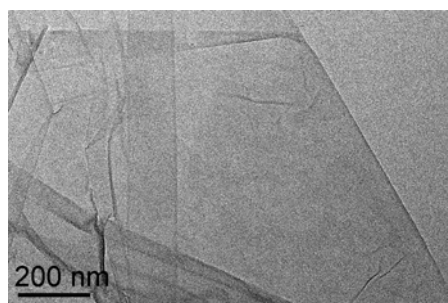
Fourier transform infrared (FTIR) spectra were recorded on a Nicolet 5700 spectrophotometer. Transmission electron microscopy (TEM) characterization was performed on a JEOL JEM-2100 electron microscope operating at 200 kV. Powder X-ray diffraction (XRD) patterns were collected using a SIEMENS Diffractometer D5000 X-ray diffractometer using a $\text{CuK}\alpha$ radiation source at 35 kV, with a scan rate of 0.02 s^{-1} in the 2θ range of $3\text{--}90^\circ$. Atomic force microscopy (AFM) images were obtained using a digital Nanoscope IIIa Atomic Force Microscope in tapping mode. X-ray photoelectron spectra of AuNPs/rGO was recorded using an X-ray photoelectron spectrometer (Kratos Axis Ultra DLD) with an aluminum (mono) $\text{K}\alpha$ source.

3. Results and Discussion

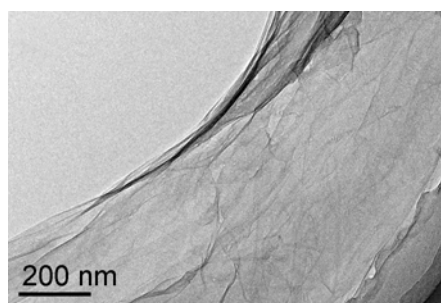
The AFM image in Fig. 3(a) shows the morphology of as-prepared GO, where the cross-sectional view indicates that the average thickness of GO sheets is about 1 nm, suggesting that the GO sheets are fully exfoliated. Figures 3(b) and 3(c) shows the typical TEM image of the prepared GO and rGO, respectively. It can be seen that, after reduced by EGCG, the morphology of the rGO does not have obvious



(a)



(b)



(c)

Fig. 3. AFM image of GO (a) and TEM images of GO (b) and rGO (c) (color online).

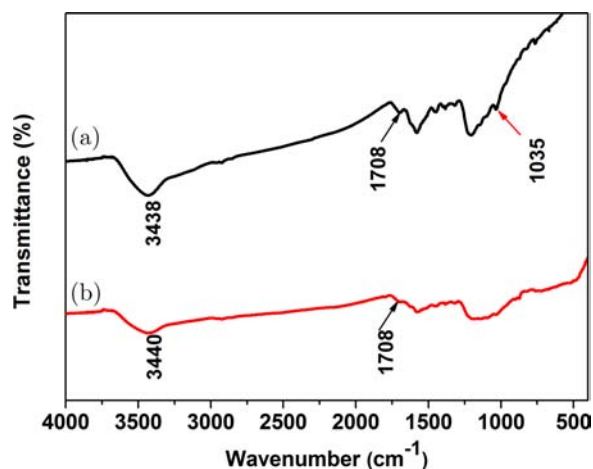


Fig. 4. FTIR spectra of GO (a) and rGO (b) (color online).

changes. And the rGO remains as an intact piece of sheet.

FTIR technique was utilized to characterize the chemical changes of GO after reduction process. As shown in Fig. 4, the peaks from the range of 900 cm^{-1} to 1500 cm^{-1} can be ascribed to the functional groups (epoxy groups and carboxyl groups) of GO.³³ Curve a and b show an evident broad absorption peak at 3438 cm^{-1} and 3440 cm^{-1} respectively, which are assigned to the O–H stretching vibration of hydroxyls. After the reduction, the

peaks at 1708 cm^{-1} assigned to carboxyl groups and 1055 cm^{-1} assigned to epoxy groups are decreased significantly, clearly indicating the removal of oxygen containing groups of GO. In addition, the aqueous GO is light brown, after reduction, it turned to black (as shown in Fig. 1), suggesting the successful reduction of GO.

Besides, according to some reductants that have the common characteristics to EGCG, such as tannic acid and tea polyphenols that have been reported in the literature,^{34,35} we proposed a procedure for the preparation of rGO. However, most of the epoxide groups are believed to be removed more easily than hydroxyl and carboxyl during the reduction, therefore, the mechanism of epoxy groups on GO that converted to carboxyl groups may proceed via a two-step SN_2 nucleophilic reaction and elimination with the release of H_2O ,³⁷ which is demonstrated in Fig. 5. As is well known, that GO can be easily dissolved in water solution is mainly caused by the oxygen-containing groups. Usually, the removal of surface oxygen-containing groups in GO will lead to irreversible aggregation, therefore, a stabilizer is always needed to prevent or reduce the aggregation. According to previous literatures,³⁵ the interaction between stabilizer and rGO were considered to be π - π and van der Waals interactions. While the

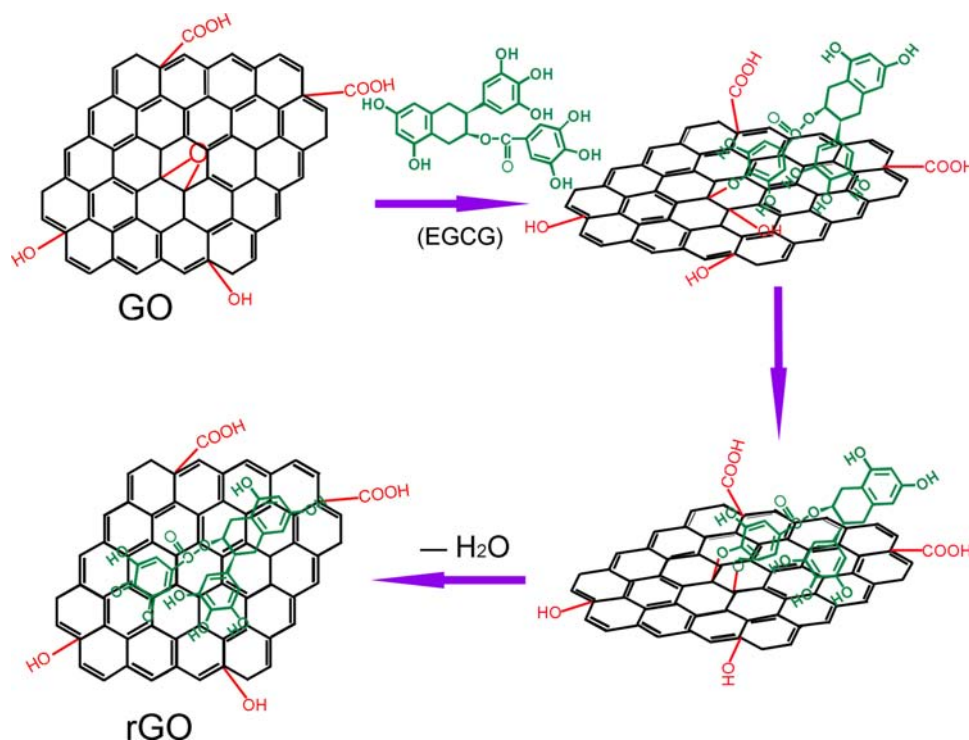


Fig. 5. Proposed reaction pathway for the chemical reduction of GO by EGCG (color online).

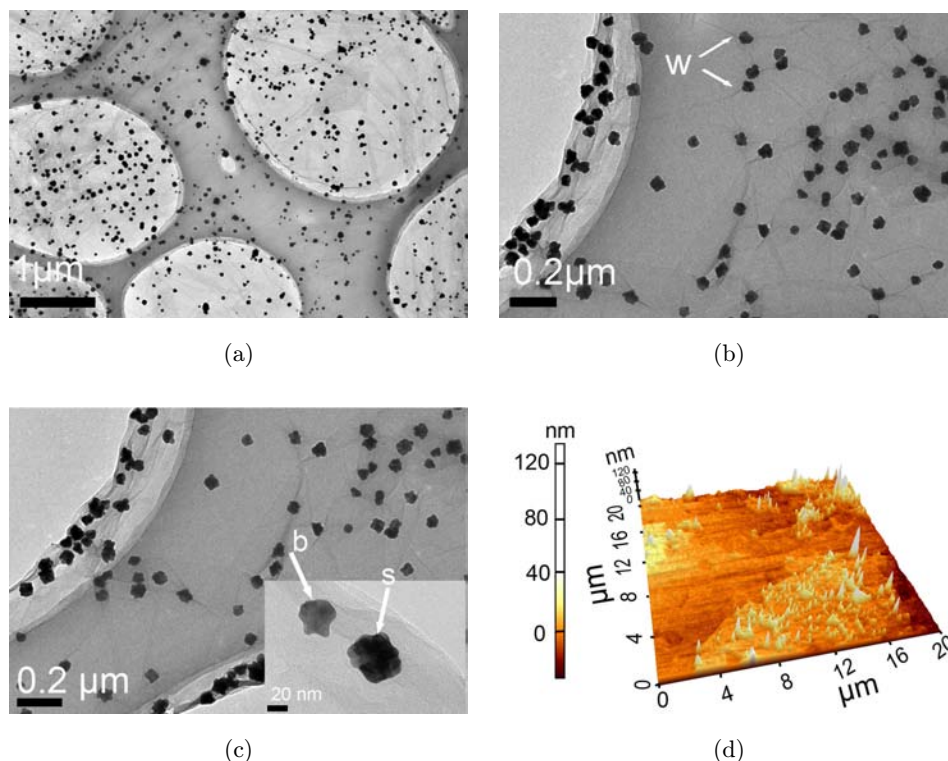


Fig. 6. TEM images of AuNPs/rGO nanocomposite under various magnifications (a), (b) and (c); AFM image of AuNPs/rGO (d) (color online).

interaction between oxidized EGCG and rGO is believed to mainly be π - π interaction. Finally, due to the strong interactions between rGO and O-EGCG that avoids the aggregates of rGO sheets, the colloidal solution exhibits good stability and solubility in water without any addition of surfactant.

Figures 6(a)–6(c) display the TEM images of AuNPs/rGO nanocomposite under various magnifications. It is observed from Fig. 6(a) that there is a homogeneous and dense coverage of AuNPs on the surface of rGO sheets and the diameters of AuNPs vary from 20 nm to 50 nm. As shown in Figs. 6(b) and 6(c), the AuNPs/rGO displays the characteristic of wrinkled morphology (darker lines, labeled as “W”). On one hand, the wrinkles are caused by the surface chemical property of rGO itself, on the other hand, the loading of AuNPs can also lead rGO to wrinkle, accordingly, flower-like AuNPs are apt to form around the wrinkles. Besides, it is believed that Au ions can nucleate on both sides of the rGO sheets when exposed to the solvent, therefore, it can be seen from the inset of Fig. 6(c) that the AuNPs appearing darker (labeled as “s”) were probably attached to the surface of rGO and the others labeled as “b” were on the back of the sheets.

Because of the shielding effect of rGO sheets, the AuNPs that on the back of the sheets were given lesser average surface-electron density, resulting in lighter appearance than the surface AuNPs. Figure 6(d) shows the AFM image of AuNPs/rGO in three dimensions, and the small white acuminations represent AuNPs. As a result, rGO supported nanocomposite is prepared successfully with AuNPs anchored onto both sides of the sheets.

To further characterize the deposition of the AuNPs on the surface of rGO, the XRD patterns of the GO, rGO and AuNPs/rGO were collected as shown in Fig. 7. The as-prepared GO shows a characterized peak at $2\theta = 9.6^\circ$, corresponding to an interlayer d-spacing of 0.92 nm. Compared to GO, the rGO shows a peak centered at 4.9° , indicating that the interlayer distance increases to 2.1 nm. The expanded interlayer distance can result from the attachment of EGCG molecules among the GO layers. Besides, another broad peak is located at 24.5° , implying a smaller interlayer distance of 0.35 nm, which can result from the restack of graphene layers. The AuNPs/rGO exhibits the typical peaks of AuNPs at 2θ value of 38.2° , 44.5° , 64.6° , 77.8° , 82.0° , matching to Au (111), Au (200),

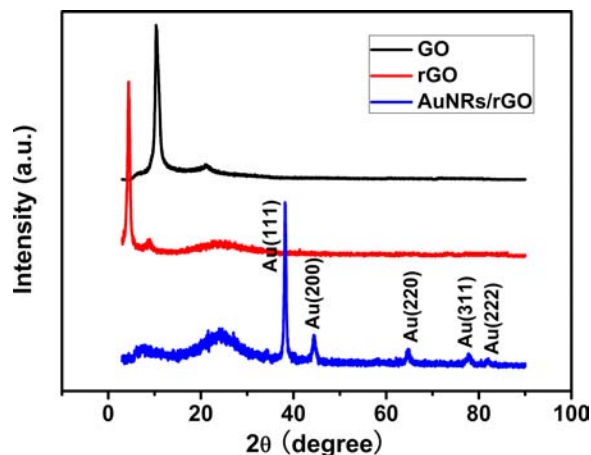


Fig. 7. Powder XRD patterns of GO, rGO and AuNPs/rGO (color online).

Au (220), Au (311) and Au (222) crystal face, respectively, which suggests the formation of face-centered cubic AuNPs.

The binding of rGO with AuNPs was also confirmed by UV-Vis spectroscopy (see Fig. 8). The optical absorption of GO and rGO in the visible light region cannot be observed. The AuNPs/rGO nanocomposite shows an obvious peak at 560 nm, which can result from the surface plasmon absorption of AuNPs, compared with that of rGO, which further indicates that the AuNPs are loaded on the surface of GO sheets.

The chemical state of AuNPs in the nanocomposite was identified by XPS measurement and the resultant Au 4f spectrum is shown in Fig. 9. As observed in Fig. 9, the intense doublets that emerged at 84.42 eV and 88.02 eV correspond well

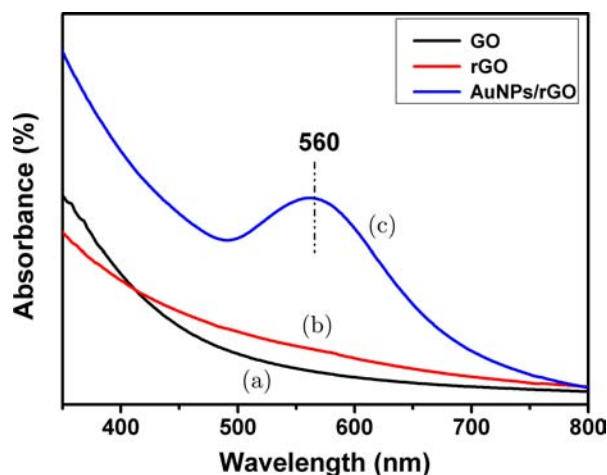


Fig. 8. UV-Vis spectra of GO (a), rGO (b) and AuNPs/rGO (c) (color online).

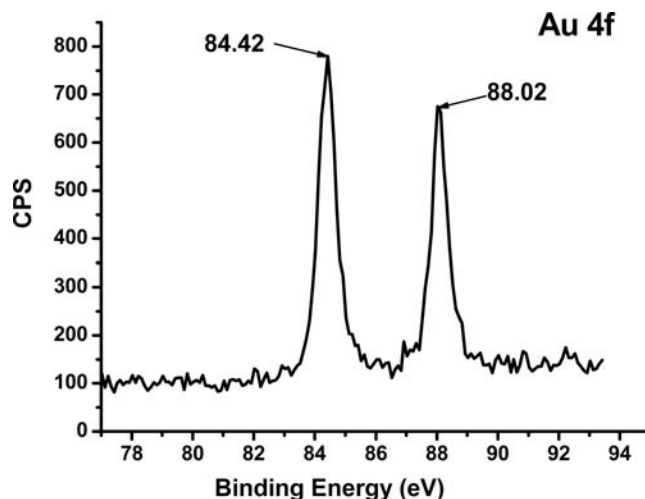


Fig. 9. XPS survey scans of Au 4f region of AuNPs/rGO.

with Au 4f₇ and Au 4f₅ binding energies, respectively. Compared with zero valent Au⁰ (84.0 eV and 87.7 eV), there is a shift of about 0.42 eV and 0.95 eV, respectively. Above changes of the binding energy indicate the different chemical environment between the AuNPs in the composite and Au⁰.³⁶ The relatively higher binding energy can be attributed to the interaction of AuNPs with EGCG molecules. The surface Au atoms of AuNPs exposed to the surrounding stabilizer with passive charges would donate electron to stabilizer, causing a positive shift in Au 4f core level. As discussed above, due to the chelating interactions of Au ions with EGCG during the synthesis, EGCG serves as a reducer as well as a stabilizer. All the above observations suggest the successful decoration of AuNPs onto rGO sheets. Most important, due to the synergistic effect of polyhydroxy EGCG, AuNPs/rGO can be homodispersed in aqueous solution stably.

4. Conclusions

In this work, the synthesis method of AuNPs/rGO nanocomposite was reported and a systematical characterization of the nanocomposite material was presented. The method is simple, green, low cost, which can be easily realized under mild conditions. Above all, the water soluble rGO was prepared via a chemical reduction process, the strong interactions between rGO and the oxidized EGCG enabled the good dispersion of rGO in aqueous solution. Based on the prepared rGO, AuNPs with the diameter of ~20–50 nm were decorated on both sides of the rGO sheets, as a result, the AuNPs/rGO nanocomposite

material that can be well dispersed in water was obtained. Therefore, this nanocomposite prepared via the green, facile strategy reported here would have many potential applications, such as electronic devices and biocompatible materials.

Acknowledgments

We acknowledge the support of the project of the National Natural Science Foundation of China (NSFC) (51243001, 51373154), the 521 Talent Project of Zhejiang Sci-Tech University.

References

1. A. K. Geim and K. S. Novoselov, *Nat. Mater.* **6**, 183 (2007).
2. S. Ghosh, I. Calizo, D. Teweldebrhan *et al.*, *Appl. Phys. Lett.* **92**, 151911 (2008).
3. S. H. Hur and J. Park, *Asia-Pac. J. Chem. Eng.* **8**, 218 (2013).
4. P. Blake, P. D. Brimicombe, R. R. Nair *et al.*, *Nano Lett.* **8**, 1704 (2008).
5. C. W. Twombly, J. S. Evans, I. I. Smalyukh *et al.*, *Opt. Express* **21**, 1324 (2013).
6. Z. Bo, Y. Yang, J. H. Chen *et al.*, *Nanoscale* **5**, 5180 (2013).
7. Y. Wang, R. Yang, Z. W. Shi *et al.*, *Acs Nano* **5**, 3645 (2011).
8. O. K. Kwon, K. S. Kim, J. Park *et al.*, *Comput. Mater. Sci.* **67**, 329 (2013).
9. Y. U. Jung, S. Oh, S. Choa *et al.*, *Curr. Appl. Phys.* **13**, 1331 (2013).
10. J. J. Liang, L. Huang, N. Li *et al.*, *Acs Nano* **6**, 4508 (2012).
11. N. Al-Aqtash, H. Li, L. Wang *et al.*, *Carbon* **51**, 102 (2013).
12. S. J. He, K. K. Liu, S. Su *et al.*, *Anal. Chem.* **84**, 4622 (2012).
13. T. Wu, L. Zhang, J. P. Gao *et al.*, *J. Mater. Chem. A* **1**, 7384 (2013).
14. K. Jasuja, J. Linn, S. Melton *et al.*, *Phys. Chem. Lett.* **1**, 1853 (2010).
15. A. Guimont, E. Beyou, P. Alcouffe *et al.*, *Polymer* **54**, 4830 (2013).
16. V. J. Surya, K. Iyakutti, H. Mizuseki *et al.*, *Comput. Mater. Sci.* **65**, 144 (2012).
17. H. J. Yin, H. J. Tang, D. Wang *et al.*, *Acs Nano* **6**, 8288 (2012).
18. Y. Q. Hu, Z. H. Xue, H. X. He *et al.*, *Biosens. Bioelectron.* **47**, 45 (2013).
19. L. Li, H. M. Lu and L. Deng, *Talanta* **113**, 1 (2013).
20. J. Gao, F. Liu, Y. L. Liu *et al.*, *Chem. Mater.* **22**, 2213 (2010).
21. C. Z. Zhu, S. J. Guo, Y. X. Fang *et al.*, *Acs Nano* **4**, 2429 (2010).
22. D. R. Dreyer, R. S. Ruoff and C. W. Bielawski, *Angew. Chem. Int. Ed.* **49**, 9336 (2010).
23. C. P. Fu, Y. F. Kuang, Z. Y. Huang *et al.*, *Chem. Phys. Lett.* **499**, 250 (2010).
24. K. Jasuja, J. Linn, S. Melton *et al.*, *J. Phys. Chem. Lett.* **1**, 1853 (2010).
25. N. Y. Cheng, J. Q. Tian, Q. Liu *et al.*, *ACS Appl. Mater. Interfaces* **5**, 6815 (2013).
26. C. F. Hu, J. H. Rong, J. H. Cui *et al.*, *Carbon* **51**, 255 (2013).
27. Y. J. Zhang, W. B. Hu, B. Li *et al.*, *Nanotechnology* **22**, 345601 (2011).
28. X. Y. Qi, K. Pu, X. Z. Zhou *et al.*, *Small* **6**, 663 (2010).
29. Y. C. Si and E. T. Samulski, *Nano Lett.* **8**, 1679 (2008).
30. H. Zhu, M. L. Du, M. Zhang *et al.*, *Sens. Actuators B* **185**, 608 (2013).
31. P. Wang, H. Zhu, S. Y. Bao *et al.*, *J. Phys. D: Appl. Phys.* **46**, 345303 (2013).
32. W. S. Hummers and R. E. Offeman, *J. Am. Chem. Soc.* **80**, 1339 (1958).
33. X. Liu, X. Y. Wang, P. Y. He *et al.*, *J. Solid State Electrochem.* **16**, 3929 (2012).
34. Y. Wang, Z. X. Shi and J. Yin, *ACS Appl. Mater. Interfaces* **3**, 1127 (2011).
35. Y. D. Lei, Z. H. Tang, R. J. Liao *et al.*, *Green Chem.* **13**, 1655 (2011).
36. H. Zhu, M. L. Du, M. L. Zou *et al.*, *J. Mater. Chem.* **22**, 9301 (2012).
37. R. J. Liao, Z. H. Tang, Y. D. Lei *et al.*, *J. Phys. Chem. C* **115**, 20740 (2011).



Synthesis and deposition of ultrafine noble metallic nanoparticles on amino-functionalized halloysite nanotubes and their catalytic application



Meiling Zou^a, Mingliang Du^{b,*}, Ming Zhang^b, Tingting Yang^a, Han Zhu^a, Pan Wang^a, Shiyong Bao^a

^a Department of Materials Engineering, College of Materials and Textile, Zhejiang Sci-Tech University, Hangzhou 310018, PR China

^b Key Laboratory of Advanced Textile Materials and Manufacturing Technology, Zhejiang Sci-Tech University, Ministry of Education, Hangzhou 310018, PR China

ARTICLE INFO

Article history:

Received 14 June 2014

Received in revised form 13 October 2014

Accepted 17 October 2014

Available online 18 October 2014

Keywords:

A. Nanostructures

D. Catalytic properties

ABSTRACT

Using epigallocatechin gallate (EGCG) as both a green reductant and stabilizer, ultrafine noble metal nanoparticles (Rh NPs, Pt NPs, Pd NPs) are synthesized and in situ deposited within amino-functionalized halloysite nanotubes (N-HNTs) via a facile and eco-friendly process. These noble metal nanoparticles with extremely small size (~ 1.5 nm) are dispersed densely and uniformly on both outside and inside surface of N-HNTs. Rh deposited N-HNTs (Rh–N-HNTs) was investigated as a model composite catalyst and applied in the catalytic reduction of 4-nitrophenol (4-NP), and it exhibited amazing activity and recycle stability. Due to the green and flexibility of the technique described here, noble metal nanoparticles, metal nanoalloy, or metal oxide nanoparticles with ultrafine particle size also can be loaded densely and uniformly on the surface of diverse amino-functionalized nanotubes, nanofibers or nanoporous, and these composites may be applicable in catalysis, photocatalysis, and electrochemical areas.

© 2014 Elsevier Ltd. All rights reserved.

1. Introduction

With the fast development of nanoscience and nanotechnology, much attention has been paid to the synthesis of noble metal nanoparticles (NPs). Because of their remarkable chemical and physical properties compared to bulk metals, applications using noble metal NPs in a wide range of areas, including electronic and optical devices [1], energy generation and storage [2], chemical sensors [3–5], catalysis [6–10], hybrid material [11], and even biological materials [12–14], have all been explored. It has been realized that noble metal NPs show characteristic size-dependent properties (e.g., catalytic, electronic, optical, and thermodynamic property) with significant size-effect at 1–10 nm diameters [15–17]. For example, the position of plasmon band of metallic NPs and their bandwidth reflected from UV–vis spectra are greatly depended on the size of NPs.

From the view point of practical applications, it is of great value to find a facile method for the preparation of uniform small size noble metal NPs with high stability. There are already many methods for the preparation of noble metal NPs, but most are complex, time-consuming, or strict in synthetic conditions. However, the aggregation of small-sized noble metal NPs is always inevitable in catalytic reactions due to the high surface energy of the NPs, thus resulting in remarkable reduction of the catalytic activities and impossible reusability. To overcome these disadvantages, noble metal NPs are immobilized in/onto cheap solid supports, such as organic polymers [18], metal oxides [19,20], composites [21], various inorganic supports [22–24], and so on, aiming to prevent NPs from aggregation and enhance their stability. It has been proved as an effective way to combine the unique electronic and mechanical properties of the supports, including nanotubes, nanofibers, core-shell NPs, hollow nanospheres, etc., with the size- and shape-dependent physicochemical properties of metal NPs [25–27]. And these hybrid nanomaterials have presented promising application in catalysis, sensor, and surface enhanced Raman spectroscopy (SERS) [28].

Among those nanostructured supports, nanotube is one of the most interesting nanostructures, which is regarded as a potential

* Corresponding author. Tel.: +86 571 86843255; fax: +86 571 86843255.

E-mail addresses: du@zstu.edu.cn, psduml@gmail.com, psduml@163.com (M. Du).

candidate for catalyst supports due to its high surface area to volume ration. halloysite nanotubes (HNTs) are a promising catalyst support because of the inherent hollow nanotubular structure and different outside and inside chemistry essence, with about 15 nm lumen, 50 nm external diameter, and 1000–2000 nm in length. However, since HNTs are relatively chemically inert, activating their surface is an essential prerequisite for depositing NPs. Chemical functionalization is a convenient and widely used way to modify HNTs, as well as to improve the dispersibility [29–31].

Inspired by above considerations, in the present work we developed a facile functionalization of HNTs by *N*- β -aminoethyl- γ -aminopropyl trimethoxysilane (AEAPTMS), aimed at the preparation of chemically modified nanotube surface capable of binding noble metal NPs. The amino groups functionalized HNTs (N-HNTs) were then purified and used as catalyst carriers. An additional goal was to avoid the use of environmental intolerance reductant like NaBH_4 , dimethylhydrazine, hydrazine, etc., thus, EGCG was accepted as a green reductant to reduce the noble metallic ions. Noble metal NPs (Rh NPs, Pt NPs, Pd NPs) with ultrafine size were successfully immobilized on the outside and inside surface of N-HNTs densely and uniformly via an in situ reduction approach under a mild condition. In general, the decrease of particle size can lead to an increase of the catalytic activity because of the large surface-to-volume of smaller NPs, finally, the catalytic activities and reusability of N-HNTs deposited with noble metal NPs were evaluated by the catalytic reduction of 4-nitrophenol (4-NP).

2. Experimental

2.1. Materials

Chloroplatinic acid ($\text{H}_2\text{PtCl}_6 \cdot \text{H}_2\text{O}$), palladium chloride (PdCl_2), rhodium chloride (RhCl_3) were all obtained from Aladdin chemistry Co., Ltd. Epigallocatechin gallate (EGCG) was purchased from Xuancheng Baicao Plant Industry and Trade Company and used as received without further purification. AEAPTMS was acquired from Sinopharm Chemical Reagent Co., Ltd., China. Aqueous solutions were prepared using Milli-Q water of 18 M Ω , and other reagents were of analytical grade and used as supplied.

2.2. Synthesis of amino-functionalized HNTs (N-HNTs)

N-HNTs were prepared in a facile approach using water and ethanol as solvents, AEAPTMS as functionalization agent according to the synthesis procedure in our previous work [32]. In a typical procedure, HNTs were firstly purified via washing/centrifugation process and dried at 80 °C in a vacuum oven for a whole night. 95 g ethanol water solution (95%) was adjusted to pH 5 with acetic acid, and then 5 g AEAPTMS was dissolved in above mixture and 15 min was required for hydrolysis of AEAPTMS under vigorously stirring. Next, 10 g HNTs were added and the whole mixture was kept refluxing at 80 °C for 6 h. The product was purified via washing/centrifugation process with ethanol and deionized water to remove dissociative AEAPTMS or hydrolysis byproduct. Last, the functionalized HNTs were dried in vacuum oven under at 80 °C for 12 h and used for further experiments.

2.3. Loading of noble metal NPs (Rh, Pt, Pd) on N-HNTs

To prepare rhodium and platinum NPs decorated silanized HNTs (Rh–N-HNTs, Pt–N-HNTs), 100 mg of the purified N-HNTs powder was added in 50 mL deionized water, and the suspension was dispersed ultrasonically for 1 h at room temperature. Then 10 mL rhodium chloride (10 mM) or 10 mL chloroplatinic acid

(10 mM) was added dropwise to the dispersion of N-HNTs, and the mixture was kept under vigorous stirring for 2 h at room temperature. Subsequently, 30 mg EGCG dissolved in 5 mL H_2O was added and then the mixture was heated to 65 °C. After reaction for 6–7 h, the color of the sample changed, suggesting the formation of noble metal NPs, and the products were purified and centrifuged for three times using ethanol and deionized water, respectively, to remove excess EGCG, meanwhile, the supernatant was tested by UV–vis spectrophotometer to make sure the catalysts are clean before evaluation of catalytic activity. To prepare palladium NPs decorated N-HNTs (Pd–N-HNTs), 35 °C was maintained during reduction process, and other synthesis steps were the same as mentioned above. According to the X-ray photoelectron spectra analysis, the relative ratio of metal NPs loaded on Rh–N-HNTs, Pt–N-HNTs, and Pd–N-HNTs is 1.41%, 1.37%, and 1.18%, respectively.

2.4. Evaluation of catalytic activity

The catalytic activity of the synthesized catalysts (Rh–N-HNTs, Pt–N-HNTs, Pd–N-HNTs) was measured under identical catalytic reduction reaction of 4-NP–4-AP. Typically, 5 mg catalyst was added into fresh made NaBH_4 solution (100 mL, 25 mM) under vigorous stirring for 20 min at room temperature to make sure the catalyst dispersed uniformly in the solution. Subsequently, 4-NP aqueous solution (5 mL, 1 mM) was added, and the yellow suspension became colorless within 10 min. Meanwhile, the absorption spectra of the supernatant, were recorded by UV–vis spectrophotometer with an interval of 60 s. Typically, about 3 mL of the solution was withdrawn from the reaction system using a syringe, and then the syringe was equipped with a one-off filter. Thus, the supernatant was obtained by injecting the solution through the filter to the cuvette for test, leaving the HNTs loaded with metal NPs on the filter. The aperture of the membrane in the filter is 0.22 μm , which is efficient for the filtration of the catalyst. The maximum values of the absorption peaks at 400 nm for the obtained supernatant in the UV–vis spectra were recorded in order to evaluate the efficiency of the catalyst. Rh–N-HNTs catalyst was selected as an example and used for five successive cycles. The catalysts were separated after reaction by centrifugation at 8000 rpm for 5 min. The sediment was purified and centrifuged for several times with deionized water, and reused for next cycle reaction and the yellow suspension became colorless within 10 min every time. As a control, another sample was carried out without catalyst under the same condition.

2.5. Characterization

Fourier transform infrared (FT-IR) spectra were recorded on a Nicolet 5700 spectrophotometer. TEM images were obtained with a JSM-2100 transmission electron microscopy (JEOL, Japan) at an acceleration voltage of 200 kV. XRD patterns of the HNTs characterized with a SIEMENS Diffraktometer D5000 X-ray diffractometer using $\text{Cu K}\alpha$ radiation source at 35 kV, with a scan rate of $2\theta \text{ s}^{-1}$ in the 2θ range of 10–80°. The morphology of HNTs and N-HNTs were observed by a ULTRA-55 field-emission scanning electron microscopy (FE-SEM) at an acceleration voltage of 3 kV. X-ray photoelectron spectra of N-HNTs, Rh–N-HNTs, Pt–N-HNTs, and Pd–N-HNTs were recorded using an X-ray photoelectron spectrometer (Kratos Axis Ultra DLD) with an aluminum (mono) $\text{K}\alpha$ source (1486.6 eV). The aluminum $\text{K}\alpha$ source was operated at 15 kV and 10 mA. The catalytic reduction reaction of 4-NP–4-AP was recorded at the absorption band 300–500 nm in the UV–vis spectra using a U-3010 UV–vis spectrophotometer (Hitachi).

3. Results and discussion

3.1. Morphology, characteristics of HNTs, and functionalization of HNTs using AEPTMS

The structure and morphology of HNTs were observed by TEM and FE-SEM. Fig. 1a and b is the typical FE-SEM images of the purified HNTs at different magnification, which display the cylinder-shaped nanostructure and polydispersity in length. The TEM image in Fig. 1c shows the hollow tubular structure of HNTs with the inner and outer diameter of about 15–20 nm and 40–70 nm, respectively. What is more, Fig. 1d shows the XRD patterns of the HNTs, revealing the silicate nature of the clay mineral.

The FT-IR spectra of the HNTs, N-HNTs, Rh-N-HNTs were used to investigate the composition and structure of the resultant samples. The characteristic peaks of HNTs occurred at 3698 cm^{-1} , 3623 cm^{-1} , and 1635 cm^{-1} are attributed to O–H stretching of inner-surface hydroxyl groups, O–H stretching of inner hydroxyl groups, and deformation of water, respectively. Another two characteristic peaks at 1107 and 1033 cm^{-1} correspond to in-plane stretching of Si–O in HNTs. Compared with the curves of N-HNTs in Fig. 2b and Rh-N-HNTs in Fig. 2c, most of the peaks for HNTs maintained, which indicates that the main crystal structures of HNTs are preserved in N-HNTs and Rh-N-HNTs after modification and loading of Rh NPs. The newly emerged peaks at 2927 cm^{-1} , 2860 cm^{-1} appear in curve b and curve c are attributed to C–H asymmetric and symmetric stretching vibration, respectively. Besides, a broad band with a maximum at 3440 cm^{-1} occurred in sample b and sample c, which is assigned to the N–H stretching vibration, indicating that silane coupling agent (AEPTMS), the sole source for C–H and N–H, has been successfully grafted onto HNTs. What's more, the intensity of Si–O in-plane stretching in curve b and curve c become relatively narrow and increase, implying the Si–O groups in AEPTMS have been successfully grafted onto the HNTs. The above FT-IR results demonstrate that HNTs are easily modified by AEPTMS and the amine groups ($-\text{NH}_2$, $-\text{NH}-$) designed as the functional group are successfully detected in N-HNTs and Rh-N-HNTs.

3.2. In situ synthesis of noble metallic nanoparticles on N-HNTs

Since HNTs are functionalized with amino groups by APTEMS, they are expected to serve as substrates for complexation of noble metallic NPs, in which amino groups are the active sites [33]. Amino groups can electrostatically complex with aqueous negative-charged ions (RhCl_6^{2-} , PtCl_6^{2-} , and PdCl_4^{2-}), especially when they are exposed in acid condition that can promote the protonation of amino groups and exhibit adsorption ability for metallic ions. Subsequently, NPs are in-situ formed by chemical reduction process. In this work, we chose EGCG as both a mild and environment-friendly reducing agent and stabilizer. RhCl_3 solution was first selected as an example due to the excellent physical and chemical properties in various catalytic reactions [34].

FE-SEM images in Fig. 3a show that the morphology and structure of Rh-N-HNTs do not get noticeable change, indicating the main crystal structure of HNTs are preserved after loading Rh nanoparticles (Rh NPs). As shown in Fig. 3c,d, and f, ultrafine dots are found to exist both on the inside and outside surface of N-HNTs, and these Rh NPs distribute densely and uniformly. The chemical analysis by energy-dispersive X-ray spectroscopy (EDS, inset in Fig. 3b) confirms that these small dots are Rh NPs. Fig. 3f shows the HRTEM image of Rh-N-HNTs, the lattice finger of an interplanar spacing of 0.21 nm is according with the (111) plane of Rh NPs. In addition, the sample appearance changed from oyster white to field gray during reducing process, which is believed to be caused by plasmon resonance on Rh nanoparticle surface. The average diameter of Rh NPs is calculated about 1.2 nm and the particle distribution is shown in the inset in Fig. 3b. XRD pattern of Rh-N-HNTs exhibited no Bragg reflection can be obviously detected, which can be ascribed to the ultrafine particle size and low content of Rh NPs on N-HNT (not shown).

To verify the chelating effect of Rh NPs with amino groups, XPS survey was performed in order to get more detailed information of Rh atoms in Rh-N-HNTs. The chemical state of Rh NPs immobilized on the functionalized HNTs is presented in Fig. 4. As observed in Fig. 4a, the intense doublets emerged at 312.5 eV and 307.8 eV correspond well with Rh $3d_3$ and Rh $3d_5$ binding energies,

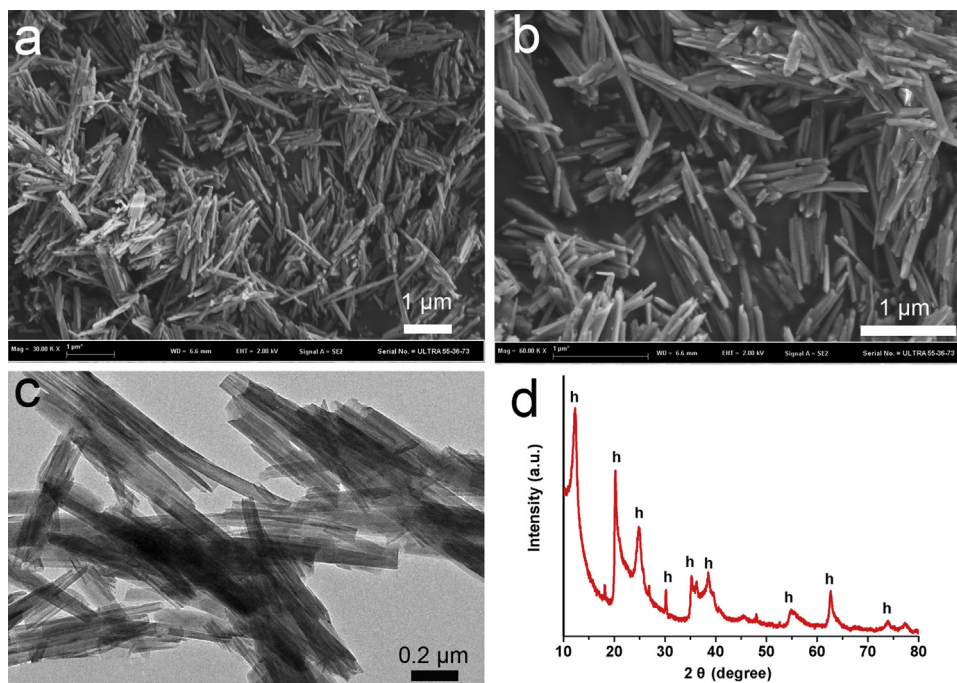


Fig. 1. (a) and (b) FE-SEM images of purified HNTs at different higher magnification; (c) TEM image of HNTs; (d) XRD patterns of HNTs (h: HNTs).

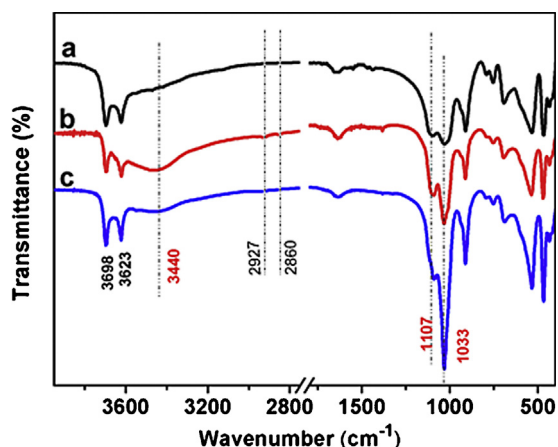


Fig. 2. FT-IR spectra of (a) HNTs, (b) N-HNTs, and (c) Rh-N-HNTs.

respectively. Compared with the zero valent Rh^0 (311.9 eV at Rh 3d₃, 307.2 eV at Rh 3d₅), the changes in binding energy indicate that there exist interaction between Rh NPs and surrounding chemicals, which is mainly caused by the chelating effect from amino groups. Because Rh NPs could be stabilized and firmly attached to the $-\text{NH}_2$ and $-\text{NH}-$ through the strong metal/amine

coordination interactions between the empty d orbital of Rh atom and the free pair of electrons on the N atom of the amino groups. Hence, the N atoms for N-HNTs and Rh-N-HNTs were testified by XPS, and the results are shown in Fig. 4b and c. In Fig. 4b, two peaks occurred at 401.5 eV and 399.3 eV, standing for two types of N ($-\text{NH}_2$, $-\text{NH}-$) in AEAPTMS grafted on HNTs. However, the binding energies of N 1s observed in Fig. 4c shift to 402.1 eV and 400.1 eV, respectively, which can be attributed to the strong interaction between Rh NPs and amino groups. Overall, above results confirm the chelating effects between Rh NPs and amino groups. Therefore, the amino modified HNTs successfully act as supports for ultrafine Rh NPs which are in situ synthesized at the active sites provided by amino groups on N-HNTs.

Similarly, owing to the expected coordination between PtCl_6^{2-} , PdCl_4^{2-} , and $-\text{NH}_2$, the N-HNTs was exploited as scaffolds to prepare Pt NPs and Pd NPs with the reduction of EGCG. SEM studies of Pt-N-HNTs and Pd-N-HNTs (not shown) also revealed that the nanotubes were several micrometers in length and no metal nanoparticles can be clearly distinguished under the present resolution the same to Rh-N-HNTs sample, indicating that Pt NPs and Pd NPs are ultrafine too. TEM images of Pt-N-HNTs and Pd-N-HNTs show that Pt NPs, and Pd NPs are distributed on the surface of N-HNTs densely and uniformly, as evidenced in Fig. 5. As shown in Fig. 5a and b, an abundance of Pt NPs with an average diameter about 1.3 nm (inset in Fig. 5c) can be seen on both outside and

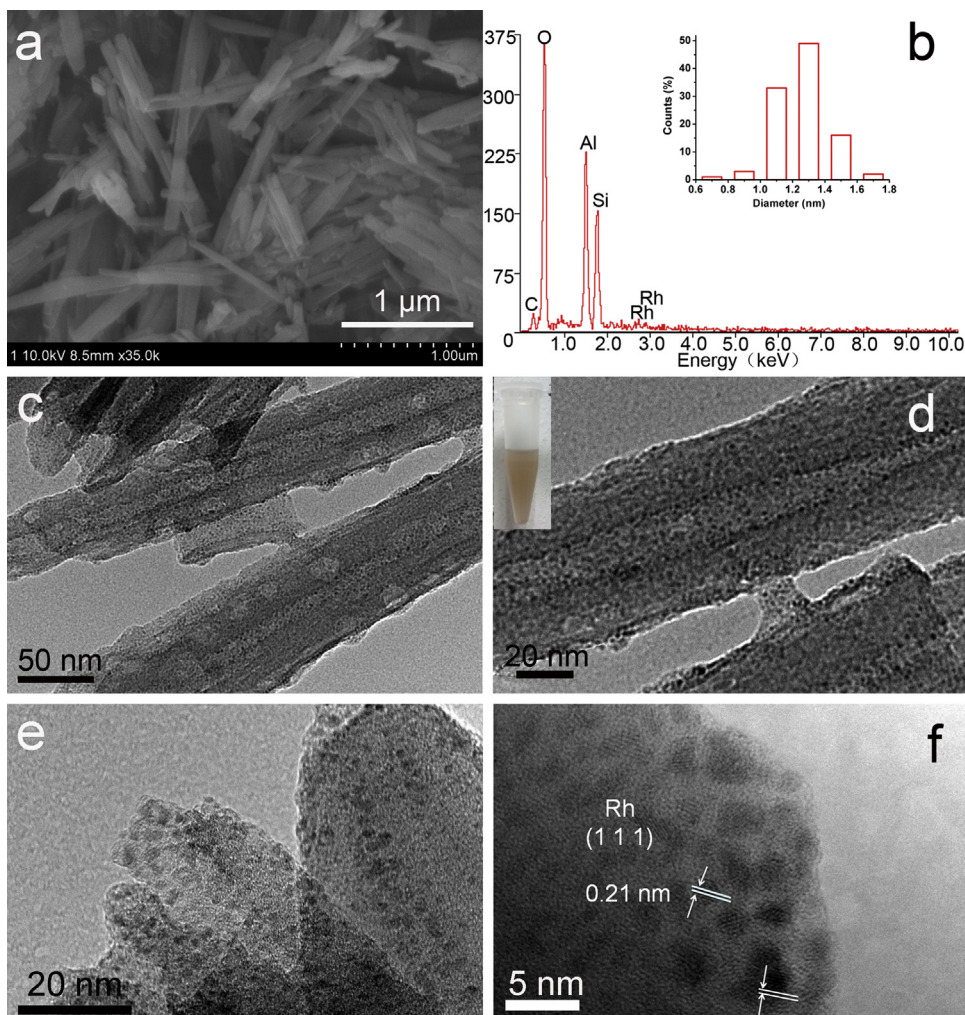


Fig. 3. (a) FE-SEM image of Rh-N-HNTs; (b) EDX spectrum of Rh-N-HNTs, the inset is the particle size distribution of Rh NPs on N-HNTs; (c)–(f) TEM images of Rh-N-HNTs under different magnifications, the inset in (d) shows the corresponding digital image of Rh-N-HNTs suspension.

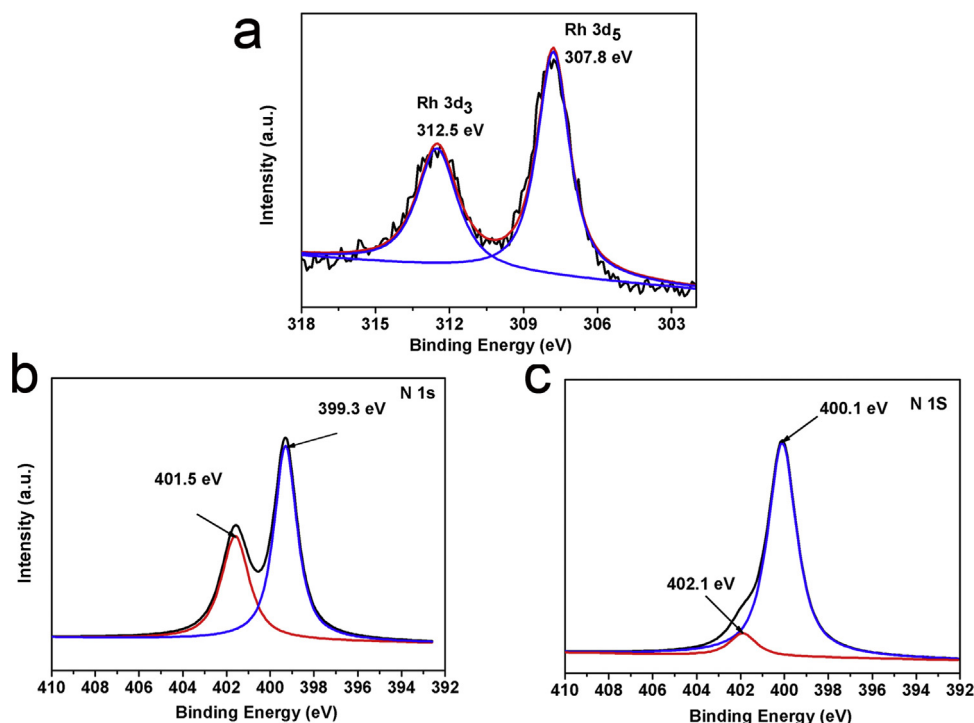


Fig. 4. XPS spectra of (a) Rh 3d of Rh-HNTs; (b) N 1s of N-HNTs and (c) N 1s of Rh-N-HNTs.

inside surface of N-HNTs. In addition, the appearance of the N-HNTs suspension turned from oyster white to claybank with the reduction of PtCl_6^{2-} , suggesting the formation of Pt NPs, and it is in accordance with the EDS result in Fig. 5c.

For the preparation of Pd-N-HNTs, the synthetic process is a little different from the protocol of Rh-N-HNTs, and Pt-N-HNTs in temperature. In this work, H_2PdCl_4 solution was prepared by dissolving PdCl_2 powder in diluted hydrochloric acid (pH 2). It is believed that acid condition would promote the protonation of amino groups, so more dissociative PdCl_4^{2-} will chelate with amino groups by electrostatic attraction. Furthermore, if the reduction is performed under relative high temperature, Pd crystal

nucleus would be synthesized in a very short time and are apt to aggregation to form large NPs. Therefore, the reduction temperature of PdCl_4^{2-} in the present study was set at 35 °C. Subsequently, the precursor PdCl_4^{2-} is reduced to Pd NPs with the addition of EGCG, giving rise to a clear-brown suspension (inset in Fig. 5e). The average Pd particle size is near 1.4 nm, which can be seen from the TEM images in Fig. 5d and e and the size distribution histogram in Fig. 5f. The EDS spectrum in Fig. 5f confirms the presence of Pd in Pd-N-HNTs.

According to above results, it is supposed that the chelating effects of noble metal ions with the amino groups grafted on HNTs and the phenolic hydroxyls in EGCG molecules play a crucial role in

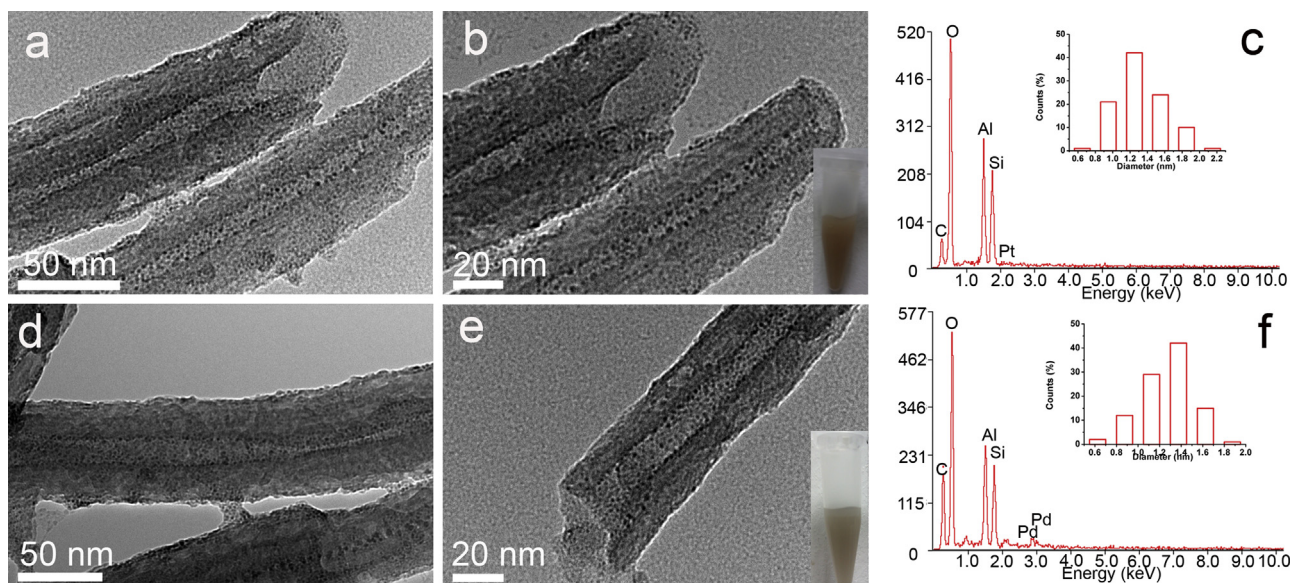


Fig. 5. TEM images of (a) and (b) Pt-N-HNTs, (c) and (d) Pd-N-HNTs; EDS spectra of Pt-N-HNTs (e), Pd-N-HNTs (f). The insets in (b) and (e) show the corresponding digital image of the suspension of each sample. The insets in (c) and (f) are the size distribution histograms of Pt and Pd NPs, respectively.

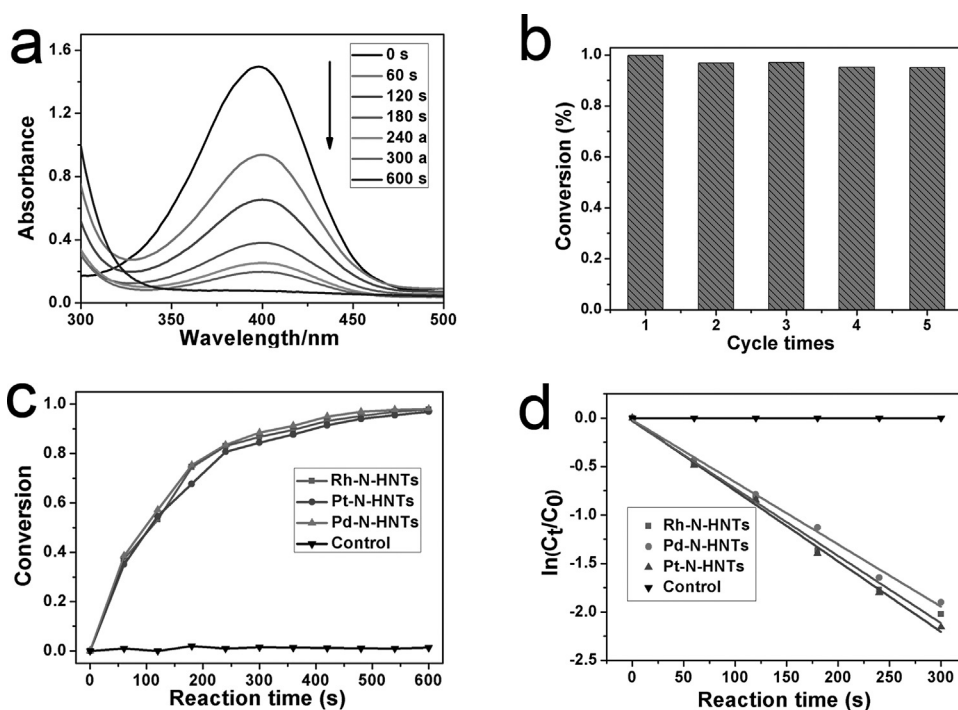


Fig. 6. (a) Time-dependent UV-vis absorbance of 4-NP catalyzed by Rh-N-HNTs; (b) catalytic conversion of 4-NP by using Rh-N-HNTs for five cycles; (c) time-dependent conversion of 4-NP reduction catalyzed by Rh-N-HNTs, Pt-N-HNTs, Pd-N-HNTs, N-HNTs, respectively; (d) $\ln(C_t/C_0)$ versus reaction time.

the synthesis of ultrafine NPs. The N-HNTs possess a large amount of amino groups, which can “anchor” noble metal ions in the solution through chelating effect. With the addition of EGCG, multiple phenolic hydroxyls were introduced to the reaction system, resulting in increased binding sites for noble metal ions through chelating effect. The high density phenolic hydroxyls groups in EGCG acted as the reducing agent and reduced the noble metal ions to metal NP accompanying the oxidation of phenolic hydroxyls to quinones, finally, the synthesized noble metal NPs were firmly fixed on the N-HNTs with the stabilization effect

caused by the quinones. Besides, mainly because of the space steric hindrance caused by the basal material (N-HNTs), the neighboring small NPs cannot easily collide with each other to aggregate to form large NPs.

3.3. Catalytic performance

The catalytic reduction of aromatic nitrocompounds using noble metal NPs in the presence of NaBH_4 has been widely investigated for the efficient preparation of aromatic

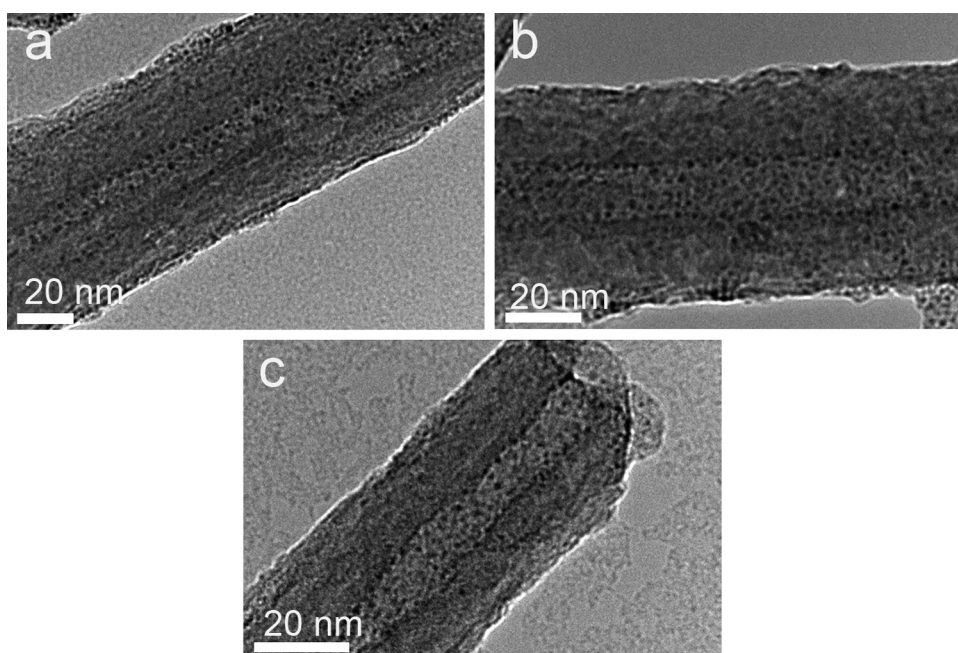


Fig. 7. TEM images of (a) Rh-N-HNTs, (b) Pt-N-HNTs, and (c) Pd-N-HNTs after catalytic reactions.

aminocompounds [35–40]. Therefore, the reduction of 4-NP–4-AP with an excess amount of NaBH_4 was used as a model system to evaluate the catalytic activity of the prepared nanocomposite catalysts. The results showed that the reaction did not proceed in the absence of nanocomposite catalysts during a long period of time. After the nanotubular catalyst, Rh–N–HNTs, was added, the color of the mixture changed from yellow to colorless within 600 s, indicating the complete conversion of 4-NP–4-AP. Fig. 6a shows the UV–vis spectra of the reaction mixture containing Rh–N–HNTs catalyst recorded at different time during the reaction process. The characteristic absorption peak of 4-NP at 400 nm gradually decreased. After reaction for a given time, the Rh–N–HNTs catalyst was separated by simple centrifugation from the mixture and washed several times by deionized water, then reused in the next cycle reaction. As shown in Fig. 6b, the Rh–N–HNTs catalyst was recycled for five times, and there is almost no decrease in reaction conversion. These results clearly indicate that Rh–N–HNTs catalyst has good catalytic efficiency and high stability.

The catalytic activities of Rh–N–HNTs, Pt–N–HNTs, and Pd–N–HNTs are compared in the reduction of 4-NP. As Fig. 6c shows, the reaction conversion is calculated from C_t/C_0 , where C_t is the 4-NP concentration at time t and C_0 is the initial 4-NP concentration, measured from the relative intensity of UV–vis absorbance (A_t/A_0) at 400 nm. In the presence of Pt–N–HNTs and Pd–N–HNTs catalyst, the reaction completed within 600 s, similar to Rh–N–HNTs in reaction efficiency. Fig. 7d shows the $\ln(C_t/C_0)$ versus reaction time for the reduction of 4-NP by using the three kind of catalysts, and the apparent rate constant were directly calculated from the slopes of the straight lines. The reaction rate constant are calculated to be $k_{\text{Rh-N-HNTs}} \sim 0.0069 \text{ s}^{-1}$, $k_{\text{Pt-N-HNTs}} \sim 0.00727 \text{ s}^{-1}$, $k_{\text{Pd-N-HNTs}} \sim 0.00642 \text{ s}^{-1}$, respectively.

In fact, the morphology and structure of the three catalysts, including the size and the density of noble metal NPs, did not show obvious change after five cycles of the catalytic reactions, as shown in Fig. 7. Above results exhibit that the noble metal NPs anchored on the outside and inside surface of HNTs with high specific surface area and chemical stability have perfect catalytic activity and efficiency, which can be applied to many other catalytic systems.

4. Conclusions

In summary, ultrafine noble metal NPs (Rh, Pt, and Pd) with the diameter less than 2 nm have been successfully synthesized by in situ green reduction. They are immobilized densely and uniformly on both the inside and outside surface of amino functionalized HNTs. The as-prepared Rh–N–HNTs, Pt–N–HNTs, and Pd–N–HNTs nanocomposite catalysts exhibited excellent catalytic activity in the reduction of 4-NP and Rh–N–HNTs showed satisfactory cycling stability. Considering the fact that amino groups can host a series of ions, the N–HNTs are anticipated to be exploited as a platform to synthesize different metal, metal alloy, or metal oxide nanoparticles, the resulting materials may have great use in catalysis and photoelectric conversion application due to their availability, formability, high specific surface area, and chemical stability.

Acknowledgements

This work was supported by the project of the National Natural Science Foundation of China (NSFC) (51373154), and the 521 Talent Project of Zhejiang Sci-Tech University.

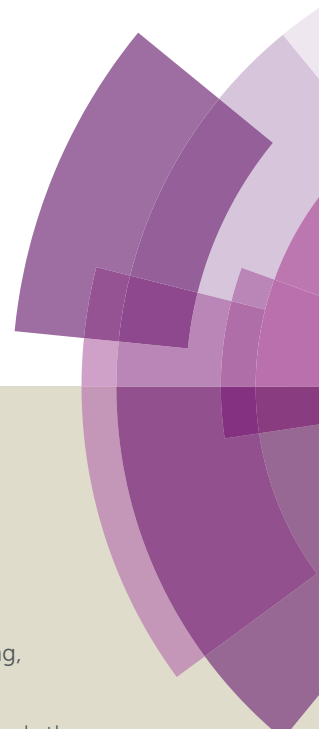
References

- [1] G.V. Hartland, Optical studies of dynamics in noble metal nanostructures, *Chem. Rev.* 111 (2011) 3858–3887.
- [2] H. Kobayashi, H. Morita, M. Yamauchi, R. Ikeda, H. Kitagawa, Y. Kubota, K. Kato, M. Takata, Nanosize-induced hydrogen storage and capacity control in a non-hydride-forming element: rhodium, *J. Am. Chem. Soc.* 133 (2011) 11034–11037.
- [3] S. Mubeen, T. Zhang, B.Y. Yoo, M.A. Deshusses, N.V. Myung, Palladium nanoparticles decorated single-walled carbon nanotube hydrogen sensor, *J. Phys. Chem. C* 111 (2007) 6321–6327.
- [4] M. Segev-Bar, A. Landman, M. Nir-Shapira, G. Shuster, H. Haick, Tunable touch sensor and combined sensing platform: toward nanoparticle-based electronic skin, *ACS Appl. Mater. Interfaces* 5 (2013) 5531–5541.
- [5] B.R. Sathe, Rhodium nanoparticle-carbon nanosphere hybrid material as an electrochemical hydrogen sensor, *RSC Adv.* 3 (2013) 5361–5365.
- [6] X. Du, J. He, Amino-functionalized silica nanoparticles with center-radially hierarchical mesopores as ideal catalyst carriers, *Nanoscale* 4 (2012) 852–859.
- [7] Y. Zhang, X. He, J. Ouyang, H. Yang, Palladium nanoparticles deposited on silanized halloysite nanotubes: synthesis, characterization and enhanced catalytic property, *Sci. Rep.* 3 (2013) 2948–2953.
- [8] S. Mahshid, C. Li, S.S. Mahshid, M. Askari, A. Dolati, L. Yang, S. Luo, Q. Cai, Sensitive determination of dopamine in the presence of uric acid and ascorbic acid using TiO_2 nanotubes modified with Pd, Pt and Au nanoparticles, *Analyst* 136 (2011) 2322–2329.
- [9] H.J. Yin, H.J. Tang, D. Wang, Y. Gao, Z.Y. Tang, Cluster/graphene hybrids for high-performance oxygen reduction reaction, *ACS Nano* 6 (2012) 8288–8297.
- [10] T.Y. Chen, Y.T. Liu, H.M. Nguyen, L.J. Fan, C.Y. Wu, T.J. Luo, C.H. Lee, Y.W. Yang, T. C. Wen, T.L. Lin, Ruthenium core-activated platinum monolayer shell high redox activity cathodic electrocatalysts for dye-sensitized solar cells, *J. Mater. Chem. A* 1 (2013) 5660–5669.
- [11] D. Tongsakul, S. Nishimura, K. Ebitani, Platinum/gold alloy nanoparticles-supported hydroxylate catalyst for selective aerobic oxidation of polyols in base-free aqueous solution at room temperature, *ACS Catal.* 3 (2013) 2199–2207.
- [12] S. Kundu, M. Jayachandran, The self-assembling of DNA-templated Au nanoparticles into nanowires and their enhanced SERS and catalytic applications, *RSC Adv.* 3 (2013) 16486–16498.
- [13] C. Perez-Campana, V. Gomez-Vallejo, M. Pigivilla, A. Martin, T. Calvo-Fernandez, S.E. Moya, T. Reese, J. Llop, Biodistribution of different sized nanoparticles assessed by positron emission tomography: a general strategy for direct activation of metal oxide particles, *ACS Nano* 7 (2013) 3498–3505.
- [14] W. Zhao, I.M. Hsing, Facile and rapid manipulation of DNA surface density on gold nanoparticles using mononucleotide-mediated conjugation, *Chem. Commun.* 46 (2010) 1314–1316.
- [15] S. Link, M.A. El-Sayed, Size and temperature dependence of the plasmon absorption of colloidal gold nanoparticles, *J. Phys. Chem. B* 103 (1999) 4212–4217.
- [16] M.P. Mallin, C.J. Murphy, Solution-phase synthesis of sub-10 nm Au–Ag alloy nanoparticles, *Nano Lett.* 2 (2002) 1235–1237.
- [17] J.R. Morones, J.L. Elechiguerra, A. Camacho, K. Holt, J.B. Kouri, J.T. Ramirez, M.J. Yacaman, The bactericidal effect of silver nanoparticles, *Nanotechnology* 16 (2005) 2346–2353.
- [18] H. Niu, S. Wang, T. Zeng, Y. Wang, X. Zhang, Z. Meng, Y. Cai, Preparation and characterization of layer-by-layer assembly of thiols/Ag nanoparticles/polydopamine on PET bottles for the enrichment of organic pollutants from water samples, *J. Mater. Chem.* 22 (2012) 15644–15653.
- [19] Y. Zhang, Q. Xiang, J. Xu, P. Xu, Q. Pan, F. Li, Self-assemblies of Pd nanoparticles on the surfaces of single crystal ZnO nanowires for chemical sensors with enhanced performances, *J. Mater. Chem.* 19 (2009) 4701–4706.
- [20] J. Fang, S. Lebedkin, S. Yang, H. Hahn, A new route for the synthesis of polyhedral gold mesocages and shape effect in single-particle surface-enhanced Raman spectroscopy, *Chem. Commun.* 47 (2011) 5157–5159.
- [21] A. Azetsu, H. Koga, A. Isogai, T. Kitaoka, Synthesis and catalytic features of hybrid metal nanoparticles supported on cellulose nanofibers, *Catalysts* 1 (2011) 83–96.
- [22] J. Kim, S. Byun, A.J. Smith, J. Yu, J. Huang, Enhanced electrocatalytic properties of transition-metal dichalcogenides sheets by spontaneous gold nanoparticle decoration, *J. Phys. Chem. Lett.* 4 (2013) 1227–1232.
- [23] A.Y. Polyakov, L. Yadgarov, R. Popovitz-Biro, V.A. Lebedev, I. Pinkas, R. Rosentsveig, Y. Feldman, A.E. Goldt, E.A. Goodilin, Decoration of WS_2 nanotubes and fullerene-like MoS_2 with gold nanoparticles, *J. Phys. Chem. C* 118 (2014) 2161–2169.
- [24] K. Jasuja, J. Linn, S. Melton, V. Berry, Microwave-reduced uncapped metal nanoparticles on graphene: tuning catalytic, electrical, and Raman properties, *J. Phys. Chem. Lett.* 1 (2010) 1853–1860.
- [25] X. Chen, Z. Cai, X. Chen, M. Oyama, AuPd bimetallic nanoparticles decorated on graphene nanosheets: their green synthesis, growth mechanism and high catalytic ability in 4-nitrophenol reduction, *J. Mater. Chem. A* 2 (2014) 5668–5674.
- [26] X. Huang, H. Wu, X. Liao, B. Shi, One-step, size-controlled synthesis of gold nanoparticles at room temperature using plant tannin, *Green Chem.* 12 (2010) 395–399.
- [27] M. El-Sayed, Small is different: shape-, size-, and composition-dependent properties of some colloidal semiconductor nanocrystals, *Acc. Chem. Res.* 37 (2004) 326–333.
- [28] J. Huang, L. Zhang, B. Chen, N. Ji, F. Chen, Y. Zhang, Z. Zhang, Nanocomposites of size-controlled gold nanoparticles and graphene oxide: formation and applications in SERS and catalysis, *Nanoscale* 2 (2010) 2733–2738.
- [29] M.L. Du, B.C. Guo, D.M. Jia, Thermal stability and flame retardant effects of halloysite nanotubes on poly(propylene), *Eur. Polym. J.* 42 (2006) 1362–1369.

- [30] J. Pan, H. Yao, L. Xu, H. Ou, P. Huo, X. Li, Y. Yan, Selective recognition of 2,4,6-trichlorophenol by molecularly imprinted polymers based on magnetic halloysite nanotubes composites, *J. Phys. Chem. C* 115 (2011) 5440–5449.
- [31] Y. Zhang, H. Yang, Co_3O_4 nanoparticles on the surface of halloysite nanotubes, *Phys. Chem. Miner.* 39 (2012) 789–795.
- [32] M.L. Zou, M.L. Du, H. Zhu, C.S. Xu, Y.Q. Fu, Green synthesis of halloysite nanotubes supported Ag nanoparticles for photocatalytic decomposition of methylene blue, *J. Phys. D: Appl. Phys.* 45 (2012) 325302–325309.
- [33] Y. Lin, Y. Qiao, Y. Wang, Y. Yan, J. Huang, Self-assembled laminated nanoribbon-directed synthesis of noble metallic nanoparticle-decorated silica nanotubes and their catalytic applications, *J. Mater. Chem.* 22 (2012) 18314–18320.
- [34] R. Palaniappan, G.G. Botte, Effect of ammonia on Pt, Ru, Rh, and Ni cathodes during the alkaline hydrogen evolution reaction, *J. Phys. Chem. C* 117 (2013) 17429–17441.
- [35] Z. Zhang, C. Shao, P. Zou, P. Zhang, M. Zhang, J. Mu, Z. Guo, X. Li, C. Wang, Y. Liu, In situ assembly of well-dispersed gold nanoparticles on electrospun silica nanotubes for catalytic reduction of 4-nitrophenol, *Chem. Commun.* 47 (2011) 3906–3908.
- [36] J. Zhang, G. Chen, D. Guay, M. Chaker, D. Ma, Highly active PtAu alloy nanoparticle catalysts for the reduction of 4-nitrophenol, *Nanoscale* 6 (2014) 2125–2130.
- [37] J. Lee, J.C. Park, J.U. Bang, H. Song, Precise tuning of porosity and surface functionality in Au@SiO_2 nanoreactors for high catalytic efficiency, *Chem. Mater.* 20 (2008) 5839–5844.
- [38] S. Harish, J. Mathiyarasu, K.L.N. Phani, V. Yegnaraman, Synthesis of conducting polymer supported Pd nanoparticles in aqueous medium and catalytic activity towards 4-nitrophenol reduction, *Catal. Lett.* 128 (2009) 197–202.
- [39] S.J. Hoseini, M. Rashidi, M. Bahrani, Platinum nanostructures at the liquid–liquid interface: catalytic reduction of *p*-nitrophenol to *p*-aminophenol, *J. Mater. Chem.* 21 (2011) 16170–16176.
- [40] S. Kundu, K. Wang, H. Liang, Photochemical generation of catalytically active shape selective rhodium nanocubes, *J. Phys. Chem. C* 113 (2009) 18570–18577.

Journal of Materials Chemistry A

Accepted Manuscript



This article can be cited before page numbers have been issued, to do this please use: M. Zou, J. Zhang, H. Zhu, M. Du, Q. wang, M. Zhang and X. Zhang, *J. Mater. Chem. A*, 2015, DOI: 10.1039/C5TA02538A.



This is an *Accepted Manuscript*, which has been through the Royal Society of Chemistry peer review process and has been accepted for publication.

Accepted Manuscripts are published online shortly after acceptance, before technical editing, formatting and proof reading. Using this free service, authors can make their results available to the community, in citable form, before we publish the edited article. We will replace this *Accepted Manuscript* with the edited and formatted *Advance Article* as soon as it is available.

You can find more information about *Accepted Manuscripts* in the [Information for Authors](#).

Please note that technical editing may introduce minor changes to the text and/or graphics, which may alter content. The journal's standard [Terms & Conditions](#) and the [Ethical guidelines](#) still apply. In no event shall the Royal Society of Chemistry be held responsible for any errors or omissions in this *Accepted Manuscript* or any consequences arising from the use of any information it contains.



Journal of Materials Chemistry A

COMMUNICATION

3D dendritic WSe₂ catalyst grown on carbon nanofiber mats for efficient hydrogen evolutionReceived 00th January 20xx,
Accepted 00th January 20xxMeiLing Zou,^{a,1} JunFeng Zhang,^{b,1} Han Zhu,^a MingLiang Du,^{a,*} QingFa Wang,^{b,**} Ming Zhang,^a
XiangWen Zhang^b

DOI: 10.1039/x0xx00000x

www.rsc.org/

3D dendritic WSe₂ on conductive carbon nanofiber mats (d-WSe₂/CFM) was designed and synthesized by a diffusion-controlled CVD method. The d-WSe₂/CFM was directly used as cathode for HER. The substantially improved HER performance are ascribed to the novel 3D structure with effectively exposed edge sites.

Electrocatalytic production of hydrogen from water splitting has been developed as an effective approach for reducing our reliance on hydrocarbon fuels.^{1,2} Various catalysts have been investigated for hydrogen evolution reactions (HER).³⁻⁵ Although platinum (Pt) or doped Pt catalyst are found to be highly active, the high cost heavily impedes its wide application in a large scale.⁶⁻⁸ Therefore, a number of alternative catalysts, such as transition metal dichalcogenides (TMDs) MX₂ (M=Mo, W and X=S, Se), are being extensively studied since their electrocatalytic activities were identified.⁹⁻¹² Both experimental and computational studies has highlighted that the HER activity of TMDs correlates with the active edge sites,¹³ consequently, hierarchically constructing TMDs with high edge fraction is of high importance to improve HER performance. For example, the density of edge sites of 2H MoS₂ is highly addressed since it dominates the HER activity while the basal plane is believed to be inert.¹⁴⁻¹⁶ As one of the most promising TMDs, WSe₂ has been investigated in the fields of batteries, field-effect transistors, diode, and so on.¹⁷⁻²⁰ Recently, the study on WSe₂ for HER are given on rational design of WSe₂ catalyst with more exposure of active edge sites and the results shows that nanostructured WSe₂ is also a promising and appealing HER electrocatalyst.^{12,21} These results motivate us to design hierarchical

WSe₂ with the aim at enhancing its HER performance. However, as far as we know, it is still of great challenge to control the growth of WSe₂. In our previous study, the hierarchical structural TMDs were assembled on electrospun carbon nanofibers substrate, exhibiting excellent performance in electrochemical hydrogen evolution applications.²²⁻²⁴ This communication will provide a more efficient and facile approach to construct hierarchical WSe₂ electrode for HER with both high effective density of edge sites and high conductive carbon nanofiber mat substrate for HER.

According to classical crystal growth theory, dendritic growth, layer-by-layer (LBL) growth and screw-dislocation-driven (SDD) growth are the three basic growth types.²⁵ Generally, a high supersaturation condition is required for both dendritic growth and LBL growth.^{26,27} SDD growth is much more favorable at lower supersaturation than former ones.^{28,29} Under conditions where a rough interface is assumed, such as high supersaturation, the crystal is bounded by rounded noncrystallographic interfaces. If morphological instability occurs on such a rough interface, the crystal takes dendritic form.²⁵ The generated structure via dendritic growth can, thus, be fully dominated by changing the vapor concentration in chemical vapor deposition (CVD) process.

In this study, we proposed a method to synthesize 3D dendritic WSe₂ with carbon nanofiber mats (CFM) as the conductive substrate by using CVD method. In this method, the diffusion flux of Se vapor inversely depends on the lateral distance away from the left edge of the furnace.³⁰ At the upstream of the furnace, the Se vapor concentration is supersaturated, then a rough reaction and growth interface is constructed, leading to morphological instability occurs on such a rough interface, resulting in the formation of WSe₂ nanostructure with dendritic crystal structure. However, at the downstream, rose-like WSe₂ nanostructure formed due to the reduced driving force caused by the much lower Se vapor concentration. Therefore, the WSe₂ nanosheet growth is subject to strong influences of the diffusion of Se vapor through the boundary layer of Ar gas flows. Finally, the generated structures are tailored by the diffusion controlled concentration of Se vapor.

The obtained dendritic WSe₂ exhibits a rather low overpotential, higher current density at -300 mV vs RHE, and a small series resistance for HER even at a relatively low coverage of

^a Key Laboratory of Advanced Textile Materials and Manufacturing Technology of the Ministry of Education, College of Materials and Textile, Zhejiang Sci-Tech University, 310018, P. R. China

^b Key Laboratory for Green Chemical Technology of the Ministry of Education, School of Chemical Engineering and Technology, Tianjin University, 92 Weijian Road, Tianjin, 300072, P. R. China

† Electronic supplementary information (ESI) available: Experimental details, the EDS analysis and optical image of d-WSe₂/CFM. TEM and HAADF-STEM analysis of TS-WSe₂/CFM. XRD and Raman characterizations of d-WSe₂/CFM and r-WSe₂/CFM. Photo of the working electrode for d-WSe₂/CFM. The magnified SEM images of CFM and WO₃/CFM. CV plots of d-WSe₂/CFM electrode at 100 mV s⁻¹ for 1000 cycles in 0.5 M H₂SO₄. See DOI: 10.1039/x0xx00000x

COMMUNICATION

Journal Name

WSe₂ and low atom fraction of W and Se (Figure S1). The excellent HER performance is correlated to the high dense edge sites and the high conductivity of substrates.

The facile CVD approach for WSe₂ with different hierarchical structures on CFM is exhibited as below, in which (NH₄)₆H₂W₁₂O₄₀ and PAN were selected as the precursors for W and CFM, respectively (see Supporting Information). Firstly, W-PAN FM was prepared by electrospinning their DMF solution. Then W-PAN FM on boat was transferred to the chamber of quartz furnace tube. Secondly, a heat treatment was employed to pre-oxide PAN FM and decompose (NH₄)₆H₂W₁₂O₄₀ into WO₃. Se vapor was then introduced at saturated vapor pressure with Ar. Another heat treatment was applied leading to graphitization of PAN FM and generation of WSe₂ by selenization of WO₃ and the CFM with WSe₂ grown on was finally obtained (Figure S2 A). The boat's lateral distance from the upstream was adjusted in order to adjust the vapor concentration. The synthetic route is illustrated in Figure 1A. More detailed information about preparation can be found in SI. The obtained CFM with a thickness of 15 μm (Figure S2 B) exhibit good flexibility and excellent conductivity, and were used as electrodes directly. The WO₃ content within fiber decreases significantly after selenization as compared to that within WO₃/CFM (Figure S2, C and D).

Since the vapor concentration of Se can be diffusion-controlled by the lateral distance from upstream, its influence on the generated structure of WSe₂ on CFM is illustrated in Figure 1. A number of flower-like WSe₂ in the size of about 2~5 μm was obtained at three positions (Figure 1A, (a), (b) and (c)). It's interesting to find that three types of microstructures were obtained. Position (a) generated a novel dendritic WSe₂ on CFM (Figure 1B and 1E), which is defined as d-WSe₂/CFM. As shown in Figure 1D and 1G, position (c) can grow smooth leaves of WSe₂ on CFM with a vivid rose-like shape, which is defined as r-WSe₂/CFM. The leaves with bended triangular or hexangular contour can be distinguished for both d-WSe₂ (Figure 1E, and Figure S3 A) and r-WSe₂ (Figure 1G and Figure S3 C). The structure generated at position of (b) exhibited a transition morphology (Figure 1C, F and Figure S3B). The sample at position (b) is defined as TS-WSe₂/CFM. The structure evolution of WSe₂ is suggested to be Se vapor concentration sensitive and could be well diffusion-controlled at different lateral distance from upstream. When the location is close to the upstream, the vapor concentration is believed to be high supersaturation while a much lower concentration can be achieved at a faraway distance. The adjusted vapor concentrations at different locations thus lead to various structures, which is consistent with previous report.³¹

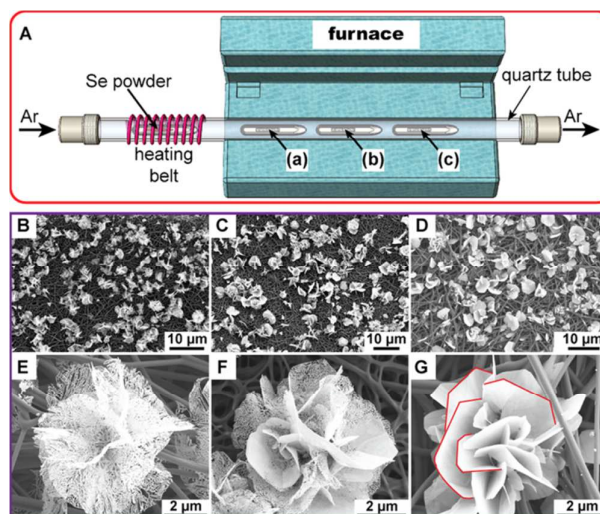


Figure 1. Schematic illustration of WSe₂ growth at different position in a quartz furnace tube. SEM images of d-WSe₂/CFM, TS-WSe₂/CFM and r-WSe₂/CFM at B, C and D low-, as well as E, F, and G high-magnification at positions (a), (b) and (c) in (A), respectively.

The d-WSe₂/CFM was fully characterized by TEM, selected area electron diffraction (SAED), high-angle annular dark field (HAADF) STEM, EELS spectra, element mapping and XPS spectra. As shown in Figure 2A, d-WSe₂ branches with 10-80 nm in diameter grew freely and artistically (Figure 2A). The effective density of edge sites on d-WSe₂/CFM is believed to be much higher in comparison to that of r-WSe₂/CFM. The light and shade contrast indicates the change in the thickness (layer number) of WSe₂ branches. The lattice distance observed on the terraces is 3.8 Å (left inset in Figure 2A), consistent with (100) planes of 2H-WSe₂.³² The SAED (right inset in Figure 2A) clearly suggests that dendritic WSe₂ is configured in 2H phase,³² in good accordance with the observed triangular or hexangular morphology in Figure 1. As shown in EELS (Figure 2C) and high-resolution element mapping (Figure 2D), both W and Se elements are homogeneously distributed within branches. X-ray photoelectron spectroscopy (XPS) was conducted to investigate the chemical composition of d-WSe₂. Two obvious peaks at 34.2 and 32.1 eV (Figure 2E) are ascribed to W 4f_{5/2} and W 4f_{7/2}, respectively.³³ In Figure 2F, Se 3d_{5/2} and Se 3d_{3/2} at 54.2 and 55.0 eV indicate divalent Se ion in good agreement with binding energy values for WSe₂ crystals.³³ Additional two weak peaks at around 37.5 and 35.7 eV, correspondingly assigned to W 4f_{5/2} and W 4f_{7/2}, are due to a fraction of WO₃ (Figure S3D).³³ The TS-WSe₂/CFM was also characterized, as shown in Figure S3 E and F.

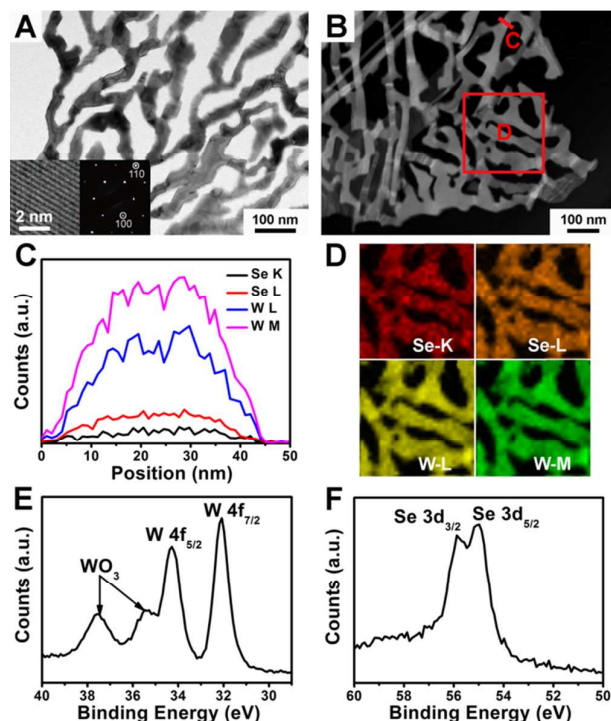


Figure 2. A) TEM image of dendritic WSe₂ (left inset, HRTEM image; right inset, the corresponding SAED pattern). B) HAADF STEM images of d-WSe₂. C) The EELS spectra and D) high-resolution element mapping of the selected region in Figure B. E) and F) XPS analysis of W 4f and S 2p peaks of d-WSe₂/CFM, respectively.

The XRD was also employed to evaluate the crystal structure of d-WSe₂ and r-WSe₂. As shown in Figure S4, the diffraction peaks are in consistent with the standard pattern of hexagonal WSe₂ (JCPDS card No. 38-1388). The thickness obtained from the full width at half-maximum of (002) according to Scherrer equation is 1.2 nm, indicating 2 layers of Se-W-Se.³⁴ The XRD result indicates the same the crystal structure d-WSe₂ and r-WSe₂. Raman spectroscopy was also exploited to further obtain structural evidence of the catalysts (Figure S5). As both E_{2g}¹ and A_{1g} modes are very closed to each other, at 250 and 253 cm⁻¹,²¹ accordingly, only one peak for WSe₂ is observed. The above Raman result for the two hierarchical structures further substantiates the same crystal structure. Two broad peaks at 1354.5 cm⁻¹ and 1587.6 cm⁻¹ correspond to the D and G band of the CFM. The intensity ratio of D and G bands (*I_D*/*I_G*) is 1.15. The presence of graphitic is expected to achieve a high conductive CFM substrate.³⁵

The d-WSe₂/CFM was directly used as hydrogen evolution cathode to highlight the merits of the novel architecture. The configuration of d-WSe₂/CFM electrode is shown in Figure S6. CFM, WO₃/CFM, WSe₂ NPs (Figure S7) and r-WSe₂/CFM electrodes were also tested as control. The electrochemical experiment was conducted in a standard three-electrode electrochemical cell setup in 0.5 M H₂SO₄ electrolyte. A resistance test was obtained (~8 Ω) via electrochemical impedance spectroscopy (EIS) and *iR* compensation was applied. Figure 3A shows the polarization curves at 5 mV s⁻¹ with current density normalized by geometric surface area. Initial cleaning of the electrocatalyst surface was performed by cycling

between 0–1.2 V vs. RHE at 100 mV s⁻¹ for 100 cycles at 25 °C under Ar bubbling. Both d-WSe₂/CFM and r-WSe₂/CFM show onset HER activity near –150 mV vs. RHE, while CFM, WO₃/CFM and CVD synthesized WSe₂ NPs show negligible HER activity. A current density of 31.7 mA cm⁻² is achieved at –300 mV vs RHE for d-WSe₂/CFM, which is the highest value for WSe₂ catalyst to the best of our knowledge as shown in Table S1.^{12, 21, 36, 37} An enhancement in cathodic current density can also be observed for d-WSe₂/CFM as compared to that of r-WSe₂/CFM (Figure 3A), indicating that the dendritic structure is more active since its highly dense edge sites is beneficial for the hydrogen evolution. However, r-WSe₂ is also a novel structure for WSe₂ and may be found application for other research fields. Tafel slope is associated with the elementary steps in HER. The first step of HER is a discharge step (Volmer reaction) in which protons are adsorbed to active sites on the surface of the catalysts and combined with electrons to form adsorbed hydrogen atoms.²¹ It is followed by a combination step (Tafel reaction) or a desorption step (Heyrovsky reaction). From the Tafel slope calculated (Figure 3B), we estimated the rate determining steps of our catalyst. As shown in Table S1, 80 mV dec⁻¹ and 163 mV dec⁻¹ were obtained for d-WSe₂/CFM and r-WSe₂/CFM, respectively. The high Tafel slope (163 mV dec⁻¹) of r-WSe₂/CFM, similar to the chemical exfoliated WSe₂ (120 mV dec⁻¹, ref. 36), indicates that the rate-determining step is the discharge step, with a very small surface coverage of adsorbed hydrogen. The significant decrease in Tafel slope can be observed for d-WSe₂/CFM (80 mV dec⁻¹), which is attributed to the unique dendritic structure of WSe₂ that reduces free energy barrier of the discharge step.¹² The electrochemical double layer capacitance (EDLC) was employed to estimate the active surface areas of the 3D electrodes,³⁸ as shown in Figure S8. The EDLC of d-WSe₂/CFM is about 2.6 times larger than that of r-WSe₂/CFM, indicating a highly effective surface area of d-WSe₂. EIS was also conducted to study the electrode kinetics at –0.25 V vs RHE. The EIS results could well exhibit the advantage of the d-WSe₂/CFM quantitatively. As shown in Figure 3C, nyquist plots reveals a significant decrease in charge-transfer resistance (RCT) for d-WSe₂/CFM (~0.2 Ω) as compared to that of r-WSe₂/CFM (~1.2 Ω), WO₃/CFM (~610 Ω) and CFM (~260 Ω). The small resistances show the advantage of the facile approach for active electrocatalyst on conductive substrate, which enables simple and effective electrical integration that minimize Ohmic losses.³⁹ The HER catalytic activities of d-WSe₂/CFM, and r-WSe₂/CFM are believed associated with their different morphologies and electronic properties, which play very important roles in the overall HER performance.³⁹ The as-synthesized 3D dendritic WSe₂ electrode with a small Tafel slope, large available surface area as well as small resistances is a promising candidate for HER applications.

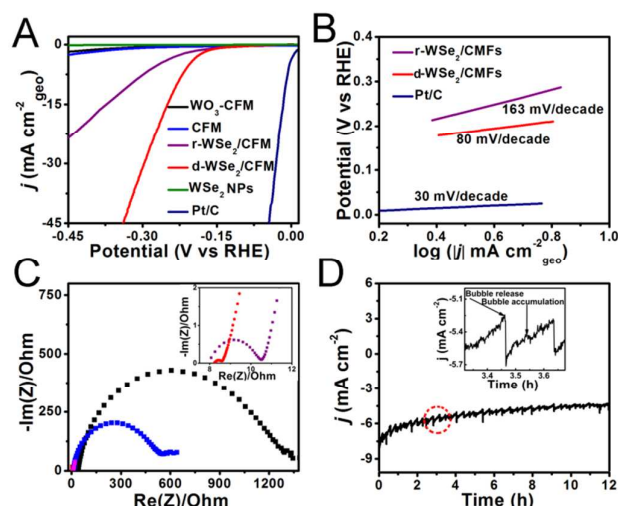


Figure 3. A) Polarization curves (after iR correction) obtained with several catalysts as indicated. B) Corresponding Tafel plots for r -WSe₂/CFM, d -WSe₂/CFM and Pt/C. C) EIS Nyquist plots collected at a bias voltage of -0.250 V vs RHE. D) Time dependence of current density under static overpotential of -0.215 V vs RHE. Inset is the enlargement of the area denoted by the dash circle.

Furthermore, two types of durability tests of d -WSe₂/CFM were also conducted. The CV test for 1000 cycles (Figure S9) indicated that excellent stability of the electrode. The SEM and TEM images of d -WSe₂/CFM after 1000 cycles were also obtained (Figure S10). In fact, the morphology and structure of d -WSe₂/CFM do not get obvious change after 1000 CV cycles, further indicating the good stability of the catalyst. The other durability test, time dependence of current density at a constant potential for a period of time (Figure 3D) implied that the current density reach a constant after an acceptable slight decrease. Although a serrate shape of current was observed that is relative to the alternate processes of bubble accumulation and the bubble release.

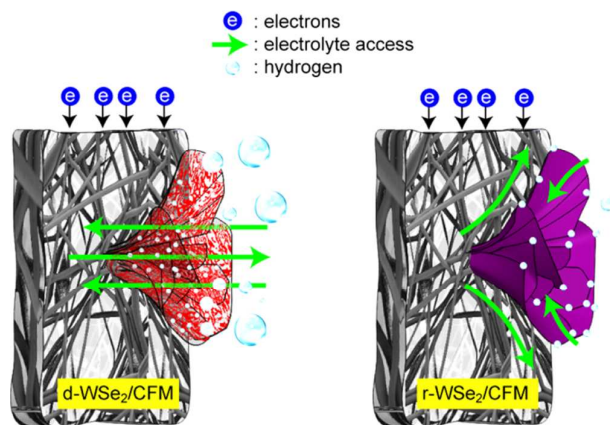


Figure 4. Schematic illustration of electrochemical behavior of d -WSe₂/CFM and r -WSe₂/CFM for HER.

The electrochemical behaviors of d -WSe₂/CFM and r -WSe₂/CFM are illustrated in Figure 4. Electrons can transfer through the carbon nanofiber to WSe₂ catalyst that grown on the CFM.

Hydrogen ions at the active sites of WSe₂ catalyst are reduced by the transferred electrons, followed by release of hydrogen gas. For the d -WSe₂/CFM, the electrolyte containing hydrogen ions can access large amount of edge sites through the dendritic structure, leading to much more hydrogen bubbles released from the electrode. r -WSe₂/CFM exhibits a relatively poorer performance due to the less edge sites on the smooth leaves of WSe₂.

Conclusions

In summary, dendritic WSe₂ on conductive CFM was designed and synthesized by a diffusion-controlled CVD method. The d -WSe₂/CFM exhibits remarkable enhancement in HER performance due to the effectively exposed edge sites. Moreover, the much lower charge-transfer resistance of d -WSe₂/CFM, the high conductivity of carbon nanofiber and the formed 3D structure are experimentally verified and well correlated to the improvement of HER activity. Above all, a facile method for synthesizing 3D structural electrode was established. It will open up a new pathway for developing more efficient HER catalysts in the near future.

Acknowledgements

This work was supported by the National Natural Science Foundation of China (NSFC) (Grant No. 51373154 and 21203137) and the 521 Talent Project of Zhejiang Sci-Tech University.

Notes

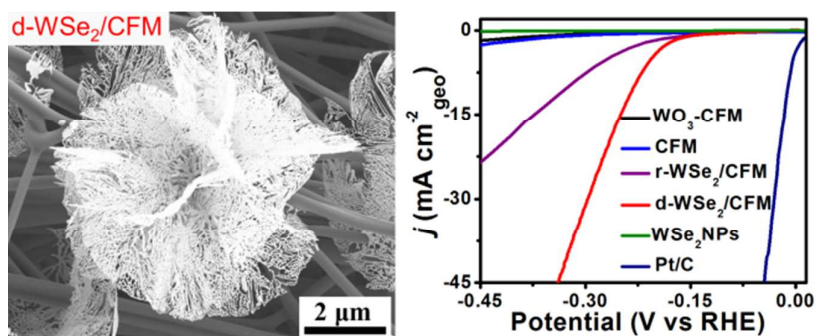
¹These authors contributed equally.

*Corresponding author

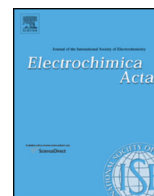
References

- I. Dincer, C. Acar, *Int. J. Hydrogen Energy*, DOI: <http://dx.doi.org/10.1016/j.ijhydene.2014.12.035>.
- Y. Zheng, Y. Jiao, M. Jaroniec and S. Z. Qiao, *Angew. Chem. Int. Edit.*, 2015, **54**, 52-65.
- Y. H. Chang, C. T. Lin, T. Y. Chen, C. L. Hsu, Y. H. Lee, W. Zhang, K. H. Wei and L. J. Li, *Adv. Mater.*, 2013, **25**, 756-760.
- D. V. Esposito, S. T. Hunt, Y. C. Kimmel and J. G. Chen, *J. Am. Chem. Soc.*, 2012, **134**, 3025-3033.
- W. F. Chen, J. T. Muckerman and E. Fujita, *Chem. Comm.*, 2013, **49**, 8896-8909.
- H. H. Li, C. H. Cui, S. Zhao, H. B. Yao, M. R. Gao, F. J. Fan and S. H. Yu, *Adv. Energy Mater.*, 2012, **2**, 1182-1187.
- X. Cao, Y. Han, C. Gao, Y. Xu, X. Huang, M. Willander and N. Wang, *Nano Energy*, 2014, **9**, 301-308.
- C. Wang, M. Chi, G. Wang, D. van der Vliet, D. Li, K. More, H. H. Wang, J. A. Schlueter, N. M. Markovic and V. R. Stamenkovic, *Adv. Funct. Mater.*, 2011, **21**, 147-152.
- S. Shin, Z. Jin, D. H. Kwon, R. Bose and Y. S. Min, *Langmuir*, 2014, **31**, 1196-1202.
- H. Tang, K. Dou, C. C. Kaun, Q. Kuang and S. Yang, *J. Mater. Chem. A*, 2014, **2**, 360-364.

- 11 M. A. Lukowski, A. S. Daniel, C. R. English, F. Meng, A. Forticaux, R. J. Hamers and S. Jin, *Energ. Environ. Sci.*, 2014, **7**, 2608-2613.
- 12 K. Xu, F. Wang, Z. Wang, X. Zhan, Q. Wang, Z. Cheng, M. Safdar and J. He, *ACS Nano*, 2014, **8**, 8468-8476.
- 13 C. Tsai, K. Chan, F. Abild-Pedersen and J. K. Nørskov, *Phys. Chem. Chem. Phys.*, 2014, **16**, 13156-13164.
- 14 D. Y. Chung, S. K. Park, Y. H. Chung, S. H. Yu, D. H. Lim, N. Jung, H. C. Ham, H. Y. Park, Y. Piao, S. J. Yoo and Y. E. Sung, *Nanoscale*, 2014, **6**, 2131-2136.
- 15 X. L. Zheng, J. B. Xu, K. Y. Yan, H. Wang, Z. L. Wang and S. H. Yang, *Chem. Mater.* 2014, **26**, 2344-2353.
- 16 D. Y. Chung, S. Park, Y. Chung, S. Yu, D. Lim, N. Jung, H. C. Ham, H. Park, Y. Piao, S. J. Yoo and Y. Sung, *Nanoscale*, 2014, **6**, 2131-2136.
- 17 B. Liu, T. Luo, G. Mu, X. Wang, D. Chen and G. Shen, *ACS Nano*, 2013, **7**, 8051-8058.
- 18 H. Fang, S. Chuang, T. C. Chang, K. Takei, T. Takahashi and A. Javey, *Nano Lett.*, 2012, **12**, 3788-3792.
- 19 R. Cheng, D. Li, H. Zhou, C. Wang, A. Yin, S. Jiang, Y. Liu, Y. Chen, Y. Huang and X. Duan, *Nano Lett.*, 2014, **14**, 5590-5597.
- 20 W. Zhang, M. H. Chiu, C. H. Chen, W. Chen, L. J. Li and A. T. S. Wee, *ACS Nano*, 2014, **8**, 8653-8661.
- 21 H. Wang, D. Kong, P. Johanes, J. J. Cha, G. Zheng, K. Yan, N. Liu and Y. Cui, *Nano Lett.*, 2013, **13**, 3426-3433.
- 22 H. Zhu, M. L. Du, M. Zhang, M. L. Zou, T. T. Yang, S. L. Wang, J. M. Yao and B. C. Guo, *Chem. Commun.*, 2014, **50**, 15435-15438.
- 23 H. Zhu, M. L. Du, M. Zhang, M. L. Zou, T. T. Yang, Y. Q. Fu and J. M. Yao, *J. Mater. Chem. A*, 2014, **2**, 7680-7685.
- 24 H. Zhu, F. L. Lyu, M. L. Du, M. Zhang, Q. F. Wang, J. M. Yao and B. C. Guo, *ACS Appl. Mater. Inter.*, 2014, **6**, 22126-22137.
- 25 I. Sunagawa, *Forma*, 1999, **14**, 147-166.
- 26 S. Jin, M. J. Bierman and S. A. Morin, *J. Phys. Chem. Lett.*, 2010, **1**, 1472-1480.
- 27 G. Zhang, S. Sun, M. Cai, Y. Zhang, R. Li and X. Sun, *Sci. Rep.*, 2013, **3**, 1526.
- 28 L. Chen, B. Liu, A. N. Abbas, Y. Ma, X. Fang, Y. Liu and C. Zhou, *ACS Nano*, 2014, **8**, 11543-11551.
- 29 A. Zhuang, J. J. Li, Y. C. Wang, X. Wen, Y. Lin, B. Xiang, X. Wang and J. Zeng, *Angew. Chem.*, 2014, **126**, 6543-6547.
- 30 C. Li, L. Huang, G. P. Snigdha, Y. Yu and L. Cao, *ACS Nano*, 2012, **6**, 8868-8877.
- 31 S. Wang, Y. Rong, Y. Fan, M. Pacios, H. Bhaskaran, K. He and J. H. Warner, *Chem. Mater.*, 2014, **26**, 6371-6379.
- 32 J. K. Huang, J. Pu, C. L. Hsu, M. H. Chiu, Z. Y. Juang, Y. H. Chang, W. H. Chang, Y. Iwasa, T. Takenobu and L. J. Li, *ACS Nano*, 2013, **8**, 923-930.
- 33 H. Wang, D. Kong, P. Johanes, J. J. Cha, G. Zheng, K. Yan, N. Liu and Y. Cui, *Nano Lett.*, 2013, **13**, 3426-3433.
- 34 J. Xie, H. Zhang, S. Li, R. Wang, X. Sun, M. Zhou, J. Zhou, X. W. Lou and Y. Xie, *Adv. Mater.*, 2013, **25**, 5807-5813.
- 35 S. Chen, J. Duan, Y. Tang, B. Jin and S. Zhang Qiao, *Nano Energy*, 2015, **11**, 11-18.
- 36 A. Y. S. Eng, A. Ambrosi, Z. Sofer, P. Šimek and M. Pumera, *ACS Nano*, 2014, **8**, 12185-12198.
- 37 J. M. Velazquez, F. H. Saadi, A. P. Pieterick, J. M. Spurgeon, M. P. Soriaga, B. S. Brunshwig and N. S. Lewis, *J. Electroanal. Chem.*, 2014, **716**, 45-48.
- 38 D. S. Kong, H. T. Wang, Z. Y. Lu, Y. Cui, *J. Am. Chem. Soc.* 2014, **136**, 4897-4900
- 39 M. A. Lukowski, A. S. Daniel, F. Meng, A. Forticaux, L. Li, S. Jin, *J. Am. Chem. Soc.*, 2013, **135**, 10274-10277.



3D dendritic WSe₂ on conductive carbon nanofiber mats (d-WSe₂/CFM) was synthesized and directly used as hydrogen evolution cathode.



Controlled morphology evolution of electrospun carbon nanofiber templated tungsten disulfide nanostructures



Meiling Zou, Ying Jiang, Meng Wan, Ming Zhang, Han Zhu, Tingting Yang, Mingliang Du*

Department of Materials Engineering, College of Materials and Textiles, Zhejiang Sci-Tech University, Hangzhou 310018, PR China

ARTICLE INFO

Article history:

Received 13 May 2015

Received in revised form 29 June 2015

Accepted 5 July 2015

Available online 8 July 2015

Keywords:

tungsten disulfide

sulfur vapor

chemical vapor deposition

hydrogen evolution reaction

ABSTRACT

Three-dimensional (3D) WS₂-nanoflower decorated and two-dimensional (2D) WS₂-nanosheet (NS) wrapped carbon nanofiber (CNF) nanostructures are constructed through a simple approach using (NH₄)₂WS₄ contained electrospun polyacrylonitrile nanofibers (W-PAN NFs) and S powder as the precursor. (NH₄)₂WS₄ are thermally decomposed into WS₂ nanoparticles (NPs) during a pre-oxidation treatment of W-PAN NFs. Interestingly, the introducing of S vapor during the carbonization of W-PAN NFs results in unexpected migration of WS₂ nanoparticles (WS₂ NPs) from the inside of CNFs to the surface to form WS₂ NSs or WS₂ nanoflowers. It is believed that S not only controls the initial nucleation of WS₂ on the surface of CNFs but also induces the migration of WS₂ NPs and directs the growth of WS₂ into various morphologies. The synthesized catalysts are directly used as the electrode for hydrogen evolution reaction (HER) and they exhibit good electrocatalytic activity.

© 2015 Elsevier Ltd. All rights reserved.

1. Introduction

The discovery of the unique properties of graphene has prompted intensive studies into layered semiconducting transition metal dichalcogenides (TMDCs). These materials, such as those in the class MX₂ (M = Mo, W and X = Se, S), have electronic properties complementary to those of semimetallic graphene [1–10]. In recent years, the preparation of thinly-layered TMDCs has been of great interest to researchers due to their favourable properties, including semiconductivity, superconductivity, and superior field emissivity, and the ability to form charge density waves. These characteristics are of great importance for a number of applications, such as electronic devices, catalysis, supercapacitors, and battery systems [11–17].

Combinations of TMDCs with other functional materials have been widely studied as candidate components for a wide range of applications. Carbon nanomaterials ranging from 1D carbon nanotubes (CNTs) or CNFs, to 2D graphene nanosheets (NS) and 3D carbon fiber papers have been investigated as TMDC substrates due to their large specific surface areas, outstanding electronic conductivities, and high charge mobilities [13,18–24]. For instance, 2D WS₂ NS grown on a reduced graphene oxide (rGO) support were recently tested as a catalyst for enhancing the hydrogen evolution

reaction. The superior catalytic performance of this hybrid material was attributed to the enhanced charge transfer kinetics that arose from the rapid electron transfer between the catalytic WS₂ NS and the rGO support [20].

WS₂ is a 2D, anisotropic material with a trigonal prismatic structure, formed by stacks of “sandwiches” consisting of a layer of W atoms between two layers of S atoms [25]. This structure gives rise to remarkable physical and chemical properties. However, the development of reliable methods for the batch production of layered WS₂ has lagged behind comparable efforts for MoS₂. Moreover, significant work is still required to explore the fundamental characteristics of WS₂ and adapt it for use in practical applications. Synthesis of high-quality WS₂ with 2D NS-like structures is of key importance in order to realize the potential of this material [26–28]. WS₂ sheets with thicknesses from one single layer to a few layers have been obtained via mechanical and chemical exfoliation [26,29,30]. These methods limit the amount of control that can be exerted over the physical features of the exfoliated sheets [29]. Solvothermal reactions are another path that may be used for the production of WS₂ NSs, but this method often results in solvent residues on the surfaces of the NSs, which are difficult to remove and may negatively impact the intrinsic properties of the NSs.

As is well known, chemical vapor deposition (CVD) has been used to grow several-layer nanoflakes of WS₂. One such process uses WO₃ thin films as a precursor material which is then

* Corresponding author. Tel: +86-571-86843763; Fax: +86-571-86843255.

E-mail address: du@zstu.edu.cn (M. Du).

subjected to a rapid sulfurization process under an inert environment (or in a mixed atmosphere with H_2 gas) [31–38]. Unfortunately, due to the structural differences between WO_x and MoO_3 , sulfurization of the WO_x precursor tends to lead to the formation of 0D fullerene-like or 1D nanotube/nanorod-like WS_2 nanostructures [39,40]. As such, the lack of a facile, reliable method for the synthesis of WS_2 NSs has also prevented research into hybrid materials combining WS_2 and carbonaceous materials such as CNFs, despite their high potential for use in a number of applications.

In recent years, our group has studied the synthesis of TMDCs with controllable size, and hybrid materials on CNFs. These hybrid materials have high surface area and exhibit excellent performance in electrochemical catalytic applications [41–43]. In this work, the synthesis of 2D WS_2 NSs and 3D WS_2 nanoflowers on electrospun CNFs is reported using $(NH_4)_2WS_4$ -containing electrospun PAN NFs (W-PAN NFs) as the precursor material.

Firstly, uniformly-distributed WS_2 nanoparticles (NPs) with diameters of ~ 3 nm were thermally decomposed from $(NH_4)_2WS_4$ contained in the W-PAN NFs. Subsequently, the PAN NFs contained WS_2 NPs were carbonized under higher temperature at Ar atmosphere. Furthermore, an efficient route has been developed to transfer these WS_2 NPs from inside CNFs into 3D WS_2 nanoflowers or 2D WS_2 NS forms grown on the outside surfaces of CNFs. This is accomplished by sublimating S powder into the Ar gas flow as a multifunctional reagent during carbonization of W-PAN NFs. Interestingly, the morphology of the resulting WS_2 can be tailored by adjusting the amount of S present in the system. A possible reaction pathway and a formation mechanism for 3D WS_2 surface nanoflowers and 2D WS_2 NSs were proposed. The synthesized catalysts were directly assembled as catalytic electrodes for electrocatalytic hydrogen production, which not only exploited the merits of CNFs, such as high surface area and good conductivity, but also avoided the usage of polymer binder to immobilize the catalyst which will benefit the practical application of the catalysts. The synthesized electrode treated by a small amount of S vapour (10 g) exhibits the best HER performance among these electrodes, in which the WS_2 catalyst with 3D flower like nanostructure exposed more active edge sites and the conductive CNFs provides a short path for fast charge transfer and transport.

2. Experimental

2.1. Synthesis of PAN nanofibers (PAN NFs) and $(NH_4)_2WS_4$ contained PAN nanofibers (W-PAN NFs) Mats

The PAN NFs were synthesized by electrospinning method. Typically, 3.86 g PAN powder was dissolved in 30 mL dimethyl formamide (DMF, 99.5%) under magnetic stirring to get a homogeneous solution. Therefore, the mass fraction of PAN in the DMF solution was 12 wt%. The solutions were transferred into a syringe with a stainless copper needle at the tip and then electrospun under a fixed voltage of 12 kV and the needle to collector distance was 12 cm with the flow rate at 0.01 mL min^{-1} . During electrospinning process the temperature was $25 \pm 2^\circ\text{C}$ and the humidity was 45 %RH. The electrospun fibers were collected onto a piece of aluminium foil. W-PAN NFs were prepared by adding additional $(NH_4)_2WS_4$ powder in above PAN/DMF solution by electrospinning under the same condition. The concentration of $(NH_4)_2WS_4$ is 10 wt% based on the weight of PAN powder.

2.2. Preparation of carbon nanofibers (CNFs) and carbon nanofiber templated WS_2 nanostructures (WS_2 -CNFs) Mats

The PAN and W-PAN NFs mats were collected and peeled off from the aluminium foil, cut into pieces, placed into a boat, and put into a CVD furnace for heat treatment. Typically, the nanofibrous mats were heated to 280°C from room temperature within 1 h, and maintained for 6 h for the sufficient pre-oxidation of the nanofibrous mats as well as the thermal decomposition of $(NH_4)_2WS_4$. The furnace was then heated to 1000°C within 2.5 h under Ar flow (150 sccm) and maintained for another 8 h for the graphitization of the nanofibrous mats. Finally, the products were cooled to room temperature under Ar atmosphere.

2.3. CVD Growth Process of S treated WS_2 -CNFs (S_x - WS_2 -CNFs, where $x = 10$ or 100) Mats

The W-PAN NFs mats with a certain size were placed in a boat and put at the center of the furnace. After 6 h thermal treatment of W-PAN NFs mats under air condition, the pressure in the chamber was reduced to 50 Pa for 10 min, and Ar (150 sccm) was then allow into the reaction tube, reaching a pressure of 400 Pa. The furnace was heated to 1000°C within 2.5 h, then a boat with 10 or 100 mg of S powder was placed outside the furnace. This zone was wrapped with a heating belt, which was heated to a temperature of 150°C . The furnace was maintained at 1000°C for another 8 h. The typical thermal treatment under S vapor environment and temperature ramps for both the furnace and the heating belt is shown in Fig. S1.

2.4. Electrochemical characterization

The as-grown WS_2 catalysts on CNFs were tested in 0.5 M H_2SO_4 (aq) electrolyte (deaerated by N_2). The catalysts were cut into $1 \times 1 \text{ cm}^{-2}$ with the cross section diameter about 15–20 μm and fixed in a Teflon electrode clamp and directly used as the working electrode. Using a Pt mesh as the counter electrode, and a saturated calomel electrode ($E(\text{RHE}) = E(\text{SCE}) + 0.265 \text{ V}$ after calibration) as the reference electrode. Linear sweep voltammetry (LSV), cyclic voltammetry (CVs) and electrochemical impedance spectroscopy (EIS) are recorded by CHI660E workstation (Shanghai Chenhua, Shanghai). LSV were conducted beginning at +0.3 V and ending at -0.6 V with a scan rate of 5 mV s^{-1} . EIS measurements were carried out at a constant -0.25 V vs RHE, while sweeping the frequency from 5 MHz to 20 mHz.

2.5. Characterization

The thermal properties of $(NH_4)_2WS_4$ powder, pure electrospun PAN NFs and W-PAN NFs with $(NH_4)_2WS_4$ content of 10 wt% were carried out on a Perkin-Elmer Pyris 1 Thermogravimetric analyzer (TGA) with a heating rate of 20°C/min from 20 to 800°C in a nitrogen atmosphere. The morphology of the prepared samples was observed by a JSM-6700F FE-SEM (JEOL, Japan) at an acceleration voltage of 3 kV. Transmission electron microscope (TEM) images and SAED patterns of all the samples were obtained with a JSM-2100 transmission electron microscopy (JEOL, Japan) at an acceleration voltage of 200 kV. X-ray photoelectron spectra of the samples were recorded using an X-ray photoelectron spectrometer (Kratos Axis Ultra DLD) with an aluminum (mono) $K\alpha$ source (1486.6 eV). Raman spectra were recorded by a Renishaw inVia Raman microscope using a 514.5 nm laser excitation source. The high-angle annular dark field scanning TEM (HAADF STEM) images, EDS mapping images, and were collected by a STEM (Tecnai G2 F30 S-Twin, Philips-FEI) at an acceleration voltage of 300 kV.

3. Results and discussion

In the present investigations, we prepared CNFs by carbonizing an electrospun PAN NFs precursor. Fig. S2 a and b show SEM images of the electrospun PAN NFs with homogeneously distributed diameters in the range 300–400 nm. After the pre-oxidation and carbonization treatments at 1000 °C, the diameter of the graphitized CNFs was reduced significantly to approximately 200 nm (Fig. S2 c and d). Thermal studies of the PAN NFs, W-PAN NFs with a $(\text{NH}_4)_2\text{WS}_4$ concentration of 10 wt%, and $(\text{NH}_4)_2\text{WS}_4$ powder were carried out using TGA analysis, as shown in Fig. S3. The $(\text{NH}_4)_2\text{WS}_4$ powder began to lose weight at approximately 200 °C and was fully decomposed to WS_2 at 345 °C in the N_2 atmosphere. The pure PAN NFs began to degrade at approximately 305 °C. However, the W-PAN NFs degraded at a relatively lower temperature of approximately 280 °C because of the decomposition of the $(\text{NH}_4)_2\text{WS}_4$. The decomposition of $(\text{NH}_4)_2\text{WS}_4$ is believed to also destroy its interactions with PAN chains and accelerate the thermal decomposition of PAN NFs, leading to the lower thermal stability of W-PAN NFs. Moreover, the final weight loss of PAN NFs was almost 100%, whereas that of W-PAN NFs was approximately 97% because of WS_2 residue produced, which was the decomposition product of $(\text{NH}_4)_2\text{WS}_4$ in the precursor.

Fig. 1 a and b show SEM images of electrospun W-PAN precursor NFs with a $(\text{NH}_4)_2\text{WS}_4$ concentration of 10 wt%. Evidently, the electrospun W-PAN nanofibers are straight, homogeneously distributed and exhibit a relatively large diameter compared to that of PAN NFs, probably because of the increased viscosity of PAN/DMF solution when $(\text{NH}_4)_2\text{WS}_4$ was added. The morphology of WS_2 -CNFs (Fig. 1 c and d) is similar to that of W-PAN NFs, except that the diameter of the fibers is greatly decreased after the thermal treatments. The inset in Fig. 2d shows the EDS spectra of WS_2 -CNFs. The atomic ratio of W to S was approximately 1:2, suggesting efficiently decomposition of $(\text{NH}_4)_2\text{WS}_4$ to WS_2 species. An O peak was also observed in the spectrum of WS_2 -CNFs, which may indicate that a small portion of WS_2 NPs on the surface of CNFs

was oxidized to WO_x during the pre-oxidation process of W-PAN in air. WS_2 NPs on the surface of WS_2 -CNFs are too small to be observed.

Fig. 2a, b, and c show TEM images of WS_2 -CNFs at different magnifications. A large amount of WS_2 NPs with an ultrafine diameter (~ 3 nm) are observed uniformly embedded in CNFs backbone. Further insight into the morphology and distribution of WS_2 NPs was obtained through HAADF STEM images, which are shown in Fig. 2d and e. The small and bright dots are recognized as WS_2 NPs and are uniformly distributed in CNFs. Fig. 2f shows the spatially resolved C, O, W and S elemental maps obtained from mapping the area in image e. The element distributions verify the homogenous dispersion of ultrafine WS_2 NPs inside the CNFs. In addition, as shown in Fig. 2c, the CNFs exhibit disordered surface regions with stacks of graphite sheets. These graphitic layers are either very loosely attached, discontinuous or collapsed, thus resulting in decreased sp^2 hybridization and providing numerous defects on the surfaces of CNFs.

As most of the WS_2 NPs are embedded in CNFs rather than exposed on their surface, which may cause inefficient contact during the catalytic reactions, thus, activation and migration of the WS_2 NPs to the surface of CNFs is essential to realize their potential applications. Recently, we discovered that WS_2 NPs exhibit unexpected behaviour and migrate from the inside of CNFs to the surface to form a large number of 3D flower-like WS_2 nanostructures when a small amount of S powder (10 mg) was mildly sublimated and carried by an Ar flow during the carbonization of W-PAN. The sample prepared using this process is denoted as S_{10} - WS_2 -CNFs. The typical thermal treatment under an S vapor environment and the temperature ramps used in the synthesis procedure are shown in Fig. S1.

As shown in Fig. 3a, the synthesized WS_2 nanoflowers are separated from one another with diameters in the range of 5–10 μm . More details of the morphologies are revealed in Fig. 3b. As evident in this image, each nanoflower with slightly helical twisted petals is more likely to be rolled up from separated WS_2 NSs, which

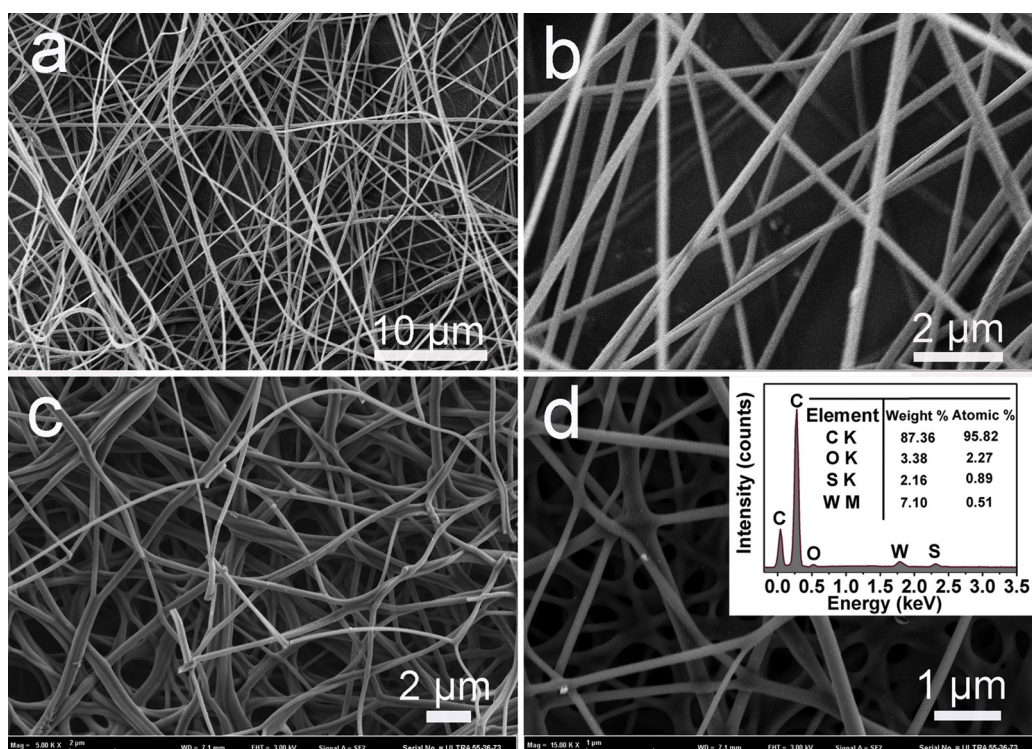


Fig. 1. (a and b) SEM images of W-PAN NFs and (c and d) WS_2 -CNFs carbonized from W-PAN NFs precursors with a $(\text{NH}_4)_2\text{WS}_4$ concentration of 10 wt%.

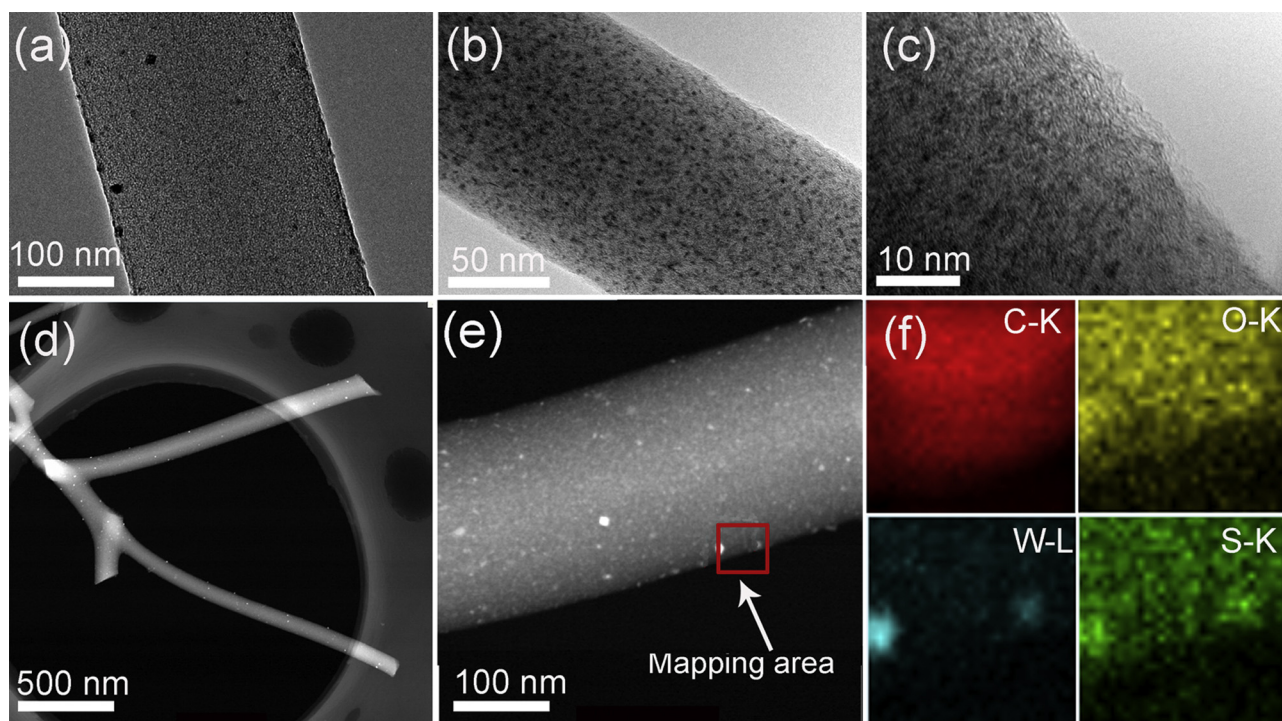


Fig. 2. (a, b, and c) TEM images and (d, e) HAADF STEM images of WS₂-CNFs at various magnifications; (f) spatially resolved C, O, W and S elemental maps obtained from the mapping area in image (e).

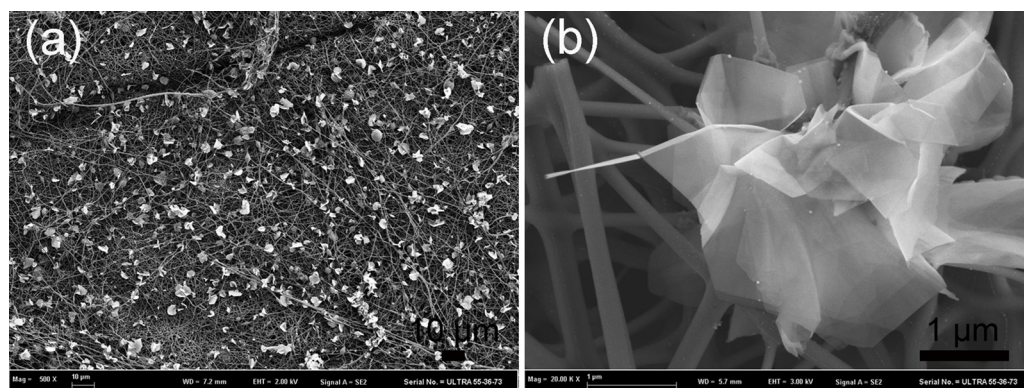


Fig. 3. (a and b) SEM images of S₁₀-WS₂-CNFs.

is quite different from previously reported WS₂ flakes with close stacking [44]. Each individual NS is typically between hundreds of nanometers and several micrometers in size and is highly anisotropic in morphology, giving rise to a lateral dimension/thickness ratio of several thousand.

The results from TEM measurements and SAED characterizations of S₁₀-WS₂-CNFs are presented in Fig. 4a–f. Fig. 4a is typical of a rather small, randomly observed WS₂ nanoflower that contains several loosely stacked WS₂ NSs. An individual NS (Fig. 4b) exhibits high crystallinity and a honeycomb-like structure, and the SAED pattern taken for an individual NS reveals a well-indexed pure hexagonal structure of 2H-WS₂ (Fig. 4c). The HRTEM and SAED results indicate that the petals of WS₂ nanoflowers are consisted of single crystals. The TEM images in Fig. 4d and e give close-up views of the NSs of WS₂ nanoflowers attached to CNFs surfaces. Skew-stacked and folded WS₂ NSs can be observed, as indicated in the SAED pattern in Fig. 4f. The edges of the folded WS₂ NSs (Fig. 4e) clearly indicate that the NSs are multilayered (5–10 layers), with an

interlayer spacing of 0.62 nm, which corresponds to the (002) planes of WS₂. One possible reason for the rolling nature of the WS₂ nanoflowers is that 2D NSs are relatively unstable and prefer to form a closed structure by rolling up to decrease the number of dangling bonds as well as the total energy of the system [41].

Composition analysis of the S₁₀-WS₂-CNFs was carried out using HAADF STEM and EDS element mapping. Fig. 4g and h present HAADF STEM images of S₁₀-WS₂-CNFs. Fig. 4g presents a single WS₂ nanoflower attached to CNFs, and the inset shows an SEM image of a similar structure. As shown in Fig. 4g, the region that appears brighter compared to the flat zones are resulted from the folded edges of the WS₂ nanoflowers, which again indicate that WS₂ nanoflowers are constructed by WS₂ NSs. In addition, as evident from Fig. 4h, ultrafine WS₂ NPs are covered on the surfaces of the CNFs. However, the density of WS₂ NPs is significantly reduced compared with that of WS₂-CNFs (Fig. 2e), which further proves that the inside WS₂ NPs have migrated outside and formed WS₂ NSs and then rolled up to 3D nanoflower-like WS₂ structures.

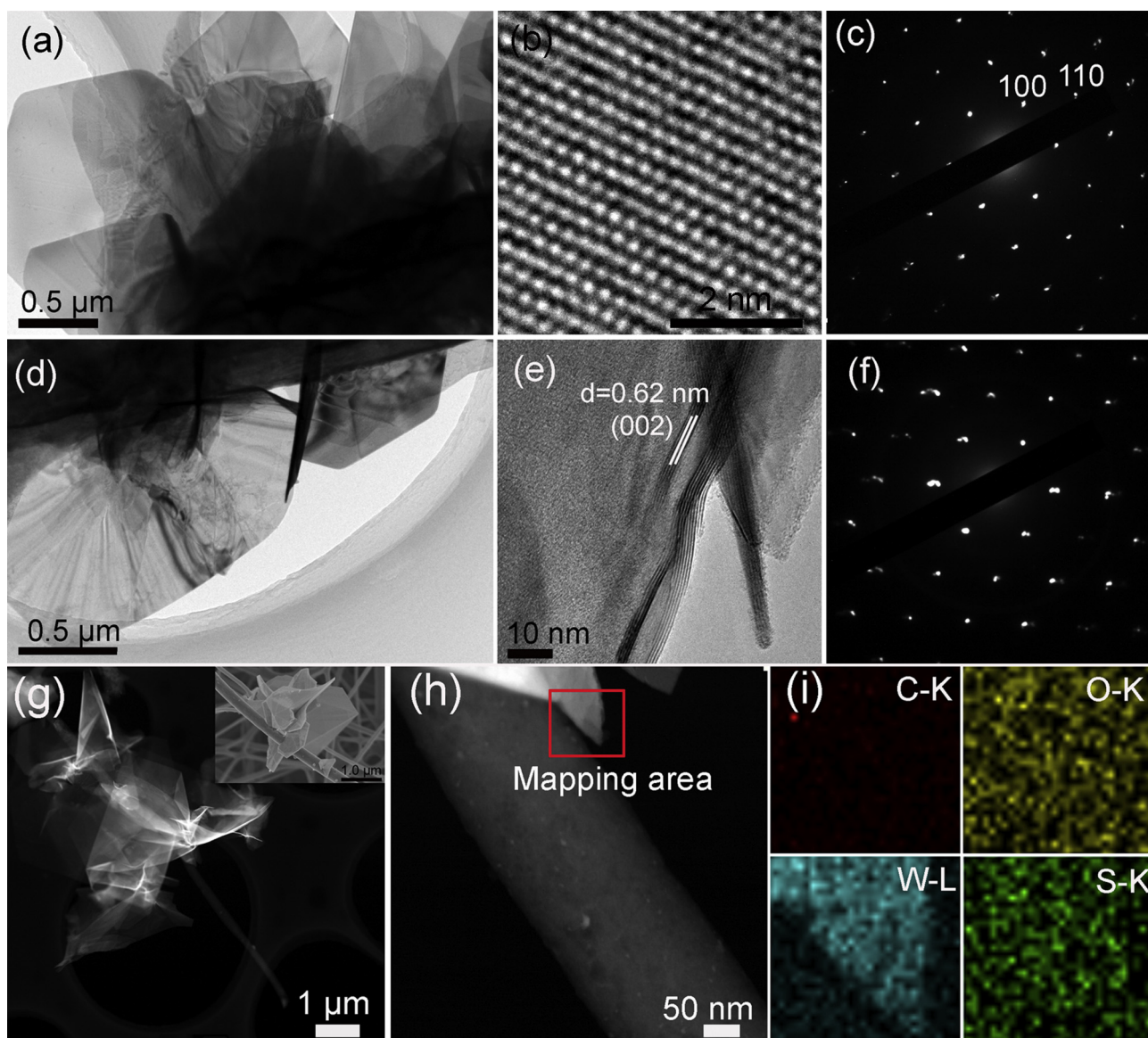


Fig. 4. (a and d, b and e, c and f) Low-magnification TEM images, HRTEM images, and electron diffraction patterns of selected areas (SAED), respectively. (g and h) HAADF STEM images of S_{10} -WS₂-CNFs. (i) Element maps taken from the mapping area in image h.

The aforementioned results clearly suggest that most of the WS₂ NPs reassemble to WS₂ NSs, only leaving a few of the WS₂ NPs embedded inside or on the surface of CNFs. According to previous reports based on scanning tunnelling microscopy of triangular WS₂ crystals and density functional theory calculations for WS₂ clusters, under the conditions of high S availability in the present experiment, the edges of WS₂ NSs are predicted to be tungsten-terminated crystallographic zigzag edges capped by two additional S atoms, which is energetically preferred [45,46]. Due to the highly exposed rims and edges of the WS₂ nanoflowers as well as the improved charge transport caused by the CNF backbone, the S_{10} -WS₂-CNFs nanostructure synthesized here may exhibit promising electrocatalytic performance [47–49].

XPS was used to investigate the chemical state of W and S on the surfaces of the samples at each stage in the synthesis. All the spectra were calibrated by the C 1s peak at 284.50 eV. Fig. 5a displays the spectrum oxidized (NH₄)₂WS₄ (O-(NH₄)₂WS₄) that has been exposed to an air environment at 280 °C for 6 h. The W 4f_{5/2} and W 4f_{7/2} peaks of O-(NH₄)₂WS₄ are located at 38.09 and 35.94 eV, respectively, indicating a +6 oxidation state of W. The

presence of intense W⁶⁺ peaks in the XPS data demonstrates that (NH₄)₂WS₄ was efficiently decomposed and fully converted into WO₃. The W 4f_{7/2-5/2} and S 2p_{3/2-1/2} spectra of pre-oxidized W-PAN NFs (P-W-PAN NFs), WS₂-CNFs and S_{10} -WS₂-CNFs are shown in Fig. 5b and 5c, respectively. For the S_{10} -WS₂-CNFs sample, doublet peaks for the binding energy of W 4f_{5/2} and 4f_{7/2} appear at 34.64 and 32.46 eV, indicating an oxidation state of W⁴⁺ (Fig. 5b), and doublet peaks for S 2p_{1/2} and S 2p_{3/2} appear at 162.15 and 163.32 eV, indicating S²⁻ (Fig. 5c). These peaks are identical to those of pure, highly crystalline WS₂. In the case of the P-W-PAN NFs sample, doublet peaks for the binding energy of W 4f_{5/2} and W 4f_{7/2} are observed at 38.10 and 35.94 eV, respectively, corresponding to W⁶⁺. However, the peak for S²⁻ is not observed (Fig. 5c), suggesting that the WS₂ NPs originating from decomposition of (NH₄)₂WS₄ and located on the surface of the P-W-PAN NFs were completely oxidized to WO₃ during the long pre-oxidation treatment process. In the case of WS₂-CNFs obtained by further carbonization of the P-W-PAN NFs in an Ar environment at 1000 °C for 8 h, the W 4f XPS spectrum (Fig. 5b) shows two sets of peaks. These peaks were fitted after deconvolution of the W 4f

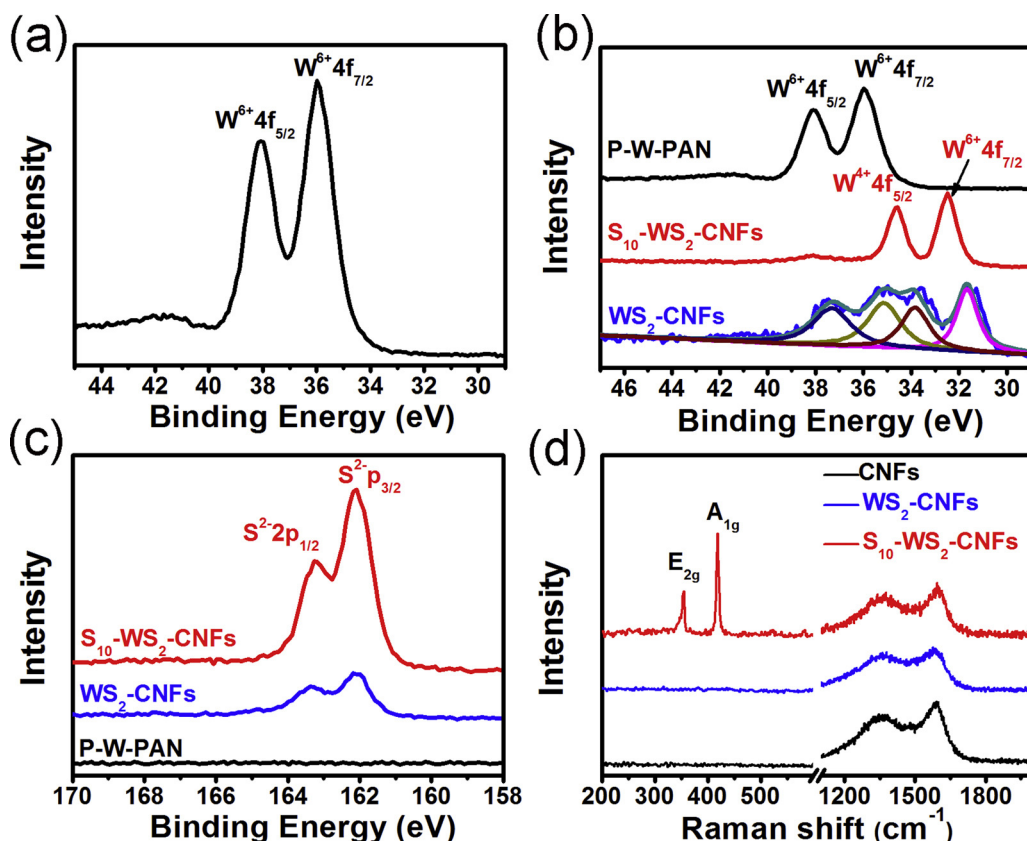


Fig. 5. Chemical composition analysis of (a) $O-(NH_4)_2WS_4$ by XPS for W 4f. (b) W 4f and (c) S 2p XPS spectra of the P-W-PAN NFs, WS_2 -CNFs and S_{10} - WS_2 -CNFs. (d) Raman spectrum of the CNFs, WS_2 -CNFs and S_{10} - WS_2 -CNFs.

peaks. The $W 4f_{5/2}$ and $W 4f_{7/2}$ peaks located at 38.09 and 35.94 eV correspond to W^{6+} , whereas the peaks located at 34.64 and 32.46 eV correspond to W^{4+} . The S 2p XPS spectrum (Fig. 5c) for WS_2 -CNFs exhibits doublet peaks at 162.15 and 163.32 eV, in accordance with the 2H phase of WS_2 . The aforementioned results suggest that WO_3 NPs and WS_2 NPs coexist on the surfaces of the WS_2 -CNFs. The emergence of new W^{4+} peaks compared to the spectrum of the P-W-PAN NFs is likely caused by the shrinking of the P-W-PAN NFs under the elevated temperature from 280 °C to 1000 °C during sample preparation, which would result in a portion of the inside WS_2 NPs being exposed on the outside surface of the WS_2 -CNFs.

The compositions and phases of the as-prepared CNFs, WS_2 -CNFs and S_{10} - WS_2 -CNFs samples were further confirmed by Raman spectroscopy, as shown in Fig. 5d. The D and G bands of the CNFs at 1354.50 and 1587.60 cm^{-1} , respectively, can be clearly observed in all the three samples. In the Raman spectrum of S_{10} - WS_2 -CNFs, the peaks distinguished at 353.60 and 418.37 cm^{-1} for WS_2 correspond to the E_{2g} and A_{1g} modes, respectively. The peak intensities for different vibration modes depend on the layer orientations [50]. The A_{1g} mode of S_{10} - WS_2 -CNFs is much more intense than the E_{2g} mode, indicating that the WS_2 is terminated by edges on the surface. A peak for WS_2 is not observed for WS_2 -CNFs.

Based on the above results and discussion, a possible reaction procedure and formation mechanism called “inside-out” mechanism for the formation of 3D nanoflower-like WS_2 on CNFs is proposed in Fig. 6. First, a homogenous dispersion of $(NH_4)_2WS_4$ in PAN NFs can be realized through electrospinning. Then, during a pre-oxidation treatment of the W-PAN NFs, $(NH_4)_2WS_4$ is gradually decomposed to form WS_2 NPs uniformly distributed inside the P-W-PAN NFs. Simultaneously, the WS_2 NPs close to the outside surface of P-W-PAN NFs are generally oxidized under these air rich

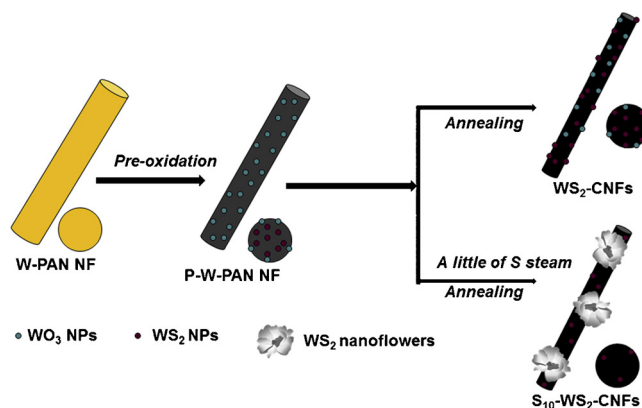


Fig. 6. Illustration of the proposed synthesis of WS_2 NPs and WS_2 nanoflowers on CNFs.

conditions to form small WO_3 NPs. After further carbonization at 1000 °C in an Ar atmosphere, the diameters of WS_2 -CNFs are greatly reduced, which enables a portion of WS_2 NPs inside the CNFs to break through the CNFs, leading to the coexistence of WO_3 NPs and WS_2 NPs on the outside surfaces of WS_2 -CNFs. By introducing a small amount of S vapor during the carbonization process, the WS_2 NPs inside CNFs are reassembled and converted into 3D nanoflower-like WS_2 on the surfaces of CNFs. Without doubt, the S vapor plays a critical role in the formation of the 3D WS_2 nanoflowers. Briefly, the surface WO_3 NPs are first reduced by S vapor to form volatile suboxides WO_{3-x} , which are then further sulfurized to WS_2 species on the surfaces of CNFs. We believe that the newly sulfurized WO_3 NPs may act as nucleation sites during

the earliest stages of growth of WS₂ NSs and they can “fill” the defects of CNFs and attach with the carbon molecules through van der Waals bonds. Because S is highly reactive, WS₂ NPs inside CNFs are activated by the S vapor. In addition, the active S vapor facilitates the diffusion of W and S species inside CNFs to the surface of CNFs, toward the expanding clusters. Lateral growth can eventually promote the coalescence of neighbouring WS₂ by rolling up, leading to a large variety of 3D nanoflower-like WS₂ structures on the surfaces of CNFs. In conclusion, S acts not only as a reducing agent to sulfurize the surface WO₃ NPs but also as a catalyst to induce and direct the growth of 2D WS₂ NSs. Notably, CNFs can be regarded as a storehouse of WS₂ NPs for subsequent construction of the resulting 3D WS₂ nanoflowers, leading to a suitable diffusion rate of WS₂ that is controlled by the space constraints of the CNFs. Thus, the WS₂ nucleation and growth steps are governed by the active S vapor and the CNFs. In this case, 10 mg of S is not sufficient to totally complete the sulfurization and growth. As a result, a small portion of WS₂ NPs remained inside or on the surfaces of CNFs, as detected by SEM and TEM.

To further explore and substantiate that S vapor is indeed influence the nucleation and growth of WS₂ NSs, we also

conducted control studies by changing the amount of S powder. A sample prepared using an S content of 100 mg (we denote this sample as S₁₀₀-WS₂-CNFs) was examined by SEM and TEM and the results are shown in Fig. 7. Both large and small pieces of WS₂ NSs coexisted, as seen in the low magnification SEM image in Fig. 7a. The large pieces of WS₂ NSs are obviously separated with diameters as large as 10 μm. Fig. 7b shows a magnified SEM image, as shown in Fig. 7b, smaller WS₂ NSs (~5 μm) with irregular shapes were randomly and separately distributed on the surface of CNFs backbone. The morphologies of the WS₂ NSs can be classified into two types: those that wrapping at the surfaces of CNFs and those that “standing” on the surfaces of CNFs, as shown in the TEM images in Fig. 7c and d, respectively. Fig. 7c shows the first type of WS₂ NS morphology. In this case, the surfaces of CNFs are wrapped with WS₂ NSs, and this interesting behaviour is likely caused by the rolling of WS₂ NSs along the CNFs' axis. Overlapping WS₂ NSs can be identified, and this result is further supported by the SAED pattern inset in Fig. 7c. The SAED pattern unambiguously suggests that WS₂ NSs are also configured in the 2H phase. Fig. 7b and d show WS₂ NSs “standing” on CNFs. In this case, a portion of large WS₂ NSs are gathered on CNFs, in particular, no WS₂ NPs can be

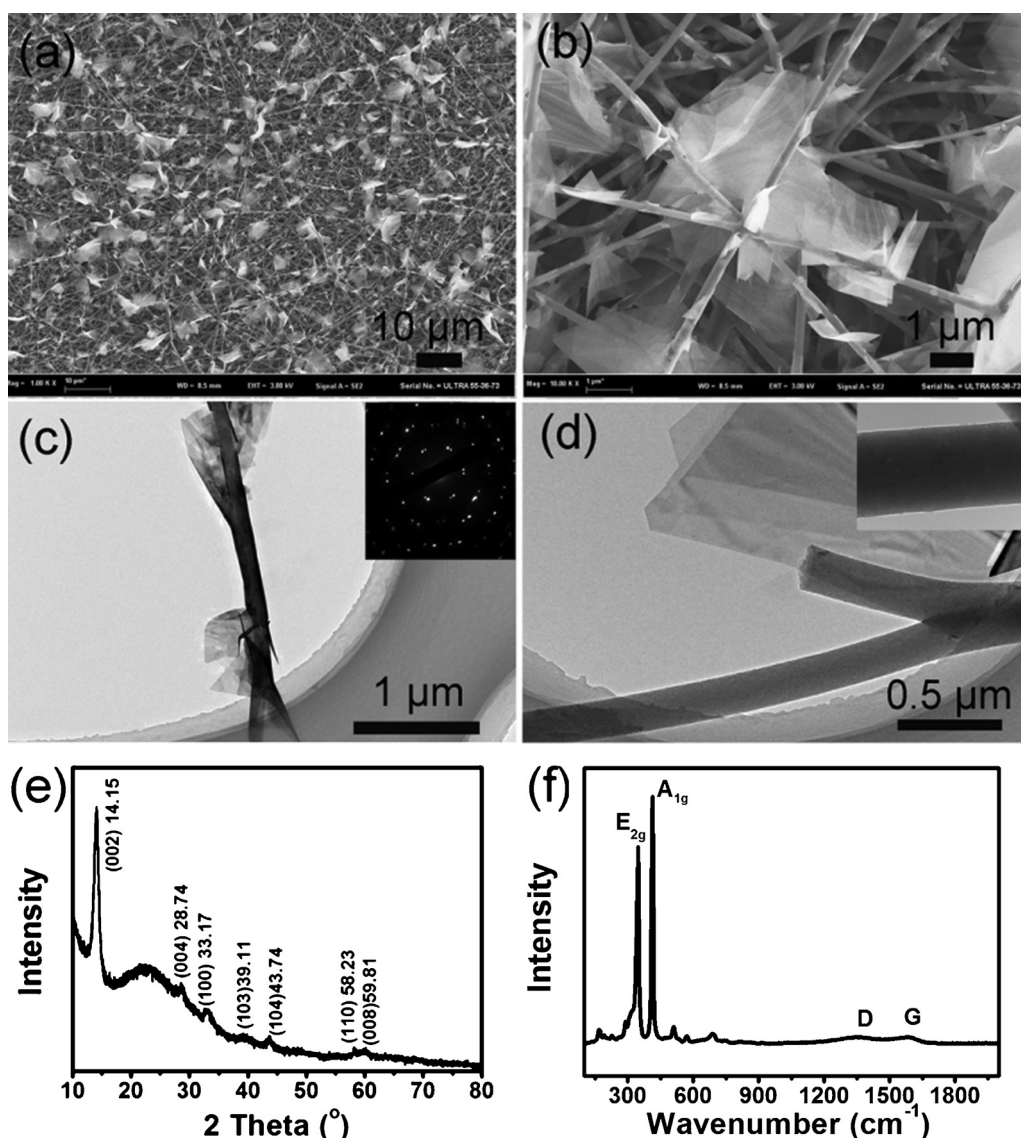


Fig. 7. (a and b, c and d, e, f) SEM images, TEM images, Raman and XRD patterns of S₁₀₀-WS₂-CNFs, respectively. The insets in (b) and (c) show the SAED pattern of the corresponding WS₂ NSs and the TEM image of CNF, respectively.

observed in CNF backbone (inset in Fig. 7d), indicating the complete removal of WS₂ NPs from the inside CNFs and their conversion into WS₂ NSs. The XRD measurement was also employed to evaluate the crystal structure of S₁₀₀-WS₂-CNFs. As shown in Fig. 7e, the diffraction peaks are all in consistent well with the standard pattern of hexagonal WS₂ (JCPDS card No. 08-0237) and no diffraction peaks of WO₃ can be observed. In addition, we conducted Raman spectroscopy on this sample. As shown in Fig. 7f, the two peaks located at 353.59 and 418.37 cm⁻¹ match well with the E_{2g} and A_{1g} vibration modes of WS₂, respectively. The distinct Raman peaks ascribed to the D (1354.50 cm⁻¹) and G (1587.60 cm⁻¹) bands of carbon was significantly decreased because of the increased density of WS₂ NSs covering the sidewalls of CNFs. We reasonably inferred that a higher concentration of S vapor promotes the reduction of WO₃ to provide a more WO_{3-x}-rich environment for the growth of WS₂ NSs. The number of nucleation sites is substantially increased and, meanwhile, the sulfurization and growth of WS₂ NSs are also expedited. Some large pieces of WS₂ NSs appear, which may be resulted from the fast growth rate of WS₂ NSs as well as the coalescence of small pieces of WS₂ NSs. Moreover, because of the excellent affinity of WS₂ NSs for the CNF side walls, the scrolling of a mass of WS₂ NSs along CNF backbones to reduce the total energy of the system and form more stable structures is favourable. Therefore, when more S vapor is introduced, WS₂ NSs tend to wrap CNFs rather than gather together and roll up to form 3D flower-like WS₂.

As described above, it is believed that the highly exposed rims and edges of the WS₂ nanoflowers and the high charge transport efficiency of S₁₀-WS₂-CNFs nanostructure may benefit to the electrocatalytic performance. In the present investigations, the catalytic activities of S₁₀-WS₂-CNFs, S₁₀₀-WS₂-CNFs and WS₂-CNFs

samples were examined in a standard three-electrode electrochemical cell setup with 0.5 M H₂SO₄ electrolyte. The catalysts were directly used as the working electrode, avoiding the usage of a polymer binder to immobilize the catalyst on the electrode surfaces, such as glassy carbon electrode, which will benefit the practical application of the catalysts. CVs were taken several cycles to bubble away the surface contaminates and stabilize the catalysts. The potential values are all plotted with reference to the standard reversible hydrogen electrode (RHE) and the current measurements were normalized by the geometric area of the tested samples.

As shown in Fig. 8a, compared to WS₂-CNFs and S₁₀₀-WS₂-CNFs, S₁₀-WS₂-CNFs exhibits lower onset overpotential (η) of about 150 mV, while CNFs show negligible HER activity. In addition, the current density of S₁₀-WS₂-CNFs was higher than that of other electrocatalysts in the whole potential region. For example, the cathodic current density (j) of S₁₀-WS₂-CNFs is 9.3 mA cm⁻² at -300 mV, which is 4.3 and 12.2 times higher than the current density of S₁₀₀-WS₂-CNFs and WS₂-CNFs, respectively, suggesting the better HER performance. As the Tafel slope is associated with the elementary steps in HER, the Tafel plots derived from Fig. 8a are shown in Fig. 8b, where the linear portions were fitted to the Tafel equation ($\eta = b \log j + a$, where b is the Tafel slope) to calculate the slopes [51]. The first step of HER is a discharge step (Volmer reaction) in which protons are adsorbed to active sites on the surface of the catalysts and combined with electrons to form adsorbed hydrogen atoms. It is followed by a combination step (Tafel reaction) or a desorption step (Heyrovsky reaction). From the Tafel slope calculated, the Tafel slope of S₁₀-WS₂-CNFs is 110 mV dec⁻¹, which outperformed the S₁₀₀-WS₂-CNFs (127 mV dec⁻¹) and WS₂-CNFs (147 mV dec⁻¹), respectively. The relatively small Tafel

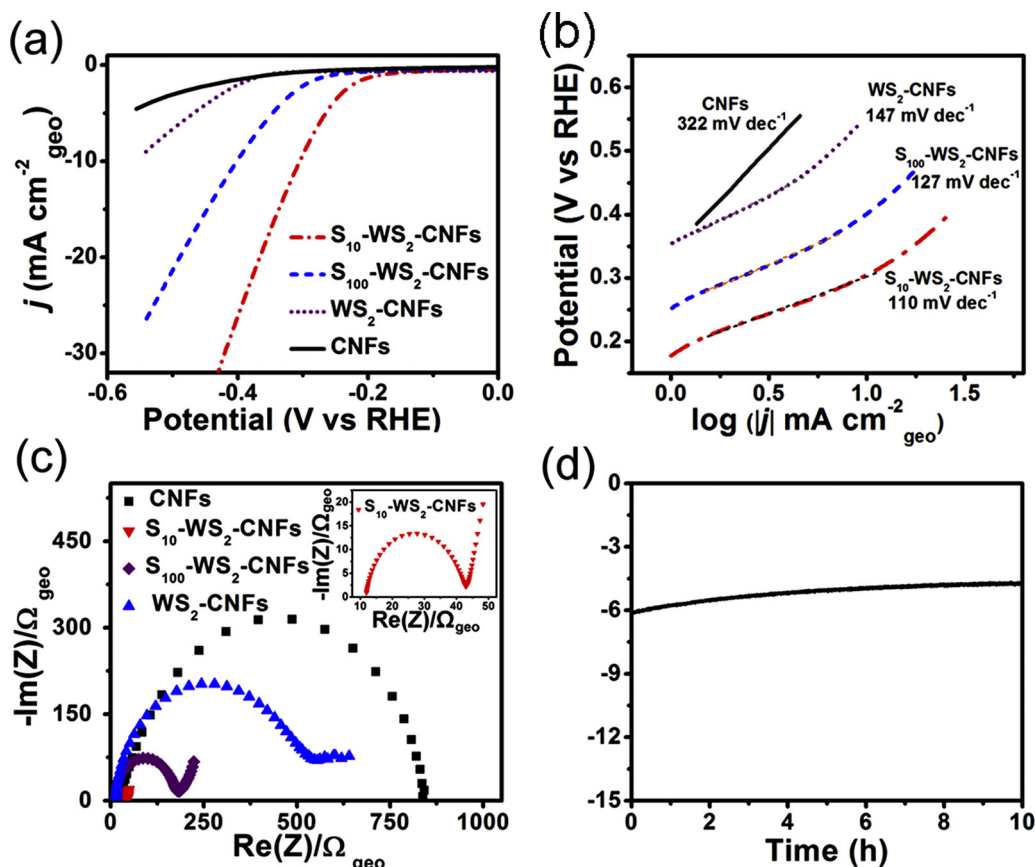


Fig. 8. (a) Polarization curves obtained with several catalysts as indicated. (b) Corresponding Tafel plots. (c) EIS Nyquist plots collected at a bias voltage of -0.25 V vs RHE. (d) Time dependence current density of S₁₀-WS₂-CNFs under static overpotential of -0.28 V vs RHE in 0.5 M H₂SO₄.

slope of S_{10} - WS_2 -CNFs sample observed here is desirable to drive a large catalytic current density at lower overpotential, which is a desired property for the practical application of HER catalysts. These results demonstrate dramatic effect of the WS_2 morphologies on their HER performance. The CNFs support substantially increased the conductivity of all the synthesized catalysts and provided high surface area to contact with electrolyte. Therefore, the enhanced HER activity of S_{10} - WS_2 -CNFs can be mainly ascribed to its unique morphology of 3D flower like WS_2 catalyst. Compared to S_{100} - WS_2 -CNFs and WS_2 -CNFs, S_{10} - WS_2 -CNFs dispersed 3D flower like WS_2 on the surface of CNFs without aggregation and exposed more active edge sites for HER. In case of WS_2 -CNFs, it exhibited fairly lower performance for HER, because the WS_2 NPs were dispersed in the CNFs, resulting in that the active catalytic sites were almost hindered. Therefore, the introduction of S vapour to the synthesis system is crucial in exploiting the HER activity of the catalysts.

Electrochemical impedance spectroscopy (EIS) measurements were conducted for further characterization of the synthesized catalysts. Fig. 8c shows the corresponding Nyquist plots of these electrocatalysts. The semicircle in the Nyquist plot of each sample represents the charge transfer process at the interface between electrocatalyst and electrolyte, which is consisted of charge transfer resistance (R_{ct}) and corresponding capacitance. As is known, R_{ct} value varies inversely to the electrocatalytic activity. Fig. 8c shows a decreased charge-transfer resistance (R_{ct}) for S_{10} - WS_2 -CNFs ($\sim 15 \Omega$) relative to S_{100} - WS_2 -CNFs ($\sim 90 \Omega$), WS_2 -CNFs ($\sim 270 \Omega$) and CNFs ($\sim 400 \Omega$), indicating the smaller charge transfer resistance of S_{10} - WS_2 -CNFs. Thus, such a low R_{ct} value of S_{10} - WS_2 -CNFs indicates that its high electrocatalytic activity for HER could be ascribed to its high electron transfer and increased number of exposed active sites.

Due to the capacitance of the catalysts is proportional to the contact area between the catalysts and electrolyte. The electrochemically active surface areas of these catalysts were also tested by the CV method to measure the electrochemical double-layer capacitance (C_{dl}). CV curves were obtained at various scan rates (5, 10, 15, etc. $mV s^{-1}$) at 0.1–0.2 V vs RHE, as shown in Fig. S4 a, b and c. The halves of the positive and negative differences current density at 0.15 V vs RHE vs the scan rate are plotted in Fig. S4 d. The C_{dl} of these electrodes are calculated to be 55, 46 and $10 mF cm^{-2}$ for S_{10} - WS_2 -CNFs, S_{100} - WS_2 -CNFs, WS_2 -CNFs, confirming that S_{10} - WS_2 -CNFs electrode possesses the largest active surface area among these electrodes. Time dependence current density of S_{10} - WS_2 -CNFs electrode under static overpotential of $-0.28 V$ vs RHE in 0.5 M H_2SO_4 was further conducted to estimate the stability of the electrode. The current density exhibits acceptable slight degradation even after 10 h, which might be resulted from the remaining of H_2 bubbles on the surface of the electrode that hindered the reaction or the consumption of H^+ of the electrolyte. The SEM images, TEM image, and EDS result of the S_{10} - WS_2 -CNFs electrode after 10 h electrolysis are given in Fig. S5, reveals the good stability of the electrode.

All the results above reveal the better HER performance for S_{10} - WS_2 -CNFs. The improved HER activity is primarily attributed to the abundant exposed edge sites caused by 3D structure of WS_2 , as well as the high electric conductivity of the underlying CNFs. S_{100} - WS_2 -CNFs electrode shows inferior activity when compared to S_{10} - WS_2 -CNFs electrode, and this may be caused by the scrolling of WS_2 NSs along the CNF that decreases the exposed edges, as the edges are the efficient catalytic sites for HER [20,28,30]. Compared with previously reported WS_2 nanostructures such as WS_2 grown on reduced graphene oxide [20], which should be immobilized on carbon gassy electrode with polymer binder to perform their HER activity, however, in our present investigation, the CNFs mats based WS_2 catalysts can be directly

used as the electrode rather than loaded on other support materials, which will benefit the large-scale production, long-time stability and practical application.

4. Conclusions

In summary, we developed a simple and efficient strategy for fabricating 3D nanoflower-like or 2D NS-like WS_2 on CNFs. WS_2 nanoparticles (WS_2 NPs) inside CNFs exhibited unexpected behaviour and migrated from the inside to the surfaces of CNFs to form WS_2 NSs or WS_2 nanoflowers with the introduction of S vapor. S plays an important role in controlling the growth and conversion of WS_2 on CNF backbones and WS_2 with different morphologies were achieved by altering the concentration of S vapor. Due to the highly exposed rims and edges of the WS_2 nanoflowers as well as the improved charge transport, the S_{10} - WS_2 -CNFs nanostructure synthesized here exhibit promising electrocatalytic performance. We believe that this new method can provide useful guidance for the development of CNF-based TMDC. Additionally, the novel WS_2 /CNFs nanocomposites prepared here may be potential candidates for a variety of applications in optoelectronics, solar energy conversion, and electrocatalysis.

Acknowledgements

This work was supported by the National Science Foundation of China (NSFC) (Grant No. 51373154), the Program for Innovative Research Team of Zhejiang Sci-Tech University and the 521 Talent Project of Zhejiang Sci-Tech University.

Appendix A. Supplementary data

Supplementary data associated with this article can be found, in the online version, at <http://dx.doi.org/10.1016/j.electacta.2015.07.033>.

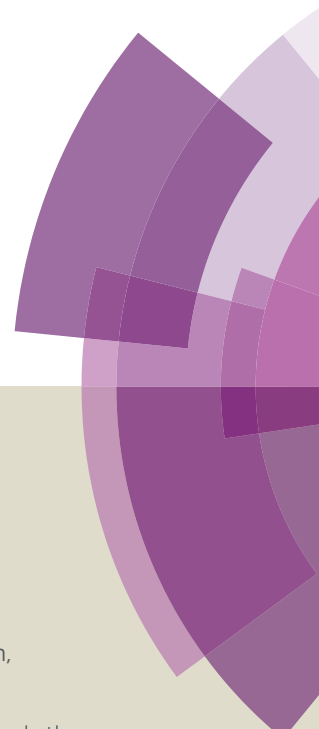
References

- [1] R.L.D. Whitby, W.K. Hsu, T.H. Lee, C.B. Boothroyd, H.W. Kroto, D.R.M. Walton, Complex WS_2 nanostructures, *Chem. Phys. Lett.* 359 (2002) 68.
- [2] X. Huang, Z. Zeng, H. Zhang, Metal dichalcogenide nanosheets: preparation, properties and applications, *Chem. Soc. Rev.* 42 (2013) 1934.
- [3] Z. Chen, A.J. Forman, T.F. Jaramillo, Bridging the gap between bulk and nanostructured photoelectrodes: the impact of surface states on the electrocatalytic and photoelectrochemical properties of MoS_2 , *J. Phys. Chem. C* 117 (2013) 9713.
- [4] G. Cunningham, M. Lotya, C.S. Cucinotta, S. Sanvito, S.D. Bergin, R. Menzel, M.S. P. Shaffer, J.N. Coleman, Solvent exfoliation of transition metal dichalcogenides: dispersibility of exfoliated nanosheets varies only weakly between compounds, *ACS nano* 6 (2012) 3468.
- [5] C. Zhi, Y. Bando, C. Tang, H. Kuwahara, D. Golberg, Large-scale fabrication of boron nitride nanosheets and their utilization in polymeric composites with improved thermal and mechanical properties, *Adv. Mater.* 21 (2009) 2889.
- [6] J.N. Coleman, M. Lotya, A. O'Neill, S.D. Bergin, P.J. King, U. Khan, K. Young, A. Gaucher, S. De, R.J. Smith, I.V. Shvets, S.K. Arora, G. Stanton, H. Kim, K. Lee, G.T. Kim, G.S. Duesberg, T. Hallam, J.J. Boland, J.J. Wang, J.F. Donegan, J.C. Grunlan, G. Moriarty, S. Shmeliov, R.J. Nicholls, J.M. Perkins, E.M. Grieveson, K. Theuvsissen, D.W. McComb, P.D. Nellist, V. Nicolosi, Two-dimensional nanosheets produced by liquid exfoliation of layered materials, *Science* 331 (2011) 568.
- [7] B. Liu, T. Luo, G.Y. Mu, X.F. Wang, D. Chen, G.Z. Shen, Rechargeable Mg-ion batteries based on WSe_2 nanowire cathodes, *ACS nano* 7 (2013) 8051.
- [8] J.K. Huang, J. Pu, C.L. Hsu, M.H. Chiu, Z.Y. Juang, Y.H. Chang, W.H. Chang, Y. Iwasa, T. Takenobu, L.J. Li, Large-area synthesis of highly crystalline WSe_2 monolayers and device applications, *ACS nano* 8 (2014) 923.
- [9] D. Merki, S. Fierro, H. Vrubel, X. Hu, Amorphous molybdenum sulfide films as catalysts for electrochemical hydrogen production in water, *Chem. Sci.* 2 (2011) 1262.
- [10] Y. Yan, B. Xia, X. Ge, Z. Liu, J.Y. Wang, X. Wang, Ultrathin MoS_2 nanoplates with rich active sites as highly efficient catalyst for hydrogen evolution, *ACS Appl. Mater. Interfaces* 5 (2013) 12794.
- [11] M.A. Lukowski, A.S. Daniel, F. Meng, A. Forticaux, L. Li, S. Jin, Enhanced hydrogen evolution catalysis from chemically exfoliated metallic MoS_2 nanosheets, *J. Am. Chem. Soc.* 135 (2013) 10274.

- [12] C.S. Rout, P.D. Joshi, R.V. Kashid, D.S. Joag, M.A. More, A.J. Simbeck, M. Washington, S.K. Nayak, D.J. Late, Superior field emission properties of layered WS₂-RGO nanocomposites, *Sci. Rep.* 3 (2013) 3282.
- [13] H.T. Wang, Z.Y. Lu, D.S. Kong, J. Sun, T.M. Hymel, Y. Cui, Electrochemical tuning of MoS₂ nanoparticles on three-dimensional substrate for efficient hydrogen evolution, *ACS nano* 8 (2014) 4940.
- [14] X. Zheng, J. Xu, K. Yan, H. Wang, Z. Wang, S. Yang, Space-confined growth of MoS₂ nanosheets within graphite: the layered hybrid of MoS₂ and graphene as an active catalyst for hydrogen evolution reaction, *Chem. Mater.* 26 (2014) 2344.
- [15] H. Zhong, G. Yang, H. Song, Q. Liao, H. Cui, P. Shen, C.X. Wang, Vertically aligned graphene-like SnS₂ ultrathin nanosheet arrays: excellent energy storage, catalysis, photoconduction, and field-emitting performances, *J. Phys. Chem. C* 116 (2012) 9319.
- [16] X. Fang, C. Hua, C. Wu, X. Wang, L. Shen, Q. Kong, J. Wang, Y. Hu, Z. Wang, L. Chen, Synthesis and electrochemical performance of graphene-like WS₂, *Chem. Eur. J.* 19 (2013) 5694.
- [17] Y. Shi, Y. Wang, J.I. Wong, A.Y. Tan, C.L. Hsu, L.J. Li, Y.C. Lu, H.Y. Yang, Self-assembly of hierarchical MoS₂/CNT nanocomposites (2 < x < 3): towards high performance anode materials for lithium ion batteries, *Sci. Rep.* 3 (2013) 2169.
- [18] K. Chang, W.X. Chen, L-cysteine-assisted synthesis of layered MoS₂/graphene composites with excellent electrochemical performances for lithium ion batteries, *ACS nano* 5 (2011) 4720.
- [19] I. Zafropoulou, M.S. Katsiotis, N. Boukos, M.A. Karakassides, S. Stephen, V. Tzitzios, M. Fardis, R.V. Vlodea, S.M. Alhassan, G. Papavassiliou, In situ deposition and characterization of MoS₂ nanolayers on carbon nanofibers and nanotubes, *J. Phys. Chem. C* 117 (2013) 10135.
- [20] J. Yang, D. Voiry, S.J. Ahn, D. Kang, A.Y. Kim, M. Chhowalla, H.S. Shin, Two-dimensional hybrid nanosheets of tungsten disulfide and reduced graphene oxide as catalysts for enhanced hydrogen evolution, *Angew. Chem. Int. Ed.* 52 (2013) 13751.
- [21] J. Wu, G. Yue, Y. Xiao, M. Huang, J. Lin, L. Fan, Z. Lan, J.Y. Lin, Glucose aided preparation of tungsten sulfide/multi-wall carbon nanotube hybrid and use as counter electrode in dye-sensitized solar cells, *ACS Appl. Mater. Interfaces* 4 (2012) 6530.
- [22] Y. Li, H. Wang, L. Xie, Y. Liang, G. Hong, H. Dai, MoS₂ nanoparticles grown on graphene: an advanced catalyst for the hydrogen evolution reaction, *J. Am. Chem. Soc.* 133 (2011) 7296.
- [23] Z. Wang, K. Zhao, H. Li, Z. Liu, Z. Shi, J. Lu, K. Suenaga, S.K. Joung, T. Okazaki, Z. Jin, Z. Gu, Z. Gao, S. Iijima, Ultra-narrow WS₂ nanoribbons encapsulated in carbon nanotubes, *J. Mater. Chem.* 21 (2011) 171.
- [24] H. Tang, K. Dou, C.C. Kaun, Q. Kuang, S. Yang, MoSe₂ nanosheets and their graphene hybrids: synthesis, characterization and hydrogen evolution reaction studies, *J. Mater. Chem. A* 2 (2014) 360.
- [25] M. Tehrani, C.C. Luhrs, M.S. Al-Haik, J. Trevino, H. Zea, Synthesis of WS₂ nanostructures from the reaction of WO₃ with CS₂ and mechanical characterization of WS₂ nanotube composites, *Nanotechnology* 22 (2011) 285714.
- [26] C. Nethravathi, A.A. Jeffery, M. Rajamathi, N. Kawamoto, R. Tenne, D. Golberg, Y. Bando, Chemical unzipping of WS₂ nanotubes, *ACS nano* 7 (2013) 7311.
- [27] F. Hoshyargar, T.P. Corrales, R. Branscheid, U. Kolb, M. Kappl, M. Panthofer, W. Tremel, Hybrid chalcogenide nanoparticles: 2D-WS₂ nanocrystals inside nested WS₂ fullerenes, *Dalton. Trans* 42 (2013) 14568.
- [28] L. Cheng, W. Huang, Q. Gong, C. Liu, Z. Liu, Y. Li, H. Dai, Ultrathin WS₂ nanoflakes as a high-performance electrocatalyst for the hydrogen evolution reaction, *Angew. Chem. Int. Ed.* 126 (2014) 1.
- [29] M.A. Ibrahim, T.W. Lan, J.K. Huang, Y.Y. Chen, K.H. Wei, L.J. Li, C.W. Chu, High quantity and quality few-layers transition metal disulfide nanosheets from wet-milling exfoliation, *RSC Adv* 3 (2013) 13193.
- [30] M.A. Lukowski, A.S. Daniel, C.R. English, F. Meng, A. Forticaux, R.J. Hamers, S. Jin, Highly active hydrogen evolution catalysis from metallic WS₂ nanosheets, *Energy Environ. Sci.* 7 (2014) 2608.
- [31] A. Anto Jeffery, C. Nethravathi, M. Rajamathi, Controlled synthesis and transfer of large-area WS₂ sheets: from single layer to few layers, *J. Phys. Chem. C* 118 (2014) 1386.
- [32] N. Peimyoo, J.Z. Shang, C.X. Cong, X.N. Shen, X.Y. Wu, E.K.L. Yeow, T. Yu, Nonblinking, intense two-dimensional light emitter: monolayer WS₂ triangles, *ACS nano* 7 (2013) 10985.
- [33] S. Tongay, W. Fan, J. Kang, J. Park, U. Koldemir, J. Suh, D.S. Narang, K. Liu, J. Ji, J. Li, R. Sinclair, J. Wu, Tuning interlayer coupling in large-area heterostructures with CVD-grown MoS₂ and WS₂ monolayers, *Nano Lett.* 14 (2014) 3185.
- [34] A.L. Elias, N. Perea-Lopez, A. Castro-Beltran, A. Berkdemir, R. Lv, S. Feng, A.D. Long, T. Hayashi, Y.A. Kim, M. Endo, *ACS nano* 7 (2013) 5235.
- [35] H.G. Fuchtbauer, A.K. Tuxen, P.G. Moses, H. Topsoe, F. Besenbacher, J.V. Lauritsen, Morphology and atomic-scale structure of single-layer WS₂ nanoclusters, *Phys. Chem. Chem. Phys.* 15 (2013) 15971.
- [36] Y. Zhang, Y.F. Zhang, Q.Q. Ji, J. Ju, H.T. Yuan, J.P. Shi, T. Gao, D.L. Ma, M.X. Liu, Y.B. Chen, X.J. Song, H.Y. Hwang, Y. Cui, Z.F. Liu, Controlled growth of high-quality monolayer WS₂ layers on sapphire and imaging its grain boundary, *ACS nano* 7 (2013) 8963.
- [37] N. Zink, H.A. Therese, J. Pansiot, A. Yella, F. Banhart, W. Tremel, In situ heating TEM study of onion-like WS₂ and MoS₂ nanostructures obtained via MOCVD, *Chem. Mater.* 20 (2008) 65.
- [38] T.F. Jaramillo, K.P. Jorgensen, J. Bonde, J.H. Nielsen, S. Horch, I. Chorkendorff, Identification of active edge sites for electrochemical H₂ evolution from MoS₂ nanocatalysts, *Science* 317 (2007) 100.
- [39] B. Gao, H. Fan, X. Zhang, Hydrothermal synthesis of single crystal MoO₃ nanobelts and their electrochemical properties as cathode electrode materials for rechargeable lithium batteries, *J. Phys. Chem. Solids* 73 (2012) 423.
- [40] D. Chen, M. Liu, L. Yin, T. Li, Z. Yang, X. Li, B. Fan, H. Wang, R. Zhang, Z. Li, H. Xu, H. Lu, D. Yang, J. Sun, L. Gao, Single-crystalline MoO₃ nanoplates: topochemical synthesis and enhanced ethanol-sensing performance, *J. Mater. Chem.* 21 (2011) 9332.
- [41] H. Zhu, M.L. Du, M. Zhang, M.L. Zou, T.T. Yang, S.L. Wang, J.M. Yao, B.C. Guo, The design and construction of 3D rose-petal-shaped MoS₂ hierarchical nanostructures with structure-sensitive properties, *Chem. Commun.* 50 (2014) 15435.
- [42] H. Zhu, M.L. Du, M. Zhang, M.L. Zou, T.T. Yang, Y.Q. Fu, J.M. Yao, In situ growth of Rh nanoparticles with controlled sizes and dispersions on the cross-linked PVA-PEI nanofibers and their electrocatalytic properties towards H₂O₂, *J. Mater. Chem. A* 2 (2014) 7680.
- [43] H. Zhu, F.L. Lyu, M.L. Du, M. Zhang, Q.F. Wang, J.M. Yao, B.C. Guo, Design of two-dimensional, ultrathin MoS₂ nanoplates fabricated within one-dimensional carbon nano fibers with thermosensitive morphology: high-performance electrocatalysts for the hydrogen evolution reaction, *ACS Appl. Mater. Interfaces* 6 (2014) 22126.
- [44] V.G. Pol, S.V. Pol, A. Gedanken, Micro to Nano Conversion: A one-step, environmentally friendly, solid state, bulk fabrication of WS₂ and MoS₂ nanoplates, *Cryst. Growth Des* 8 (2008) 1126.
- [45] H.R. Gutierrez, N. Perea-Lopez, A.L. Elias, A. Berkdemir, B. Wang, R. Lv, F. Lopez-Urias, V.H. Crespi, H. Terrones, M. Terrones, Extraordinary room-temperature photoluminescence in triangular WS₂ monolayers, *Nano Lett.* 13 (2013) 3447.
- [46] S. Najmaei, Z. Liu, W. Zhou, X.L. Zou, G. Shi, S.D. Lei, B.I. Yakobson, J. Idrobo, P.M. Ajayan, J. Lou, Vapour phase growth and grain boundary structure of molybdenum disulphide atomic layers, *Nat. Mater.* 12 (2013) 754.
- [47] C.J. Liu, U. Burghaus, F. Besenbacher, Z.L. Wang, Preparation and characterization of nanomaterials for sustainable energy production, *ACS nano* 4 (2010) 5517.
- [48] J.R. McKone, A.P. Pieterick, H.B. Gray, N.S. Lewis, Hydrogen evolution from Pt/Ru-coated p-Type WSe₂ Photocathodes, *J. Am. Chem. Soc.* 135 (2013) 223.
- [49] J. Kim, S. Byun, A.J. Smith, J. Yu, J. Huang, Enhanced electrocatalytic properties of transition-metal dichalcogenides sheets by spontaneous gold nanoparticle decoration, *J. Phys. Chem. Lett.* 4 (2013) 1227.
- [50] Y.Q. Zhu, W.K. Hsu, H. Terrones, N. Grobert, B.H. Chang, M. Terrones, B.Q. Wei, H.W. Kroto, D.R.M. Walton, C.B. Boothroyd, Morphology, structure and growth of WS₂ nanotubes, *J. Mater. Chem.* 10 (2000) 2570.
- [51] Y.W. Tan, P. Liu, L.Y. Chen, W.T. Cong, Y. Ito, J.H. Han, X.W. Guo, Z. Tang, T. Fujita, A. Hirata, M.W. Chen, Monolayer MoS₂ films supported by 3D nanoporous metals for high-efficiency electrocatalytic hydrogen production, *Adv. Mater.* 26 (2014) 8023.

Journal of Materials Chemistry A

Accepted Manuscript



This article can be cited before page numbers have been issued, to do this please use: M. Zou, J. Chen, L. Xiao, H. Zhu, T. Yang, M. Zhang and M. Du, *J. Mater. Chem. A*, 2015, DOI: 10.1039/C5TA04426J.



This is an *Accepted Manuscript*, which has been through the Royal Society of Chemistry peer review process and has been accepted for publication.

Accepted Manuscripts are published online shortly after acceptance, before technical editing, formatting and proof reading. Using this free service, authors can make their results available to the community, in citable form, before we publish the edited article. We will replace this *Accepted Manuscript* with the edited and formatted *Advance Article* as soon as it is available.

You can find more information about *Accepted Manuscripts* in the [Information for Authors](#).

Please note that technical editing may introduce minor changes to the text and/or graphics, which may alter content. The journal's standard [Terms & Conditions](#) and the [Ethical guidelines](#) still apply. In no event shall the Royal Society of Chemistry be held responsible for any errors or omissions in this *Accepted Manuscript* or any consequences arising from the use of any information it contains.



Journal of Materials Chemistry A

ARTICLE

WSe₂ and W(Se_xS_{1-x})₂ nanoflakes grown on carbon nanofibers for the electrocatalytic hydrogen evolution reaction

MeiLing Zou, JiaDong Chen, LongFei Xiao, Han Zhu, TingTing Yang, Ming Zhang, MingLiang Du*

Received 00th January 20xx,
Accepted 00th January 20xx

DOI: 10.1039/x0xx00000x

www.rsc.org/

Transition metal dichalcogenides (TMD) have recently attracted substantial attention due to their potential application to the catalysis of the hydrogen evolution reaction (HER). In this study, triangular WSe₂ and W(Se_xS_{1-x})₂ nanoflakes uniformly dispersed on the surface of electrospun carbon nanofiber mats were synthesized in a chemical vapor deposition (CVD) system. The morphology and structure of these products were systematically characterized, revealing that WSe₂ nanoflakes are configured in the 2H phase with high crystallinity, and the W(Se_xS_{1-x})₂ nanoflakes are configured in the alloy form without any obvious phase separation. The hybrid catalyst mats were directly used as hydrogen evolution cathodes to investigate their HER activity. Excellent HER performances, including low overpotential, high current density and long-term stability, were achieved by optimizing the content of the initial W precursor and the appropriate substitution of selenium with sulfur, which was resulted from the appropriate cover density and thickness of the WSe₂ nanoflakes and the defective structure of the W(Se_xS_{1-x})₂ nanoflakes.

Introduction

Sustainable hydrogen production is an essential prerequisite of the future hydrogen economy, and the electrochemical hydrogen evolution reaction (HER) has been suggested as an efficient route to the sustainable production of H₂.¹⁻⁴ In recent years, active research has continued to develop non-precious metal-based electrocatalysts for HER, including metal sulfides,⁵⁻⁷ metal selenides,⁸⁻¹⁰ metal boride,^{11, 12} metal carbides,¹³⁻¹⁵ metal phosphides,¹⁶⁻¹⁸ and heteroatom-doped nanocarbons.¹⁹⁻²¹ Among the various candidates, layered transition metals (transition metal dichalcogenides, TMD) are of particular interest. Recently, WSe₂, a typical TMD, was demonstrated as a promising HER catalyst; it has a similar structure to that of MoS₂ in which tungsten atoms are sandwiched between selenium atoms in a hexagonal arrangement by strong covalent bonds, and the neighboring layers are bound by weak van der Waals interactions.^{22, 23}

Experimental and computational studies have highlighted that the HER activity of WSe₂ correlates with the number of catalytically active sites.^{24, 25} Many studies have also suggested that the exposed edges or defects serve as the catalytically active sites.^{26, 27} Therefore, the ability to control the synthesis

of nanosized WSe₂ with an abundant amount of edge sites or defects is an effective strategy to obtain an efficient WSe₂ HER electrocatalyst. For example, vertically aligned WSe₂ with preferentially exposed active edge sites was obtained through selenization of a W thin film magnetron sputtered on an Si substrate or carbon fiber paper, which improved the HER performance.²⁶ In our recent investigation, we also demonstrated that 3D dendritic WSe₂ on carbon nanofibers with a high fraction of exposed active edge sites is a highly efficient electrocatalyst for HER.²⁸ In addition to structural engineering, another process to tune the HER activity of TMD can be realized by tailoring their chemical composition. Generally, the incorporation of transition metals, such as Co, Ni, and Fe, into TMD can enhance their catalytic activity for HER.²⁹⁻³¹ Furthermore, partial or full substitution of chalcogens into TMD by other chalcogens has led to satisfactory HER performance.^{27, 32, 33} For example, the introduction of selenium to substitute for sulfur in MoS₂ continuously modulates the d-band electronic structure of molybdenum, resulting in tuned hydrogen adsorption free energy, as well as electrocatalytic activity.³²

Motivated by the success of WSe₂ nanostructures synthesized by chemical vapor deposition (CVD), the present study investigated the growth of WSe₂ nanoflakes and the substitution of selenium with sulfur in WSe₂ to modify its physical and chemical properties. Many experimental studies have suggested that the conductivity of TMD with electrolyte is also indispensable for excellent HER performance.³⁴⁻³⁶ Among the various substrates for HER catalysts, electrospun carbon nanofiber mats (CFM) prepared from electrospun polyacrylonitrile nanofiber mats (PAN FM) after thermal treatments are promising candidates with a large specific

Key Laboratory of Advanced Textile Materials and Manufacturing Technology of the Ministry of Education, College of Materials and Textiles, Zhejiang Sci-Tech University, 310018, P. R. China

Electronic Supplementary Information (ESI) available: Schematic for the set-up used for the growth of W(Se_xS_{1-x})₂ nanoflakes on CFM; SEM images of WO₃-C-10; cross-sectional SEM images of the synthesized catalysts; SEM images of WSe₂-C-y to detect the thickness of the WSe₂ nanoflakes; element maps of W(Se_{0.4}S_{0.6})₂-C-10; EELS spectra; digital photograph of the catalyst mat; CV plots of the catalytic electrodes; Impedance spectra; representative SEM images of the electrodes after chronoamperometric response test for 12h; **The movie of bubble release.** See DOI: 10.1039/x0xx00000x

surface area and favorable high conductivity.³⁷ Synthesizing WSe₂ or W(Se_xS_{1-x})₂ alloy nanoflakes on CFM exploits the merits of CFM and avoids the usage of a polymer binder to immobilize the catalyst on the electrode surfaces, which will benefit the practical application of the catalysts.

In this study, we present the design and fabrication of WSe₂ and W(Se_xS_{1-x})₂ alloy nanoflakes on flexible CFM (W(Se_xS_{1-x})₂-C-y, where x is the atom fraction of chalcogen, and y is the initial mass fraction of the W precursor in PAN powder) via a CVD method. First, WO₃ nanoparticles (WO₃ NPs) were thermally decomposed from (NH₄)₆H₂W₁₂O₄₀ contained in the electrospun PAN FM precursor. Subsequently, WSe₂ or W(Se_xS_{1-x})₂ alloy nanoflakes were synthesized through CVD (Figure S1). In this process, the temperature gradient of the furnace was used to synthesize W(Se_xS_{1-x})₂-C-y, which has been successfully used in previous studies to grow compositionally tunable chalcogenide alloy nanoflakes.^{38, 39} The loading amount of WSe₂ nanoflakes on CFM was tuned by adjusting the initial W precursor in the electrospun PAN FM substrate, and the substitution of selenium with sulfur was realized using selenium along with sulfur powder as the reductants. W(Se_xS_{1-x})₂-C-y directly served as the working electrodes in a three-electrode system and exhibited excellent electrocatalytic properties for HER, displaying a relatively low overpotential, small Tafel slope, high exchange current density and good stability.

Experimental

Ammonium metatungstate hydrate contained PAN FM (W-PAN FM) was prepared via electrospinning following a previous method.²⁸ The WSe₂ or W(Se_xS_{1-x})₂ nanoflakes on the CFM were synthesized through CVD. First, W-PAN FM was cut into suitable flat pieces, placed on an alumina boat, and then moved into the middle of the heating zone of a slender quartz tube for heat treatments. The furnace was heated to 280 °C from room temperature and was maintained at this temperature for 6 h for the sufficient pre-oxidation of the PAN nanofibers, as well as the thermal decomposition of (NH₄)₆H₂W₁₂O₄₀ to form uniformly dispersed WO₃ NPs. Subsequently, a boat loaded with 5 mmol of Se (or 2.5 mmol S + 2.5 mmol Se) powder was placed upstream at a distance of approximately 20 cm from the center of the furnace (Figure S1). Prior to heating to higher temperatures, an Ar flow was introduced into the system at a rate of 150 sccm for 20 min to ensure favorable conditions for the sample synthesis. The furnace was then ramped to 1000 °C at 5 °C min⁻¹ and was maintained at this temperature for another 6 h to sufficiently reduce the WO₃ NPs inside of the PAN nanofibers and to completely graphitize the PAN nanofibers. During this time, the pressure inside of the tube and the flow rate of Ar were maintained at 1 Torr and 150 sccm, respectively. After the treatment, the temperature was allowed to return to room temperature.

Characterizations

The morphology of the prepared samples was observed on a JSM-6700F FE-SEM (JEOL, Japan) at an acceleration voltage of 3 kV. Transmission electron microscopy (TEM) and scanning

transmission electron microscopy (STEM) were performed using a transmission electron microscope (Tecnai G2 F30 S-Twin, Philips-FEI) at an acceleration voltage of 300 kV. X-ray diffraction (XRD) patterns of the hybrid films were obtained on a diffractometer (Bruker AXS D8) using Cu K_α radiation (k = 0.15418) with a 2θ scan from 5 to 80 degrees at a step of 0.02. X-ray photoelectron spectra of the samples were recorded using an X-ray photoelectron spectrometer (Kratos Axis Ultra DLD) with an aluminum (mono) K_α source (1486.6 eV). Raman spectra were recorded using a Renishaw inVia Raman microscope with a 532 nm laser excitation source.

Electrochemical Measurements

The HER performances of the as-grown catalysts were tested in 0.5 M H₂SO₄ (aq) electrolyte (deaerated by N₂). The catalysts mats were cut into 1 × 1 cm² pieces, fixed in a Teflon electrode clamp, and used as the working electrode. A Pt mesh and a saturated calomel electrode (E(RHE) = E(SCE) + 0.244 V) were used as the counter and reference electrodes, respectively. Cyclic voltammograms (CVs) were obtained for 400 cycles to bubble away the surface contaminates and simultaneously stabilize the catalysts. The potential values were plotted with reference to the standard reversible hydrogen electrode (RHE), and the current measurements were normalized to the geometric area of the tested samples. The performance of the hydrogen evolution catalysts was measured using linear sweep voltammetry beginning at +0.3 V and ending at -0.50 V vs RHE with a scan rate of 2 mV s⁻¹. Electrochemical impedance spectroscopy (EIS) was performed when the working electrode was biased at a constant value of -0.15 V vs RHE while sweeping a frequency from 5 MHz to 10 mHz. A chronoamperometric response was required under a static overpotential of -0.2 V vs RHE. All electrochemical studies were performed on a CHI660E workstation (Shanghai Chenhua, Shanghai) in a three-electrode configuration.

Results and discussion

In this study, there were four major steps involved in the detailed growth of WSe₂ nanoflakes on CFM: (1) the thermal decomposition of (NH₄)₆H₂W₁₂O₄₀ contained in the PAN nanofibers to create uniformly dispersed WO₃ NPs (Figure S2), (2) the sublimation and transport of Se vapor by a forced flow of Ar carrier gas, (3) the diffusion of Se vapor from the gas phase onto WO₃ NPs contained on the CFM substrate to reduce the surface WO₃ NPs on the CFM to form volatile suboxides WO_{3-x}, and (4) the rapid selenization of WO_{3-x} NPs into WSe₂ species for the lateral growth or incorporation of WSe₂ nanoflakes on CFM. Because selenium is highly reactive at high temperatures, the WO₃ NPs inside of the carbon nanofibers are activated by the selenium vapor and transform gradually to the outside surface of the CFM to participate in further selenization and growth. As shown in Figure 1, triangular WSe₂ nanoflakes were synthesized on CFM with various coverages using a simple CVD method. The CFM consisting of carbon nanofibers 0.2~0.3 μm in diameter is a three-dimensional substrate after thermal treatments. Figure 1a-c presents the SEM images of WSe₂-C-10, WSe₂-C-20 and WSe₂-C-30, respectively. In previous reports, WSe₂ was

typically only deposited onto the surface of the substrate, such as Si substrates or carbon fiber paper. However, in the present investigation, WSe₂ nanoflakes with triangular morphologies are dispersed uniformly onto the surface of nearly each carbon nanofiber of the three-dimensional CFM (Figure S3), and high HER activity of the catalysts was anticipated due to the high specific area of the CFM and the abundant number of exposed edges of WSe₂.

A typical TEM image of a representative sample (WSe₂-C-10) shows that the obtained WSe₂ nanostructures are bent triangular nanoflakes with edge lengths of 200-500 nm (Figure 1d) on the surface of the carbon nanofibers. Figure 1e shows the high-resolution transmission electron microscopy (HRTEM) image of a typical nanoflake that demonstrates the single-

crystalline nature of the 2D structure with a lattice spacing of 2.8 Å, in agreement with the (100) plane of WSe₂. Elemental mapping on the WSe₂-C-10 sample shows the uniform chemical composition throughout the material (Figure 1f). The differences in the thicknesses of the WSe₂ nanoflakes among these three samples (Figure S4) were also revealed by TEM studies, and the thickness of the WSe₂ nanoflakes increased by increasing the W precursor in the carbon nanofibers. Most of these WSe₂-C-10 triangular nanoflakes have 6-8 layers, whereas WSe₂-C-30 has as many as 15 layers. The differences in thickness of the WSe₂ nanoflakes may result in significant changes in the electrocatalytic activity of the catalysts, which is discussed later.

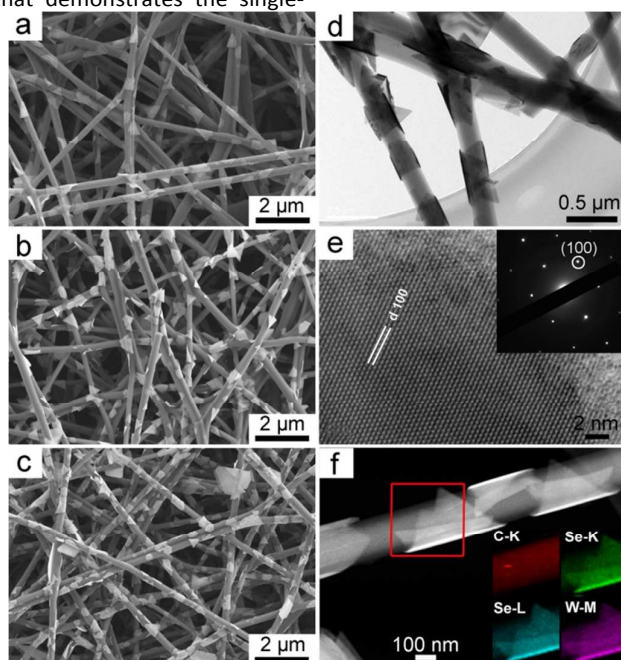


Figure 1. SEM images of (a) WSe₂-C-10, (b) WSe₂-C-20 and (c) WSe₂-C-30; (d) low-magnification TEM image of WSe₂-C-10; (e) HRTEM image of a WSe₂ nanosheet of WSe₂-C-10; (f) high-angle annular dark field (HAADF) STEM image of WSe₂-C-10; inset contains the element maps obtained from the mapping area in image f.

The incorporation of other chalcogens into WS₂ and MoS₂ will enhance their catalytic activity for HER.^{32, 33} For WSe₂, the hydrogen binding energy at the selenide W-edge is too weak ($\Delta G_H = 170$ mV), and theoretical calculations suggest that the substitution of an appropriate portion of selenium by sulfur may help attain a ΔG_H value more close to thermoneutral, leading to improved HER activity.²⁴ Inspired by this strategy, we synthesized W($\text{Se}_x\text{S}_{1-x}$)₂ alloy nanoflakes on CFM and explored their influence on the spectroscopic properties and electrochemical activities of the material. PAN FM containing 10 and 20% (NH₄)₆H₂W₁₂O₄₀ was selected as the representative precursor, and Figures 2a and b present the SEM images of the final products, respectively. Bent triangular nanoflakes were dispersed uniformly on the surface of each carbon nanofiber (Figure S2). The edge lengths of the second sample were approximately two times longer than the lengths of the first sample. TEM combined with energy-dispersive X-ray spectroscopy (EDS) was used to investigate the microstructure and elemental composition of these nanoflakes (Table S1).

Figure 2c shows the typical TEM image of the first sample, and the inset in Figure 2c shows the HRTEM image of the alloy nanoflake with a honeycomb-like structure. The EDS spectrum shown in Figure 1d demonstrates that the nanoflakes consist of W, S, and Se elements with an Se mole fraction [x, Se/(S+Se)] of ~0.4, indicating the composition of the nanoflake as W($\text{Se}_{0.4}\text{S}_{0.6}$)₂, denoted as sample W($\text{Se}_{0.4}\text{S}_{0.6}$)₂-C-10. Analogously, the second sample was denoted as W($\text{Se}_{0.2}\text{S}_{0.8}$)₂-C-20. Note that the increase in the W precursor facilitates the substitution of selenium with sulfur, leading to an increased S mole fraction in the alloy nanoflakes. This observation is reasonable because S is more active than Se at high temperatures, and a faster substitution and growth of the alloy nanoflakes is subsequently promoted, resulting in an increased lateral dimension and decreased Se mole fraction in the alloy nanoflakes. The increased edge lengths would cause decreases in the density of active edge sites, and finally affect the HER activity.^{40]}

EDS element mapping was applied to investigate the spatial distribution of constituent elements within the $W(\text{Se}_x\text{S}_{1-x})_2$ alloys (Figure S5), confirming the homogeneous distribution of W, Se and S elements across the entire substrate. Furthermore, the representative high-resolution element images of $W(\text{Se}_{0.4}\text{S}_{0.6})_2$ -C-10 obtained from STEM are shown in Figures 2e and f. W, Se and S show high spatial correlation over the examined area, suggesting a single-phase construction of nanoscale S and Se with no phase separation of WSe_2 and WS_2 . Moreover, line-scan electron energy loss spectroscopy (EELS) from the indicated position revealed that

the signal intensity of each element changed consistently with the thickness of the alloy nanoflakes (Figure S6). Further insight into the morphology of the alloy nanoflakes revealed many dislocations and distortions compared with single-component WSe_2 nanoflakes (Figure 3). As indicated in many previous studies, these defects typically serve as active sites and can crack the crystal to expose specific crystal planes, subsequently increasing the accessible internal surface area, which may dramatically improve the electrocatalytic HER performance.^{27, 40}

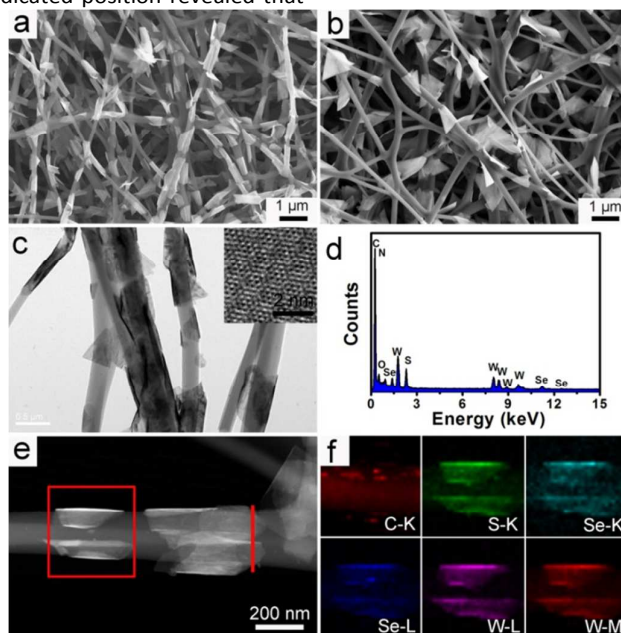


Figure 2. SEM images of (a) $W(\text{Se}_{0.4}\text{S}_{0.6})_2$ -C-10 and (b) $W(\text{Se}_{0.2}\text{S}_{0.8})_2$ -C-20; (c) low-magnification TEM image of $W(\text{Se}_{0.4}\text{S}_{0.6})_2$ -C-10; inset is the HRTEM of the $W(\text{Se}_{0.4}\text{S}_{0.6})_2$ nanoflake; (d) EDS spectrum from the region in image c; (e) HAADF STEM image of $W(\text{Se}_{0.4}\text{S}_{0.6})_2$ -C-10; (f) corresponding element maps obtained from the mapping area in image e.

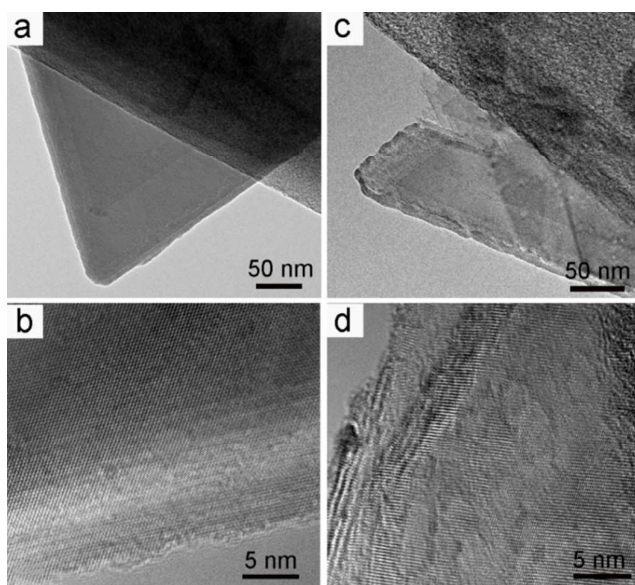


Figure 3. TEM images of (a and b) WSe_2 -C-10 and (c and d) $W(\text{Se}_{0.4}\text{S}_{0.6})_2$ -C-10.



Journal of Materials Chemistry A

ARTICLE

The structural information of the products was investigated by XRD and Raman analysis. As shown in Figure 4a, all of the diffraction peaks in the XRD patterns can be assigned to hexagonal 2H-tungsten dichalcogenide (JCPDS card No. 38-1388), revealing the high purity of the products. The good crystallinity of all of these samples may benefit their electrochemical stability in acidic electrolytes. Moreover, the substitution of selenium by sulfur leads to an upshift of all of the main diffraction peaks, which further implies their mixing at the atomic level.³² As shown in Figure 4b, two broad peaks at 1200-1600 cm^{-2} of all five samples are ascribed to the D and G bands of the carbon nanofiber substrate. Only one prominent peak in the WSe_2 -C-y samples is distinctly observed

below 1000 cm^{-2} , where the A_{1g} and E_{2g} peaks of WSe_2 are expected because these two modes are closely located at 253 and 250 cm^{-2} , respectively.²⁶ With the introduction of sulfur, these vibrational modes shift to higher frequencies, suggesting that the interaction between sulfur and selenium atoms enhances the related W-Se modes and increases their vibrational frequencies. Meanwhile, two pronounced peaks assigned to the 2H WS_2 -like E_{2g} (351.9 cm^{-2}) and A_{1g} (415.8 cm^{-2}) modes emerge. Compared with the respective E_{2g} and A_{1g} peaks at 353.6 and 418.4 cm^{-1} of pure WS_2 nanoflakes, the blue-shift of these two peaks is diagnostic of typical $\text{W}(\text{Se}_x\text{S}_{1-x})_2$ alloys.³²

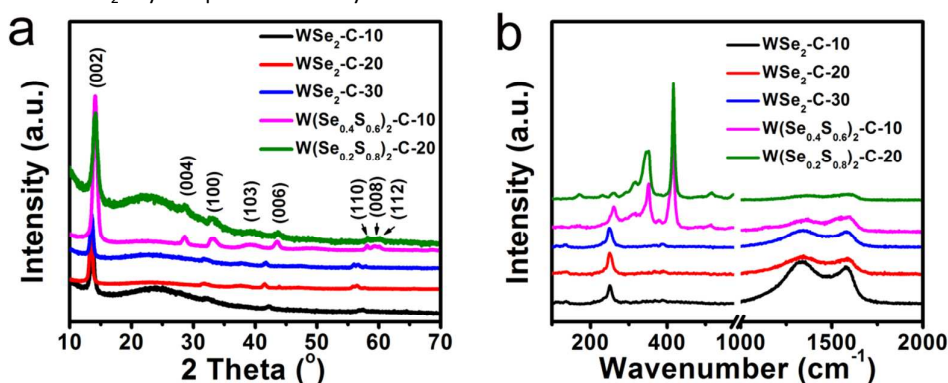


Figure 4. Spectroscopic characterizations of various samples: (a) XRD, (b) Raman.

We also investigated the chemical states of tungsten and chalcogen in WSe_2 and $\text{W}(\text{Se}_x\text{S}_{1-x})_2$ alloys using XPS analysis. Figure 5a-c illustrates the W 4f, Se 3d and S 2p high-resolution spectra of these samples. In Figure 5a, the two obvious peaks at 32.6 and 34.7 eV in the WSe_2 -C-y samples are the characteristic peaks of W 4f_{7/2} and W 4f_{5/2}, respectively. The substitution of selenium causes a small shift in these peaks to higher binding energies, which agrees with previously reported values for the WSe_2 and WS_2 systems.³² Similar changes can also be observed in the Se 3d and S 2p XPS spectra. The peaks at approximately 54.5 and 55.4 eV are attributed to the Se 3d_{5/2} and Se 3d_{3/2} binding energies, respectively, as shown in Figure 5b. Meanwhile, with increasing sulfur content, the peaks of selenium shift to higher binding energies. Note that with an increasing S concentration from 0.6 to 0.8, the S 2p_{3/2}

and S 2p_{1/2} peaks of the alloy nanoflakes appear to be dominant with a slight downshift compared with bulk WS_2 .⁶

Based on the above discussion, WSe_2 and $\text{W}(\text{Se}_x\text{S}_{1-x})_2$ with bent triangular morphologies were successfully prepared on the surface of electrospun carbon nanofibers. All of the resulting nanoflakes were rich in exposed edges, which is critical to HER electrocatalysis. The cover density of WSe_2 can be adjusted by varying the initial $(\text{NH}_4)_6\text{W}_{12}\text{O}_{40}$ precursor in the electrospun PAN nanofibers. Increasing the W precursor will lead to increased thickness of the WSe_2 nanoflakes. In addition, using a simple method, we successfully synthesized $\text{W}(\text{Se}_x\text{S}_{1-x})_2$ alloy nanoflakes with an abundant amount of defects on the carbon nanofibers. Due to the higher activity of S over Se at high temperatures, increasing the W precursor decreases the Se/S ratio and greatly increases the edge length of the alloy nanoflakes.



Journal of Materials Chemistry A

ARTICLE

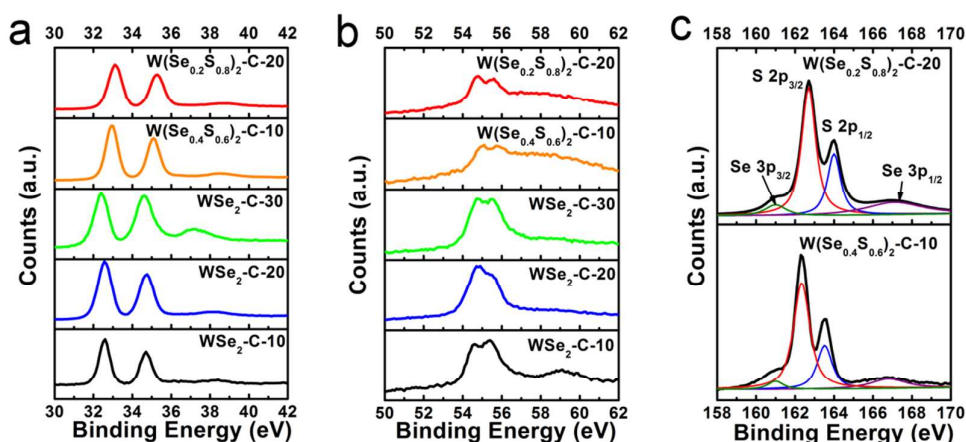


Figure 5. (a-c) High-resolution XPS spectra of W 4f, Se 3d and S 2p of various samples, respectively.

The HER catalytic activity of WSe_2 and $\text{W}(\text{Se}_x\text{S}_{1-x})_2$ nanoflakes on carbon nanofibers was evaluated in 0.5 M H_2SO_4 with a typical three-electrode electrochemical cell setup. Because these various catalysts were directly assembled as the working electrode in HER, the catalyst thickness was taken into consideration. The cross-sectional images of these catalysts were recorded, as shown in Figure S3 a-j, indicating the comparable thickness of each sample and the homogenous distribution of the WSe_2 (or $\text{W}(\text{Se}_x\text{S}_{1-x})_2$) nanosheets throughout the hybrid catalysts. Generally, electrospin-derived neat CFM are brittle, whereas these hybrid catalysts are flexible (Figure S7), which may be due to the high density of flexible WSe_2 nanoflakes alongside the carbon nanofiber backbone, as well as the suitable thickness of these catalyst mats.

Figure 6a shows the polarization curves of the final products normalized to the geometric area of the electrode. CFM and WSe_2 NPs show negligible activity, whereas $\text{W}(\text{Se}_x\text{S}_{1-x})_2$ -C-y samples exhibit robust HER activity with small onset potentials over the range of 80-110 mV and with the cathodic current increasing rapidly under more negative potentials. Interestingly, WSe_2 -C-20 demonstrates the best catalytic activity with an overpotential (η) of 158 mV at a current density of 10 mA cm^{-2} (Table 1), in contrast to other samples, such as WSe_2 -C-10 (213 mV) and WSe_2 -C-30 (188 mV). This exceptional HER activity is further illustrated by comparing the Tafel slopes of WSe_2 -C-20 (98 mV dec^{-1}) with other samples (Figure 6b and Table 1). For WSe_2 -C-y samples, WSe_2 -C-30 has the highest cover density of the WSe_2 nanoflakes, and its HER performance is better than that of WSe_2 -C-10 but is inferior to that of WSe_2 -C-20. Previous reports have indicated that the HER efficiency is related to the thickness of TMD because the high interlayer potential barrier may result in a lower interlayer electron hopping efficiency, consequently reducing the HER activity.⁴¹ We can conclude that the increased

thickness of the WSe_2 nanoflakes in WSe_2 -C-30 (Figure S4) is a major cause for its reduced catalytic activity, suggesting that the thickness and cover density of WSe_2 nanoflakes can be optimized to balance the catalytic activity. With the substitution of selenium by sulfur, $\text{W}(\text{Se}_{0.4}\text{S}_{0.6})_2$ -C-10 and $\text{W}(\text{Se}_{0.2}\text{S}_{0.8})_2$ -C-20 showed a greatly improved HER efficiency over WSe_2 -C-10 and WSe_2 -C-30 that was slightly inferior to WSe_2 -C-20 (Figure 6a and b). The overpotential to achieve an electrocatalytic current density of 10 mA cm^{-2} for $\text{W}(\text{Se}_{0.4}\text{S}_{0.6})_2$ -C-10 and $\text{W}(\text{Se}_{0.2}\text{S}_{0.8})_2$ -C-20 is 174 and 178 mV, respectively. One major cause for the good catalytic behavior of these two samples may be the unique defect-rich alloy nanoflakes, which impart additional active edge sites (Figure 3). Moreover, the band gap of $\text{W}(\text{Se}_{0.4}\text{S}_{0.6})_2$ and $\text{W}(\text{Se}_{0.2}\text{S}_{0.8})_2$ is approximately 1.69 and 1.65 eV, respectively, and slightly larger than bulk WSe_2 with band gap of 1.6 eV.^{42]} However, the substitution of selenium with sulfur atoms lead to lower Tafel slopes, which is probably afforded by the much increased active edge sites of the alloy nanoflakes. The $\text{W}(\text{Se}_{0.4}\text{S}_{0.6})_2$ -C-10 exhibited a better HER performance than $\text{W}(\text{Se}_{0.2}\text{S}_{0.8})_2$ -C-20, which could result from the markedly longer edge length of $\text{W}(\text{Se}_{0.2}\text{S}_{0.8})_2$ that reduces the density of the active sites. We also synthesized WS_2 -C-20 as a control. The SEM image and the polarization curve can be seen in Figure S8. The edge length of WS_2 is comparable to $\text{W}(\text{Se}_{0.2}\text{S}_{0.8})_2$ and much larger than WSe_2 , which can be resulted from the much activity nature of S than Se at high temperature that accelerated the reduction of WO_3 NPs and the growth of WS_2 nanosheets. The onset potential of WS_2 -C-20 is about -200 mV and larger than that of $\text{W}(\text{Se}_{0.2}\text{S}_{0.8})_2$ -C-20, indicating the favorable adsorption of H_{ads} on the S substituted edge.

We also estimated the relative difference in electrochemically active surface areas among these electrodes using a simple cyclic voltammetry (CV) method. The electrostatic capacities of these electrodes under 0-0.8 V vs

RHE at a scan rate of 0.1 V s⁻¹ were recorded (Figure S8 a). Typically, the exchange current density (*j*₀) is expected to be proportional to the catalytically active surface area. The *j*₀ values of these electrodes calculated from the Tafel plots in Figure 6b are summarized in Table 1. An alternative approach to estimate the effective surface area is to measure the capacitance of the double layer (*C*_{dl});⁸ thus, CV plots under a potential range (0.1–0.2 V vs RHE) in which no faradic current was observed at various scan rates (0.5–5 mV s⁻¹) were recorded (Figure S9 b–f). Subsequently, the *C*_{dl} of these electrodes were collected and are shown in Figure 6c and Table 1. The electrochemical effective surface areas of WSe₂-C-20 (430 mF cm⁻²), WSe₂-C-30 (313 mF cm⁻²) and W(Se_{0.4}S_{0.6})₂-C-10 (376 mF cm⁻²) are approximately 1.78, 1.3 and 1.56 times larger than WSe₂-C-10 (241 mF cm⁻²), respectively. This increase in electrochemically active surface area demonstrates the proliferation of active sites, which improves the catalytic performance. Impedance measurements were performed at η = 150 mV (Figure S10), and the charge transfer resistances of these electrodes vary in a trend that agrees with the CV results.

At a potential below the onset potential during the test, many bubbles are generated on the electrode surface (see Movie S1 of the W(Se_xS_{1-x})₂-C-10 electrode at a constant potential of –0.4 V vs RHE as an example). These bubbles are easily released from the CFM surface, which is a highly desirable property for the practical application of HER catalysts. To evaluate the catalyst durability in acidic environments, potentiostatic electrolysis cycling was performed at –0.2 V vs RHE for 12 h. As shown in Figure 6d, the current densities of these electrodes remained stable for 12 h, and the slight decrease in current density could be ascribed to the continuously released bubbles generated from the surface of the CFM and to the consumption of H⁺ during the tests. The representative SEM images of these electrodes after the 12 h cycling test are given in Figure S11, showing no obvious changes in morphology. This excellent durability shows promise for practical long-term applications of the catalysts. The comparison of some state-of-the-art WS₂ and WSe₂ HER electrocatalysts was summarized in Table S2, revealing the excellent HER performance of the electrodes synthesized in this study.

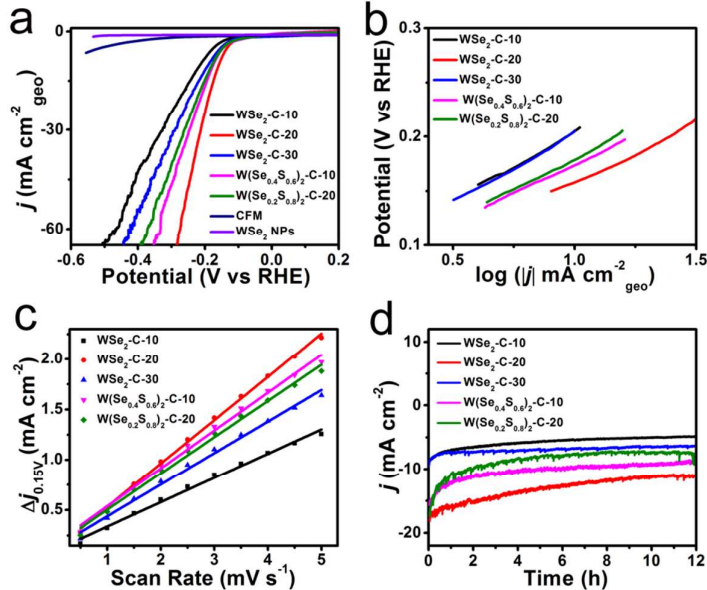


Figure 6. (a) Polarization curves obtained for several electrodes as indicated; (b) corresponding Tafel plots; (c) linear fitting of the capacitive currents of the catalysts vs scan rates; (d) time dependence of current density under a static overpotential of –0.2 V vs RHE.

Table 1. Electrocatalytic performance of the five different catalysts.

	WSe ₂ -C-10	WSe ₂ -C-20	WSe ₂ -C-30	W(Se _{0.4} S _{0.6}) ₂ -C-10	W(Se _{0.2} S _{0.8}) ₂ -C-20
η @ <i>j</i> = 10 mA cm ⁻² (mV)	213	158	188	174	178
Tafel slope (mV dec ⁻¹)	117	98	116	106	106
<i>j</i> ₀ (mA cm ⁻²)	0.195	0.240	0.204	0.229	0.214
<i>C</i> _{dl} (mF cm ⁻²)	241	430	313	376	359

Conclusions

Triangular WSe₂ and W(Se_xS_{1-x})₂ nanoflakes with an abundant amount of exposed edges uniformly dispersed on the surface of conductive electrospun CFM were synthesized in a CVD

system. The cover density of WSe₂ nanoflakes can be easily controlled by adjusting the initial W precursor, while the thickness of the nanoflakes increases with the increasing W precursor. W(Se_xS_{1-x})₂ nanoflakes with no obvious phase separation were also synthesized, and the partial substitution

ARTICLE

Journal of Materials Chemistry A

of selenium with sulfur makes the basal planes of the $\text{W}(\text{Se}_x\text{S}_{1-x})_2$ nanoflakes substantially more defective than the WSe_2 nanoflakes. The products were directly used as hydrogen evolution cathodes to highlight the merits of these catalysts. All of these electrodes exhibited low overpotential, high exchange current density, and long-term stability for HER. More importantly, the excellent HER performance can be obtained either by adjusting the suitable cover density and thickness of the WSe_2 nanoflakes or by optimizing the substitution of selenium with sulfur. The present study provides a simple method for the synthesis of CFM-based TMD, which may have promising applications in other fields.

Acknowledgements

This study was supported by the National Natural Science Foundation of China (NSFC) (Grant no. 51373154), Program for Innovative Research Team of Zhejiang Sci-Tech University and the 521 Talent Project of Zhejiang Sci-Tech University.

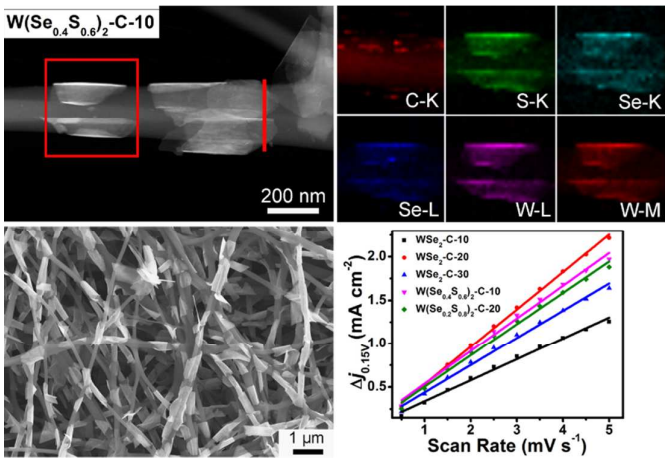
Notes and references

- X. Zou and Y. Zhang, *Chem. Soc. Rev.*, 2015, DOI: 10.1039/C4CS00448E.
- C. G. Morales-Guio, L. A. Stern and X. Hu, *Chem. Soc. Rev.*, 2014, **43**, 6555-6569.
- H. H. Li, C. H. Cui, S. Zhao, H. B. Yao, M. R. Gao, F. J. Fan and S. H. Yu, *Adv. Energy Mater.*, 2012, **2**, 1182-1187.
- C. Wang, M. Chi, G. Wang, D. van der Vliet, D. Li, K. More, H. H. Wang, J. A. Schlueter, N. M. Markovic and V. R. Stamenkovic, *Adv. Funct. Mater.*, 2011, **21**, 147-152.
- X. Zheng, J. Xu, K. Yan, H. Wang, Z. Wang and S. Yang, *Chem. Mater.*, 2014, **26**, 2344-2353.
- M. A. Lukowski, A. S. Daniel, C. R. English, F. Meng, A. Forticaux, R. J. Hamers and S. Jin, *Energy Environ. Sci.*, 2014, **7**, 2608-2613.
- C. Y. Lin, D. Mersch, D. A. Jefferson and E. Reisner, *Chem. Sci.*, 2014, **5**, 4906-4913.
- D. Kong, H. Wang, Z. Lu and Y. Cui, *J. Am. Chem. Soc.*, 2014, **136**, 4897-4900.
- M. R. Gao, Z. Y. Lin, T. T. Zhuang, J. Jiang, Y. F. Xu, Y. R. Zheng and S. H. Yu, *J. Mater. Chem.*, 2012, **22**, 13662-13668.
- F. H. Saadi, A. I. Carim, J. M. Velazquez, J. H. Baricuatro, C. C. L. McCrory, M. P. Soriaga and N. S. Lewis, *ACS Catal.*, 2014, **4**, 2866-2873.
- M. D. Scanlon, X. Bian, H. Vrubel, V. Amstutz, K. Schenk, X. Hu, B. Liu and H. H. Girault, *Phys. Chem. Chem. Phys.*, 2013, **15**, 2847-2857.
- H. Vrubel and X. Hu, *Angew. Chem.*, 2012, **51**, 12703-12706.
- X. Fan, H. Zhou and X. Guo, *ACS Nano*, 2015, **9**, 5125-5134.
- K. Zhang, Y. Zhao, S. Zhang, H. Yu, Y. Chen, P. Gao and C. Zhu, *J. Mater. Chem. A*, 2014, **2**, 18715-18719.
- C. Wan, Y. N. Regmi and B. M. Leonard, *Angew. Chem.*, 2014, **53**, 6407-6410.
- J. Tian, Q. Liu, A. M. Asiri and X. Sun, *J. Am. Chem. Soc.*, 2014, **136**, 7587-7590.
- T. Wang, K. Du, W. Liu, Z. Zhu, Y. Shao and M. Li, *J. Mater. Chem. A*, 2015, **3**, 4368-4373.
- P. Jiang, Q. Liu and X. Sun, *Nanoscale*, 2014, **6**, 13440-13445.
- I. Y. Jeon, D. Yu, S. Y. Bae, H. J. Choi, D. W. Chang, L. Dai and J. B. Baek, *Chem. Mater.*, 2011, **23**, 3987-3992.
- Y. Hou, Z. H. Wen, S. M. Cui, S. Q. Ci, S. Mao and J. H. Chen, *Adv. Funct. Mater.*, 2015, **25**, 872-882.
- S. Gao, G. D. Li, Y. Liu, H. Chen, L. L. Feng, Y. Wang, M. Yang, D. Wang, S. Wang and X. Zou, *Nanoscale*, 2015, **7**, 2306-2316.
- A. Y. S. Eng, A. Ambrosi, Z. Sofer, P. Šimek and M. Pumera, *ACS Nano*, 2014, **8**, 12185-12198.
- J. M. Velazquez, F. H. Saadi, A. P. Pieterick, J. M. Spurgeon, M. P. Soriaga, B. S. Brunschwig and N. S. Lewis, *J. Electroanal. Chem.*, 2014, **716**, 45-48.
- C. Tsai, K. Chan, F. Abild-Pedersen and J. K. Nørskov, *Phys. Chem. Chem. Phys.*, 2014, **16**, 13156-13164.
- T. F. Jaramillo, K. P. Jørgensen, J. Bonde, J. H. Nielsen, S. Hørch and I. Chorkendorff, *Science*, 2007, **317**, 100-102.
- H. Wang, D. Kong, P. Johanes, J. J. Cha, G. Zheng, K. Yan, N. Liu and Y. Cui, *Nano Lett.*, 2013, **13**, 3426-3433.
- K. Xu, F. Wang, Z. Wang, X. Zhan, Q. Wang, Z. Cheng, M. Safdar and J. He, *ACS Nano*, 2014, **8**, 8468-8476.
- M. L. Zou, J. F. Zhang, H. Zhu, M. L. Du, Q. F. Wang, M. Zhang and X. W. Zhang, *J. Mater. Chem. A*, 2015, **3**, 12149-12153.
- D. Merki, H. Vrubel, L. Rovelli, S. Fierro and X. Hu, *Chem. Sci.*, 2012, **3**, 2515-2525.
- X. J. Lv, G. W. She, S. X. Zhou and Y. M. Li, *RSC Adv.*, 2013, **3**, 21231-21236.
- J. Li, W. Tang, H. Yang, Z. Dong, J. Huang, S. Li, J. Wang, J. Jin and J. Ma, *RSC Adv.*, 2014, **4**, 1988-1995.
- Q. Gong, L. Cheng, C. Liu, M. Zhang, Q. Feng, H. Ye, M. Zeng, L. Xie, Z. Liu and Y. Li, *ACS Catal.*, 2015, **5**, 2213-2219.
- V. Kiran, D. Mukherjee, R. N. Jenjeti and S. Sampath, *Nanoscale*, 2014, **6**, 12856-12863.
- A. J. Smith, Y. H. Chang, K. Raidongia, T. Y. Chen, L. J. Li and J. Huang, *Adv. Energy Mater.*, 2014, **4**, 1400398.
- H. Wang, Z. Lu, D. Kong, J. Sun, T. M. Hymel and Y. Cui, *ACS Nano*, 2014, **8**, 4940-4947.
- J. Kim, S. Byun, A. J. Smith, J. Yu and J. Huang, *J. Phys. Chem. Lett.*, 2013, **4**, 1227-1232.
- H. Zhu, M. Du, M. Zhang, M. Zou, T. Yang, Y. Fu and J. Yao, *J. Mater. Chem. A*, 2014, **2**, 7680-7685.
- H. Li, X. Duan, X. Wu, X. Zhuang, H. Zhou, Q. Zhang, X. Zhu, W. Hu, P. Ren, P. Guo, L. Ma, X. Fan, X. Wang, J. Xu, A. Pan and X. Duan, *J. Am. Chem. Soc.*, 2014, **136**, 3756-3759.
- A. Pan, R. Liu, M. Sun and C.-Z. Ning, *J. Am. Chem. Soc.*, 2009, **131**, 9502-9503.
- J. Xie, H. Zhang, S. Li, R. Wang, X. Sun, M. Zhou, J. Zhou, X. W. Lou and Y. Xie, *Adv. Mater.*, 2013, **25**, 5807-5813.
- Y. Tan, P. Liu, L. Chen, W. Cong, Y. Ito, J. Han, X. Guo, Z. Tang, T. Fujita, A. Hirata and M. W. Chen, *Adv. Mater.*, 2014, **26**, 8023-8028.
- Q. Fu, L. Yang, W. H. Wang, A. Han, J. Huang, P. W. Du, Z. Y. Fan, J. Y. Zhang and B. Xiang, *Adv. Mater.*, 2015, DOI: 10.1002/adma.201500368.
- D. Voiry, H. Yamaguchi, J. W. Li, R. Silva, D. C. B. Alves, T. Fujita, M. W. Chen, T. Asefa, V. B. Shenoy, G. Eda and M. Chhowalla, *Nat. Mater.*, 2013, **12**, 850-855.

WSe₂ and W(Se_xS_{1-x})₂ nanoflakes grown on carbon nanofibers for the electrocatalytic hydrogen evolution reaction

MeiLing Zou, JiaDong Chen, LongFei Xiao, Han Zhu, TingTing Yang, Ming Zhang, MingLiang Du*

Triangular W(Se_xS_{1-x})₂ nanoflakes uniformly dispersed on the surface of electrospun carbon nanofiber mats were synthesized. The hybrid catalyst mats were directly used as hydrogen evolution cathodes and exhibit excellent HER performances.



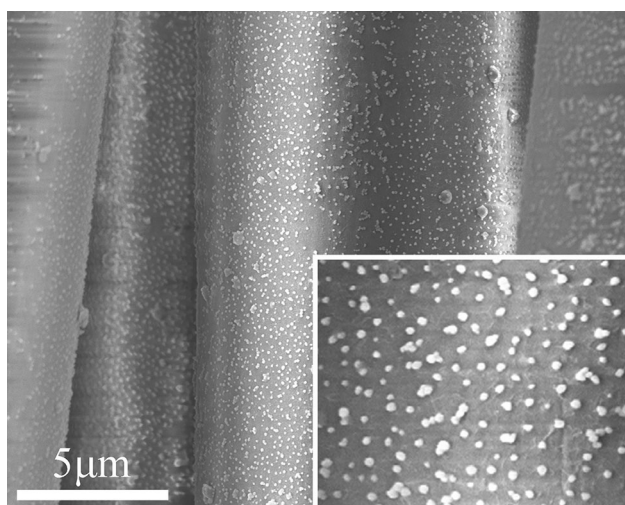
Storable silicon/shape memory polyurethane hybrid sols prepared by a facile synthesis process and their application to aramid fibers

Jianrui Chen · Xixi Li · Yaofeng Zhu ·
Wenbin Jiang · Yaqin Fu

Received: 31 October 2014 / Accepted: 29 January 2015 / Published online: 5 March 2015
© Springer Science+Business Media New York 2015

Abstract In this study, silicon/shape memory polyurethane (SiO_2/SMPU) hybrid sols were prepared using a sol–gel process without water. The structural, mechanical, thermal, and optical properties of the SiO_2/SMPU sols were studied. Results indicated that the hybrid sols exhibited uniform size distribution and good dispersion. In addition, the hybrid sols were characterized by transparency and excellent storability even after 6 months when stored in an inert atmosphere. The application of these hybrid sols was also investigated, and it was found that they effectively improve the quality of aramid fibers by enhancing their UV resistance and the binding strength between the coating and the fiber.

Graphical Abstract



Keywords Hybrid sol · Sol–gel · Storable · Aramid fiber · UV resistance · Binding strength

1 Introduction

In the twenty-first century, the field of coatings is expected to contribute to high levels of scientific and technological development [1, 2]. Inorganic coatings are derived from abundant resources and have wide applications in industry, particularly in ceramics and metal plating [3, 4]. However, the disadvantages of weak ductility and easy crack shrinkage limit their application to flexible substrates. Meanwhile, organic coatings can be applied to an array of products. For example, polyurethane (PU) coatings are valued in the paint industry for their superior bonding, durability, and high gloss [5, 6]. Despite many advances in organic coatings technology, single-layer organic coatings have difficulty meeting the performance requirements of highly demanding applications.

New coatings or composite materials with promising properties can be obtained by introducing nanoscale inorganic fillers into the polymer matrix of organic coatings [7, 8]. Among these inorganic fillers, SiO_2 hybrids are commonly used because of their high stability, high heat resistance, radiation resistance, and excellent mechanical properties. Hence, SiO_2/PU composite coatings have gained considerable academic and industrial attention [9–11]. To improve the homogeneous dispersion of nanoparticles, numerous studies have focused on the surface modification of nanoparticles [12, 13] and on methods for incorporating inorganic nanofillers into organic matrices [14–16]. Among these methods, the sol–gel process has been found to demonstrate optimal performance. This process combines the advantages of the inorganic material (e.g., rigidity and

J. Chen · X. Li · Y. Zhu · W. Jiang · Y. Fu (✉)
The Key Laboratory of Advanced Textile Materials and
Manufacturing Technology Ministry of Education, Zhejiang
Sci-Tech University, Hangzhou 310018, Zhejiang, China
e-mail: fyq01@zstu.edu.cn

thermal stability) and the organic polymer (e.g., flexibility, dielectric properties, ductility, and processability). Thus, the sol–gel process serves a major role in the development of advanced functional materials [17–19]. However, water-containing sols have their limitations such as low storage stability (short gel times) and the need for the use of fresh sols at the start of each process. Therefore, coatings that can be conveniently stored for extended periods of time are needed for industrial applications.

Shape memory polymers (SMPs) have attracted a great deal of attention in recent years owing to their ability to maintain a temporarily deformed shape and return to their original shape by application of an external stimulus, including heat, light, water, electrical, chemical, or magnetic field [20, 21]. In particular, shape memory polyurethane (SMPU) is the most extensively and specifically investigated SMPs for its flexible molecular design and its promising applications such as self-healing, medical devices, water vapor permeability, damping, and shock resistance based on its shape memory effect [22–24]. In addition, their intelligent properties make them ideal as alternative polymeric matrix materials in place of traditional PUs. However, research on the preparation of a SiO_2 /SMPU composite coating is limited [25].

Herein, we describe novel, storable SiO_2 /SMPU hybrid sol coatings with uniform size distributions and good dispersion. The coatings are prepared in situ using a sol–gel process with SMPU, 3-aminopropyltriethoxysilane (KH-550), and tetraethoxysilane (TEOS) as precursors, the solid acid *p*-toluenesulfonic acid (PTSA) as the catalyst, and moisture in the air as the source of water for the hydrolysis reaction. Further, the properties and application to aramid fibers were investigated.

2 Experimental

2.1 Materials

The liquid SMPU (Diary, MS-4510) was supplied by Diaplex Co. Ltd., Japan. TEOS, KH-550, PTSA, *N,N*-dimethylacetamide (DMAc), 85 wt% phosphoric acid, acetone, and 99.7 wt% absolute ethanol were provided by Hangzhou Mike Chemical Instrument, China. Twaron 2200 aramid fibers with a diameter of 13 μm were supplied by Teijin Japan.

2.2 Preparation of SiO_2 /SMPU hybrid sols

First, a SiO_2 precursor solution (Solution A) consisting of PTSA/TEOS/DMAc in a mass ratio of 0.1:10:100 was prepared. Next, a solution of modified SMPU resin (Solution B) was prepared by mixing the SMPU resin and KH-550 in a

mass ratio of 100:2. Solutions A and B were then mixed to achieve an equivalent PTSA/TEOS/KH-550 mass ratio of 0.1:10:2. The mixed solution was maintained for 2 days in a Teflon container that was sealed with tin foil having several pores. Several types of hybrid sols were fabricated according to different ratios as shown in Table 1.

2.3 Preparation of SiO_2 /SMPU hybrid films

The sols were initially gelled in air at room temperature for 5 days and then dried in an oven at 40 °C for 24 h, 60 °C for 24 h, 80 °C for 24 h, and 130 °C for 24 h. The film thickness was controlled by using the same amount of total materials and a Teflon container of the same size.

2.4 Modification of aramid fibers

Aramid fibers were dipped in the sol coating (1/50 diluted solution) for 6 min using vertical dip-coating at a rate of 60 mm/min. The samples were then maintained at room temperature until dry and subsequently heated to 70 °C at a heating rate of 0.5 °C/min, cooled, and then finally stored.

3 Characterization

3.1 Electron microscopy

The morphology and dispersion of the hybrid sols were examined using a transmission electron microscope (TEM) (JEM-2100F, JEOL, Japan) operated at 200 kV.

3.2 Tensile test

The mechanical properties of the hybrid films were determined using an Instron 3367R4415 universal testing instrument (Canton, MA, USA) at a rate of 50 mm/min in accordance with ISO527:1993.

3.3 Thermogravimetric analysis (TGA)

The thermal properties of the hybrids were investigated by TGA using a STA 503 WinTA instrument. In each case, 10 mg

Table 1 Recipes for SiO_2 /SMPU hybrid sol preparations

Sample	S0	S2.5	S5	S10	S20
DMAc/g	45	45	45	45	45
TEOS/g	0	0.75	1.5	3	6
PTSA/g	0	0.0075	0.015	0.03	0.06
KH-550/g	0	0.15	0.3	0.6	1.2
SMPU/g	30	30	30	30	30

of the specimen was heated from room temperature to 800 °C at a heating rate of 20 °C/min under a nitrogen atmosphere.

3.4 Ultraviolet–visible (UV–Vis) spectrophotometry

An UV–Vis spectrophotometer (Lambda 900, China) was employed to evaluate the transmittance of the hybrids in the wavelength range from 200 nm to 800 nm. The samples for UV–Vis transmittance measurements were prepared by cutting the cast films into 0.2-mm-thick pieces.

3.5 UV resistance tests

UV radiation tests were conducted by exposing fibers to a homemade UV chamber (254 nm, 4,000–4,600 $\mu\text{W}/\text{cm}^2$) for different lengths of time following the accelerated photoaging procedure. The single-fiber tensile strength was then assessed using a universal testing instrument (KES-G1, Japan) at a rate of 6.0 mm/min in accordance with GJB993-1990.

3.6 Thermal shock tests

Thermal shock tests were conducted by exposing the coated fibers to rapid cold–hot environments. The samples were placed in the oven 200 °C within 1 min and then placed in the refrigerator 0 °C cooling in 1 min, repeated for three cycles. The morphology of the tested samples was examined using a field emission scanning electron microscope (Ultra 55, Zeiss, Germany).

4 Results and discussion

4.1 Morphology of the SiO_2 /SMPU hybrid sols

Dispersion and particle size are two key indicators of the quality of coatings. Typical TEM images of the SiO_2 /SMPU hybrid sols are shown in Fig. 1. The size of the SiO_2 particles increased as the amount of TEOS increased and was 11.9, 17.1, 36.1, and 61.7 nm for S2.5, S5, S10, and S20, respectively. Moreover, the SiO_2 particles had an irregular spherical shape that may be attributed to the hydrolysis of KH-550, which then formed a new cross-linking structure with the SiO_2 sol molecules generated from the TEOS [26]. Therefore, excellent dispersion and a controllable nanoparticle size were achieved, leading to a coating system with high stability.

The hybrid sols were more stable under an inert atmosphere and without the addition of deionized water, as shown in Fig. 2. In fact, upon the addition of deionized water, the sols rapidly became cloudy and opaque. However, when stored in an inert atmosphere, the hybrid sols were highly

stable and transparent and did not gel, even after 6 months, as shown in Fig. 3. This observation indicates that the SiO_2 /SMPU hybrid sol prepared in this study is storable and can be conveniently utilized in industrial applications.

4.2 Mechanical properties

The macroscopic mechanical properties of a composite material reflect its intrinsic interaction capacity. Therefore, the stress–strain curves of the pure SMPU and SiO_2 /SMPU hybrids were obtained and are shown in Fig. 4. The broken elongation of the composites decreased with increasing silica concentration. Notably, however, the hybrids with 2.5, 5, and 10 wt% (theoretical value) silica did not rupture, even with a strain of 200 %, thus demonstrating excellent toughness. The yield strength of the hybrids increased from 21 to 37 MPa, whereas the tensile strength increased from 43 to 55 MPa, an improvement of 76 and 28 %, respectively. The enhanced properties are attributed to the effects of the nanoscale structure and the stronger interactions between the organic matrix and the inorganic materials [27]. However, the tendency decreased with a further increase in SiO_2 content. When the silica content continued to increase to 20 wt% (S20), the yield strength, tensile strength, and elongation were decreased to 33, 50 MPa, and 160 %, due to the higher concentration of particles, which hindered the movement of the chain segments and weakened the size effects of the nanoparticles.

4.3 Thermal properties

Thermal stability serves as an essential function in determining both the technological applications and processing conditions for polymeric hybrids and is typically evaluated using TGA. The thermal decomposition behavior of the SMPU and SiO_2 /SMPU hybrids is depicted in Fig. 5. Two thermal decomposition stages appeared in all of samples that are attributed to the decomposition of the soft and hard segments of the SMPU [28]. The onset temperature of the first stage for S2.5 was approximately 329 °C, which is 29 °C higher than that of the pure SMPU, although the improvement effect gradually weakened as the silica content increased. Moreover, the onset temperatures of the second stage for all of the SiO_2 /SMPU hybrids were 6–13 °C higher than that of the pure SMPU (412 °C). Consequently, it can be concluded that adding silica improved the thermal stability of the SMPU, possibly due to the good dispersion and interfacial adhesion between the silica and the matrix.

4.4 Optical properties

The optical properties of the pure SMPU and SiO_2 /SMPU hybrid coating films were investigated using UV–Vis

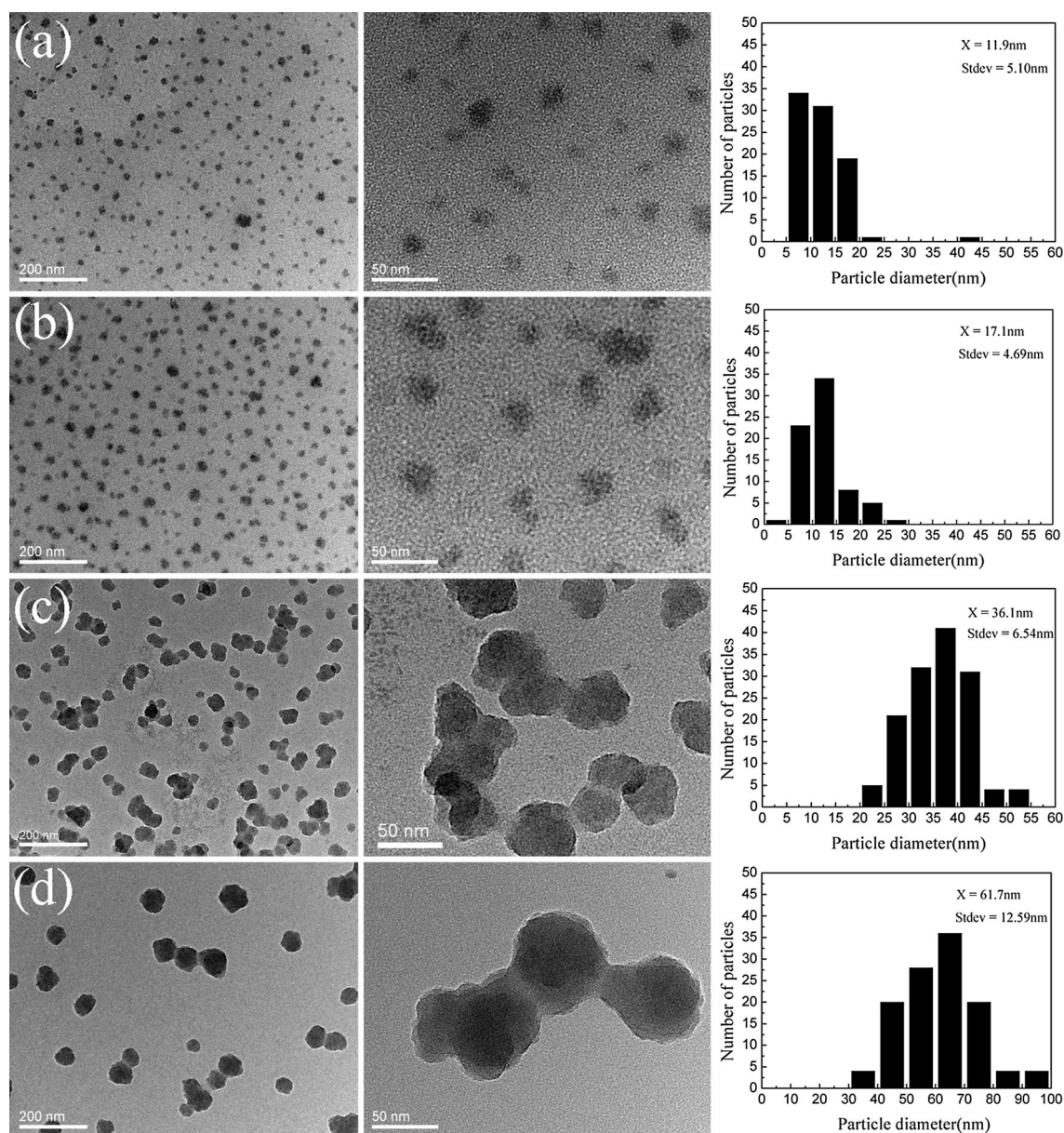


Fig. 1 TEM images of the SiO₂/SMPU hybrid sols: **a** S2.5, **b** S5, **c** S10, and **d** S20

spectroscopy. The spectra, as shown in Fig. 6, of the film samples exhibit strong absorbance in the 250- to 300-nm range and a lack of absorbance (transparency) in the 300- to 800-nm range. In addition, the transmittance was similar for all of the samples with increasing SiO₂ content (S0–S20) and reached values as high as 90 %, although it slightly decreased for S5, S10, and S20. Overall, all the samples exhibited good optical transmittance in the visible region. These results indicate that the presence of the silicon unit does not affect the optical transmittance. Such transparent materials can be applied as coatings for lenses and optical fibers.

4.5 Application

An aramid fiber was used to verify the ability of the sols in improving the UV resistance of a coated material. Aramid fiber was selected as the test substrate because it is an important high-performance fiber that is known to be prone to degradation under UV irradiation [29]. Figure 7 shows the tensile strength of uncoated and hybrid sol-coated fibers before UV irradiation. The results show that the tensile strength of hybrid sol-coated fibers has been significantly improved and the S10-TF with the optimal tensile strength, which may be attributed to a special “pizza-like” structure

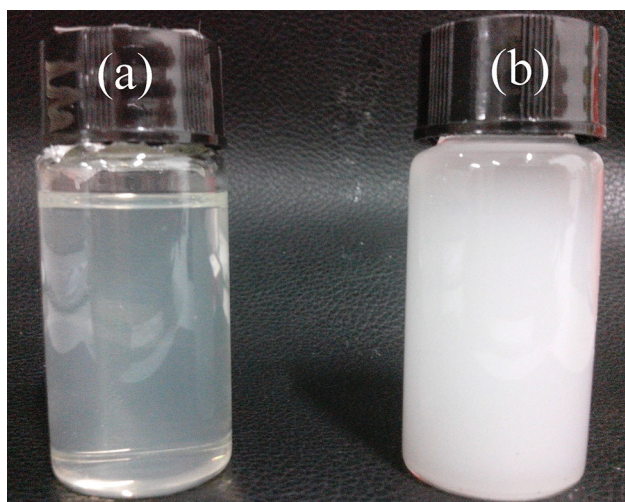


Fig. 2 Images of **a** the S10 hybrid sol and **b** the S10 sol with deionized water

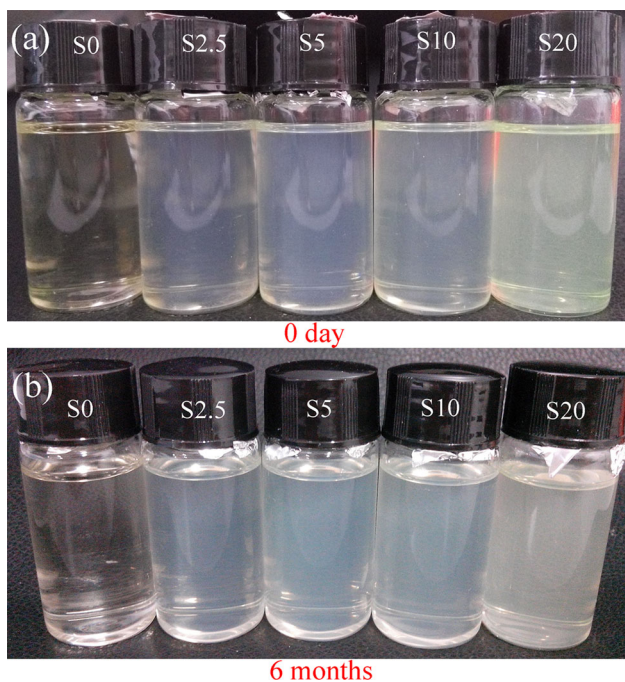


Fig. 3 Images of the SiO₂/SMPU hybrids sols **a** at day 0 and **b** after storage for 6 months

of hybrid material coated on the surface of aramid fiber [30]. Figure 8 shows the tensile strength of uncoated and S10 coated fibers after UV irradiation for different lengths of time. The tensile strength of the uncoated fiber declined dramatically within the first 24 h, while the tensile strength of the coated fiber was reduced by just half compared with that of the uncoated sample. Moreover, the retention rate for the tensile strength of the coated and uncoated fibers under UV irradiation after 192 h decreased to 44.0 and

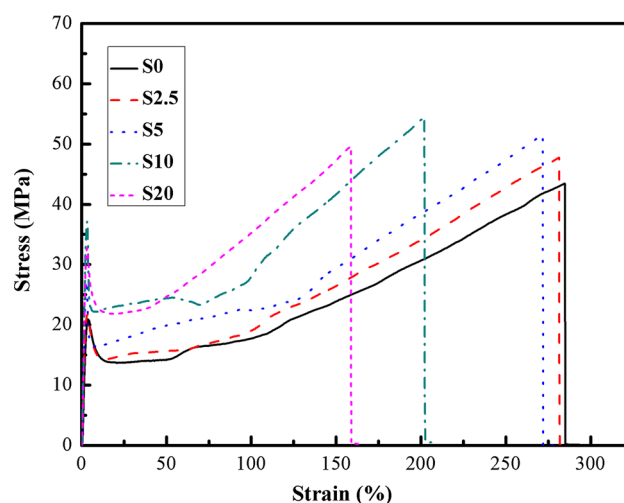


Fig. 4 Stress–strain curves of SMPU and SiO₂/SMPU hybrid films with different silica contents

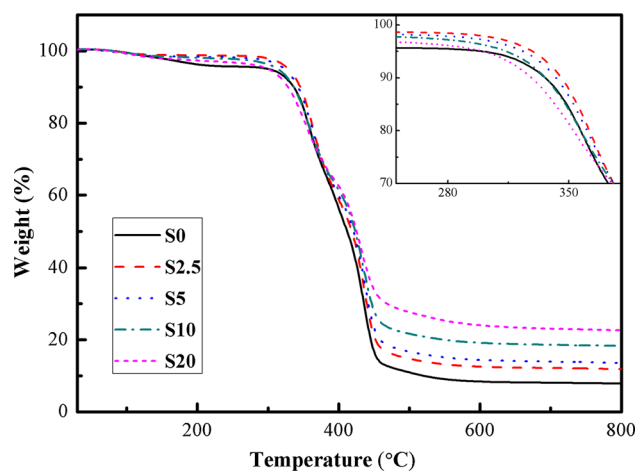


Fig. 5 TGA curves for the SMPU and SiO₂/SMPU hybrid films with different silica contents

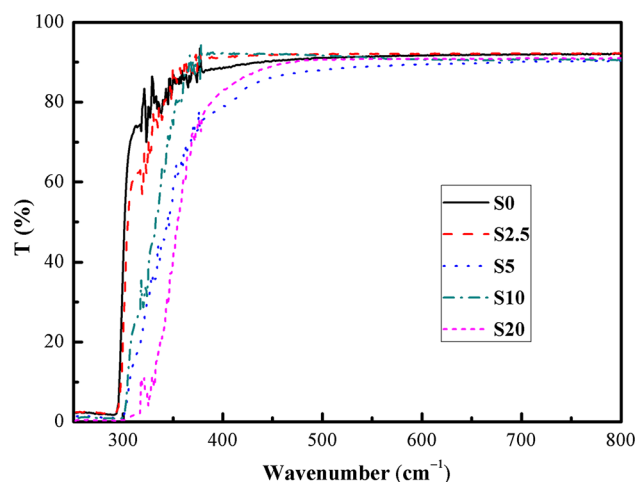


Fig. 6 UV–Vis transmittance spectra for the SMPU and SiO₂/SMPU hybrid films with different silica contents

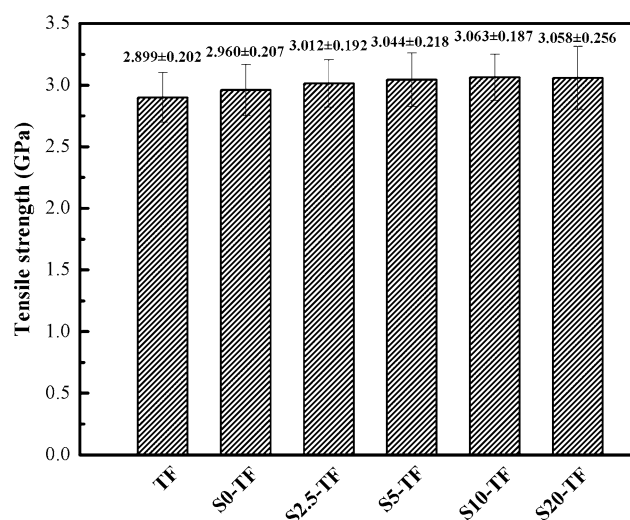


Fig. 7 Tensile strength of uncoated and coated with hybrid sols-coated monofilament aramid fibers

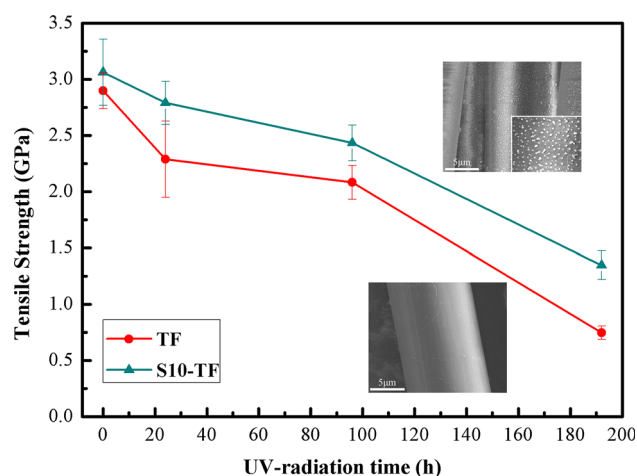
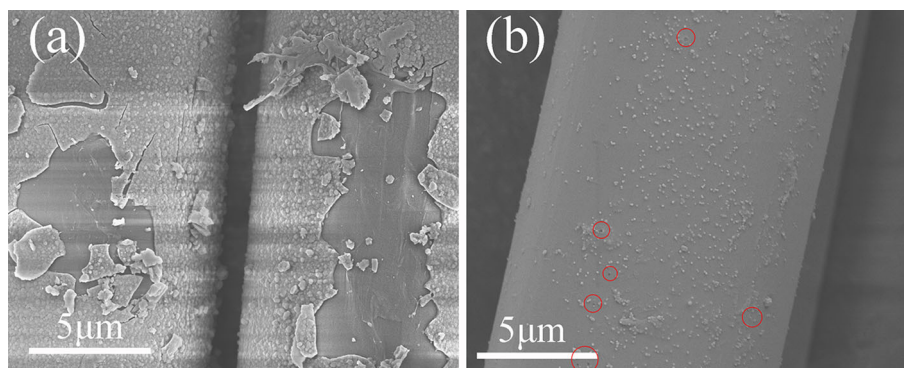


Fig. 8 Influence of UV irradiation time on the tensile strengths of aramid fibers, both uncoated and coated with the S10 hybrid sol

22.9 %, respectively. The corresponding values for the coated fibers were higher than those for the uncoated fibers, particularly upon short-term irradiation (for example,

Fig. 9 SEM images of aramid fibers with the different coatings after thermal shock tests **a** silica sol coating and **b** S10 hybrid sol coating



24 h). These results can be attributed to the photo-stabilization of the nanosized SiO_2 particles in the coating, which absorbed the 254-nm UV light, thus preventing degradation of the organic bonding in the aramid fibers. They also indicate that the aramid fibers have a higher UV resistance when surface treated by the hybrid coating.

The combined strength of the coating and the substrate is an important indicator of the quality of the coating. In particular, good thermal shock stability reflects good interfacial bonding strength between the coating and the substrate. Therefore, thermal shock tests were conducted on aramid fibers coated with the S10 sol hybrid coating and an inorganic silica sol previously reported by us [31] for comparison. Figure 9 shows the SEM images of two aramid fibers with the different coatings after the thermal shock tests. The silica membrane detached from the fiber surface over a large area, thus exposing the smooth substrate (Fig. 9a). This result may be attributed to the weak ductility of the inorganic coating and the inability to adapt to the sharp temperature change and resultant stresses. However, the surface of the aramid fiber with the hybrid coating exhibited only a slight amount of particle shedding in a crater-shaped hole (encircled in red), but the overall membrane did not appear to have any cracks and other damage (Fig. 9b). This result indicates that the protective performance of the hybrid coating under variable temperature environments is greater than that of the single inorganic coating. On the one hand, ductility and self-healing properties enhance the SMPU components, and hybrid coating results in a lower thermal expansion coefficient difference between the aramid fiber and the organic coating. On the other hand, a suitable amount of SiO_2 increases the heat resistance and helps avoid rapid crack development in a single direction.

5 Conclusions

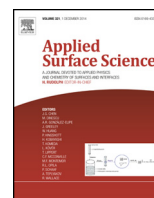
Readily usable SiO_2 /SMPU hybrid sols that have high storage stability under an inert atmosphere have been

prepared using a novel sol–gel process without water. The incorporation of nanosilica particles with uniform size distribution and good dispersion improved the mechanical and thermal stability of SMPU, while the SMPU improved the ductility and self-healing properties of the substrate. Combining the advantages of both materials, the SiO₂/SMPU hybrid sols were shown to exhibit UV resistance and strong adhesion to aramid fibers. It is expected that these sols, when applied to aramid fibers, can improve their quality by enhancing their service life and the interfacial strength of fiber-reinforced composites. Thus, this capability has the potential to widen the applications of aramid fibers.

Acknowledgments This work has been supported by National Natural Science Foundation of China (Grant No. 51473147); authors are very grateful.

References

- Dušek K, Dušková-Smrčková M (2000) Network structure formation during crosslinking of organic coating systems. *Prog Polym Sci* 25:1215–1260
- Lee D, Rubner M-F, Cohen R-E (2006) All-nanoparticle thin-film coatings. *Nano Lett* 6:2305–2312
- Spear K-E (1989) Diamond—ceramic coating of the future. *J Am Ceram Soc* 72:171–191
- Lennon A, Yao Y, Wenham S (2013) Evolution of metal plating for silicon solar cell metallisation. *Prog Photovolt Res Appl* 21:1454–1468
- Türting O, Kayaman-Apohan N, Kahraman M-V, Menceloğlu Y, Güngör A (2008) Nonisocyanate based polyurethane/silica nanocomposites and their coating performance. *J Sol Gel Sci Technol* 47:290–299
- Rahman M-M, Hasneen A, Lee W-K, Lim K-T (2013) Preparation and properties of sol–gel waterborne polyurethane adhesive. *J Sol Gel Sci Technol* 67:473–479
- Schaefer D-W, Justice R-S (2007) How nano are nanocomposites? *Macromolecules* 40:8501–8517
- Dong Y, Ding J, Wang J, Fu X, Hu H, Li S, Yang H, Xu C, Du M, Fu Y (2013) Synthesis and properties of the vapour-grown carbon nanofiber/epoxy shape memory and conductive foams prepared via latex technology. *Compos Sci Technol* 76:8–13
- Pagliaro M, Ciriminna R, Palmisano G (2009) Silica-based hybrid coatings. *J Mater Chem* 19:3116–3126
- Zhou S, Wu L, Sun J, Shen W (2002) The change of the properties of acrylic-based polyurethane via addition of nano-silica. *Prog Org Coat* 45:33–42
- Rahman I-A, Padavettan V (2012) Synthesis of silica nanoparticles by sol–gel: size-dependent properties, surface modification, and applications in silica-polymer nanocomposites—a review. *J Nanomater* 2012:1–15. doi:[10.1155/2012/132424](https://doi.org/10.1155/2012/132424)
- Kango S, Kalia S, Celli A, Njuguna J, Habibi Y, Kumar R (2013) Surface modification of inorganic nanoparticles for development of organic–inorganic nanocomposites—a review. *Prog Polym Sci* 38:1232–1261
- Gao X, Zhu Y, Zhao X, Wang Z, An D, Ma Y, Guan S, Du Y, Zhou B (2011) Synthesis and characterization of polyurethane/SiO₂ nanocomposites. *Appl Surf Sci* 257:4719–4724
- Li Y, Han B, Liu L, Zhang F, Zhang L, Wen S, Lu Y, Yang H, Shen J (2013) Surface modification of silica by two-step method and properties of solution styrene butadiene rubber (SSBR) nanocomposites filled with modified silica. *Compos Sci Technol* 88:69–75
- Sadeghi M, Mehdi-Talakesh M, Ghalei B, Shafiei M (2013) Preparation, characterization and gas permeation properties of a polycaprolactone based polyurethane–silica nanocomposite membrane. *J Membr Sci* 427:21–29
- Glomann T, Schneider G-J, Allgaier J, Radulescu A, Lohstroh W, Farago B, Richter D (2013) Microscopic dynamics of polyethylene glycol chains interacting with silica nanoparticles. *Phys Rev Lett* 110:178001
- Zou H, Wu S, Shen J (2008) Polymer/silica nanocomposites: preparation, characterization, properties, and applications. *Chem Rev* 108:3893–3957
- Sanchez C, Julian B, Belleville P, Popall M (2005) Applications of hybrid organic–inorganic nanocomposites. *J Mater Chem* 15:3559–3592
- Lionti K, Toury B, Boissière C, Benayoun S, Miele P (2013) Hybrid silica coatings on polycarbonate: enhanced properties. *J Sol Gel Sci Technol* 65:1–9
- Behl M, Razzaq M-Y, Lendlein A (2010) Multifunctional shape-memory polymers. *Adv Mater* 22:3388–3410
- Leng J, Lan X, Liu Y, Du S (2011) Shape-memory polymers and their composites: stimulus methods and applications. *Prog Mater Sci* 56:1077–1135
- Jorcin J-B, Scheltjens G, Van-Ingelgem Y, Tourwé E, Van-Assche G, De-Graeve I, Van-Mele B, Terryn H, Hubin A (2010) Investigation of the self-healing properties of shape memory polyurethane coatings with the ‘odd random phase multi-sine’ electrochemical impedance spectroscopy. *Electrochim Acta* 55:6195–6203
- Mondal S, Hu J-L (2007) Water vapor permeability of cotton fabrics coated with shape memory polyurethane. *Carbohydr Polym* 67:282–287
- Ji F-L, Hu J-L, Li T-C, Wong Y-W (2007) Morphology and shape memory effect of segmented polyurethanes. Part I: with crystalline reversible phase. *Polymer* 48:5133–5145
- Sedat-Gunes I, Cao F, Jana S-C (2008) Evaluation of nanoparticulate fillers for development of shape memory polyurethane nanocomposites. *Polymer* 49:2223–2234
- Soleimani-Dorcheh A, Abbasi M-H (2008) Silica aerogel; synthesis, properties and characterization. *J Mater Process Technol* 199:10–26
- Chen Y, Zhou S, Yang H, Wu L (2005) Structure and properties of polyurethane/nanosilica composites. *J Appl Polym Sci* 95:1032–1039
- Xia H, Song M (2006) Preparation and characterisation of polyurethane grafted single-walled carbon nanotubes and derived polyurethane nanocomposites. *J Mater Chem* 16:1843–1851
- Zhang H, Zhang J, Chen J, Hao X, Wang S, Feng X, Guo Y (2006) Effects of solar UV irradiation on the tensile properties and structure of PPTA fiber. *Polym Degrad Stab* 91:2761–2767
- Chen J, Zhu Y, Ni Q, Fu Y, Fu X (2014) Surface modification and characterization of aramid fibers with hybrid coating. *Appl Surf Sci* 321:103–108
- Yang H, Wang J, Wu H, Fu Y (2013) Effect of silica sol modification on the tensile property of carbon fiber/epoxy composites. *Chin J Mater Res* 27:108–112



Surface modification and characterization of aramid fibers with hybrid coating



Jianrui Chen, Yaofeng Zhu, Qingqing Ni, Yaqin Fu*, Xiang Fu

The Key Laboratory of Advanced Textile Materials and Manufacturing Technology Ministry of Education, Zhejiang Sci-Tech University, Hangzhou Zhejiang 310018, China

ARTICLE INFO

Article history:

Received 17 July 2014

Received in revised form

29 September 2014

Accepted 29 September 2014

Available online 7 October 2014

Keywords:

Aramid fiber

Hybrid coating

Surface modification

Interfacial adhesion

ABSTRACT

Aramid fibers were modified through solution dip-coating and interfacial in situ polymerization using a newly synthesized SiO_2 /shape memory polyurethane (SiO_2 /SMPU) hybrid. Fourier transform infrared and X-ray photoelectron spectroscopy indicated that the synthesized SiO_2 /SMPU hybrid successfully coated the fiber surface. The surface morphology of the aramid fibers and the single fiber tensile strength and interfacial shear strength (IFSS) of the composites were determined. The IFSS of the fiber coated with the hybrid improved by 45%, which benefited from a special “pizza-like” structure on the fiber surface.

© 2014 Elsevier B.V. All rights reserved.

1. Introduction

Fiber-reinforced polymer composites are widely used in aerospace, automobiles, and industries because of their outstanding properties, such as high specific strength, low density, and flexible design [1,2]. Composite interfaces must efficiently transfer stress from the matrix to the fibers to optimize the mechanical performance of fiber-reinforced polymer composites [3,4]. Therefore, the fiber–matrix interface has been a research hotspot.

Aramid fibers are high-performance fibers that have attracted commercial and academic interest because their highly crystalline structure offers high specific toughness ratio and strength [5,6]. However, aramid fiber-reinforced polymer composites demonstrate poor interfacial adhesion because aramid fibers exhibit chemical resistance to the active groups of the polymer matrix [7,8].

Many prominent researchers investigated different methods to improve the interface of aramid fiber-reinforced polymer composites. One of these methods is modifying the aramid fiber surface through chemical or physical treatments, such as coupling agent and surface grafting, plasma treatment, γ -rays, and ultrasound [9–13], or modifying the original resin matrix to match the aramid fiber [14,15].

Coating is an important fiber surface modification method that has shown promising interface improvement. This method has the

advantages of retaining the main fiber structure, fixing defects on the fiber surface, and being suitable for complex-shaped samples [16–18]. Many coating treatments have been used to modify the aramid fiber surface, but limited success has been achieved. Lange et al. [19] found that polyurethane varnish coating can significantly improve the interfacial properties of aramid/epoxy resin composites. Zou et al. [20] reported that nano- SiO_2 coating using the sol–gel method can improve the mechanical properties of aramid filaments. However, studies have rarely analyzed the potential use of inorganic nanofiller/polyurethane hybrid materials in fiber coating.

Aramid fibers were modified in the present work by solution dip-coating and interfacial in situ polymerization using a newly synthesized SiO_2 /shape memory polyurethane (SiO_2 /SMPU) hybrid. The microstructure of the SiO_2 /SMPU hybrid was investigated. The aramid fiber surface topography and SiO_2 nanoparticle distribution of the hybrid coating the aramid fiber were determined through scanning electron microscopy. The tensile properties of the coated aramid fibers were tested in the fiber direction using universal testing instruments. The adhesion between the modified aramid fibers and the resin matrix was also evaluated through interfacial shear strength (IFSS) to analyze the fiber–matrix interface properties.

2. Experimental

Aramid fibers (Twaron2200, with 13 μm diameter) were supplied by Teijin Japan and liquid shape memory polyurethane (Diary, MS-4510) was supplied by Diaplex Co. Ltd. Japan.

* Corresponding author. Tel.: +86 571 86843607; fax: +86 571 86843607.
E-mail address: fyq01@zstu.edu.cn (Y. Fu).

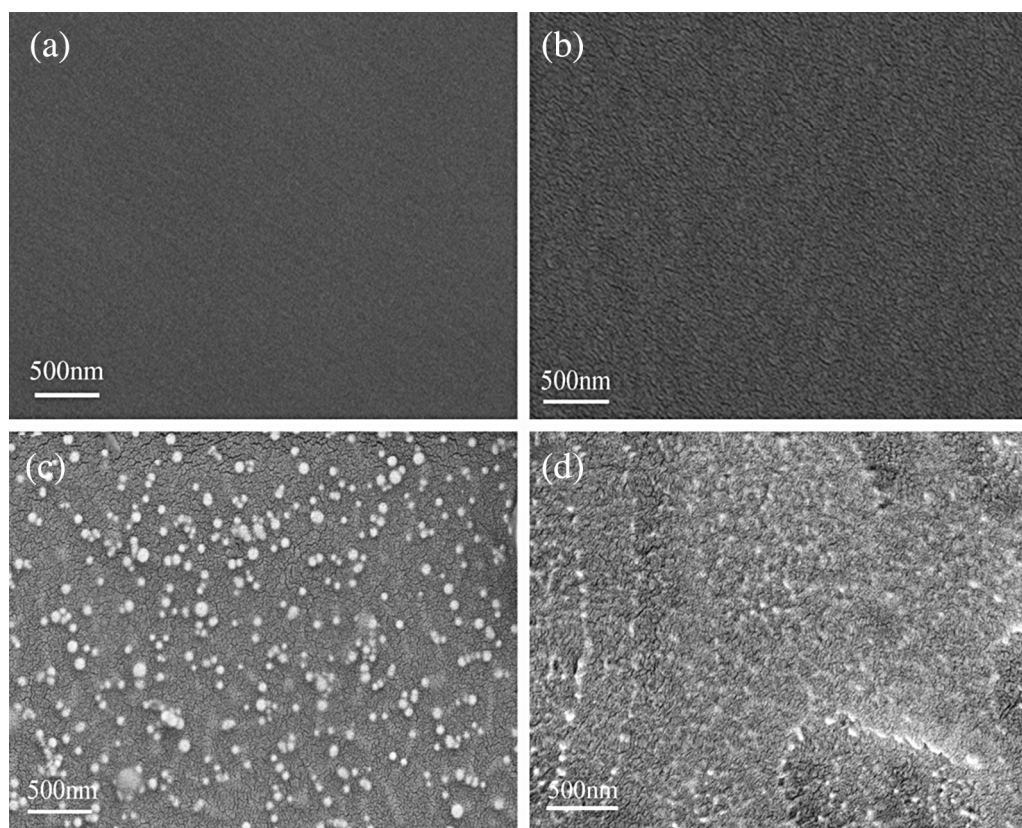


Fig. 1. SEM images of pure SMPU (a) surface and (b) cross-section, and SiO₂/SMPU (c) surface and (d) cross-section.

Tetraethoxysilane (TEOS), 3-aminopropyltriethoxysilane (KH550), p-toluenesulfonic acid (PTSA), N,N-dimethylacetamide (DMAc), phosphoric acid, acetone, and absolute ethanol were of analytical grade.

2.1. SMPU/SiO₂ hybrid synthesis

The SiO₂ precursor (solution A) was prepared by mixing PTSA, TEOS, and DMAc at a mass ratio of 0.1:10:100 under stirring at 25 °C for 2 h. The modified SMPU resin (solution B) was prepared by mixing SMPU resin and KH550 at a mass ratio of 100:2 under stirring at 50 °C for 2 h. The SiO₂/SMPU hybrid was synthesized by mixing solutions A and B under stirring at 50 °C for 2 h. The equivalent PTSA/TEOS/KH550 was ensured to be 0.1:10:2. The final hybrid used to coat the aramid fibers was prepared by mixing the SiO₂/SMPU hybrid and DMAc at a mass ratio of 2:100.

2.2. Surface modification of aramid fibers

The aramid fibers were washed in acetone and subjected to functionalized pretreatment using 30% aqueous phosphoric acid solution at 40 °C for 2 h. The sample was dried and marked as TF. TF was coated with pure SMPU and SiO₂/SMPU through the dipping method and then dried at room temperature for 2 days. The samples were designated as SMPU–TF and S–TF, respectively.

2.3. Preparation of single fiber-reinforced composite

SMPU was poured into molds fixed with single aramid fibers. The molds were heated in an oven to 40 °C for 24 h, 60 °C for 24 h, 80 °C for 24 h, and 24 h at 130 °C.

2.4. Characterization

The morphology of the SiO₂/SMPU materials and S–TF were examined through field-emission scanning electron microscopy (F-ESEM) (ULTRA 55, ZEISS, Germany). Attenuated-total-reflection infrared spectra were recorded using a Nicolet5700 FT-IR spectrometer (Thermo Electron, USA) to analyze the chemical structures of the aramid fibers. X-ray photoelectron spectroscopy (XPS) was performed using an ESCALAB MARK II X-ray photoelectron spectrometer (VG, U.K.).

The tensile strength of the coated fibers was determined using a universal testing instrument (KES-G1, Japan) at a rate of 6.0 mm/min in accordance with GJB993-1990. Single-fiber fragmentation testing was performed by a Leica DM2700P polarizing microscope. The IFSS was calculated according to the saturated number of cracks throughout the fiber using the equation:

$$IFSS = k \frac{\sigma_f d}{2l}$$

where k is the correction factor for aramid fiber ($k=0.889$) [21], σ_f is the ultimate fiber strength at the critical length, d is the fiber diameter, and \bar{l} is the average fiber fragment length.

3. Results and discussion

3.1. Characterization and analysis of SiO₂/SMPU hybrid structure

Typical SEM images of SMPU and SiO₂/SMPU hybrid are shown in Fig. 1. SiO₂ particles with sizes ranging from 30 to 50 nm are evenly distributed both on the surface (Fig. 1c) and on the cross-section (Fig. 1d) compared with the smooth SMPU (Fig. 1a and 1b). This result can be attributed to the fact that the hydrolysis

condensation of the system is well controlled through the anhydrous sol–gel method, which uses water in air as the hydrolysis reaction source [15]. Meanwhile, SMPU and TEOS interact through the amino and alkoxy groups of KH550, respectively. This interaction not only forms covalent bonds between the organic polymer and inorganic silica but also prevents particle agglomeration. Therefore, the nanoparticles exhibit excellent dispersion and suitable size, and the sizing system shows stability even after six months.

3.2. Structure and properties of the aramid fiber surface

The FTIR spectra of the TF and S-TF samples are shown in Fig. 2. The characteristic bands of TF at 3320 and 1543 cm^{-1} are attributed to the N–H vibration of the primary amine in Twaron. Absorption peaks at 2958, 1729, 1610, and 1222 cm^{-1} are absent in TF but present in S-TF. This result can be ascribed to the characteristic peaks of polyurethane. The sharp absorption peak at 1067 cm^{-1} can also be ascribed to the characteristic peaks of Si–O–Si, which are created because of the formation of sizing through the hydrolysis and condensation of the precursor (SMPU + KH550 + TEOS). The absorption peaks are relatively weak because of the relatively low amount of hybrid coated on the fibers.

The chemical microstructure of S-TF as determined through XPS is shown in Fig. 3. The wide-scan spectra of the TF (Fig. 3a) and S-TF (Fig. 3c) surfaces contain C 1s, N 1s, and O 1s peaks. The N 1s peak intensity of S-TF is lower than that of TF. This result indicates that

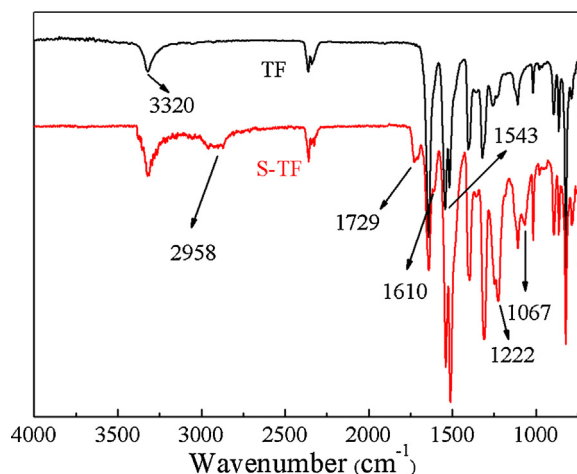


Fig. 2. FTIR spectra of TF and S-TF fibers.

the coating on the S-TF surface has a lower nitrogen ratio than that on the TF surface. Fig. 3b shows that the N 1s core-level spectrum of the TF surface contains only two peaks. These peaks can be ascribed to the N–H and N–C species at binding energies (BEs) of 399.5 and 399.1 eV, respectively, caused by TF synthesis. The N 1s core-level spectrum of S-TF (Fig. 1d) can be curve-fitted with three peak components, with a new one for the N–Si species at a BE of 397.8 eV.

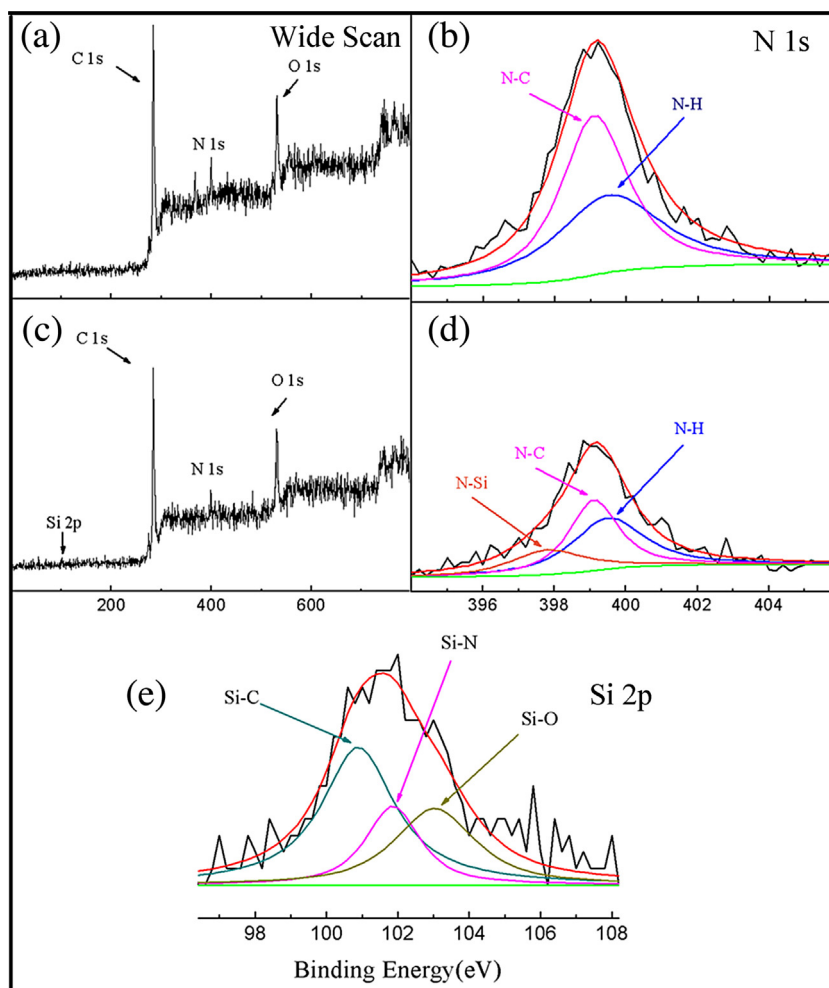


Fig. 3. XPS spectra of (a and b) TF and (c, d and e) S-TF fibers.

Table 1
Elemental composition of the sample surfaces.

Sample	Atomic percent				Atomic ratio O/N
	C 1s	O 1s	N 1s	Si 2p	
TF	76.84	15.44	7.72	0	2.00
S-TF	76.32	16.32	5.02	2.34	3.25

The Si 2p core-level spectrum of S-TF (Fig. 3e) can be curve-fitted with three peak components, namely, 28.9% Si–O, 51.1% Si–C, and 20.0% Si–N. This result suggests that silicon exists in the forms of SiO₂ and covalent cross-linking oxide.

The surface elemental composition of the samples is listed in Table 1. The O/C ratio is increased and the oxygen element is increased by 6% after the modification. The nitrogen element ratios of TF and S-TF are 7.72 and 5.02, respectively, and the O/N ratios of TF and S-TF are 2.00 and 3.25, respectively. The increase in O/N on the polar surface probably contributes to the adhesion between the fiber and the matrix [22]. The S-TF surface contains 2.34% Si. FTIR and XPS analyses indicate the successful coating of the SiO₂/SMPU hybrid onto the aramid fiber surface.

Fig. 4 shows the surface morphology of the aramid fibers. Slight lines and grooves as well as plush-like microfibers can be observed on the TF surface (Fig. 4a). The SMPU-TF surface contains a coarse SMPU membrane (Fig. 4b). However, the S-TF surface contains an integrated compact membrane with embedded and semi-embedded particles (Fig. 4c and 4d). The great number of particles uniformly scattered on the fiber surface plays an important role in increasing the specific surface area.

Single-fiber tensile testing was performed to characterize in-plane strength (Fig. 5). Coating increases fiber strength; S-TF is stronger than SMPU-TF. This result and mechanism can be explored as follow: a special structure was introduced onto the S-TF surface

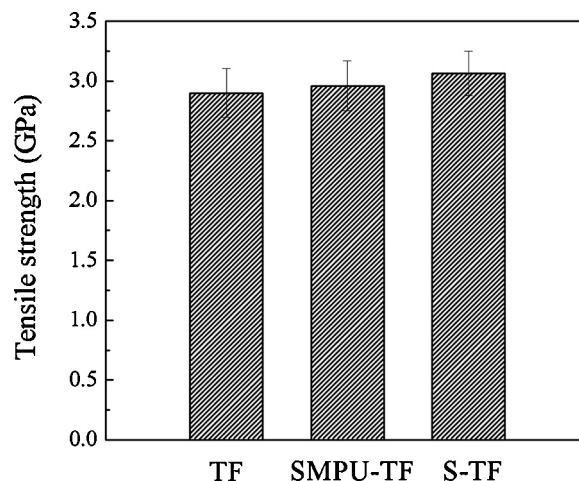


Fig. 5. Tensile strength of monofilament aramid fibers modified through different methods.

with some reactive groups after acidification. Reactive groups react with silicon hydroxyl groups and form Si–O–Si bonds during drying. As a result, a silicon-oxide network structure is constructed. This structure improves network structure uniformity, enhances stress transfer, and then improves fiber anti-load capacity and tensile strength. This phenomenon can be referred to as the “surround effect” of hybrid membrane. SEM and XPS spectral analyses show that the SMPU/SiO₂ hybrid on the aramid fiber surface has a “pizza-like” structure (Fig. 6). SiO₂ particles are located outside and covalent cross-linking oxide membranes are located inside this structure. The formation of this structure is a major advantage because previous fiber surface modification efforts to increase

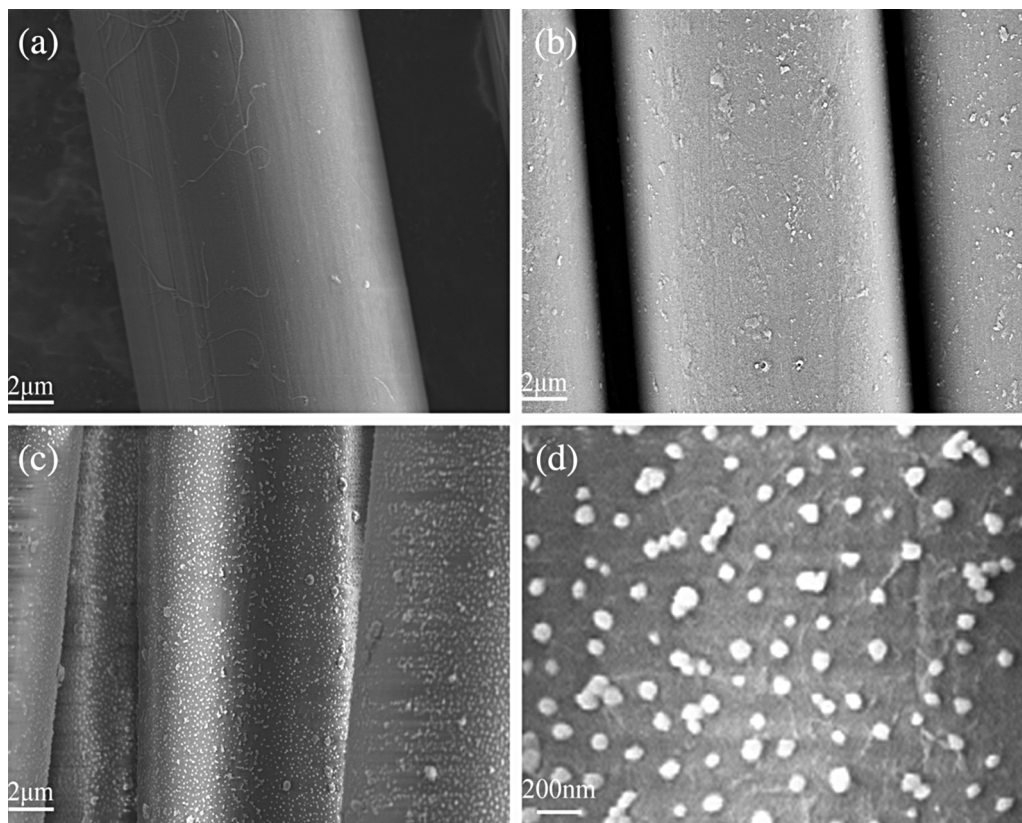


Fig. 4. SEM images of the aramid fibers surface (a: TF; b: SMPU-TF; c and d: S-TF).

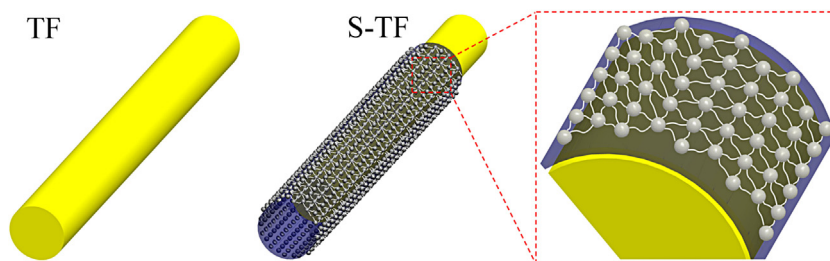


Fig. 6. Schematic of aramid fiber modified with SiO₂/SMPU hybrid.

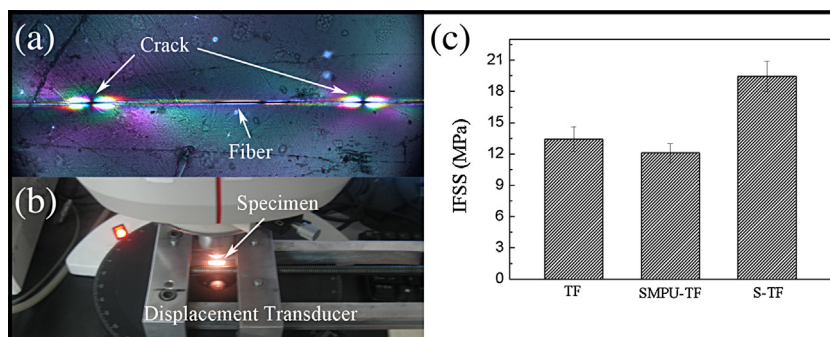


Fig. 7. Single-fiber segmentation results. (a) Micrograph of the typical fiber cracks, as observed in situ during the test. (b) Microtensile frame used in the testing, with a specimen in its jaws. (c) showing a 45% increase in single-fiber interfacial strength. The three fibers tested were TF, SMPU-TF, and S-TF.

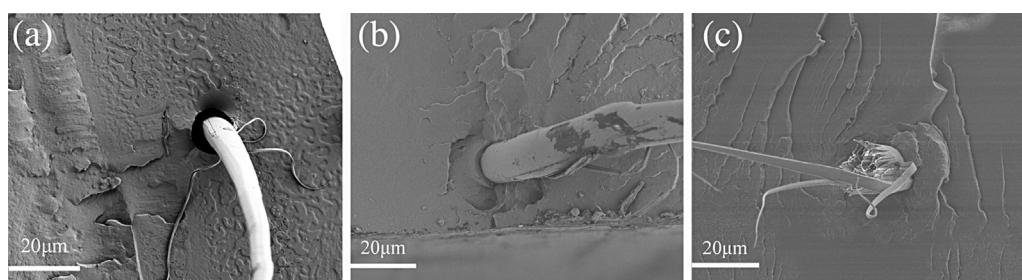


Fig. 8. Brittle cross-section morphology of the aramid fiber/SMPU composites: (a) TF fiber/SMPU, (b) SMPU-TF fiber/SMPU, and (c) S-TF fiber/SMPU.

adhesion with the matrix improve interfacial properties but at the cost of fiber strength.

3.3. Evaluation of interfacial adhesion

The interfacial properties of the fiber after surface treatment were evaluated through single fiber fragmentation. This process is widely used to assess interfacial strength [23]. The samples were placed in a screw-driven microtensile test stage, stress was applied on the specimen, and the specimen was monitored using an optical microscope under polarized light (Fig. 7a). The number of fragments was counted under increasing strain using this system to identify the saturation point (Fig. 7b). The number of fragments was then used to determine critical length. The interfacial shear strength of each case studied is plotted in Fig. 7c. The interfacial strength of S-TF is 45% higher than that of TF. The interfacial adhesion between the aramid fiber and the polymer matrix is significantly increased after the modification. However, the counter interfacial strength of SMPU-TF is decreased. Therefore, the new structure of the S-TF surface indicates strong adhesion between the fiber and the matrix.

The cross-sections of the specimens under SEM are illustrated in Fig. 8. Fig. 8a shows that the TF forms plastic flow necking near the fracture in the longer range. This finding may be attributed to the acidification pretreatment [24]. However, the SMPU membrane

detaches from the SMPU-TF surface, and the fiber surface shows irregular mottles (Fig. 8b). This result may be attributed to the different thermal expansion coefficients of the pure SMPU coating and aramid fibers [25]. However, axial splitting and many fibrillated and petaloid microfibers are found in S-TF (Fig. 8c). This result suggests that S-TF exhibits more consumed fracture energies and better interfacial bonding than TF. The excellent interfacial adhesion is expected to exert the “hammer ball effect” on the particles from the “pizza-like” structure coating. The links point between the matrix and the fiber, showing that the “pizza” combines with the two interfaces by covalently linking the cross-linking oxide membrane to the fiber and linking the SiO₂ particles to the matrix. The “hammer ball” is pulled when the reinforced fibers are forced, and the stress is efficiently transferred from the matrix to the fibers. The SEM micrographs of the fracture surface of the species correspond well to the IFSS testing results.

4. Conclusions

A novel SiO₂/SMPU hybrid was synthesized by the anhydrous sol-gel method, and nanoparticles of excellent dispersion and suitable size were successfully obtained. The aramid fibers were modified using the synthesized hybrid. FTIR, XPS, and SEM indicated that the hybrid was formed on the aramid fiber surface

after modification. Hybrid modification increased single fiber tensile strength by 5.7% and improved the IFSS of the S–KF composite by 45%. A “pizza-like” structure was also formed in the hybrid on the fiber surface during coating. The interfacial phase structure possessed both inorganic composition and organic structure. This special phase structure can improve performance, particularly at the interfacial bonding area. Hybrid modification effectively and conveniently improved the interface properties between the fibers and the matrix as well as the mechanical properties of aramid fibers. This method is expected to be an important direction for future research on aramid fiber surface modification.

Acknowledgments

The authors gratefully acknowledge the Instrumental Analysis Center of Zhejiang Sci-Tech University for the use of their characterization facilities. We also thank the technicians for their assistance in the analyses and for the technical discussions.

References

- [1] C.E. Bakis, L.C. Bank, V.L. Brown, E. Cosenza, J.F. Davalos, J.J. Lesko, A. Machida, S.H. Rizkalla, T.C. Triantafillou, Fiber-reinforced polymer composites for construction-state-of-the-art review, *J. Compos. Constr.* 6 (2002) 73–87.
- [2] F.M. AL-Oqla, S.M. Sapuan, Natural fiber-reinforced polymer composites in industrial applications: feasibility of date palm fibers for sustainable automotive industry, *J. Clean. Prod.* 66 (2014) 347–354.
- [3] F.Z. Arrakhiz, M.E. Achabya, M. Malha, M.O. Bensalah, O. Fassi-Fehri, R. Bouhfid, K. Benmoussa, A. Qaiss, Mechanical and thermal properties of natural fibers reinforced polymer composites: Doum/low density polyethylene, *Mater. Des.* 43 (2013) 200–205.
- [4] S.S. Nair, D.C. Hurley, S. Wang, T.M. Young, Nanoscale characterization of interphase properties in maleated polypropylene-treated natural fiber-reinforced polymer composites, *Polym. Eng. Sci.* 53 (2013) 888–896.
- [5] I.M. Daniel, O. Ishai, *Engineering Mechanics of Composite Materials*, 2nd ed., Oxford University Press, New York, 2006.
- [6] J.M. García, F.C. García, F. Serna, J.L. de la Peña, High-performance aromatic polyamides, *Prog. Polym. Sci.* 35 (2010) 623–686.
- [7] W. Wang, R. Li, M. Tian, L. Liu, H. Zou, X. Zhao, L. Zhang, Surface silverized meta-aramid fibers prepared by bio-inspired poly(dopamine) functionalization, *ACS. Appl. Mater. Interfaces* 5 (2013) 2062–2069.
- [8] G.J. Ehlert, H.A. Sodano, Zinc oxide nanowire interphase for enhanced interfacial strength in lightweight polymer fiber composites, *ACS. Appl. Mater. Interfaces* 1 (2009) 1827–1833.
- [9] T. Ai, R. Wang, W. Zhou, Effect of grafting alkoxysilane on the surface properties of Kevlar fiber, *Polym. Compos.* 28 (2007) 412–416.
- [10] T.M. Liu, Y.S. Zheng, J. Hu, Surface modification of aramid fibers with new chemical method for improving interfacial bonding strength with epoxy resin, *J. Appl. Polym. Sci.* 118 (2010) 2541–2552.
- [11] M. Su, A. Gu, G. Liang, L. Yuan, The effect of oxygen-plasma treatment on Kevlar fibers and the properties of Kevlar fibers/bismaleimide composites, *Appl. Surf. Sci.* 257 (2011) 3158–3167.
- [12] Y.H. Zhang, Y.D. Huang, L. Liu, K.L. Cai, Effects of γ -ray radiation grafting on aramid fibers and its composites, *Appl. Surf. Sci.* 254 (2008) 3153–3161.
- [13] L. Liu, Y.D. Huang, Z.Q. Zhang, Z.X. Jiang, L.N. Wu, Ultrasonic treatment of aramid fiber surface and its effect on the interface of aramid/epoxy composites, *Appl. Surf. Sci.* 254 (2008) 2594–2599.
- [14] T.K. Lin, S.J. Wu, J.G. Lai, S.S. Shyu, The effect of chemical treatment on reinforcement/matrix interaction in Kevlar-fiber/bismaleimide composites, *Compos. Sci. Technol.* 60 (2000) 1873–1878.
- [15] L. Xu, Y. Fu, M. Du, Investigation on structures and properties of shape memory polyurethane/silica nanocomposites, *Chin. J. Chem.* 29 (2011) 703–710.
- [16] B. Wei, H.L. Cao, S.H. Song, Surface modification and characterization of basalt fibers with hybrid sizings, *Compos. Part A* 42 (2011) 22–29.
- [17] B. Mahltig, H. Haufe, H. Böttcher, Functionalization of textiles by inorganic sol–gel coatings, *J. Mater. Chem.* 15 (2005) 4385–4398.
- [18] B.S. Shim, W. Chen, C. Doty, C. Xu, N.A. Kotov, Smart electronic yarns and wearable fabrics for human biomonitoring made by carbon nanotube coating with polyelectrolytes, *Nano Lett.* 8 (2008) 4151–4157.
- [19] P.J. de Lange, E. Mäder, K. Mai, R.J. Young, I. Ahmad, Characterization and micromechanical testing of the interphase of aramid-reinforced epoxy composites, *Compos. Part A* 32 (2001) 331–342.
- [20] J. Zou, Y.C. Zhang, H.Y. Wu, Y.P. Qiu, Nano effects of helium plasma treatment nano-SiO₂ coating Kevlar filaments, *Mater. Sci. Forum* 610 (2009) 692–699.
- [21] P.J. Herrera-Franco, L.T. Drzal, Comparison of methods for the measurement of fiber/matrix adhesion in composites, *Composites* 23 (1992) 2–27.
- [22] P.J. de Lange, P.G. Akker, E. Mäder, S.L. Gao, W. Prasithphol, R.J. Young, Controlled interfacial adhesion of Twaron® aramid fibers in composites by the finish formulation, *Compos. Sci. Technol.* 67 (2007) 2027–2035.
- [23] B.W. Kim, J.A. Nairn, Observations of fiber fracture and interfacial debonding phenomena using the fragmentation test in single fiber composites, *J. Compos. Mater.* 36 (2002) 1825–1858.
- [24] G. Li, C. Zhang, Y. Wang, P. Li, Y. Yu, X. Jia, H. Liu, X. Yang, Z. Xue, S. Ryu, Interface correlation and toughness matching of phosphoric acid functionalized Kevlar fiber and epoxy matrix for filament winding composites, *Compos. Sci. Technol.* 68 (2008) 3208–3214.
- [25] L.B. Xu, Y.Q. Fu, Q.Q. Ni, Interfacial properties of aramid/SMPU-SiO₂ composites, *Acta Polym. Sin.* 10 (2011) 1132–1137.

Fabrication and properties of KMnO_4 -treated functionalized biaxially oriented polypropylene (BOPP) films coated with a hybrid material

Jing Wang · Yaofeng Zhu · Yaqin Fu

Received: 6 November 2013 / Accepted: 7 April 2014 / Published online: 16 April 2014
© Springer Science+Business Media New York 2014

Abstract KMnO_4 -treated functionalized biaxially oriented polypropylene (BOPP) films coated with a hybrid material were synthesized, and the abrasion resistance properties of the resultant films were examined. The presence of functional groups was confirmed using Fourier-transform infrared spectroscopy, transmittance measurements were performed using an ultraviolet–visible spectrophotometer, and the intensities of the films were measured using a universal testing machine. The abrasion resistance and roughness of the composite films were significantly affected by modification of the BOPP film. The transmittance of the modified films obviously improved with the addition of Al_2O_3 sol, and the mechanical properties of the treated films were improved by the coatings. The abrasion resistance of one of the functionalized films (sample S159) increased by 79.5 % compared with that of the original film.

Keywords Abrasion resistance · Biaxially oriented polypropylene · Surface modification · KMnO_4

1 Introduction

Biaxially oriented polypropylene (BOPP) films are important commercial polyolefin films widely used in food packaging, as a protective coating of other films, and printing [1–4]. However, the relatively low adhesion and

scratch resistance of BOPP films restrain their wider application [5, 6]. Application of sol–gel coatings is the most commonly employed method for protecting BOPP films from direct contact with scratching particles. However, BOPP films exhibit very low surface tension, especially in the polar regions of the polymers; this low surface tension leads to incomplete wettability, which causes low interfacial interactions between the highly crosslinked coating and the polypropylene films. Thus, to improve the application prospects of BOPP films, surface modification techniques must be introduced.

The most commonly used surface treatment techniques for BOPP films include plasma treatment [7, 8], ion beam treatment [9], corona discharge [10], surface grafting [11], and chemical oxidation [12, 13]. Favaro et al. [14] demonstrated that the surface wettability of polypropylene films can be significantly improved by treatment with KMnO_4 solution. In their study, the adhesion of KMnO_4 -treated PP films improved, but the treated films were washed with HCl solution, which is not eco-friendly and could be harmful to researchers and end-users. Jeon et al. [15] prepared hard coating films based on organosilane-modified boehmite nanoparticles under UV/thermal dual curing. Wan et al. [16] and Lioni [17] synthesized hybrid materials using a sol–gel technique with the addition of water to successfully improve the abrasion resistance of the substrate. However, studies on the preparation of sol–gel solutions in the absence of water are limited [18]. Wang et al. [19] synthesized hybrid materials using a sol–gel technique without the addition of water; the resulting material had a low reaction rate, resulted in a more stable and easy-to-store sol system, and successfully improved the abrasion resistance of BOPP films. However, curing conditions were fairly rigorous at -55°C and 0.01 MPa and thus impractical for industrial applications.

J. Wang · Y. Zhu · Y. Fu (✉)
The Key Laboratory of Advanced Textile Materials and
Manufacturing Technology Ministry of Education, Zhejiang Sci-
Tech University, Hangzhou 310018, Zhejiang, China
e-mail: fyq01@zstu.edu.cn

In the current study, KMnO_4 solution was used to modify the surface of BOPP films to improve their adhesion, and oxalic acid solution, which is more eco-friendly than HCl , was used to wash the treated films. A sol–gel method in which the sol is synthesized without the addition of deionized water was used to prepare uniformly dispersed nanoparticles, and Al_2O_3 sol was added to the SiO_2 sol to maintain the high transmittance of treated BOPP films. The BOPP films were then coated with the hybrid material using a dip-coating technique.

2 Experimental

2.1 Materials

BOPP films (thickness = 47 μm) were supplied by Zhejiang Kelly Packaging Materials Company (China). KMnO_4 , 98 % (w/v) H_2SO_4 solution, tetraethoxysilane (TEOS), *p*-toluene sulfonic acid (PTSA), absolute ethanol (99.7 wt%), oxalic acid, aluminum tri-sec-butoxide (ASB), and 3-triethoxysilylpropylamine (KH550) were provided by Hangzhou Mike Chemical Instrument (China). All chemicals were used without further purification.

2.2 Surface modification of BOPP films

The BOPP films were washed with deionized water and dried in a baking oven prior to modification. The films were oxidized in 0.3/0.1 M $\text{KMnO}_4/\text{H}_2\text{SO}_4$ solution at 60 °C for 6 h, yielding films with good adhesion properties [14]. Afterward, the BOPP films were washed with oxalic acid solution to remove any oxidation residue from their surface.

2.3 Preparation of surface modifier

A total of 30.00 g of TEOS, 0.30 g of PTSA, and 200 mL of ethanol were added to a small reaction vessel at room temperature under stirring for 2 h. The obtained homogeneous mixture was marked solution A. Exactly 6.00 g of KH550 and 200 mL of ethanol were added to another small reaction vessel at room temperature under stirring for 2 h, and the resulting mixture was marked solution B. Solution B was added to solution A using the titrimetric method under stirring for 2 h. The resulting Sol 1 was stored in a fresh vessel and isolated from air. In the same manner, a total of 10.00 g of ASB and 200 mL of ethanol were added to a small reaction vessel at room temperature under stirring for 2 h. The resulting solution was marked solution C. Exactly 0.10 g of PTSA and 200 mL of ethanol were added to a small reaction vessel at room temperature under stirring for 2 h. The resulting solution was marked solution D. Solution C was added to solution D using the titrimetric

Table 1 Sol compositions obtained using different ratios of the raw materials

Formula	TEOS/ASB (g)	PSTA (g)	KH550 (g)	EtOH (mL)
1	15/0	0.15	3	200
2	15/1	0.16	3	240
3	15/3	0.18	3	320
4	15/9	0.24	3	560
5	0/15	0.15	0	600

method under stirring for 2 h, thereby forming Sol 5. Sol 1 was mixed with Sol 5 at varying ratios, as shown in Table 1, to form different sol solutions.

2.4 Coating and curing

BOPP films modified with the $\text{KMnO}_4/\text{H}_2\text{SO}_4$ solution were dipped into the sol solutions for 10 min, and the films were collected at a rate of 2 mm/s. The coated films were aged at 25 °C in the air for 24 h and then dried at 100 °C for 0.5 h. In this study, six samples labeled S150u, S150, S151, S153, S159, and S015 were prepared to determine the effects of the nanocomposite coatings on the BOPP films. S150u refers to the pristine film without treatment with $\text{KMnO}_4/\text{H}_2\text{SO}_4$ solution but coated with Sol 1. S150, S151, S153, S159, and S015 refer to the films treated with $\text{KMnO}_4/\text{H}_2\text{SO}_4$ solution and coated with Sol 1, Sol 2, Sol 3, Sol 4, and Sol 5, respectively.

2.5 Characterization

Changes in the surface functional groups were recorded on a Fourier-transform infrared (FTIR) spectrometer (Nicolet 5700, Thermo Electron Scientific Instruments Corp, USA). The surface topography of the BOPP films was analyzed after the abrasion test using a field-emission scanning electron microscope (Ultra 55, Zeiss, Germany) at an operating voltage of 3 kV. Sol dispersion was examined using a transmission electron microscopy (TEM) system (JEM-2100F, JEOL, Japan) operated at 200 kV. Transmittance measurements were performed using an ultraviolet–visible spectrophotometer (TU-1901, Persee, China), and the measured wavelengths were range from 400 to 800 nm. The transmission values were averaged from 400 to 800 nm, and each sample was measured six times. The chemical binding of the coated films was investigated by X-ray photoelectron spectroscopy (K-Alpha, Thermo Fisher Scientific, USA). The instrument was equipped with a monochromatic $\text{Al-K}\alpha$ X-ray source ($h\nu = 1,468.6$ eV), and the XPS analysis chamber was evacuated to a pressure of 2×10^{-9} mbar or lower before collecting XPS spectra. Spectra was collected using an X-ray spot size of 400 μm

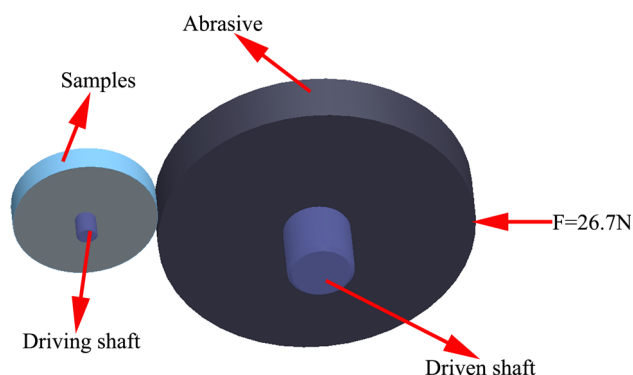


Fig. 1 Schematic of the abrasion tester

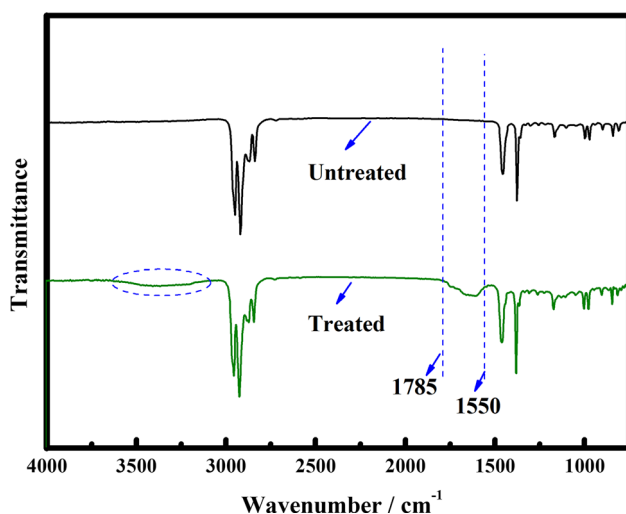


Fig. 2 FTIR-ATR spectra of BOPP films with and without 0.3 M KMnO_4 solution treatment

and pass energy of 100 eV, with 1 eV increments, at a 90° takeoff angle. The tensile property of the films was measured using a universal testing machine (INSTRON 3367,

USA), and ten samples with identical characteristics were tested. The abrasion resistance of the films was analyzed using an Akron abrasion tester (MH-74, China) (Fig. 1) at a loading of 26.7 N for 200 circles. Samples were cut into 214 mm × 12.7 mm sizes for abrasion testing. Mass loss (M_L) was defined as:

$$M_L = \frac{M_0 - M_f}{M_0} \times 100 \%$$

where M_0 is the weight of samples before the abrasion test and M_f is the weight of samples after the abrasion test.

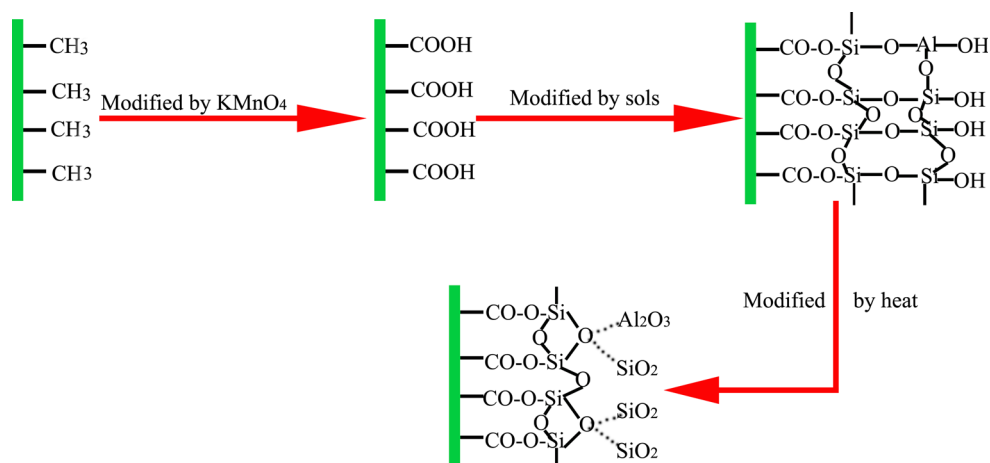
3 Results and discussion

3.1 Effects of surface modification and mixed sol analyzed by FTIR

Figure 2 shows the FTIR spectra of raw BOPP films and modified BOPP films with KMnO_4 solution. The main spectral changes found in the region between 1,785 and 1,550 cm^{-1} in the modified and untreated polymers are attributed to the different carbonyl groups that formed on the modified film surfaces. The mechanism diagram of preparation of BOPP composite films is shown in Fig. 3. In Fig. 2, the spectra of the treated BOPP films exhibit significant absorption bands at approximately 1,785 and 1,550 cm^{-1} , which correspond to $-\text{C}=\text{O}$ and $-\text{C}-\text{O}$ stretching vibrations, respectively. The treated films also show a broad band at around 3,200 cm^{-1} , which is attributed to $\text{O}-\text{H}$ stretching vibrations. The spectra of the BOPP films indicate that surface modification using the KMnO_4 solution can significantly promote the formation of oxygen-containing functional groups.

Figure 4 shows the FTIR spectra of the mixed sols. The absorption peak at 951 cm^{-1} attributed to $\text{Si}-\text{OH}$ stretching vibrations shifted to 905 cm^{-1} upon addition of the Al_2O_3 sol. When the Al_2O_3 sol is added to the SiO_2 sol, the

Fig. 3 The mechanism diagram of preparation of BOPP composite films



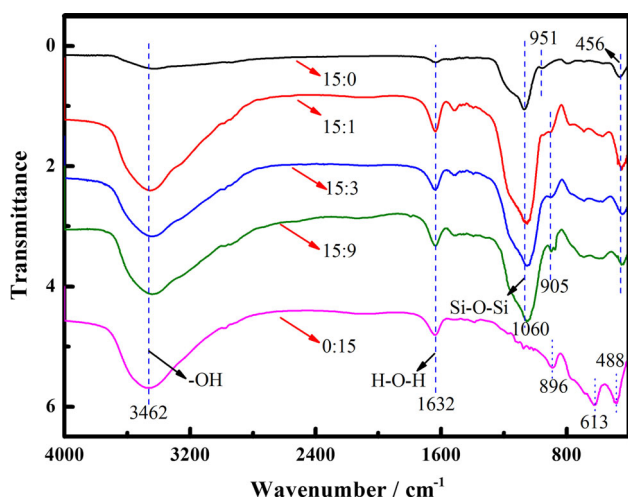


Fig. 4 FTIR spectra of various sols

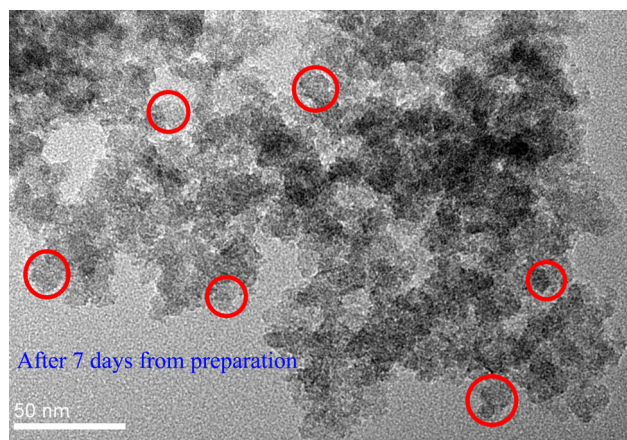


Fig. 5 TEM image of the sol (TEOS/ASB = 15:0) after 7 days from preparation

Si-OH groups are replaced by Si-O-Al; thus, the peak at 905 cm^{-1} is attributed to Si-O-Al stretching vibrations. These findings confirm that the Si-O-Al group is formed in the mixed sol system.

3.2 Morphologies of the nanoparticles and sols

The morphology of the nanoparticles was investigated using TEM. Figure 5 shows that the average size of the nanoparticles is 20 nm. The formation of nanoparticles in the presence of water in air showed a low reaction rate and led to a more stable, transparent, and easy-to-store sol system compared with a water system. Figure 6 shows that the sols remain stable when isolated from air without addition of deionized water. The sols remained transparent even after aging for 30 days, which indicates that the sols prepared in this study may be conveniently stored and utilized in industrial applications.

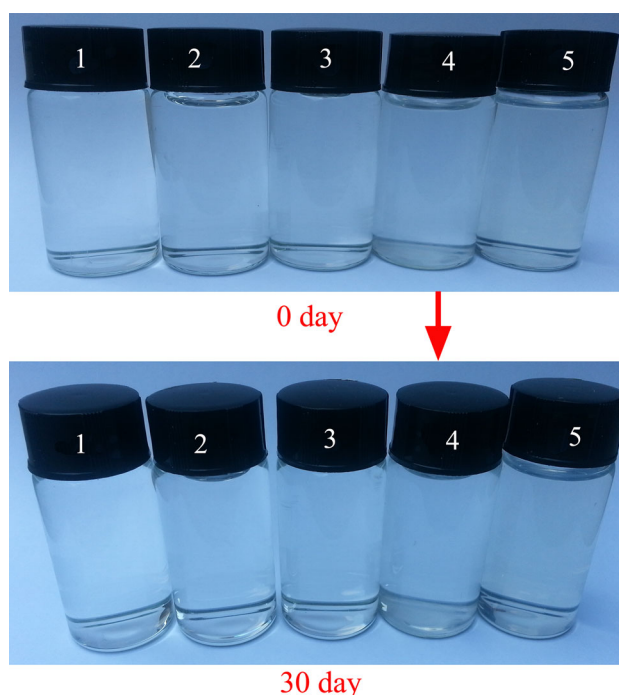


Fig. 6 Sol aging at different time points

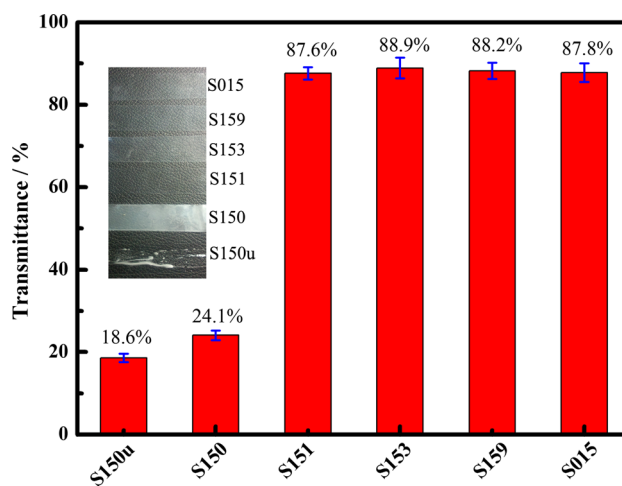


Fig. 7 Transmittance in the visible range of samples coated with various sols

3.3 Effect of surface modification on the transmittances of coated BOPP films

S150u, S150, S151, S153, S159, and S015 exhibited visible range (400–800 nm) transmittances of 18.6, 24.1, 87.6, 88.9, 88.2, and 87.8 %, respectively (Fig. 7). Compared with S150u, S150 exhibited considerably higher transmittance because surface modification can enhance interfacial interactions between the highly crosslinked coating and polypropylene films and smoothens the coating considerably.

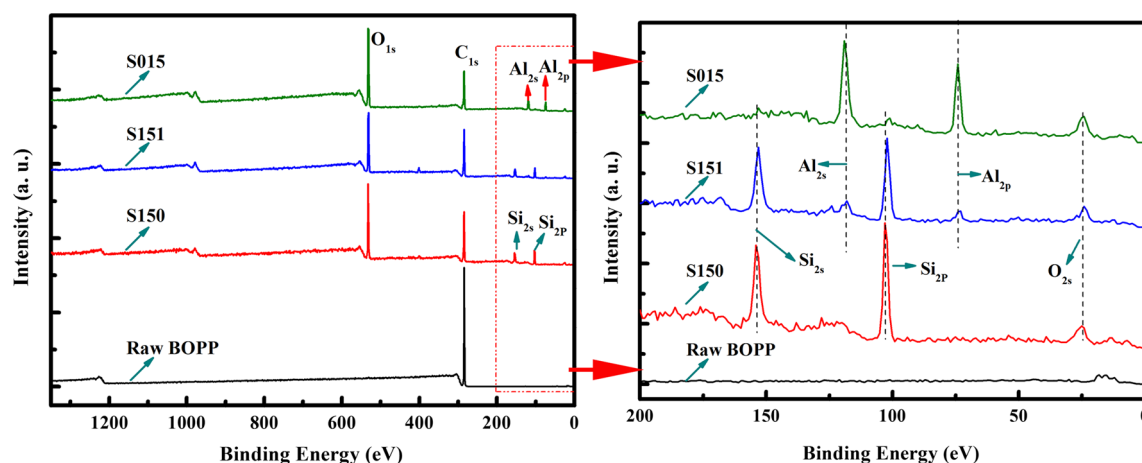


Fig. 8 XPS spectra of raw and various coated films

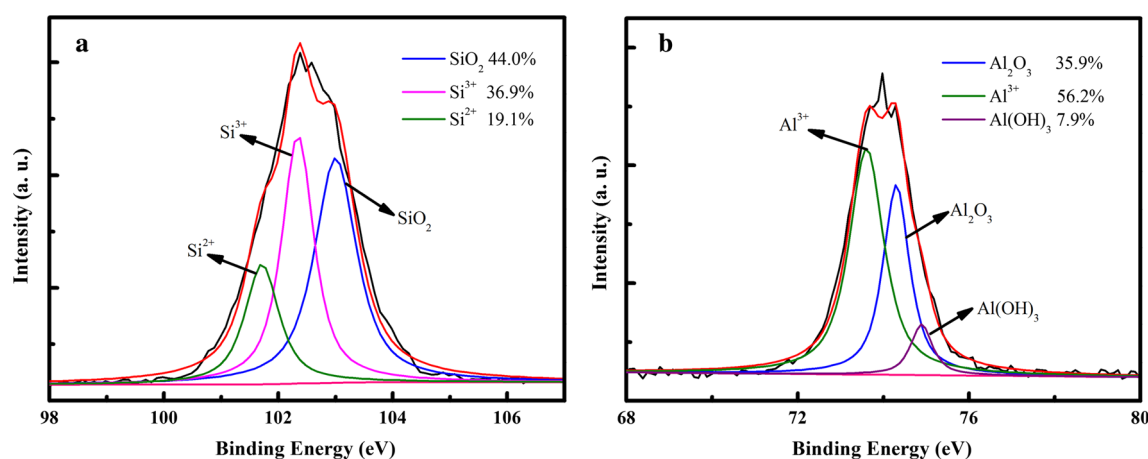


Fig. 9 **a** Si2p spectra of sample S150 and **b** Al2p spectra of sample S015

S151, S153, S159, and S015, where were coated with the Al_2O_3 sol, were all transparent, which suggests that coating with the Al_2O_3 sol produces films with high transmittance.

3.4 XPS study of the coated films

Figure 8 compares the XPS spectra of the uncoated and coated films. According to the data in the NIST X-ray Photoelectron Spectroscopy database, the appearance of $\text{Al}2s$ at 119.2 eV and $\text{Al}2p$ at 74.3 eV confirms the formation of Al_2O_3 . The formation of SiO_2 is also proven. All binding energies were referenced to the $\text{C}1s$ hydrocarbon peak at 283 eV. The raw BOPP film is not oxidized by air, since $\text{O}1s$ peaks were not observed. To analyze changes in the chemical composition of the BOPP film surface as well as their

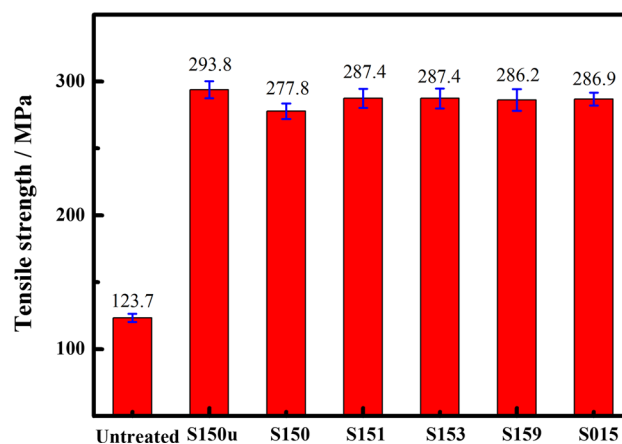


Fig. 10 Tensile strength of the samples

chemical binding states, the spectra of Al2p and Si2p were investigated, as shown in Fig. 9. On the basis of the mechanism diagram of preparation of BOPP composite films (Fig. 3), the peaks were split to concrete compositions. The spectra obtained indicate that Al and Si elements in the films mainly exist as Al^{3+} and SiO_2 , respectively. Various covalent bonds improved interfacial interactions between the highly crosslinked coating and the polypropylene films.

3.5 Effects of surface coating on the mechanical properties of the BOPP films

The samples were tested to study the effects of coating on their mechanical properties. The tensile strengths of the samples are shown in Fig. 10. The coating considerably

affected the mechanical properties of the BOPP films. Compared with the raw BOPP film, treated films exhibit significantly increased tensile strength. During the preparation of different sols, no water was added to the sol–gel systems. The precursors were hydrolyzed by air moisture in the process of gel, which effectively controls the rate of hydrolysis and results in finer and more uniform nanoparticles. Thus, sols can easily infiltrate the surface of the BOPP films and ultimately improve their mechanical properties. The tensile strength of S150 was slightly lower than that of S150u because surface modification can produce flatter and more uniform coatings without agglomeration.

3.6 Effect of surface coating on the abrasion resistance of BOPP films

The samples were subjected to abrasion treatment to study the effects of the coatings on the abrasion resistance of BOPP films. The surface morphologies of the BOPP films after the abrasion test are shown in Figs. 11 and 12. The raw film sample contained deep grooves, as shown in Fig. 11. Scratches on the surfaces of samples S150u and S150 can clearly be seen, but these scratches are shallower than those in the raw film sample. These results indicate that the abrasion resistance of the films is improved by the SiO_2 sol coating and surface modification. Figure 12 further shows shallow grooves on the surfaces of S151, S153, S159, and S015, which indicate significant improvements in abrasion resistance compared with those of the raw film, S150u, and S150 samples. This result shows that addition of the Al_2O_3 sol improves interfacial interactions between

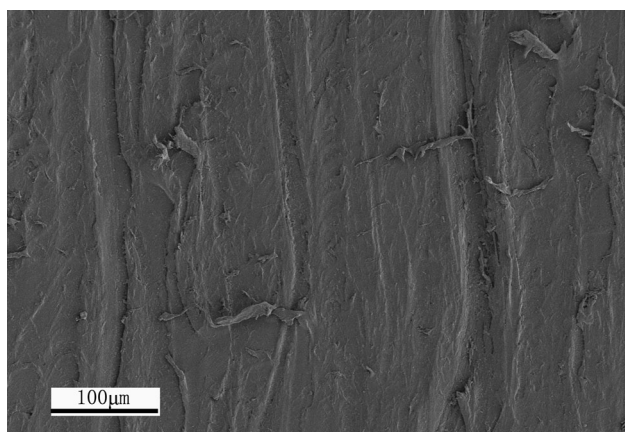


Fig. 11 SEM image of the surface of the raw film after abrasion test

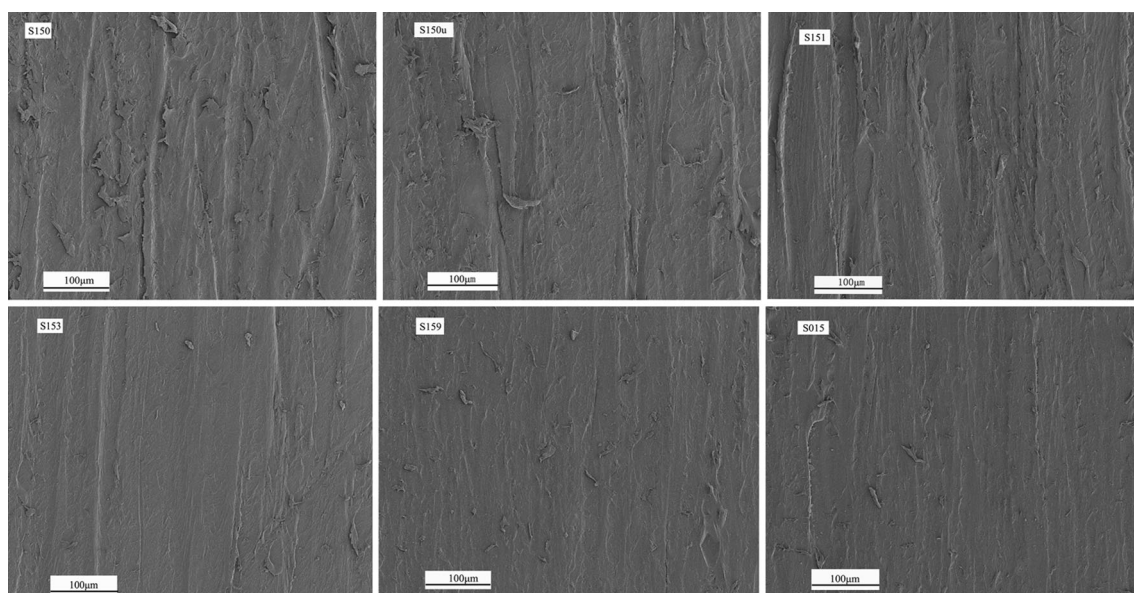


Fig. 12 SEM image of the surfaces of the treated films after abrasion test

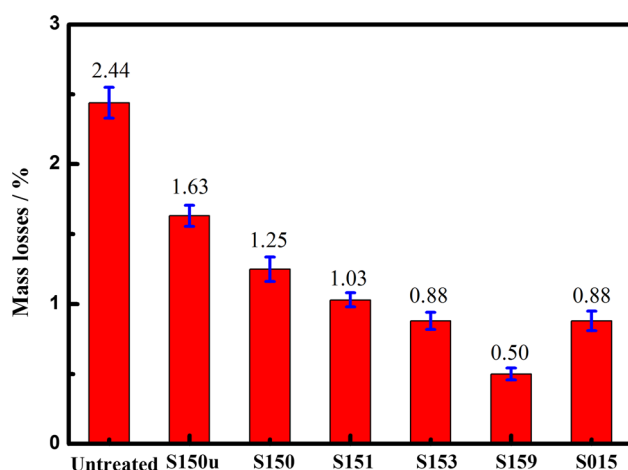


Fig. 13 Mass losses of the samples after the abrasion test

the BOPP film and the coating, thereby resulting in higher abrasion resistance.

The MLs of the samples are shown in Fig. 13. The MLs of S150u, S150, S151, S153, S159, and S015 were 2.44, 1.63, 1.25, 1.03, 0.88, 0.50, and 0.88 %, respectively. These results suggest that surface modification of BOPP films through $\text{KMnO}_4/\text{H}_2\text{SO}_4$ and coating treatment can significantly improve the abrasion resistance of the resultant films. The use of mixed sols obtained by addition of the Al_2O_3 sol to the SiO_2 sol can further improve the abrasion resistance of BOPP films. These findings were confirmed by SEM observations and are attributed to the strengthening effects of the nanoparticles on the film surfaces [20] as well as the presence of polar groups, both of which significantly improve the interfacial properties of the films [21]. In the current study, comparison of the results of the raw film sample with those of S159 showed that the abrasion resistance of the modified BOPP film increased by 79.5 %.

4 Conclusion

Several surface modification conditions were applied to BOPP films. Modification with KMnO_4 solution significantly increased interactions between the BOPPs films and the coating. The coating containing with Al_2O_3 sol produces films with high transmittance. Uniformly dispersed nanoparticles were obtained by the sol–gel method, and the sols remained stable without the addition of deionized water. BOPP films exhibited high abrasion resistance after modification, and a maximum improvement of 79.5 % was observed.

Acknowledgments The authors gratefully acknowledge the Instrumental Analysis Center of Zhejiang Sci-Tech University for allowing the use of their characterization facilities. We also thank the technicians for their assistance in the analyses and for the technical discussions.

References

- Lin Y, Hiltner A, Baer E (2010) A new method for achieving nanoscale reinforcement of biaxially oriented polypropylene film. *Polymer* 51:4218–4224
- Kalapat N, Amornsakchai T (2012) Surface modification of biaxially oriented polypropylene (BOPP) film using acrylic acid-corona treatment: part I. Properties and characterization of treated film. *Surf Coat Technol* 27:594–601
- Pandiyaraj K-N, Selvarajan V, Deshmukh R-R, Gao C (2009) Modification of surface properties of polypropylene (PP) film using DC glow discharge air plasma. *Appl Surf Sci* 255:3965–3971
- Tamura S, Kuramoto I, Kanai T (2012) The effect of molecular structure of polypropylene on stretchability for biaxially oriented film. *Polym Eng Sci* 52:1383–1393
- Dasari A, Rohrmann J, Misra R-D-K (2002) Micro-and nanoscale evaluation of scratch damage in poly (propylene)s. *Macromol Mater Eng* 287:889–903
- Xiang C, Sue HJ, Chu J, Coleman B (2001) Scratch behavior and material property relationship in polymers. *J Polym Sci, Part B: Polym Phys* 39:47–59
- Xie J, Xin D, Cao H, Wang C, Zhao Y, Yao L, Ji F, Qiu Y (2011) Improving carbon fiber adhesion to polyimide with atmospheric pressure plasma treatment. *Surf Coat Technol* 206:191–201
- Vesel A, Mozetic M (2012) Surface modification and ageing of PMMA polymer by oxygen plasma treatment. *Vacuum* 86:634–637
- Hite D-A, Colombe Y, Wilson A-C, Brown K-R, Warring U, Jordens R, Jost J-D, McKay K-S, Pappas D-P, Leibfried D, Wineland D-J (2012) 100-fold reduction of electric-field noise in an ion trap cleaned with in situ argon-ion-beam bombardment. *Phys Rev Lett* 109:103001
- Bian X, Chen L, Yu D, Wang L, Guan Z (2012) Impact of surface roughness on corona discharge for 30-year operating conductors in 500-kV ac power transmission line. *IEEE Trans Power Deliver* 27:1693–1695
- Kyomoto M, Moro T, Takatori Y, Kawaguchi H, Nakamura K, Ishihara K (2010) Self-initiated surface grafting with poly (2-methacryloyloxyethyl phosphorylcholine) on poly (ether-etherketone). *Biomaterials* 31:1017–1024
- Li J, Wang M, Shen Y (2012) Chemical modification on top of nanotopography to enhance surface properties of PDMS. *Surf Coat Technol* 206:2161–2167
- Ji W-G, Hu J-M, Liu L, Zhang J, Cao C (2007) Improving the corrosion performance of epoxy coatings by chemical modification with silane monomers. *Surf Coat Technol* 201:4789–4795
- Fávaro S-L, Rubira A-F, Muniz E-C, Radovanovic E (2007) Surface modification of HDPE, PP, and PET films with KMnO_4/HCl solutions. *Polym Degrad Stab* 92:1219–1226
- Jeon S-J, Lee J-J, Kim W, Chang T, Koo S (2008) Hard coating films based on organosilane-modified boehmite nanoparticles under UV/thermal dual curing. *Thin Solid Films* 516:3904–3909
- Wan Y, Sun B, Liu W, Qi C (2012) Tribological performance of fatty acid modification of sol–gel TiO_2 coating. *J Sol Gel Sci Technol* 61:558–564

17. Lioni K, Toury B, Boissière C, Benayoun S, Miele P (2013) Hybrid silica coatings on polycarbonate: enhanced properties. *J Sol Gel Sci Technol* 65:1–9
18. Xu L, Fu Y, Du M (2011) Investigation on structures and properties of shape memory polyurethane/silica nanocomposites. *Chin J Chem* 29:703–710
19. Wang J, Zhu Y, Fu Y (2013) Abrasion resistance of biaxially oriented polypropylene films coated with nanocomposite hard coatings. *Appl Surf Sci* 285P:697–701
20. Xu T, Zhao J, Xu K, Xu Q (1997) Study on the tribological properties of ultradispersed diamond containing soot as an oil additive. *Tribol Trans* 40:178–182
21. Lakshmi R-V, Bharathidasan T, Basu B-J (2011) Superhydrophobic sol-gel nanocomposite coatings with enhanced hardness. *Appl Surf Sci* 257:10421–10426



Abrasion resistance of biaxially oriented polypropylene films coated with nanocomposite hard coatings



Jing Wang, Yaofeng Zhu, Yaqin Fu*

The Key Laboratory of Advanced Textile Materials and Manufacturing Technology Ministry of Education, Zhejiang Sci-Tech University, Hangzhou, Zhejiang 310018, China

ARTICLE INFO

Article history:

Received 11 July 2013

Received in revised form 22 August 2013

Accepted 23 August 2013

Available online 30 August 2013

Keywords:

Abrasion resistance

Biaxially oriented polypropylene

Sol-gel

Surface modification

KMnO₄

ABSTRACT

KMnO₄-treated, functionalized, biaxially oriented polypropylene (BOPP) films coated with nano-silica hybrid material were synthesized. The abrasion resistance of the films was examined using a reciprocating fabric abrasion tester. Functional groups were confirmed by Fourier-transform infrared spectroscopy. Contact angle measurements were performed on the BOPP film surface to quantify the effectiveness of the functionalization. Results indicate that the abrasion resistance and roughness of the composite film were significantly affected by the modification of the BOPP film. Water surface contact angle of the modified BOPP films decreased from 90.1° to 71.4°, when KMnO₄ concentration increased from 0 M to 0.25 M. Wettability of the BOPP films clearly improved after KMnO₄ treatment. Abrasion resistance of the functionalized films coated with hybrid materials improved by 27.4% compared with that of the original film.

© 2013 Elsevier B.V. All rights reserved.

1. Introduction

Biaxially oriented polypropylene (BOPP) films are some of the most important commercial polyolefin films because of their excellent properties, such as chemical resistance, toughness, and high thermal stability [1–3]. These films are widely used in food packaging, as protective coating for other films, in printing, and other applications. However, BOPP films have low scratch resistance and lack adhesiveness [4,5].

Sol-gel coatings are frequently used to improve the scratch resistance of polymeric materials. However, the interfacial interaction between highly crosslinked coatings and polypropylene films is low, thereby requiring further modification of the polymer surface. A number of surface modification techniques can be used to improve interfacial interactions, including plasma treatment [6], ion beam treatment [7], corona discharge [8,9], surface grafting [10], and chemical oxidation [11]. Bles et al. [12] reported the use of chromosulfuric acid to modify polypropylene surfaces. This method increases friction by enhancing the interactions of the films using a sapphire indenter. Bellel et al. [13] showed that the surface wettability of polypropylene films can be significantly improved by depositing thin SiO_x layers on the surface. Jeon et al. [14] prepared hard coating films using organosilane-modified boehmite nanoparticles under UV/thermal dual curing. Yin and Wang [15] and Dinelli

et al. [16] synthesized hybrid materials using a sol-gel technique by adding water to improve the abrasion resistance of the substrate. However, research on the preparation of a sol-gel solution in the absence of water is limited [17].

In the current study, KMnO₄ solution was used to modify the surface of BOPP films to improve adhesion. Using KMnO₄ solution for chemical oxidation is more eco-friendly than using other solutions. A sol-gel method in which the sol was synthesized without adding deionized water was used to prepare uniformly dispersed nanosilica. The nanosilica hybrid materials were then coated on the BOPP films using a dip-coating technique.

Abrasion resistance is used to characterize shear deformation imposed by a hard material on another softer material [18–20]. In the present study, KMnO₄ solution was used to modify the surface of polypropylene film to enhance the abrasion resistance of films coated with nanosilica hybrid materials.

2. Experimental

2.1. Materials

BOPP films (thickness = 47 μm) were supplied by the Zhejiang Kelly Packaging Materials Company (China). KMnO₄, 98% (w/v) H₂SO₄ solution, 37% (w/v) HCl solution, tetraethoxysilane (TEOS), *p*-toluene sulfonic acid (PTSA), 99.7 wt% absolute ethanol, and 3-triethoxysilylpropylamine (KH550) were provided by Hangzhou Mike Chemical Instrument (China). All chemicals were used without further purification.

* Corresponding author. Tel.: +86 13958199325; fax: +86 571 86843151.
E-mail address: fyq01@zstu.edu.cn (Y. Fu).

Table 1

Factors and levels used in 2^2 factorial design for the chemical surface oxidation of BOPP films.

Factor	Name	Units	Level (−1)	Level (+1)
A	Time	h	2	4
B	KMnO ₄ /H ₂ SO ₄ concentration	mol L ^{−1}	0.05/0.10	0.25/0.10

2.2. Surface modification of BOPP films

The BOPP films were washed with deionized water and dried in a baking oven prior to modification. The films were then cut into 210 mm × 70 mm pieces and then oxidized in KMnO₄/H₂SO₄ solution at 50 °C. Time and KMnO₄/H₂SO₄ concentration were the two parameters varied for the surface modification treatment (Table 1). Afterwards, the films were washed with HCl solution to remove any oxidation residue from the surface of BOPP films. The films were then dried for 30 min at 100 °C.

2.3. Nanosilica sol synthesis

A total of 25.000 g TEOS, 0.250 g PTSA, and 50 mL ethanol were added to a small reaction vessel at room temperature under stirring for 2 h. The homogeneous mixture obtained was marked as Solution A. Meanwhile, 5.000 g 3-triethoxysilylpropylamine and 50 mL ethanol were added to another small reaction vessel at room temperature under stirring for 2 h. The resulting mixture was marked as Solution B. Solution B was then added to Solution A using the titrimetric method under stirring for 2 h. The obtained sol was stored in a fresh vessel and isolated from air.

2.4. Coating and curing

The BOPP films modified by the KMnO₄/H₂SO₄ solution were immersed in the sol solution for 10 min, and then collected at a rate of 2 mm/min. The coated films were aged for 24 h and then freeze-dried at −55 °C and 0.01 MPa in a vacuum for 24 h. The aged films were cured for 1 h at 100 °C. In this study, three samples, labeled F, FC, and FMC, were prepared to determine the effect of the nanocomposite hard coating on BOPP film. F refers to pristine film without KMnO₄/H₂SO₄ solution and coating treatment. FC refers to film untreated with KMnO₄/H₂SO₄ solution but treated with coating. FMC refers to film treated with 0.25 M KMnO₄/H₂SO₄ solution for 4 h and with coating.

2.5. Characterization

The wettability of the specimens treated and untreated with KMnO₄ was measured with a water contact angle (OCA 20, Dataphysics, Germany). Changes in the surface functional groups were recorded on a Fourier-transform infrared (FTIR) spectrometer (Nicolet 5700, Thermo Electron Scientific Instruments Corp, USA). Surface topography of the BOPP films before and after the abrasion test was analyzed using a field-emission scanning electron microscope (Ultra 55, Zeiss, Germany) at an operating voltage of 3 kV. Sol dispersion was examined using a transmission electron microscope (TEM) (JEM-2100F, JEOL, Japan) operated at 200 kV. Abrasion resistance of the films was analyzed using a reciprocating wear tester (shown in Fig. 1) with abrasives (1000 Cw, 3M, USA) at a loading of 9 N 1000 times and lasting for about 30 min. The area of contact was 150 mm × 70 mm. Mass loss (M_L) was defined as

$$M_L = \frac{M_0 - M_f}{M_0} \times 100\%$$

where M_0 is the weight of the samples before the abrasion test, and M_f is the weight of the samples after the abrasion test.

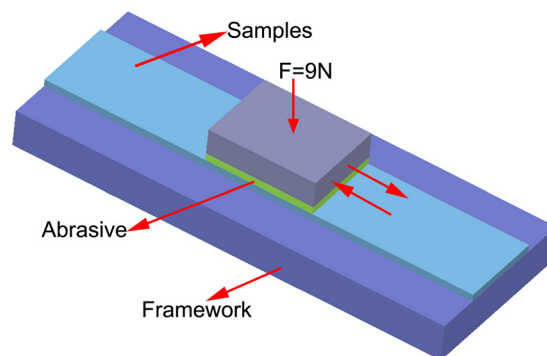


Fig. 1. Schematic of reciprocating wear tester.

3. Results and discussion

3.1. Factors of transmittance

The transmittance spectra show significant differences between the modified BOPP films washed with HCl solution and those that were unwashed (Fig. 2). The results show that the HCl solution can remove any oxidation residue, which makes the treatment ineffective on transmittance. Furthermore, the transmittance of the BOPP films were significantly affected by the drying condition (Fig. 3), indicating that the BOPP films have higher transmittance after freeze drying compared with thermal drying. This result may be because the nano-silica hybrid material treated with freeze drying had uniform, well-dispersed particles with no agglomeration.

3.2. Contact angle

Fig. 4 shows the water surface contact angles of the unmodified BOPP films and those modified by different treatments. Comparing the untreated films with those modified under extreme conditions (0.25 M, 4 h) shows that the BOPP films exhibited increased wettability, when the contact angle was decreased from 90.1° to 71.4°. This decrease was similar to that seen in a previous study using a different oxidation technique [21]. Comparing the condition (0.05 M, 2 h) with the condition (0.05 M, 4 h), the films presented a larger decrease in water contact angle, from 79.8° to 74.5°. This result was due to the increased number of functional groups

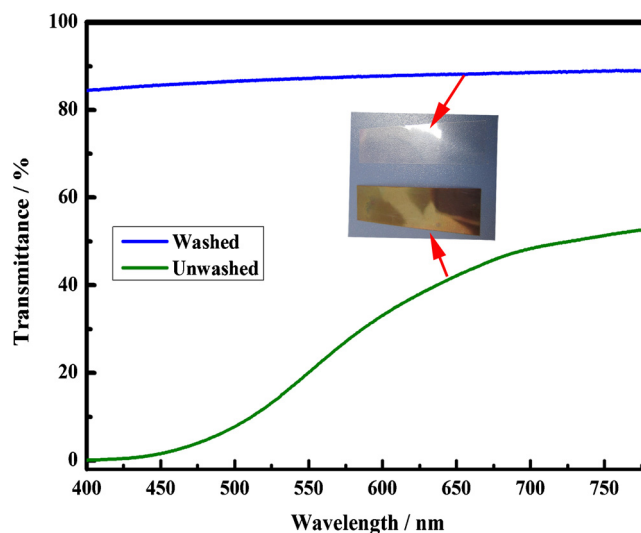


Fig. 2. Transmittance spectra in the visible range for samples untreated and treated with KMnO₄ solution.

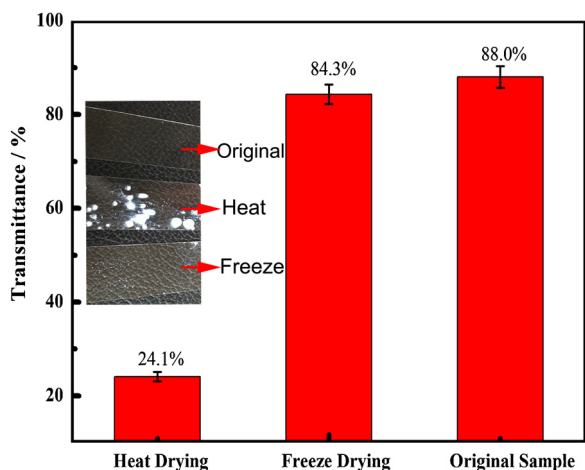


Fig. 3. Transmittance in the visible range for samples with varied drying conditions.

successfully introduced onto the surface of the BOPP films with prolonged time. The water contact angle of the films also decreased from 74.5° to 71.4° between treatments (0.05 M, 4 h) and (0.25 M, 4 h). This increase in solution concentration may have favored the hydrolysis reaction involving the breaking and movement of oxidized polymer chains away from the film surface, and may explain the aforementioned inversion. KMnO_4 concentration affected the water contact angle more than the time of modification.

3.3. Effects of surface modification as analyzed by attenuated total reflectance (ATR)–FTIR

Figs. 5 and 6 show the FTIR spectra of the BOPP films modified under different conditions. The absorption peaks at 2944, 2912, 1455, and 1373 cm^{-1} were attributed to CH_3 non-symmetric stretching vibrations, symmetric C–H stretching vibrations, CH_3 non-symmetric changing angle vibrations, and symmetric changing angle vibrations, respectively. The main spectral changes found in the region between 1740 and 1600 cm^{-1} in the modified and untreated polymers were attributed to the different carbonyl groups that formed on the modified film surfaces.

Fig. 5 shows no significant change in absorption peaks, indicating that the treatment time is not a major factor affecting film modification. Fig. 6 shows that the (0.05 M, 4 h) BOPP film exhibited small absorption bands at approximately 1740 and 1600 cm^{-1} ,

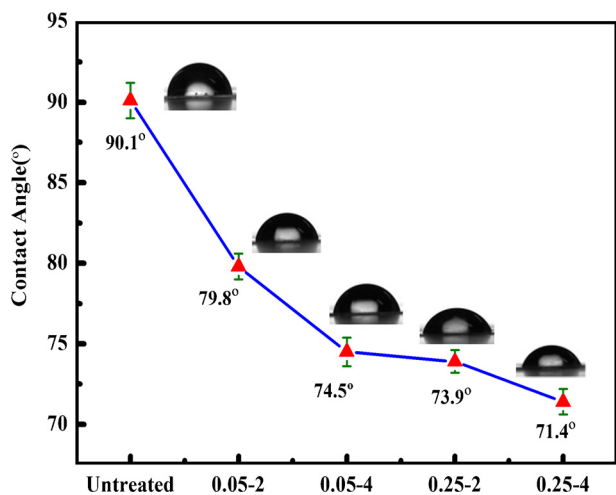


Fig. 4. Drop water contact angle of BOPP film surfaces placed under different oxidation conditions.

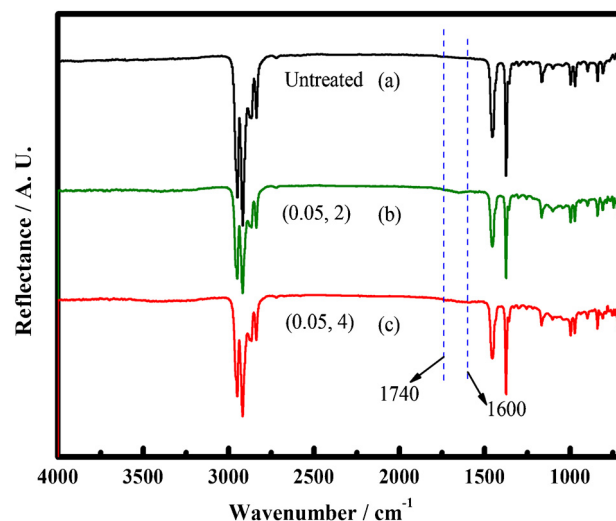


Fig. 5. FTIR-ATR spectra of BOPP films treated with 0.25 M KMnO_4 solution for different times: (a) 0 h; (b) 2 h; (c) 4 h.

which may correspond respectively to COO^- and C=O stretching vibrations. The (0.25 M, 4 h) BOPP film showed an intensification of the band at 1740 cm^{-1} , a broad band at around 3200 cm^{-1} attributed to O–H stretching vibrations, and a large shoulder at 1094 cm^{-1} corresponding to C–O stretching vibrations. The spectra of the BOPP films indicated that increasing the KMnO_4 solution concentration can significantly promote the oxidation of these films.

3.4. Morphology of nanoparticles and sols

The morphology and dispersion of silica nanoparticles were investigated using TEM. Fig. 7 shows that the average size of the silica nanoparticles was 30 nm, and that the silica nanoparticles were generally spherical and relatively uniformly dispersed. Nanoparticles can strengthen the abrasion resistance of films [22]. As shown in Fig. 8, the SiO_2 sol can be more stable under isolation from air without adding deionized water. At the same time, the SiO_2 sol rapidly becomes muddy and opaque after the addition of deionized water. Fig. 9 shows that the SiO_2 sol remains transparent after aging for 30 days, indicating that the SiO_2 sol prepared in this work is convenient for storage and application in the industry.

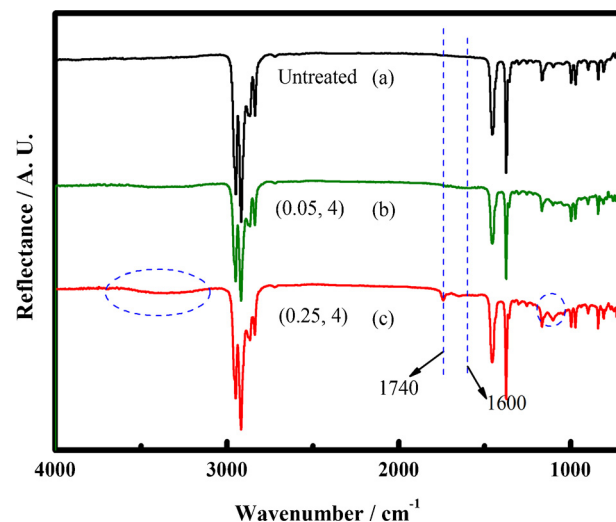


Fig. 6. FTIR-ATR spectra of BOPP film treated with KMnO_4 solution at different concentrations for 4 h: (a) 0 M; (b) 0.05 M; (c) 0.25 M.

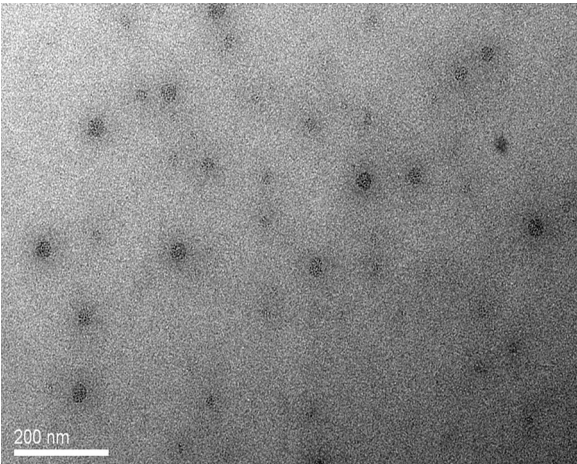


Fig. 7. TEM image of the sol.



Fig. 8. Photograph of two sols: (A) without deionized water, and (B) with deionized water.

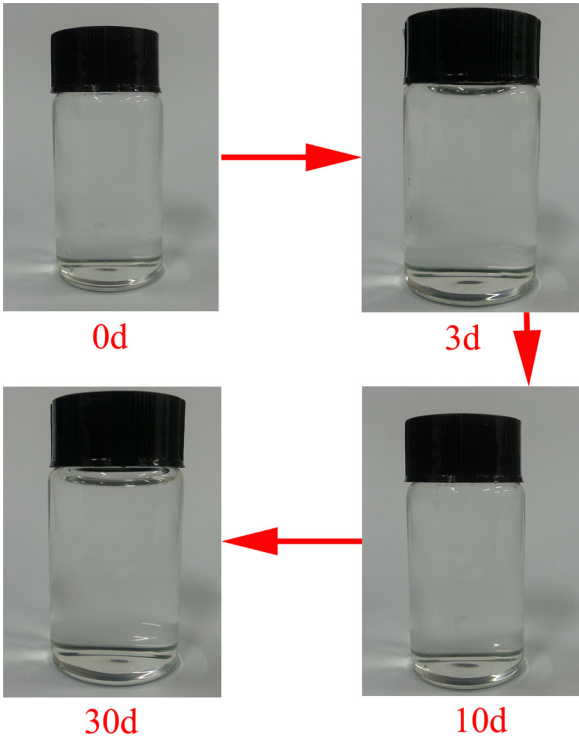


Fig. 9. Sol aging with different times.

3.5. Abrasion resistance

The surface morphologies of BOPP films before and after the abrasion test are shown in Fig. 10. Sample F exhibited deep grooves, as seen in Fig. 10(d). Meanwhile, the scratch on the surface of Sample FC was clear, as shown in Fig. 10(e), but not as deep as that on Sample F, indicating that abrasion resistance was improved by the coating. In Fig. 10(f), the grooves on the surface of FCM are shallow, indicating significant improvement compared with Samples F and FC. This result shows that the surface modification of the films

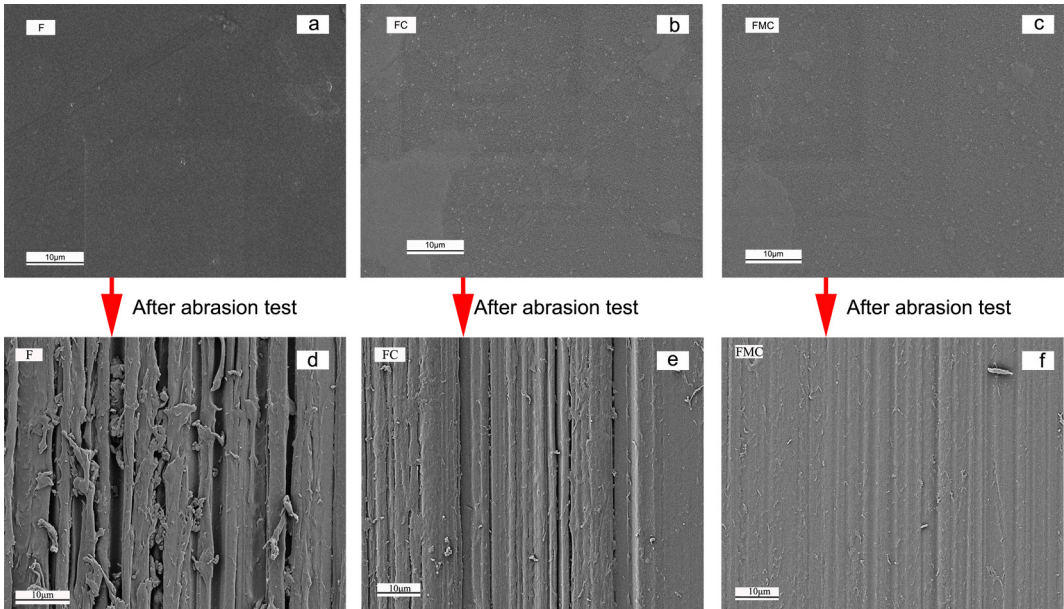


Fig. 10. SEM image of the sample surfaces: (a–c) before abrasion test; (d–f) after abrasion test.

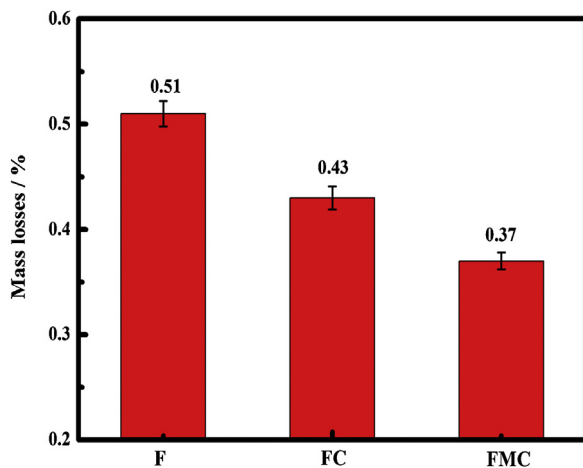


Fig. 11. Mass losses of samples after the abrasion test.

improved the interfacial interaction between the BOPP film and the coating, resulting in higher abrasion resistance.

The losses in mass of the samples are shown in Fig. 11. The mass losses of Samples F, FC, and FMC were 0.51%, 0.43%, and 0.37%, respectively. These results suggest that the surface modification of BOPP films by means of $\text{KMnO}_4/\text{H}_2\text{SO}_4$ and coating treatments can improve the abrasion resistance of these films. These findings, confirmed by SEM observations, were attributed to the strengthening effect of nanoparticles on the film surface [23] and to the presence of polar groups. Consequently, the interfacial property was high [24]. In the current study, a comparison of Sample F with FMC showed that the abrasion resistance of the modified BOPP films increased by 27.4%.

4. Conclusion

A series of surface modification conditions was applied to BOPP films. The results show that increased KMnO_4 concentration and prolonged treatment time can significantly increase the interaction between BOPP films and the coating. The KMnO_4 -treated BOPP films have no effect on transmittance when washed with HCl solution. Uniformly dispersed spherical silica nanoparticles were obtained using the sol–gel method, and the sol can remain stable without the addition of deionized water. The BOPP films exhibited high abrasion resistance after modification, with a maximum improvement of 27.4%.

Acknowledgments

The authors gratefully acknowledge the Instrumental Analysis Center of Zhejiang Sci-Tech University for the use of their characterization facilities. We also thank the technicians for their assistance in the analyses and for the technical discussions.

References

- [1] N. Kalapat, T. Amornsakchai, Surface modification of biaxially oriented polypropylene (BOPP) film using acrylic acid-corona treatment: Part I. Properties and characterization of treated films, *Surf. Coat. Technol.* 207 (2012) 594–601.
- [2] J. Ho, T.R. Jow, High field conduction in biaxially oriented polypropylene at elevated temperature, *IEEE. Trans. Dielectr. Electr. Insul.* 19 (2012) 990–995.
- [3] N. Dilsiz, H. Yavuz, S. Cörekçi, M. Cakmak, Plasma surface functionalization of biaxially oriented polypropylene films with trimethyl borate, *Adv. Mater. Chem. Phys.* 1 (2011) 50–55.
- [4] J. Chu, L. Rumao, B. Coleman, Scratch and mar resistance of filled polypropylene materials, *Polym. Eng. Sci.* 38 (1998) 1906–1914.
- [5] M.L. Maspocho, J. Gamez-Perez, E. Gimenez, O.O. Santana, A. Gordillo, Influence of processing on ethylene–propylene block copolymers: structure and mechanical behavior, *J. Appl. Polym. Sci.* 93 (2004) 2866–2878.
- [6] A. Sarani, N.D. Geyter, A.Y. Nikiforov, R. Morent, C. Leys, J. Hubert, F. Reniers, Surface modification of PTFE using an atmospheric pressure plasma jet in argon and argon + CO_2 , *Surf. Coat. Technol.* 206 (2012) 2226–2232.
- [7] S. Venkatachalam, H. Nanjo, K. Kawasaki, Y. Wakui, H. Hayashi, T. Ebina, Preparation and characterization of nanocrystalline ITO thin films on glass and clay substrates by ion-beam sputter deposition method, *Appl. Surf. Sci.* 257 (2011) 8923–8928.
- [8] L.H. Xua, Z.P. Fang, P.A. Song, M. Peng, Effects of corona discharge on the surface structure, morphology and properties of multi-walled carbon nanotubes, *Appl. Surf. Sci.* 256 (2010) 6447–6453.
- [9] S. Tripatanasuwan, D.H. Reneker, Corona discharge from electrospinning jet of poly(ethylene oxide) solution, *Polymer* 50 (2009) 1835–1837.
- [10] M. Kyomoto, T. Moro, Y. Takatori, H. Kawaguchi, K. Nakamura, K. Ishihara, Self-initiated surface grafting with poly(2-methacryloyloxyethyl phosphorylcholine) on poly(ether-ether-ketone), *Biomaterials* 31 (2010) 1017–1024.
- [11] R. Mazeikiene, G. Niaura, A. Malinauskas, Chemical oxidation of aniline and N-methylaniline: a kinetic study by Raman spectroscopy, *Spectrochim. Acta B* 106 (2013) 34–40.
- [12] M.H. Blees, G.B. Winkelman, A.R. Balkenende, J.M.J.D. Toonder, The effect of friction on scratch adhesion testing: application to a sol–gel coating on polypropylene, *Thin Solid Films* 359 (2000) 1–13.
- [13] A. Bellel, S. Sahli, Z. Ziari, P. Raynaud, Y. Segui, D. Escaich, Wettability of polypropylene films coated with SiO_x plasma deposited layers, *Surf. Coat. Technol.* 201 (2006) 129–135.
- [14] S.J. Jeon, J.J. Lee, W. Kim, T.S. Chang, S.M. Koo, Hard coating films based on organosilane-modified boehmite nanoparticles under UV/thermal dual curing, *Thin Solid Films* 516 (2008) 3904–3909.
- [15] Y. Yin, C. Wang, Organic–inorganic hybrid silica film coated for improving resistance to capsaicin oil on natural substances through sol–gel route, *J. Sol–Gel. Sci. Technol.* 64 (2012) 743–749.
- [16] M. Dinelli, E. Fabbri, F. Bondioli, TiO_2 – SiO_2 hard coating on polycarbonate substrate by microwave assisted sol–gel technique, *J. Sol–Gel. Sci. Technol.* 58 (2011) 463–469.
- [17] L. Xu, Y. Fu, M. Du, Investigation on structures and properties of shape memory polyurethane/silica nanocomposites, *Chin. J. Chem.* 29 (2011) 703–710.
- [18] V. Jardret, P. Morel, Viscoelastic effects on the scratch resistance of polymers: relationship between mechanical properties and scratch properties at various temperatures, *Prog. Org. Coat.* 48 (2003) 322–331.
- [19] B.J. Briscoe, S.K. Sinha, Scratch Resistance, Localised damage characteristics of polymer surfaces—a review, *Materialwiss. Werkst.* 34 (2003) 989–1002.
- [20] H. Jiang, R.L. Browning, M.M. Hossain, H.J. Sue, M. Fujiwara, Quantitative evaluation of scratch visibility resistance of polymers, *Appl. Surf. Sci.* 256 (2010) 6324–6329.
- [21] N.Y. Cui, N.M.D. Brown, Modification of the surface properties of a polypropylene (PP) film using an air dielectric barrier discharge plasma, *Appl. Surf. Sci.* 189 (2002) 31–38.
- [22] H. Zhang, L. Tang, Z. Zhang, L. Gu, Y. Xu, C. Eger, Wear-resistant and transparent acrylate-based coating with highly filled nanosilica particles, *Tribol. Int.* 43 (2010) 83–91.
- [23] X. Tao, Z.J. Zheng, X. Kang, X.Q. Ji, Study on the tribological properties of ultradispersed diamond containing soot as an oil additive, *Tribol. T.* 40 (1997) 178–182.
- [24] R.V. Lakshmi, T. Bharathidasan, B.J. Basu, Superhydrophobic sol–gel nanocomposite coatings with enhanced hardness, *Appl. Surf. Sci.* 257 (2011) 10421–10426.

Mechanical and Abrasion Properties of Polyethylene Terephthalate Films Coated with SiO₂/Epoxy Hybrid Material

WANG Jing (王靖), FU Xiang (付翔), DING Juan (丁娟), WU Hui-min (吴惠敏), FU Ya-qin (傅雅琴)*

The Key Laboratory of Advanced Textile Materials and Manufacturing Technology, Ministry of Education, Zhejiang Sci-Tech University, Hangzhou 310018, China

Abstract: Hybrid materials were prepared using a silane coupling agent, tetraethoxysilane (TEOS) as the precursor, dilute hydrochloric acid as the catalyst, and epoxy as the matrices. The films coated with hybrid materials were expected to improve abrasion resistance and mechanical properties. The morphology, mechanical properties, adhesion, and abrasion resistance of the polyethylene terephthalate (PET) films were characterized using an atomic force microscope, a tensile testing machine, a bagger knife, and a reciprocating fabric abrasion tester. The result of research indicated that the modification significantly affected the abrasion resistance and roughness. The tensile strength and abrasion resistance of the modified PET films increased by 40% and 50% respectively at 3% TEOS mass fraction.

Key words: polyethylene terephthalate (PET) films; surface modification; sol-gel; abrasion resistance
CLC number: TB383

Document code: A

Article ID: 1672-5220(2013)06-0521-04

Introduction

Polyethylene terephthalate (PET) films are widely-used materials for soft packaging, electrical insulation, photography, and decoration because of their low cost, excellent gas barrier ability, high transparency, and high dimensional stability^[1-3]. However, PET films have very poor scratch resistance^[4] and unsatisfactory mechanical properties^[5], which limit their development. Epoxy resins are widely used as adhesives^[6-8], coatings^[9], casting materials^[10], and matrix resin for composites^[11-12], because of their excellent mechanical properties, low cost, good adhesion, and chemical stability. Thus, a composite of epoxy resin and polyester film seems promising. However, modification only by epoxy resin cannot satisfy the application of higher requirement in mechanical properties and abrasion resistance^[13-14]. SiO₂ is usually used as an abrasion material because of its extreme hardness and high thermostability. However, SiO₂ alone is difficult to be used as coating. The introduction of an organic group to coating has good prospects^[15-16]. To improve mechanical properties, epoxy resins are used in coating to prepare epoxy resin/silica hybrids^[17]. However, little research has been reported in early articles about preparing a sol-gel solution without adding water.

Epoxy resin is most commonly used for top coats in aerospace coating systems because of its high abrasion resistance. In this paper, the sol-gel was prepared using a silane coupling agent, tetraethoxysilane (TEOS) as the precursor, and dilute hydrochloric acid as the catalyst. The sol-gel is used as a modifier to prepare epoxy resin/silica hybrids. The properties of the hybrid materials and the relationship of the contents of silica and silane coupling agents with the tribological properties of the epoxy resin/silica hybrid thin film

are concluded in the article.

1 Experimental

1.1 Materials

The reagents used were TEOS, coupling agent (KH550), ethyl alcohol, sodium hydroxide, epoxy resin E-51, and 10% by weight diluted hydrochloric acid, provided by Hangzhou Mike Chemical Instrument Co., Ltd., China. The substrate was PET films (thickness = 271 μm) from Hangzhou Zheng Bang Plastic Company, China. All these chemicals were used without further purification.

1.2 Surface modification of PET films

The films were rinsed with deionized water and dried in a baking oven prior to modification. The sample films were then cut into 10 mm × 100 mm sizes and oxidized in 2% by weight NaOH solution at 90 °C. After 40 min, the films were pulled out, rinsed with deionized water, and dried in a baking oven for further use.

1.3 Preparation of surface modifier

Epoxy resin and a curing agent were added to a small reaction vessel at room temperature. TEOS, silane coupling agent, ethyl alcohol, and diluted hydrochloric acid were then added to the same reaction vessel. The reaction vessel was placed in a water bath at 60 °C under stirring for 15 min. Six parameters of surface modifier were shown in Table 1.

Table 1 Formula of the modifier

Formula	Epoxy /g	Amilan /g	TEOS /g	EtOH /g	HCl /mL	KH550 /g
1	6	4	—	—	—	—
2	6	4	0.3	0.066	0.2	—
3	6	4	0.3	0.066	0.2	0.3
4	6	4	0.5	0.066	0.2	—
5	6	4	0.5	0.066	0.2	0.5

1.4 Coating deposition

A viscous flow modifier was uniformly coated on the modified PET films. The samples were then dried in a baking oven at 70 °C for 3 h and kept sealed until further use. The samples were named EP, TEP3, TKEP3, TEP5, and TKEP5 based on the content of their TEOS and silane coupling agent: "3" and "5" stand for the mass fraction of TEOS at 3% and 5%, respectively, and "K" denotes the surface modifier containing the silane coupling agent.

1.5 Characterization

The surface roughness of the coating films was analyzed using an atomic force microscopy (AFM) system (XE-100E, Park Systems, Korea). Transmittance measurements were

Received date: 2013-03-22

Foundation item: Scientific Research Foundation for the Returned Overseas Chinese Scholars, Ministry of Education of China (No. 2005-383)

* Correspondence should be addressed to FU Ya-qin, E-mail: fyq01@zstu.edu.cn

performed using an ultraviolet and visible spectrophotometer (TU-1901, Persee, China). The intensity of the films was measured with GB/T 1040. 3-2006 by a universal testing machine (INSTRON 3367, America). The improvement of strength T_f is defined as

$$T_f/\% = \frac{T_f - T_0}{T_0} \times 100,$$

where T_0 is the strength of PET sample, and T_f is the strength of samples.

The adhesion of the films was determined using a cross-cut tester (QFH, Shanghai High Precision Instrument, China). The hardness of the films was analyzed with abrasives (CS-17, 3M, America) at 9 N loading 1 000 times. The improvement of abrasion resistance M_f is defined as

$$M_f/\% = \frac{M_0 - M_f}{M_0} \times 100,$$

where M_0 is the abrasion loss of PET sample, and M_f is the abrasion loss of samples.

2 Results and Discussion

In the presence of sodium hydroxide, hydrolysis can produce hydroxyl and carboxyl groups that can improve the adhesion of PET films^[18-20]. The structure of the product created by the reaction between the silane coupling agent and TEOS is shown in Fig. 1. When the modifier is coated on the films, the amino group of the curing and silane coupling agents easily reacts with the hydroxyl group of the surface of PET films and epoxy resin. The connection between the modifier and PET films can be firm, which affects the mechanical properties.

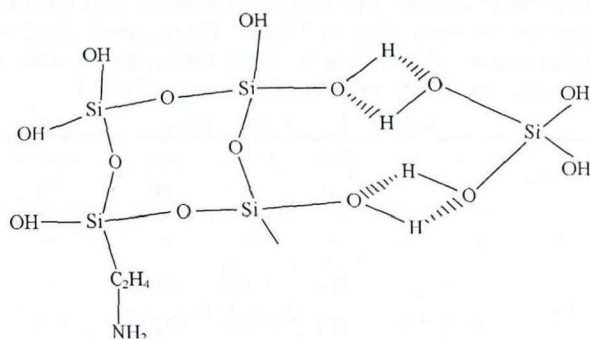


Fig. 1 Schematic diagram of TEOS and silane coupling agent product structure

2.1 Effect of modifier on the surface morphology, abrasion properties, and transmittance

The surface of materials considerably affects scratch resistance and application^[21]. Thus, the surface roughness of the samples was observed by XE-100E before and after modification. The results are shown in Figs. 2-4 and Table 2.

The surface roughness R_a of untreated films is 4.04 nm (Fig. 2), whereas that of PET films treated with epoxy resin is 1.13 nm (Fig. 3). The surface becomes smoother because uncured epoxy resins have good liquidity at 60 °C and can thus fill the holes on the surface. Figures 4(a) - (d) show the AFM images of PET film samples modified under different conditions. The surface of these films is glossier than those shown in Figs. 2 and 3. TEOS and the silane coupling agent make the film surface smoother. In fact, the addition of silane coupling agent increases the fluidity of epoxy resin and improves the surface smoothness of PET films.

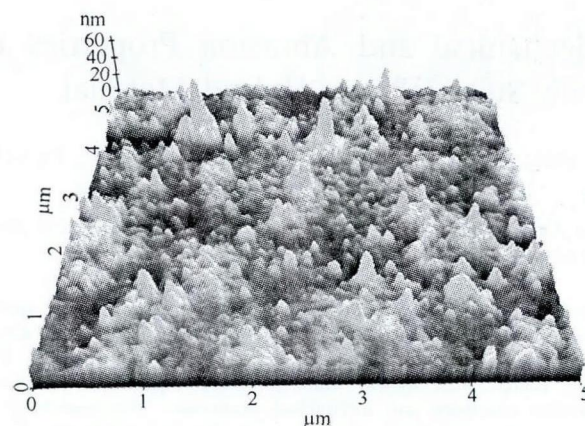


Fig. 2 Surface morphology of unmodified PET film

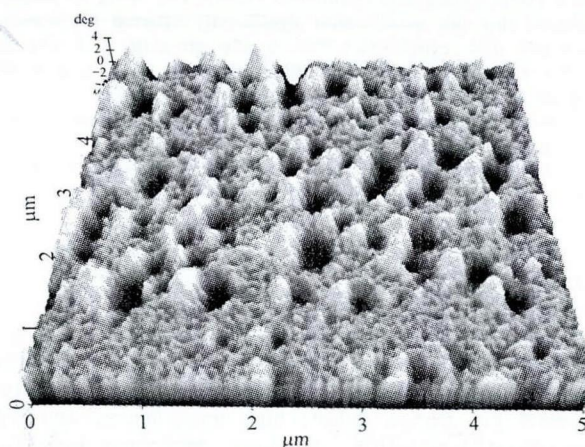
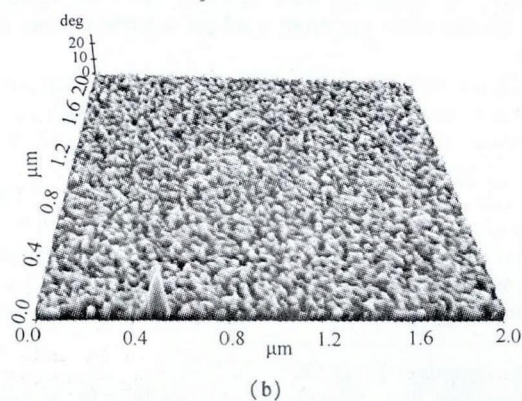
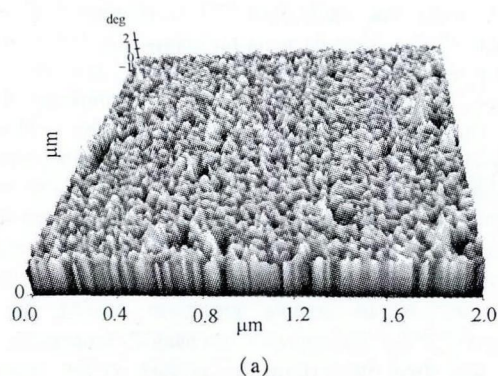


Fig. 3 Surface morphology of PET film modified with epoxy



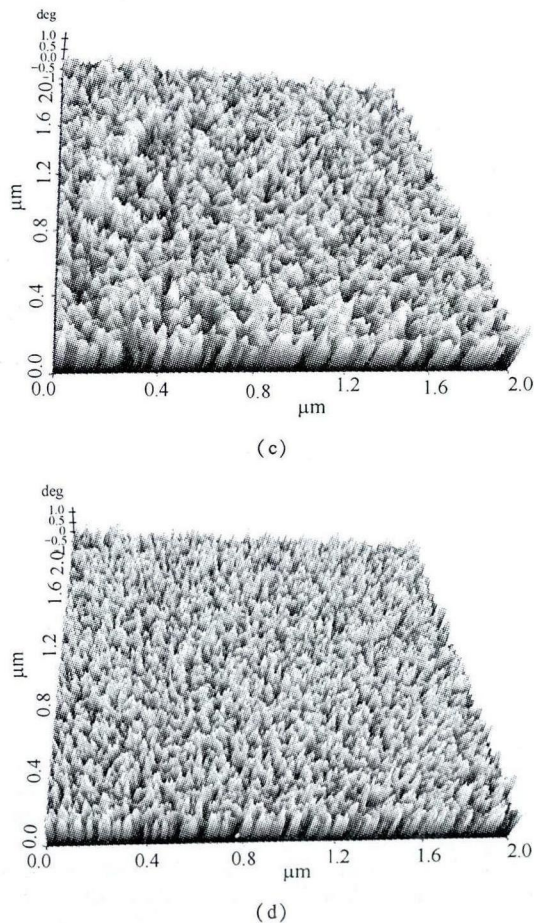


Fig. 4 Surface morphologies of PET films modified with hybrid materials: (a) TEP3; (b) TEP5; (c) TKEP3; and (d) TKEP5

Table 2 Surface roughness of samples

Samples	PET	EP	TEP3	TKEP3	TEP5	TKEP5
R_a/nm	4.040	1.130	0.328	0.294	0.330	0.286

The levels of bonding fastness of the coatings are generally divided from 0 to 5, with 0 as the best bonding fastness. And with levels up, the bonding fastness become worse. After a scratch test, the surface of the sample was observed with a magnifying glass. The adhesive properties of the modifier with the PET surface are shown in Table 3.

Table 3 Assessment of adhesive power level

Sample	EP	TEP3	TKEP3	TEP5	TKEP5
Appearance	Smooth	Peeling a little	Smooth	Peeling a little	Smooth
Level	0	1	0	1	0

Epoxy resin and the modifying agent containing a coupling agent have good adhesion to PET, whereas hybrid materials without a coupling agent have relatively poor adhesive fastness (Table 3). Given that the coupling agent has dual functional groups that can produce a coupling effect with sodium hydroxide-treated PET, bond performance can be improved.

The samples of PET, EP, and TKEP3 had visible range transmittances of 89.2%, 88.1%, and 87.8%, respectively (Fig. 5). EP and TKEP3 samples had a little lower transmittance than untreated PET film. But the samples all were transparent, which suggested that PET films coated with hybrid

materials did not much affect the transmittance.

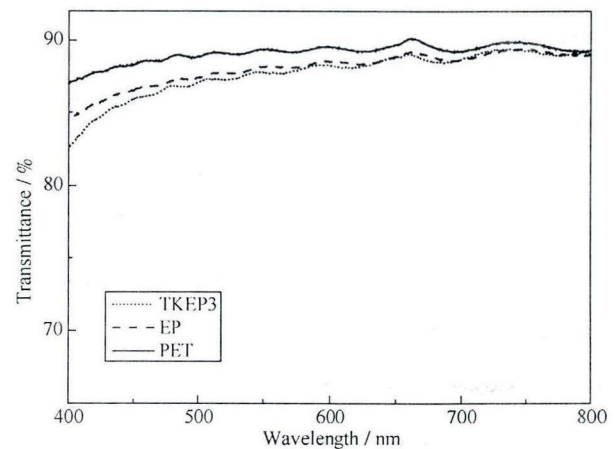


Fig. 5 Transmittance spectra in the visible range for samples of PET, EP, and TKEP3

2.2 Effect of surface modification on the mechanical properties of PET films

The mechanical properties of the samples were tested to study the impact of modification on them. The tensile curves of the samples are shown in Fig. 6.

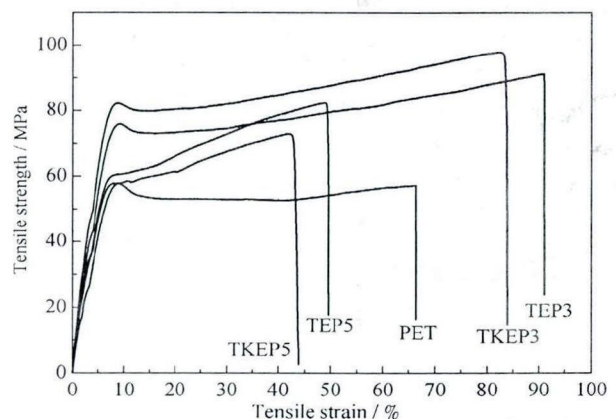


Fig. 6 Tensile curves of samples

The modifier remarkably affects the mechanical properties of PET (Fig. 6 and Table 4). Compared with raw PET, TEP3 and TKEP3 have significantly increased tensile strength and elongation at break. In the preparation of TEP3 and TKEP3, the addition of TEOS, ethanol, and KH550 decreases the viscosity of the system and increases mobility. Consequently, epoxy resin easily infiltrates the holes on the surface of the PET carrier, enabling the PET films to combine with the epoxy hybrid materials and ultimately improve the mechanical properties. On the other hand, no water was added to the sol-gel systems other than a small amount of water in the catalyst. Air moisture hydrolyzes TEOS and the coupling agent in the sol-gel process of the system, which effectively controls the rate of hydrolysis. Thus, the SiO_2 particles in the sample are smaller and more uniform, thereby enabling the self-healing of the PET surface as well as increasing the strength and elongation of the material.

Table 4 Mechanical properties of samples

Sample	PET	EP	TEP3	TKEP3	TEP5	TKEP5
Tensile strength/MPa	57.2	63.3	85.7	97.7	75.4	69.7
Tensile strain/%	66.2	64.6	88.9	83.5	51.2	48.6

Modified TEP5 and TKEP5 have significantly improved strength but decreased elongation. The increments in inorganic particles and stress concentration make the materials more brittle. The shape of each curve is also substantially the same, and the curves show the typical tensile shape of a single material (Fig. 6). The bonding between the modifier and PET is excellent, and the interface presents typical cohesive damage. Overall, when the mass fraction of TEOS is 3%, the tensile strength and elongation of modified PET films significantly increase. From the data of Table 4, at 3% mass fraction of TEOS and coupling agent KH550, the strength of the modified PET films increases by 70%, comparing with samples of PET.

2.3 Effect of surface modification on the abrasion resistance of the PET films

The samples were subjected to abrasion treatment to study the impact of modification on the abrasion resistance of PET. The results are shown in Table 5. The surface treatment of PET films improves their abrasion resistance (Table 5). A significant difference is observed among different modifiers. The wear resistance of PET films treated with the modifier and added with a coupling agent significantly improves, and the amount of wear decreases by more than 40%. What's more, the sample TKEP5 has the best abrasion resistance, with the maximum abrasion of the films improved by 57.7%. These improvements are due to the excellent bonding among the epoxy resin, PET films, and inorganic silica particles, which improves the abrasion resistance of epoxy resin. The coupling agent also improves the interfacial bonding among silica, epoxy resin, and PET.

Table 5 Abrasion loss of samples

Sample	PET	EP	TEP3	TKEP3	TEP5	TKEP5
Abrasion loss/mg	52	45	27	25	30	22

3 Conclusions

(1) PET films coated with hybrid materials are smooth and free of cracks based on visual observation. AFM images show that epoxy resin modified with TEOS has better appearance than unmodified epoxy resin and thus fulfills appearance requirements.

(2) The strength of PET films coated with hybrid materials is significantly better than those coated with unmodified epoxy. At 3% TEOS mass fraction, the strength and elongation at break significantly improve.

(3) The adhesion of PET films coated with the hybrid materials added with a coupling agent is excellent and prevents coating shedding. Epoxy can be improved with a coupling agent in the sol-gel system.

(4) The PET films have good abrasion resistance after modification, with the maximum abrasion of the films being 57.7%.

References

- [1] Jeon D H, Lee K H, Park H J. The Effects of Irradiation on Physicochemical Characteristics of PET Packaging Film [J]. *Radiation Physics and Chemistry*, 2004, 71(5): 1059-1064.
- [2] Zeng K, Bai Y P. Improve the Gas Barrier Property of PET Film with Montmorillonite by *in situ* Interlayer Polymerization [J]. *Materials Letters*, 2005, 59(27): 3348-3351.
- [3] Pandiyaraj K N, Selvarajan V, Deshmukh R R, *et al.* Adhesive Properties of Polypropylene (PP) and Polyethylene Terephthalate (PET) Film Surfaces Treated by DC Glow Discharge Plasma [J]. *Vacuum*, 2008, 83(2): 332-339.
- [4] Hsiang H I, Chang Y L, Chen C Y, *et al.* Silane Functional Effects on the Rheology and Abrasion Resistance of Transparent SiO₂/UV-Curable Resin Nano-composites [J]. *Materials Chemistry and Physics*, 2010, 120(2/3): 476-479.
- [5] Zhang Y, Ma X Q, Li Y C, *et al.* Study of Toughened and Strengthened Unsaturated Polyester Resin by Nanometer Silicon Dioxide [J]. *China Plastics*, 2004, 18(2): 35-39. (in Chinese)
- [6] Lapique F, Redford K. Curing Effects on Viscosity and Mechanical Properties of a Commercial Epoxy Resin Adhesive [J]. *International Journal of Adhesion & Adhesives*, 2002, 22(4): 337-346.
- [7] Ameli A, Papini M, Schroeder J A, *et al.* Fracture R-Curve Characterization of Toughened Epoxy Adhesives [J]. *Engineering Fracture Mechanics*, 2010, 77(3): 521-534.
- [8] Azari S, Papini M, Spelt J K. Effect of Adhesive Thickness on Fatigue and Fracture of Toughened Epoxy Joints - Part II: Analysis and Finite Element Modeling [J]. *Engineering Fracture Mechanics*, 2011, 78(1): 138-152.
- [9] Shah R S, Wang Q, Lee M L. Cycloaliphatic Epoxy Resin Coating for Capillary Electrophoresis [J]. *Journal of Chromatography A*, 2002, 952(1/2): 267-274.
- [10] Koerner H, Hampton E, Dean D, *et al.* Generating Triaxial Reinforced Epoxy/Montmorillonite Nanocomposites with Uniaxial Magnetic Fields [J]. *Chemistry of Materials*, 2005, 17(8): 1990-1996.
- [11] Chen G X, Kim H S, Shim J H, *et al.* Role of Epoxy Groups on Clay Surface in the Improvement of Morphology of Poly (l-lactide)/Clay Composites [J]. *Macromolecules*, 2005, 38(9): 3738-3744.
- [12] Tamura K, Yokoyama S, Pascua C S, *et al.* New Age of Polymer Nanocomposites Containing Dispersed High-Aspect-Ratio Silicate Nanolayers [J]. *Chemistry of Materials*, 2008, 20(6): 2242-2246.
- [13] Wei C, Tan S T, Wang X Y, *et al.* Effects of Liquid Crystalline Polyurethane on the Structure and Properties of Epoxy [J]. *Journal of materials science letters*, 2002, 21(9): 719-722.
- [14] Zhu Y G, Li Z Q, Zhang D, *et al.* PET/SiO₂ Nanocomposites Prepared by Cryomilling [J]. *Journal of Polymer Science Part B: Polymer Physics*, 2006, 44(8): 1161-1167.
- [15] Saccani A, Toselli M, Pilati F *et al.* Effects of Organic-Inorganic Hybrid Coatings on Durability of Cross-Linked Polyethylene [J]. *Polymer Degradation and Stability*, 2011, 96(12): 2080-2087.
- [16] Kessmana A J, Huckaby D K P, Snyder C R, *et al.* Tribology of Water and Oil Repellent Sol-Gel Coatings for Optical Applications [J]. *Wear*, 2009, 267(1/2/3/4): 614-618.
- [17] Qi C, Gao H, Yan F, *et al.* Study on Preparation and Tribological Properties of Epoxy Resin/SiO₂ Hybrid Thin Film [J]. *Journal of Applied Polymer Science*, 2005, 97(1): 38-43.
- [18] Tanahashi M, Yao T, Kokubo T *et al.* Apatite Coated on Organic Polymers by Biomimetic Process: Improvement in Its Adhesion to Substrate by NaOH Treatment [J]. *Journal of Applied Biomaterials*, 1994, 5(4): 339-347.
- [19] Ren X, Kocer H B, Kou L, *et al.* Antimicrobial Polyester [J]. *Journal of Applied Polymer Science*, 2008, 109(5): 2756-2761.
- [20] Kosmidis V A, Achilias D S, Karayannidis G P. Poly (ethylene terephthalate) Recycling and Recovery of Pure Terephthalic Acid. Kinetics of a Phase Transfer Catalyzed Alkaline Hydrolysis [J]. *Macromolecular Materials and Engineering*, 2001, 286(10): 640-647.
- [21] Bellel A, Sahli S, Ziari Z *et al.* Wettability of Polypropylene Films Coated with SiO₂ Plasma Deposited Layers [J]. *Surface and Coatings Technology*, 2006, 201(1/2): 129-135.

证书号第1835439号



发明专利证书

发明名称：用于短流程缫丝的丝条预干燥装置及预干燥方法

发明人：傅雅琴；王靖；陈文兴；江文斌；吴惠敏

专利号：ZL 2013 1 0249879.9

专利申请日：2013年06月24日

专利权人：浙江理工大学

授权公告日：2015年11月04日

本发明经过本局依照中华人民共和国专利法进行审查，决定授予专利权，颁发本证书并在专利登记簿上予以登记。专利权自授权公告之日起生效。

本专利的专利权期限为二十年，自申请日起算。专利权人应当依照专利法及其实施细则规定缴纳年费。本专利的年费应当在每年06月24日前缴纳。未按照规定缴纳年费的，专利权自应当缴纳年费期满之日起终止。

专利证书记载专利权登记时的法律状况。专利权的转移、质押、无效、终止、恢复和专利权人的姓名或名称、国籍、地址变更等事项记载在专利登记簿上。



局长
申长雨

申长雨



证书号第2138164号



发明专利证书

发明名称：一种修饰芳纶纤维表面的方法

发明人：傅雅琴；陈剑锐；朱曜峰

专利号：ZL 2014 1 0369866.X

专利申请日：2014年07月30日

专利权人：浙江理工大学

授权公告日：2016年07月06日

本发明经过本局依照中华人民共和国专利法进行审查，决定授予专利权，颁发本证书并在专利登记簿上予以登记。专利权自授权公告之日起生效。

本专利的专利权期限为二十年，自申请日起算。专利权人应当依照专利法及其实施细则规定缴纳年费。本专利的年费应当在每年07月30日前缴纳。未按照规定缴纳年费的，专利权自应当缴纳年费期满之日起终止。

专利证书记载专利权登记时的法律状况。专利权的转移、质押、无效、终止、恢复和专利权人的姓名或名称、国籍、地址变更等事项记载在专利登记簿上。



局长
申长雨

申长雨



证书号第 3337903 号



实用新型专利证书

实用新型名称：一种用于短流程缫丝的丝条预干燥装置

发 明 人：傅雅琴；王靖；陈文兴；江文斌；吴惠敏

专 利 号：ZL 2013 2 0360073.2

专利申请日：2013 年 06 月 24 日

专 利 权 人：浙江理工大学

授权公告日：2013 年 12 月 25 日

本实用新型经过本局依照中华人民共和国专利法进行初步审查，决定授予专利权，颁发本证书并在专利登记簿上予以登记。专利权自授权公告之日起生效。

本专利的专利权期限为十年，自申请日起算。专利权人应当依照专利法及其实施细则规定缴纳年费。本专利的年费应当在每年 06 月 24 日前缴纳。未按照规定缴纳年费的，专利权自应当缴纳年费期满之日起终止。

专利书记载专利权登记时的法律状况。专利权的转移、质押、无效、终止、恢复和专利权人的姓名或名称、国籍、地址变更等事项记载在专利登记簿上。



局长

田力普

